The Eurasia Proceedings of Science, Technology, Engineering & Mathematics

EPSTEM

VOLUME 36 ICBAST CONFERENCE

ISSN: 2602-3199
ISBN: 978-625-6959-80-4

ICBAST 2025: 5th International Conference on Basic Sciences and Technology (ICBAST)
August 28- 31, 2025 Budapest, Hungary
Edited by: Prof.Dr. Mehmet Ozaslan - Gaziantep University, Türkiye

The Eurasia Proceedings of Science, Technology, Engineering & Mathematics (EPSTEM)
ISSN: 2602-3199

ICBAST 2025

International Conference on Basic Sciences and Technology (ICBAST)

Proceedings Book

Editor

Mehmet Ozaslan
Gaziantep University, Türkiye

ISBN: 978-625-6959-80-4

Published by the ISRES Publishing

Address: Askan Mah. Akinbey Sok. No: 5-A/Konya/TÜRKİYE

Web: www.isres.org

Contact: isrespublishing@gmail.com

Dates: August 28- 31, 2025

Location: Budapest, Hungary

https://2025.icbast.net

About Editor

Prof Dr. Mehmet Ozaslan
Department of Biology, Gaziantep University, Türkiye
Website: mehmetozaslan.com
E-mail: ozaslanmd@gantep.edu.tr

Language Editor

Lecturer Ceren Dogan
School of Foreign Languages, Necmettin Erbakan University, Türkiye
Email: cerendogan@erbakan.edu.tr

CONFERENCE PRESIDENT

Prof. Dr. Mehmet Ozaslan - Gaziantep University, Türkiye

SCIENTIFIC BOARD

Ágnes Csiszárik-Kocsir, Óbuda University, Hungary
Bálint Blaskovics, Corvinus University, Hungary
Besnik Hajdari - University "isa Boletini" Mitrovica, Kosovo
Bogdan Patrut - Alexandru Ioan Cuza Üniversitesi , Romania
Chalavadi Sulochana - Gulbarga University, India
Csaba Antonya - Transilvania University of Brasov, Romania
Dariusz Jacek Jakóbczak - Technical University of Koszalin, Poland
Dehini Rachıd -University of Bechar, Algeria
Eleonora Guseinoviene - Klaipeda University, Lithuania
Elena Krelja Kurelovic - Polytechnic of Rijeka, Croatia
Eva Trnova - Masaryk University, Czech Republic
Farhad Balash - Kharazmi University, Iran
Fundime Miri - University of Tirana, Albania
Gabriel Delgado-Toral - Universidad Nacional Autónoma de México, Mexico
Gordana Savıc - University of Belgrade, Serbia
Hasan Mlinaku, VUZF, Sofia in Bulgaria
Irina Andreeva - Peter The Great St. Petersburg Polytechnic University, Russia
Isti Hıdayah - Semarang State University, Indonesia
János Varga, Óbuda University, Hungary
Jose Manuel Lopez Guede - University of Basque Country, Spain
Kamil Yurtkan - Cyprus International University, Cyprus
Katsina Christopher Bala - Federal University of Technology, Minna, Nigeria
Khitam Shraim - Palestine Technical University, Palestine
Marija Stanıć - University of Kragujevac, Serbia
M. Hanefi Calp - Karadeniz Technical University, Turkey
Mohamed Ahmed - Mansoura University, Egypt
Mousa Attom- American University of Sharjah, U.A.E.
Nicu Bızon - Pitesti University, Romania
Oszkár Dobos - Obuda University, Hungary
Pandian Vasant - Teknology Petronas University, Romania
Rajnalkar Laxman - Gulbarga University, India
Richárd Horváth, Óbuda University, Hungary
Sanaa Al-Delaımy - Mosul University, Iraq
Shadi Aljawarneh - Jordan University of Science and Technology, Jordan
Shynar Baımaganbetova - Nazarbayev University, Kazakhstan
Svetlana Khan - Almaty University of Power Engineering and Telecommunications, Kazakhstan
Yiyang Chen - Soochow University (CN), China
Zipporah Pewat Duguryil - Federal College of Education, Nigeria
Zoltán Rajnai, Óbuda University, Hungary

ORGANIZING COMMITTEE

Ágnes Csiszárik-Kocsir, Óbuda University, Hungary
Aynur Aliyeva - Institute of Dendrology of Anas, Azerbaijan

Editorial Policies

ISRES Publishing follows the steps below in the procedings book publishing process.
In the first stage, the papers sent to the conferences organized by ISRES are subject to editorial oversight. In the second stage, the papers that pass the first step are reviewed by at least two international field experts in the conference committee in terms of suitability for the content and subject area. In the third stage, it is reviewed by at least one member of the organizing committee for the suitability of references. In the fourth step, the language editor reviews the language for clarity.

Review Process

Abstracts and full-text reports uploaded to the conference system undergo a review procedure. Abstracts will be evaluated on the basis of abstracts/proposals. The conference system allows the full text to be sent if the abstract is accepted. Participants must wait for the evaluation results after uploading their article abstracts to the conference system. If their abstracts are accepted, they can upload their full texts to the conference system. The full texts are then sent to at least two reviewers for review. The conference has a double-blind peer-review process. Any paper submitted for the conference is reviewed by at least two international reviewers with expertise in the relevant subject area. Based on the reviewers' comments, papers are accepted, rejected or accepted with revision. If the comments are not addressed well in the improved paper, then the paper is sent back to the authors to make further revisions. The accepted papers are formatted by the conference for publication in the proceedings.

Aims & Scope

Engineering, technology and basic sciences are closely related fields. Developments and innovations in one of them affect the others. Therefore, the focus of the conference is on studies related to these three fields. Studies in the fields of engineering, technology and basic science are accepted to the conference even if they are not associated with other fields. The conference committee thinks that a study in only one field (for example, mathematics, physics, etc.) will contribute to other fields (for example, engineering, technology, etc.) in future studies, even if it is not associated with the presentation at the conference. In line with this perspective, studies in the following fields are accepted to the conference: Biology, Chemistry, Engineering, Mathematics, Physics and Technology.

The aim of the conference is to bring together researchers and administrators from different countries, and to discuss theoretical and practical issues in all fields of Engineering, Technology and Basic Sciences.

The Eurasia Proceedings of Science, Technology, Engineering & Mathematics (EPSTEM)
ISSN: 2602-3199

Articles: 1- 31

CONTENTS

The Eurasia Proceedings of Science, Technology, Engineering & Mathematics (EPSTEM)
ISSN: 2602-3199

The Eurasia Proceedings of Science, Technology, Engineering & Mathematics (EPSTEM)
ISSN: 2602-3199

The Eurasia Proceedings of Science, Technology, Engineering and Mathematics (EPSTEM), 2025

Volume 36, Pages 1-10

ICBAST 2025: International Conference on Basic Sciences and Technology

Epichlorohydrin-Crosslinked Nano-TiO_2/Plum Kernel Shell/Chitosan Hydrogel Beads for the Efficient Removal of Hexavalent Chromium from Aqueous Solutions

Serife Parlayici
Konya Technical University

Erol Pehlivan
Konya Technical University

Abstract: The removal of hexavalent chromium [Cr (VI)] from industrial wastewater remains a significant environmental challenge due to its extreme toxicity and serious risks to both human health and the ecosystem. This study aims to develop and evaluate a sustainable and efficient adsorbent for Cr (VI) removal from aqueous solutions. To achieve this, composite hydrogel beads composed of nano-TiO_2, plum kernel shell, and chitosan were synthesized using a sol-gel method and crosslinked with epichlorohydrin ($nTiO_2$–PKS–Cts@ECH). The morphological and structural characteristics of the biosorbent were analyzed using scanning electron microscopy (SEM) and Fourier-transform infrared spectroscopy (FTIR). Important operational factors, such as pH, adsorbent dose, contact time, and starting Cr (VI) concentration, were optimized using batch adsorption experiments. The equilibrium data were evaluated using the Langmuir, Freundlich, and Dubinin–Radushkevich isotherm models, with the Langmuir model showing the best fit, indicating monolayer adsorption and a maximum capacity of 97.09 mg/g. Kinetic analysis demonstrated that the adsorption process followed a pseudo-second-order model, suggesting that chemisorption, electrostatic attraction, and reduction collectively constitute the rate-limiting steps. Overall, the findings highlight the high potential of $nTiO_2$–PKS–Cts@ECH as a promising and eco-friendly biosorbent for the effective removal of Cr (VI) from contaminated water systems.

Keywords: Nano-TiO_2, Chitosan, Plum kernel shell, Epichlorohydrin, Chromium (VI)

Introduction

The high toxicity, mobility, and carcinogenic characteristics of heavy metals, especially hexavalent chromium [Cr (VI)], make them a serious hazard to human health and water quality (Mahmoud et al., 2022, Billah et al., 2022). Cr (VI), which is frequently released from processes like electroplating, leather tanning, and textile production, can remain in aquatic environments and build up in living things, having detrimental effects on the environment and biology. The development of economical and environmentally friendly alternatives is still a top environmental concern because traditional treatment techniques, including as chemical reduction, membrane filtration, and ion exchange, can have high operating costs, generate sludge, or have poor removal efficiency (Mahmoud et al., 2024.

Because of its porous structure, large surface area, and profusion of reactive functional groups including hydroxyl, carboxyl, and phenolic groups, the plum kernel shell's structure is crucial to its effectiveness in eliminating Cr (VI) from aqueous solutions. Shell part of the plum seed consists mainly of carbon and oxygen represents the elemental composition characteristic of organic substances, since they are the main components of organic molecules (Usmonova and Salixanova, 2025). Strong adsorption interactions with Cr (VI) ions are made possible by these structural characteristics via surface complexation, ion exchange, and electrostatic

attraction. Its mechanical stability and chemical reactivity are also improved by the shell's lignocellulosic composition, which is mostly composed of cellulose, hemicellulose, and lignin. This allows for activation or modification to further increase the shell's adsorption capacity. For the treatment of water contaminated with toxic Cr (VI), this low-cost, renewable, and natural biomass provides an effective and environmentally friendly alternative.

Chitosan, a naturally occurring biopolymer formed from chitin, has drawn interest among other biosorbents due to its abundance of functional groups (such as -OH and -NH_2) that aid in metal ion binding, as well as its biodegradability and biocompatibility (Jiménez-Gómez & Cecilia, 2020). Chitosan, a naturally occurring biopolymer, is useful in many fields, including environmental protection and healthcare (Al-Obaidi, 2023 etal., 2023; Alsuhaibani et al., 2024, Ke et al., 2021). However, the actual use of native chitosan is limited by its mechanical constraints, which include low stability and solubility in acidic environments. Crosslinking with substances like epichlorohydrin and adding inorganic and bio-based fillers have been investigated as ways to improve the structural integrity and adsorption effectiveness of chitosan in order to get around these drawbacks. As a powerful crosslinking agent that improves the structural integrity and functional performance of composite materials, epichlorohydrin is essential to the creation of sophisticated hydrogel-based adsorbents. Epichlorohydrin crosslinks chitosan with nano-TiO_2 particles and plum kernel shell biomass to help create a stable three-dimensional polymeric network. Crosslinking chitosan with epichlorohydrin expands the spacing between chitosan chains, which enhances the rate of adsorption, even when the material is in a dry state (Rocher et al., 2010). The hydrogel beads' mechanical strength and chemical durability are increased by this crosslinking, which also helps to create a porous matrix with improved adsorption capacity and active site accessibility.

The combination of nanomaterials with biopolymers has created new avenues for the creation of high-performing hybrid adsorbents in recent years. In environmental applications, nano-TiO_2—which is well-known for its photocatalytic activity, thermal stability, and wide surface area—has shown beneficial benefits when paired with biopolymer matrices. Nano-TiO_2 with biomaterial can effectively degrade persistent organic pollutants that are resistant to biodegradation (Guo et al., 2025). The adsorption capabilities of the hybrid system are further improved by the availability and affordability of porous carbonaceous material from agricultural by-products like plum kernel shell (PKS), which has a high lignocellulosic content. A highly efficient adsorbent for the removal of Cr (VI) may be produced by combining these elements into a single, functionalized composite.

This study focuses on creating and testing new hydrogel beads made from a composite of titanium dioxide nanoparticles, plum kernel shells, and chitosan, which are crosslinked with epichlorohydrin. The purpose of these beads is to act as a versatile adsorbent for removing Cr (VI) from water. Researchers developed the composite beads to combine the unique properties of each ingredient. They then conducted experiments to see how factors like pH, contact time, initial Cr (VI) concentration, and the amount of adsorbent used affected how well the nano-composite beads removed the Cr (VI). The results suggest that these hybrid hydrogel beads are a promising, effective, and eco-friendly option for cleaning up water contaminated with Cr (VI).

Results and Discussion

Materials and Experimentation

The supplier of the chitosan (degree of deacetylation, DD=75–85%) was Sigma-Aldrich. The acetic acid (CH_3COOH, >99 % purity), HCl, NaOH and $K_2Cr_2O_7$ salt (purity: ≥99.9 %) were provided by the Merck Company. TiO_2 nano-particles were obtained from Sigma-Aldrich (St Louis, MO, USA). The epichlorohydrin (ECH) cross-linker was obtained from Merck (Darmstadt, Germany). All relevant chemicals used in the experiments were of analytical grade. Plum kernels were collected from an orchard near Konya, Türkiye, and their shells were used in the synthesis of adsorbents. In the preparation of the composite adsorbent, an IKAMAG-RO15 model mechanical stirrer, a GFL 3033 model thermostatic shaker, and a pH meter with glass electrodes (Orion 900S2) were used. A UV-visible spectrophotometer (Schmadzu UV-1700) was used for the determination of MB (λmax: 664 nm). The FT-IR spectrum was recorded on a Bruker VERTEX 70 FT-IR spectrometer. The microstructure of the adsorbent was examined using scanning electron microscopy (SEM, Nova Nano SEM 200, FEI Company).

Preparation of Raw Material

Plum kernels were separated from the fruit, the they were cleaned of dirt, washed, and dried. The dried kernels were first ground into powder using a mill and sieved to a particle size of 125 µm. The powdered kernel shells were then washed several times with 0.1 mol L^{-1} HCl, followed by several times with distilled water, and dried at room temperature for 24 hours. This prepared PKS powder was used in composite synthesis.

Synthesis of Adsorbent

The preparation process of $nTiO_2$–PKS–Cts@ECH is shown in Figure 1. A viscous gel was prepared by dissolving 3 g of chitosan in 300 mL of acetic acid (0.1 mol L^{-1}) solution. Then, 1.5 g of PKS and 1.5 g of $nTiO_2$ were added to the homogenate gel and stirred at room temperature for 12 h. The mixed solution was slowly dropped into a precipitation bath containing 200 mL of 5% NaOH and 300 mL of 6% ethyl alcohol to form small beads and left to stand for 24 h. The beads were filtered and washed several times with deionized water until the pH of the solution phase became neutral. The beads were cross-linked in 1% ECH solution at 50 °C for 6 h. After the reaction, the composite spheres were filtered and rinsed repeatedly with deionized water, then allowed to dry for 24 h and stored until use.

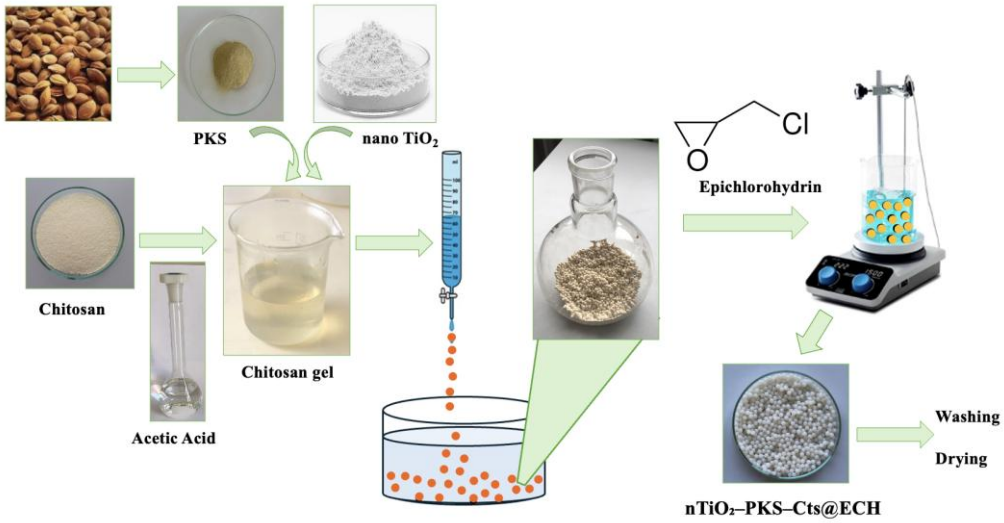

Figure 1. Schematic steps of $nTiO_2$–PKS–Cts@ECH beads synthesis

Batch Adsorption Experiments

To evaluate the adsorption efficiency of Cr (VI) removal from aqueous solutions using $nTiO_2$–PKS–Cts@ECH beads, batch adsorption experiments were conducted. First, a Cr (VI) stock solution was prepared by weighing 2.83 g of $K_2Cr_2O_7$ (≥99.0%) and dissolving it in distilled water to 1000 mg/L (Masuku et al., 2024). Subsequent dilutions with distilled water were performed to reach the desired initial Cr (VI) concentration for the adsorption tests. To determine the effect of various parameters on the adsorption efficiency and capacity of $nTiO_2$–PKS–Cts@ECH beads, experiments were systematically conducted using varying factors such as solution pH, initial concentration, adsorbent dosage, temperature, and contact time. For this purpose, pH (2, 3, 4, 5, 6, 7, 8, and 9), dye initial concentration (10, 25, 50, 75, 100, 150, 200, 250, 400, and 500 mg L^{-1}), adsorbent dosage (0.5, 1.0, 1.5, 2.0, 3.0, and 4 g L^{-1}), contact time (5, 15, 30, 45, 60, 90, 120, 180, 240, 300, and 360 min) and temperature (25, 35, 45, and 55 °C) parameters were optimized. The composite beads were mixed with Cr (VI) solutions of known concentrations under regulated conditions. Cr (VI) ions remain in the solution after the adsorption process were determined by UV-Vis spectrophotometry by analyzing the beads at regular intervals after filtration. Changes between the initial and final Cr (VI) concentrations were used to calculate the adsorption capacity (q_e, mg/g) and removal efficiency (%).

$$q_e = \frac{C_{0,Cr(VI)} - C_{e,Cr(VI)}}{m} V \quad (1)$$

$$Removal\ (\%) = \frac{C_{0,Cr(VI)} - C_{e,Cr(VI)}}{C_{0,Cr(VI)}} 100 \quad (2)$$

Structural and Morphological Characterization of the Nano-Composites

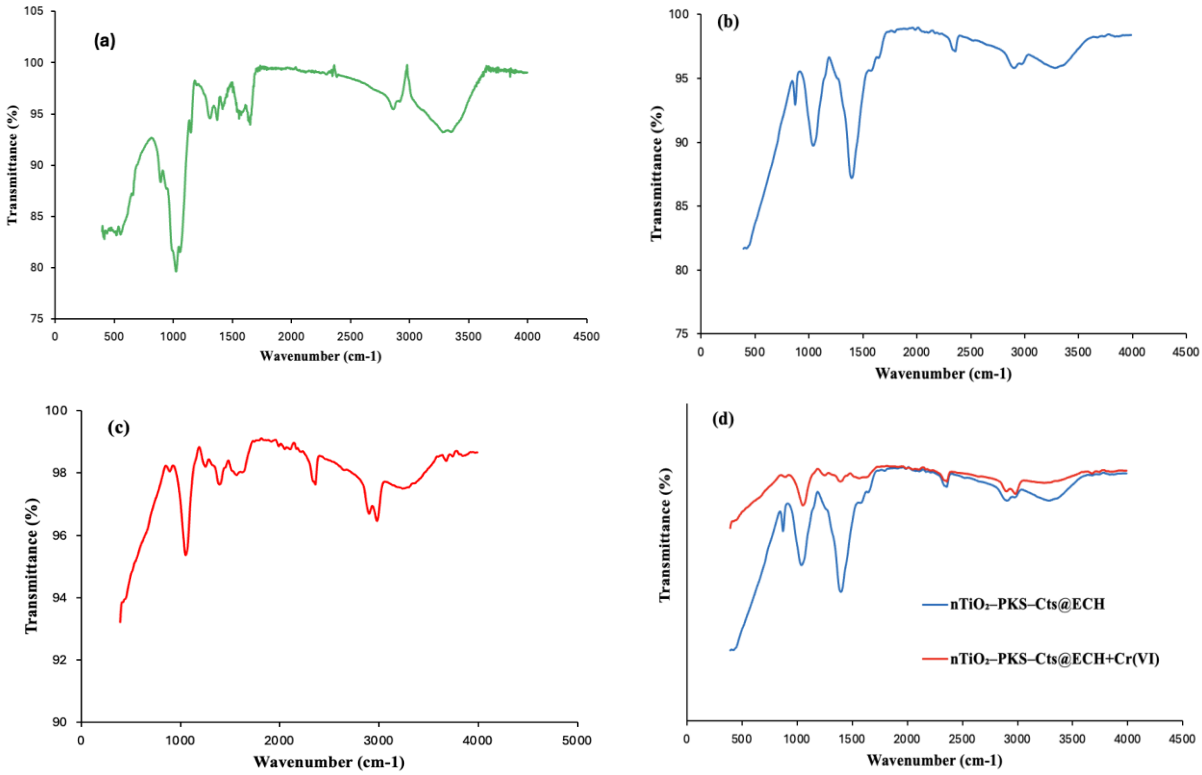

Figure 2. FT-IR diagram of chitosan (a), nTiO₂–PKS–Cts@ECH (b), nTiO₂–PKS–Cts@ECH+ Cr (VI) (c) and comparison of Cr (VI) adsorption before and after (d)

Figure 2(a-d) shows the FT-IR spectra of chitosan, nTiO₂–PKS–Cts@ECH, nTiO₂–PKS–Cts@ECH, and the composite before and after Cr (VI) adsorption. FT-IR analysis identifies key functional groups, providing insight into the molecular interactions within the nTiO₂–PKS–Cts@ECH structure and highlighting potential active sites responsible for Cr (VI) ion adsorption. N-H and O-H groups in chitosan are also observed around 3350 cm-1 (Khan et al. 2024). In addition, the absorption bands at 2919 and 2867 cm-1 can be attributed to C-H symmetric and asymmetric stretching, respectively (Teshome et al., 2024).

The amide II peak in chitosan is observed at 1560 cm-1 and 1375 cm-1, and characteristic peaks belonging to NHCOCH3 stretching are observed. The absorption band at 1026 cm-1 is due to the symmetric stretching of C-O-C bonds (Parlayıcı & Pehlivan, 2024). These bands are characteristics typical of polysaccharide and are found in other polysaccharide spectra, such as xylan, glucans and carrageenans. These features confirm that Cht is rich in amino groups, which play a crucial role in its adsorption capabilities. When the spectrum of nTiO₂–PKS–Cts@ECH was examined (Figure 2b), the peaks around 3371 and 3278 cm-1 belonged to hydroxyl and amino groups, respectively. Smaller peaks included the peak at 2865 cm-1 matching C-H bonds, the peak at 1646 cm-1 generally seen in type I amides, and the peak at 1582 cm-1 associated with type II amide groups. The peaks appearing at 1425 and 1375 cm-1 represented CH3N-acetylglucosamine and -CH2 groups, respectively. The peaks at 1068 and 1026 cm-1 indicated the presence of C-O bonds. The peak of the C-O vibration indicated the presence of hemicellulose in the biosorbent. Oxygen in TiO2 was observed at 1090–1200 cm-1 and the band at 500 cm-1 was due to Ti-O vibrations.

In the figure, the FT-IR spectrum of nTiO₂–PKS–Cts@ECH before adsorption was compared with the spectrum of nTiO₂–PKS–Cts@ECH after Cr (VI) adsorption. When the spectra before and after the adsorption of Cr (VI) were compared (Figure 2d), differences in the positions and peak intensities of the absorbance peaks were revealed. After the adsorption of Cr (VI), the asymmetric stretching vibration at 3371 cm-1 was significantly disrupted, suggesting that chemical interactions occurred between Cr (VI) ions and hydroxyl groups on the nTiO₂–PKS–Cts@ECH surface. The peak observed at 1375 cm-1 before adsorption shifted to 1396 cm-1 after Cr (VI) adsorption, and the peak intensity became smaller. Slight shifts and distortions in the C–O band (1068 to 1026 cm-1) and the amine (N–H) band (3278 cm-1) were observed. FT-IR post-adsorption spectra indicate that functional groups play a role in the adsorption processes.

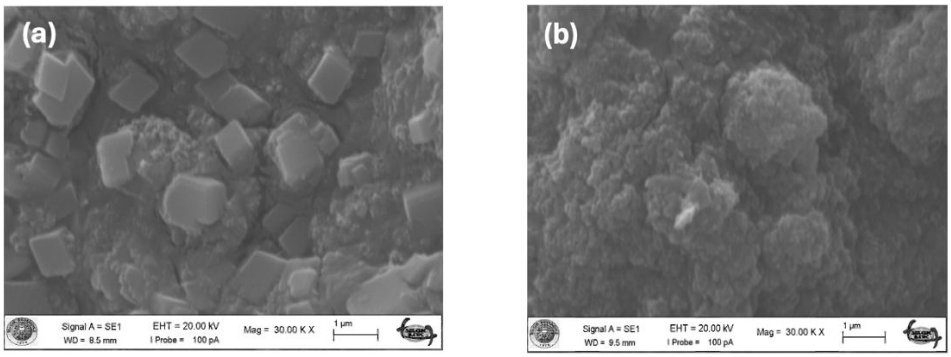

Figure 3. SEM image of (a) nTiO₂–PKS–Cts@ECH before MB adsorption (b) nTiO₂–PKS–Cts@ECH composite after MB adsorption

SEM was used to study the surface of the nTiO₂–PKS–Cts@ECH composite. The images in Figure 3a show the original, porous structure of the composite before it was used to treat Cr (VI). After the composite was used to adsorb Cr (VI) ions, the SEM images in Figure 3b clearly show that the surface became more homogenous and saturated. This visual change indicates that the pores and active sites on the adsorbent's surface have been successfully occupied by the Cr (VI) ions.

Results of the Batch Adsorption Experiments

Effect of nTiO₂–PKS–Cts@ECH Dosage

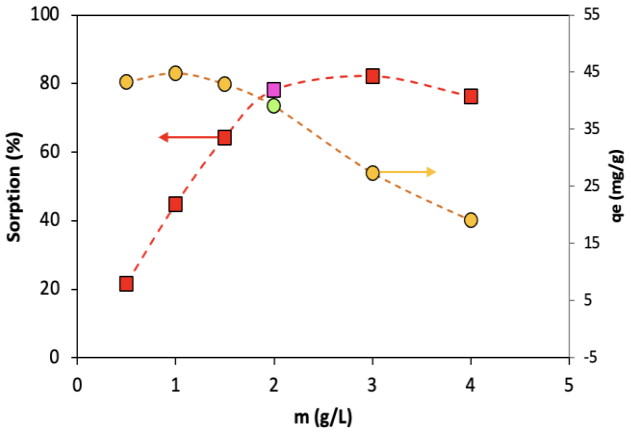

Figure 4. Effect of nTiO₂–PKS–Cts@ECH composite dosage

The amount of Cr (VI) retention was examined by adsorption experiments at different adsorbent doses (0.5, 1.0, 1.5, 2.0 , 3.0 and 4.0 g/L). In Figure 4, the adsorption capacities and sorption% values are plotted against the varying amount of adsorbent. Generally, as the adsorbent dose increases, the Cr (VI) retention capacity of the adsorbent first increases to a certain value and then decreases. At the same time sorption % increased up to this value again and after the dose was increased then it reached a stable value. In case the amount of nTiO₂–PKS–Cts@ECH increases from 0.5.0-2.0 g/L, the adsorption is increased quickly for the Cr (VI). After 2.0 g/L of nTiO₂–PKS–Cts@ECH dosages, it was observed that the adsorption remained stationary and small increment in the adsorption value was obtained. The capacity of adsorbent increased proportional to the adsorbent dose until 2.0 g/L.

Effect of pH

The effectiveness of the nTiO₂–PKS–Cts@ECH beads in removing Cr (VI) is largely dependent on the pH of the aqueous solution. Cr (VI) is mostly found as $HCrO_4^-$ and $Cr_2O_7^{2-}$ ions at lower pH values (Zewde et al., 2024; Nishad et al., 2025), especially in the acidic range (usually around pH 2–4). pH values at different values (2, 3, 4, 5, 6, 7, 8, 9) were tried in the solution phase for the adsorption of Cr (VI). From the figure, it is observed that the adsorption capacity decreases as the pH increases. These ions are more easily adsorbed onto

the protonated surface of the hydrogel beads because of increased electrostatic attraction. With its many amino groups, the chitosan component gets highly protonated in acidic environments, which raises the positive surface charge and enhances its ability to interact with negatively charged Cr (VI) species. Further aiding elimination, the TiO_2 nanoparticles might also help reduce Cr (VI) to some extent. On the other hand, the removal efficiency tends to drastically decline when the pH rises toward neutral or alkaline conditions.Functional groups on the adsorbent surface deprotonate, which lowers the electrostatic interaction between the adsorbent and anionic Cr (VI) species. At higher pH, these species also start to transition toward the CrO_4^{2-} form. Furthermore, chromate species and hydroxide ions may compete more for active sites at higher pH values, which would further inhibit adsorption. This highlights the significance of pH modification in real-world water treatment applications employing this composite material, as the ideal pH for Cr (VI) removal using these hydrogel beads usually lies in the acidic range.

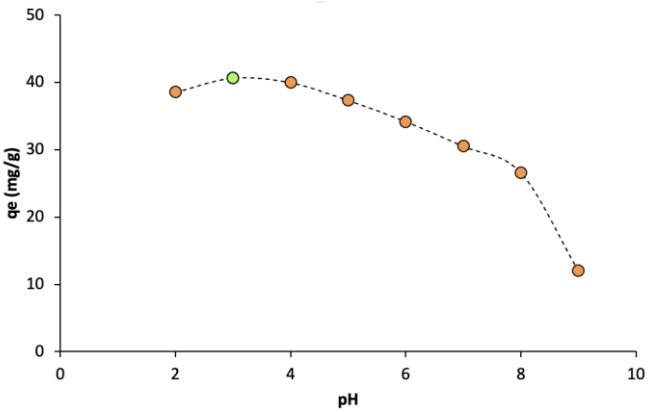

Figure 5. The effect of pH on Cr (VI) ions adsorption.

Effect of Cr (VI) Initial Concentration

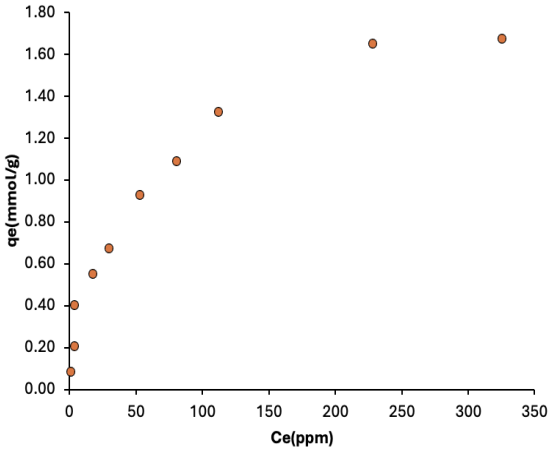

Figure 6. Effect of Cr (VI) ions concentration

An adsorption isotherm graph for removing Cr (VI) using nano-composite was given in the Figure 6. The graph, which plots the amount of Cr (VI) adsorbed (q_e) against its equilibrium concentration (Ce), shows a relationship typical of a monolayer adsorption process. The adsorption capacity was assessed by varying the Cr (VI) initial concentration (10, 25, 50, 75, 100, 150, 200, 250, 400 and 500 ppm). For $nTiO_2$–PKS–Cts@ECH, the adsorption was increased by enhancing the Cr (VI) concentration and could enhance the mass transfer between the liquid and solid phases to maximize the utilization of the active sites on the composite adsorbent. An increase in the Cr (VI) concentration enhanced the difference in adsorption capacity of the nano-composite. Initially, as the concentration of Cr (VI) increases, the amount adsorbed rises quickly. This steep increase indicates that the composite beads have a high affinity for Cr (VI) at low concentrations and that there are many available binding sites. Isotherm models are also important tools for understanding the mechanism of adsorption between the aqueous solution and the adsorbent. For this purpose, Langmuir, Freundlich, and D-R isotherm models were considered in the presented study. As the Cr (VI) concentration continues to increase, the rate of

adsorption slows down until the curve eventually flattens out. This plateau, or saturation point, signifies that most of the available active sites on the hydrogel beads are now occupied. At this point, the composite beads have reached its maximum adsorption capacity and can no longer effectively remove more Cr (VI) from the solution. This behavior is often characteristic of the Langmuir isotherm model, which suggests that the adsorption takes place on uniform sites on the adsorbent's surface (Chanajaree et al., 2021; Parlayıcı & Pehlivan, 2025). By applying the Langmuir model equation, the maximum Cr (VI) adsorption capacity of $nTiO_2$–PKS–Cts@ECH is 97.09 mg/g. Reduction, electrostatic interaction, and chemical adsorption together or some of them are active on the adsorption of the Cr (VI).

Table 1. Adsorption isotherm parameters for removal of Cr (VI) ions.

Model	Equation	Parameters for dye			
Langmuir	$\frac{C_e}{q_e} = \frac{C_e}{A_s} + \frac{1}{K_b A_s}$	**Q_m** 97.09	**K_b** 0.0255	**R^2** 0.985	**R_L** 0.282
Freundlich	$\ln q_e = \ln K_f + \frac{1}{n} \ln C_e$	**K_f** 6.001	**n** 1.99	**R^2** 0.924	
D-R	$\text{In } q_e = \ln q_m - \beta \varepsilon^2$	**X_m** 104.58	**K** 0.004	**E** 11.18	**R^2** 0.951

Effect of Contact Time and Kinetic Studies

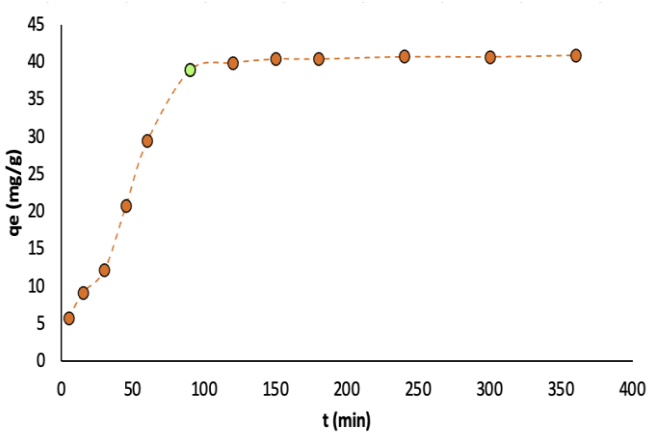

Figure 7. Effect of contact time on adsorption.

The effect of contact time on Cr (VI) adsorption was examined at different contact times (5, 15, 30, 45, 60, 90,120, 150, 180, 240, 300 and 360 min), 2.0 g/L adsorbent dosage, pH 3, 100 ppm Cr (VI) concentration, and 25 °C temperature to see how it affected the results. During the first 60 minutes, the adsorption process proceeds quickly, and the adsorption capacity increases significantly from about 6 mg/g to 29 mg/g. The time it took to attain equilibrium was influenced by the type of the adsorbent and the quantity of accessible active adsorption sites. The high number of easily accessible active sites on the composite beads' surface is what causes this quick early phase. After that, as the active sites are gradually occupied, the rate of adsorption starts to decrease. After around 90 minutes, the system starts to stabilize. The mass transfer resistance of the adsorbate from the bulk solution to the internal pores of the composite beads becomes the rate-limiting step as a result of this plateau, which shows that most of the accessible adsorption sites have been saturated.

Kinetic Models for Equlibrium

The adsorption kinetics curves for Cr (VI) removal by $nTiO_2$–PKS–Cts@ECH are shown in Figure 8. Table 2 presents the parameter results of both pseudo-first-order and pseudo-second-order kinetic models used to evaluate the adsorption data. The pseudo-second-order model provided a superior fit to the experimental results compared to the pseudo-first-order model. This is confirmed by the higher correlation coefficient (R^2) obtained for the pseudo-second-order model. Consequently, the adsorption process is more accurately explained by pseudo-second-order kinetics, indicating that chemisorption and electrostatic atraction is likely the dominant mechanism (Yuan & Lu, 2024).

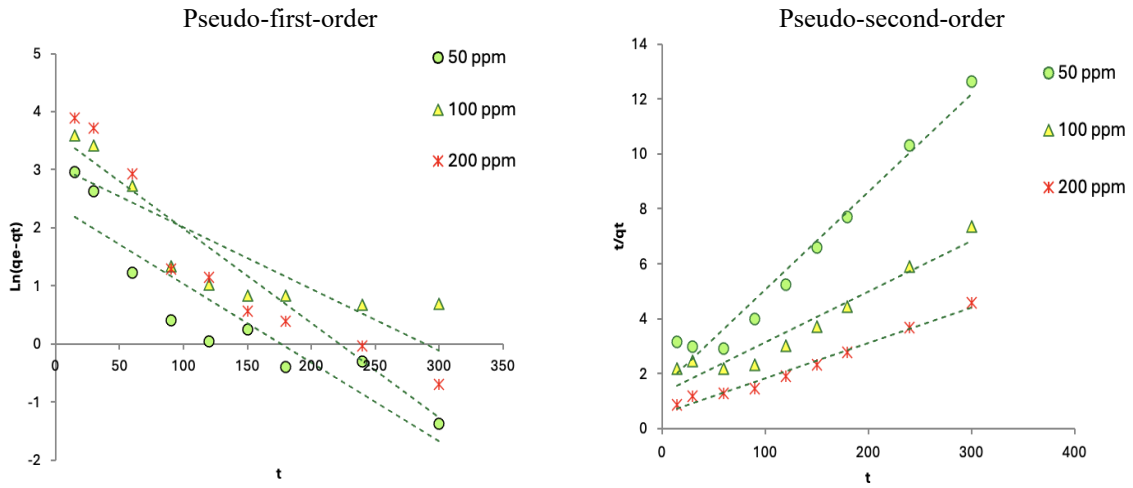

Figure 8. Kinetics for Cr (VI) ions adsorption onto nTiO₂–PKS–Cts@ECH composite.

Table 2. Comparison of the pseudo-first-order, pseudo-second-order adsorption rate constants and calculated and experimental q_e values obtained at different initial Cr (VI) concentrations.

		Pseudo-first-order			Pseudo-second-order		
C_o(ppm)	q_e exp	k_1	q_e	R^2	k_2	q_e	R^2
50	23.990	0.014	10.85	0.829	0.0009	28.01	0.968
100	42.775	0.011	21.69	0.709	0.0003	54.05	0.929
200	66.147	0.016	36.92	0.884	0.0003	77.52	0.981

Thermodynamic Studies

The effect of temperature on the adsorption of Cr (VI) onto nTiO₂–PKS–Cts@ECH was investigated (Figure 9), and the thermodynamic constants are given in Table 3. Negative ΔS° values reflect a decreased degree of disorder at the adsorbent-Cr (VI) interface in the solution phase during Cr (VI) adsorption onto the nTiO₂–PKS–Cts@ECH surface. A negative ΔH° value for Cr (VI) indicates that the adsorption of Cr (VI) onto nTiO₂–PKS–Cts@ECH is an exothermic process. Negative ΔG° values indicated that the adsorption of Cr (VI) onto nTiO₂–PKS–Cts@ECH is thermodynamically spontaneous and natural (Akiode et al., 2023). Additionally, the increase in ΔG° with increasing temperature indicates that the Cr (VI) adsorption process becomes more favorable at lower temperatures.

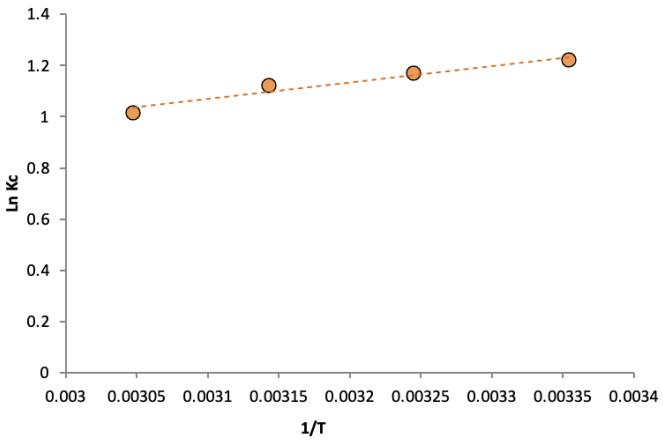

Figure 9. The impact of temperature on Cr (VI) adsorption.

Table 3. Thermodynamic parameters for adsorption of Cr (VI)

ΔS°	**ΔH°**	**ΔG° (J mol^{-1})**				
(J K^{-1}mol^{-1})	J mol^{-1}	T=298.15K	T=308.15K	T=318.15K	T=328.15K	R^2
-7.590	-5327.81	-3064.76	-2988.86	-2912.96	-2837.05	0.944

Conclusion

The $nTiO_2$–PKS–Cts@ECH nano-composite beads demonstrated considerable promise as a sustainable and highly efficient biosorbent for the removal of Cr (VI) from aqueous systems. Synthesized through the sol–gel method and stabilized via epichlorohydrin cross-linking, these nano-composite beads exhibited adsorption performance strongly influenced by operational factors such as solution pH, adsorbent dosage, contact duration, and the initial Cr (VI) concentration. Equilibrium analysis revealed that the Langmuir isotherm provided the best fit, consistent with a monolayer adsorption mechanism and yielding a maximum adsorption capacity of 97.09 mg/g. Kinetic modeling indicated a pseudo-second-order process, highlighting chemisorption, electrostatic interactions, and reduction as the governing mechanisms. Optimal removal occurred under acidic conditions, where protonated bead surfaces facilitated the uptake of dominant Cr (VI) species ($HCrO_4^-$ and $Cr_2O_7^{2-}$). Thermodynamic parameters confirmed that adsorption was spontaneous and exothermic, though less favorable at elevated temperatures. SEM imaging further illustrated that the porous structure of the hydrogel became saturated following Cr (VI) uptake. The results indicate that $nTiO_2$–PKS–Cts@ECH is a highly promising material for cleaning polluted water sources, specifically for removing Cr (VI).

Scientific Ethics Declaration

* The authors declare that the scientific ethical and legal responsibility of this article published in EPSTEM journal belongs to the authors.

Conflict of Interest

* The authors declare that they have no conflicts of interest

Funding

* This research received no specific grant from any funding agency in the public, commercial, or not-for-profit sectors.

Acknowledgements or Notes

* This article was presented as an oral presentation at the International Conference on Basic Sciences and Technology (www.icbast.net) held in Budapest/Hungary on August 28-31, 2025.

References

Akiode, O. K., Adetoro, A., Anene, A. I., Afolabi, S. O., & Alli, Y. A. (2023). Methodical study of chromium (VI) ion adsorption from aqueous solution using low-cost agro-waste material: Isotherm, kinetic, and thermodynamic studies. *Environmental Science and Pollution Research*, *30*(16), 48036-48047.

Al-Obaidi, N. S., Sadeq, Z. E., Mahmoud, Z. H., Abd, A. N., Al-Mahdawi, A. S., & Ali, F. K. (2023). Synthesis of chitosan-TiO2 nanocomposite for efficient Cr (VI) removal from contaminated wastewater sorption kinetics, thermodynamics and mechanism. *Journal of Oleo Science*, *72*(3), 337-346.

Alsuhaibani, A. M., Alayyafi, A. A., Albedair, L. A., El-Desouky, M. G., & El-Bindary, A. A. (2024). Efficient fabrication of a composite sponge for Cr (VI) removal via citric acid cross-linking of metal-organic framework and chitosan: adsorption isotherm, kinetic studies, and optimization using Box-Behnken design. *Materials Today Sustainability*, *26*, 100732.

Billah, R. E. K., Shekhawat, A., Mansouri, S., Majdoubi, H., Agunaou, M., Soufiane, A., & Jugade, R. (2022). Adsorptive removal of Cr (VI) by chitosan-SiO2-TiO2 nanocomposite. *Environmental Nanotechnology, Monitoring & Management*, *18*, 100695.

Chanajaree, R., Sriuttha, M., Lee, V. S., & Wittayanarakul, K. (2021). Thermodynamics and kinetics of cationic/anionic dyes adsorption on cross-linked chitosan. *Journal of Molecular Liquids*, *322*, 114507.

Guo, J., Zhou, T., Guo, H., Ge, C., & Lu, J. (2025). Application of nano-TiO2@ adsorbent composites in the treatment of dye wastewater: A review. *Journal of Engineered Fibers and Fabrics*, *20*, 15589250251329450.

Jiménez-Gómez, C. P., & Cecilia, J. A. (2020). Chitosan: A natural biopolymer with a wide and varied range of applications. *Molecules*, *25*(17), 3981.

Ke, C. L., Deng, F. S., Chuang, C. Y., & Lin, C. H. (2021). Antimicrobial actions and applications of chitosan. *Polymers*, *13*(6), 904.

Khan, M. K., Abdulhameed, A. S., Alshahrani, H., & Algburi, S. (2024). Chitosan/functionalized fruit stones as a highly efficient adsorbent biomaterial for adsorption of brilliant green dye: Comprehensive characterization and statistical optimization. *International Journal of Biological Macromolecules*, *263*, 130465.

Mahmoud, M. E., Elsayed, S. M., Mahmoud, S. E. M., Aljedaani, R. O., & Salam, M. A. (2022). Recent advances in adsorptive removal and catalytic reduction of hexavalent chromium by metal–organic frameworks composites. *Journal of Molecular Liquids*, *347*, 118274.

Mahmoud, M. E., El-Said, G. F., Ibrahim, G. A., & Elnashar, A. A. (2024). Effective removal of hexavalent chromium from water by sustainable nano-scaled waste avocado seeds: Adsorption isotherm, thermodynamics, kinetics, and error function. *Biomass Conversion and Biorefinery*, *14*(13), 14725-14743.

Masuku, M., Nure, J. F., Atagana, H. I., Hlongwa, N., & Nkambule, T. T. (2024). Pinecone biochar for the Adsorption of chromium (VI) from wastewater: Kinetics, thermodynamics, and adsorbent regeneration. *Environmental Research*, *258*, 119423.

Nishad, V., Kumar, S., & Sastry, S. V. A. R. (2025). Kinetics, isotherms and thermodynamics studies of Cr (VI) removal using zero-valent iron nanoparticles synthesized from Aegle marmelos (Bael) plant extract. *Nanotechnology for Environmental Engineering*, *10*(3), 66.

Parlayıcı, S., & Pehlivan, E. (2024). Methylene blue removal using nano-TiO2/MWCNT/Chitosan hydrogel composite beads in aqueous medium. *Chemosphere*, *365*, 143244.

Parlayıcı, S., & Pehlivan, E. (2025). Highly efficient hexavalent chromium removal using nano-Fe3O4/pomegranate peel biochar/Alginate composite as an advanced biosorbent. *Turkish Journal of Analytical Chemistry*, *7*(1), 22-32.

Rocher, V., Bee, A., Siaugue, J. M., & Cabuil, V. (2010). Dye removal from aqueous solution by magnetic alginate beads crosslinked with epichlorohydrin. *Journal of Hazardous Materials*, *178*(1-3), 434-439.

Teshome, S., Kassahun, S. K., & Tiruneh, S. N. (2024). Response surface statistical modeling for optimization of methylene blue adsorption from aqueous solution using chitosan/graphite composites: Isotherm and kinetics studies. *Separation Science and Technology*, *59*(2), 205-223.

Usmonova, Z., & Salixanova, D. (2025). Plum fruit peel as a raw material for obtaining activated carbon adsorbents. In *AIP Conference Proceedings* (Vol. 3304, No. 1, p. 040029). AIP Publishing LLC.

Yuan, J., & Lu, W. (2024). Adsorption of Cr (VI) from aqueous solutions using inorganic clays modified magnetic chitosan adsorbent: Kinetic and thermodynamic study. *Desalination and Water Treatment*, *319*, 100442.

Zewde, Z., Asere, T. G., & Yitbarek, M. (2024). Porous biochars derived from brewery waste for the treatment of Cr (VI)-contaminated water. *PLoS One*, *19*(11), e0314522.

Author(s) Information

Serife Parlayici
Konya Technical University, Faculty of Engineering and Natural Sciences, Department of Chemical Engineering, Rauf Orbay Street. 42250, Selçuklu/Konya, Türkiye

Erol Pehlivan
Konya Technical University, Faculty of Engineering and Natural Sciences Department of Chemical Engineering Rauf Orbay Street. 42250, Selçuklu/Konya, Türkiye
Contact e-mail: *erolpehlivan@gmail.com*

To cite this article:

Parlayici, S. & Pehlivan E. (2025). Epichlorohydrin-crosslinked nano-TiO_2/plum kernel shell/chitosan hydrogel beads for the efficient removal of hexavalent chromium from aqueous solutions *The Eurasia Proceedings of Science, Technology, Engineering and Mathematics (EPSTEM), 36,* 1-10.

The Eurasia Proceedings of Science, Technology, Engineering & Mathematics (EPSTEM)
ISSN: 2602-3199

The Eurasia Proceedings of Science, Technology, Engineering and Mathematics (EPSTEM), 2025

Volume 45, Pages 11-20

ICBAST 2025: International Conference on Basic Sciences and Technology

Influence of Calcium on the Thermal Oxidation of Ca-Doped CoO and of CaO-Coated Cobalt

Nacer Halem
Mouloud Mammeri University of Tizi-Ouzou

Zohra Halem
University Mohand Oulhadj

Ouardia Halem
Mouloud Mammeri University of Tizi-Ouzou

Mariora Abrudeanu
University of Pitesti

Georgette Petot-Ervas
SPMS Laboratory

Abstract: The present study concerns the influence of calcium on the thermal oxidation of Ca-doped $Co_{1-x}O$ and of CaO-coated cobalt. We have found that calcium enhanced the thermal oxidation of $Co_{1-x}O$ single crystals while a CaO coating leads to a decrease of the oxidation kinetic of cobalt polycrystals, at T<1200°C. From a formal treatment, based on the thermodynamic of irreversible processes, we have shown that the increase of the thermal oxidation of Ca-doped $Co_{1-x}O$ is due to the increase of the diffusion coefficient of cobalt in Ca-doped samples, while the beneficial effect of a CaO coating on the cobalt oxidation is due to the shift of the $Co/Co_{1-x}O$ phase boundary to higher P_{O_2}, leading to a decrease of the driving force of diffusion in the oxide scale.

Key words: Oxygen chemical potential gradient, Diffusion driving force, Diffusion, Kinetic demixing

Introduction

Although it is recognized that at high temperature transport of reactants plays a crucial role in metal oxidation processes (Kofstad, 1988; Wagner, 1951; Wagner, 1975), metal corrosion studies are generally performed from observations performed at room temperature (Kofstad, 1988). These analyses are influenced by reactions occurring during cooling, such as the formation of precipitates, for instance. It is then understandable that important mechanisms still remain unexplained.

The purpose of this work was to investigate the influence of sputter-coatings CaO on to Co polycrystalline surfaces, prior to oxidation. This allows to eliminate calcium effects on metal diffusion processes and to understand the difference observed with the oxidation of Ca-doped $Co_{1-x}O$ single crystals, in their stability range. The results have been analyzed taking into account the thermodynamic and transport properties of pure and Ca-doped $Co_{1-x}O$ single crystals, at equilibrium and under non equilibrium conditions, and a formal treatment based on the thermodynamic of irreversible processes (Petot-Ervas, 1990).

Theoretical Background

- Selection and peer-review under responsibility of the Organizing Committee of the Conference

General Equations

Oxidation of $Co_{1-x}O$ is governed by cation exchanges with cationic vacancies α times negatively ionized (V^{α}'), whose concentrations depend on both, temperature (T) and oxygen partial pressure (P_{O2}) in thermodynamic equilibrium with the sample [5,6]. By application of the mass action law to the equation of formation of the prevailing defects in undoped $Co_{1-x}O$ ($½O_2 <=> O_O + V^{\alpha}' + \alpha h^{\circ}$) and according to the charge neutrality condition, one can show that (Kofstad ,1972; Philibert , 1991; Atkinson ,1985):

$$[h^{\circ}] = \alpha[V_{Co}^{\alpha'}] = AK_V^{1/(\alpha+1)} (P_{O2})^{1/2(\alpha+1)} \quad (1)$$

where K_V is the equilibrium constant of formation of defects, P_{O2} the oxygen partial pressure in the surrounding atmosphere, O_O an oxygen ion on its normal site, h° an electron hole, $A = \alpha^{1/(\alpha+1)}$ and square brackets denote concentrations in mole fraction.

The thermodynamic and transport properties of undoped and Ca-doped $Co_{1-x}O$ single crystals were determined from electrical conductivity measurements (Halem, 2022):

$$\sigma = e\,\mu\,p = \sigma_o (P_{O2})^{1/2(\alpha+1)} \exp(-\Delta H_{\sigma})/RT) \quad (2)$$

where e is the electrical charge of electrons, p the hole concentration per cm^3, μ the hole mobility, regarded generally as a thermally activated hopping process ($\mu = \mu_o \exp -\Delta H_{\mu}/RT$), ΔH_{σ} the enthalpy of conductivity, with $\Delta H_{\sigma} = (\Delta H_{\mu} + \Delta H_V)/(1+\alpha)$, ΔH_V the enthalpy of formation of the defects, ΔH_{μ} the hole enthalpy of mobility and α the mean electrical charge of the cobalt cationic vacancies, which can be determined from the slopes (Eqs.1,2) , (Atkinson ,1985; Halem , 2022).

$$(d\ln\sigma / d\ln P_{O2})_T = 1/2(\alpha+1) \quad (3)$$

One can recall that the thermodynamic properties of undoped and Ca-doped $Co_{1-x}O$ single crystals show that calcium has a reducing behaviour in $Co_{1-x}O$, leading to both, the formation of singly ionized cobalt cations (Co^{+}) and the shift of the Co/CoO and CoO/Co_3O_4 phase boundaries to higher and lower $P_{O2,}$ respectively (Halem, 2022). This reduction behavior, of elastic nature, is due to local strains when larger homovalent solute cations are present in oxides (Atkinson, 2012). The thermodynamic properties of Ca-doped samples are then governed by the formation of extrinsic defects ($Ca_{Co}^{x} <=> Ca_{Co}^{\bullet} + e'$), which influence the concentration of intrinsic defects (Eq.1) through the electroneutrality condition:

$$\alpha[V_{Co}^{\alpha'}] + [e'] = [h^{\circ}] + [Ca_{Co}^{\bullet}] \quad (4)$$

Transport Processes Under Non-Equilibrium Conditions

Statement of the Problem

Under non equilibrium conditions, fluxes of cations (J_i) and cationic vacancies (J_V) appear in p-type semi conducting oxides, coupled through the condition (Petot-Ervas, 1990; Kofstad ,1972; Schmalzried, 1986)

$$J_V + \Sigma J_i = 0 \quad (5)$$

Taking into account that no electrical current flows through the film ($I_t = FJ_h = 0$) and assuming a virtual local equilibrium between electrically charged species and neutral atoms ($A + \alpha h^{\circ} <=> A^{\alpha+}$) (Wagner, 1951; Wagner, 1975) has shown that in a p-type semi-semiconducting oxide the cationic fluxes in the "z" direction, with respect to the oxygen sublattice (or laboratory reference frame) can be written:

$$J_i = -\frac{C_i}{RT} D_i \frac{d\eta_i^{\alpha+}}{dz} = -\frac{C_i}{RT} D_i \left(\frac{d\mu_i^{\alpha+}}{dz} + z_i F \frac{d\Phi}{dz}\right) = -\frac{C_i}{RT} D_i \frac{d\mu_i}{dz} \quad (6)$$

where $d\mu_i/dz = RT d\ln a_i$ is the chemical potential gradient of the neutral species, $d\eta_i\alpha+/dz$ the electrochemical potential gradient of the charged species, F the Faraday constant, Φ the Nernst potential, $C_i = x_i C_M$ the cation concentration per unit volume (mol/cm^3), D_i the diffusion coefficient of cations i, z_i their valence and C_M the concentration of cationic sites in the lattice.

To express Eq.6 in a form including measurable parameters, it was assumed (Petot-Ervas, 1990) that in the solid solution (AO-BOγ) the concentration of BOγ ($x_{BO\gamma} = m$) is low enough ($x_{AO} << m$) that the Raoult law may be applied ($a_{AO} \approx x_{AO} = 1-m$). Therefore, taking into account the local equilibrium between the different species in each element of volume ($1/2O_2 + A <=> AO$, $\gamma/2O_2 + B <=> BO_\gamma$), it follows (Petot-Ervas, 1990):

$$J_A = -\frac{C_A}{RT} D_A \frac{d\mu_A}{dz} = C_M D_A \left[\frac{dm}{dz} + (1-m)\, d\ln a_O/dz\right] = C_M D_A \left[\frac{dm}{dz} + (1-m)\, \mathcal{F}\right] \quad (7)$$

$$J_B = -\frac{C_B}{RT} D_B \frac{d\mu_B}{dz} = -C_M D_B \left[\frac{dm}{dz} - m\gamma\, d\ln a_O/dz\right] = -C_M D_B \left[\frac{dm}{dz} - m\gamma\, \mathcal{F}\right] \quad (8)$$

where $\mathcal{F}$ is the external driving force of diffusion depending of the oxygen potential gradient ($d\ln a_O/dz$) across the oxide ($a_O = P_{O_2}^{1/2}$), which can be related to the cationic vacancy concentration gradient ($V^{\alpha\prime}$) (Eq.1) :

$$\mathcal{F} = d\ln a_O/dz = \tfrac{1}{2}\, d\ln P_{O_2}^{1/2} = (1+\alpha)\, d\ln[V^{\alpha\prime}]/dz \quad (9)$$

The previous equations (Eqs 7,8) show that the cationic fluxes are influenced by the kinetic demixing of cations (dm/dz) which occur in multi component oxides However, when the concentration of solute cations is very low (xCo>>xCa), the flux of solute cations can be neglected and the shift velocity of the oxidation front (Eqs.11,12) can be written:

$$v_{oxid} = J_V / C_M = -(J_A^{2+} + J_B^{\delta+})/C_M \approx -J_A^{2+}/C_M \quad (10)$$

Substituting Eq.7 in Eq.10, assuming that kinetic demixing processes (dm/dz) can be neglected, one obtains for the oxidation rate of a p-type semiconducting oxide (AO,BOγ) in presence of a driving force ($\mathcal{F}$):

$$v_{oxid} = -D_A \left[\frac{dm}{dz} + (1-m)\, \mathcal{F}_{(\text{Ca-doped CoO})}\right] \approx -D_A\, \mathcal{F}_{(\text{Ca-doped CoO})} \quad (11)$$

while for a pure oxide: $v_{oxid} = -J_A^{2+}/C_M = -D_A\, \mathcal{F}_{(CoO)}$ (12)

where $m = x_{Ca}$ and $(1-m) = x_{Co}$ are the mole fractions of calcium and cobalt cations in the cationic sublattice, respectively.

Kinetic Demixing in Ca-doped $Co_{1-x}O$ Single Crystals

From a practical point of view, experiments were performed in presence of an applied electric field. The experimental arrangement is described previously ((Monceau ,1994**)**. The driving force is then due to the cationic vacancy concentration gradient (Eq.9), which depends of the electric field, E (Monceau ,1994**)**:

$$\mathcal{F} = q_i E/kT. \quad (14)$$

where $q_i=z_ie$ is the charge of the diffusing species and k the Boltzman constant.

This driving force (Eq.14) leads to a flux of cations "i" toward the direction of the cathode, coupled to a flux of cationic vacancies in the opposite direction (Fig.1). During the transport processes the conservation of sites implies that (Eq.5):

$$J_V= -\Sigma J_i \quad (15)$$

New lattice sites are then formed at the surface where cations arrive and the shift velocity of displacement of this surface (v_i), with respect to the laboratory reference state (Schmalzried, 1986), (Monceau ,1994**),** (Mahiouz ,2018), is given by:

$$v_i=\Sigma J_i/C_i \quad (16)$$

Consequently, a concentration gradient (dx_i/dz) sets up progressively in an oxide (A,B,O) if the diffusion coefficients of cations A^{2+} and $B^{\alpha+}$ are different (Eqs.7,8).

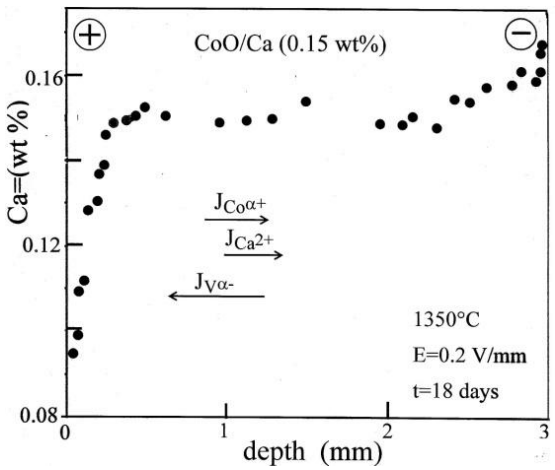

Figure 1. Kinetic demixing profile of a Ca^{2+} - doped $Co_{1-x}O$ single crystal, maintained in air under 0.2V, for 18 days at 1350°C.

In Fig.1, we have reported the kinetic demixing results in a Ca (0.15 wt%)-doped $Co_{1-x}O$ single crystal maintained under an applied electrical field (E) of 0.2 V/mm in flowing air, at 1350°C for 18 days. Starting from a homogeneous parallelepipedic single-crystal of 3mm long, EPMA analysis show an enrichment of calcium near the cathode. Therefore, it follows (Eqs.7,8) that:

$$D_{Ca}>D_{Co} \quad (17)$$

It should be noted that this result is in discrepancy with the results reported in literature for undoped $Co_{1-x}O$ single crystals (Fig.2), in equilibrium with the surrounding atmosphere (Dieckman ,1984), (Chen , 1980).

$$D^*_{Ca} < D^*_{Co} \quad (18)$$

This difference was explained by correlation effects (Eq.19), whose primary cause is due to the Ca^{2+}: size (Ca^{2+}: r=0.1nm, Co^{2+}: r=0.074nm, Co^{3+}/0.063nm]. Calcium influences the binding enthalpy (Δh_A) and the jump frequency (w) of a vacancy and a neighbouring cation close to a Ca^{2+} (Chen ,1980) :

$$(D^*_{Ca} / D^*_{Co}) = (w_{Ca}/w_{Co})\,(f_{Ca}/f_{Co})\exp(-\Delta h_A/kT) \quad (19)$$

where f_{Co} is the cobalt correlation factor in undoped $Co_{1-x}O$ (f_{Co}=0.78) and f_{Ca} a complicated function of all the jump frequencies in the vicinity of calcium cations in a Ca- doped $Co_{1-x}O$ samples (Philibert , 1991)

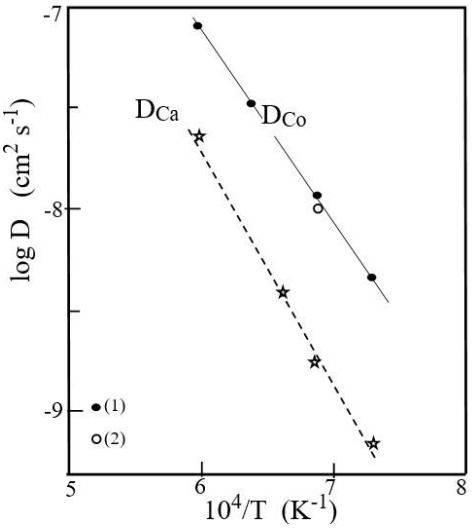

Figure 2. Arrhenius plot of the self-diffusion coefficient of cobalt (Dieckman ,1984), (Chen , 1980). and of the diffusion coefficient of Ca^{2+} [16] in undoped $Co_{1-x}O$ single crystal, at P_{O2}=0.21 atm.

Experimental Results

Oxidation in the Stability Range Of Undoped and Ca-doped $Co_{1-x}O$ Single Crystals

Oxidation Results

The experiments have been performed by measuring the electrical conductivity of a single crystal as a function of time, following a sudden change in external P_{O2} (Farhi ,1978), at constant temperature. Just after the change of P_{O2}, the point defect concentrations near the gas/oxide interface (Eqs1,4) correspond to the new imposed equilibrium conditions. Therefore, a defect concentration gradient sets up near the surface, leading to defect fluxes in the oxide. They develop in the bulk and decrease then, to disappear after a time ″t″, when the new equilibrium conditions are reached. The effective diffusion coefficient of the defects, being due to a vacancy concentration gradient (dx_V/dz), is called chemical diffusion coefficient ($\widetilde{D}$). According to the Fick law, the coupled fluxes of cations (J_i) and cationic vacancies (J_V) can be written (Kofstad ,1972; Philibert , 1991; Halem , 2022),

$$J_V=-\Sigma J_i =-\widetilde{D}\ (dx_V/dz) \qquad (20)$$

The chemical diffusion coefficient ($\widetilde{D}$) allows to determine the mean penetration depth (Δz) of the oxidation (or reduction) front in the oxide, after a time t, and to evaluate the time to reach the new thermodynamical equilibrium conditions of the sample (Kofstad ,1972; Farhi ,1978)

$$\Delta z=\sqrt{\widetilde{D}t} \qquad (21)$$

As an example, we have reported in Fig.3 the electrical conductivity results after 5000 s, at 1000°C. They were obtained with a brick–shape sample (5x2x2mm) of undoped and Ca-doped $Co_{1-x}O$ single crystals after an abrupt change of P_{O2}, between 10^{-3}atm (argon) and 0.21atm (air). These results show that calcium increases the oxidation kinetics from the beginning of the oxidation. One can recall that the first terms of the general equation of these representations are rapidly negligible when the time increases and the simplified relation is given by the following expression (Farhi ,1978) :

$$\left(\frac{\sigma(t)-\sigma_\infty}{\sigma_0-\sigma_\infty}=\left(\frac{8}{\pi^2}\right)^3 \exp\left[-\pi^2\left(\frac{1}{H^2}+\frac{1}{L^2}+\frac{1}{l^2}\right)\widetilde{D}t\right]\right). \qquad (22)$$

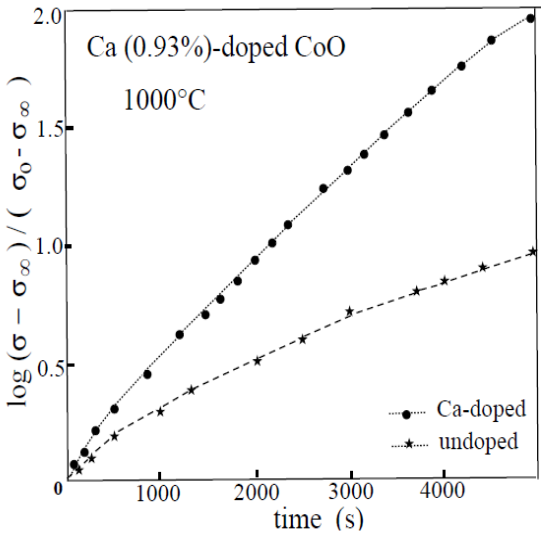

Figure 3. Re-equilibration kinetics of pure and Ca-doped $Co_{1-x}O$ single crystal after an abrupt change of P_{O2} (argon ⇨ air), followed by electrical conductivity measurements as a function of time, at 1000°C.

The chemical diffusion was then determined from the linear plots of log $(\sigma(t)-\sigma_\infty)/\sigma_0-\sigma_\infty)$ as a function of time. The Arrhenius plots of the values of $\tilde{D}$ obtained with undoped and Ca-doped $Co_{1-x}O$ single crystals are reported in Fig.4. In agreement with the results reported in Fig.3, they show that calcium leads to an increase of the chemical diffusion, i.e. of the oxidation kinetic of $Co_{1-x}O$ in it stability range (Halem, 2022). The kinetic demixing processes being negligible ($x_{AO}<<x_{BO\gamma}$), the chemical diffusion coefficient of undoped and of diluted solid solution (AO-BOγ) can be expressed by the relation (Kofstad ,1972; Philibert , 1991; Halem , 2022):

$$\tilde{D} = (1+\alpha)\, D_V \qquad (23)$$

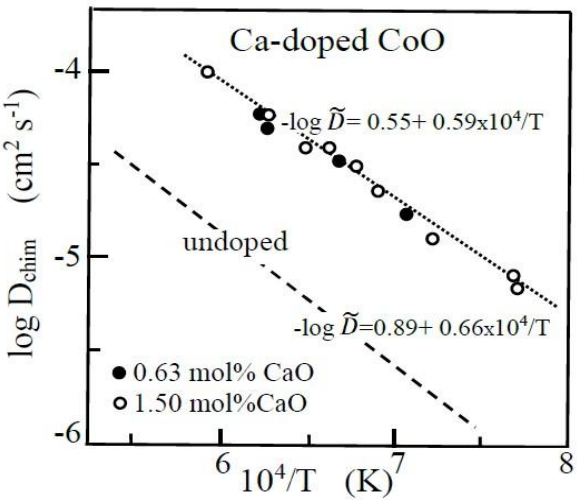

Figure 4. Arrhenius plots of the chemical diffusion coefficient of undoped and Ca-doped $Co_{1-x}O$ single crystals.

According to the close values of the mean charge (α) of the cationic vacancies in doped and undoped single crystals, for $P_{O2}>10^{-3}$atm [8], the greater chemical diffusion coefficient values determined for the doped samples (Fig.4) is due to an increase of the diffusion coefficient of the cationic vacancies:

$$D_V\text{ (Ca-doped CoO)} > D_V\text{ (undoped CoO)} \qquad (24)$$

Therefore, taking into account that the diffusion coefficient of the cationic vacancies depends of the diffusion coefficient of cations

$$x_V D_V = x_{Co} D_{Co} + x_{Ca} D_{Ca} \approx D_{Co} \quad (25)$$

and that the concentration of electron holes and cationic vacancies are not significantly influenced by calcium in the doped samples, for $P_{O2}>10^{-3}$atm (Halem , 2022), it follows that:

$$D_{Co}(\text{Ca-doped CoO}) > D_{Co}(\text{undoped CoO}) \quad . \quad (26)$$

Consequently, for $P_{O2}>10^{-3}$ atm, the higher oxidation rate of Ca-doped $Co_{1-x}O$ single crystals (Figs 3,4) is mainly due to an increase of the cobalt diffusion coefficient (D_{Co}) in these samples.

Thermal Oxidation of Uncoated and CaO-coated Cobalt Polycristals

Oxidation Results

Metal specimens were square cobalt coupons (0.4cm^2 by 01cm thick), sintered from high purity Johnson Mattey cobalt powders. As described previously (Mahiouz ,2018), (Aïdrous ,2014), the coupons were first oxidized at 1250°C. The oxide scale was removed on one main surface (0.4cm^2), which was then polished to a 1μm diamond finish. The coating deposition on this face was achieved by sputtering a CaO target in an ambient of $7x10^{-2}$ mbar argon, during one hour and under the deposition energy of a few eV, causing no sample heating during deposition. Deposited films were uniform in thickness (≤50nm), without crack and spall.

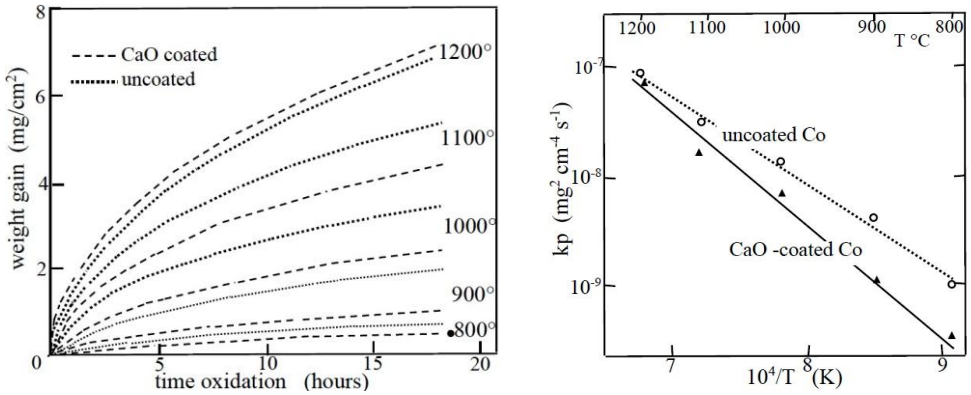

Figure 6.a. Weight gain versus time of uncoated and CaO coated cobalt polycrystals, under P_{O2}=0.21 atm.

Oxidation experiments were performed in a Setaram thermobalance (Mahiouz ,2018), (Aïdrous ,2014), (Halem, 2016) by following the weight-gain as a function of time, from 800° to 1200°C (Fig.6a). At temperatures lower than 1200°C, these results show that CaO coatings reduce the oxidation rates. Furthermore, in agreement with the Wagner theory (Kofstad, 1988), these results follow parabolic law (Fig.6b), and the weight gain per unit area (Δ m/s) can be expressed by the following relation:

$$(\Delta \text{ m/s}) = k_p \sqrt{t} + k_o \quad (27)$$

where kp is a parabolic rate constant.

3.3.2 Composition of scales

T

The calcium profile through the oxidation layers developed on CaO-coated cobalt was determined on fracture sections, by EPMA analyses. At 900°C, the profile presents a maximum in a localized zone, which coincides approximately with the position of the initial cobalt surface. From either side of this maximum, the amount of calcium is low and increases in the outer layer, in agreement with the kinetic demixing of calcium in Ca-doped $Co_{1-x}O$ single crystals (Fig.1). When the temperature increases, the calcium becomes progressively more diluted in the thicker layers. At 1100°C, its shows only a small increase close to the metal/oxide interface, due to equilibrium segregation.

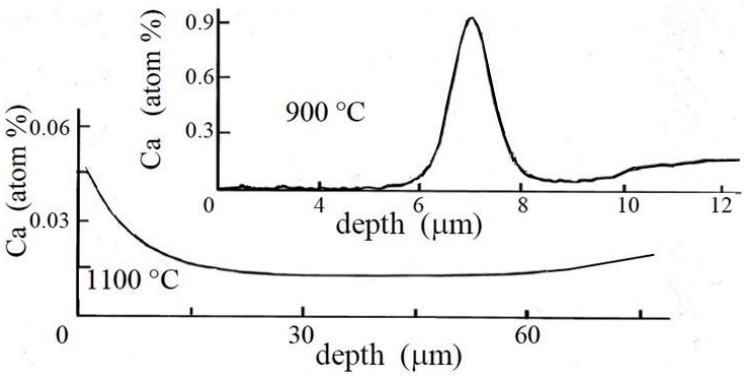

Figure 7. Calcium concentration–depth profiles in oxide films, after 18h of oxidation at 900°C and 1100°C. Metal/oxide interface taken as initial position of analysis.

Discussion

The results reported previously show that CaO coatings reduce the oxidation kinetics of cobalt at T<1200°C (Fig 6). They have been analyzed taking into account the thermodynamic and transport properties of undoped and Ca-doped $Co_{1-x}O$ single crystals [8].

Taking into account that the calcium concentration is low in oxidation layers developed on CaO-coated cobalt (Fig.7), their rate of growth can be described by Eqs.11,12:

CaO-coated cobalt polycrystals: $v_{oxid} \approx - D_{Co}\, \mathcal{F}_{(Ca\text{-doped CoO})}$ (28)

uncoated cobalt polycrystals: $v_{oxid} = - D_{Co}\, \mathcal{F}_{(CoO)}$ (29)

with $\mathcal{F} = d\ln a_O/dz = d\log (P_{O2})^{1/2}/dz$ (30)

These relations predict that the rate of oxidation of coated and uncoated cobalt polycrystals depends of the diffusion coefficient of cobalt (D_{Co}) and of the driving force of diffusion ($\mathcal{F}$).

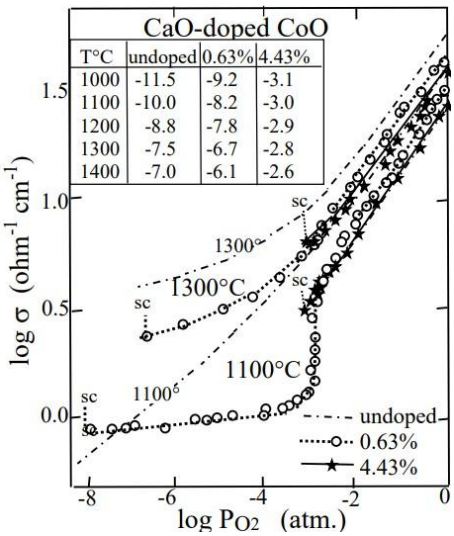

Figure 8. Influence of the calcium concentration on the electrical conductivity of undoped and Ca-doped $Co_{1-x}O$, at 1100° and 1300°C (Halem,2022) The dissociation pressure of undoped and Ca-doped $Co_{1-x}O$ single crystals is reported in the Table between 1000° and 1400°C. It is also indicated (sc) on the □ plots

Concerning the driving force of diffusion (Eq.30), it depends of the oxygen potential gradient across the oxidation scale. The shift of the $Co/Co_{1-x}O$ phase boundary to higher P_{O2} [8] in Ca-doped $Co_{1-x}O$ single crystals (Fig.8), all the more important that the calcium amount in the oxide is high, leads to a decrease of the oxygen potential

gradient ($dlna_O/dz$) across the oxidation layer. It follows a decrease of F and of the oxidation kinetics of the CaO-coated $Co_{1-x}O$ polycrystals, as it was observed experimentally, at T<1200°C(Fig.6).

When the temperature increases, the calcium concentration in the oxidation layer (Fig.7) decreases. The transport processes are then controlled progressively by the same parameters of the uncoated samples and, at T=1200 °C, the experimental results (Fig.6) show that the oxidation rates of uncoated and CaO-coated cobalt polycrystals are practically the same.

Conclusion

This set of results was analyzed taking into account the thermodynamic and transport properties of undoped and Ca-doped $Co_{1-x}O$ single crystals and a formal treatment, based on the thermodynamic of irreversible process. From the general expressions obtained, it was shown that the rate of oxidation is mainly controlled by a competitive effect of D_{Co} and F.

Concerning the oxidation of undoped and Ca-doped CoO single crystals, the results being obtained in the same oxygen partial pressure range (same driving force of diffusion), they are only influenced by the diffusion of cations. In agreement with the increase of D_{Co} in Ca-doped $Co_{1-x}O$ single crystals (Eq.26), they show that calcium leads to an increase of the oxidation kinetic in the stability range of the oxide.

Concerning the CaO-coated cobalt polycrystals, the shift of the $Co/Co_{1-x}O$ phase boundary to higher P_{O2} (Fig.8) in Ca-doped $Co_{1-x}O$ single crystals to higher P_{O2}, all the more important that the calcium amount in the oxide is high, leads an decrease of the driving force of diffusion (F) and of the oxidation kinetics of the CaO-coated polycrystal (Fig.6). When the temperature increases, the calcium concentration in the oxidation layer decreases with the thickening of the layer. The oxidation kinetics are then progressively controlled by the same parameters than uncoated samples and, at T=1200°C, the experimental results show that the oxidation rates of uncoated and CaO-coated Co samples are practically the same.

Scientific Ethics Declaration

* The authors declare that the scientific ethical and legal responsibility of this article published in EPSTEM journal belongs to the authors.

Conflict of Interest

* The authors declare that they have no conflicts of interest

Funding

* This research received no specific grant from any funding agency in the public, commercial, or not-for-profit sectors.

Acknowledgements or Notes

* This article was presented as a poster presentation at the International Conference on Basic Sciences and Technology (www.icbast.net) held in Budapest/Hungary on August 28-31, 2025.

* The authors thank N.Halem (LEC2M, Tizi Ouzou), G.Baldinozzi and C.Petot (Centraesupelec, laboratoire SPMS) for useful discussions.

References

Aïdrous, H., Cieniek, L., Halem, N., Kusinski, J., Petot, C., & Petot-Ervas, G. (2014). Thermodynamic and transport properties of Ca-doped nickel oxide and relevance to the oxidation of CaO-coated nickel. *Solid State Ionics, 261*, 117-124.

Atkinson, A. (1985). Transport processes during the growth of oxide films at elevated temperature. *Reviews of Modern Physics, 57*(2), 437-470.

Boussetta, H. (1992). *Thèse de doctorat*. Université de Tunis.

Chen, W. J., & Peterson, N. L. (1980). Isotope effect for cation diffusion in CoO. *Journal of Physics and Chemistry of Solids, 41*, 647-652.

Dieckmann, R. (1984). Point defects and transport properties of binary and ternary oxides. *Solid State Ionics, 12*, 1-22.

Farhi, R., & Petot-Ervas, G. (1978). Electrical conductivity and chemical diffusion measurements in nickel oxide at high temperature. *Journal of Physics and Chemistry of Solids, 39*, 1169-1173.

Halem, Z., Kusinski, J., Halem, N., Baldinozzi, G., & Petot-Ervas, G. (2022). Influence of CaO on the thermodynamic and transport properties of cobaltous oxide. *Solid State Ionics, 382*, 115946.

Halem, Z., Halem, N., Abrudeanu, M., Chekroude, S., Petot, C., & Petot-Ervas, G. (2016). Transport properties of Al- or Cr–doped nickel oxide relevant to the thermal oxidation of dilute Ni–Al and Ni–Cr alloys. *Solid State Ionics, 297*, 13-19.

Kofstad, P. (1972). *Nonstoichiometry, diffusion and electrical conductivity in binary metal oxides*. Wiley-Interscience.

Kofstad, P. (1988). *High temperature corrosion*. Elsevier Applied Science.

Mahiouz, N., Halem, Z., Halem, N., & Petot-Ervas, G. (2018). Transport properties of Ce-doped nickel oxide and relevance on the thermal growth of oxide scales on CeO_2-coated nickel. *Solid State Ionics*, 14943.

Monceau, D., Filal, M., Tebtoub, M., Petot, C., & Petot-Ervas, G. (1994). Kinetic demixing of ceramics in an electric field. *Solid State Ionics, 73*, 221-225.

Monceau, D., Petot, C., & Petot-Ervas, G. (1991). Kinetic demixing profile calculations under a chemical potential gradient. *Solid State Ionics, 45*, 231-235.

Petot-Ervas, G., & Petot, C. (1990). The influence of impurities segregation phenomena on the oxido-reduction of oxides. *Journal of Physics and Chemistry of Solids, 51*(8), 901-906.

Philibert, J. (1991). *Atom movements: Diffusion and mass transport in solids*. Les Éditions de Physique.

Schmalzried, H. (1986). Behavior of semi-conducting oxides in oxygen potential gradients. In *Reactivity of Solids*. 117–137.

Wagner, C. (1951). *Atom movements*. American Society for Metals.

Wagner, C. (1975). Equations for transport in oxides of transition metal oxides. *Progress in Solid State Chemistry, 10*, 3–16.

Zahn, D., Heitjans, P., & Maier, J. (2012). From composites to solid solutions: Modeling of ionic conductivity in the CaF_2–BaF_2 system. *Chemistry – A European Journal, 18*, 6225-6229.

Author(s) Information

Nacer Halem
Laboratory LEC2M, Mouloud Mammeri University of Tizi-Ouzou, Tizi Ouzou, Algeria
Contact e-mail: *nacer.halem@ummto.dz*

Zohra Halem
University Mohand Oulhadj, Bouira, Algeria.

Ouardia Halem
LEC2M Laboratory, Mouloud Mammeri University of Tizi-Ouzou, Tizi Ouzou, Algeria

Mariora Abrudeanu
LSIM I134, University of Pitesti, 110040 Pitesti, Romania

Georgette Petot-Ervas
SPMS Laboratory, Paris, France

To cite this article:

Halem, N., Halem, Z., Halem, O., Abrudeanu, M., & Petor-Ervas, G. (2025). Influence of calcium on the thermal oxidation of Ca-doped CoO and of CaO-coated cobalt. *The Eurasia Proceedings of Science, Technology, Engineering and Mathematics (EPSTEM), 36,* 11-20

The Eurasia Proceedings of Science, Technology, Engineering & Mathematics (EPSTEM)
ISSN: 2602-3199

The Eurasia Proceedings of Science, Technology, Engineering and Mathematics (EPSTEM), 2025

Volume 36, Pages 21-27

ICBAST 2025: International Conference on Basic Sciences and Technology

Reinforcement Analysis of a Water Tank Wall by External Prestressing

Hocine Hammoum
Mouloud Mammeri University of Tizi-Ouzou

Karima Bouzelha
Mouloud Mammeri University of Tizi-Ouzou

Amar Aliche
Mouloud Mammeri University of Tizi-Ouzou

Abstract: Water storage structures age and deteriorate over time, which can make them vulnerable. There are many reinforcement methods available to rehabilitate them. Our research focuses on a system for reinforcing the wall of a concrete tank, subjected to hydrostatic pressure, by additional external prestressing. The role of the latter will be to relieve the wall of hydrostatic or even hydrodynamic tensile stresses, and allow it to return to an acceptable service state. This technique of adding external prestressing cables was initially introduced in the reinforcement and rehabilitation of civil engineering structures, mainly from the 1970s. In this study, a deterministic analysis is developed for the dimensioning of the external prestressing necessary to absorb part of the hydrostatic pressure exerted on the wall, taking into account the different instantaneous and deferred stress losses. Additionally, the hydrodynamic effect is evaluated by the Westergaard method, to analyze the stress state induced by the fluid-structure interaction with respect to the seismic action. In a second step, a reliability analysis is developed by considering three random variables, including the compressive strength of the concrete, the seismic intensity and the eccentricity of external prestressing cables. This reliability analysis is conducted using a computer code developed with Matlab© software based on the Monte Carlo simulations method to assess the probability of failure in tension of the circular wall for different seismic intensities. The developed approach was applied, for a practical example, whose dimensions are realistic. Fragility curves are developed representing the failure probability in the different levels of seismic acceleration.

Keywords: Tanks, External prestressing, Reliability, Seismic acceleration, Failure probability

Introduction

External prestressing is a construction technique that has been used for several years and is in fact a special case of post-tensioning. The use of external prestressing in bridge construction is experiencing spectacular growth after having been used to reinforce old structures. It consists of placing the prestressing cables in sheaths that are no longer embedded but external to the concrete in the running part. These sheaths are only placed in the concrete at the ends of the element and installed in "deflection bosses". This device is widespread in practice on civil engineering structures; this prestressing makes it possible to significantly increase the rigidity of a reinforced concrete structure. It is natural in arches, vaults, and circular structures as is the case for a circular water reservoir.

This study involves the rehabilitation of a drinking water reservoir in service, circular in shape and with a capacity of 5000 m^3. It has a serious defect, which makes this structure in its current state unacceptable from a health point of view; they do not offer sufficient health protection to the stored water. During a survey carried out on the tank to identify the origin of the leaks, it was found that the cylindrical tank had cracked, visible from

- Selection and peer-review under responsibility of the Organizing Committee of the Conference

the outside, at the tank-radiator interface, and more precisely above the gusset plate. The rehabilitation project will include additional prestressing.

The Tension at the Origin

This tension represents the actual stress transmitted to the prestressing steel by the jack, obtained by a combination of measuring the hydraulic pressure in the jack and measuring the elongation of the cable during tensioning. Most jacks are calibrated by manufacturers based on load cells and are generally accurate to within a few percent. The prestressed concrete regulation (BPEL) recommends, for the evaluation of the maximum tension at tensioning also called tension at origin, and noted σ_{p0} the following relationship:

$$\sigma_{p0} = \min(0.8f_{prg}; 0.9f_{peg})$$

Where, f_{prg} and f_{peg} are respectively the guaranteed breaking stress, and the conventional elastic limit.

Combinations of Actions

The combinations that define the actions to be taken into account for the justification of prestressed concrete structures intended to retain liquids are taken from Fascicule 74, as follows:
Ultimate Limit States (ULS), under fundamental combinations:

$$C1: P_t + 1.5Q$$
$$C2: P_t + 1.3Q$$

Ultimate limit states (ULS), under accidental combinations:

$$C3: P_t + Q + F_a$$

Serviceability Limit States (SLS), Rare to Frequent Combinations:

$$C4: P_t + Q$$

Where, P_t, Q and F_a designate respectively the prestressing force, the live load which is represented by the hydrostatic loads and the accidental action which is represented by the hydrodynamic loads.

Allowable Constraints

The allowable compressive stress of the concrete, calculated in homogeneous section with the prestressing force P_t, is given by:

$$\sigma_{bc} = 0.6f_{c28}$$

The allowable tensile stress of the concrete, calculated in homogeneous section is given by:
Under the effect of rare combinations, inside the embedding section: $\sigma_{bt} = f_{t28}$
Under the effect of rare combinations, outside the embedding section: $\sigma_{bt} = 1.10f_{t28}$
Under the effect of frequent combinations, inside the embedding section: $\sigma_{bt} = 0$
Under the effect of frequent combinations, outside the embedding section: $\sigma_{bt} = 1.5f_{t28}$
Allowable tensile and compressive stresses for fc28=45 MPa are given in Table 4.5

Table 1. Allowable tensile and compressive stresses.

	Tensile stress [MPa]		Compressive stress [MPa]	
	Rare	Frequent	Rare	Frequent
outside the embedding section	-3.63	-4,95	27,00	
inside the embedding section	-3,30	0,00		

For external prestressing, the allowable stresses for outside the embedding section must be considered.

Deterministic Analysis

The structure that is the subject of this study is a circular reinforced concrete tank, with a capacity of 5000 m^3, placed on the ground, to which is applied external prestressing. The geometric characteristics of this structure are summarized in the table.

Table 2. Geometric characteristics of the tank.

Parameters	Values	Unit
Theoretical capacity of tank V	5000	m^3
Internal Diameter	24.00	m
Water height	11.00	m
Real volume Vr	4 976.28	m^3
Deflection f	2.50	m
Radius of curvature R	30.05	m

The hydrodynamic calculation of the tank is performed by the Westergaard method, considering the characteristic values of seismic acceleration and compressive strength of concrete. The tensile stresses at the level of the internal fibers (full reservoir) and the compressive stresses at the level of the external fibers (empty reservoir) are evaluated for different combinations of action. The calculation results showed that these stresses are lower than the allowable stresses, which allows us to conclude that the tank is not at risk of failure. The prestressing forces at different levels of the tank wall, and at different abscissas, along the cables, are considered after all prestress losses (instantaneous and delayed).

We note, however, that the significant values of the tensile constraints are obtained for the C3 combination, taking into account the seismic action and this at the level of the bottom sections of the wall. The latter are graphically presented under the C3 combination in the first two sections of the bottom of the wall, as a function of the cable length X.

The significant values of the compressive stresses are obtained for the C1, C2, C3 combinations, at the level of the external fibers when the tank is empty. The latter are graphically presented under the C1, C2, C3 combinations in the first two sections of the bottom of the wall, as a function of the cable length X. We find that the compressive and tensile stresses at different levels of the tank wall, and at different abscissas, along the cables, are lower than the allowable compressive and tensile stresses.

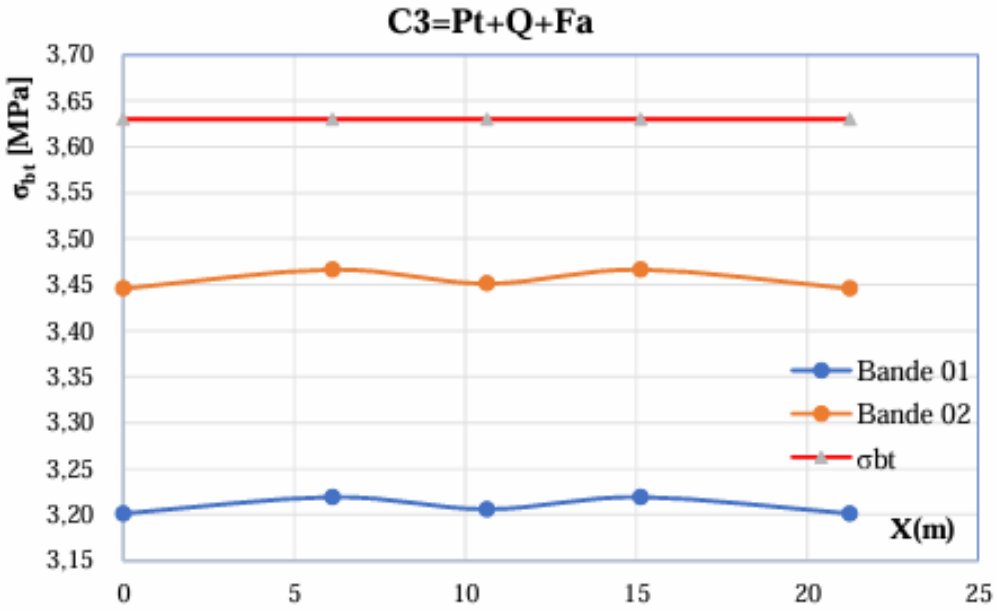

Figure 1. Tensile stresses in the internal fiber of the first two sections of the circular wall, under C3 combination (Tank full).

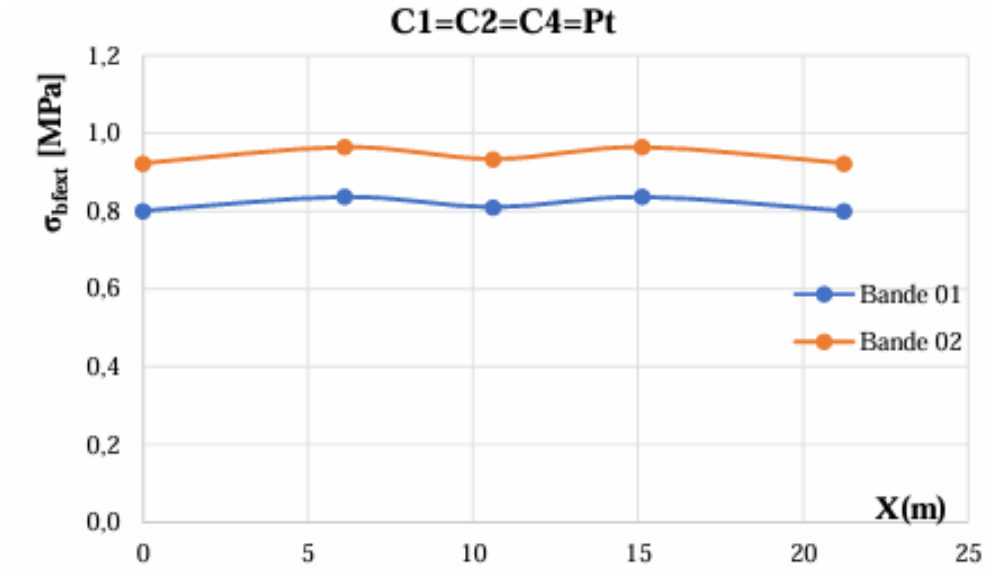

Figure 2. Compressive stresses in the external fiber of the first two sections of the circular wall, under C1, C2, C3 combinations (Tank empty).

Reliability Analysis

In the structural reliability approach, influencing parameters are considered as random variables. Reliability theory is based on a probabilistic approach to structural safety based on the Monte Carlo method, which recognizes a limit state criterion and the variability of the parameters involved in this criterion (Aoues, 2018). The structure is ultimately considered safe if the probability of failure is less than a reference value called the allowable failure probability. This study, which aims to conduct a reliability analysis of an externally prestressed concrete tank, is conducted in this context. The random variables considered are the seismic zone acceleration coefficient (A), the compressive strength of the concrete (fc), and the eccentricity (e) of the prestressing cables. The normal distribution is fitted for both parameters (A) and (fc), and the uniform distribution is fitted for the eccentricity (e). The limit state criterion used is tensile stress.

The Probabilistic Approach

The probabilistic approach is the method that relies on reliability theory to assess the probability of failure or the reliability index of the structure. The operating mode of the structure is, as with the semi-probabilistic approach, described by a limit state, but the uncertainties related to the input parameters are introduced in the form of a probability law assigned to each variable. These probability laws are established from statistical studies on the parameters concerned. The probabilistic approach consists of calculating the probability of exceeding the limit state criterion, called the probability of failure P_f, which is compared to an allowable probability of failure P_f^{adm} (Ballière et al, 2012).

$$P_f = P(G \leq 0) \leq P_f^{adm}$$

To quantify the risk of failure of a concrete tank due to loss of stability, it is necessary to define the different limit state functions G(X) which define its behavior. These functions delimit the domain of proper functioning as well as that of failure of the structure. A limit state function G(X) can be written in the following form depending of the structural resistance R(X) and the applied loading S(X) (Lemaire, 2005):

$$G(X) = R(X) - S(X)$$

The limit state function considered in this study corresponds to the failure mode of the tank due to loss of tensile strength of its wall at the serviceability limit state (SLS). It is given as follows:

$$G(X) = \sigma_{bt}^{adm} - \sigma_{max}$$

σ_{bt}^{adm} is the allowable tensile stress of the concrete given by Fascicle 74 (See Table 1).

σ_{max} being the maximum applying tensile stress.

The probability of failure is calculated by considering, in a first time, two random variables (A and f_c). The probability of failure at the tensile limit state as a function of the different seismic zones and coefficients of variation is illustrated Figure 3.

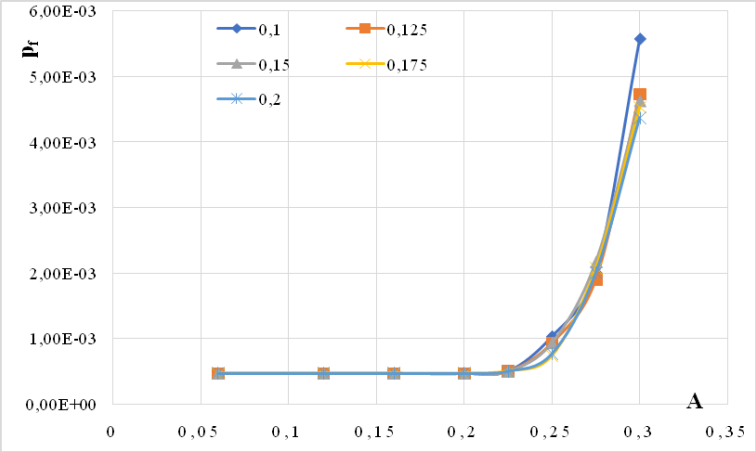

Figure 3. Probability of failure as a function of the different seismic zones and coefficients of variation

The prestressed concrete tank is of consequence class 2 (CC2), because the losses in terms of human life, economic, social and environmental will be considerable in the case of the structure failing. This leads us to take as admissible values of the reliability index β; 4.7 for an equal reference duration of one year and 3.8 for a reference duration of 50 years, which correspond to admissible failure probability values of 10^{-3} and 10^{-6} respectively, in accordance with Eurocode 2 (table 3).

Table 3. Relationship between β and P_f.

Category	Values						
β	1.28	2.33	3.09	3.72	4.26	4.75	5.20
P_f	10^{-1}	10^{-2}	10^{-3}	10^{-4}	10^{-5}	10^{-6}	10^{-7}

Table 4 illustrates the allowable values of β according to the consequence class.

Table 4. Minimum values of β according to the consequence class.

Reliability class	Reference period (1 year)	Reference period (50 years)
RC2	4.7	3.8

The analysis of the results shows that in the low and medium seismicity zone (IIa), the probability of failure is lower than the allowable probability ($P_f^{adm} = 10^{-3}$) regardless of the coefficient of variation; it is concluded that the tank is stable. On the other hand, the probability of failure P_f is higher than this allowable value in the high and the very high seismicity zone. The tank is therefore not suitable for these two zones.

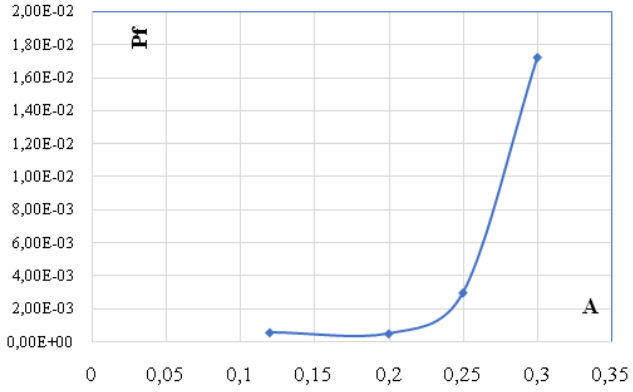

Figure 4. Probability of failure as a function of the different seismic zones and coefficients of variation

In a second step, the probability of failure is calculated by considering as random variable the eccentricity (e) and the compressive strength of the concrete (fc) for the different seismic zones. The results are illustrated in Figure 2.

Conclusion

This study focused on the deterministic analysis of the cylindrical wall of a tank placed on the ground in externally prestressed concrete, under hydrostatic and hydrodynamic stress. The Westergaard method was used to approach the hydrodynamic stress. It was possible to highlight that certain input parameters such as the eccentricity (e), the compressive strength (fc) and the zone acceleration coefficient (A) had a considerable influence on the variation of the tensile stresses, particularly in the internal fiber when the tank is full, as well as on the compression stresses in the external fiber when the tank is empty. The reliability approach based on the Monte Carlo method, which takes into account uncertainties, concludes that the analyzed structure is stable in low and medium seismicity zones (IIa). Conversely, in high seismicity zones (IIb) and in very high seismicity zones (III), the structure presents a probability of failure (Pf) beyond the admissible values recommended by Eurocode 2 which stipulates that $10^{-6} \leq P_f \leq 10^{-3}$, this demonstrates that this kind of rehabilitation is not suitable for these seismic zones. The uncertainty in eccentricity is by far the most influential and dominant in reliability calculation, which leads us to recommend careful implementation of external prestressing cable trays.

Scientific Ethics Declaration

*The authors declares that the scientific ethical and legal responsibility of this article published in EPSTEM journal belongs to the authors.

Conflict of Interest

*The authors declare that they have no conflicts of interest

Funding

*The authors wish to thank the Algerian Ministry of higher education and scientific research for funding the University education research project (PRFU – N° A01L02UN150120220004).

Acknowledgements or Notes

*This article was presented as an oral presentation at the International Conference on Basic Sciences and Technology (www.icbast.net) held in Budapest/Hungary on August 28-31, 2025.

*The information on data of concrete compressive strength has been kindly provided by Eurl ECE of Tizi Ouzou (Algeria).

References

Aoues, Y. (2008). *Optimisation fiabiliste de la conception et de la maintenance des structures* (PhD thesis). Blaise Pascal University of Clermont, France.

Ballière A. et al., (2012). *Théorie de la fiabilité, application à l'évaluation structurale des ouvrages d'art*. Rapport d'étude.

Carlton M. A, & Devore J. L. (2014). *Probability with applications in engineering*. Springer edition.

Dehmous, H. (2007). *Fiabilité et micromécanique des matériaux composites Application à la passerelle de Laroin* (PhD thesis). Institut National Polytechnique de Toulouse.

DTR B.C.2.2, (1988). *Charges permanentes et charges d'exploitations.* CNERIB, Alger.

Eurocode 2 (2003). *Bases de calcul des structures, norme européenne.* Retrieved from https://www.febelcem.be /fileadmin/user_upload/autres-publications/fr/EC2Condense.pdf

Fascicule 74 (1998). *Construction des réservoirs et châteaux d'eau en béton armé, en béton précontraint ou en maçonnerie*. Retrieved from https://piles.cerema.fr/IMG/pdf/fascicule_74_cctg_1998_construction_reservoirs_beton_ cle795f61.pdf

Guerrin, A., & Lavaur, R. C. (1972). *Traité de béton armé tome 6, réservoirs, châteaux d'eau et piscines*. Eyrolles edition.

Haddad, L., & Sellam, Y. (2017). *Analyse mécano-fiabiliste d'un réservoir surélevé soumis à l'action du vent* (Master's thesis). Mouloud Mammeri University.

Rychilk, I., & Ryden, J. (2006). *Probability and risk analysis, an introduction for engineers*. Springer.

Author(s) Information

Hocine Hammoum
Mouloud Mammeri University of Tizi Ouzou, Department of civil engineering, 15000 Tizi Ouzou, Algeria.
Contact e-mail: *hocine.hammoum@ummto.dz*

Amar Aliche
Mouloud Mammeri University of Tizi Ouzou, Department of civil engineering, 15000 Tizi Ouzou, Algeria.

Karima Bouzelha
Mouloud Mammeri University of Tizi Ouzou, Department of civil engineering, 15000 Tizi Ouzou, Algeria.

To cite this article:

Hammoum, H., Bouzelha, K., & Aliche, A. (2025). Reinforcement analysis of a water tank wall by external prestressing. *The Eurasia Proceedings of Science, Technology, Engineering and Mathematics (EPSTEM), 36*, 21-27.

The Eurasia Proceedings of Science, Technology, Engineering & Mathematics (EPSTEM)
ISSN: 2602-3199

The Eurasia Proceedings of Science, Technology, Engineering and Mathematics (EPSTEM), 2025

Volume 36, Pages 28-38

ICBAST 2025: International Conference on Basic Sciences and Technology

Reliability Analysis of a Gravity Adduction of Water Supply System: Case Study

Karima Bouzelha
Mouloud Mammeri University of Tizi-Ouzou

Hocine Hammoum
Mouloud Mammeri University of Tizi-Ouzou

Melissa Rezki
Mouloud Mammeri University of Tizi-Ouzou

Hafidh Belabes
Mouloud Mammeri University of Tizi-Ouzou

Abstract: The gravitational transfer of drinking water through gravity-fed supply pipes from a departure tank to a receiving tank often follows very complex and winding itineraries. The longitudinal profiles of these itineraries consist of a succession of singular points (top and bottom points). A common mistake made by inexperienced engineers is to ignore these specific features and focus only on the levels of the departure and receiving tanks. The problem becomes even more complex when the longitudinal profile forms a siphon, where the transferred water undergoes a significant drop to the lowest point before rising again to reach the receiving tank. This paper focuses on the study of a practical case of a siphon in a gravity-fed water supply system connecting two tanks over a distance of 15.25 km. By using a Geographic Information System (GIS), a Digital Elevation Model (DEM) was generated along the pipeline itinerary to highlight the terrain's complexity and the singular points of the pathway. A deterministic analysis was conducted to evaluate the service life of the siphon-shaped gravity-fed water supply system. This analysis revealed that uncertainties in the gravity adduction, particularly regarding the internal roughness of the pipeline, can directly impact operating pressures at singular points and, consequently, affect the system's lifetime. Additionally, a reliability-based analysis was performed, accounting for the random variability of roughness. The limit state function is governed by the normal operating conditions and failure criteria of the water supply system. The failure probabilities of the gravity adduction with respect to these limit state functions were computed using the classical Monte Carlo simulation method and then compared to the allowable failure probability for civil engineering structures.

Keywords: Gravity-fed water supply, Siphon, Deterministic analysis, Reliability analysis, Failure probability

Introduction

Gravity-fed water Transfer is extremely sensitive to topography, particularly in Kabylia region, where villages are perched on hilltops or mountains forming a segment of the mountain system. The transfer of water by gravity via supply pipes from one tank to another is subject to very Pressure drops**.** At these low points (siphon), there is extreme hydrostatic pressure, which puts a severe strain on the pipes. This is exacerbated by water hammer.

Usually, in design offices, the analysis and design of drinking water addictions are based on deterministic approaches, and the calculation parameters are considered by engineers as constant values. However, the

literature has shown that, in general, variables such as the consumption rate, the Hazem Williams coefficient and the peak coefficient are considered to be random (Jung, 2010 ; Seifollahi, 2013 ; Basupi, 2015; Hwang, 2017). To this end, reliability theory is increasingly used to take account of the randomness and uncertainty inherent in these different parameters (Tori et al., 2012 ; Galaitsi et al.2016 ; Batsirai et al, 2018).

This scientific approach leads to the estimation of the probability of failure of these structures. Several methods are used to calculate the probability of failure of a drinking water supply network (Gheisi, 2016; Goulter, 2000; Pandey, 2020; Sirsant, 2023). The Monte Carlo method is still the most widely used because of its simplicity and effectiveness. To describe the variability of random parameters, the normal distribution and the betta distribution are the most commonly used to generate the probability low distributions (Jung, 2010; Basupi, 2015; Hwang 2017).

In this article, the hydraulic behaviour (pressure) of the Oued Aissi siphon is examined, which is an adduction pipe linking Larbaa Nath Irathen tank to Béni Douala tank over a length of 15.25 km. This pipeline, which began in 1946, served a project involving 100 villages and was supplied from the Souk El Djema dam (Ain El Hammam). This project was resumed in 1963. The pipe at siphon level, with a nominal pressure PN100 was swept away by the flood of April 1974, then repaired and put back into service. In view of the high nominal pressures and the vulnerability of the pipe due to the river crossing, this supply line was decommissioned at the end of 1976. Using a deterministic calculation of velocities and pressures, we will attempt to provide technical and hydraulic explanations for these repeated ruptures, which led the hydraulic department of Tizi Ouzou to abandon this siphon. In addition, the adopted reliability analysis allows the random variability of Hazen William's roughness coefficient to be taken into account. The results of the calculation of the probability of failure highlighted the sensitivity of the pressure and velocity criteria to the random variability of the roughness.

Presentation of the Gravity Supply

The Oued Aissi supply network starts from a tank with a capacity of 1000 m³ located in Aboudid (LNI) at level of 1035 m (Figure 1). The water will be conveyed to tank with a capacity of 1000 m³ located at Djouad (Beni Douala) at level of 880.27 m (Figure 1).

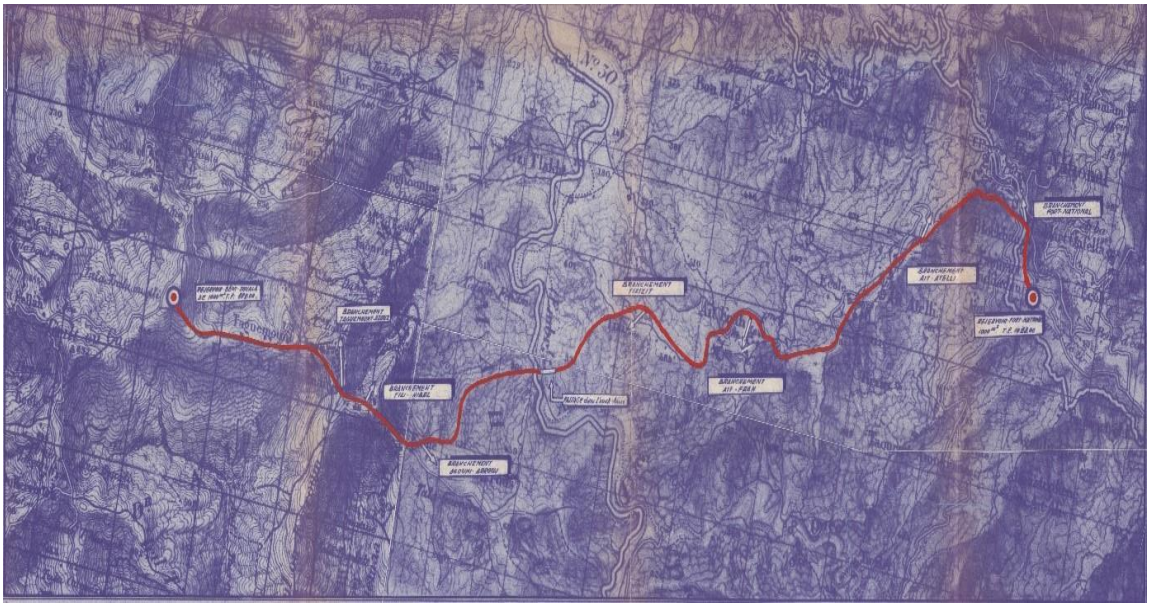

Figure 1. Sketch of the route of the gravity-fed water supply, overlaid on a topographic map

The steel supply pipe is made up of 64 sections. The corresponding lengths and altitudes are taken from the longitudinal profile of the network (Figure 2). Several tapping points are successively made along this pipe to supply 7 villages. The flow rate through the network varies according to the different tapping points (Table 1). Figures 1 illustrate the route sketch and longitudinal profile of this pipeline, respectively. This figure highlights the topographical configuration of the project, which is referred to as a siphon. If the difference in altitude between the departure tank and the receiving tank is only 154.73 m, the water must undergo a fall of 871.62 m before it can rise to the receiving tank.

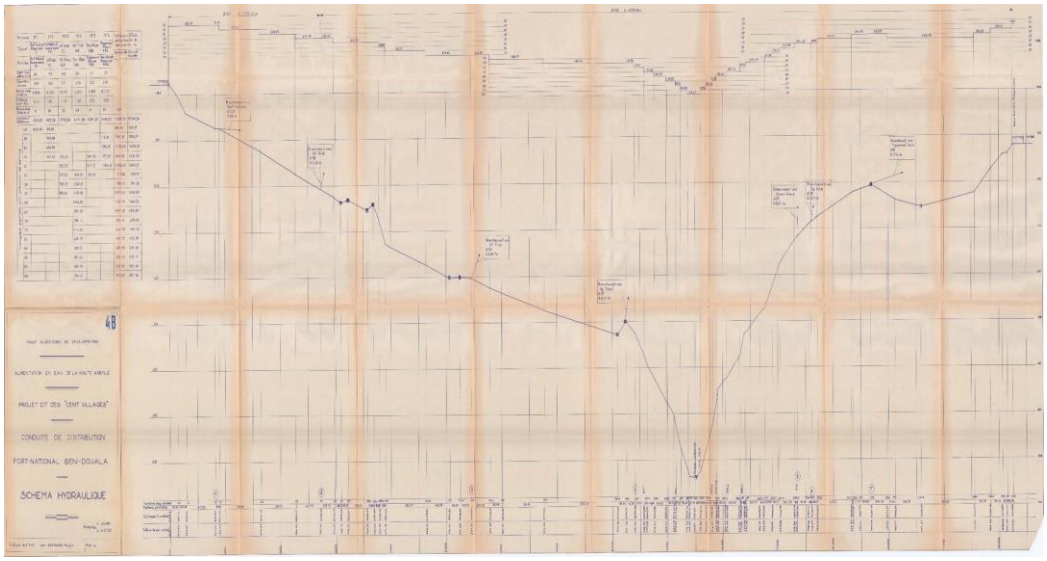

Figure 2. Longitudinal profile of the gravity pipeline

Table 1. Flow transiting by the addiction pipe

Pipeline section	1,00	2,00	3,00	4,00	5,00	6,00
Departure	LNI tank	LNI Tizi N'Smlal	Ait Atelli	Ait Ferah	Tizi Hibel	Taguemount Azouz
Arrival	LNI Tizi N'Smlal	Ait Atelli	Ait Ferah	Tizi Hibel	Taguemount Azouz	BD tank
Transited flow (l/s)	99,00	71,00	68,32	64,54	61,13	52,07
Tapping flow (l/s)	28,00	2,68	3,78	3,41	9,06	-

Digital Terrain Model (DTM)

To generate a Digital Terrain Model along the pipeline route (Larbaa Nath Irathen - Beni douala), a semi of 1406 points was carried out on the staff map (Oued Aissi-Takhoukht-Mechtras) at a scale of 1:25,000 (Figure 3), using GIS (Geographic Information System).

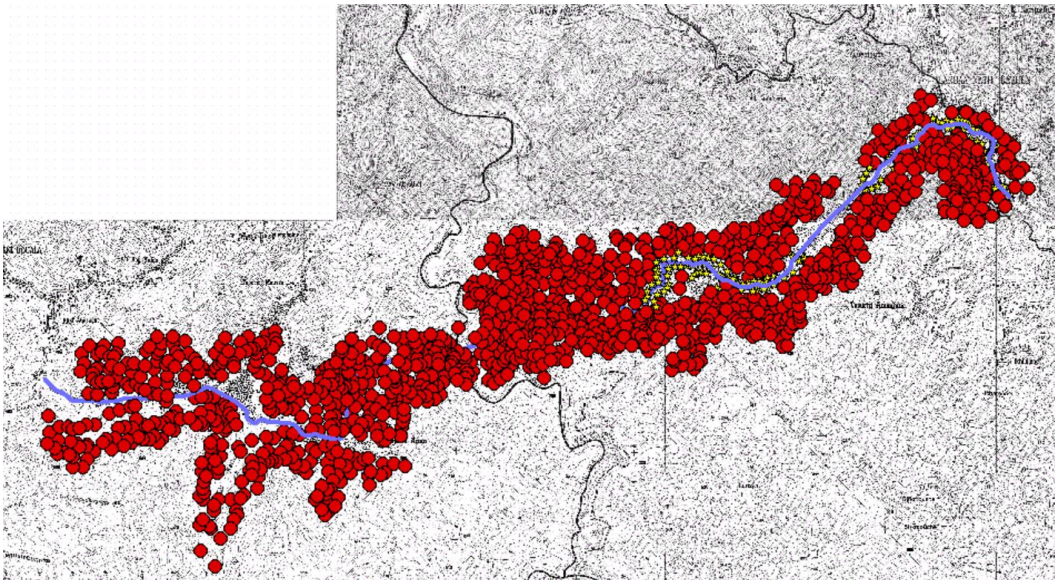

Figure 3. Topographic survey.

To give meaning to this graphical representation and show the difference in altitude between the various sampled points, a thematic map is created (Figure 4). We observe that the altitude ranges from 200 m to 950 m.

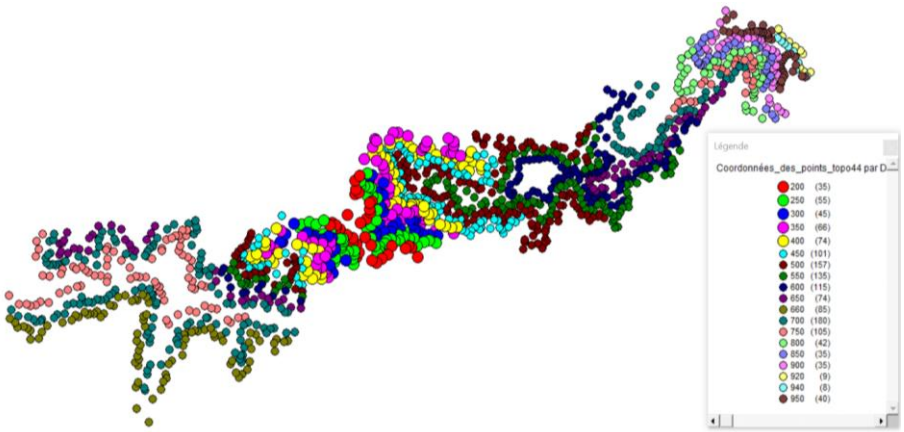

Figure 4. Analyse thématique des altitudes.

For each surveyed point, the X, Y, and Z coordinates were recorded in an Excel file and then imported into Surfer software to generate the DTM along the route of the Oued Aissi gravity pipeline (Figure 5). This DTM provides an accurate and detailed representation of the siphon, clearly highlighting the significant elevation differences between the departure tank and the receiving tank. Thus, it serves as a relevant tool for understanding terrain complexity, optimizing route analysis, and supporting decision-making related to the installation or maintenance of the hydraulic network.

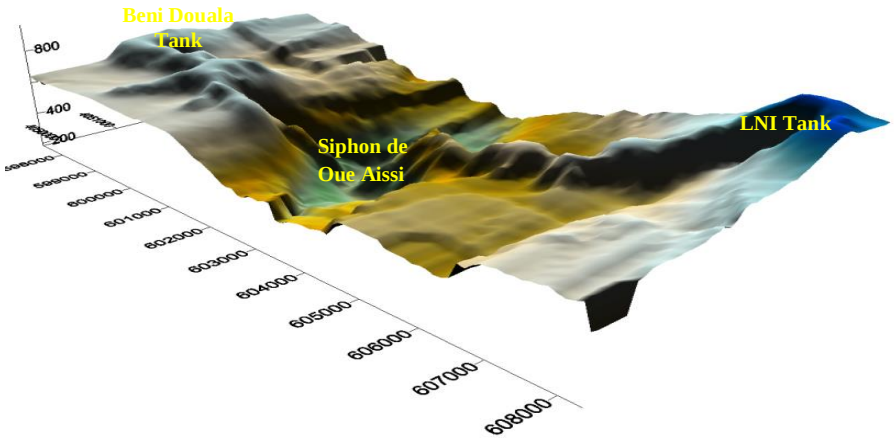

Figure 5. Digital Terrain Model along the pipeline route (Larbaa Nath Irathen - Beni douala).

Hydraulic Calculation of Gravity Supply Network

The purpose of the hydraulic calculation of the gravity supply network pipe is to determine the flow velocity V(m/s) and piezometric level Hi (m) in the various sections of the pipe. Two standard diameters are adopted, DN300 and DN250. The flow velocity V(m/s) in the pipeline is determined using the continuity equation:

$$V = \frac{4\,Q}{\pi\,DN^2} \tag{1}$$

To ensure the proper functioning of the network, the piezometric level (or Hydraulic head) H^i at node (i) must satisfy the following condition:

$$H_{min\,adm} < H^i \leq H_{max\,adm} \tag{2}$$

Where:

$$H^i = H^{i-1} - \Delta H \tag{3}$$

ΔH: Total head losses (linear and singular), given by:

$$\Delta H = 1.15\,j\,L \tag{4}$$

Where L is the length of the pipeline and j is the unit head loss, given by the Hazen-Williams formula:

$$j = 1.218 * 10^{10} \frac{Q^{1.852}}{chw^{1.852} * DN^{4.871}} \quad (5)$$

chw designate the Hazen-Williams roughness coefficient, equal to 136 for a new pipe and 95 for an old pipe. The minimum admissible service head is verified to ensure that water can enter the tank. It is given by:

$$H^i_{minadm} = NTE^i + 10 \quad (6)$$

Where 10 m represents the minimum service pressure and (NTE) the Natural Terrain Elevation. The maximum admissible head at a node (i) of the pipeline is obtained using the following equation:

$$H^i_{maxadm} = NTE^i + PN \quad (7)$$

Where PN is the nominal pressure of the pipe, in meters, selected from the catalogue based on the maximum pressures (P_{max}) and minimum pressures (P_{min}). The maximum and minimum pressure at any node (i) of the pipelinein according to water hammer are given by the following equations:

$$P^i_{max} = H^i_{geo} + B \quad (8)$$
$$P^i_{min} = H^i_{geo} - B \quad (9)$$

Where, Hgeo and B designate respectively the geometric height of the node (i) and the water hammer pressure at the same node (i). This water hammer is given by the following equation:

$$B = a\frac{v}{g} \quad (10)$$

a: Celerity of the water hammer wave, given by Allievi

$$a = \frac{9900}{\sqrt{48{,}90 + K\frac{DN}{e}}} \quad (11)$$

Where K and e designate respectively the coefficient depending on the pipe material (steel, K = 0.50), and the pipe wall thickness [m]. The calculation results show that for the various sections the velocities are between (V_{min}=0.5 m/s) and (V_{max}=1.5 m/s), in accordance with the condition required by the regulations (Figure 6).

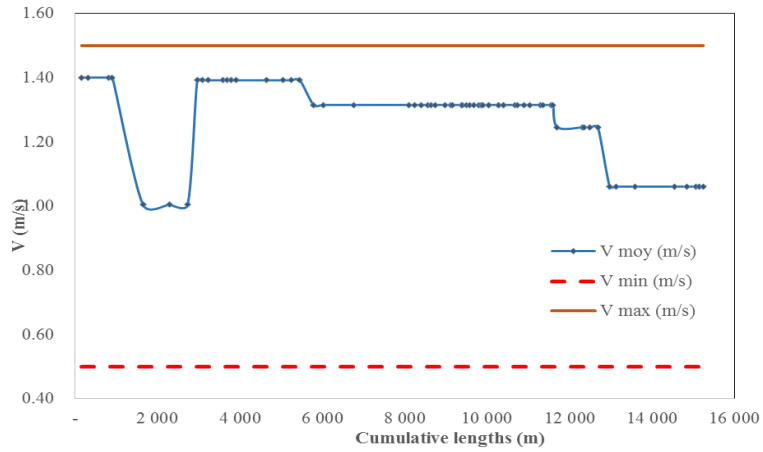

Figure 6. Velocity calculation results

For the pressures, Oued Aissi gravity feed network was modelled for both the commissioning phase (chw=136) and over 30 year (chw=95). The calculation results of the piezometric levels are shown in Figures 7 and 8. It can be seen that at commissioning, the piezometric line (H^i) is within the maximum and minimum allowable pressure range across all section. This deterministic analysis of velocities and pressures indicates that Oued

Aissi gravity feed network is properly designed at the time of commissioning, in accordance with hydraulic regulations. It should also be pointed out that the pressures at the Siphon are very high. To this end, we have adopted pipes of PN90 and PN100. Over a 30-year period (Chw=95), the results show that the piezometric level falls below the minimum admissible pressure at the last three nodes (63, 64 and 65). This, of course, leads to network malfunction, as the water will not reach the receiving tank. This means that the network is not properly dimensioned with regard to the hydraulic conditions required by the regulations. These nodes must therefore be points of attention for the infrastructure manager.

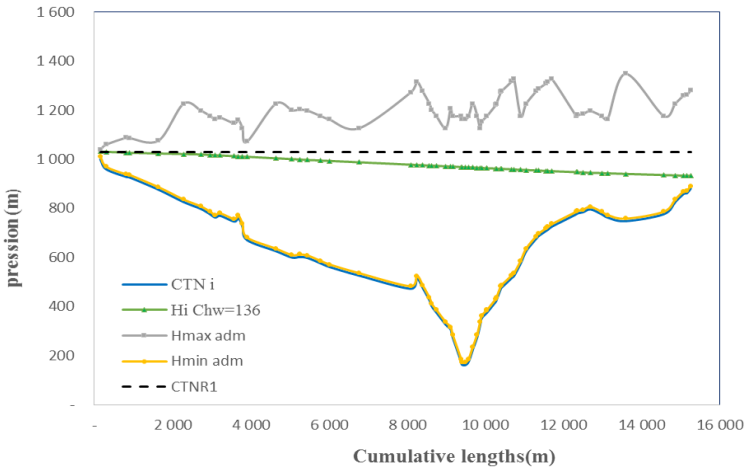

Figure 7. Piezometric line position at commissioning.

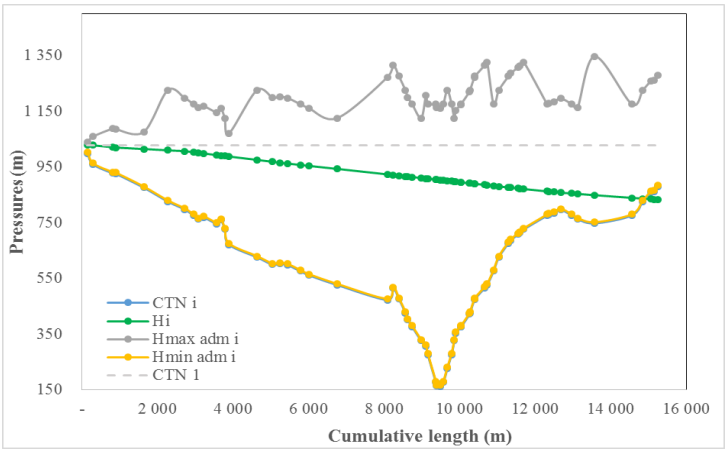

Figure 8. Piezometric line position over 30 years.

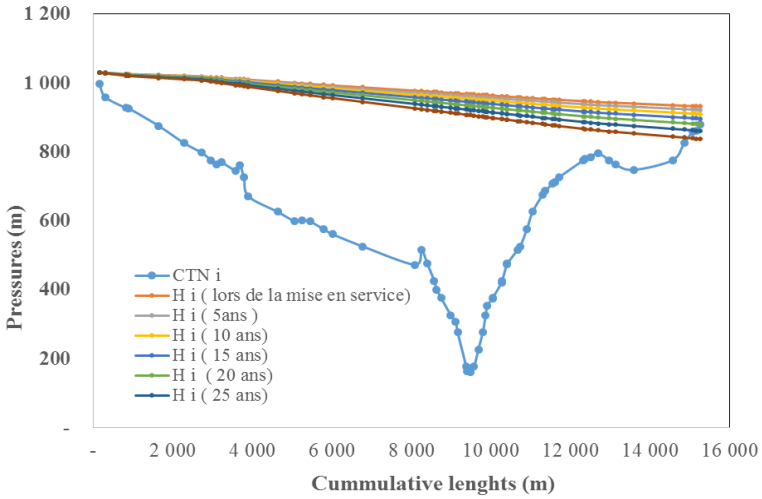

Figure 9. Evolution of piezometric levels.

To analyse the lifetime of Oued Aissi gravity feed network, we considered a linear evolution of the Chw coefficient. The results of the piezometric levels evolution as a function of time (figure 9) show that the piezometric line decreases with time and therefore with the Hazen-Williams coefficient, falling below the CTN at around 20 years of service.

To obtain the exact year of the network failure, we superimposed the evolution over time of the piezometric level of the network with the natural ground level, as shown in figure 10. The results show that after 19 years of service, the initial design flow (99 l/s) cannot be insured. This would lead to a flow deficit and therefore a reduction in the supply. Under these conditions, after simulating the situation for 30 years, it turns out that the pipe could only provide 90 l/s.

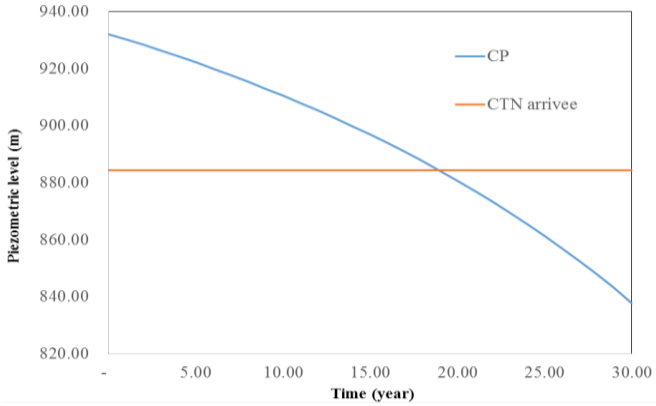

Figure 10. Analyse of the lifetime of Oued Aissi gravity feed network

The gravity supply network is analyzed under the condition of an instantaneous valve closure. For this purpose, the overpressures and underpressures induced by the water hammer (B) at each node were calculated according to relation 10. The results of these calculations are presented in Figure 11. It is observed that when the valve closes instantaneously, the overpressures exceed the permissible limits at several nodes (37, 59, and 61), which may damage the pipes and lead to leaks as well as weakened joints and connections. Particular attention should be paid to these nodes, especially in the vicinity of siphons.

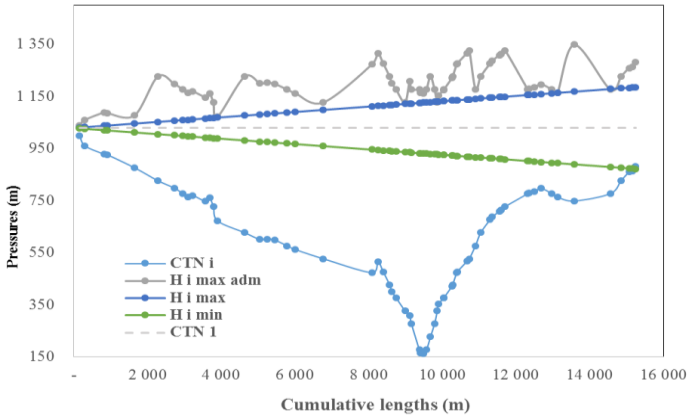

Figure 11: Pressures acting at instantaneous closure of the valve.

Finally, for a better analysis of the gravity feed failure, we propose a reliability study, taking into account the uncertain aspect of pipe roughness, throught the Hazen Williams coefficient (Chw).

Failure Mode and Limit State Function

In reliability theory, the failure of a system is defined by the general form of a limit state function G(X) (Lemaire, 2005), which defines its behaviour, as follows:

$$G(X) = R(X) - S(X) \tag{12}$$

Where X is the vector of random variables xi. The basic principle of structural design is that the ultimate resistance R(X) must be greater than the live load S(X) (Lemaire, 2005). The probabilistic approach consists of calculating the probability of the limit state criterion being exceeded, called probability of failure P_f, which is compared with a permissible probability of failure, which is is equal to 10^{-3} for civil engineering structures (Bouzelha et al, 2024):

$$P_f = P(G(X) \leq 0) \leq P_f^{adm} \tag{13}$$

In this study, the limit state function G(X) is defined by the failure of the water supply network in service, resulting from the ageing of the pipes. This ageing is mainly due to the increase in the roughness of the internal walls, which leads to a significant rise in head losses. The criterion for justifying this limit state is to check that the piezometric head H(X), taking into account the head losses, is greater than the minimum admissible head; previously defined:

$$G = H(X) - H_{min\ adm}(X) \tag{14}$$

Evolution of the Failure Probability

The failure probability P_f is given by the integral of the probability density function, as follows:

$$P_f = \int_{D_f} f_X(x_1, x_2, \dots\dots, x_1) dx_1, dx_2, \dots\dots, dx_n \tag{15}$$

The analytical evaluation of this integral is difficult and requires advanced mathematical skills. Several numerical approaches are proposed in the literature (Lemaire, 2005) such as the Monte Carlo simulation method and the First-Order Reliability Method (FORM), and the Second-Order Reliability Method (SORM). In this study, the calculation of the failure probability P_f is conducted with the classical Monte Carlo method. The principle of this method is based on generating a large number of random samples, denoted N_t, according to their joint probability distribution. For each sample, the response of the limit state function is evaluated (Figure 10). A failure indicator I_{di} is then introduced to identify the failure condition of the system based on the limit state function G(X), such that:

$$I_{di} = \begin{cases} 1 & \text{if } G(x) \leq 0 \\ 0 & \text{if } G(x) > 0 \end{cases} \tag{16}$$

The failure probability Pf is evaluated, for the predefined failure mode, by the following relationship.

$$P_f = \frac{\sum_{i=1}^{N_t} I_{di}}{N_t} \tag{17}$$

Random Variables and Distribution Laws

The behaviour of the water supply network is affected by numerous uncertainties linked to the geometry of the pipes, the characteristics of the materials and the hydraulic characteristics. The main source of uncertainty retained in our case study is the roughness of the pipes which wears away over time, thus affecting pressure losses and, above all, pressures in the network. This roughness is expressed by the Hazen-Williams coefficient. This random variable is generated using the normal distribution in accordance with the literature (Seifollahi et al, 2013; Xu et al. 1999). The probability density function of the normal distribution is given by expression (18) and illustrated in Figure 10 for different values of C_v

.

$$f(x) = \frac{1}{\sigma\sqrt{2\pi}} \exp\left(-\frac{(x-\mu)^2}{2\sigma^2}\right) \tag{18}$$

x is the random variable, μ is the mean of the distribution, and σ the standard deviation.

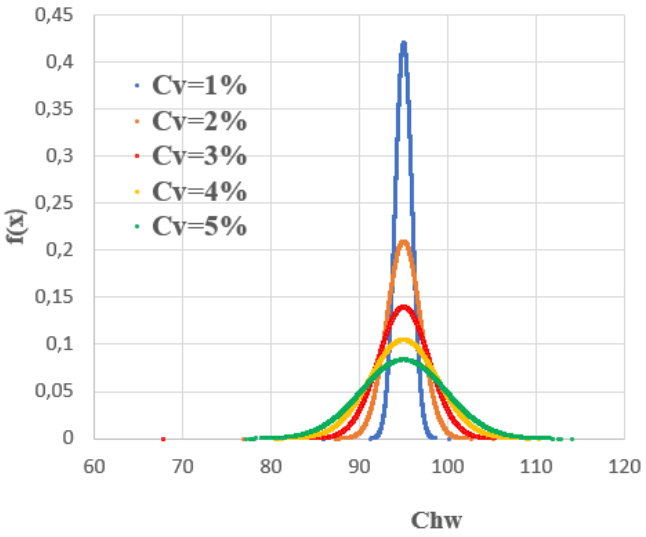

Figure 10. Density function of the normal distribution.

Results and Discussion

The probability of failure P_f is obtained using Monte Carlo simulations. The number of the number of samples (N_t) is fixed at 30 000.00, after a convergence test (Figure11).

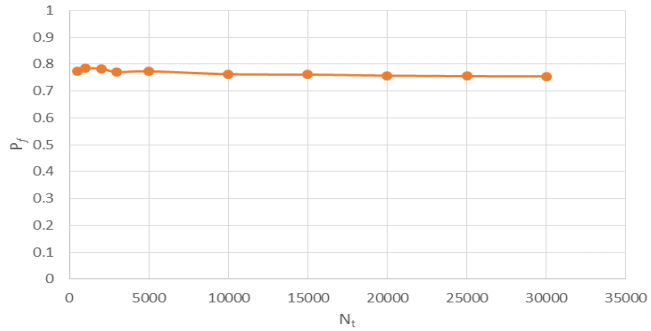

Figure 11. Variation of the failure probability as function of the number of draws.

The evolution of the probability of failure P_f as a function of time, for different coefficients of variation ranging from 1% to 5%, is illustrated in Figure 12. We note the sensitivity of the pressure criterion to the random variability of the pipe roughness.

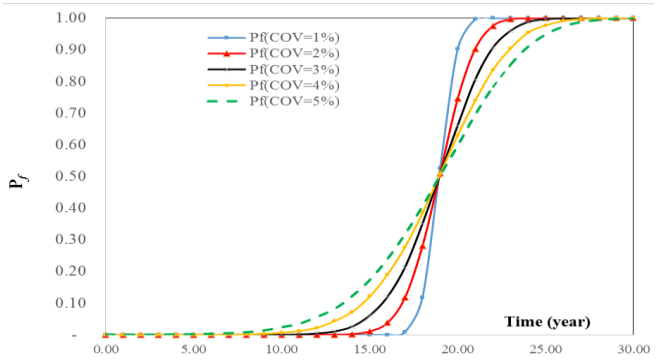

Figure 12. Probability of failure as a function of coefficient of variation.

It is observed that the failure probability is zero during the first ten years of service. Between ten and thirteen years, P_f remains below the admissible probability ($P_f^{adm}=10^{-3}$). After thirteen years, the failure probability increases with time, as the network continues to age. The admissible probability is reached between 13 and 16

years, depending on the coefficient of variation C_v. In other words, the risk of network failure is likely to occur earlier than predicted by deterministic calculations (19 years), due to uncertainties related to roughness.

Conclusion

The combined analysis of the Digital Terrain Model (DTM) and the deterministic and probabilistic approaches applied to the Oued Aissi gravity-fed water supply network has led to several key practical insights essential for ensuring the long-term sustainability of the system. These include the importance of the DTM in the design and analysis of the pipeline route, as well as the limitations of the deterministic approach, which does not take into account the random variability of certain key parameters, particularly pipe roughness. In addition, several causes of failure or malfunction have been identified, such as:

- *Pipeline aging*, resulting in a gradual increase in internal roughness, leads to significant head losses and a drop in piezometric pressure. Over time, the pressure falls below the admissible value at the last three nodes, preventing water from reaching the receiving tank.
- *Insufficient flow*, observed from the 19th year of operation, when the design flow rate of 99 l/s can no longer be maintained, leading to a supply deficit.
- *Random variability of roughness*, highlighted by the probabilistic analysis, anticipates failures between 13 and 16 years, which are not predicted by the deterministic approach.

These findings underscore the need for an adaptive network management, incorporating monitoring, preventive maintenance, and progressive redimensioning to ensure the long-term reliability of the service.

Scientific Ethics Declaration

*The authors declare that the scientific ethical and legal responsibility of this article published in EPSTEM journal belongs to the authors.

Conflict of Interest

*The authors declare that they have no conflicts of interest

Funding

*The authors wish to thank the Algerian Ministry of higher education and scientific research for funding the University education research project (PRFU – N° A01L02UN150120220004).

Acknowledgements or Notes

*This article was presented as an oral presentation at the International Conference on Basic Sciences and Technology (www.icbast.net) held in Budapest/Hungary on August 28-31, 2025.

*The information on data of the Oued Aissi siphon has been kindly provided by Water Resources Department of Tizi Ouzou (Algeria).

References

Basupi, I., & Kapelan, Z. (2015). Flexible water distribution system design under uncertainty. *Journal of Water Resources Planning and Management*, *141*(4), 786–797.

Batsirai, M., Suhrcke, M., & Hunter, P. R. (2018). Reliability of water supplies in low and middle-income countries: A structured review of definitions and assessment criteria. *Journal of Water, Sanitation and Hygiene for Development*, *8*(2), 142–164.

Bonnin, J. (1986). *Hydraulique urbaine appliquée aux agglomérations de petite et moyenne importance*. Eyrolles.

Bouzelha, K., Hammoum, H., Aliche, A., Aoues, Y., & Amiri, O. (2024). Contribution to calibration of partial safety factors for RC water tank design. *Structural Engineering International*, *34*(3), 404-413.

Galaitsi, S. E., Russell, R., Bishara, A., Durant, J. L., Bogle, J., & Huber-Lee, A. (2016). Intermittent domestic water supply: A critical review and analysis of causal-consequential pathways. *Water*, *8*(7), 274.

Gheisi, A., Forsyth, M., & Naser, G. (2016). Water distribution systems reliability: A review of research literature. *Journal of Water Resources Planning and Management*, *142*(11).

Goulter, I., Walski, T. M., Mays, L. W., Sakarya, A. B. A., Bouchart, F., & Tung, Y. K. (2000). Reliability analysis for design. In L. W. Mays (Ed.), *Water distribution systems handbook*. McGraw-Hill.

Hammoum, H., & Bouzida, R. (2010). *Pratique des Systèmes d'information Géographiques (SIG): Application sous Mapinfo*. Pages Bleues.

Hwang, H., Lansey, K., & Jung, D. (2018). Accuracy of first-order second-moment approximation for uncertainty analysis of water distribution systems. *Journal of Water Resources Planning and Management*, *144*(2), 04017088.

Jung, D., Chung, G., & Kim, J. H. (2010). Optimal design of water distribution systems considering uncertainties in demands and roughness coefficients. In *Water Distribution Systems Analysis 2010* (pp. 1390-1399).

Lemaire, M., Chateauneuf, A., & Mitteau, J. (2005). *Fiabilité des structures*. Lavoisier.

Pandey, P., Dongre, S., & Gupta, R. (2020). Probabilistic and fuzzy approaches for uncertainty consideration in water distribution networks: A review. *Water Supply*, *20*(1), 13–27.

Seifollahi-Aghmiuni, S., Bozorg Haddad, O., & Mariño, M. A. (2013). Water distribution network risk analysis under simultaneous consumption and roughness uncertainties. *Water Resources Management*, *27*(7), 2595–2610.

Sirsant, S., Hamouda, M. A., & Shaaban, M. F. (2023). Advances in assessing the reliability of water distribution networks: A bibliometric analysis and scoping review. *Water*, *15*(5), 986.

Torii, A. J., & Lopez, R. H. (2012). Reliability analysis of water distribution networks using the adaptive response surface approach. *Journal of Hydraulic Engineering*, *138*(3), 227–236.

Xu, C., & Goulter, I. C. (1999). Reliability-based optimal design of water distribution networks. *Journal of Water Resources Planning and Management*, *125*(6), 352–362.

Author(s) Information

Karima Bouzelha
Mouloud Mammeri University of Tizi-Ouzou, Department of civil engineering, 15000 Tizi Ouzou, Algeria.
Contact e-mail: *karima.bouzelha@ummto.dz*

Hocine Hammoum
Mouloud Mammeri University of Tizi-Ouzou, Department of civil engineering, 15000 Tizi Ouzou, Algeria.

Melissa Rezki
Mouloud Mammeri University of Tizi-Ouzou, Department of civil engineering, 15000 Tizi Ouzou, Algeria.

Hafidh Belabes
Mouloud Mammeri University of Tizi-Ouzou, Department of civil engineering, 15000 Tizi Ouzou, Algeria.

To cite this article:

Bouzelha, K., Hammoum, H., Rezki, M., & Belabes, H. (2025). Reliability analysis of a gravity adduction of water supply system: Case study. *The Eurasia Proceedings of Science, Technology, Engineering and Mathematics (EPSTEM), 36,* 28-38.

The Eurasia Proceedings of Science, Technology, Engineering & Mathematics (EPSTEM)
ISSN: 2602-3199

The Eurasia Proceedings of Science, Technology, Engineering and Mathematics (EPSTEM), 2025

Volume 36, Pages 39-47

ICBAST 2025: International Conference on Basic Sciences and Technology

Fabrication and Characterization of FeMnCo/Nanofiber for Radar Absorbing Material by Electrospinning

Kadir Asrin Sari
Özdemir Bayraktar Aerospace Technologies Vocational and Technical Anatolian High School

Umit Erdem
Kırıkkale Unıversity

Ugur Sari
Kırıkkale University

Abstract: With the rapid advancement of modern radar technologies, the development of materials capable of attenuating or eliminating electromagnetic wave reflection has become a critical area of research in electromagnetic interference (EMI) shielding and radar stealth engineering. These materials are not only essential for reducing radar detectability in military applications but also for safeguarding sensitive electronic systems and minimizing electromagnetic exposure in biological systems. This study focuses on the fabrication and characterization of a high-performance radar absorbing material effective in the X-band and Ku-band frequency ranges, which are commonly used in advanced defense radar systems. A novel nanocomposite was developed by incorporating 40 wt% FeMnCo alloy particles into a polyacrylonitrile (PAN) matrix via electrospinning. The resulting nanofiber architecture exhibited a uniform, cross-linked network with fiber diameters ranging from 200 to 400 nm, as confirmed by Scanning Electron Microscopy (SEM). X-ray Diffraction (XRD) confirmed uniform nanofiber formation and phase stability. Electromagnetic wave absorption properties were evaluated using a Vector Network Analyzer (VNA). The composite exhibited broadband absorption behavior with reflection loss (RL) values below -20 dB across both the X and Ku bands, indicating excellent radar attenuation performance. A minimum RL of -67.59 dB was recorded at 15.40 GHz, demonstrating the material's strong potential for stealth and EMI shielding applications. The findings highlight the synergistic effect of ferromagnetic FeMnCo alloy particles and the high surface area of the nanofibrous morphology in enhancing dielectric and magnetic loss mechanisms. This work contributes to the growing field of radar absorbing materials by offering a scalable and efficient approach to next-generation stealth technologies and electromagnetic protection systems. Future studies may focus on optimizing the composite's thickness, multi-layer configurations, and environmental durability to further improve real-world applicability and long-term performance.

Keywords: Electromagnetic wave absorption, Radar absorbing material (RAM), Nanofiber, Electrospinning

Introduction

The development of materials with the ability to absorb electromagnetic (EM) waves is of critical importance in areas such as radar systems, electromagnetic pollution control, and communication security (Abdalla et al., 2023; Ruiz-Perez et al., 2022). Today, both civil and military security challenges necessitate the development of specialized materials designed to prevent radar systems from detecting objects through electromagnetic waves, and intensive research efforts are being conducted in this context (Du et al., 2024; Saeed et al., 2024). Radar absorbing materials (RAMs) are strategic materials that find wide application in low-visibility technologies for military systems, in coatings designed to mitigate the effects of electromagnetic radiation, and in protective

clothing (Kim et al., 2023). These materials operate primarily through two different mechanisms to suppress or eliminate reflected electromagnetic waves (Kim et al., 2023; Ruiz-Perez et al., 2022). The first mechanism involves the attenuation of EM waves within the material through dielectric and magnetic losses, whereby the wave energy is dissipated and converted into heat. The second mechanism is based on the penetration of the wave into the material, its reflection from the back surface, and its return to the inner front surface, thereby generating multiple internal reflections (Figure 1).

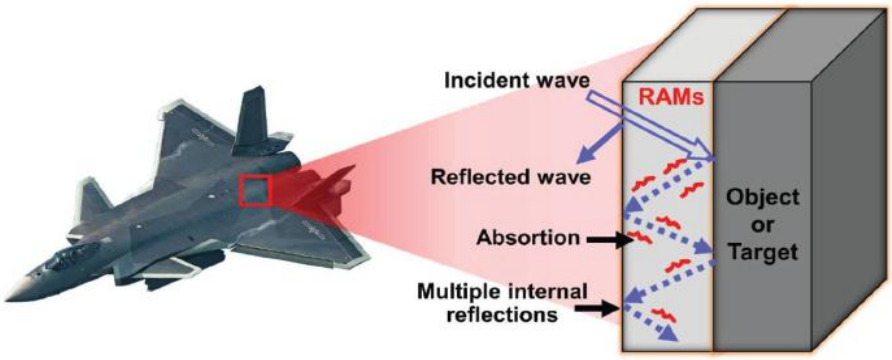

Figure 1. Attenuation mechanism of EM waves in RAMs (Kim et al., 2023)

In conventional RAMs, metals, metal powders, ferrites, conductive polymers, and various dielectric materials have been employed as the absorbing phase (Abdalla et al., 2023; Huang et al., 2020). However, these materials are often limited in practical applications due to their high density, poor corrosion resistance, heavy structures, or low absorption efficiency within restricted frequency bands (Jia et al., 2018). Consequently, research efforts have shifted toward the development of next-generation RAMs that are lightweight, electrically and magnetically conductive, thermally stable, corrosion-resistant, and capable of achieving high absorption over a broad frequency range (Huang et al., 2020; Kim et al., 2023). In recent years, advancements in materials science have facilitated the replacement of traditional absorbers with innovative approaches based on carbon-based materials, ceramics, and nanofiber architectures (Cai et al., 2024). Among these, the electrospinning technique has attracted significant attention, as it enables the fabrication of lightweight, flexible nanofiber structures with high surface area (Li et al., 2023). Moreover, this method allows the incorporation of various additives to further enhance the absorption performance of the nanofibers (Abdalla et al., 2023; Huang et al., 2020).

Transition metals such as Fe, Ni, and Co have attracted considerable attention as magnetic absorbers due to their high magnetization and permeability and are frequently employed as dopants in electrospinning processes (Wang et al., 2019; Xu et al., 2024). In particular, magnetic oxides such as Fe_3O_4 (Bayat et al., 2014; Pan et al., 2020) and $MgFe_2O_4$ (Liao et al., 2022) have been widely used as additives in electrospun nanofibers. Liu et al. (2016) reported that CoO-doped nanofibers exhibited a minimum reflection loss (RL) of –25.7 dB at a thickness of 2 mm. For magnetic oxides, electromagnetic absorption mainly arises from magnetic losses, as their electrical conductivity is relatively low. This limitation can be overcome by incorporating alloys that combine strong magnetic properties with good electrical conductivity. For instance, Chai et al. (2024) fabricated FeCo alloy nanoparticle-doped nanofibers, achieving effective absorption performance at a thickness of 1.2 mm and a frequency of 4.2 GHz. Similarly, Du et al. (2024) demonstrated that FeCoNi-doped carbon nanofibers achieved strong absorption with a minimum RL of –69.3 dB at 6.8 GHz with a thickness of 1.82 mm.

In the current literature, research on nanofiber-based electromagnetic wave absorbers using magnetic alloys as additives instead of ferromagnetic metal oxides is relatively limited. In particular, there are no studies using magnetic alloy particles obtained in ingot form as additives in nanofiber-based electromagnetic wave absorbers. This highlights the novelty of our work in developing ultrathin, lightweight, and broadband effective EM wave absorbers. In this study, radar absorbing materials with lightweight, flexible, and broadband high-absorption capability were developed by integrating FeMnCo-based magnetic alloys into electrospun nanofiber matrices. Through this approach, the synergistic effects of dielectric and magnetic losses were harnessed to overcome the performance limitations of conventional RAMs and address the current gap in literature. Accordingly, PAN nanofiber doped with ferromagnetic FeMnCo alloy particles were fabricated via electrospinning, and its electromagnetic wave absorption properties were investigated. The microstructure and absorption characteristics of nanofibers containing 40 wt% FeMnCo alloy were systematically studied.

Method

In this study, FeMnCo doped nanofiber was produced by electrospinning solutions containing alloy particles. The FeMnCo alloy used was prepared from bulk material containing 17.3% Mn and 4.6% Co by weight. As reported in the literature (Sarı & Kırındı, 2010), this alloy was heated in a furnace at 1200 °C for 12 hours and then rapidly immersed in room-temperature water to acquire ferromagnetic properties. This magnetic property was the primary reason for its selection in this study.

The alloy was obtained in powder form using a diamond file. The resulting FeMnCo alloy particles were combined with polyacrylonitrile (PAN) polymer and dimethylformamide (DMF) used as a solvent to prepare a solution suitable for electrospinning. The fabrication steps are schematically presented in Figure 2. In the first step, 1.11 g of PAN was dissolved in 10 mL of DMF to reach a concentration of 10% (by weight). Then, 40% (approximately 5.4 g) of FeMnCo alloy particles were added to this solution. The mixture was continuously stirred on a magnetic stirrer for 24 hours to ensure a homogeneous distribution. The homogenized solution was transferred to a 10 mL syringe and subjected to electrospinning. Electrospinning parameters were set as 14 kV applied voltage, 1 mL/h feed rate, and 17 cm tip-collector distance. After the solvent evaporated, the fibers formed were collected on aluminum foil and dried at room temperature to obtain the nanofiber structure.

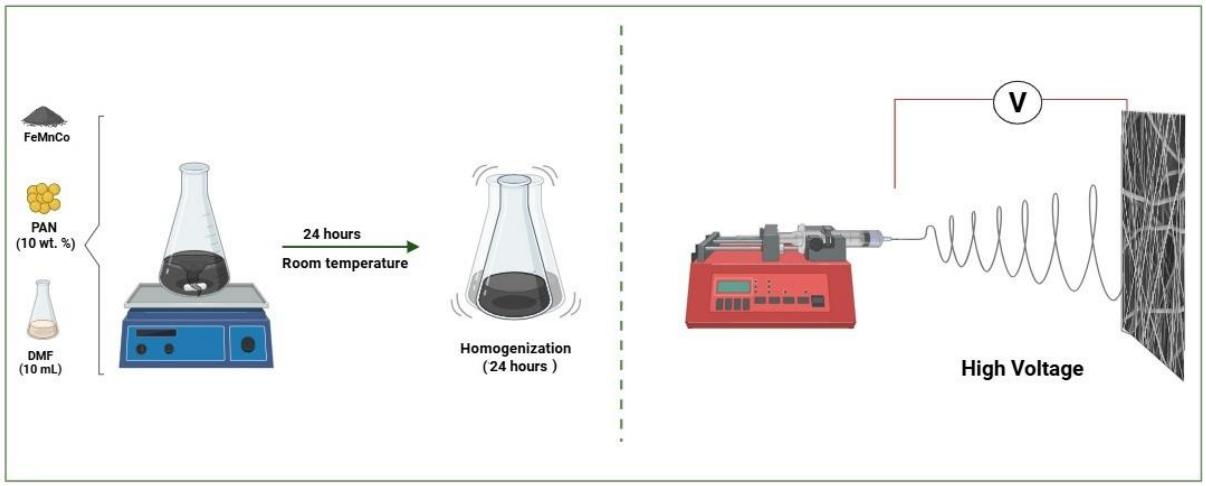

Figure 2. FeMnCo doped PAN nanofiber fabrication scheme

The surface morphology of the produced nanofiber was examined by scanning electron microscope (SEM, HITACHI SU5000). X-Ray diffraction (XRD) measurements to determine the phase structures of the nanofiber sample were carried out on a Bruker D8 Advance instrument using CuKα (λ = 0.15406 nm) radiation and a 2θ range of 10°–80°. EM wave absorption performance was evaluated by reflection loss (RL) measurements. RL tests were performed with a Keysight N5224B vector network analyzer; samples for X-band (8–12 GHz, WR90 adapter) and Ku-band (12–18 GHz, WR62 adapter) measurements were prepared in accordance with the waveguide dimensions.

Results and Discussion

Morphological and Structural Analysis

The surface morphology of FeMnCo doped nanofiber is presented in Figure 3. SEM-based morphological studies show that the fibers are distinctly one-dimensional, with an average diameter ranging from 200 to 400 nm and a very high length-to-diameter ratio along the long axis. These thin-diameter and long fiber structures provide a high specific surface area, allowing electromagnetic waves to travel longer distances within the material and, therefore, contributing to greater energy loss due to multiple interactions (Li et al., 2023). In addition, a three-dimensional, cross-linked, and anisotropic network morphology formed by the overlapping of fibers in different orientations was observed in SEM images. Such structures allow the deflection of electromagnetic waves, the formation of multiple internal reflections, and enhanced energy absorption through increased scattering (Cai et al., 2024). These fibers doped with the FeMnCo alloy are expected to have high electrical conductivity due to the presence of metallic conductive phases in the polymer matrix. Such a conductive network structure enables the EM waves to undergo multiple scattering between the fibers and their energy to be gradually absorbed (Erdem et al., 2025; Cai et al., 2024).

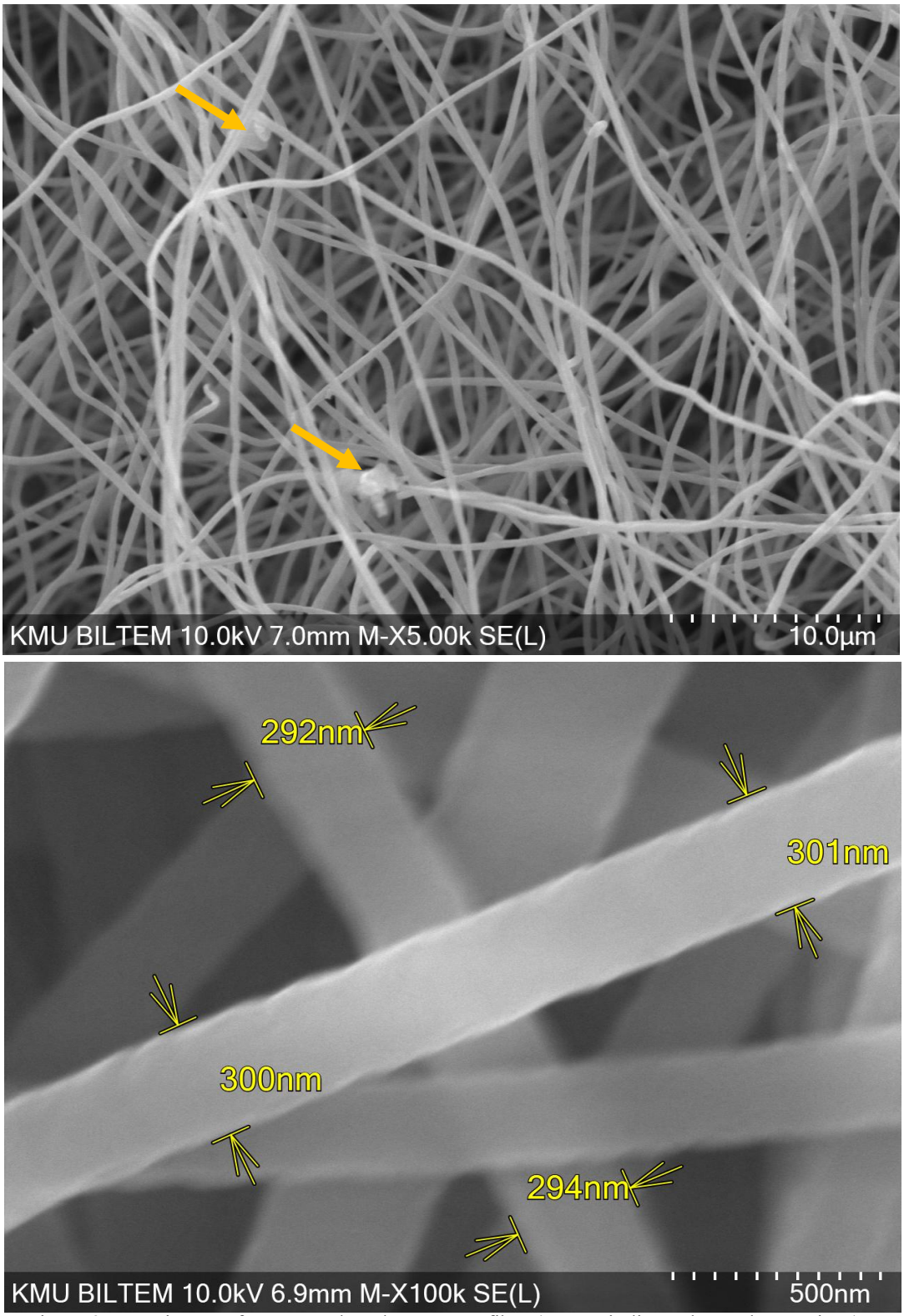

Figure 3. SEM image of FeMnCo doped PAN nanofiber (arrows indicate the agglomerations)

Detailed SEM analyses of the nanofiber sample indicated the presence of distinct particle agglomerations (dense clusters) in some areas (see Figure 3). Alloy powders were obtained by mechanically abrading the FeMnCo alloy ingot with a diamond file and then homogenized in the PAN solution using a magnetic stirrer. Because this method provides low-energy mixing, it is possible that the powder particles are not fully dispersed and may form dense clusters in places. These clusters can lead to morphological defects such as bead formation, increased roughness, and discontinuities on the fiber surface, disrupting the continuity of the conductive network within the composite and thus reducing EM absorption performance (Karbowniczek et al., 2022).

Alternatively, using a high-shear homogenizer instead of a magnetic fish stirrer could significantly reduce the risk of agglomeration by more effectively dispersing the alloy particles in the solution. Furthermore, instead of using the powders obtained after filing, subjecting them to size reduction and surface activation using ball mills or mechanical grinding methods could contribute to a more uniform particle distribution and a more suitable distribution for electrospinning. Such improvements could improve electromagnetic absorption performance by allowing for a more uniform fiber morphology and, consequently, the formation of a more stable conductive network (Erdem et al., 2025).

The crystal structure and phase combinations of the FeMnCo-nanofiber sample were investigated in detail by XRD analysis, and the resulting diffraction pattern is presented in Figure 4. Two broad diffraction peaks characteristic of polyacrylonitrile (PAN), used as the polymer matrix, were identified in the diffraction pattern. The first of these peaks is observed in the range of approximately 10–20° and corresponds to the (110) plane of carbon, and the second is located in the range of 25–34° and represents the (002) plane of carbon (Dong et al., 2022; Kahraman et al., 2018). These broad peaks confirm the presence of amorphous and semi-crystalline regions of PAN and also reveal the irregular packing structure of the carbon chains. In addition to the peaks belonging to PAN in Figure 4, sharp diffraction peaks specific to the FeMnCo alloy phases are also observed. This indicates the presence of metallic alloy phases in the nanofiber structure obtained by the electrospinning method. In particular, the coexistence of peaks corresponding to the martensite and austenite phases of the FeMnCo alloy in the diffraction pattern is striking. As reported by Sarı and Kırındı (2010), three different crystal structures can be found stable in the FeMnCo alloy under appropriate heat treatment conditions: α′-martensite with a BCC crystal structure, ε-martensite with a HCP crystal structure, and γ-austenite with a FCC crystal structure. Of these phases, α′-martensite, in particular, stands out as the phase that determines the ferromagnetic properties of the alloy due to its high magnetic moment.

In the diffraction pattern seen in Figure 4, three distinct diffraction peaks corresponding to the (311), (110), and (200) planes of the α′-martensite phase (Wang et al., 2018), the (111), (200), and (220) planes of the γ-austenite phase (Wang et al., 2020), and the diffraction peak corresponding to the (002) plane specific to the ε-martensite phase are clearly defined (Sarı & Kırındı 2010). These results indicate the coexistence of a triple phase in the nanofiber structure and the high microstructural diversity of the material. In addition, the coexistence of different crystalline phases can create synergistic effects on the mechanical strength, electrical conductivity, and electromagnetic wave absorption capacity of the material. In this context, the obtained XRD results reveal that the FeMnCo-nanofiber composites provide a multiphase microstructure optimization in terms of both structural and functional properties.

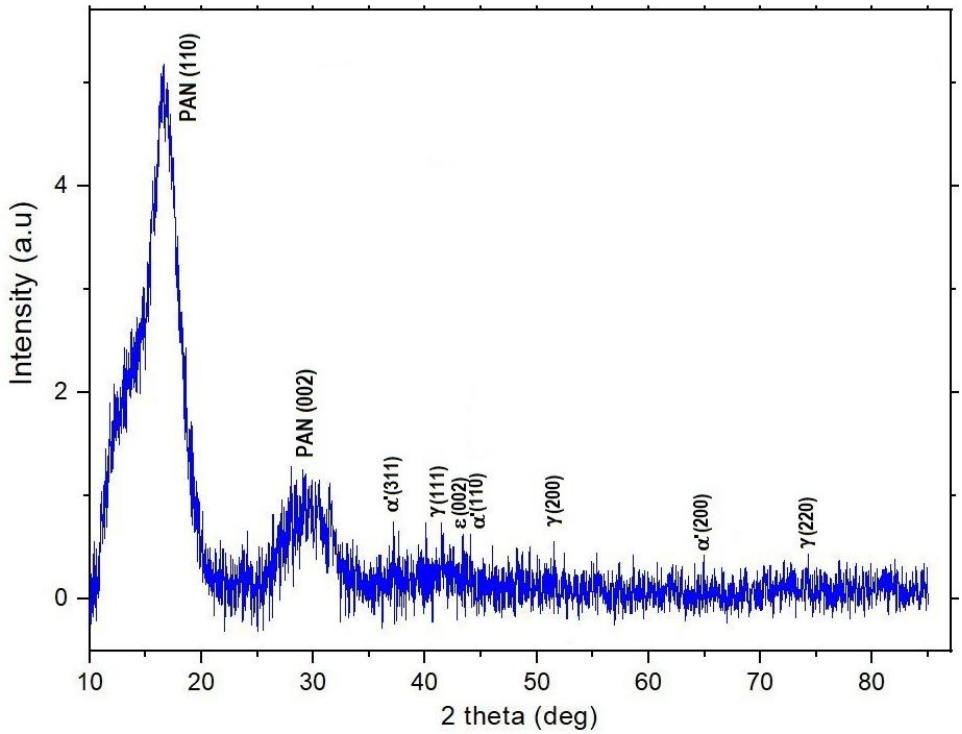

Figure 4. X-ray pattern of FeMnCo-nanofiber

Electromagnetic Absorption Performance

The EM wave absorption properties of the FeMnCo-doped nanofiber composite were evaluated using reflection loss (RL) values obtained in the frequency range of 8–18 GHz. As shown in Figure 5, the measured RL values are generally below the -20 dB level across both the X-band (8–12 GHz) and Ku-band (12–18 GHz). In literature, a limiting value of -10 dB is defined as the minimum acceptable performance criterion demonstrating that the material can absorb at least 90% of electromagnetic waves (Li et al., 2018; Ruiz-Perez et al., 2022). The values below -20 dB obtained in this study indicate that the composite can achieve high-efficiency EM wave absorption. The highest absorption performance of the nanofiber sample with a thickness of 1.2 mm was achieved with an RL value of -67.59 dB measured at a frequency of 15.40 GHz. This magnitude represents almost complete absorption at the relevant frequency, indicating that the reflection of EM waves from the material surface is negligible. As stated in the literature, for the electromagnetic absorption mechanism to be effective, the incident wave must enter the material with the lowest possible reflection (Kim et al., 2023). This is related not only to the low RL value but also to the impedance matching (Erdem et al., 2025).

Dong et al. (2022) carbonized PAN nanofibers produced by electrospinning by heat treatment and achieved a minimum RL value of -12.75 dB in the Ku band. Compared to our study, the PAN nanofiber doped with FeMnCo alloy in this study showed a significant performance improvement compared to the previous study, reaching RL values of -20 dB and below in both the X and Ku bands. This result indicates that the FeMnCo doping significantly improves the EM wave absorption capacity of PAN nanofibers. The incorporation of FeMnCo alloy particles into the composite indicates that dielectric loss and magnetic loss mechanisms are activated together in electromagnetic wave absorption (Erdem et al., 2025; Xu et al., 2024). FeMnCo is a multi-component alloy that combines high electrical conductivity and strong ferromagnetic properties. Conductive alloy particles dispersed within the fiber matrix extend the path of incident electromagnetic waves within the material, amplifying multiple scattering and surface polarization effects, thereby increasing dielectric losses. Dielectric loss occurs when a portion of the electromagnetic wave's energy is converted into electric current as it passes through the material and is converted into heat due to the material's internal resistance (Xu et al., 2024).

In terms of magnetic losses, the ferromagnetic nature of Fe and Co elements, along with the ferromagnetic properties of the FeMnCo alloy (Sarı & Kırındı, 2011), can lead to hysteresis losses, magnetic resonance, and eddy current losses within the material (Erdem et al., 2025). In such materials exposed to a changing magnetic field, the constant realignment of the internal magnetic field to match the external field consumes energy; this energy loss leads to the conversion of electromagnetic waves into thermal energy, thus effective absorption (Xu et al., 2024). In conclusion, the superior EM wave absorption performance observed in FeMnCo doped PAN nanofiber can be explained by the synergistic effect of high impedance matching, multiple scattering effect, and combined dielectric–magnetic loss mechanisms. These findings suggest that metallic alloy reinforcement is an effective strategy to optimize EM wave absorption in nanofiber-based polymer composites.

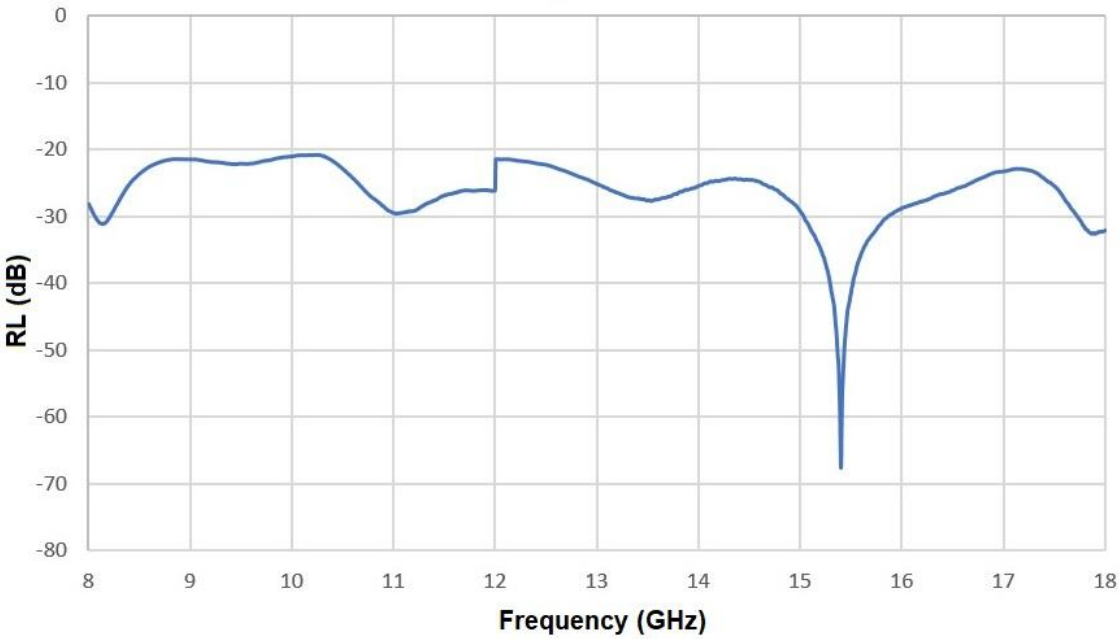

Figure 5. RL curve of FeMnCo-nanofiber in the 8–18 GHz range

Conclusion

In this study, the morphological, structural, and electromagnetic wave absorption properties of FeMnCo alloy-doped PAN nanofiber were systematically investigated. SEM analyses revealed that the electrospun nanofibers exhibited a thin diameter (200–400 nm), a high aspect-to-diameter ratio, and a three-dimensional network-like morphology. This morphology, thanks to the high specific surface area and multiple scattering mechanisms, allowed electromagnetic waves to travel longer distances within the material and increased energy losses. XRD results showed that the composite structure contained amorphous and semi-crystalline regions of PAN, as well as α'-martensite, γ-austenite, and ε-martensite phases of FeMnCo alloy. This microstructure is believed to enhance both the electrical conductivity and magnetic properties of the material, thereby enhancing its electromagnetic absorption capacity.

EM absorption performance evaluations revealed that FeMnCo-PAN nanofiber composites exhibit reflection loss values below -20 dB in the frequency range of 8–18 GHz and reach a maximum RL value of -67.59 dB at 15.40 GHz. These values demonstrate that the material can achieve highly efficient EM wave absorption in both the X and Ku bands. The superior performance achieved can be explained by the high impedance matching provided by the FeMnCo alloy doping, the multiple scattering effect caused by the conductive particles, and the synergistic effect of simultaneously activating dielectric–magnetic loss mechanisms.

In conclusion, FeMnCo-doped PAN nanofiber composite stand out as lightweight, flexible, and manufacturable materials that exhibit high electromagnetic wave absorption capacity over a wide frequency range. These properties give these composites a high potential for use in advanced technology applications such as electromagnetic interference shielding, radar absorbing surfaces, and wave absorption coatings.

Recommendations

To improve the electromagnetic absorption performance of FeMnCo-doped PAN nanofiber, the use of a high-efficiency homogenizer and controlled ball mill instead of a filing method and magnetic stirrer in alloy powder preparation is recommended. This approach can positively contribute to the electromagnetic properties of the material by reducing alloy particle size and improving homogeneous distribution. Furthermore, systematic optimization of FeMnCo ratios and fiber thickness, as well as layered integration of different dielectric and magnetic phases, may further enhance absorption performance. Thermal, humidity, and mechanical strength tests can be performed to assess the material's suitability for long-term use.

Scientific Ethics Declaration

*The authors declare that the scientific ethical and legal responsibility of this article published in EPSTEM journal belongs to the authors.

Conflict of Interest

*The authors declare that they have no conflicts of interest.

Funding

*This work was supported by the Scientific and Technological Research Council of Türkiye (TÜBİTAK, 2224-A, Project No: 1919B022502481).

Acknowledgements or Notes

*This article was presented as an oral presentation at the International Conference on Basic Sciences and Technology (www.icbast.net) held in Budapest/Hungary on August 28-31, 2025.

*The authors acknowledge the support of the Scientific and Technological Research Council of Turkiye for participation in the international scientific event.

References

Abdalla, I., Cai, J., Lu, W., Yu, J., Li, Z., & Ding, B. (2023). Recent progress on electromagnetic wave absorption materials enabled by electrospun carbon nanofibers. *Carbon*, 118300.

Bayat, M., Yang, H., Ko, F. K., Michelson, D., & Mei, A. (2014). Electromagnetic interference shielding effectiveness of hybrid multifunctional Fe3O4/carbon nanofiber composite. *Polymer*, *55*(3), 936-943.

Cai, W. J., Jiang, J. G., Zhang, Z. D., Liu, Z. X., Zhang, L. J., Long, Z. K., & Bi, K. (2024). Carbon nanofibers embedded with Fe–Co alloy nanoparticles via electrospinning as lightweight high-performance electromagnetic wave absorbers. *Rare Metals*, *43*(6), 2769-2783.

Dong, S., Li, J., Zhang, S., Li, N., Li, B., Zhang, Q., & Ge, L. (2022). Excellent microwave absorption performance of PAN-based Fe/C nanofibers with low loading fillers. *Colloids and Surfaces A: Physicochemical and Engineering Aspects, 655*, 130280.

Du, C., Zhang, Y., Wan, G., Wu, L., Li, L., Mou, P., Li, L., Xiong, H., & Wang, G. (2024). Multi-interfaced FeCoNi@C/carbon cloth composites for eliminating electromagnetic wave pollution. *DeCarbon, 6*, 100065.

Huang, W., Tong, Z., Wang, R., Liao, Z., Bi, Y., Chen, Y., Wang, C., & Ma, Y. (2020). A review on electrospinning nanofibers in the field of microwave absorption. *Ceramics International*, *46*(17), 26441-26453.

Jia, Z., Lan, D., Lin, K., Qin, M., Kou, K., Wu, G., & Wu, H. (2018). Progress in low-frequency microwave absorbing materials. *Journal of Materials Science: Materials in Electronics*, *29*, 17122-17136.

Kahraman, H. T., Yar, A., Avcı, A., & Pehlivan, E. (2018). Preparation of nanoclay incorporated PAN fibers by electrospinning technique and its application for oil and organic solvent absorption. *Separation Science and Technology, 53*(2), 303–311.

Karbowniczek, J. E., Ura, D. P., & Stachewicz, U. (2022). Nanoparticles distribution and agglomeration analysis in electrospun fiber-based composites for desired mechanical performance of poly(3-hydroxybutyrate-co-3-hydroxyvalerate) (PHBV) scaffolds with hydroxyapatite (HA) and titanium dioxide (TiO_2) towards medical applications. *Composites Part B: Engineering, 241*, 110011.

Kim, S. H., Lee, S. Y., Zhang, Y., Park, S. J., & Gu, J. (2023). Carbon-based radar absorbing materials toward stealth technologies. *Advanced Science*, *10*(32), 2303104.

Liao, Z., Ma, M., Bi, Y., Tong, Z., Chung, K. L., Li, Z., Wang, S., Yu, H., & Zhong, X. (2022). MoS2 decorated on one-dimensional MgFe2O4/MgO/C composites for high-performance microwave absorption. *Journal of Colloid and Interface Science*, *606*, 709-718.

Li, L., Chen, Z., Pan, F., Guo, H., Wang, X., Cheng, J., Guo, Y., Zhang, X., Wang, Y., & Lu, W. (2023). Electrospinning technology on one-dimensional microwave absorbers: Fundamentals, current progress, and perspectives. *Chemical Engineering Journal, 470*, 144236.

Liu, H., Li, Y., Yuan, M., Sun, G., Li, H., Ma, S., Gu, J., & Zhang, Y. (2018). In situ preparation of cobalt nanoparticles decorated in N-doped carbon nanofibers as excellent electromagnetic wave absorbers. *ACS Applied Materials & Interfaces*, *10*(26), 22591-22601.

Liu, T., Guo, Y. F., Yan, Y. M., Wang, F., Deng, C., Rooney, D., & Sun, K. N. (2016). CoO nanoparticles embedded in three-dimensional nitrogen/sulfur co-doped carbon nanofiber networks as a bifunctional catalyst for oxygen reduction/evolution reactions. *Carbon*, *106*, 84-92.

Pan, J., Guo, H., Wang, M., Yang, H., Hu, H., Liu, P., & Zhu, H. (2020). Shape anisotropic Fe3O4 nanotubes for efficient microwave absorption. *Nano Research*, *13*, 621-629.

Ruiz-Perez, F., López-Estrada, S. M., Tolentino-Hernández, R. V., & Caballero-Briones, F. (2022). Carbon-based radar absorbing materials: A critical review. *Journal of Science: Advanced Materials and Devices*, *7*(3), 100454.

Saeed, M., Haq, R. S. U., & Yi, J. (2024). Recent advances in carbon nanotubes, graphene and carbon fibers-based microwave absorbers. *Journal of Alloys and Compounds, 5*, 1-15.

Xu, W., Liu, N., & Lu, Z. (2024). Recent progress of iron-based magnetic absorbers and its applications in elastomers: A review. *Materials*, *17*(16), 4058.

Wang, Y., Gao, X., Lin, C., Shi, L., Li, X., & Wu, G. (2019). Metal organic frameworks-derived Fe-Co nanoporous carbon/graphene composite as a high-performance electromagnetic wave absorber. *Journal of Alloys and Compounds*, *785*, 765-773.

Wang, F., Sun, Y., Li, D., Zhong, B., Wu, Z., Zuo, S., Yan, D., Zhuo, R., Feng, J., & Yan, P. (2018). Microwave absorption properties of 3D cross-linked Fe/C porous nanofibers prepared by electrospinning. *Carbon, 134*, 264–273.

Wang, Y., Wang, H., Ye, J., Shi, L., & Feng, X. (2020). Magnetic CoFe alloy@ C nanocomposites derived from ZnCo-MOF for electromagnetic wave absorption. *Chemical Engineering Journal*, *383*, 123096.

Author(s) Information

Kadir Asrin Sari
Özdemir Bayraktar Aerospace Technologies Vocational and Technical Anatolian
High School, Ankara-Türkiye

Umit Erdem
Kırıkkale Unıversity, Vocational School,
Department of Electronics and Automatıon,
Kırıkkale–Türkiye

Uğur Sari
Kırıkkale University Science and Mathematics Education Department,
Kırıkkale-Türkiye
Contact e-mail: *usari05@yahoo.com*

To cite this article:

Sari, K.A., Erdem, U., & Sari, U. (2025). Fabrication and characterization of FeMnCo/Nanofiber for radar absorbing material by electrospinning. *The Eurasia Proceedings of Science, Technology, Engineering and Mathematics (EPSTEM), 36,* 39-47.

The Eurasia Proceedings of Science, Technology, Engineering & Mathematics (EPSTEM)
ISSN: 2602-3199

The Eurasia Proceedings of Science, Technology, Engineering and Mathematics (EPSTEM), 2025

Volume 36, Pages 48-58

ICBAST 2025: International Conference on Basic Sciences and Technology

Cutting-edge Global Technologies for Extraction and Processing of Critical and Strategic Raw Materials: A Review

Yoan Hristov
University of Mining and Geology "St. Ivan Rilski"

Vessela Petrova
University of Mining and Geology "St. Ivan Rilski"

Abstract: To some extent, each country defines critical minerals differently, but in general, they are strategic commodities that have no substitutes, that are mined and processed in a similar way in the relevant regions of the world, and that encompass the raw materials needed to produce advanced technological products such as renewable energy equipment, electronics, batteries, and electric vehicles. In recent years, the global mining industry has had to deal with increasing public pressure to adopt more sustainable practices and to cope with growing environmental and social demands. The rise of digital transformation, fuelled by advances in artificial intelligence, blockchain, big data, the Internet of Things, robotics, 3D printing, nano- and biotechnology, quantum computing, network algorithms, machine learning, and other emerging technologies, presents a unique opportunity for the mining industry to innovate and improve its productivity. These technologies can enhance operational efficiency, reduce environmental impact, improve the sustainability of production chains, and encourage more responsible resource extraction.

Keywords: Critical raw materials, Technologies, Mining, Extraction, Processing

Introduction

In recent years, the demand for critical and strategic raw materials has been steadily growing, due to the role of these raw materials in the production of clean energy, modern digital technologies, defence industry equipment and modern technological products. Other key drivers influencing the increased demand for these elements are the escalating geopolitical tension, environmental regulations and the emerging resource nationalism in recent months. Therefore, ensuring a secure, sustainable and efficient supply of these important critical and strategic raw materials is becoming a national and global priority.

Table 1. Global lithium production by country (Statista.com, 2025)

Country	Metric tons
Australia	88,000
Chile	49,000
China	41,000
Zimbabwe	22,000
Argentina	18,000
Brazil	10,000
Canada	4,300
Namibia	2,700
Portugal	380

Raw materials containing lithium, cobalt, nickel, rare earth elements, which are essential for the production of batteries for electric cars, wind turbines, semiconductors, and at the same time have some other applications in the high-tech sector, have been in particular demand recently (European Commission, 2023). This growing demand is reflected in the global distribution of lithium production, which also underscores the strategic dominance of a limited number of countries in the supply chain (Table 1).

The geopolitical implications of lithium resource concentration are underscored by this data, which also highlights the urgent need for technological innovation and the deployment of advanced methods to ensure supply chain resilience. In a similar vein, silicon-another critical raw material essential for semiconductors, electronics, and clean energy systems-warrants close examination. Understanding its global production landscape is equally crucial for assessing supply chain security and technological readiness (Table 2).

Table 2. Global silicon production by country in 2024 (Statista.com, 2025)

Country	Production (1,000 metric tons)
China	7400
Russia	520
Brazil	390
Norway	300
Kazakhstan	137
Malaysia	130
France	110
Iceland	90
Bhutan	80
Germany	60
India	60
Canada	50
South Africa	50
Spain	45
Australia	40
Poland	30
Other countries	208

The overwhelming concentration of silicon production in a small number of nations, as indicated in Table 2, emphasizes the significance of technological innovation and digital resilience to lessen reliance and enhance strategic autonomy. Some traditional methods of raw material extraction and processing, such as the well-known energy-intensive approaches of pyrometallurgy and hydrometallurgy, have recently begun to be considered environmentally and economically unsustainable (Ali et al., 2017). In this regard, it is quite logical that scientific research and subsequent industrial innovations are directed towards more advanced modern technologies such as bioleaching, extraction of materials with ionic liquid solvents, deep-sea mining, resource modelling using AI technologies, as well as some plasma separation systems (Binnemans et al., 2013; Padinhattath et al., 2025; Quijada-Maldonado et al., 2020; Saldaña et al., 2022, 2023) Although these new technologies are quite young, they are still promising and can bring better efficiency, reduce the environmental footprint of activities, and also provide an opportunity to use such unconventional sources as electronic waste and tailings.

Major global strategic frameworks, such as the European Raw Materials Alliance Declaration and the US Department of Energy's Critical Materials Strategy, also emphasize value chains that need to be developed through the introduction of modern innovation in supply chains. At the same time, the importance of taking into account the principles of the circular economy and the use of extracted resources in a closed loop to ensure sustainability is also emphasized. According to the declaration of the European Raw Materials Alliance, raw materials are crucial for European industrial ecosystems, contributing over €2 trillion in added value and employing more than 30 million Europeans. They are essential for achieving the European Green Deal and the EU's green and digital transitions (European Raw Materials Alliance (ERMA), n.d.). For its part, the US Department of Energy's Critical Materials Strategy has a goal to foster scientific innovation and develop technologies that will ensure resilient and secure critical mineral and material supply chains independent of resources and processing from foreign processing and resource control (U.S. Department of Energy, n.d.).

These initiatives are designed to lessen EU reliance on important critical raw materials from third countries and to gain the US increased capacity for domestic production for reasons of national security and economic sustainability. The ERMA and DOE projects are designed to support creation of a more sustainable and environmentally responsible supply chain for critical minerals by focusing on sustainable sourcing and reuse technologies and policies. Technologies that enable low-emission recovery, enhanced traceability, and adaptive mining systems are not only altering the technical environment but also the geopolitics of raw material access.

As demand for these materials grows, especially for technologies like electric vehicles, renewable energy, and high-tech electronics, the development of advanced and sustainable methods of extraction and processing become increasingly important.

Objective and Research Question:

The objective of this review is to identify, categorize, and critically assess cutting-edge technologies for the sustainable extraction and processing of critical and strategic raw materials. The analysis focuses on evaluating their sustainability, scalability, and compatibility with digital transformation and climate objectives, with particular attention to advanced robotics, artificial intelligence, and automation systems as core enablers of Mining 4.0. Emerging methods such as bioleaching, ionic liquids, deep-sea mining, and plasma separation are also considered in the background scope. Ultimately, reducing dependence on critical materials and creating resilient industrial ecosystems depends on the successful development, testing, and deployment of these innovations in industrial activity.

Guided by this objective, the central research question addressed in this paper is: What are the most promising emerging technologies for sustainable and efficient extraction and processing of critical and strategic raw materials, and how do they align with global digitalization and environmental goals?

Method

We conducted a structured narrative review drawing on Scopus, Web of Science, ScienceDirect and IEEE Xplore for the period 2010–2025 (emphasis on 2020–2025). The search strategy combined three main dimensions: materials such as lithium, rare earth elements, cobalt, nickel, and silicon; technologies including advanced robotics, artificial intelligence, and automation systems; and, as a background scope, emerging methods such as bioleaching, ionic liquids, deep-sea mining, and plasma separation. To ensure alignment with sustainability considerations, additional qualifiers were used, including life cycle assessment (LCA), energy and water use, technology readiness level (TRL), and scale-up potential. Database searches were complemented with backward and forward citation chasing as well as authoritative reports from standards bodies and government agencies.

Sources were included if they were peer-reviewed or otherwise authoritative, contained explicit process descriptions, and were directly relevant to the extraction or processing of critical or strategic raw materials. Excluded were purely conceptual papers without process detail, duplicate publications, and superseded reports. Rather than aiming for exhaustive count-based screening, we applied theoretical saturation and triangulated evidence across multiple sources for each technology. For every case, we extracted information on the input material, process type, Technology Readiness Level (TRL 1–9), application scale (laboratory, pilot, demonstration, or industrial), and sustainability indicators such as energy demand, water consumption, reagent use and toxicity, recovery rates, and waste generation. A quantitative meta-analysis was not feasible due to heterogeneous reporting; therefore, results were synthesized thematically and summarized in a TRL × sustainability scorecard.

Cutting-edge Technologies for Extraction and Processing Operations

The cutting-edge technologies for mining and processing of critical and strategic raw materials, which are discussed in this chapter, include three distinct categories – high-tech robots, artificial intelligence and advanced automation systems. Their application in industrial practice can lead to increased efficiency, on the one hand, and safety of mining operations, on the other. The introduction of such technologies in mining has the potential to revolutionize the industry by reducing costs, increasing productivity and, last but not least, minimizing environmental impact.

In this regard, resource engineering is gradually but steadily entering a new transformative era thanks to new generation technologies for mining and processing of raw materials important for industrial independence. In addition to improving operational efficiency and basic safety, advances in high-tech robots, artificial intelligence and advanced automation systems are leading to the rationalization of value chains throughout the mineral industry. To optimise the extraction and processing of critical materials, which processes are characterized by

high complexity and labour intensity, the introduction of new digital technological tools into operation is essential.

Advanced Robotics in Harsh Environments and Safety

In recent years, there has been a wider application of robotic systems in practice, especially in dangerous and inaccessible environments, which include deep underground mines, oceanic crusts and polar regions. To increase the safety of exploration activities in such areas, exploration robots are used, the application of which helps to improve monitoring and, accordingly, minimize the risks to the lives of personnel. At the same time, such robots are particularly applicable in the study of underground galleries, in which chemical leaks may occur, and the same applies to ensuring the safety of archaeological excavations (Liu et al., 2015). Complex robotic systems used in mining operations are usually equipped with modern equipment, including cameras and sensors for collecting information, which allows the transmission of real-time feedback to the operators serving them. At the same time, modern robots can be programmed to work independently and also be guided remotely, as these capabilities improve productivity and safety in the work environment. Automated robotic systems are undergoing constant development and over time become more complex and sophisticated, integrating the latest hardware and software innovations, resulting in improved operational efficiency and reliability. These robotic systems increasingly integrate artificial intelligence, enabling real-time situational assessment and autonomous decision-making based on sensor data (Kokkinis et al., 2024). Some of the devices now also have built-in artificial intelligence, which allows them to make their own assessment of the current situation and make independent decisions based on real-time data analysis. Research data shows that the implementation of automated mining systems in practice leads to improvements in overall operational productivity, while at the same time significantly reducing the possibility of human error.

For example, the Minebot (see Figure 1), which was developed at the University of Leeds, has the ability to reconfigure itself to the environment in which it is located and is designed specifically for underground exploration with the option to pass through narrow boreholes. The weight of the robot is about 2.7 kg, which allows it to function in tunnels up to 200 m long.

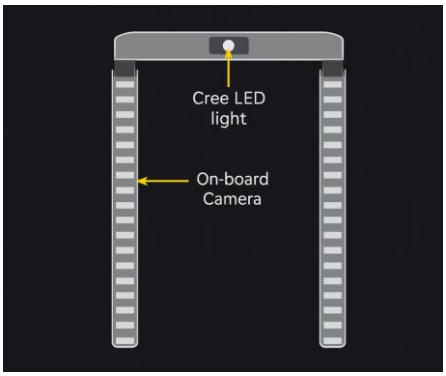

Figure 1. Schematic visualization of the fully deployed configuration of the *Minebot*, created by the authors based on technical descriptions and imagery in Liu et al. (2015).

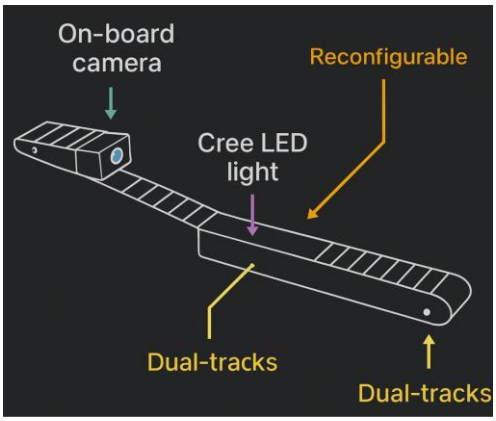

Figure 2. Schematic visualization of the Minebot in snake-like configuration, created by the authors based on technical descriptions and imagery in Liu et al. (2015).

The specialized design allows it to move on two rails and the so-called snake-shaped transformation (see Figure 2), through which the robot is able to overcome various obstacles (Liu et al., 2015). Optionally, this robot, as well as others in its class, can be equipped with 3D ceramic-packaged multifunctional sensors, intelligent navigation systems and an adaptive high-speed wireless network, which allows it to both communicate with the surface and make decisions autonomously based on collected real data. The high level of autonomy and adaptability of this Minebot robot makes it a valuable tool for effective and operational underground exploration.

By taking on dangerous tasks such as navigation, mapping and manipulation, autonomous robots designed for underground mining environments aim to improve safety. One such robot, named Julius (named after engineer Julius Ludwig Weisbach), is designed for underground operations. It uses a UR5 robotic arm (see Figure 3), sophisticated optical sensors and a four-wheeled mobile platform to communicate with the IoT infrastructure and control smart sensor boxes (SSBs).

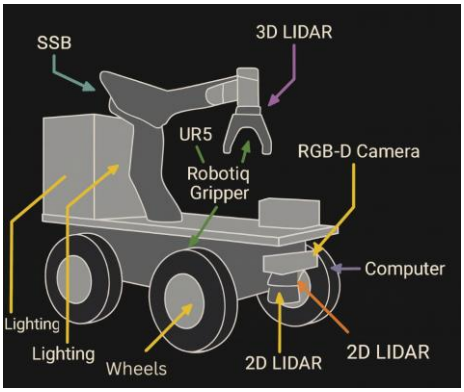

Figure 3. Schematic visualization of the Julius robot, created by the authors based on technical descriptions and imagery in Lösch et al. (2018).

Visual odometry and sophisticated sensor fusion are used to ensure more accurate navigation in the difficult-to-navigate underground passages, as GNSS signals are not available at such depths. Initial tests have yielded good results and show that the robot can navigate autonomously even in the presence of mud in the passages, while also being able to create 2D occupancy grid maps when the relevant area is sufficiently well lit (Lösch et al., 2018). The mapping results that the robot demonstrates are encouraging given the challenges that the dark and humid and almost liquid environment presents. The robot's operating time reaches three to four hours, and its compact design allows it to reach extremely narrow trenches or gaps. With the help of a robotic arm, the robot's manipulation capabilities are also increased, which gives it better chances of effective interaction with the components of the surrounding intelligent infrastructure. Such and similar systems will be essential for the development of Mining 4.0, as scientists' efforts are aimed at generally improving the autonomous functionality of robots, the precision of navigation controllers, and improving manipulation capabilities for working in complex, inaccessible and dangerous environments.

To improve further the autonomy and safety of robotic platforms in similar challenging environments, advanced terrain understanding becomes paramount. A major factor in this is traversability analysis-how a robot can evaluate and estimate the navigability of a terrain through sensory input and modelling techniques. Therefore, traversability analysis is an integral part of advanced robotics in harsh environments that directly impacts the safety and efficiency of UGVs. Xue, Fu, Xiao, Fan, Zhao & Dai (2023) proposed a new LiDAR-based terrain modelling method that gives a solution to problems posed by complex terrains-rugged off-road environments. Unlike traditional single-frame methods, the proposed approach exploits multi-frame information fusion through Normal Distributions Transform (NDT) mapping to produce stable and complete models of the terrain. Spatial-temporal Bayesian Generalized Kernel (BGK) inference and bilateral filtering further improve accuracy as well as edge preservation in predicting terrain elevation—apparently important for unobserved regions to be modelled reliably. Geometric connectivity between cells in the terrain is used in analysing traversability with an evaluation and an assignment of travel costs; therefore, slopes, ditches, and road curbs are distinguished from one another. Experiments with available datasets and in custom off-road scenarios show much better performance—state-of-the-art realtime modelling of terrain plus traversability analysis. The generated cost maps provide richer information for path planning. It allows UGVs to select safer and more efficient routes (Xue et al., 2023). It improves the robustness of autonomous navigation in dynamic and unstructured environments. Besides, it contributes a lot to enhancing operational safety. This is a valuable advancement in robotics for harsh

environments. Future work will focus on negative obstacle detection and computational efficiency improvements.

LiDAR-based terrain and traversability model utilising may have valuable applications in mining since mines are generally located in rough terrains and require vehicles to be operated remotely for safety as well as efficiency. The laser scanning allows enough time of assessment of the setup environment of the mine despite several adverse challenges (Kumar Singh et al., 2023). Providing better accuracy in drilling, mapping, and ore handling, these autonomous and semi-autonomous robots keep human operators out of harm's way. Robotic platforms can map ore bodies in real-time with minimal disturbance to surrounding geology by being equipped with LIDAR as well as multispectral sensors. These robots are capable of navigating through hazardous, confined spaces that are unsafe for people to enter. By boosting output and lowering worker risks, this technology is completely changing the mining sector. Employing robots to perform these duties can also help businesses cut down on downtime brought on by safety concerns and the expenses related to accidents and injuries. All things considered, the use of semi-autonomous and autonomous robots in mining operations is opening the door to a more secure and productive sector.

In summary, advanced robotics improve operational safety and efficiency in challenging mining environments by enabling remote monitoring, autonomous navigation, and manipulation. However, limitations remain in terms of cost, robustness, and scalability, which require further research and development.

Artificial Intelligence and Automation Systems for Predictive Mining and Mineral Processing

Artificial intelligence has significantly enhanced predictive maintenance in the mining and mineral processing industry. Machine learning algorithms can facilitate the prediction of equipment failure, optimise scheduling of maintenance activities, and improve operational performance. Structured data from sensors together with unstructured data like logs of previous maintenance activities are used in current predictive models for estimating the Remaining Useful Life (RUL) of equipment (Dayo-Olupona et al., 2023). Lessons under supervised learning and unsupervised learning as well as deep learning include anomaly detection and fault diagnosis as well as degradation pattern prediction. For instance, Random Forests and Neural Networks among other ML models have given high accuracies towards predicting failures related to equipment and optimisation of maintenance strategies. Internet-of-Things (IoT) integrated with cyber-physical systems leads to real-time monitoring while digital twins enable support for proactive maintenance planning. Challenges about data quality, cost-effectiveness, and scalability remain even with all these advancements. Future research should therefore focus on model adaptability, external factors, and real-time decision-making to unleash the full potential of AI in predictive maintenance. This will drive the mining industry to work better, have less downtime, and operate sustainably.

Beyond artificial intelligence, advanced automation systems—including autonomous haulage systems (AHS), automated drilling rigs, and robotic inspection drones—are also reshaping the mining landscape (Cerna et al., 2023). These systems, integrated with AI analytics, enable round-the-clock operations, improve workplace safety, and reduce human error. Automation hardware combined with predictive software tools ensures not only efficiency but also the agility required to respond to changing geological conditions and operational demands.

The training of powerful artificial intelligence requires high-quality, consistent, and comprehensive datasets. The mining industry, however, mostly works with fragmented and noisy data. In addition to this, the cost of implementing the AI solution –hardware and software plus the skilled personnel to operate– will impose a big burden on small operations. Another problem is scalability: when built at a particular site but then applied to different geological conditions and different operational environments. Further study should first focus on creating adaptable AI models capable of learning external factors including environmental variations, market dynamics, and regulatory constraints. This will facilitate real-time decision-making supported by AI to enhance predictive maintenance in reducing downtime and achieving optimal utilization of resources. With the help of cloud computing development joined to IoT and digital twins, AI will assist in real-time monitoring as well as immediate adjustments in mining operations; thus improving cost-effectiveness and scalability in different mining scenarios (Yang et al., 2024). Therefore, such a challenge has to be accomplished toward more sustainable, efficient, resilient practices through the full potential breakthroughs promised by AI in predictive mining and mineral processing.

Artificial Intelligence and Machine Learning have already proven their considerable potential in the sphere of predictive mining and mineral processing by enhancing data analysis and decision-making capabilities. Indeed,

ML techniques could be applied at any stage within the scope of mineral exploration activities, starting from a regional-scale targeting exercise down to resource definition with the use of complex geoscientific datasets—geochemical, geophysical, or hyperspectral (Davies et al., 2025). For instance, Random Forest algorithms have so far been among the best performers in geological parameter prediction as well as mineral prospectivity mapping exercises when compared to other ML models in terms of accuracy and computational efficiency. It is important to note, however, that the usability of ML tools depends on the interdisciplinary cooperation between geoscientists and data scientists through novel techniques applied to prepare data as well as human creativity in addressing special complexity in geoscientific challenges. Technological development amalgamated with human expertise is essential for attaining sustainable exploration success and improvement in discovery rates of critical mineral deposits.

Artificial intelligence (AI) has made a practice of being used as a revolutionary tool in predictive mining as well as mineral processing by throwing unique solutions for optimisation and consistency improvements. Applications of AI to concentration of minerals have thus far exhibited immense potential with gravity-based separation, density-based separation, magnetic and electric separation, and sensor-based sorting. Neural networks (NNs), support vector machines (SVMs), and random forests (RFs) (Gomez-Flores et al., 2022). Machine Learning models have so far been applied in prediction concerning grading, recovery, or efficiency in separation. Since multilayer perceptron NNs are supervised learning models that were used to predict recoveries in Falcon concentrators they can be used for the optimisation of operating parameters relating to magnetic separators. Sensor-based sorting is also made more accurate through machine vision techniques under problematical conditions through Artificial Intelligence. Difficulties stay, as there is a need for larger datasets and better instrumentation integration hydrodynamic modelling with AI tools. A future study should be about the application of AI to turbulence control and drag optimisation in addition to open-access dataset development for improved predictive capability and innovation facilitation in mineral processing.

An important use of deep learning models is that involving Convolutional Long Short-Term Memory (ConvLSTM) networks for real-time monitoring of the quality of mineral flotation froth (Bendaouia et al., 2024). The spatial and temporal information from video sequences representing the flotation process is input simultaneously with these models to predict chemical composition grades for minerals so that adjustment of flotation parameters can be done accurately, thereby improving mineral recovery rates. Traditionally implemented laboratory analysis or even X-ray fluorescence (XRF)-based monitoring would have high running costs and maintenance issues as well as latency problems that these AI approaches could solve since they are low-cost, low-maintenance, real-time insights.

AI can be applied in differential flotation, a complex process in which several mineral products such as zinc, copper, iron, and lead are derived. As a result of froth characteristic analysis (texture and bubble size) accurate model-based control optimisation can be ensured for optimal flotation performance with reduced reagent consumption—increased profitability with improved environmental sustainability (Bendaouia et al., 2024). The AI industrial models developed herein also ensure flexibility and consistency when implemented within on-premises architectures to provide the needed information for dynamic process control, which depicts the Mineral Process Automation as an evolution towards Industry 4.0 technologies.

Having laid a firm foundation in improved results of controlling flotation with AI input, these enhancements speak to the larger transformative power that artificial intelligence has over the mining sector. As automation further develops, Artificial Intelligence is being integrated towards predictive maintenance and strategy decisions considerably enabling nimbler, informed by data and environmentally sustainable mineral processing operations across the complete value chain. Artificial intelligence (AI) has, therefore, increasingly come into play in predictive mining and mineral processing across the spectrum to improve efficiency and effectiveness decision making. Real-time insights and predictive maintenance are enabled by AI from all the data being collected in operations within the mining industry. For example, Vale’s investments included an Artificial Intelligence Centre based in Brazil that monitors AI initiatives being piloted globally within its extensive operations for process optimisation and downtime reduction that centralised, AI-driven systems might bring (Storey, 2025). These applications show how transformative artificial intelligence can become toward the improvement of equipment reliability as well as operational safety.

According to Storey (2025), "digitalization technologies, such as artificial intelligence and the Internet of Things (IoT) use those data to drive innovation, increase operational efficiency and productivity, lower costs, improve safety, increase overall business agility and unlock new revenue streams". All of these advancements point to a paradigm shift in mining operations management as well as a technological shift, putting intelligent systems at the centre of an industrial transformation that is resilient, sustainable, and value-driven.

Recent advances in artificial intelligence (AI) have radically transformed the future of mining and mineral processing. In effect, AI will offer highly creative solutions to hitherto longstanding problems. An example involves the integration of neuro-symbolic AI together with knowledge graphs, balancing between-based machine learning models and expert geological reasoning (Chen et al., 2025). More particularly, this hybrid methodology exploits large language models (LLMs) for extracting those symbolic rules embedded within geology literature and then dynamically knowledge graphs that reflect domain-specific insights.

They are incorporated into the machine learning workflow; hence, guiding the predictions to conform to geological principles as well as improving accuracy and transparency. For example, regarding copper deposits, neuro-symbolic AI models have been tested for their ability to indicate important geochemical elements Cu Fe and S with coherent explanations on mineralization patterns. This degree of interpretability is augmented further with tools such as SHAP (SHapley Additive exPlanations) values by which the importance of individual features concerning predictions can be measured (Chen et al., 2025). Incorporating expert knowledge into AI models improves predictive accuracy and increases trust among geoscientists, supporting more sustainable mineral exploration and processing. Such breakthroughs make Artificial Intelligence the building block of insightful, value-based business metamorphosis.

Artificial intelligence does not only improve its prediction validation, but geoscientists trust and validate it too, thereby making it a transformer in sustainable mineral exploration and processing. A key feature of the Multi-Model Decision System (MMDS) is that domain knowledge has been injected into AI systems for better capability to emulate complex geological processes and to more accurately predict mineral prospectivity (Soltani et al., 2025). The MMDS system applies state-of-the-art deep learning models such as Deep Neural Networks (DNN), Deep Belief Networks (DBN), Decision Forests (DF), and 1D Convolutional Neural Networks (1D-CNN) to create individual prediction synergies by lowering uncertainty, resulting in strong spatial patterns for mineralization.

The decision-making engine inspired by the MARCOS model weighs based on the performance of each model. The better models naturally get to have a significantly large effect on final predictions. This approach improves not only predictive accuracy but also aligns with geoscientific principles and therefore builds trust among professionals in this discipline. These prospectivity maps, which come out of MMDS have shown much better spatial coincidence with known mineral deposits and hence could be considered very good tools for finding lower risk exploration targets (Soltani et al., 2025). Such development put artificial intelligence as an essential input factor for informed, value-based decisions in mineral exploration leading to better and more efficient resource management.

Scoring Method

Each technology is rated on Efficiency, Sustainability, Scalability (1–5; higher is better) using extracted indicators (energy kWh/t, water m^3/t, reagents/toxicity, recovery %, waste reduction %, CAPEX/OPEX class, pilot/industrial evidence). Readiness is assessed using the Technology Readiness Level (TRL, 1–9). For compactness in Table 3, TRLs are grouped into three bands: Pilot (TRL 5–6), Applied (TRL 7–8), and Mature (TRL 9). Assignments are based on reported scale (lab/pilot/plant), evidence of operational deployments, and independent corroboration; where sources diverge, the lower defensible TRL is used. Technologies at ≤ TRL 4 are flagged as Pre-pilot in the text and omitted from Table 3. The following comparative table synthesizes these families together with robotics/AI/automation.

Table 3. Comparative Assessment of Technologies for Sustainable Resource Extraction

Technology	Efficiency	Sustainability	Scalability	Readiness band (mapped TRL)	TRL (1-9)
Advanced robotics	High	Medium	Medium	Applied (TRL 7-8)	7-8
Artificial intelligence	Medium	High	Medium	Applied (TRL 7-8)	8
Automation systems	High	Medium	High	Mature (TRL 9)	9

Legend: High (H) = 4–5; Medium (M) = 3; Low (L) = 1–2 (rating scale: 1–5)

TRL bands follow standard EC/NASA definitions. Individual TRLs reflect the most conservative interpretation of the available evidence.

In conclusion, AI technologies contribute to more efficient and sustainable mining operations by enabling predictive maintenance, resource mapping, and process optimisation. Remaining challenges concern data quality, scalability limitations, and the effective integration of domain-specific expertise.

Digital and autonomous technologies act as enablers rather than substitutes for process innovation. Policy instruments (e.g., localization incentives, reporting standards for energy/water, and pilot-to-demo financing) accelerate the transition from **TRL 4–6** to **TRL 7–9**. For operators, prioritizing sensor-based sorting, AI-assisted control, and selective separations typically yields early energy/water gains while preparing flowsheets for circular routes (e.g., black mass recycling).

Evidence across technologies is heterogeneous and often limited to pilot scale; sustainability indicators (energy, water, reagents, recovery) are inconsistently reported. We therefore used a structured narrative synthesis without PRISMA counts, focusing on triangulation. Future work should standardize reporting, develop open datasets for benchmarking AI-enabled control, and track TRL progression from pilot to commercial deployments.

Conclusion

The global demand for critical and strategic raw materials is driven by advances in green technologies, digitalization, and evolving geopolitical dynamics. This has put a lot of pressure on the mining and processing sectors to come up with new methods. This review examined how advanced robotics, artificial intelligence, and automation systems are transforming the extraction and processing of critical raw materials across the value chain.

Cutting-edge robotics is already improving safety and productivity in extreme mining conditions by enabling real-time surveillance, self-navigation, and exact manipulation within danger zones. At the same time, artificial intelligence has proven useful for predictive maintenance, mineral prospectivity mapping, process optimisation, and autonomous decision-making. These innovations reduce environmental effects and operating costs as well as allow the recovery of unconventional resources (e.g., electronic waste and tailings), which go straight toward the goals of a circular economy.

Digital innovation, properly matched with principles of sustainability, is an obvious path to improved efficiency, responsibility, and scalability of the extraction and processing of strategic materials. Challenges that remain, however, include problems with data quality and integration costs, in addition to system scalability and adequate interdisciplinary collaboration that have to be addressed through sustained investment leveraged by international cooperation integrated with domain expertise and data science.

Ultimately, resilience and sustainability in the supply of critical raw materials depend on the continued development, deployment, and scaling of such high technologies. As digitalization is changing the face of mining activities across the world, there is a need for stakeholders to embrace a proactive and cooperative approach that will ensure technological advancement supports industrial competitiveness as well as environmental stewardship and long-term global resource security.

This review contributes to the literature by synthesizing emerging technological innovations in mining, highlighting their advantages and limitations, and identifying research gaps. It provides a comparative assessment of technologies based on efficiency, scalability, and environmental performance, offering insights for stakeholders aiming to align digitalization with sustainability goals in the mining industry.

Scientific Ethics Declaration

*The authors declares that the scientific ethical and legal responsibility of this article published in EPSTEM Journal belongs to the authors.

Conflict of Interest

*The authors declare that they have no conflicts of interest

Funding

* This research received no specific grant from any funding agency in the public, commercial, or not-for-profit sectors.

Acknowledgements or Notes

*This article was presented as an oral presentation at the International Conference on Basic Sciences and Technology (www.icbast.net) held in Budapest/Hungary on August 28-31, 2025.

*This work has been carried out in the framework of the National Science Program "Critical and strategic raw materials for a green transition and sustainable development", approved by the Resolution of the Council of Ministers № 508/18.07.2024 and funded by the Ministry of Education and Science (MES) of Bulgaria.

References

Ali, S., Giurco, D., Arndt, N., Nickless, E., Brown, G., Demetriades, A., Durrheim, R., Enriquez, M., Kinnaird, J., Littleboy, A., Oberhänsli, R., Salem, J., Schodde, R., Schneider, G., Vidal, O., & Yakovleva, N. (2017). Mineral supply for sustainable development requires resource governance. *Nature*, *543*, 367–372.

Bendaouia, A., Abdelwahed, E. H., Qassimi, S., Boussetta, A., Benzakour, I., Amar, O., & Hasidi, O. (2024). Artificial intelligence for enhanced flotation monitoring in the mining industry: A ConvLSTM-based approach. *Computers & Chemical Engineering*, *180*, 108476.

Binnemans, K., Jones, P. T., Blanpain, B., Van Gerven, T., Yang, Y., Walton, A., & Buchert, M. (2013). Recycling of rare earths: A critical review. *Journal of Cleaner Production*, *51*, 1–22.

Cerna, G. E. P., Hernández, J. R. C., Herazo, J. C. M., & Castillo, A. P. (2023). Evaluation of the overall effectiveness (OEE) of autonomous transportation system (AHS) equipment and its impact on mine design. Open pit mine case study. *Procedia Computer Science*, *224*, 468–473.

Chen, W., Zhang, J., Li, W., Que, X., Li, C., & Ma, X. (2025). Integrating neuro-symbolic AI and knowledge graph for enhanced geochemical prediction in copper deposits. *Applied Computing and Geosciences*, *27*, 100259.

Davies, R. S., Trott, M., Georgi, J., & Farrar, A. (2025). Artificial intelligence and machine learning to enhance critical mineral deposit discovery. *Geosystems and Geoenvironment*, *4*(2), 100361.

Dayo-Olupona, O., Genc, B., Celik, T., & Bada, S. (2023). Adoptable approaches to predictive maintenance in mining industry: An overview. *Resources Policy*, *86*, 104291.

European Critical Raw Materials Act-European Commission. (n.d.). Retrieved July 23, 2025, from https://single-market-economy.ec.europa.eu/publications/european-critical-raw-materials-act_en

European Raw Materials Alliance (ERMA). (n.d.). European raw materials alliance (ERMA). Retrieved May 28, 2025, from https://erma.eu/

Gomez-Flores, A., Ilyas, S., Heyes, G. W., & Kim, H. (2022). A critical review of artificial intelligence in mineral concentration. *Minerals Engineering*, *189*, 107884.

Kokkinis, A., Frantzis, T., Skordis, K., Nikolakopoulos, G., & Koustoumpardis, P. (2024). Review of automated operations in drilling and mining. *Machines*, *12*, 845.

Kumar Singh, S., Pratap Banerjee, B., & Raval, S. (2023). A review of laser scanning for geological and geotechnical applications in underground mining. *International Journal of Mining Science and Technology*, *33*(2), 133–154.

Liu, J., Ma, B.-Y., Fry, N., Pickering, A., Whitehead, S., Somjit, N., Richardson, R. C., & Robertson, I. D. (2015). Exploration robots for harsh environments and safety. *IFAC-PapersOnLine*, *48*(10), 41–45.

Lösch, R., Grehl, S., Donner, M., Buhl, C., & Jung, B. (2018). Design of an autonomous robot for mapping, navigation, and manipulation in underground mines. *2018 IEEE/RSJ International Conference on Intelligent Robots and Systems (IROS)*, 1407–1412.

Padinhattath, S. P., Shaibuna, M., & Gardas, R. L. (2025). Ionic liquids and deep eutectic solvents: A brief prologue and their applications in sustainable extraction and separation processes. *Journal of the Indian Chemical Society*, *102*(4), 101638.

Quijada-Maldonado, E., Olea, F., Sepúlveda, R., Castillo, J., Cabezas, R., Merlet, G., & Romero, J. (2020). Possibilities and challenges for ionic liquids in hydrometallurgy. *Separation and Purification Technology*, *251*, 117289.

Saldaña, M., Jeldres, M., Galleguillos Madrid, F. M., Gallegos, S., Salazar, I., Robles, P., & Toro, N. (2023). Bioleaching modeling-a review. *Materials*, *16*(10), 3812.

Saldaña, M., Neira, P., Gallegos, S., Salinas-Rodríguez, E., Pérez-Rey, I., & Toro, N. (2022). Mineral leaching modeling through machine learning algorithms − a review. *Frontiers in Earth Science*, *10*.

Soltani, Z., Hassani, H., & Esmaeiloghli, S. (2025). Multi-model decision system: An ensemble deep learning model to enhance predictive power in mineral prospectivity mapping. *Ore Geology Reviews*, *184*, 106768.

Storey, K. (2025). Digitalization in mining and the rise of the urban miner. *The Extractive Industries and Society*, *24*, 101718.

U.S. Department of Energy. (n.d.). *2021 DOE critical materials strategy. Energy.gov.* Retrieved May 28, 2025, from https://www.energy.gov/eere/ammto/2021-doe-critical-materials-strategy

Xue, H., Fu, H., Xiao, L., Fan, Y., Zhao, D., & Dai, B. (2023). Traversability analysis for autonomous driving in complex environment: A LiDAR-based terrain modeling approach. *Journal of Field Robotics*, *40*(7), 1779–1803.

Yang, F., Zuo, R., & Kreuzer, O. P. (2024). Artificial intelligence for mineral exploration: A review and perspectives on future directions from data science. *Earth-Science Reviews*, *258*, 104941.

Author(s) Information

Yoan Hristov
University of Mining and Geology "St. Ivan Rilski"
"Prof. Boyan Kamenov" Str., 1700 Sofia, Bulgaria
Contact e-mail: *yoan.hristov@mgu.bg*

Vessela Petrova
University of Mining and Geology "St. Ivan Rilski"
"Prof. Boyan Kamenov" Str., 1700 Sofia, Bulgaria

To cite this article:

Hristov, Y. & Petrova, V. (2025). Cutting-edge global technologies for extraction and processing of critical and strategic raw materials: A review. *The Eurasia Proceedings of Science, Technology, Engineering and Mathematics (EPSTEM), 36,* 48-58.

The Eurasia Proceedings of Science, Technology, Engineering & Mathematics (EPSTEM)
ISSN: 2602-3199

The Eurasia Proceedings of Science, Technology, Engineering and Mathematics (EPSTEM), 2025

Volume 36, Pages 59-72

ICBAST 2025: International Conference on Basic Sciences and Technology

Innovative Technologies for Waste Reduction in the Extraction and Processing of Critical Raw Materials

Vessela Petrova
University of Mining and Geology "St. Ivan Rilski"

Abstract: This study addresses the pressing challenge of substantial waste generation during the extraction and processing of critical raw materials (CRMs), which are essential for emerging technologies and the transition to a sustainable economy. While previous research has documented individual technologies and practices, it has often lacked an integrated, cross-regional perspective and a strategic framework for implementation. To fill this gap, this study develops an integrated conceptual model of zero-waste mining systems, informed by a systematic comparative analysis of innovative technologies and best practices from Europe, Australia, and Canada. The research adopts a mixed-method approach combining a comprehensive literature review, in-depth case studies, and a strategic SWOT analysis to evaluate the feasibility, scalability, and transferability of advanced waste-reduction technologies. Key findings demonstrate that precision mining techniques, sensor-based selective extraction, advanced flotation and leaching methods, and tailings valorization can significantly reduce waste—by up to 60%—while enhancing resource recovery and generating additional economic value. The proposed conceptual model synthesizes these practices within the circular economic framework, emphasizing the need for technological integration, supportive regulatory environments, and cross-industry collaboration. This study contributes to the literature by offering a systematic, cross-regional synthesis of innovative CRM waste-reduction strategies and proposing a transferable model that bridges the gap between descriptive case evidence and actionable strategies for sustainable mining. The findings provide both theoretical and practical insights, supporting policymakers, practitioners, and researchers in advancing circular economy principles in the CRM sector.

Keywords: Critical raw materials, Mining waste, Innovative technologies, Sustainable development

Context and Significance of the Problem

Critical raw materials (CRMs) are defined as minerals, metals, and other naturally occurring resources considered economically essential and whose supply is subject to significant risk due to geopolitical, environmental, technological, or economic factors (European Commission, 2020). According to the European Commission, the criticality of a raw material is assessed based on two primary criteria: economic importance and supply risk (European Commission, 2023). Economic importance refers to the degree to which a material is vital for strategic sectors of the economy, such as advanced manufacturing, renewable energy technologies, digital technologies, defense, and aerospace (Graedel et al., 2015). Supply risk, conversely, measures vulnerability due to concentration of production in specific countries, political instability in supplier nations, low substitutability, and limited recycling possibilities (Buijs & Sievers, 2012). The strategic significance of CRMs stems largely from their essential role in facilitating high-technology applications and enabling sustainable transitions. Rare earth elements (REEs), lithium, cobalt, and graphite exemplify this, as they are critical for batteries, electric vehicles, renewable energy infrastructure, and digital technologies (Achzet & Helbig, 2013, World Bank, 2020). For instance, lithium and cobalt are indispensable components in lithium-ion batteries, fundamental for electric vehicles (EVs) and energy storage systems, crucial elements in achieving global climate targets (World Bank, 2020). CRMs also carry geopolitical significance, influencing international trade dynamics, economic security, and national strategic autonomy (Humphries, 2019). A notable example is

China's dominance in rare earth production, historically accounting for up to 85% of global output, creating vulnerabilities for economies dependent on these materials (Kalantzakos, 2018). Such concentration enhances geopolitical leverage, enabling producer nations to exert economic and political influence globally (O'Sullivan et al., 2017). Given these circumstances, strategies to mitigate CRM-related risks have become paramount. Approaches include diversification of supply sources, development of alternative materials, increasing recycling rates, and improving material efficiency and circularity within value chains (Ali et al., 2017). Therefore, the strategic management of critical raw materials is not merely an economic issue but a multifaceted challenge encompassing environmental, technological, and geopolitical dimensions.

Waste Generation in Extraction and Processing Processes: Scale and Implications

Waste generation during mining and mineral processing activities constitutes one of the most significant environmental and ecological challenges facing contemporary industrial society. The scale of waste produced in mining and processing operations is immense, often surpassing the volume of the extracted valuable minerals by orders of magnitude (Lottermoser, 2010). For instance, according to estimates, the global mining industry generates approximately 100 billion tonnes of waste annually, comprising mainly waste rock, tailings, slag, and wastewater (Franks et al., 2021). Tailings, which are the fine-grained residues left after mineral processing, are particularly problematic due to their sheer volume and potential toxicity. Tailings are typically stored in large tailings dams or impoundments, which pose significant structural and environmental risks (Azam & Li, 2010; Santamarina et al., 2019). Incidents such as the Brumadinho tailings dam collapse in Brazil in 2019, resulting in severe environmental destruction and loss of human life, illustrate the potentially catastrophic consequences associated with tailings mismanagement (Santamarina et al., 2019). Beyond structural risks, waste generated in mining and processing activities contributes significantly to environmental contamination, affecting soil, water, and air quality. Acid mine drainage (AMD), a common byproduct of sulfide mineral oxidation in mining waste, represents one of the most severe environmental issues, leading to contamination of groundwater, surface water, and degradation of aquatic ecosystems (Akcil & Koldas, 2006). Heavy metals and toxic substances such as mercury, arsenic, cadmium, and lead can persist in ecosystems, bioaccumulating in flora and fauna, and posing severe health risks to human populations (Franks et al., 2021). Recent studies emphasize that advancements in geoscientific research and technological development are playing an increasingly important role in shaping more sustainable waste management practices in the mining industry (Kisyov et al., 2024). Moreover, as Tomova stated the extraction of mineral resources inherently produces varying amounts of extractive waste, necessitating complex and carefully planned waste management approaches. The management of extractive waste is a multifaceted process involving numerous technical, environmental, and regulatory considerations. It requires a comprehensive understanding of the entire mining cycle—including the extraction method, beneficiation processes, and mineral treatment techniques—to ensure that waste is handled in a way that minimizes long-term environmental and safety risks (Tomova, 2023). Furthermore, waste from mining and processing has long-term implications for land use and biodiversity. Vast areas of land become unusable for agriculture or habitation due to contamination or physical disruption by mining waste, significantly impacting local ecosystems and biodiversity (Bridge, 2004). The ecological footprint of mining waste disposal often persists for decades or even centuries after operations cease, underscoring the urgent need for sustainable waste management practices. (Hristova et al., 2024) Given the magnitude of these environmental, health, and safety impacts, innovative waste management strategies, including waste reduction, recycling, reuse, and remediation, have become critical components in achieving sustainability in the mining sector (Lottermoser, 2010). Such strategies not only reduce the environmental footprint of mining operations but also mitigate long-term ecological and socio-economic consequences.

Purpose and Research Questions

The primary purpose of this research is to develop and evaluate an integrated framework for zero-waste mining systems, grounded in innovative technologies and circular economy principles. To achieve this, the study addresses the following research questions:

1. To what extent do precision mining and sensor-based extraction technologies reduce waste and enhance resource efficiency compared to conventional practices?
2. How transferable and scalable are innovative waste-reduction practices across different geopolitical and geological contexts?
3. What are the critical success factors, barriers, and enabling conditions for implementing zero-waste mining systems within the circular economy paradigm?

These questions guide the subsequent methodological choices, comparative analysis, and strategic evaluation undertaken in this study.

Research Methods

This study employs a mixed-methods approach combining systematic literature review, in-depth case study analysis, and strategic evaluation. First, a systematic review of academic articles, technical reports, and policy documents was conducted using databases such as Scopus, Web of Science, and institutional repositories. Keywords included “critical raw materials,” “circular economy,” “mining waste,” and “innovative technologies.” Second, four case studies (Sweden, Germany, Australia, Canada) were purposively selected based on three criteria: (a) relevance to critical raw materials and waste reduction, (b) availability of documented outcomes and data, and (c) diversity of regional and technological contexts. Finally, a comparative evaluation was performed using both economic and environmental indicators (e.g., waste reduction rates, resource recovery efficiency, cost savings, and GHG emissions) and a SWOT analysis to assess the feasibility, scalability, and potential risks of the identified practices. This rigorous methodological design ensures transparency, reproducibility, and applicability of the findings across different mining contexts.

Theoretical Aspects and Principles of the Circular Economy

Minimizing Waste and Pollution through Efficient and Environmentally Friendly Technologies

The minimization of waste and pollution is fundamental to achieving sustainability within the circular economy framework. Efficient and environmentally friendly technologies play a crucial role in this process by significantly reducing resource consumption, emissions, and environmental impacts associated with industrial activities, particularly in mining and raw materials processing (Ghisellini et al., 2016, Dimov et al, 2020). Technological advancements aimed at waste and pollution reduction encompass various strategies, including cleaner production methods, process optimization, and the adoption of closed-loop systems. Cleaner production technologies focus on reducing waste generation at the source through process improvements, raw material substitution, and enhanced operational efficiency (Tsai & Chou, 2009). For instance, flotation techniques, bioleaching, and solvent extraction have significantly lowered hazardous waste generation in mineral processing operations compared to conventional methodologies (Brierley & Brierley, 2013). Moreover, the implementation of advanced waste management technologies such as waste-to-energy processes, industrial symbiosis, and recycling technologies enhances resource recovery and minimizes environmental burdens (Van Berkel et al., 2009). Industrial symbiosis, a practice where waste or by-products from one industrial process become valuable resources for another, effectively reduces waste disposal needs and conserves resources, illustrating significant environmental and economic benefits (Chertow, 2007). The adoption of innovative technologies for pollution control, including advanced filtration systems, bioremediation, and phytoremediation, has proven effective in mitigating environmental contamination. These technologies actively contribute to the rehabilitation of contaminated sites, ensuring ecosystems' protection and promoting biodiversity recovery (Mulligan et al., 2001). An essential aspect of waste and pollution minimization technologies is their capacity to enhance overall efficiency, sustainability, and resilience in production processes. Sustainable technological solutions support achieving long-term environmental goals while delivering economic benefits by optimizing resource usage, reducing operational costs, and complying with increasingly stringent environmental regulations (Korhonen et al., 2018). Therefore, integrating efficient and environmentally friendly technologies into industrial processes represents a vital component of circular economy strategies, offering substantial potential to minimize waste, reduce pollution, and foster sustainable economic development. This study advances the academic discourse on sustainable critical raw material (CRM) management by not merely synthesizing existing technological solutions, but by providing a comparative, cross-regional analysis of best practices contextualized within the circular economy framework, underpinned by a conceptual model for integrated zero-waste mining systems. The proposed model incorporates insights from European and international case studies and delineates pathways for technology transfer and policy alignment.

Preserving the Value of Products and Materials through Reuse, Repair, and Recycling

Preserving the value of products and materials is a central principle of the circular economy, designed to prolong the lifespan and enhance the utility of resources through reuse, repair, and recycling. These strategies play a critical role in reducing environmental pressures, minimizing waste generation, and optimizing resource

efficiency, thereby promoting sustainable economic practices (Stahel, 2016). Reuse involves the repeated utilization of products or components in their original form or with minimal modification, effectively extending product lifespan and reducing the demand for new resources. The reuse strategy significantly mitigates environmental impacts associated with resource extraction, processing, and production, leading to considerable savings in energy and raw materials (Ghisellini et al., 2016). For instance, reusable packaging solutions, such as pallets, crates, and containers, have demonstrated significant environmental and economic advantages compared to single-use alternatives (Singh & Ordoñez, 2016). Repair further preserves the value of products by maintaining their functionality and delaying disposal. Repair activities encompass maintenance, refurbishment, and remanufacturing processes, each contributing to reduced material consumption and waste generation. Refurbishing and remanufacturing restore products to a condition comparable to new items, supporting the retention of high product value and functionality at lower environmental costs (Ellen MacArthur Foundation, 2013). A prominent example includes the remanufacturing of automotive parts and electronic components, widely recognized for their economic and environmental benefits (King et al., 2006). Recycling represents a fundamental approach within the circular economy aimed at reclaiming valuable materials from end-of-life products. Recycling not only prevents waste from entering landfills or incineration processes but also recovers valuable resources, reducing dependency on primary raw material extraction and lowering associated environmental impacts (Geyer et al., 2016). Effective recycling systems rely on technological advancements in sorting, processing, and re-manufacturing, as well as comprehensive management practices to ensure high-quality secondary materials suitable for industrial reuse (Graedel & Reck, 2012). Collectively, reuse, repair, and recycling strategies significantly contribute to preserving resource value, promoting sustainability, and supporting a resilient circular economy. These practices offer pathways toward sustainable resource management, enhancing economic efficiency, and achieving environmental stewardship goals.

Restoring Natural Systems through Sustainable Resource Management and Reducing Negative Environmental Impacts

Restoration of natural systems is a foundational objective within the circular economy, emphasizing the sustainable management of resources and the systematic reduction of negative environmental impacts. This principle addresses the urgent need to rehabilitate ecosystems that have been degraded by industrial activity, pollution, and unsustainable resource extraction practices (Costanza et al., 2017). Sustainable resource management entails practices designed to balance ecological sustainability with economic and social needs, thus ensuring the long-term health of ecosystems. This includes the application of sustainable forestry, responsible mining, regenerative agriculture, and integrated water management practices. Each of these strategies prioritizes resource regeneration and ecosystem resilience, reducing pressures on natural environments while promoting biodiversity and ecological health (Sayer et al., 2013). Effective restoration of ecosystems often involves direct intervention methods, including ecological restoration projects that target habitat rehabilitation, biodiversity recovery, and the restoration of ecosystem functions. For example, mine site rehabilitation projects aim to restore landscapes through reforestation, soil amendment, and ecological engineering, significantly reducing erosion, improving water quality, and enhancing biodiversity (Bradshaw, 2000). Reducing negative environmental impacts also requires mitigating pollution through sustainable practices, waste minimization, and the reduction of emissions. Advanced pollution control technologies, such as bioremediation, phytoremediation, and advanced water treatment systems, are crucial in mitigating contaminants in air, water, and soil, thus actively restoring the health of natural systems (Mulligan et al., 2001). Further, enhancing ecosystem services through sustainable practices has broad implications for climate change mitigation, such as carbon sequestration via reforestation and soil restoration projects. These practices not only restore ecological functions but also deliver socio-economic benefits, including improved human health, enhanced water security, and increased resilience to climate change (Costanza et al., 2017).

Beyond the operational principles described above, this study situates its analysis within broader theoretical frameworks, including industrial ecology, socio-technical transition theory, and resilience thinking. These perspectives emphasize the interconnectedness of technological, organizational, and environmental systems, highlighting the necessity of systemic change over isolated interventions. Incorporating these theories enriches the understanding of how circular economy principles can drive sustainable transformation in resource-intensive industries.

Classification of Innovative Technologies

Effective waste reduction in the extraction and processing of critical raw materials involves various innovative technologies. This study classifies these technologies according to the stages of mining and processing operations.

Technologies in Mining Operations

Minimally Invasive and Precision Mining Technologies

Precision mining involves advanced techniques aimed at accurately identifying and extracting valuable minerals while minimizing environmental disturbance and waste generation. Technologies such as automated and remotely controlled machinery, drones for aerial surveying, and robotics significantly improve the precision of extraction processes. These technologies facilitate targeted excavation, drastically reducing the volume of unnecessary overburden removed and minimizing ecological impacts (Dunbar et al., 2012). Additionally, the integration of GPS and advanced data analytics provides real-time geological insights, optimizing mining operations for maximum resource efficiency and reduced environmental footprints.

Sensor-Based Technologies for Selective Extraction and Waste Reduction

Sensor-based technologies employ advanced detection systems to differentiate valuable ore from waste rock, facilitating selective extraction practices. These technologies utilize sensors such as X-ray fluorescence (XRF), near-infrared (NIR) spectroscopy, and laser-induced breakdown spectroscopy (LIBS), enabling real-time ore sorting and significantly reducing the handling of barren material (Lessard et al., 2014). By implementing these sensor-based solutions, mining operations can achieve higher resource recovery rates, reduce processing energy consumption, and substantially lower waste generation. This selective approach not only enhances economic viability but also contributes directly to the environmental sustainability of mining activities.

Technologies in Raw Material Processing

Innovative Flotation and Separation Technologies with Reduced Waste

Advances in flotation and separation technologies have considerably enhanced the efficiency of raw material processing. Modern flotation methods, including column flotation, froth flotation with improved reagents, and microbubble techniques, increase the selectivity and recovery rates of valuable minerals, thus significantly reducing waste generation. Additionally, advanced separation methods such as gravity separation, magnetic separation, and electrostatic separation technologies have been refined to achieve higher purity of extracted materials, minimizing the amount of residual waste produced.

Recycling and Reuse of Waste Materials and By-products

Technological innovations in recycling and reuse processes have enabled effective valorization of waste materials and by-products from mining operations. Techniques such as hydrometallurgical recycling, pyrometallurgical recycling, and bioleaching allow for the extraction of valuable components from previously discarded materials. The reuse of tailings and slag in construction materials, road building, and other industrial applications exemplifies practical approaches that extend the lifecycle of waste materials, thereby significantly reducing environmental impacts and enhancing resource efficiency.

Integrated Technological Systems (Zero Waste & Circular Integrated Solutions)

Examples of Best Practices and Implemented Projects in Europe and Globally

Integrated technological systems aim for comprehensive waste minimization by employing a holistic approach combining various advanced technologies. A prominent example is the Zero Waste mining initiative in Sweden, where mining operations integrate precision extraction, waste reuse, and recycling technologies, drastically reducing their ecological footprint. Similarly, in Germany, the "Green Mining" project incorporates sensor-

based sorting, advanced recycling techniques, and waste valorization, resulting in significant reductions in waste output and enhanced environmental performance.

Globally, Canada's mining industry has implemented integrated circular solutions, combining flotation innovations and advanced sensor technologies with sustainable waste management practices. Australia's "Circular Economy in Mining" project further illustrates successful integration of comprehensive waste management systems that emphasize resource recovery and minimal environmental impact. These international practices demonstrate the viability and scalability of integrated technological systems, underscoring their role in promoting sustainability within the mining sector.

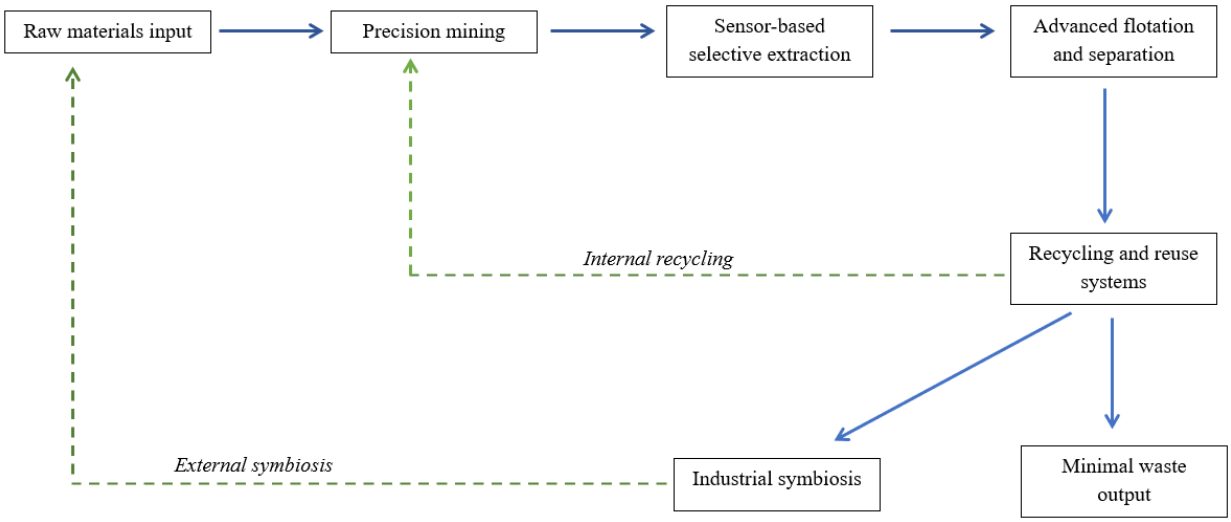

Figure 1. Conceptual model of an integrated zero-waste and circular economy system in mining operations, developed by the author based on synthesis of case study data

The figure illustrates a conceptual framework of an integrated zero waste and circular economy system implemented in mining operations. The main process flow begins with raw materials input and proceeds through precision mining, sensor-based selective extraction, advanced flotation and separation, and finally to recycling and reuse systems, resulting in minimal waste output. Internal recycling loops allow materials recovered during recycling and reuse to be reintroduced into processing operations or utilized through industrial symbiosis, rather than directly into mining operations. External industrial symbiosis enables the exchange of by-products with other industries, which can be fed back as raw material inputs. The system highlights the integration of technological, managerial, and collaborative practices to achieve enhanced resource efficiency and sustainability.

Review of Best Practices and Case Studies

To elucidate the practical implications and effectiveness of innovative technologies aimed at waste minimization in the extraction and processing of critical raw materials, this section presents a review of exemplary case studies from Europe and other global regions. These cases demonstrate how technological, managerial, and systemic innovations contribute to advancing the principles of the circular economy in the mining sector.

European Examples of Successful Technological Innovations

Case 1: Sweden — Recycling and Waste Minimization in Rare Earth Element Mining

Sweden has emerged as a pioneer in implementing advanced recycling technologies and waste minimization practices, particularly in the context of rare earth element (REE) mining. The LKAB (Luossavaara-Kiirunavaara AB) initiative in northern Sweden integrates residue valorization from iron ore tailings, extracting REEs and phosphorus as by-products (Binnemans & Jones, 2020). This approach not only mitigates the ecological footprint of mining but also addresses supply risks for critical materials. The project exemplifies a closed-loop strategy, where tailings that were traditionally considered waste are transformed into valuable resources, aligning with circular economy principles and significantly reducing the need for primary extraction.

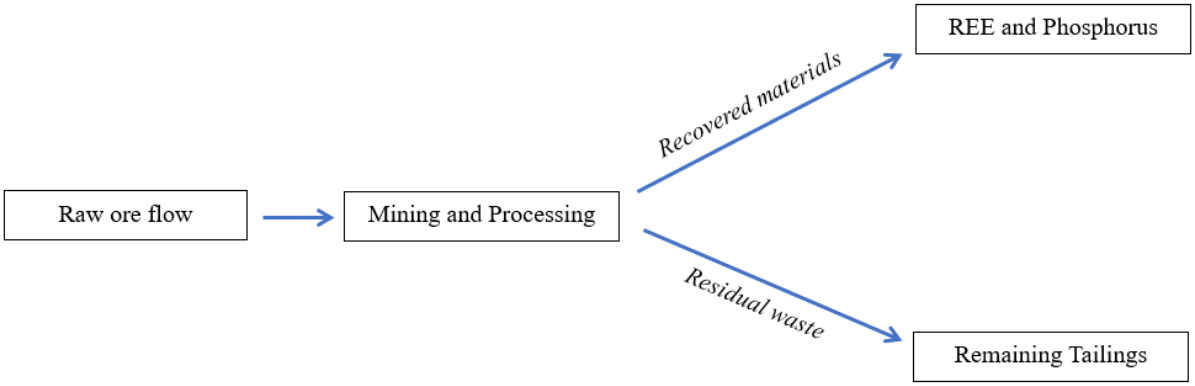

Figure 2. Material flow in the Swedish case study: Tailings valorization, adapted from Binnemans & Jones (2020)

The figure illustrates the material flow in the Swedish case study, where mining and processing of raw ore generate both residual tailings and recovered rare earth elements (REE) and phosphorus. Through innovative valorization of tailings, these materials are extracted as valuable by-products, significantly reducing the amount of waste and contributing to a more sustainable mining process.

Case 2: Germany — Lithium and Rare Metal Processing Practices

Germany has made significant strides in developing sustainable processing routes for lithium and rare metals. The Zinnwald Lithium Project, located in Saxony, employs energy-efficient roasting and leaching techniques to recover lithium from mica-rich ores while minimizing waste generation (Schulz et al., 2021). Furthermore, research consortia such as LiBRi (Lithium Recovery from Brines) have explored membrane-based separation and solvent extraction methods to enhance recovery rates and reduce chemical waste. These efforts exemplify how Germany integrates process innovation, resource efficiency, and environmental stewardship into its critical material supply chains.

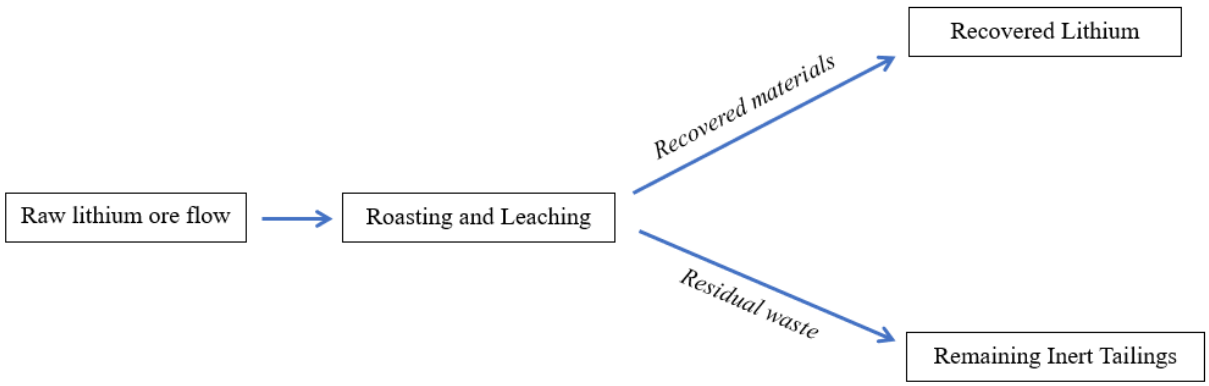

Figure 3. Material flow in the German case study: Lithium-efficient leaching, adapted from Schulz et al. (2021)

The figure presents the material flow in the German case study, where raw lithium ore undergoes roasting and leaching processes. This results in the recovery of lithium while producing minimal inert tailings. The innovative leaching techniques enhance resource efficiency and reduce chemical and solid waste generation.

International Examples

Case 3: Australia — Innovative Technologies for Reuse of Mining Waste

Australia has been at the forefront of developing technologies to convert mining waste into secondary products, contributing to both economic and environmental objectives. The Cooperative Research Centre for Transformations in Mining Economies (CRC TiME) supports projects that repurpose tailings and slag for construction materials, such as geopolymer concrete and road base aggregates (Parsons et al., 2022). These

initiatives exemplify industrial symbiosis, where waste streams from mining operations are reintegrated into other industrial processes, thereby reducing landfill use and greenhouse gas emissions.

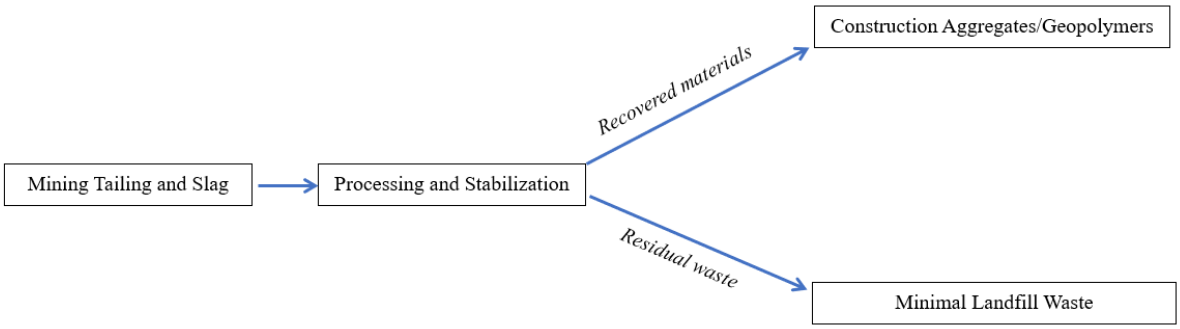

Figure 4. Material flow in the Australian case study: Tailings to construction materials, adapted from Parsons et al. (2022)

This figure depicts the Australian case study, in which mining tailings and slag are processed and stabilized to produce construction aggregates and geopolymer materials. This approach demonstrates an effective reuse of mining waste in other industrial applications, minimizing landfill disposal and lowering CO_2 emissions (Author research).

Case 4: Canada — Application of Sensor and Digital Technologies for Precision Waste Management

In Canada, the mining industry has increasingly adopted sensor-based and digital technologies to improve waste management practices. Companies such as Teck Resources have deployed real-time monitoring systems using IoT (Internet of Things) and machine learning algorithms to optimize ore sorting and tailings deposition (Keenan & Kemp, 2020). These technologies enable selective extraction and precise control over waste streams, enhancing resource efficiency and minimizing environmental risks. The integration of such digital solutions underscores Canada's commitment to technologically advanced and environmentally responsible mining operations.

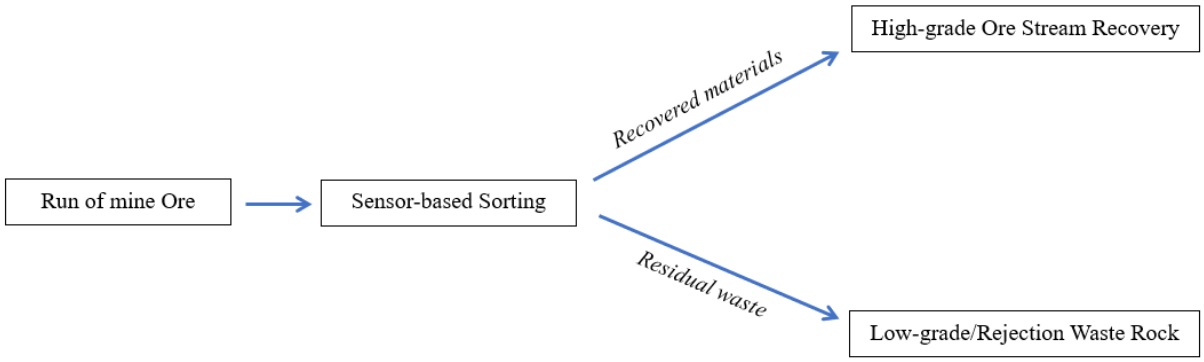

Figure 5. Material flow in the Canadian case study: Sensor-based sorting, adapted from Keenan & Kemp (2020)

The figure shows the material flow in the Canadian case study, where run-of-mine ore is processed through sensor-based sorting. This results in a high-grade ore stream and a reduced amount of low-grade waste rock. The use of sensor and digital technologies improves selectivity, enhances recovery rates, and minimizes waste generation (Author research).

Table 1 provides a comparative overview of the four case studies analyzed in this study, summarizing the key technological innovations, achieved waste reduction rates, estimated resource recovery quantities, and additional environmental or economic benefits. The Swedish case demonstrates the valorization of tailings with substantial recovery of rare earth elements (REE) and phosphorus. The German case highlights lithium recovery through efficient leaching, minimizing chemical and solid waste. The Australian case exemplifies the transformation of mining tailings and slag into construction materials, achieving the highest recorded waste reduction (60%). The Canadian case showcases sensor-based sorting technologies that improve selectivity and optimize resource

utilization. This synthesis underscores the diversity of approaches and their effectiveness in supporting circular economy principles within the mining sector.

Table 1. Summary of best practices and case studies in mining waste reduction, compiled from Binnemans & Jones (2020); Schulz et al. (2021); Parsons et al. (2022); Keenan & Kemp (2020).

Case Study	Innovation	Waste Reduction (%)	Resource Recovery (t/year)	Additional Benefits
Sweden	Tailings valorization	50	1,500 REE & Phosphorus	Reduced land use
Germany	Lithium-efficient leaching	35	800 Lithium	Lower chemical consumption
Australia	Tailings to construction materials	60	2,000 Aggregates	Lower CO_2 emissions
Canada	Sensor-based sorting	40	1,200 High-grade ore	Improved selectivity

The values presented in Table 1 are not original empirical results but indicative estimates synthesized from reported ranges in the cited literature. They are intended solely to illustrate the order of magnitude of potential improvements, rather than to provide precise or site-specific measurements. (Binnemans & Jones, 2020; Schulz et al., 2021; Parsons et al., 2022; Keenan & Kemp, 2020)

Comparative Analysis and Evaluation of the Effectiveness of Technologies

To assess the relevance and impact of the innovative technologies and practices presented in the case studies, this section offers a comparative evaluation grounded in economic and environmental performance indicators, complemented by a SWOT analysis that synthesizes their strengths, weaknesses, opportunities, and threats.

Economic and Environmental Indicators for Technology Assessment

The effectiveness of waste-reduction technologies in mining is best evaluated using a combination of quantitative and qualitative indicators that capture their economic viability and environmental benefits (Hilson & Murck, 2000; Tost et al., 2018). Table 1 (see Section 4) already summarizes the tangible benefits of the four case studies; here we expand on the core metrics typically employed in such evaluations.

Key Economic Indicators:

- *Cost savings per ton of ore processed ($/t):*
  Reflects the reduction in operating costs through improved resource efficiency and reduced disposal fees.
- *Capital expenditure (CAPEX) payback period (years):*
  Measures the time required to recover investments in innovative technologies.
- *Incremental revenue from by-products (% of total revenue):*
  Assesses the additional income generated by valorizing materials previously considered waste.
- *Productivity gains (%):*
  Quantifies improvements in throughput or reduction in downtime due to more efficient processes.

Key Environmental Indicators:

- *Waste reduction rate (%):*
  Quantifies the proportion of material diverted from landfills or tailings.
- *Resource recovery efficiency (%):*
  Measures the proportion of valuable materials successfully recovered from ores and waste streams.
- *Reduction in greenhouse gas (GHG) emissions (t CO_2-eq/year):*
  Assesses climate impact mitigation through energy savings and reduced material losses.
- *Land and water footprint reduction (%):*
  Evaluates the minimized use of land and water resources due to improved practices.

For example, the Swedish tailings valorization project demonstrates both high waste reduction (~50%) and significant incremental revenue from REE and phosphorus sales, while the Australian case emphasizes the environmental co-benefits of lowering CO_2 emissions and diverting waste to construction materials. The Canadian sensor-based sorting shows notable productivity gains and resource efficiency but requires higher initial capital investment compared to conventional techniques.

SWOT Analysis of the Presented Practices

A SWOT analysis provides an integrated perspective on the internal and external factors that shape the feasibility and scalability of the technologies.

Table 2. SWOT analysis of the innovative practices investigated, conceptualized by the author based on case study synthesis

STRENGTHS	*WEAKNESSES*
Demonstrated capacity to reduce waste significantly	High initial capital investment
Enhanced resource recovery and generation of secondary revenues streams	Technological complexity and maintenance requirements
Alignment with circular economy and sustainability objectives	Limited applicability in specific geological settings
Compliance with environmental regulations and improved stakeholder legitimacy	
OPPORTUNITIES	*THREATS*
Growing demand for sustainable, responsibly sourced materials	Market volatility and price fluctuations
Supportive policy frameworks and regulatory incentives	Regulatory uncertainties and delays
Potential for industrial symbiosis and cross-sectoral collaborations	Technological obsolescence due to rapid innovation
Increasing stakeholder expectations for ESG performance	Potential operational disruptions during implementation
	Organizational resistance to change in traditional operations

This comparative and strategic assessment underlines that the innovative practices examined hold substantial potential for improving the sustainability of mining operations. However, realizing these benefits requires careful consideration of economic feasibility, context-specific applicability, and proactive risk mitigation strategies.

Table 2 provides a SWOT (Strengths, Weaknesses, Opportunities, and Threats) analysis of the innovative practices investigated. The analysis highlights their proven ability to reduce waste, recover resources, and align with sustainability goals as key strengths, while also recognizing challenges such as high upfront costs and technological complexity. Opportunities emerge from increasing demand for sustainable materials, supportive policy frameworks, and the potential for industrial symbiosis, whereas external threats include market volatility, regulatory delays, and resistance to change. This strategic assessment emphasizes the importance of balancing technological innovation with economic feasibility and adaptive management to maximize the impact of these practices.

Discussion and Directions for Future Research

This section reflects on the findings of the study, contextualizing them within broader technological, regulatory, and strategic frameworks. It also outlines potential pathways for transferring and disseminating the analyzed technologies and identifies promising avenues for further research and development in advancing the circular economy within the mining sector. The findings contribute novel insights by systematically mapping and comparing the technological, economic, and regulatory dimensions of innovative waste-reduction practices in CRM extraction and processing. In particular, the study highlights the transferability potential and constraints of these innovations, offering a strategic framework that can inform both scholarly debates and policy-making.

Analysis of Key Technological and Regulatory Challenges

While the innovative practices examined have demonstrated significant potential to reduce waste and improve resource efficiency, several technological and regulatory barriers remain. From a technological perspective, challenges include the high complexity and maintenance requirements of sensor-based and automated systems (Tost et al., 2018), as well as the limited applicability of certain techniques in specific geological or operational contexts. Furthermore, the scaling of tailings valorization and industrial symbiosis often depends on site-specific factors, such as mineral composition and regional industrial networks, which may not always be replicable elsewhere.

On the regulatory side, the successful implementation of such technologies is contingent upon supportive policy frameworks and streamlined permitting processes. Yet, regulatory uncertainty and inconsistent environmental standards across jurisdictions may deter investment and innovation (Hilson & Murck, 2000). Moreover, the lack of standardized metrics for measuring sustainability performance in mining complicates the benchmarking and monitoring of these initiatives.

Potential for Global Transfer and Dissemination of the Analyzed Technologies

The case studies reviewed in this research, though situated in specific regional and institutional contexts, offer valuable insights for global application. The technologies and practices exemplify principles—such as material valorization, selective extraction, and waste reuse—that are transferable across a range of mining settings. Industrial symbiosis, for instance, has been successfully demonstrated in Australia and could be adopted in other mining-intensive regions with adequate infrastructure and policy support. Similarly, sensor-based sorting technologies, as piloted in Canada, could be tailored to diverse ore types globally, provided appropriate calibration and adaptation. Nonetheless, effective transfer and dissemination require not only technological adaptation but also institutional and cultural changes within the mining sector. International collaborations, knowledge-sharing platforms, and capacity-building programs can play pivotal roles in fostering uptake and scaling of these innovations (Velenturf & Jensen, 2016).

Prospects and Opportunities for Integrating Circular Economy Principles in Mining

Looking ahead, the integration of circular economy principles in mining holds considerable promise but calls for intensified interdisciplinary research and cross-sectoral cooperation. Future research could focus on developing more energy-efficient and low-carbon technologies, improving life-cycle assessment methods, and exploring business models that incentivize circular practices. Moreover, further empirical studies are needed to quantify the long-term economic and environmental benefits of the innovations discussed, especially in developing country contexts where data remains scarce. Additionally, there is growing potential in leveraging digitalization and artificial intelligence to enhance predictive capabilities and optimize resource flows within mining operations (Keenan & Kemp, 2020). Policymakers and industry leaders should also work collaboratively to harmonize sustainability standards and incentivize circular innovations through targeted financial and regulatory mechanisms.

While the innovative practices examined show clear potential to reduce waste and improve resource efficiency, their broader adoption faces challenges. Key constraints include high upfront costs, technological complexity, and varying geological and institutional contexts. These barriers underscore the need for adaptive management, supportive policies, and further empirical research to ensure sustainable implementation of zero-waste mining systems.

Conclusion

This study has examined innovative technologies and best practices for reducing waste and enhancing resource efficiency in the extraction and processing of critical raw materials, through a review of European and international case studies, comparative analyses, and strategic evaluations. The findings underscore the significant potential of integrating circular economy principles into mining operations to simultaneously address environmental, economic, and social challenges associated with resource extraction. This research contributes to existing literature by developing a synthesized model of integrated technological and managerial solutions for

zero-waste mining operations, grounded in empirical case studies and evaluated through a robust SWOT analysis. It thus bridges the gap between descriptive case evidence and prescriptive strategies, providing a foundation for future empirical testing and theoretical refinement.

Summary of Key Findings

The reviewed case studies demonstrate that integrating advanced technologies—such as precision mining, sensor-based extraction, flotation, and tailings valorization—can substantially reduce waste, enhance resource recovery, and generate additional economic value. These innovations align with circular economy principles by transforming residual materials into valuable by-products and improving operational efficiency. However, their successful implementation depends on addressing technological, financial, and regulatory challenges, and requires systemic integration of technological, managerial, and policy measures.

Recommendations for Practice and Policy

To accelerate the adoption and scaling of these practices, the following recommendations are proposed:

- *For industry practitioners:* Invest in capacity building and technological innovation, prioritizing site-specific assessments to select the most appropriate solutions. Foster collaborations with adjacent industries to exploit opportunities for industrial symbiosis and material reuse.
- *For policymakers:* Develop and harmonize regulatory frameworks that incentivize circular practices through subsidies, tax relief, or mandatory sustainability reporting. Establish standardized metrics for sustainability performance in mining to improve transparency and benchmarking.
- *For researchers and stakeholders:* Encourage interdisciplinary research to quantify long-term benefits, explore emerging digital and AI-driven solutions, and adapt innovations to diverse geological and socio-economic contexts.

In conclusion, advancing circular economy principles within the mining sector is both a necessity and an opportunity, promising substantial gains in sustainability and resilience of critical material supply chains. It calls for a concerted effort by industry, government, and academia to align innovation, policy, and practice toward a more sustainable and responsible mining future.

Scientific Ethics Declaration

* The author declares that the scientific ethical and legal responsibility of this article published in EPSTEM Journal belongs to the author.

Conflict of Interest

* The author declares that there is no conflict of interest

Funding

* This research received no specific grant from any funding agency in the public, commercial, or not-for-profit sectors.

Acknowledgements or Notes

* This article was presented as an oral presentation at the International Conference on Basic Sciences and Technology (www.icbast.net) held in Budapest/Hungary on August 28-31, 2025.

* This work has been carried out in the framework of the National Science Program "Critical and strategic raw materials for a green transition and sustainable development", approved by the Resolution of the Council of Ministers № 508/18.07.2024 and funded by the Ministry of Education and Science (MES) of Bulgaria.

References

Achzet, B., & Helbig, C. (2013). How to evaluate raw material supply risks—An overview. *Resources Policy, 38*(4), 435–447.

Akcil, A., & Koldas, S. (2006). Acid mine drainage (AMD): Causes, treatment and case studies. *Journal of Cleaner Production, 14*(12–13), 1139–1145.

Ali, S. H., Giurco, D., Arndt, N., Nickless, E., Brown, G., Demetriades, A., Yakovleva, N. (2017). Mineral supply for sustainable development requires resource governance. *Nature, 543*(7645), 367–372.

Azam, S., & Li, Q. (2010). Tailings dam failures: A review of the last one hundred years. *Geotechnical News, 28*(4), 50–53.

Bradshaw, A. (2000). The use of natural processes in mine site rehabilitation: Revegetation of metalliferous mine wastes. *Hydrometallurgy, 59*(2–3), 203–210.

Bridge, G. (2004). Contested terrain: Mining and the environment. *Annual Review of Environment and Resources, 29*, 205–259.

Brierley, C. L., & Brierley, J. A. (2013). Progress in bioleaching: Part B: Applications of microbial processes by the minerals industries. *Applied Microbiology and Biotechnology, 97*(17), 7543–7552.

Buijs, B., & Sievers, H. (2012). Critical thinking about critical minerals: Assessing risks related to resource security. *Polinares Working Paper, 16*.

Chertow, M. R. (2007). "Uncovering" industrial symbiosis. *Journal of Industrial Ecology, 11*(1), 11–30.

Costanza, R., de Groot, R., Sutton, P., van der Ploeg, S., Anderson, S., Kubiszewski, I., Turner, R. K. (2017). The value of the world's ecosystem services and natural capital. *Nature, 387*, 253–260.

Dimov, E., Bakyrdjieva, R., & Stratiev. N. (2020). The mining industry and the recycling of raw materials as an important element of the Bulgarian economy. *Journal of Mining and Geological Sciences, 63*, 289-292.

Ellen MacArthur Foundation. (2013). *Towards the circular economy: Economic and business rationale for an accelerated transition*. Ellen MacArthur Foundation.

European Commission. (2020). *Critical raw materials resilience: Charting a path towards greater security and sustainability*. COM(2020) 474 final. Retrieved from https://eur-lex.europa.eu/legal-content/EN/TXT/?uri=CELEX:52020DC0474

European Commission. (2023). *Critical Raw Materials Act*. Brussels: European Commission. Retrieved from https://single-market-economy.ec.europa.eu/publications/critical-raw-materials-act_en

Franks, D. M., Stringer, M., Torres-Cruz, L., Baker, E., Valenta, R. K., Thygesen, K., Ballesteros, A. (2021). Tailings facility disclosures reveal stability risks. *Nature Sustainability, 4*(5), 384–391.

Geyer, R., Jambeck, J. R., & Law, K. L. (2016). Production, use, and fate of all plastics ever made. *Science Advances, 3*(7), e1700782.

Ghisellini, P., Cialani, C., & Ulgiati, S. (2016). A review on circular economy: The expected transition to a balanced interplay of environmental and economic systems. *Journal of Cleaner Production, 114*, 11–32.

Graedel, T. E., & Reck, B. K. (2012). Metallurgy for recovering critical metals from the future's electronics. *MRS Bulletin, 37*(4), 325–331.

Graedel, T. E., Harper, E. M., Nassar, N. T., Nuss, P., & Reck, B. K. (2015). Criticality of metals and metalloids. *Proceedings of the National Academy of Sciences, 112*(14), 4257–4262.

Hristova, T., B. Evstatiev, I. Stoyanov, P. Hristov. (2024). Industry 4.0−based solid waste management and future prospects in circular economy, In *Woodhead Advances in Pollution Research, Advances in Energy from Waste*, Woodhead Publishing.

Humphries, M. (2019). *Critical minerals and U.S. public policy*. Congressional Research Service. Retrieved from https://sgp.fas.org/crs/misc/R45810.pdf

Kalantzakos, S. (2018). The geopolitics of critical minerals. *The Fletcher Forum of World Affairs, 42*(2), 57–76.

King, A. M., Burgess, S. C., Ijomah, W., & McMahon, C. A. (2006). Reducing waste: Repair, recondition, remanufacture or recycle? *Sustainable Development, 14*(4), 257–267.

Kisyov, A., Tomova, M., Koprev, I. (2024). Geophysical methods for optimizing mining waste management. In Dobrinkova, N., Fidanova, S. (Eds.), *Environmental protection and disaster risks (EnviroRisks 2024).* Springer.

Korhonen, J., Honkasalo, A., & Seppälä, J. (2018). Circular economy: The concept and its limitations. *Ecological Economics, 143*, 37–46.

Mulligan, C. N., Yong, R. N., & Gibbs, B. F. (2001). Remediation technologies for metal-contaminated soils and groundwater: An evaluation. *Engineering Geology, 60*(1–4), 193–207.

O'Sullivan, M., Overland, I., & Sandalow, D. (2017). The geopolitics of renewable energy. *Center on Global Energy Policy*. Retrieved from https://www.energypolicy.columbia.edu/sites/default/files/energy/CGEP TheGeopoliticsOfRenewables.pdf

Santamarina, J. C., Klein, K. A., & Fam, M. A. (2019). *Soils and waves: Particulate materials behavior, characterization and process monitoring*. Wiley.

Sayer, J., Sunderland, T., Ghazoul, J., Pfund, J. L., Sheil, D., Meijaard, E., van Oosten, C. (2013). Ten principles for a landscape approach to reconciling agriculture, conservation, and other competing land uses. *Proceedings of the National Academy of Sciences, 110*(21), 8349–8356.

Singh, J., & Ordoñez, I. (2016). Resource recovery from post-consumer waste: Important lessons for the upcoming circular economy. *Journal of Cleaner Production, 134*(Part A), 342–353.

Stahel, W. R. (2016). The circular economy. *Nature, 531*(7595), 435–438.

Terziyski D., (2024). Optimization of technological schemes for construction of open mine roads. *C. R. Acad. Bulg. Sci., 77*(1), 101–110.

Tomova, M. (2023). Geophysical techniques for monitoring of integrated mine waste storage facility: Case study of Southeastern Bulgaria. *The Eurasia Proceedings of Science, Technology, Engineering & Mathematics (EPSTEM), 26,* 341-347

Tsai, W. T., & Chou, Y. H. (2009). A model of cleaner production implementation and sustainability for petrochemical industry in Taiwan. *Journal of Loss Prevention in the Process Industries, 22*(3), 274–279.

Van Berkel, R., Fujita, T., Hashimoto, S., & Geng, Y. (2009). Industrial and urban symbiosis in Japan: Analysis of the Eco-Town program 1997–2006. *Journal of Environmental Management, 90*(3), 1544–1556.

World Bank. (2020). *Minerals for climate action: The mineral intensity of the clean energy transition*. Washington, DC: World Bank.

Author(s) Information

Vessela Petrova
University of Mining and Geology "St. Ivan Rilski"
Sofia, Bulgaria
Contact e-mail: *vessela.petrova@mgu.bg*

To cite this article:

Petrova, V. (2025) Innovative technologies for waste reduction in the extraction and processing of critical raw materials. *The Eurasia Proceedings of Science, Technology, Engineering and Mathematics (EPSTEM), 36,* 59-72.

The Eurasia Proceedings of Science, Technology, Engineering & Mathematics (EPSTEM)
ISSN: 2602-3199

The Eurasia Proceedings of Science, Technology, Engineering and Mathematics (EPSTEM), 2025

Volume 36, Pages 73-80

ICBAST 2025: International Conference on Basic Sciences and Technology

Investigation of Red Blood Cell Microcirculation Using the DLVO Theory

Lali Kalandadze
Batumi Shota Rustaveli State University

Nugzar Gomidze
Batumi Shota Rustaveli State University

Mirian Kontselidze
Batumi Shota Rustaveli State University

Abstract: The study of blood microcirculation has revealed specific properties that distinguish blood from Newtonian and non-Newtonian fluids. These anomalies cannot be fully explained by conventional hydrodynamic or rheological models alone. While the viscous incompressible fluid model describes blood flow well in vessels with diameters exceeding 300 μm, capillaries below this threshold exhibit non-classical flow behavior, the underlying physical mechanisms of which remain an active area of investigation. In this work, blood is modeled as a multiphase physicochemical system, represented as a suspension of cellular elements in plasma. The cellular components, particularly erythrocytes, are treated as part of an electrostatic system, where their electrical characteristics are determined not by discrete surface charges, but by the zeta potential -the electrokinetic potential at the interface between the erythrocyte membrane and the plasma. Microcirculatory dynamics are analyzed through the framework of DLVO theory. A quantitative assessment of red blood cell motion in capillaries is presented, incorporating resistance forces, hydrodynamic pressure, and gradients in electrostatic potential. The results indicate that mechanical and electrical factors substantially influence microcirculatory flow, affecting erythrocyte deformation and orientation, and inducing a directional electrostatic force gradient that governs cell movement in narrow capillaries.

Keywords: Microcirculation, Erythrocyte, Hemodynamics, Two-phase systems, Zeta potential

Introduction

Blood is a unique biological fluid. It is a heterogeneous and multiphase physicochemical system. It can be represented as formed elements (red blood cells, leukocytes, thrombocytes) suspended in plasma. That is, it is a dispersed system. Many regularities established for non-biological dispersed systems can be used to study blood flow properties. However, it should be noted that during the study of the functioning of blood microcirculation, several features were discovered that set it apart from Newtonian and non-Newtonian fluids. The regularities of hydrodynamics or rheology alone cannot explain those peculiarities. (Yaya et al 2021, Vahidkhah et al, 2016).

The rheological properties of blood are determined primarily by the processes of hydrodynamic interaction of erythrocytes and plasma, which lead to the formation and disintegration of aggregates, rotational movements of erythrocytes, as well as their redistribution and appropriate orientation in the bloodstream (Secomb, 2017). The properties of blood significantly depend on the ability of red blood cells to deform. While moving, they change their normal shape. So, for example, Guckenberger et al. (2018) experimentally and numerically found two major shapes of red blood cells, like croissants and slippers. This ability allows red blood cells with a diameter of about 8 μm to penetrate without damage through the pores of a membrane filter with a diameter of 3 μm and

a length of 12 μm. They also move freely in small capillaries with an average diameter of 10 to 2 μm (Bedggood et al., 2024). It should be noted that red blood cells completely restore their natural shape after leaving the capillaries. Free-moving healthy red blood cells never become deformed (Babaki et al., 2023). In general, the movement of blood in the vascular system is characterized by the following features:

- The decrease in hematocrit with a reduction in the diameter of the capillaries is known as the Fahraeus effect.
- The dependence of blood viscosity on the diameter of blood vessels. Viscosity remains constant when the capillary diameter exceeds 0.3 mm, but decreases with a decrease in diameters from 0.3 mm to 4-5 μm - Fahraeus-Lindqvist effect.
- The presence of a plasma layer without red blood cells near the wall of the blood vessel (acellular layer).

When capillaries are filled only with plasma, the blood flow stops, but it resumes as soon as red blood cells appear in them, and the greater the number of red blood cells there, the more intense the flow. These processes are part of the Fahraeus-Lindqvist effect (Fahraeus & Lindqvist, 1931, Köry et al., 2022, Chebbi, 2015, Ascolese et al., 2019, Farina et al 2021).

In large blood vessels with a diameter of more than 300 microns, the viscous incompressible fluid model works well; And when examining small capillaries with a diameter of less than 300 microns, abnormal properties of blood flow appear, the study of the physical basis of which is still relevant today. To explain the microcirculatory properties of blood, various theoretical models of two-phase systems are considered (Knüppel et al., 2024, Wei-Tao et al., 2014, Schenkel et al., 2021, Gracka et al., 2022). These models only quantitatively describe the movement of blood in capillaries and cannot explain its qualitative side- the features of the movement of red blood cells in small capillaries. To obtain information about changes in the physical properties of erythrocytes during blood movement in capillaries, it is important to introduce innovative methods of fluorescence spectroscopy, optical, and magneto-optical studies (gomidze et al., 2025, Kalandadze & Nakashidze 2020). These techniques will provide additional information about the complex representation of spectral and structural-dynamic changes in erythrocytes.

Understanding the microcirculation mechanism of red blood cells is very important for both medicine and biotechnology (Trejo-Soto et al., 2022, Baskaran et al., 2024, Man et al., 2023, Guven et al., 2020) since the body supplies oxygen and nutrients and removes metabolic waste products from the cells through the capillary network. To know the mechanism of microcirculation gives the ability to control the movement of red blood cells in the capillary network. Controlling the regulation of this movement is very important for the processes occurring in the body. So, for example, blocking the movement of red blood cells in the capillary network of cancer cells will lead to the “starvation” of undesirable cells and ultimately their death.

The current paper examines blood flow in capillaries with diameters of less than 10 micrometers. Microcirculatory dynamics are analyzed through the framework of the DLVO (Derjaguin–Landau–Verwey–Overbeek) theory. Erythrocytes are treated as an electrostatic system determined by the zeta potential. A quantitative assessment of red blood cell motion in capillaries is presented, incorporating resistance forces, hydrodynamic pressure, and gradients in electrostatic potential.

Some Aspects of Blood Microcirculation

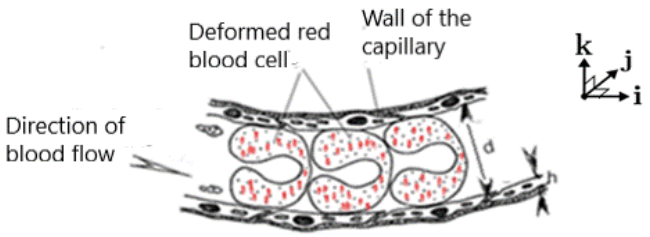

Figure 1. Model of erythrocyte movement in a thin capillary.
h - plasma layer, d - capillary diameter

As is known, neurohumoral factors control the mechanism of blood microcirculation. However, there is a second component of blood microcirculation. That is its physical aspect, according to which blood is a dispersed

system with formed elements suspended in plasma, continuously moving through blood vessels of various diameters. This movement is affected by different hydrodynamic factors. In this regard, the movement of red blood cells in capillaries attracts attention, the mechanism of which requires a complex approach. Figure 1 depicts the model of deformed erythrocyte movement in a capillary.

To estimate the pressure required to move blood through small capillaries assume that the capillary length is l=1 mm, diameter d=3 μm, average blood flow velocity v=0.5 mm/s, and dynamic viscosity of blood plasma $\eta = 2 \cdot 10^{-3}$Pa·s. To use Poiseuille's equation, assume that blood plasma, which is a Newtonian fluid, moves in a capillary, and this movement is laminar. According to Poiseuille's formula:

$$Q = \frac{\pi R^4 \Delta P}{8\eta l} \tag{1}$$

where Q is the volume of fluid flowing per unit time, R is the radius of the capillary, and ΔP is the pressure drop along the length of the capillary. From Poiseuille's formula (1) we obtain:

$$\Delta P = \frac{Q 8\eta l}{\pi R^4} = \frac{\pi R^2 v 8\eta l}{\pi R^4} = \frac{v 8\eta l}{R^2} \tag{2}$$

Substituting the corresponding values into the formula (2), it is obtained that the pressure drop along the capillary is $\Delta P = 3.6 \cdot 10^3$Pa. The pressure required in the capillary is almost 1.5 times higher than the hydrodynamic pressure created by the heart during systole. This indicates that a significantly higher pressure is needed when blood moves through the capillaries with a dynamic viscosity value of $\eta = (4-5) \cdot 10^{-3}$ Pa·s. The findings indicate that the pressure produced by the heart during systole alone is insufficient to propel blood through the capillaries. As a result, further investigation and assessment of additional mechanisms that assist in the movement of red blood cells in small capillaries are necessary.

Zeta Potential of a Deformed Red Blood Cell

Blood cells and corpuscular elements compose the electrical system (Tokumasu et al., 2012). A double layer of charges is concentrated on their surface Figure 2. The charges are also distributed inside the morphological elements of blood membranes and organelles. These complex electrical systems move continuously in blood vessels of different diameters and, certainly, are sensitive to changes in various hydrodynamic influences.

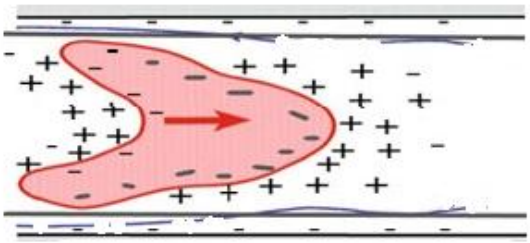

Figure 2. The electric double layer of a deformed red blood cell

It is reasonable to assume that an important role in the movement of erythrocytes in the capillary is played by the electrical forces arising between the erythrocyte membrane and the endothelial cells of the inner surface of the capillary. As is known, the electrical properties of electrolytes are expressed not by the magnitude of elementary charges, but by the zeta potential (Collini and Jackson, 2023), similarly, one can consider the electric potential at the boundary of two phases: erythrocyte and plasma. The electrical double layer causes the generation of an electrical potential, which prevents cell aggregation and therefore plays an important role in cell stabilization. Unlike the electrostatic charge of a red blood cell, which is expressed in electrostatic units, zeta potential is measured in millivolts. When its value decreases (Fontes et al., 2008, Swati et al., 2018, Karemore and Avary, 2019) the stability of the blood suspension is disrupted. Thus, the magnitude (effect) of the interaction of formed elements in the formation of red blood cell rheological properties is a function of the difference in the erythrocyte and plasma surface potential.

The surface charge of blood cell membranes is directly related to the processes of physicochemical transformations occurring on cell membranes. To release oxygen, it is necessary to shift the pH towards acidity (Bohr effect) (Hilpert et al., 1963). Ions can diffuse from the red blood cell membrane into the plasma. In the layer close to the membrane, the plasma pH decreases. Ions shield the electrostatic field of negative charges on the membrane's outer surface. Screening leads to a decrease in the electrical double layer. Therefore, when red blood cells move in small capillaries, the energy density of the electrostatic interaction between the membranes of the red blood cell and the endothelial cell (the inner layer of the capillaries) decreases. As a result, the pressure force opposing the movement of red blood cells in the capillaries is reduced.

A negative blood pH gradient $\frac{\partial(PH)}{\partial X} < 0$ induces a negative gradient of electric energy density along the capillary. Let's take the direction of blood movement as the positive X direction (Figure1). Due to a negative gradient, a tangential force $\vec{F}$ acts on the erythrocyte membrane in the direction of blood flow, which is equal to:

$$\vec{F} = -\frac{\partial U}{\partial X} \cdot S\vec{i} \tag{3}$$

where U represents the total electrostatic repulsion energy density, S denotes the erythrocyte's surface area along the capillary endothelial cell membrane, and $\vec{i}$ is the unit vector in the X-axis direction. The electric double layer of the erythrocyte membrane is formed due to the force of electrostatic attraction and thermal movement of ions. The first one tries to attract the opposite sign ions, and the second one distributes them throughout the volume. Therefore, the DLVO theory is used to estimate the force F. (Agmo et al., 2023). This theory combines the forces of Van der Waals attraction and electrostatic repulsion caused by the electric double layer. The DLVO theory considers the electrostatic part in the averaged field approximation in the limits of small surface potentials. According to the DLVO theory, the total interaction energy U of two particles per unit area will be equal to

$$U = U_m + U_{el} = 2\varepsilon_0 \varepsilon k \varphi_\delta^2 e^{-kh} - \frac{A^*}{12\pi h^2} \tag{4}$$

where U_m and U_{el} are the energies of attraction and repulsion between particles; In particular, U_m is determined by the forces of intermolecular attraction, and U_{el} by the forces of electrostatic repulsion; ε_0 is the electric constant, ε is the dielectric permittivity of the medium, φ_δ is the potential of the diffuse layer, A^* —Hamaker constants of the dispersed medium, h is the distance between particles, k - Debye–Huckel parameter represents the rate of charge decrease with distance, inversely proportional to the thickness of the diffuse layer, and is determined by the formula:

$$k = \sqrt{\frac{2F^2 I}{\varepsilon_0 \varepsilon RT}} \tag{5}$$

where I is the ionic strength of the solution, $I = 1/2 \sum_{i=1}^{n} c_i z_i^2$, c_i is the molar concentration of each ion, z_i is the ion charge.

Results and Discussion

Let's consider two parallel uniformly charged elementary surfaces- one on the membrane of an erythrocyte and the other on the endothelial cell opposite it. The charge density is denoted as σ_x, the radius of the capillary is R, and the thickness of the plasma between them is h. Since h<<R (see Figure 1), the curvature of the surfaces of both membranes can be neglected and they can be considered as flat parallel surfaces (Figure 3).

The electrostatic field is symmetrical to the h/2 plane. In the case of small fields, the magnitude of the electric potential of a unit surface is determined from the Gouy–Chapman equation:

$$\varphi(z = 0) = \left(\frac{RT}{2\varepsilon\varepsilon_0 C_0 F_0^2}\right)^{1/2} \sigma(x) \tag{6}$$

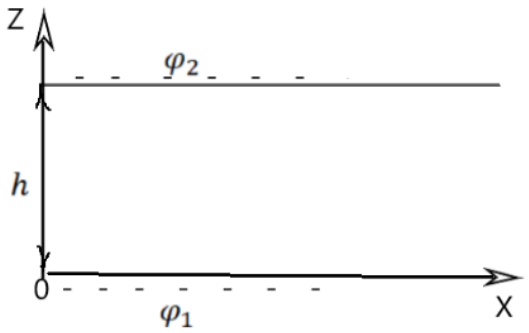

Figure3. A geometric representation of the potentials of two phases: φ_1 and φ_2 are potentials of negatively charged surfaces of the erythrocyte membrane (φ_1) and endothelial cell (φ_2); h- thickness of plasma layer

where R is the gas constant, T is the absolute temperature in the blood plasma layer, F_0 is the Faraday number, ε_0 is the electric constant, ε is the dielectric constant of the blood plasma, C_0 is the average concentration of ions in the plasma layer, $\sigma(x)$ is the surface charge density.

To determine the potential in the blood plasma layer at z=h in Debye approximation can be written:

$$\varphi(h,x) = \varphi(0,x)\, e^{-kx} \tag{7}$$

Here, k is the Debye–Huckel parameter (see equation 5).

Using formulas (12) and (14), the expression for the energy of electrostatic repulsion between units of area can be written as follows:

$$U_{el}(x) = \sigma(x)\cdot \varphi(h,x) = \sigma(x)\cdot \left(\frac{RT}{2\varepsilon\varepsilon_0 C_0 F_0^2}\right)^{1/2} \sigma(x) e^{-kx} = \sigma(x)^2 \cdot \left(\frac{RT}{2\varepsilon\varepsilon_0 C_0 F_0^2}\right)^{1/2} e^{-kx} \tag{8}$$

Considering this result (8) in formula (3), we obtain:

$$F = -\frac{\partial\left(\sigma(x)^2\cdot\left(\frac{RT}{2\varepsilon\varepsilon_0 C_0(x) F_0^2}\right)^{1/2} e^{-kx}\right)}{\partial X}\cdot S \tag{9}$$

Then the magnitude of the tangential force will therefore be

$$F = \left\{\left[2\,\sigma(x)\frac{\partial\sigma}{\partial x}\left(\frac{RT}{2\varepsilon\varepsilon_0 C_0(x) F_0^2}\right)^{\frac{1}{2}} - \frac{1}{2}\sigma(x)^2\left(\frac{RT}{2\varepsilon\varepsilon_0 C_0(x) F_0^2}\right)^{\frac{1}{2}}\frac{1}{C_0}\frac{\partial C_0(x)}{\partial x}\right] e^{-kx} - k\sigma(x)^2\left(\frac{RT}{2\varepsilon\varepsilon_0 C_0(x) F_0^2}\right)^{1/2} e^{-kx}\right\} S \tag{10}$$

According to (10), the energy U of electrostatic repulsion depends on the concentration of ions, the permittivity of the plasma, the thickness of the plasma layer, the density of the negative charge of the membrane, and the temperature of the blood.

The ζ-potential is very sensitive to the influence of various factors. This refers to the change in pH of the blood plasma during metabolism. We assumed that σ tends to increase linearly as pH increases. At point PH=7,38 $\sigma = \sigma_0$. At the isoelectric point pH=5.8 $\sigma = 0$. Thus, the function σ(pH) can be represented as (Glaser R., 2012, Kunitsyn et al., 2007):

$$\sigma = \sigma_0 + \frac{\sigma_0}{1.62}(PH - 7.38) \tag{9}$$

The normal pH of arterial blood is 7.38-7.42, although rapid changes in pH are possible during exchange reactions. Let the length of the capillary be 1 mm, the thickness of the plasma between the membranes is 2 nm, T=310 K, σ_0=3.84·10^{-2} cells/m^2, and the concentration of anions C_0=140-150 mmol/L.

Thus, combining equations (3) and (8) we can estimate the tangential force F. As a result of calculations, we get that F≈5·10^{-11} N. This means that the erythrocyte exerts additional pressure in the capillary: $\Delta P = \frac{F}{\pi r^2} = \frac{5 \cdot 10^{-11}}{3{,}14 \cdot 10^{-12}} = 16$ Pa. A maximum of 44 red blood cells ($\frac{1\ mm}{23 \cdot 10^{-3} mm} = 43{,}5$) can be placed simultaneously in a 1 mm length capillary. The sum of these red blood cells creates additional pressure $\Delta P = 44 \cdot 16$=704 Pa, which helps the blood move in the capillaries. This phenomenon is similar to the creep of the wetting fluid upward in thin capillaries, but the mechanism of these two phenomena is different.

Electrostatic tangential force F depends on the square of the surface charge density of the membrane $\sigma(x)^2$. If the surface charge density decreases, and consequently the zeta potential of the erythrocyte, then the value of F decreases sharply. This reduces the permeability of the erythrocyte through the capillary, which leads to hypoxia and tissue necrosis.

In our calculations, we assumed that the charges on the membrane surface are uniformly distributed and independent of the azimuthal coordinate. However, if the distribution of charges is uneven, there will be an additional component of force (F). This can result in the creation of a torque around the longitudinal axis of the erythrocyte, causing it to rotate along this axis. Consequently, the erythrocyte moves through the capillary like a rotating screw.

Conclusion

The study investigated the microcirculation properties of blood flow in capillaries. The paper provides a qualitative assessment of the movement of red blood cells in capillaries using hydrodynamic pressure and changes in electrical potential coefficients along the capillary. The pressure required to move blood through small capillaries was assessed. In this regard, additional mechanisms facilitating red blood cell movement in small capillaries have been considered and evaluated. The zeta potential was used to determine the electrical properties of red blood cells. According to calculations, the electrical potential induced by the double electrical layer potentially affects the surface of erythrocytes in the small capillaries and excites an electrostatic tangential force in the direction of red blood cells flow.

Scientific Ethics Declaration

*The authors declare that the scientific ethical and legal responsibility of this article published in EPSTEM journal belongs to the authors.

Conflict of Interest

*The authors declare that they have no conflicts of interest

Funding

*This work was supported by Shota Rustaveli National Science Foundation of Georgia (SRNFG) (grant number FR-24-3101)

Acknowledgements or Notes

*This article was presented as an oral presentation at the International Conference on Basic Sciences and Technology (www.icbast.net) held in Budapest/Hungary on August 28-31, 2025.

References

Agmo, H. V. (2023). An overview of surface forces and the DLVO theory. *ChemTexts 9*, 10.

Ascolese, M., Farina, A., & Fasano, A., (2019). The Fåhræus-Lindqvist effect in small blood vessels: How does it help the heart?. *J Biol Phys 45*, 379–394.

Babaki, M., Fedosov, D. A., Gholivand, A., Joeri, O., Remco, T., & Minne P. L. (2023). Competition between deformation and free volume quantified by 3D image analysis of red blood cell. *Biophysical Journal*, *122,* (9),1646-1658.

Baskaran, R. K., Rajaram, A., Link, B., Porr, B., & Franke, T. (2024). Classification of chemically modified red blood cells in microflow using machine learning video analysis, *Soft Matter*, *20*, 952.

Bedggood, P., Ding, Y., & Metha, A. (2024). Changes to the shape, orientation and packing of red cells as a function of retinal capillary size, *Biomedical Optics Express 15*, 558-578.

Chebbi, R. (2015). Dynamics of blood flow: modeling of the Fåhræus–Lindqvist effect. *J Biol Phys 41*, 313–326.

Collini, H., & Jackson, M.D. (2023). Zeta potential of crude oil in aqueous solution. *Adv. Colloid Interface Sci*., *320*, 102962.

Fahraeus, R., & Lindqvist, T. (1931). The viscosity of the blood in narrow capillary tubes, *American Journal of Physiology – Cell Physiology 96*(3), 562–568.

Farina, A., Rosso, F., & Fasano, A., (2021). A continuum mechanics model for the Fåhræus-Lindqvist effect. *Journal of Biological Physics, 47*, 253–270.

Fontes, A., Fernandes, H. P., André, A. de Thomaz, Barbosa, L. C., & Lenz, C. (2008). Measuring electrical and mechanical properties of red blood cells with double optical tweezers *Journal of Biomedical Optics, 13* (1) 014001.

Glaser, R. (2012). *Biophysics*, (2nd ed.). Springer.

Gomidze, N., Kalandadze, L., Khajishvili, M., Nakashidze, O., Jabnidze, I., Jakobia, D., & Makharadze, K. (2025). Fluorescence spectroscopy as a novel tool in hematological diagnostics. *APL Bioengineering 9* (2), 026102.

Gracka, M., Lima, R., Miranda J.M., Student, S., Melka, B., & Ostrowski, Z. (2022). Red blood cells tracking and cell-free layer formation in a microchannel with hyperbolic contraction: A CFD model validation *Computer Methods and Programs in Biomedicine, 226,* 107117.

Guckenberger, A., Kihm, A., John, T., Wagner, Ch., & Gekle, S. (2018). Numerical–experimental observation of shape bistability of red blood cells flowing in a microchannel. *Soft Matter*, *14,* 2032-2043.

Guven, G., Matthias, P. H., & Can, I. (2020). Microcirculation: Physiology, pathophysiology, and clinical application. *Blood Purification. 49*(1-2),143–150.

Hilbert, P, Fleischmann, R.G, Kempe, D., & Bartrls, H. (1963). The Bohr effect related to blood and erythrocyte PH. *American Journal of Physiology, 205*, 337-40.

Kalandadze, L., & Nakashidze, O. (2020). Influence of the size, shape and concentration of magnetic particles on the optical properties of nano-dispersive structures. *Journal of Magnetism and Magnetic Materials 500*, 166355.

Knüppel, F., Malchow, S, Sun, A, Hussong, J, Hartmann, A, Wurm, F-H., & Torner, B. (2024). Viscosity modeling for blood and blood analog fluids in narrow gap and high reynolds numbers flows. *Micromachines. 15*(6),793.

Köry J., Maini, P. K., Pitt-Francis, J. M., & Byrne, H. M. (2022). Dependence of cell-free-layer width on rheological parameters: Combining empirical data on flow separation at microvascular bifurcations with geometrical considerations, *Physical Review E, 105,* 014414.

Kunitsyn, V.G., Mokrushnikov, P.V., & Panin, L.E. (2007). Mechanism of erythrocyte microcirculation in capillary vessels at physiological changes of PH. *Bulletin of the Siberian Branch of the Russian Academy of Medical Sciences, 5,* 28–32.

Man, Y., Wu, D. H., An R., Wei Pe., Monchamp, K., Goreke, U., Sekyonda, Z., Wulftange, W. J., Federici, Ch., Bode, A., Nayak, L. V., Little, J. A., & Gurkan, U. A. (2023). Microfluidic concurrent assessment of red blood cell adhesion and microcapillary occlusion: Potential hemorheological biomarkers in sickle cell disease. *Sensors & Diagnostics, 2,* 457-467.

Megha, N., Karemore, N., M., & Avari, G., J., (2019). *Alteration in zeta potential of erythrocytes in preeclampsia patients*. IntechOpen

Schenkel, T., & Halliday, I. (2021). Continuum scale non newtonian particle transport model for hæmorheology. *Mathematics. 9*(17), 2100.

Secomb, T. W. (2017). Blood flow in the microcirculation, *Annual Review of Fluid Mechanics*. *49*(1), 443–461.

Swati, S. Gaikwad, N. Karemore, & Avari, J. G. (2018). Alterations in zeta potential and osmotic fragility of red blood cells in hyperglycemic conditions. *Pharmaceutical & Biosciences Journal*, 25-30.

Tokumasu, F., Ostera, G.R., Amaratunga, C., & Fairhurst, R.M., (2012). Modifications in erythrocyte membrane zeta potential by Plasmodium falciparum infection. *Experimental Parasitolog, 131*(2), 245-51.

Trejo-Soto, C., Lázaro, G.R., Pagonabarraga, I., & Hernández-Machado, A., (2022). Microfluidics approach to the mechanical properties of red blood cell membrane and their effect on blood rheology. *Membranes, 12*, 217.

Vahidkhah, K., Balogh, P., & Bagchi, P. (2016). Flow of red blood cells in stenosed microvessels. *Scientific Reports 6*, 28194.

Wu, W.T., Aubry, N., Massoudi, M., Kim, J., & Antaki, J. F. (2014). A numerical study of blood flow using mixture theory. *International Journal of Engineering Science*,*76*, 56-72.

Yaya, F., Römer, J., Guckenberger, A., John, T., Gekle, S., Podgorski, T., & Wagner, C. **(**2021). Vortical flow structures induced by red blood cells in capillaries. *Microcirculation 28*(5), e12693.

Author(s) Information

Lali Kalandadze
Batumi Shota Rustaveli State University
35 Ninoshvili Str., Batumi, Georgia
Contact e-mail: *Lali.kalandadze@bsu.edu.ge*

Nugzar Gomidze
Batumi Shota Rustaveli State University
35 Ninoshvili Str., Batumi, Georgia

Mirian Kontselidze
Batumi Shota Rustaveli State University
35 Ninoshvili Str., Batumi, Georgia

To cite this article:

Kalandadze, L., Gomidze, N. & Kontselidze, M. (2025). Investigation of red blood cell microcirculation using the DLVO theory. *The Eurasia Proceedings of Science, Technology, Engineering and Mathematics (EPSTEM), 36,* 73-80.

The Eurasia Proceedings of Science, Technology, Engineering & Mathematics (EPSTEM)
ISSN: 2602-3199

The Eurasia Proceedings of Science, Technology, Engineering and Mathematics (EPSTEM), 2025

Volume 36, Pages 81-92

ICBAST 2025: International Conference on Basic Sciences and Technology

Application of Taguchi to Cutting Behavior of Stainless Steels

Yusuf Sahin
OSTIM Technical University

Ahmet Saygin Ogulmus
OSTIM Technical University

Abstract: The selection of un-appropriate cutting factors in any type of metal cutting is led to higher surface roughness and larger cost because they directly affect the quality characteristics and production rate. The cutting of AISI 304 stainless steel is investigated both experimentally and theoretically at basic parameters while outputs are surface roughnesses of Ra, Rz and Rt. Taguchi L9 design is adopted in analyzing the machining results using carbide inserts. Variance analysis and regression analysis are carried out to determine effective factors and relationship between the input and responses, respectively. It is shown that the optimum surface roughness is obtained around 1.18 µm, and the optimum parameters are determined from experiment trial 7. Further, the feed rate is dominant effect on the surface roughness while the speed and the depth of cut are not effective. Moreover, the regression models are developed, the correlation coefficients of Ra, Rz and Rt are found to be around 99.15%, 99.76% and 96.77%, respectively, that are quite reasonable, but slightly more errors generated in Rt results. The present finding results exhibit that Taguchi method is an effective method for improving surface quality of cutting stainless steels. The experimental design applied to improve surface quality is also applicable to industrial practices.

Keywords: AISI 304 stainless steel, Cutting parameters, Surface roughness

Introduction

Surface roughness (SR) is very important output because of affecting the directly product's quality besides fatigue/fracture strength of component surfaces. There are various manufacturing processes used in machining the mechanical parts such as turning shaping/planning, pressing, milling, drilling, grinding or less common non-traditional process such as mechanical, thermal and electro-chemical, like water jet machining, electro discharge machining, and chemical etching. The first group is called traditional machining, which is based on removal of materials using tools that are harder than the materials (Şahin, 2003). These are not efficient in machining ceramics and composites or very tight tolerances. The second group is preferred in avoiding surface damage that often accompanies the stresses created by traditional cutting, but these are slow processes to complete the jobs. Among these groups, however, turning is mostly used with appropriate cutting inserts because of being faster one. Dimensional accuracy plays a crucial role in today's manufacturing integrity, especially in aerospace, automotive, biomedical implants, and robotics. For this reason, SR not only affects how the parts looks like, but also has big effect on mechanical performance like wear, friction, fatigue rand fracture. In recently, many researchers have, therefore, focused more and more on advanced optimization methodologies that combine experimental design methods, computational modeling, and real-time process monitoring to get consistent and reproducible SR results. This approach also leads to brings together scientists from materials science, tribology, mechanical engineering and physics.

The ten-point mean roughness (Rz) number, maximum height (Rt), and arithmetical mean roughness (Ra) are the most common parameters to measure surface roughness. Ra, which is measured in µm, is the average

distance between mean line and surface profile. Rz is the distance from mean line, concentrating on the highest peak and valley. Rt is the distance between the highest peak and the lowest peak in vertical direction. Surface control is very crucial in any metal cutting in terms of its function and longer service life. Mechanical properties like material strength and hardness affect the cutting force and surface roughness. The heat generated during the turning can cause thermal damage to the tool edge, causing early failure. Because of lower conductivity during machining AISI 304 steels, heat cannot transfer efficiently in separated chip (Kónya et al. 2024). Also, this steel may be hardened by itself during cut because it has got some alloy elements like Cr and Ni.

Many researchers examined at SR, tool life, and power of AISI 304 steels when cutting in different situations using Taguchi/RSM or Grey relation. Nehri et al. (2024) used the Taguchi approach, RSM, and ANN to study the turning of AISI 304L in order to predict wear and surface. AlO_3 plus TiCN-coated tool worked well. The results were proven to be dependable and correct through experimentation. Using Taguchi L9 design, Grey Relation Analysis, and PCA, Rathod et al. (2022) searched at tool life and surface roughness in turning same steels at higher speeds. The results indicated that speed was considerable influence for manufacturing time but depth of cut was effective for roughness. The higher speed associated with lower feed rate and depth of cut were best settings for surface roughness. Kumar et al. (2020) optimized the main cutting parameters in dry turning of AISI 304 steel using Taguchi (L9) and ANOVA to maximize metal removal rate (MRR). Feed rate was the most significant factor on MRR, followed by depth of cut and speed. Boucherit et al. (2024) applied Taguchi method and modified WPCA model to cut AISI 304 with coated carbide inserts including main parameters and nose radius. The results exhibited that contributions of feed rate and nose radius to surface roughness was about 52.4% and 26.5 %, respectively.

Su et al. (2020) presented a multi-objective optimization method of cutting parameters based on grey relational analysis (GRA) and RSM in turning AISI 304 austenitic steel. The multi-objective problem was converted into simple objective optimization problem through GRA. Optimal parameters were achieved at higher depth, lower feed rate and speed. Berkani et al. (2015) studied the empirical equations in characterizing machinability with RSM. The feed rate was the most effective, but the depth of cut affects cutting force and cutting power considerably. Binali et al. (2023) studied the turning of AISI 304 at dry and minimum quantity lubrication (MQL) environment conditions by TiC-coated insert using factorial design. The high speed resulted in 10% lower in surface roughness. Also, force decreased by 20% at low feed rate. The speed was observed as most influential factor on surface roughness, followed by feed rate. Other people study on MQL method with various oils (Binali et al. (2023) on sustainable approach; Dubey, Sharma & Singh (2021) on hybrid nano fluid MQL; Rajeswari R. (2024) on MQL with corn oil; and Singh, Dureja, Dogra & Bhatti (2018) on comprehensive MQL, Dry & Flood comparison. In addition, Nguyen et al. (2019) on green machining for the dry milling process of AISI 304, Hata, Widiatmoko, Mulyana & Azmy (2023) on wet milling optimization were studied. Nguyen et al.(2019) results revealed that the reductions in energy consumption and surface roughness were more or less 34.9 % and 57.7 %, respectively, while the improvements in power was around 28.8 % in comparison to initial factor. Hata et al. (2023) searched for the optimization of the machining parameter in wet milling process for AISI 304 and AISI 316 steels through the Taguchi method. The optimum surface roughness of AISI 304/316 stainless steel was around 0, 21-0, 24 μm, respectively. The depth of cut was the most influential parameter, but feed rate held pivotal factor on SR for AISI 316 steel. For other experimental and statistical study, Patel et al. (2015) studied the optimization and prediction of cutting force and surface roughness in end milling process of AISI 304 stainless steel. They employed Taguchi's L27 orthogonal array and regression analysis. Popan et al. (2015) also developed theoretical model using regression analysis that aimed to predict surface roughness in turning of AISI 304 stainless steel. The study analyzed the influence of basic factors on the quality. They focused on DoE methodology, specifically utilizing the Taguchi (L9) design, to explore the intricate relationships between inputs and Ra, Rt and Rz output. Taguchi technique was mostly used for process optimization and provided a structural approach to evaluate the influence of various factors using the limited numbers of tests (Sahin et al.2024). Furthermore, numerous studies investigated prediction studies on machining AISI 304 stainless steel on surface roughness, cutting forces and others based on machine learning, statistical methods and hybrid approaches. Zhou et al.(2019) on Gradient Boosting Regression Trees; Caydaş and Ekici (2012) on Support Vector Machines¸ Alajmi and Almeshal (2020) on ANFIS-QPSO and Popan et al.(2015) on Artificial Neural Network. These models showed high accuracy in predicting surface quality under different cutting conditions.

The literature survey indicates that there have been number of studies carried out on turning behavior AISI 304 stainless steels in optimizing surface roughness, material removal rate, cutting force or tool life (Adalarasan et al. 2015; Ramu et al. 2018; Elsiti and Elmunafi 2023; Sundara Bharathi et al. 2020) and application of methodology (Hamdan et al. 2012; Ramu et al.2018; Elsiti et al. 2023; Sundara Bharathi et al. 2020). However,

a limited numbers of studies was conducted at machining of AISI 304 stainless steels using statistical method, focusing on surface roughness of Ra, Rt and Rz (Ozdemir 2019; Prakash et al. 2011, Alzyod, Konya and Ficzere, 2025, Rao Rh, Rao Jag and Suresh K, 2015). The purpose of current study is, thus, to determine the optimal parameters in turning AISI 304 steel under lower speeds but not only for Ra output, but also Rt, Rz values by carbide inserts. Moreover, regression models are developed for first order at 95% confidence level. Analysis of variance are carried out to determine the effective parameters on the response.

Materials and Methods

Austenitic stainless steel (AISI 304 steel) is mostly used in manufacturing, construction and aero plane industry because it is strong, resists corrosion, cheap, and flexible. Its mechanical and physical characteristics are listed in Table 1. Its machinability is the worst due to higher mechanical and lower conductivity. Thus, selection of the right cutting tool is vital important when turning AISI 304 steel. The tool utilized for present study is un-carbide insert (P10). In this work, SNMG 120408 tool signature is chosen.

Table 1. Mechanical and physical property of AISI 304 steel

Maximum tensile strength (MPa)	Yield strength (MPa)	Hardness (HB)	Elongation (%)	Modulus of elasticity (GPa)	Thermal conductivity (W/m/K)	Density (g/cm^3)
520-720	210	215	45	193	16.2	8.0

The experiment is conducted in Metal Cutting Laboratory of Mechanical Engineering Department of OSTİM TECH. Figure 1 indicates standard lathe machine with 2.5 kW power, which is utilized in machining trials. The dimensions of test specimens are 120 mm in diameter, 500 mm in length. To carry out set of nine experiments, the specimen is partitioned into nine uniform segments, each measuring 10 mm in length, separated by 4 mm in wide and 2 mm deep slit. A fresh cutting edge is utilized before starting each test. Each surface is measured using the Time 3200 surface roughness tester. Before starting the trials, the measurement device is calibrated to make sure the data is accurate.

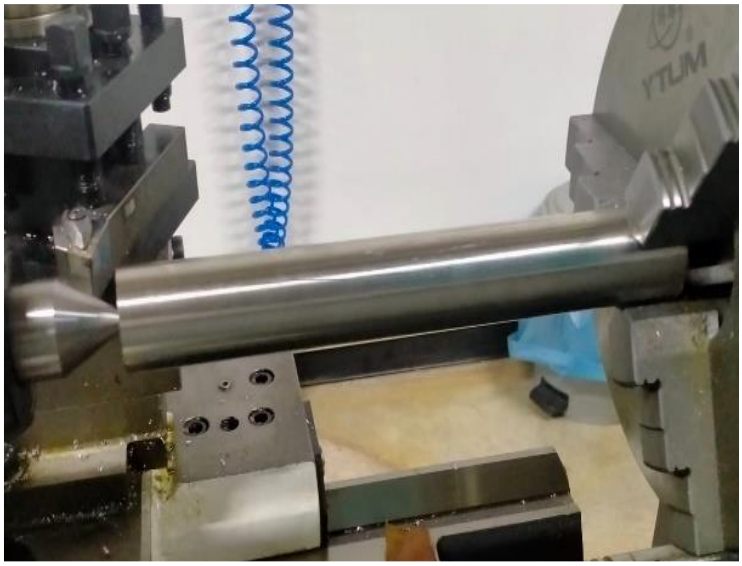

Figure 1. A standard lathe machine used for machining stainless steel through carbide insert

For this investigation, Taguchi L9 orthogonal array is chosen. Selected factors are spindle speed, feed rate, depth of cut. Each factor has three levels like low, medium and high. Table 2 shows the main factors and their levels for each parameter below. In addition, Time 3200 surface roughness tester is used in measuring SR of the tested steels to find out how to change the roughness values.

Table 2. Cutting parameters and their levels

Parameters	Level 1	Level 2	Level 3
Cutting speed (m/min)	50	79	113
Feed rate (mm/rev.)	0.08	0.11	0.18
Depth of cut (mm)	0.6	1.2	1.8

Surface Roughness Parameters

As shown in Figure 2, the industry uses some metrics for surface roughness's such as arithmetical mean roughness (Ra), maximum height (Rt), ten-point mean roughness (Rz) number. The mean line is in coordinate system (x, y) axes. The mean line goes along x-axis, while y-axis shows how much the mean line will be varied. We chose to test all three SR parameters—Ra, Rz, and Rt, rather than just Ra because we need to see both peaks and valley's changes in the shape of the machined surface. Ra gives a broad idea of average roughness, whereas Rz and Rt give more information about peak-to-valley characteristics or five to ten point measurements, as exhibited in Fig. 2 (b, c), which are very important for sealing surfaces, fatigue loading or coating adherence.

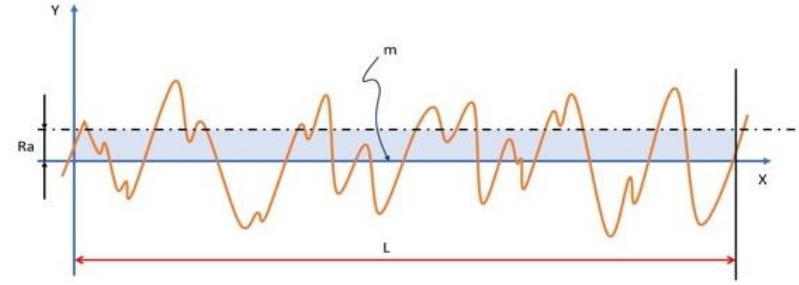

$$R_a = \frac{1}{L}\int_0^L |f(x)|dx$$

(a) Ra

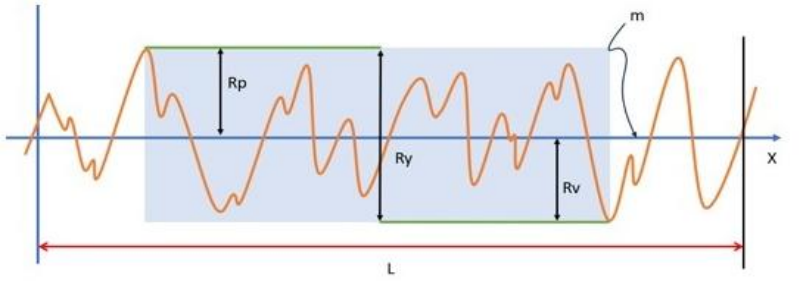

$$R_y = R_p + R_v$$

(b) Rt or Ry

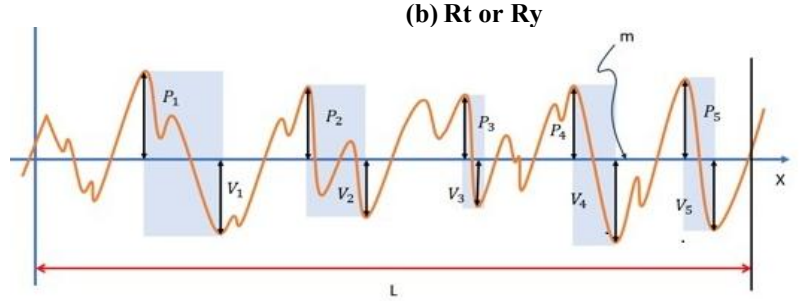

(c) Rz

$$R_z = \frac{|R_{p1} + R_{p2} + R_{p3} + R_{p4} + R_{p5}| + |R_{v1} + R_{v2} + R_{v3} + R_{v4} + R_{v5}|}{5}$$

Figure 2. Basic surface roughness parameters used for industry (P: Peaks while V: Valleys; Rp: Tallest 5 peaks within the measuring length; Yv: Lowest 5 peaks within the measurement length)

Results and Discussion

Surface Roughness of Ra

Figure 3 illustrates the primary effects plot of surface roughness represented by Ra values in turning, detailed in Table 3. The data in this figure reveals that feed rate is the most significant parameter, varying linearly with an increase in feed rate, followed by depth of cut while cutting speed is in-significant. The increased surface roughness values with increasing feed rate is attributed to the classical theory of metal machining (Sahin, 2003). Additionally, higher surface roughness produces when more friction takes place between the tool/specimen. Coated layer has not demonstrate an enhanced stability at these lower test environments. Comparable results are

noted in the previous research works (Kumar, 2020; Boucherit et al. 2024; Berhani, 2015). However, another investigation showed that the speed is effective on machining AISI 304 steels (Binali 2023; Rathod 2022).

Table 3. Taguchi L9 design and its Ra value results

Trial number	V (m/min)	f (mm/rev)	t (mm)	Ra (µm)	FITS_MEANS1 (µm)
1	1	1	1	1.793	1.7561
2	1	2	2	2.767	2.6611
3	1	3	3	6.81	6.9527
4	2	2	3	1.211	1.3537
5	2	3	1	2.738	2.7011
6	2	1	2	7.61	7.5041
7	3	3	2	1.181	1.0751
8	3	1	3	2.791	2.9337
9	3	2	1	6.82	6.7831
Average error (%)				1.48	

The lowest surface roughness is achieved with lower feed rate, higher speeds, and higher depth of cut when carbide tool is used. In other words, the optimum cutting parameter is determined from the first trial of experiment, yielding about 1.181 µm, which exhibits an excellent performance in relative to other experiments. Namely, the optimum cutting is achieved with carbide tool at V = 113 m/min, f = 0.08 mm/rev, t = 1.8 mm, which is followed by trial 7 (Figure 3). The cutting speed is an ineffective, can be disregarded. Hamdan et al. (2012) also reported that feed rate (80.85%) is the dominant parameter on SR, followed by speed (8.24%), depth of cut (7.59%), respectively. The optimal SR is achieved through the use of coated carbide in the optimization process.

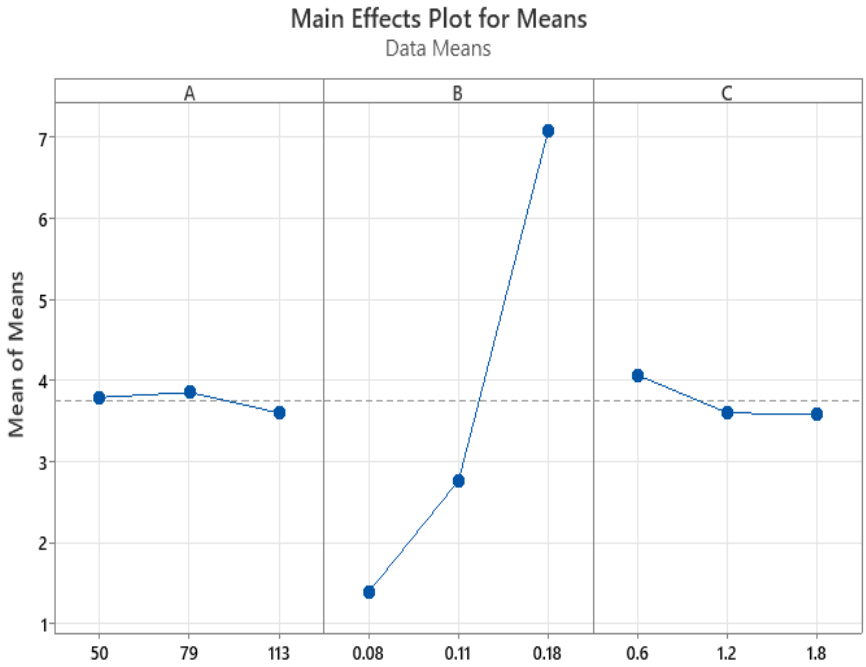

Figure 3. Main effect plots for SR of Ra in cutting the SS

Table 4 shows the results of response table for means Ra values. It is indicated that feed rate is the most significant factor on SR because it holds the topmost (rank 1), followed by depth of cut (rank 2), speed (rank 3), as observed by the slope of the line. This might be due to selecting the lower speed in the present study. The previous study indicates that feed rate is effective for SR while feed rate, depth of cut are significant on MRR for AISI 304 stainless steel (Şahin and Akbar, 2024). Among the tool tip used, sintered P10 carbide tool shows a slightly lower surface roughness about 1.297 µm, which is achieved from trial 1. For MRR, optimum levels are found at conditions of spindle speed of 1200 rpm, feed rate of 0.24 mm/rev., depth of cut of 1.5 mm when cut with or without any tool. AISI 304 stainless steels are machined at various cutting conditions using coated carbide inserts by the Taguchi approach (Şahin and Ogulmuş, 2024). The results exhibited that feed rate, speed are effective for SR, whereas feed rate and depth of cut were significant for MRR. TiCN coated carbide

indicated the lowest SR indicating at 0.68 µm, which is corresponding to trial 7. The results revealed that the optimum SR was found at higher speed/depth of cut associated with lower feed rate.

Table 4. Response table for means

Level	A (Cutting speed)	B (Feed rate)	C (Depth of cut)
1	3.790	1.395	4.065
2	3.853	2.765	3.599
3	3.597	7.080	3.576
Delta	0.256	5.685	0.488
Rank	3	1	2

Regression Equation

Regression is used for studying SR when machining stainless steels.

Regression Equation,

$$Ra = -2.624 - 0.00319\ x\ A + 57.7\ x\ B - 0.407\ x\ C \quad (1)$$

Where Ra is SR index, A is speed, B is feed rate and C is depth. This equation shows that A and C coefficients are negative while B is positive. Its coefficients (R-Sq.) is found to be 99.15%. These results exhibit good accuracy for models with experimental value.

ANOVA

ANOVA is performed; the results are listed in Table 5. The feed rate factor is statistically significant at 5% significant level for because of (p=0.002) while other factors are not found an effective because p is higher than that of 0.05. Moreover, the contribution mostly comes from the feed rate, the error term is lower when turned these steels. The correlation coefficient, R-Sq is found to be 99.15%. Feed rate is the most effective factor, contributing 98.8% to the variation in surface roughness, depth of cut and speed can be neglected.

Table 5. Analysis of variance for means

Source	DF	Seq SS	Adj SS	Adj MS	F	P-value	Pcont,%
A	2	0.1065	0.1065	0.0532	1.08	0.482	0.19
B	2	52.8134	52.8134	26.4067	534.14	0.002	98.76
C	2	0.4555	0.4555	0.2278	4.61	0.178	0.85
Residual Error	2	0.0989	0.0989	0.0494			0.184
Total	8	53.4743					

Surface Roughness of Rz

Figure 4 illustrates the main effects plot of surface roughness of Rz values in turning, with corresponding results are presented in Table 6. The data in this figure, feed rate again is the most influential parameter, exhibiting a linear relationship with increasing feed rate, followed by speed and depth of cut. Ozdemir et al. (2019) found that the fundamental factors influencing surface roughness (Ra, Rz) are determined as feed rate, depth of cut, and cutting speed. The Box-Behnken Experimental Design utilized for Ra, Rz parameters in drilling of MDF composite panels indicated (Prakash et al. 2011) that the surface roughness of the predicted model during the confirmatory test exhibits of 2.06% and 2.631% error for Ra and Rz, respectively. A recent study conducted by Alzyod et al. (2025) indicated that feed rate was the dominant factor on surface roughness, contributing to Ra and Rz high levels. Metal removal rate was also effective for feed rate and depth of cut. Rao, Ch et al. (2015) conducted surface roughness analysis of Ra, Rq and Rz in cutting EN19 steel utilizing Grey relation analysis. The models created on roughness parameters demonstrated significant results because of yielding high coefficient correlation of 0.992, 0.987 and 0.982 for Ra, Rt and Rz, respectively.

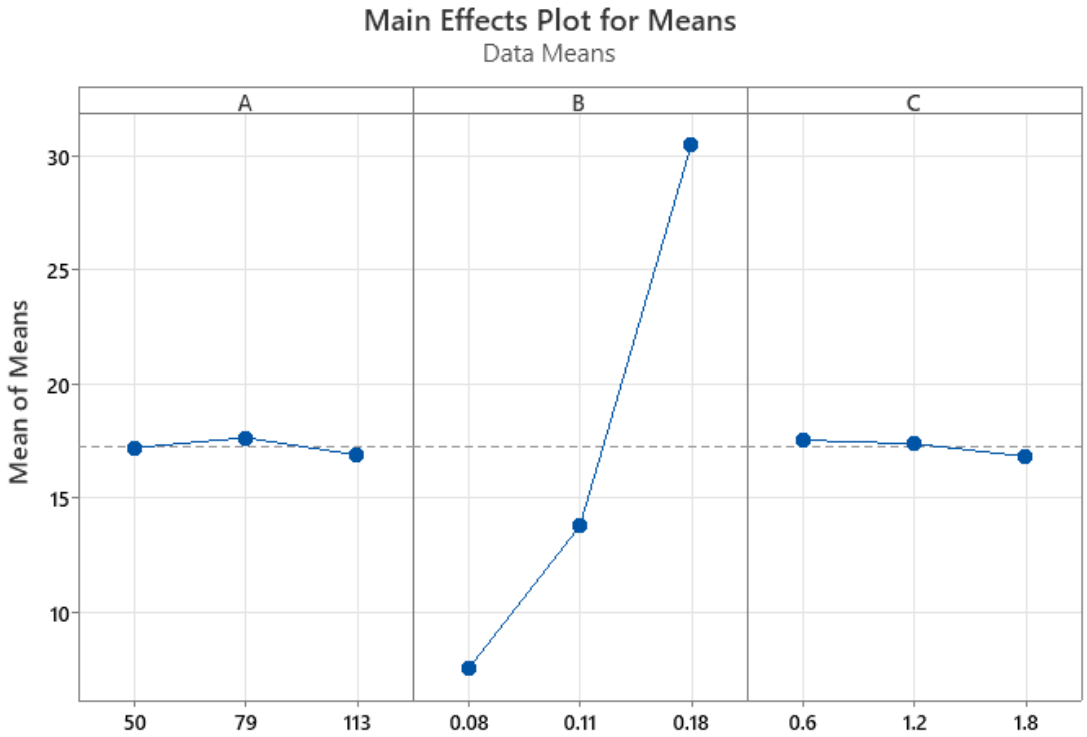

Figure 4. The main effect plots for SR of Rz in cutting the SS

Table 6. Taguchi L9 design and its Rz results

Trial number	V (m/min)	f (mm/rev)	t (mm)	Rz (µm)	FITS_MEAN S2
1	1	1	1	8.064	7.7678
2	1	2	2	13.86	13.859
3	1	3	3	29.7	29.996
4	2	2	3	7.75	8.0468
5	2	3	1	14.04	13.7439
6	2	1	2	31.145	31.1442
7	3	3	2	6.738	6.737222
8	3	1	3	13.4	13.69689
9	3	2	1	30.525	30.22889

Table 7 shows the results of response table for means Rz values. The feed rate is the most significant factor on the SR because it holds the topmost (rank 1), followed by speed/depth of cut, but no considerable difference occurred between the depth of cut (rank 3=16.826) and speed (rank 2=16.888).

Table 7. Response table for means

Level	A (Speed)	B (Feed rate)	C (Depth of cut)
1	17.208	7.517	17.536
2	17.645	13.767	17.378
3	16.888	30.457	16.826
Delta	0.757	22.939	0.710
Rank	2	1	3

Regression Equation

Regression Equation is given the following equation.

$$Rz = -10.08 - 0.00557\ x\ A + 230.9\ x\ B - 0.592\ x\ C \quad (2)$$

Where Rz is SR index. Again, it shows that A, C coefficients are negative while B is positive. Their determination coefficient (R-Sq.), R-Sq. (adj), R-Sq. (pred) are found to be 99.76%, 99.610% and 99.10%, respectively. These results exhibit good accuracy for models with experimental value.

ANOVA

ANOVA analysis is performed; the results are given in Table 8. The feed rate again is statistically significant at 5% significant level for because of (p=0.001) while other factors are not found an effective. Moreover, the error term is also lower when turned these steels, and R-Sq is found to be 99.8%. The feed rate contribution reaches to 99.7% on roughness, whereas, depth of cut/speed can be disregarded due to it's contributing of 0.10% or lower.

Table 8. Analysis of variance for means

Source	DF	Seq SS	Adj SS	Adj MS	F	P-value	Pcont, %
A	2	0.867	0.867	0.434	1.64	0.378	0.1025
B	2	843.823	843.823	421.912	1599.74	0.001	99.736
C	2	0.835	0.835	0.417	1.58	0.387	0.098
Residual Error	2	0.527	0.527	0.264			0.067
Total	8	846.053					

Surface Roughness of Rt

Figure 5 illustrates the main effects plot of surface roughness of Rt values during turning, as summarized in Table 9. The data presented in this figure, feed rate is the most effective parameter, followed by speed/depth of cut. Speed appears to be more effective than that of depth of cut. However, both parameters demonstrate a decreasing trend when increasing speed and depth of cut. Rt exhibits slightly different behavior because of coming from its definition. This can be attributed to increasing the height difference between the highest mountain and the lowest valley in overall measurement distance. Srivabut et al. (2024) examined the optimization of turning process, focusing on fundamental parameters affecting the roughness quality of wood-plastic composites (WPCs) through the Box–Behnken design and response surface methodology (RSM). Optimal conditions for the turning were identified at a spindle speed of 781 rpm, a feed rate of 0.05 mm/min, and a depth of cut of 2.8 mm with 30 wt. % wood sawdust. Under these conditions, the samples indicated Ra, Rq, and Rz values of 1.8, 2.2, and 11.3 μm, respectively.

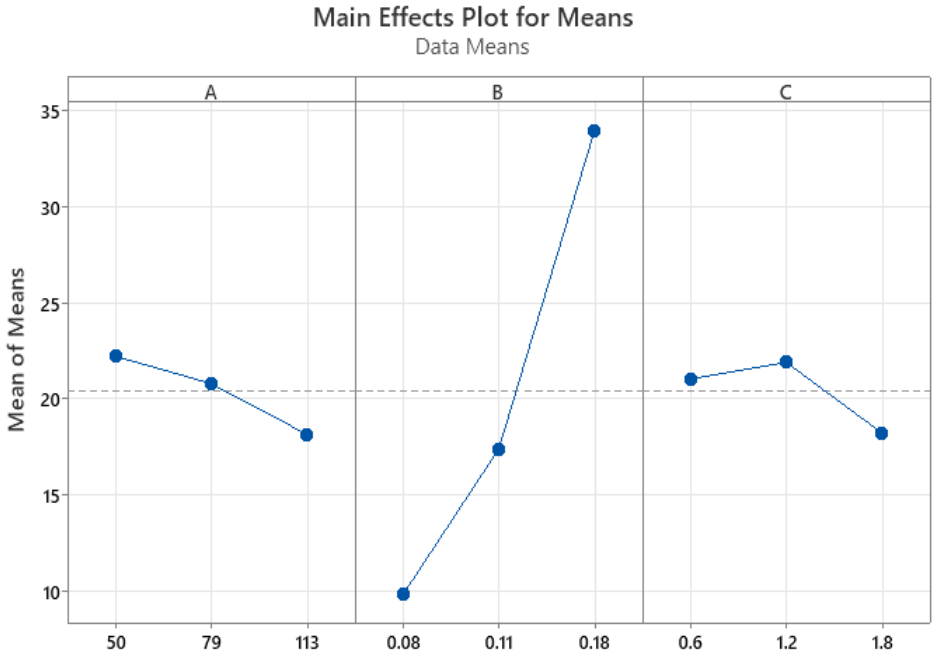

Figure 5. The main effect plots for SR of Rt in cutting the SS.

Table 9. Taguchi L9 design and its Rt results

Trial number	V (m/min)	F (mm/rev)	Depth of cut(mm)	Rt (µm)	FITS_MEANS3
1	1	1	1	12.291	12.288
2	1	2	2	22.615	20.7487
3	1	3	3	31.79	33.6574
4	2	2	3	9.869	11.7364
5	2	3	1	15.645	15.6437
6	2	1	2	36.915	35.0487
7	3	3	2	7.27	5.40377
8	3	1	3	13.94	15.8074
9	3	2	1	33.27	33.2687

Table 10 shows the results of response table for means Rt values. The feed rate is the significant effect on the SR because it holds the topmost (rank 1), followed by speed (rank 2) but again small differences appears between speed and depth of cut.

Table 10. Response table for means Rt values

Level	A	B	C
1	22.232	9.810	21.048
2	20.810	17.400	21.918
3	18.160	33.992	18.235
Delta	4.072	24.182	3.683
Rank	2	1	3

Regression Equation

Regression Equation is given the following equation.

$$Rt = -1.26 - 0.065\ x\ A + 241\ x\ B - 2.34\ x\ C \quad (3)$$

Where Rt is SR index. Again it shows that A, C coefficients are negative while B is positive. Its correlation coefficients (R-Sq.), R-Sq. (pred) are found to be 96.77% and 86.73%, respectively. The coefficients values are decreased significantly in comparison to Ra and Rz values. This can be because the vertical distance between the highest peak and lowest peak of roughness profile increased within the overall measurement length.

ANOVA

The results of variance analysis are given in Table 11. The feed rate factor is statistically significant at 5% significant level because of (p=0.000) while other factors are not found an effective because p=0.104 and p=0.231 for A and C, respectively. Moreover, R-Sq is found to be 99.1%. Similar findings are found, but slightly difference is evident because feed rate is the major factor, contributing 93% to the variation, speed has a contribution of 2.55% while depth of cut can be neglected.

Table 11. Analysis of variance

Source	DF	Adj SS	Adj MS	F-Value	P-value	Pcont. %
A	1	25.21	25.213	3.95	0.104	2.555
B	1	917.45	917.452	143.82	0.000	93.00
C	1	11.87	11.872	1.86	0.231	1.20
Error	5	31.90	6.379			3.2033
Total	8	986.43				

The existing literature survey proposes that the R-square should fall in the range from 0.8 to 1 (Chicco et al. 2021).

Confirmation Tests

The aim of confirmation test is to validate optimal testing parameters obtained from SR. The test is performed with two replicas. Predicted Ra, Rz and Rt using an optimal level is calculated from Equation (1, 2, 3),

$$Y_{pred.} = Y_m + \sum_{i=1}^{m} (Y_i - Y_m) \quad (4)$$

Where, Ym indicates total mean SR, Yi represents the mean SR at optimal condition, m is number of inputs, and its result is indicated in Table 12. Other study on the experiment is performed with the optimal level of the selected variables (V3-f1-d3) (Sahin & Öğulmus, 2024). It is reported that statistical analysis can only be deemed reliable if the error values remain below 20% (Columb & Atkinson, 2016).

Table 12. Confirmation tests with Taguchi/regression equation

	Taguchi method Eq.(1)			Regression Eq.(2)		
For Ra	Exp.(µm)	Pred.	Error (%)	Exp.(µm)	Pred.	Error (%)
A3B1C3 (Opt.)	1.15	1.07	8.9	1.15	0.899	27.9
A2B2C2 (Rand.)	2.78	2.467	4.45	2.78	2.88	3.47
For Rz	Exp.	Pred.	Error (%)	Exp.	Pred.	Error (%)
A3B1C3 (Opt.)	6.720	7.579	11.3	6.72	6.704	2.9
A2B2C2 (Rand.)	13.82	14.29	10.0	13.82	14.17	3.29
For Rt	Exp.	Pred.	Error (%)	Exp.	Pred.	Error (%)
A3B1C3 (Opt.)	6.91	5.405	27.8	6.91	6.463	6.9
A2B2C2 (Rand.)	22.60	20.748	8.96	22.60	19.18	17.83

Conclusions

The surface roughness's of Ra, Rz and Rt are developed when machining AISI 304 SS by Taguchi method. The results exhibited that the optimum surface roughness was found at cutting speed of 113 m/min, feed rate of 0.08 mm/rev, and depth of cut of 1.8 mm. At the same content, trial 7 yielded the lowest surface roughness approximately 1.18 µm, which was lower than that of the previous reported work. Further, ANOVA indicated that feed rate was a considerable influence on surface roughness with a 95% confidence level, while others were in-significant effect. Confirmation tests was conducted both Taguchi method and regression analysis. Moreover, correlation coefficients of Ra, Rz and Rt were found to be approximately 99.15%, 99.76, and 96.77%, respectively. The coefficient of Rt value was decreased slightly in comparison to Ra and Rz values. That is, Rt produced more errors but its result is within an acceptable range. These findings are significantly important for both academic researchers and the enhancement of mass production processes.

Scientific Ethics Declaration

*The authors declare that the scientific ethical and legal responsibility of this article published in EPSTEM journal belongs to the authors.

Conflict of Interest

*The author declares that there is no conflict of interest.

Funding

*This research received no internal or external funding.

Acknowledgements or Notes

*This article was presented as a/an oral presentation at the International Conference on Basic Sciences and Technology (www.icbast.net) held in Budapest/Hungary on August 28-31, 2025.

References

Adalarasan, R., Santhanakumar, & M., Rajmohan, M. (2015). Application of grey taguchi-based response surface methodology for optimizing the plasma arc cutting parameters of 304L stainless steel. *International Journal of Advanced Manufacturing Technology*, *78*, 1161–1170.

Alajmi M.S., Almeshal, A.M. (2020). prediction and optimization of surface roughness in a turning process using the ANFIS-QPSO method. *Materials*, *13*(13), 2986.

Alzyod, H., Konya, G., Ficzere, P. (2025). Maximizing material removal rate and surface smoothness in MEX parts through turning process optimization using BBD. *Progress in Additive Manufacturing,* 1-15.

Binali, R., Demirpolat, H., Kuntoglu, M., Salur, E., (2023). Different aspects of machinability in turning of aisi 304: A sustainable approach with mql. *Metals*, *13*(6), 1088.

Chandrasekaran, K., Marimuthu, P., Raja, & K.R., Manimaran, A. (2014). Multi response optimization of machining parameters for turning stainless steel using coated tools. *Applied Mechanics and Material*s, 573, 644-648.

Chicco, D., Warrens, M. J., Jurman, G. (2021). The coefficient of determination R-squared is more informative than SMAPE, MAE, MAPE, MSE and RMSE in regression analysis evaluation. *Peer Journal of Computer Science, 7, e623.*

Caydas, U., Ekici, S. (2012). Support vector machines for surface roughness prediction in CNC turning of AISO 304 austenitic stainless steel. *Journal of Intelligent Manufacturing*, 23, 639–650.

Columb, M. O., & Atkinson, M. S. (2016). Statistical analysis: Sample size and power estimations. *BJA Education, 16*(5), 159–161.

Dubey, V., Sharma, A.K., Vats, P., Pimenov, D.Y., Giasin, K., & Chuchala, D. (2021). Study of a multicriterion decision-making approach to the mql turning of AISI 304 steel using hybrid nanocutting fluid. *Materials*, *14*(23), 7207.

Elsiti, N. M. I., & Elmunafi, M. H. S. (2023). Optimization of machining parameters for turning process by using grey relational analysis. *World Journal of Advanced Research and Reviews, 17*(01), 756–761.

Nehri, Y. E., Oral, A., & Toktas, A. (2024). Optimization of machining parameters of AISI 304L stainless steel with the least error method using Taguchi, RSM, and ANN. *Australian Journal of Mechanical Engineering*, *23*(3), 538–548.

Hamdan, A., Sarhan, A. A. D., & Hamdi, M. (2012). An optimization method of the machining parameters in high-speed machining of stainless steel using coated carbide tool for best surface finish. *International Journal of Advanced Manufacturing Technology, 58*, 81–91.

Hata, A., Widiatmoko, R. Y., Mulyana, D., & Azmy, I. (2023). Optimization of cutting parameter CNC wet milling process of austenitic stainless steel on surface roughness. *Jurnal Engine*, *7*(2), 55.

Konya, G., Takacs, J., Miskolczi. I., Kovacs, Z. F. (2024). Investigation of the effects of machining parameters on cutting conditions during orthogonal turning of austenite stainless steel. *Product Engineering Architect*, *30*(1), 86–93.

Kumar, N., Siddiqui, M. S., Srivastava, R., Kumar,V., Kumar, J.(2020). Analysis and optimization of cutting parameters in dry turning of AISI 304 stainless steel using Taguchi and ANOVA method. September 2020, *National Conference on Research and Developments in Material Processing, Modelling and Characterization* 2020, 1-11.

Nguyen, T.-T., Mia, M., Dang, X.-P., Le, C.-H., & Packianather, M. S. (2019). Green machining for the dry milling process of stainless steel 304. *Proceedings of the Institution of Mechanical Engineers, Part B: Journal of Engineering Manufacture*, *234*(5), 881–899.

Ozdemir, M. (2019). Optimization with Taguchi method of influences on surface roughness of cutting parameters in CNC turning processing. *Mechanika*, *25*(5), 397–405.

Patel, D. A., Mistry, J. M., Kapatel, V. P., & Joshi, D. R (2015). Optimization and prediction of cutting force and surface roughness in end milling process of AISI 304 stainless steel. *Applied Mechanics and Materials*,*813-814*, 362-367.

Pereira, O., Rodríguez, A., Fernández-Abia, A., Barreiro, J., & López de Lacalle, L. N. (2016). Cryogenic and minimum quantity lubrication for an eco-efficiency turning of AISI 304. *Journal of Cleaner Production, 139*, 440–9.

Popan, L. A., Balc, N., Alina, P., Fratila, D., & Trif, A. (2015). Surface roughness prediction during dry turning of austenitic stainless steel AISI 304. *Applied Mechanics and Materials*, *808*, 54-59.

Prakash, S., Palanikumar, K., Lilly-Mercy, J., & Nithyalakshmi, S. (2011). Evaluation of surface roughness parameters (Ra, Rz) in drilling of Mdf composite panel using Box-Behnken experimental design (BBD). *International Journal on Design and Manufacturing Technologies*, *5*(1), 52-62.

Ramu, I., Srinivas, P., & Vekatesh, K. (2018). Taguchi based grey relational analysis for optimization of machining parameters of CNC turning steel 316 R. *IOP Conf. Series: Materials Science and Engineering, 377*, 012078.

Rao, Ch.M., Rao, KJ., Babu, KS. (2015). Analysis of process parameters in dry turning of medium carbon steel En19 by using grey relational grade and regression methods. *Int. Journal of Engineering Research and Applications, 5*(10), 07-14.

Rajeswari, R. (2024). Investigation on the effect of turning of AISI 304 stainless steel using MQL technique with corn oil. *Engineering Proceedings*, *61*(1), 35-43.

Rathod, N., Chopra, M. K., Chaurasiya, P. K., & Vidhate, U. S. (2022). Optimization of tool life, surface roughness and production time in CNC turning process using Taguchi method and ANOVA. *Annals of Data Science, 10*(5), 1179-1191.

Sahin, Y. (2003). *Talaş kaldırma prensipleri I*. Seçkin Yayıncılık, Ankara, Turkey.

Sahin, Y., & Saygın Öğünmüş, A. (2025). Optimization of cutting parameters in surface roughness and metal removal rate in cutting stainless steel by coated tool. *International Conference on Advances and Creations in Mechanical Engineering (ICACME 2025)*.

Sahin, Y., Akbar, D., Can, D. S. (2024). Optimization of the machinability behavior of AISI 304 stainless steel using Taguchi method. *7th International Conference on Recent Advances in Automotive Engineering & Mobility Research (ReCAR 2024).*

Septi, B., Mounia, K., Salim, B., Mohamed, A. Y. (2024). Evaluation of cutting parameters during dry turning of AISI 304 stainless steel and optimization through a modified WPCA approach. *Proceedings of the Institution of Mechanical Engineers, Part C: Journal of Mechanical Engineering Science*, 238(18), 9072-9091.

Sirin, E. (2024). Optimization of surface roughness and cutting temperature in turning of 1.4534 stainless steel under sustainable conditions. *Düzce University Journal of Science & Technology*, *12*, 654-668.

Sundara Bharathi, S.R., Ravindran, D., & Arul Marcel Moshi, A. (2020). Multi-response optimization of CNC turning parameters of austenitic stainless steel 303 using Taguchi-based grey relational analysis. *Transactions of the Canadian Society for Mechanical Engineering, 44*(4), 110-113.

Srivabut C, Rawangwong S, Hiziroglu S, Homkhiew C. (2024). Multi-objective optimization of turning process parameters and wood sawdust contents using response surface methodology for the minimized surface roughness of recycled plastic/wood sawdust composites. *Composite Part C: Open Access, 14*, 100477.

Sofiane-Berkani, S., Yallese, M. A., Boulanouar, L., & Mabroukic, M. (2015). Statistical analysis of AISI304 austenitic stainless steel machining using Ti(C, N)/Al2O3/TiN CVD coated carbide tool. *International Journal of Industrial Engineering Computations, 6*(4), 539-552.

Su, Y., Zhao, G., Zhao, Y., Meng, J., & Li, C. (2020). Multi-objective optimization of cutting parameters in turning AISI 304 austenitic stainless steel. *Metals*, *10*(2), 217.

Singh, T., Durej, J.S., Dogra, M., Bhatti, M. (2018). Machining performance investigation of AISI 304 stainless steel under dry, flood, and NF-MQL. *International Journal of Automotive & Mechanical Engineering, 15*(4), 5837-5862.

Zhou, T., He, L., Wu, J., Du, F., & Zou, Z. (2019). Prediction of surface roughness of 304 stainless steel and multi-objective optimization of cutting parameters based on GA-GBRT. A*pplied Science, 9*(18), 3684-3691.

Author(s) Information

Yusuf Sahin
Department of Mechanical Engineering
OSTIM Technical University
Ankara, Türkiye
Contact e-mail: *yusuf.sahin@ostimteknik.edu.tr*

Ahmet Saygin Ogulmus
Machine Program of Vocational School of Higher Education, Ostim Technical University
Ankara, Türkiye

To cite this article:

Sahin, Y., & Ogulmus, A. S. (2025). Application of Taguchi to cutting behavior of stainless steels. *The Eurasia Proceedings of Science, Technology, Engineering and Mathematics (EPSTEM), 36,* 81-92.

The Eurasia Proceedings of Science, Technology, Engineering & Mathematics (EPSTEM)
ISSN: 2602-3199

The Eurasia Proceedings of Science, Technology, Engineering and Mathematics (EPSTEM), 2025

Volume 36, Pages 93-101

ICBAST 2025: International Conference on Basic Sciences and Technology

Inhomogeneous Planar Structure Experiencing Rotary Motion: A Longitudinal Fracture Investigation

Victor Rizov
University of Architecture, Civil Engineering and Geodesy

Abstract: In different sectors of engineering various planar structures often are experiencing motion. If the motion is with acceleration the inertia loadings in most of the cases cannot be neglected when analyzing different aspects of the behavior (including fracture) of these structures. In modern engineering using of continuously inhomogeneous structural materials for making of different structural members and components is growing constantly. This is due to the excellent properties of these materials. In a result of this, the continuously inhomogeneous materials represent a very promising alternative to the homogeneous engineering materials especially in applications where the structures are subjected to extreme loadings and influences. This paper is focused on investigation of a planar inhomogeneous structure with a longitudinal crack. The structure is experiencing a rotary motion. The inertia loadings induced by the acceleration are taken into account when deriving the strain energy release rate. The members of the structure under consideration are made by a continuously inhomogeneous material having non-linear viscoelastic behavior. Obtaining of the components of the inertia loading that acts on the structure is presented in detail. A verification of the proposed approach against the method of the integral *J* is shown. A parametric study developed by applying the solution of the strain energy release rate under inertia loading is reported and discussed.

Keywords: Planar structure, Rotary motion, Inhomogeneous material, Longitudinal fracture

Introduction

It is well known that using of continuously inhomogeneous structural materials in different segments of the modern engineering has intensified in the recent years. One of the most important features of the continuously inhomogeneous structural materials is that their properties are smooth functions of coordinates. In this relation, the functionally graded materials play a very important role (Gandra et al., 2011, Rizov, 2022; El-Galy et al., 2019). They represent continuously inhomogeneous composites with two or more constituents (Mahamood & Akinlabi, 2017). The constituents are mixed-up during manufacturing so as the microstructure changes smoothly in a solid (Gasik, 2010; Radhika et al., 2020; Rizov, 2018). Thus, there is no distinct border between the constituents of these novel materials in contrast to the fiber or particle reinforced composite materials. In this way, the stress concentrations in functionally graded materials are reduced in a high degree. This is one the basic advantages of the continuously inhomogeneous (functionally graded) materials over the conventional dispersal reinforced composites. One important characteristic of the continuously inhomogeneous materials is that their constituents can be distributed in the process of production so as to achieve a desired profile of continuous properties change along a given direction in a solid. This is a prerequisite for fabrication of members of different engineering structures, mechanisms and facilities of highly efficient characteristics aimed for use in heavy conditions including under dynamic loadings.

The growing use of continuously inhomogeneous materials in various applications in which engineering structures are experiencing motion with acceleration requires conducting of different investigations and analyses of their performance under inertia loadings. The safety and reliability of these structures is closely related to

their fracture behavior (Dowling, 2007; Rizov, 2018; Rizov & Altenbach, 2019). Thus, fracture in structures experiencing motion represents an important subject that has to be studied thoroughly.

This paper is focused on longitudinal fracture in a planar structure experiencing rotary motion. The structure is continuously inhomogeneous along the thickness and length. The mechanical behavior of the structure is non-linear viscoelastic. The strain energy release rate (SERR) in the structure under inertia loading is derived. A verification against the method of the integral *J* is carried-out. A parametric study is performed.

Theoretical Model

The planar structure, $D_1D_2D_4$, has two members, D_1D_2 and D_2D_4, as shown in Figure 1.

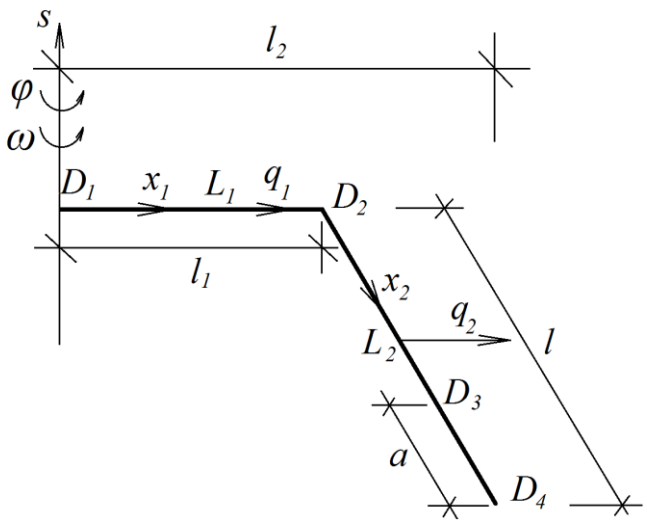

Figure 1. Planar structure, $D_1D_2D_4$, experiencing rotary motion around axis, s

The lengths of these members are l_1 and l, respectively. The thickness of each of the members is h as shown in Figure 2.

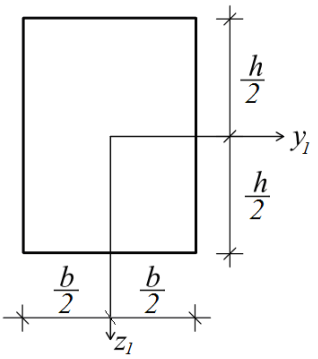

Figure 2. Cross-section of the structure

The members are made by a material that is continuously inhomogeneous along the thickness and length. Thus, the material properties change continuously along h and along the length, $l+l_1$. Besides, the material has non-linear viscoelastic behavior. The structure is experiencing rotary motion around vertical axis, s, according to the law presented in Eq. (1).

$$\varphi = \rho t\,, \tag{1}$$

where φ is the angle of rotation, ρ is a parameter, t is time.

The angular velocity, ω, and acceleration, α, of the planar structure are found by Eqs. (2) and (3), respectively.

$$\omega = \frac{d\varphi}{dt} = \rho\,, \tag{2}$$

$$\alpha = \frac{d\omega}{dt} = 0\,. \tag{3}$$

The normal acceleration, a_{n1}, of an arbitrary point, L_1, of the horizontal structural member, D_1D_2, is found by Eq. (4).

$$a_{n1} = \rho^2 x_1, \tag{4}$$

Where

$$0 \le x_1 \le l_1. \tag{5}$$

The axis, x_1, is shown in Fig. 1 (the origin of x_1 is in point, D_1).

The intensity of the inertia loading, q_1, in point, L_1, is determined by using Eq. (6).

$$q_1 = -a_{n1}m\,, \tag{6}$$

where m is the mass per unit length of the planar structure. The intensity of the inertia loading, q_1, is shown in Figure 1.

Equation (7) is applied for deriving the normal acceleration, a_{n2}, of an arbitrary point, L_2, of the inclined structural member, D_2D_4.

$$a_{n2} = \rho^2\left(l_1 + x_2 \sin\beta\right), \tag{7}$$

Where

$$0 \le x_2 \le l\,, \tag{8}$$

$$\sin\beta = \frac{l_2 - l_1}{l}\,. \tag{9}$$

The axis, x_2, and the size, l_2, are shown in Fig. 1 (the origin of x_2 is in point, D_2).

Equation (10) is used to determine the intensity of the inertia loading, q_2, in point, L_2.

$$q_2 = -a_{n2}m\,. \tag{10}$$

The intensity, q_2, is shown in Figure 1. The relation between stress, σ, strain, ε, and time given in Eq. (11) is applied for modeling the non-linear viscoelastic behavior of the planar structural member (Lukash, 1997).

$$\sigma = B\varepsilon^{\delta}\,\frac{1}{1+\lambda t^{\mu}}\,, \tag{11}$$

where B, δ, λ and μ, are material properties. The changes of these properties along h are presented by the laws given in Eqs. (12), (13), (14) and (15).

$$B = B_1 + \frac{B_2 - B_1}{h^{\psi_B}}\left(\frac{h}{2} + z_1\right)^{\psi_B}, \tag{12}$$

$$\delta = \delta_1 + \frac{\delta_2 - \delta_1}{h^{\psi_\delta}}\left(\frac{h}{2} + z_1\right)^{\psi_\delta}, \tag{13}$$

$$\lambda = \lambda_1 + \frac{\lambda_2 - \lambda_1}{h^{\psi_\lambda}}\left(\frac{h}{2} + z_1\right)^{\psi_\lambda}, \tag{14}$$

$$\mu = \mu_1 + \frac{\mu_2 - \mu_1}{h^{\psi_\mu}}\left(\frac{h}{2} + z_1\right)^{\psi_\mu}, \tag{15}$$

where

$$-\frac{h}{2} \le z_1 \le \frac{h}{2}. \tag{16}$$

In Eqs. (12) – (15), the subscripts, *1* and *2*, refer to the outer and inner surface of the structural members, z_1 is the transversal centric axis of the cross-section (Fig. 2), ψ_B, ψ_δ, ψ_λ and ψ_μ are parameters.

Equations (17) - (24) describe change of material properties along the length of the two members.

$$B_1 = B_{1D1} + \frac{B_{1D4} - B_{1D1}}{(l_1 + l_2)^{\gamma_{B1}}} x_3^{\gamma_{B1}}, \tag{17}$$

$$B_2 = B_{2D1} + \frac{B_{2D4} - B_{2D1}}{(l_1 + l_2)^{\gamma_{B2}}} x_3^{\gamma_{B2}}, \tag{18}$$

$$\delta_1 = \delta_{1D1} + \frac{\delta_{1D4} - \delta_{1D1}}{(l_1 + l_2)^{\gamma_{\delta1}}} x_3^{\gamma_{\delta1}}, \tag{19}$$

$$\delta_2 = \delta_{2D1} + \frac{\delta_{2D4} - \delta_{2D1}}{(l_1 + l_2)^{\gamma_{\delta2}}} x_3^{\gamma_{\delta2}}, \tag{20}$$

$$\lambda_1 = \lambda_{1D1} + \frac{\lambda_{1D4} - \lambda_{1D1}}{(l_1 + l_2)^{\gamma_{\lambda1}}} x_3^{\gamma_{\lambda1}}, \tag{21}$$

$$\lambda_2 = \lambda_{2D1} + \frac{\lambda_{2D4} - \lambda_{2D1}}{(l_1 + l_2)^{\gamma_{\lambda2}}} x_3^{\gamma_{\lambda2}}, \tag{22}$$

$$\mu_1 = \mu_{1D1} + \frac{\mu_{1D4} - \mu_{1D1}}{(l_1 + l_2)^{\gamma_{\mu1}}} x_3^{\gamma_{\mu1}}, \tag{23}$$

$$\mu_2 = \mu_{2D1} + \frac{\mu_{2D4} - \mu_{2D1}}{(l_1 + l_2)^{\gamma_{\mu2}}} x_3^{\gamma_{\mu2}}, \tag{24}$$

where

$$0 \le x_3 \le l_1 + l. \tag{25}$$

In Eqs. (17) – (24), the subscripts, $D1$ and $D4$, refer to sections, $D1$ and $D4$, of the plane structure, x_3 is the longitudinal centric axis, γ_{B1}, γ_{B2}, $\gamma_{\delta1}$, $\gamma_{\delta2}$, $\gamma_{\lambda1}$, $\gamma_{\lambda2}$, $\gamma_{\mu1}$ and $\gamma_{\mu2}$ are parameters.

The SERR, G, is determined by using Eq. (26).

$$G = \frac{dU^*}{bda}, \tag{26}$$

where U^* is the complementary strain energy in the planar structure, da is an elementary increase of the crack length.

The complementary strain energy is found by Eq. (27).

$$U^* = \iiint_{(V)} u_0^* dV, \tag{27}$$

where V is the volume of the structure, u_0^* is the complementary strain energy density.

Equation (28) is applied for determining of u_0^* in an arbitrary point of the structure.

$$u_0^* = \sigma\varepsilon - \int \sigma d\varepsilon, \tag{28}$$

where σ is related to strain, ε, via Eq. (11).

The strain changes along h by the law in Eq. (29).

$$\varepsilon = \kappa\left(z_1 - z_{1n}\right), \tag{29}$$

where

$$-\frac{h}{2} \le z_1 \le \frac{h}{2}. \tag{30}$$

In Eq. (29), κ is the curvature, z_{1n}, is the coordinate of the neutral axis.

The curvature and the coordinate of the neutral axis are determined by applying Eqs. (31) and (32).

$$N = \iint_{(A)} \sigma dA, \tag{31}$$

$$M = \iint_{(A)} \sigma z_1 dA, \tag{32}$$

where N and M are the axial force and the bending moment in the considered section of the structure, A is the area of the section.The axial force and the bending moment are obtained by performing reduction of the inertia loading for the considered section.

A verification of the SERR against the method of the integral *J* is carried-out (Broek, 1986). The integral *J* is obtained by Eq. (33).

$$J = J_1 + J_2 + J_3, \tag{33}$$

where J_1 and J_2 are solutions of the integral *J* in the sections of the inner and outer arms of the crack, J_3 is the solution in the section ahead of the crack tip. Equations (34), (35) and (36) are used for J_1, J_2 and J_3, respectively.

$$J_1=\int\left[u_{01}\cos\alpha_1-\left(p_{x1}\frac{\partial u_1}{\partial x}+p_{y1}\frac{\partial v_1}{\partial x}\right)\right]ds\,, \tag{34}$$

$$J_2=\int\left[u_{02}\cos\alpha_2-\left(p_{x2}\frac{\partial u_2}{\partial x}+p_{y2}\frac{\partial v_2}{\partial x}\right)\right]ds\,, \tag{35}$$

$$J_3=\int\left[u_{03}\cos\alpha_3-\left(p_{x3}\frac{\partial u_3}{\partial x}+p_{y3}\frac{\partial v_3}{\partial x}\right)\right]ds\,. \tag{36}$$

The integration is performed by the MatLab. The solution of the *J* matches the solution of the SERR which is a verification of the present analysis.

Parametric Study

A parametric study is developed with purpose to examine the peculiarities of the longitudinal fracture in a continuously inhomogeneous planar structure experiencing rotary motion. In particular, we are focused on the parameters of the motion law, the geometry of the structure, and the material inhomogeneity. The study clarifies the influence of these parameters on the SERR. The results of the parametric study are reported graphically in Figs. 3, 4, 5 and 6. The SERR is obtained for $b=0.010$ m, $h=0.015$ m, $a=0.5l$, $\psi_B=0.4$, $\psi_\delta=0.4$, $\psi_\lambda=0.4$, $\psi_\mu=0.4$, $\gamma_{B1}=0.6$, $\gamma_{B2}=0.6$, $\gamma_{\delta1}=0.6$, $\gamma_{\delta2}=0.6$, $\gamma_{\lambda1}=0.8$, $\gamma_{\lambda2}=0.8$, $\gamma_{\mu1}=0.8$ and $\gamma_{\mu2}=0.8$.

First, the effects of the parameter, ρ, of the rotary motion on the SERR are examined at $B_{1D4}/B_{1D1}=0.5$ (curve 1), $B_{1D4}/B_{1D1}=1.0$ (curve 2), and $B_{1D4}/B_{1D1}=2.0$ (curve 3) in Figure 3. The growth of the SERR that can be seen in Figure 3 with increase of the value of ρ is generated by increase of the inertia loading. Increase of B_{1D4}/B_{1D1} ratio reduces the SERR (Figure 3).

One can observe how the SERR is influenced by B_{2D4}/B_{2D1} ratio at $l/h=10$ (curve 1), $l/h=15$ (curve 2), and $l/h=20$ (curve 3) in Figure 4.

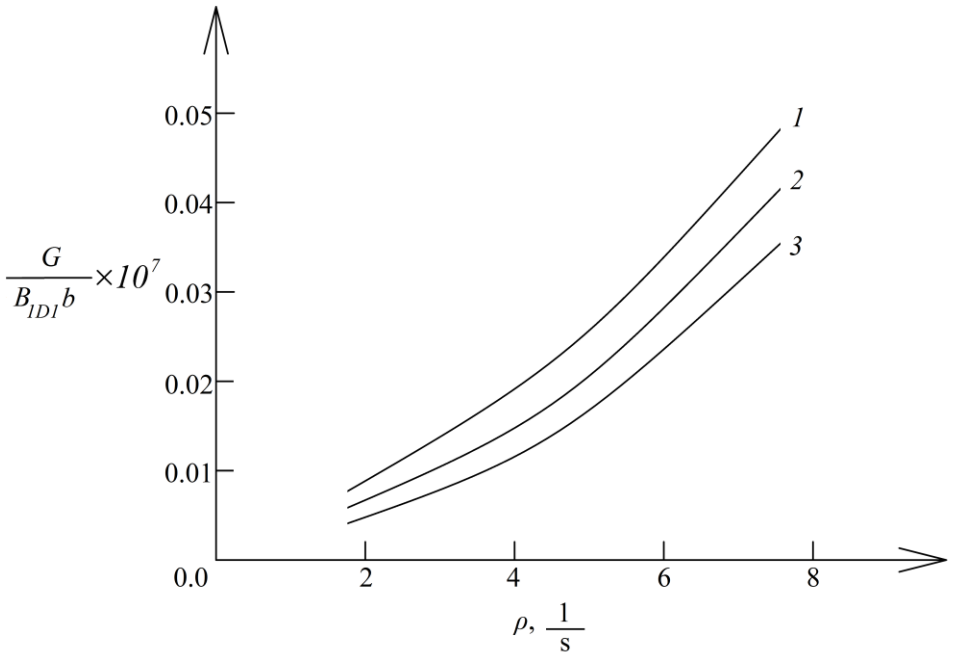

Figure 3. The SERR versus ρ

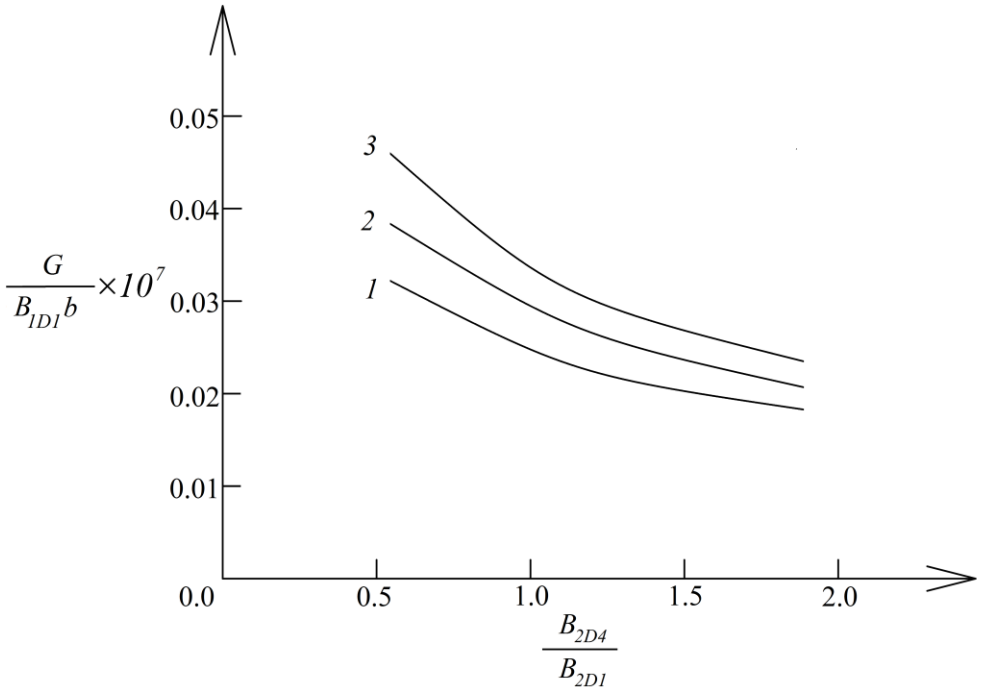

Figure 4. The SERR versus B_{2D4}/B_{2D1} ratio

The rise of the SERR with increase of l/h ratio that can be observed in Figure 4 is induced again by the growth of the inertia loading. The SERR reduces as a result of the growth of B_{2D4}/B_{2D1} ratio (Figure 4).

Figure 5 gives an idea about the effects of l_1/h ratio on the SERR at $\delta_{1D4}/\delta_{1D1}=0.5$ (curve 1), $\delta_{1D4}/\delta_{1D1}=1.0$ (curve 2), and $\delta_{1D4}/\delta_{1D1}=2.0$ (curve 3). Rise of l_1/h ratio generates a growth of the SERR (Figure 5). This is due to increase of the inertia loading induced by the rise the length, l_1. Increase of $\delta_{1D4}/\delta_{1D1}$ ratio reduces the SERR as one can see in Figure 5.

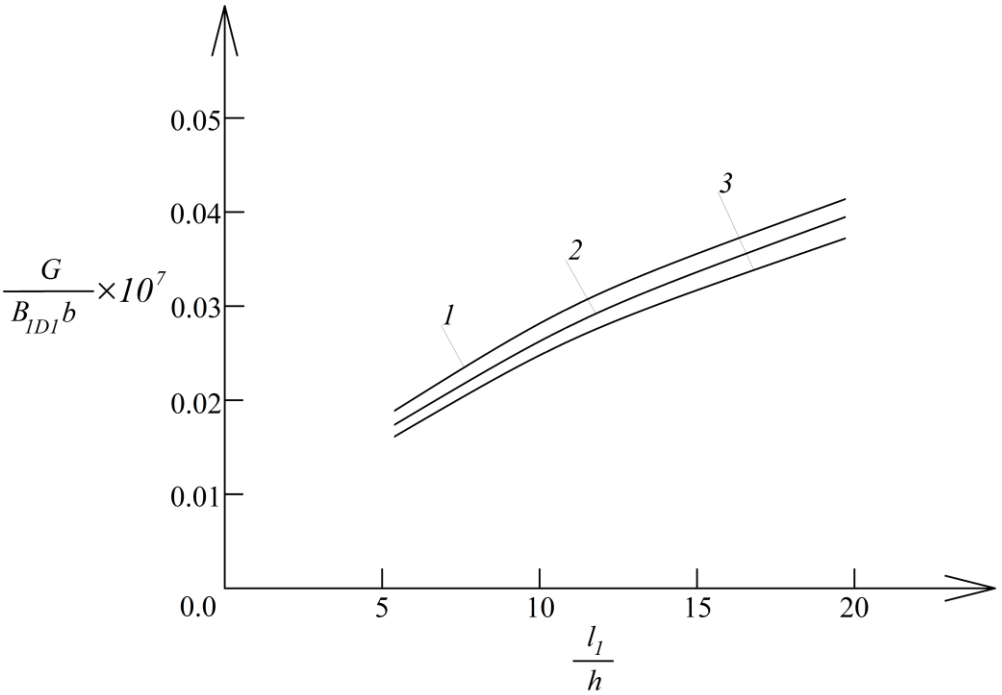

Figure 5. The SERR versus l_1/h ratio

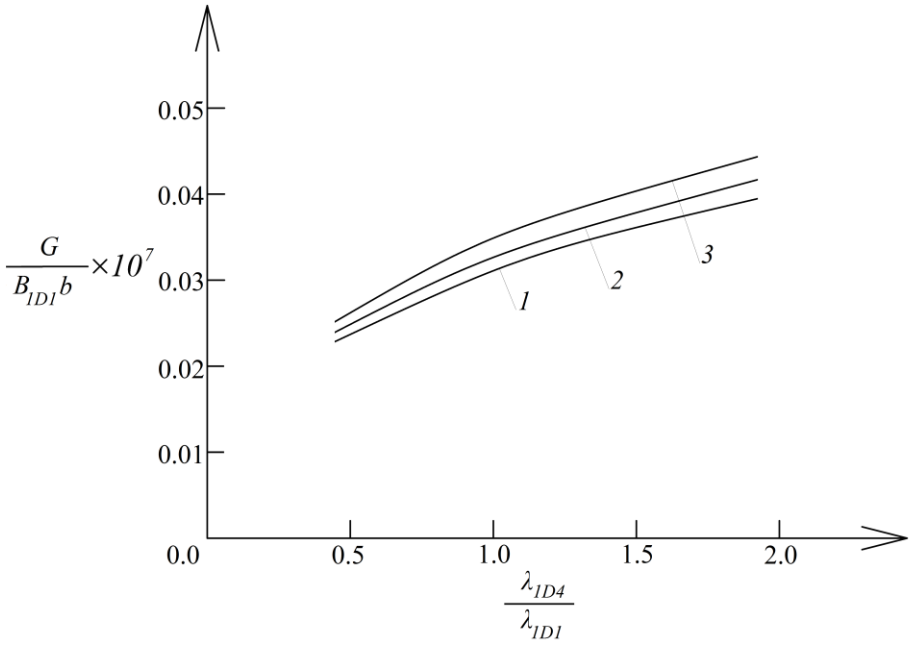

Figure 6. The SERR versus $\lambda_{1D4}/\lambda_{1D1}$ ratio

Finally, we examine how the SERR is influenced by $\lambda_{1D4}/\lambda_{1D1}$ ratio at $l_2/h=4$ (curve 1), $l_2/h=8$ (curve 2), and $l_2/h=12$ (curve 3) in Figure 6. The examination reveals that the SERR grows as a result of increase of $\lambda_{1D4}/\lambda_{1D1}$ ratio as one can observe in Figure 6. Increase of l_2/h ratio leads to also to growth of the SERR as shown in Figure 6.

Conclusion

In conclusion, it can be stated that the investigation developed in this paper throws light on the peculiarities of longitudinal fracture in continuously inhomogeneous non-linear viscoelastic planar structures experiencing rotary motion. The solution of the SERR under inertia loading derived here is used for performing a parametric study. It is found that the SERR is strongly affected by the law of rotary motion, the geometry of the planar structure and the inhomogeneity of the material. The increase of parameter, ρ, of the rotary motion induces a growth of the SERR. Increase of l/h, l_1/h and l_2/h ratios (these ratios represent geometrical parameters of the planar structure) induces also a growth of the SERR. Opposite trend, i.e. reduction of the SERR is detected when B_{1D4}/B_{1D1}, B_{2D4}/B_{2D1} and $\delta_{1D4}/\delta_{1D1}$ ratios increase.

Recommendations

The results obtained in this paper indicate that the approach can be used for analyzing longitudinal fracture in rotating planar structures. The approach can be applied also for rotating structures of more complex geometry.

Scientific Ethics Declaration

*The author declares that the scientific ethical and legal responsibility of this article published in EPSTEM journal belongs to the author.

Funding

* This research received no specific grant from any funding agency in the public, commercial, or not-for-profit sectors.

Conflict of Interest

*The author declares that he has no conflicts of interest.

Acknowledgements or Notes

*This article was presented as an oral presentation at the International Conference on Basic Sciences and Technology (www.icbast.net) held in Budapest/Hungary on August 28-31, 2025.

References

Broek, D. (1986). *Elementary engineering fracture mechanics*. Springer.

Dowling, N. (2007). *Mechanical behavior of materials*. Pearson.

El-Galy, I.M., Saleh, B.I., & Ahmed, M.H. (2019). Functionally graded materials classifications and development trends from industrial point of view. *SN Applied Sciences, 1,* 1378.

Gandra, J., Miranda, R., Vilaça, P., Velhinho, A., & Teixeira, J.P. (2011). Functionally graded materials produced by friction stir processing. *Journal of Materials Processing Technology*, *211,* 1659-1668.

Gasik, M. M. (2010). Functionally graded materials: bulk processing techniques. *International Journal of Materials and Product Technology*, *39*, 20-29.

Lukash, P. (1997). *Fundamentals of non-linear structural mechanics*. Science.

Mahamood, R. C., & Akinlabi, E. T. (2017). *Functionally graded materials.* Springer.

Radhika, N., Sasikumar, J., Sylesh, J. L., & Kishore, R. (2020). Dry reciprocating wear and frictional behaviour of B4C reinforced functionally graded and homogenous aluminium matrix composites. *Journal of Materials Research and Technology*, *9,* 1578-1592.

Rizov, V. I. (2018). Non-linear delamination in two-dimensional functionally graded multilayered beam. *International Journal of Structural Integrity, 9,* 646-663.

Rizov, V. I. (2022). Effects of periodic loading on longitudinal fracture in viscoelastic functionally graded beam structures. *Journal of Applied and Computational Mechanics, 8,* 370–378.

Rizov, V.I., & Altenbach, H. (2019). On the analysis of lengthwise fracture of functionally graded round bars. *Structural Integrity and Life*, *19*, 102–108.

Author(s) Information

Victor Rizov
University of Architecture, Civil Engineering and Geodesy
1 Chr. Smirnensky blvd., 1046 – Sofia, Bulgaria
Contact e-mail: *v_rizov_fhe@uacg.bg*

To cite this article:

Rizov, V. (2025). Inhomogeneous planar structure experiencing rotary motion: A longitudinal fracture investigation. *The Eurasia Proceedings of Science, Technology, Engineering and Mathematics (EPSTEM), 36,* 93-101.

The Eurasia Proceedings of Science, Technology, Engineering & Mathematics (EPSTEM)
ISSN: 2602-3199

The Eurasia Proceedings of Science, Technology, Engineering and Mathematics (EPSTEM), 2025

Volume 36, Pages 102-109

ICBAST 2025: International Conference on Basic Sciences and Technology

Design of S-Boxes Based on Alternative Irreducible Polynomials

Zhanat Saukhanova
L.N. Gumilyov Eurasian National University

Gulmira Shakhmetova
L.N. Gumilyov Eurasian National University

Altynbek Sharipbay
L.N. Gumilyov Eurasian National University

Alibek Barlybayev
L.N. Gumilyov Eurasian National University

Sayat Raykul
L.N. Gumilyov Eurasian National University

Altay Khassenov
L.N. Gumilyov Eurasian National University

Abstract: In the era of rapid digital technology development, the volume of information transmitted in cyberspace is significantly increasing, thereby intensifying the need to ensure confidentiality and the protection of personal data. Modern cryptographic methods are used for such purposes. One of the most widely used encryption algorithms is Advanced Encryption Standard (AES), which employs substitution box (S-box) to enhance the security of the encryption process. S-box is one of the important components of the block algorithm. The robustness of an S-box is largely determined by its architecture and algebraic basis. In this paper, a method for constructing S-boxes is proposed based on various alternative irreducible polynomials with the addition of a constant 8-bit vector, different from that used in the AES standard. A total of 16 S-boxes were constructed and their performance was evaluated using standard cryptographic criteria, including nonlinearity, strict avalanche effect, etc. The results demonstrated that the proposed S-boxes exhibit performance comparable to that of the standard AES S-box. This study is conducted within the framework of grant funding from the Science Committee of the Ministry of Education and Science of the Republic of Kazakhstan (grant No. AP19677422).

Keywords: Cryptography, Advanced encryption standard (AES), Substitution box (S-box), Irreducible polynomial

Introduction

AES is a widely used block symmetric encryption cryptosystem. The Rijndael algorithm was declared the AES standard in 2002 by the US National Institute of Standards and Technology (NIST). This algorithm provides encryption of 128 bits of plaintext using a key of 128, 192, or 256 bits. For encryption in each round of the algorithm, transformations such as ByteSub, ShiftRows, MixColumns, AddRoundKey are used (Dworkin et al., 2021). One of the important nonlinear components in the structure of the Rijndael algorithm is the cryptographic substitution table (or S-Box), which is applied at the ByteSub stage.

A cryptographic S-box is used to transform input bits into output bits to ensure their randomization and increase cryptographic strength (El Gaabouri et. al., 2024). In standard AES, the irreducible polynomial $t(x) = x^8 + x^4 + x^3 + x + 1$ and the constant 63_{16} are used to generate the S-box (Nitaj et.al., 2020). This combination is known to potential attackers. Therefore, the generation of new S-boxes with the same cryptographic properties as the traditional one expands the capabilities of block algorithms.

The use of alternative S-boxes increases the security of the cryptographic algorithm. In this paper, various irreducible polynomials and constants were considered, on the basis of which 16 new S-boxes were constructed. The proposed S-boxes were tested for cryptographic criteria such as balance, bijective, nonlinearity, Strict avalanche criterion (SAC), differential uniformity, fixed points and periods. The results showed that the proposed S-boxes have performance indicators comparable to those of the original AES S-box.

Method

Traditional S-box in Rijndael Algorithm

In the symmetric block cipher Rijndael (AES), the replacement byte (S-box) function S is represented as a composition of two mappings $S(x) = f(x) \circ g$, where $x \in \mathbb{F}_{2^8}$, defined over the Galois field $GF(2^8)$ (Daemen, 2002).

The first transformation $f(x): GF(2^8) \to GF(2^8)$ implements the calculation of the multiplicative inverse element using the formula:

$$f(x) = \begin{cases} 0, if\ x = 0, \\ x^{-1}, if\ x \neq 0. \end{cases} \quad (1)$$

Where x^{-1} denotes the multiplicative inverse in the field $GF(2^8)$, while zero remains unchanged. The multiplication operation is performed modulo the irreducible polynomial $t(x) = x^8 + x^4 + x^3 + x + 1$.

The second transformation $g: GF(2^8) \to GF(2^8)$ is an affine mapping implemented through a bitwise operation. The affine function $g(x)$ is defined by the following equation:

$$g(x) = Ax + b, \quad (2)$$

where A is an 8×8 bit matrix and b is a constant. For an element $x = (x_7, x_6, x_5, x_4, x_3, x_2, x_1, x_0)$ of the field, the mapping $(x) = y$ is computed as follows:

$$\begin{pmatrix} y_0 \\ y_1 \\ y_2 \\ y_3 \\ y_4 \\ y_5 \\ y_6 \\ y_7 \end{pmatrix} = \begin{pmatrix} 10001111 \\ 11000111 \\ 11100011 \\ 11110001 \\ 11111000 \\ 01111100 \\ 00111110 \\ 00011111 \end{pmatrix} \begin{pmatrix} x_0 \\ x_1 \\ x_2 \\ x_3 \\ x_4 \\ x_5 \\ x_6 \\ x_7 \end{pmatrix} + \begin{pmatrix} 1 \\ 1 \\ 0 \\ 0 \\ 0 \\ 1 \\ 1 \\ 0 \end{pmatrix}$$

As an example, consider the element $x = 45 = 0010\ 1101 = 0x2d$.

Let us compute the transformation of the input element $S(0x2d) = 0xd8$:

1) $0x2d = (0,0,1,0,1,1,0,1)$ has a polynomial representation $x^5 + x^3 + x^2 + 1$

2) The inverse transform of the polynomial $x^5 + x^3 + x^2 + 1$ modulo the irreducible polynomial $t(x) = x^8 + x^4 + x^3 + x + 1$ is $f(x^5 + x^3 + x^2 + 1) = x^6 + x^2$, which has the form $(0,1,0,0,0,1,0,0)$ in binary representation.

3) Apply an affine transformation:

$$\begin{pmatrix}10001111\\11000111\\11100011\\11110001\\11111000\\01111100\\00111110\\00011111\end{pmatrix}\begin{pmatrix}0\\0\\1\\0\\0\\0\\1\\0\end{pmatrix}+\begin{pmatrix}1\\1\\0\\0\\0\\1\\1\\0\end{pmatrix}=\begin{pmatrix}0\\0\\0\\1\\1\\0\\1\\1\end{pmatrix}$$

4) Thus, the output of element $0x2d$ will be element (1,1,0,1,1,0,0,0) or $0xd8$.

Proposed S-boxes

This section of the article describes the proposed method for constructing 16 cryptographically strong 8×8 S-boxes, based on the use of some irreducible polynomials selected from the list of 30 irreducible polynomials of degree 8 (Planteen, 2019) and the affine transformation employed in the AES standard. As noted in the work (Ospanov et.al., 2022), by varying the selection of specific irreducible polynomials, the choice of the initial transformation from a set of alternative transformations, the selection of a particular affine transformation matrix, and a specific shift constant, it is possible to construct various optimal S-boxes. Table 1 shows the set of components used in constructing the proposed S-boxes.

Table 1. A set of components for constructing S-boxes

S-boxes	Irreducible polynomial	Affine matrices	Constants
Sbox0	$x^8+x^7+x^2+x+1$	11011001	a3
Sbox1		11010110	72
Sbox2		01101101	18
Sbox3		01101101	a0
SBox4		00011111	3d
Sbox5		01001010	79
Sbox6	$x^8+x^4+x^3+x+1$	11101001	dc
SBox7		11010011	e7
SBox8		00011100	3e
Sbox9		11111000	5a
Sbox10	$x^8+x^6+x^5+x+1$	00001000	22
SBox11		11110001	eb
Sbox12		00000001	fb
SBox13	$x^8+x^6+x^5+x^2+1$	10010001	2b
SBox14		10000000	f8
SBox15	$x^8+x^5+x^3+x^2+1$	11110111	da

As an example, Table 2 presents one of the sixteen S-boxes, namely Sbox14, which was constructed using the irreducible polynomial $t(x)=x^8+x^6+x^5+x^2+1$. The values obtained as a result of the multiplicative inverse transformation (1) are fed into the affine mapping as a bitwise vector $x=(x_7,x_6,x_5,x_4,x_3,x_2,x_1,x_0)$, corresponding to equation (2).

$$\begin{pmatrix}y_0\\y_1\\y_2\\y_3\\y_4\\y_5\\y_6\\y_7\end{pmatrix}=\begin{pmatrix}10000000\\01000000\\00100000\\00010000\\00001000\\00000100\\00000010\\00000001\end{pmatrix}\begin{pmatrix}x_0\\x_1\\x_2\\x_3\\x_4\\x_5\\x_6\\x_7\end{pmatrix}+\begin{pmatrix}0\\0\\0\\1\\1\\1\\1\\1\end{pmatrix}$$

Table 2. Proposed SBox14

	0	1	2	3	4	5	6	7	8	9	A	B	C	D	E	F
0	F8	F9	4A	24	A1	6F	96	0D	66	AB	01	B9	CF	53	30	56
1	B7	41	63	03	36	DF	6A	42	51	88	1F	C9	9C	C7	AF	32
2	6D	BE	16	BA	07	81	37	ED	9F	A3	59	0B	B1	34	A5	65
3	1E	E3	C0	4C	39	72	52	F4	CA	4D	55	2E	61	21	9D	E5
4	00	F3	DB	17	8F	92	D9	6C	35	D4	76	48	2D	69	40	E8
5	79	85	67	F1	1A	94	33	E6	6E	FC	9E	D1	64	D6	04	5D
6	8B	11	47	19	E4	C6	A2	D0	2A	28	BD	8E	AD	1B	FE	0C
7	E1	50	10	98	1C	0E	93	BC	06	DD	26	12	78	A9	44	08
8	84	A8	4F	5F	5B	75	3D	14	71	70	CD	38	5A	7D	B2	49
9	2C	B5	EE	43	BF	D8	A0	FD	20	C4	02	EA	A4	D7	F0	AA
A	0A	D2	74	7C	05	A7	4E	7B	89	E0	CE	F5	2F	C2	F7	31
B	B3	77	FA	25	CB	C1	5E	7A	B6	E9	EF	6B	86	09	18	9A
C	73	CC	3E	22	15	7E	3A	23	F6	57	E7	AE	D5	B0	EC	DE
D	91	2B	90	29	68	B4	C3	54	60	C5	3B	3F	FB	4B	82	13
E	46	9B	AC	95	8C	0F	C8	E2	8A	99	83	27	7F	3C	DA	BB
F	87	45	58	D3	97	FF	8D	1D	B8	F2	62	EB	A6	5C	80	DC

Results and Discussion

For efficient encryption, the S-box must have strong algebraic properties that establish nonlinear relationships between its input and output values (Mahboob, 2023). This section presents the results of the analysis of the cryptographic characteristics of the 16 S-boxes we proposed. For the evaluation of S-boxes, the generally accepted tests described in the sources (Nizam Chew & Ismail, 2020), (Zahid, 2019) were used: the strict avalanche criterion (SAC), nonlinearity (NL), balanced, differential uniformity, algebraic degree, fixed points and period. The results of the comparative performance of our S-boxes with the standard AES S-box are presented in Table 3. In addition, this section includes a SageMath code listing developed to compute and verify several of the cryptographic criteria employed in the evaluation of the proposed S-boxes.

Balanced Boolean Function

A Boolean function $f(x)$ is defined as *balanced* if it satisfies the condition given in formula (3):

$$H_W\big(f(x)\big) = \sum_{x=0}^{2n-1} f(x) = 2^{n-1} \qquad (3)$$

where H_W is Hamming weight, and n is the number of Boolean variables. According to (Bejo & Adji, 2017), the Hamming weight indicates how balanced the output values are distributed, so it is one of the important cryptographic properties in the analysis of Boolean functions. In other words, the Boolean function is balanced if number of input values for which $f(x)$ =0 is equal to the number of input values for which $f(x)$ =1. This property ensures that the output values are uniform between 0 and 1, which avoids statistical bias that can be exploited in attacks. The balanced nature of the function confirms its cryptographic strength. All component Boolean functions of the proposed 16 S-box are balanced (number of 1's = number of 0's) (Table 3).

Bijectivity

An $n \times n$ S-box is bijective when it acts as a permutation: every input maps to a unique output, yielding all 2^n distinct values within $[0, 2^{n-1}]$. The all 16 proposed 8×8 S-box produces 256 unique outputs over $[0,255]$, and thus meets the bijectivity criterion (Mahboob, 2023).

Nonlinearity(NL)

The nonlinearity of an S-box is a fundamental cryptographic parameter that characterizes its resistance to linear cryptanalysis. It is defined as the Hamming distance between each component Boolean function of the S-box and the set of all affine functions. This characteristic is formally expressed as (Esa, 2022):

$$NL_f = 2^{n-1}(1 - 2^{-n}\max\ |W_f(z)|), \qquad (4)$$

where $W_f(z)$ denotes the Walish spectrum of the Boolean function, defined by:

$$W_f(z) = \sum(-1)^{f(x)\oplus x\cdot z}, \quad x, z \in \mathbb{F}(2^n).$$

Higher nonlinearity values indicate a reduced correlation between input and output bits under linear approximations, thereby enhancing the cryptographic strength of the substitution box. The theoretical upper bound for the nonlinearity of a Boolean function over the field $\mathbb{F}(2^n)$ is known to be 120, as established in (Carlet & Ding, 2007). The16 S-boxes developed in this work demonstrates an average nonlinearity of 112, which is comparable to that of the AES S-box (Table 3). The observed nonlinearity suggests that the designed S-box possesses strong resistance to linear cryptanalysis by minimizing linear correlations.

Differential Uniformity

Differential cryptanalysis is one of the most widely used cryptanalysis methods aimed at recovering plaintext or key information. The method is based on the analysis of differences between pairs of plaintexts and corresponding ciphertexts. Identifying stable dependencies between input and output differences can allow the cryptanalyst to draw conclusions about parts of the secret key. To ensure resistance to differential cryptanalysis, the S-box must have a low value of Differential Uniformity (DU). This characteristic is calculated using the following formula (Zahid, 2019):

$$DU = \max_{A_x \neq 0, B_x}[\#\{x \in Z | S(x) \oplus S(x \oplus \Delta x) = \Delta y\}] \qquad (5)$$

where, A_x and B_x – input and output masks, respectively and $Z = \{0,1, \dots, 255\}$, are Δx and Δy the input and output differentials, respectively.

For example, for 8-bit substitutions, the optimal values of differential uniformity are values no greater than 8. According to Theorem 4.1 in work (Cui et. al., 2011) AES S-box has DU = 4. All S-boxes can be considered differentially 4-unitary, which is allowed in the practice of designing secure substitutions.

Algebraic Degree

The algebraic degree of an S-box is a fundamental cryptographic metric, defined as the maximum algebraic degree among its component Boolean functions when represented in Algebraic Normal Form (ANF) (Prévost & Martin, 2025). Formally, given a vectorial Boolean function $F: \mathbb{F}_{2^n} \to \mathbb{F}_{2^n}$, the algebraic degree is:

$$\deg(F) = \max \deg(f_i), 1 \leq i \leq n \qquad (6)$$

where each f_i denotes a single-bit output coordinate of the S-box. A high algebraic degree hinders attackers' ability to express or approximate the S-box using low-degree polynomial equations, thereby strengthening its resistance to algebraic attacks and interpolation methods. In the context of 8-bit S-boxes, a degree of 7-seen, for example, in the AES S-box—is considered optimal.

Fixed Points

Fixed points are important structural properties of substitution boxes that may reveal exploitable symmetries if not properly avoided. A fixed point is an input value $x \in \mathbb{F}(2^n)$ for which the S-box returns the same value as output, i.e., $S(x) = x$. In the presented results (Table 3), all S-boxes exhibit no fixed points, indicating that for every x, $S(x) \neq x$, thereby eliminating trivial self-mappings and enhancing resistance to iterative attacks.

Periodicity of S-box

Another cryptographic property of the S-box is its periodicity. Periodicity shows how many times the S-box needs to be used to return the initial input value to its original value. Periodicity analysis allows to estimate how resistant

the S-box is to repeated attacks (Cui et. al., 2011). Formally, for a function F, that maps elements from a field $\mathbb{F}_{2^n}$ to the same field $\mathbb{F}_{2^n}$, the period of an element x is the smallest positive number p, for which $F^p(x) = x$.

The proposed S-boxes show a good result of periodicity. According to the results demonstrated in Table 3, the minimum period of cycle lengths is in the range from 2 to 10, and maximum varies from 88 to 215. The best result was shown by SBox14, in this S-box, to obtain each initial value, it is necessary to go through a period of 256 times, which indicates a single cycle of permutation. This property is highly desirable in cryptographic design because it maximizes diffusion and minimizes the risk of short cycle vulnerabilities that can be exploited in iterative attacks.

StrictAvalancheCriterion (SAC)

Another important cryptographic property of Boolean functions is the strong avalanche effect (SAC). This criterion was introduced by Webster and Tavares (Webster & Tavares, 1985) as a definition of strong S-boxes. According to SAC, changing one bit in the input of a strong S-box should change the output bit with probability close to 0.5. In formal terms, SAC is characterized by the following relation (Bejo & Adji, 2017):

$$\delta(x) = (\frac{1}{2^n}\sum_{i=1}^{n} f(x) \oplus f(x \oplus c_i^n)) \qquad (5)$$

Where c_i^n denote an n-dimensional vector with Hamming weight equal to 1 at the i-th position. A cryptographic function is said to satisfy the Strict Avalanche Criterion (SAC) if all entries in the resulting output matrix are approximately equal to 0.5. For the 16 proposed S-boxes, the SAC values were computed using the built-in by Python. Each S-box was evaluated across all 8 input bits, and the resulting average output change probabilities were recorded. The results for all S-boxes fall within the range of [0.45, 0.55], with two instances—SBox4 and SBox10—exhibiting slightly higher symmetry with values closer to [0.47, 0.53].

S-box Cryptographic Criterias Coded in Sage

To analyze such cryptographic properties as: balanced, nonlinearity, differential uniformity, algebraic degree and fixed points, the mathematical tool SageMath was used. SageMath is a free open-source mathematical platform that provides an integrated environment for performing calculations and conducting scientific research (Esslinger, 2023). Within the framework of cryptographic tasks, SageMath offers a specialized module S-Boxes and Their Algebraic Representations, which allows calculating a wide range of cryptographic characteristics, including linear and differential parameters. Listing 1 is presented below, which shows the code for determining the cryptographic criteria of the presented S-boxes. SageMath code for cryptographic evaluation of the proposed S-box:

```
from sage.crypto.sbox import SBox
from sage.crypto.boolean_function import BooleanFunction
S = SBox([
0x8c, 0x90, 0xd9, 0xc1, 0x46, 0x63, 0x53, 0xf1, 0x61, 0x32, 0x15, 0x3e, ...
# ])
# Evaluation of cryptographic criteria
S.is_balanced()                              # Balanced (should return True)
S.maximal_difference_probability_absolute()  # Differential uniformity
S.nonlinearity()                             # Nonlinearity
S.max_degree()                               # Algebraic degree
S.fixed_points()                             # Fixed points
```

Analysis of Cryptographic Properties of the Proposed S-boxes

To evaluate the strength of the proposed S-boxes, their cryptographic properties were compared with those of the AES S-box, which is widely regarded as a benchmark in symmetric key cryptography. As mentioned in work (Seitkulov et.al., 2021) the AES S-box demonstrates high cryptographic robustness, with a nonlinearity of 112, algebraic degree of 7, and differential uniformity of 4. These values are essential for ensuring resistance against linear and differential cryptanalysis.

Table 3. Cryptographic properties of the proposed 16 S-boxes

	Balanced	Nonlinearity	Differential uniformity	Algebraic degree	Fixed points	Periodicity	SAC
Sbox0	True	112	4	7	[]	[6, 154]	[0.45, 0.55]
Sbox1	True	112	4	7	[]	[2, 195]	[0.45, 0.55]
Sbox2	True	112	4	7	[]	[2, 61]	[0.45, 0.55]
Sbox3	True	112	4	7	[]	[2, 138]	[0.45, 0.55]
Sbox4	True	112	4	7	[]	[3, 213]	[0.47, 0.53]
Sbox5	True	112	4	7	[]	[2, 215]	[0.45, 0.55]
Sbox6	True	112	4	7	[]	[4, 166]	[0.45, 0.55]
Sbox7	True	112	4	7	[]	[2, 88]	[0.45, 0.55]
SBox8	True	112	4	7	[]	[10, 109]	[0.45, 0.55]
Sbox9	True	112	4	7	[]	[8, 166]	[0.45, 0.55]
SBox10	True	112	4	7	[]	[2, 123]	[0.47, 0.53]
SBox11	True	112	4	7	[]	[5, 133]	[0.45, 0.55]
SBox12	True	112	4	7	[]	[3, 198]	[0.45, 0.55]
SBox13	True	112	4	7	[]	[5, 210]	[0.45, 0.55]
SBox14	True	112	4	7	[]	[256,256]	[0.45, 0.55]
SBox15	True	112	4	7	[]	[3, 150]	[0.45, 0.55]

It should be noted that all constructed S-boxes, in terms of the main cryptographic parameters, correspond to the AES S-box. They preserve the same optimal nonlinearity and algebraic degree, and exhibit minimal differential uniformity, which is essential for secure substitution. It is also worth mentioning that the SAC values lie within the acceptable cryptographic range [0.45, 0.55], indicating a well-balanced avalanche effect. Each of the proposed S-boxes has no fixed points and satisfies the periodicity conditions. This consistency across all cryptographic criteria confirms that the our S-boxes meet the level of cryptographic strength of the s-box used in the AES standard.

Conclusion

The authors of this paper conducted a study of the construction of alternative S-boxes. A method for generating 16 new S-boxes was proposed, which consisted in using irreducible polynomials over a finite Galois field different from the standard. From the list of 30 irreducible polynomials, 5 were taken, for each of them their own unique affine matrices and individual constants were used. The use of such a set of components led to the structural diversity of the obtained S-boxes. The cryptographic resistance of the obtained S-boxes was tested according to the established criteria, such as bijectivity, balance, nonlinearity, strict avalanche criterion (SAC), differential homogeneity, algebraic degree, fixed points, and periodicity. Analysis of cryptographic metrics showed that all the proposed S-boxes meet the necessary conditions for their use as an alternative to the standard AES S-box.

Scientific Ethics Declaration

*The authors declares that the scientific ethical and legal responsibility of this article published in EPSTEM journal belongs to the authors.

Conflict of Interest

*The authors declare that they have no conflicts of interest

Funding

*This research is funded by the Science Committee of the Ministry of Education and Science of the Republic of Kazakhstan (Grant No. AP19677422).

Acknowledgements or Notes

*This article was presented as an oral presentation at the International Conference on Basic Sciences and Technology (www.icbast.net) held in Budapest/Hungary on August 28-31, 2025.

References

Bejo, A., & Adji, T. B. (2017, August). AES S-box construction using different irreducible polynomial and constant 8-bit vector. *2017 IEEE Conference on Dependable and Secure Computing* (pp. 366-369). IEEE.

Carlet, C., & Ding, C. (2007). Nonlinearities of S-boxes. *Finite Fields and Their Applications*, *13*(1), 121-135.

Cui, J., Huang, L., Zhong, H., Chang, C., & Yang, W. (2011). An improved AES S-box and its performance analysis. *International Journal of Innovative Computing, Information and Control*, *7*(5), 2291-2302.

Daemen, J., & Rijmen, V. (2002). *The design of Rijndael* (Vol. 2). New York: Springer-verlag.

Dworkin, M. J., Barker, E., Nechvatal, J. R., Foti, J., Bassham, L. E., Roback, E., & Dray Jr, J. F. (2001). *Advanced encryption standard* (AES). National Institute of Standards and Technology.

El Gaabouri, I., Senhadji, M., Belkasmi, M., & El Bhiri, B. (2024). A new S-box pattern generation based on chaotic enhanced logistic map: Case of 5-bit S-box. *Cybersecurity, 7*(1), 59.

Esa, N. F., Abdul-Latip, S. F., & Abu, N. A. (2022). A new design of substitution box with ıdeal strict avalanche criterion. *Malaysian Journal of Mathematical Sciences*, *16*(4).

Esslinger, B. (2023). *Learning and experiencing cryptography with cryptool and sagemath*. Artech House.

Mahboob, A., Nadeem, M., & Rasheed, M. W. (2023). A study of text-theoretical approach to S-box construction with image encryption applications. *Scientific Reports*, *13*(1), 21081.

Nitaj, A., Susilo, W., & Tonien, J. (2020). A new improved AES S-box with enhanced properties. *Australasian Conference on Information Security and Privacy* (pp. 125-141). Springer International Publishing.

Nizam Chew, L. C., & Ismail, E. S. (2020). S-box construction based on linear fractional transformation and permutation function. *Symmetry*, *12*(5), 826.

Ospanov, R., Seitkulov, E., & Ergalieva, B. (2022). A generalized algebraic method for constructing 8-bit rijndael S-boxes. *Bulletin of KazATK, 120*(1), 156-163.

Planteen, C. (2019). *Primitive elements and irreducible polynomials of GF (256)*. Cody Planteen.

Prévost, T., & Martin, B. (2025). A 10-bit S-box generated by Feistel construction from cellular automata. *arXiv preprint arXiv:2507.02489*.

Seitkulov, Y. N., Ospanov, R. M., & Yergaliyeva, B. B. (2021). On the cryptographic properties of S-boxes. *Engineering Journal of Satbayev University*, *143*(4), 96-103.

Webster, A. F., & Tavares, S. E. (1985). On the design of S-boxes. *Conference on the Theory and Application of Cryptographic Techniques* (pp. 523-534). Berlin, Heidelberg.

Zahid, A. H., Arshad, M. J., & Ahmad, M. (2019). A novel construction of efficient substitution-boxes using cubic fractional transformation. *Entropy*, *21*(3), 245.

Author(s) Information

Zhanat Saukhanova
L.N. Gumilyov Eurasian National University
Pushkin street 11, Astana, Kazakhstan

Gulmira Shakhmetova
L.N. Gumilyov Eurasian National University
Pushkin street 11, Astana, Kazakhstan
Contact e-mail: *sh_mira2004@mail.ru*

Altynbek Sharipbay
L.N. Gumilyov Eurasian National University
Pushkin street 11, Astana, Kazakhstan

Alibek Barlybayev
L.N. Gumilyov Eurasian National University
Pushkin street 11, Astana, Kazakhstan

Sayat Raykul
L.N. Gumilyov Eurasian National University
Pushkin street 11, Astana, Kazakhstan

Altay Khassenov
L.N. Gumilyov Eurasian National University
Pushkin street 11, Astana, Kazakhstan

To cite this article:

Saukhanova, Z., Shakhmetova G., Sharipbay A., Barlybayev A., Raykul S., & Khassenov A. (2025). Design of S-boxes based on alternative irreducible polynomials. *The Eurasia Proceedings of Science, Technology, Engineering and Mathematics (EPSTEM), 36,* 102-109.

The Eurasia Proceedings of Science, Technology, Engineering & Mathematics (EPSTEM)
ISSN: 2602-3199

The Eurasia Proceedings of Science, Technology, Engineering and Mathematics (EPSTEM), 2025

Volume 36, Pages 110-116

ICBAST 2025: International Conference on Basic Sciences and Technology

Synthesis, Characterization and Selective Fluorimetric Detection of Al^{3+} by A Schiff Base Derived From 5-Chloro-8-Hydroxyquinoline

Onder Alici
Selcuk University

Maghan I. Camara
Selcuk University

Abstract: In this study, an aldehyde derivative compound containing 5-chloro-8-hydroxyquinoline was synthesized based on literature procedures. Subsequently, the target compound, a Schiff base derivative (**HQ-BH**), was obtained via a condensation reaction between the quinoline-based aldehyde and benzaldehyde hydrazone. The chemical structure of the synthesized HQ-BH compound was confirmed using various spectroscopic techniques, including FT-IR, TOF-MS, ^{1}H-NMR, and ^{13}C-NMR. Next, the interactions of the **HQ-BH** compound with various metal ions (Li^{+}, Ni^{2+}, Co^{2+}, Ag^{+}, Al^{3+}, Mg^{2+}, Mn^{2+}, Ca^{2+}, Ba^{2+}, Cu^{2+}, Hg^{2+}, Fe^{2+}, Rb^{2+}, Fe^{3+}, Cs^{+}, Cd^{2+}) were investigated under suitable conditions using fluorescence spectrophotometry. Initially, a selectivity study was performed. The sensor **HQ-BH** did not exhibit any significant fluorescence emission at 499 nm upon excitation at 360 nm. However, upon the individual addition of each cation (20.0 equivalents), only Al^{3+} induced a distinct emission band at 499 nm with a notable enhancement in intensity. As a result of these measurements, it was concluded that the **HQ-BH** compound displays selective fluorimetric response exclusively toward Al^{3+} among all tested metal ions.

Keywords: Al^{3+}, Quinoline, Fluorescence, Schiff base

Introduction

Aluminium (Al) is one of the most abundant elements in nature and is extensively used in various industrial applications. It plays a critical role in sectors such as water treatment, food additives, pharmaceuticals, and household appliances (Aydin, 2021; Alici, 2021; Heena et al., 2023). Due to its widespread use, there is a significant risk of unintentional excessive exposure to aluminium in daily life. According to the World Health Organization (WHO), the human body can only absorb up to 7 mg/kg of Al^{3+} ions. Exposure beyond this threshold has been associated with serious health issues, including Alzheimer's disease, osteoporosis, and kidney dysfunction (Deibel et al., 1996). As a result, the reliable detection of Al^{3+} ions in environmental and biological systems have become an increasingly important research focus. In recent years, UV-visible (UV-vis) spectroscopy and fluorescence spectroscopy have emerged as leading analytical techniques for the detection of Al^{3+} ions. Fluorescent sensors have garnered significant attention due to their advantages, such as low cost, high sensitivity, rapid response, and operational simplicity (Fu et al., 2019; Yan et al., 2023). A wide range of fluorescent chemosensors with selective recognition capabilities for Al^{3+} have been developed and reported in the literature (Sen et al., 2012; Mahalakshmi et al., 2020; Ali et al., 2021; Erdemir & Malkondu, 2021). In this context, Schiff base compounds have attracted considerable interest due to their ability to form strong and stable complexes with metal ions. These compounds, which contain various donor atoms, serve as key structural motifs in macrocyclic chemistry and offer broad application potential in environmental and biomedical fields (Keypour et al., 2019; Nemati et al., 2021; Zeynali et al., 2021; Hajari et al., 2022). Moreover, the favourable electronic and structural features of Schiff bases enable the selective and efficient detection of specific metal ions, including Al^{3+} (Alici & Erdemir, 2015; Golbedaghi et al., 2022).

In this study, an aldehyde derivative compound containing 5-chloro-8-hydroxyquinoline was synthesized based on literature procedures (Wantulok et al., 2020). Subsequently, the target compound, a Schiff base derivative (**HQ-BH**), was obtained via a condensation reaction between the quinoline-based aldehyde and benzohydrazide. The chemical structure of the synthesized HQ-BH compound was confirmed using various spectroscopic techniques, including FT-IR, TOF-MS, ^{1}H-NMR, and ^{13}C-NMR. Next, the interactions of the **HQ-BH** compound with various metal ions (Li^{+}, Ni^{2+}, Co^{2+}, Ag^{+}, Al^{3+}, Mg^{2+}, Mn^{2+}, Ca^{2+}, Ba^{2+}, Cu^{2+}, Hg^{2+}, Fe^{2+}, Rb^{2+}, Fe^{3+}, Cs^{+}, Cd^{2+}) were investigated under suitable conditions using fluorescence spectrophotometry. Initially, a selectivity study was performed. The sensor **HQ-BH** did not exhibit any significant fluorescence emission at 499 nm upon excitation at 360 nm. However, upon the individual addition of each cation (20.0 equivalents), only Al^{3+} induced a distinct emission band at 499 nm with a notable enhancement in intensity. As a result of these measurements, it was concluded that the **HQ-BH** compound displays selective fluorimetric response exclusively toward Al^{3+} among all tested metal ions.

Method

Chemicals and Instruments

All necessitated chemicals are analytical grade and were obtained from Sigma-Aldrich Chemicals (Zwijndrecht, The Netherlands) and utilized with no further processing. The perchlorate salts of the cations were utilized in this study. FT-IR, TOF-MS, ^{1}H and ^{13}C-NMR spectral studies were measured by Bruker Vertex 70, Bruker Microflex LT MALDI-TOF MS, Bruker, 400 MHz, Avance NEO (Broadband) and emission spectra of the chemosensor **TDH-CB** were recorded in a Edinburgh Instruments FS5 Fluorescence Spectrophotometer.

Synthesis of 5-Chloro-8-Hydroxyquinoline-7-Carbaldehyde (HQA)

Compound (**HQA**) was prepared according to the literature (Wantulok et al., 2020).

Synthesis of the Receptor *N*'-((5-Chloro-8-Hydroxyquinolin-7-yl) Methylene) Benzohydrazide (HQ-BH)

Absolute ethanolic solutions (25 mL) of 5-chloro-8-hydroxyquinoline-7-carbaldehyde (100.00 mg, 0.481 mmol) were added to benzohydrazide (78.70 mg, 0.578 mmol) in absolute EtOH and stirred under reflux for 12 hours. After completion of the reaction, the precipitation formed was filtered off. The precipitate was washed three times with water and ethanol and dried in a vacuum oven. Finally, the Schiff base compound (**HQ-BH**) was recrystallized with hot ethanol to obtain yellow crystals.

Yield: 84 %, Melting Point: 260 ^{0}C, ^{1}H NMR (400 MHz, DMSO-d_6) δ 12.14 (s, 1H), 9.06 (dd, J = 4.2, 1.5 Hz, 1H), 9.03 (s, 1H), 8.58 (dd, J = 8.5, 1.6 Hz, 1H), 8.14 (s, 1H), 8.07 – 7.96 (m, 2H), 7.84 (dd, J = 8.5, 4.2 Hz, 1H), 7.70 – 7.64 (m, 1H), 7.61 (dd, J = 8.2, 6.5 Hz, 2H). ^{13}C NMR (100 MHz, DMSO-d_6) δ 163.52, 152.94, 150.10, 143.50, 140.07, 133.60, 133.25, 132.38, 129.01, 128.14, 127.16, 124.32, 123.78, 120.10, 117.63.

Results and Discussion

Preparation for the Receptor HQ-BH

The synthesis of the **HQ-BH** compound was carried out through a two-step reaction process. In the first step, 5-chloro-8-hydroxyquinoline was used as the starting material and subjected to a Duff reaction. Hexamethylenetetramine (HMTA) was employed as the formylating agent, and trifluoroacetic acid (TFA) served as the reaction medium. Under these conditions, a formyl group was selectively introduced at the 7-position of the aromatic ring, yielding 5-chloro-8-hydroxyquinoline-7-carbaldehyde (**HQA**). In the second step, the obtained **HQA** was reacted with benzohydrazide via a condensation reaction. This transformation, which involves the formation of a Schiff base, occurs through the reaction of the aldehyde group with the hydrazide, forming an aryl-hydrazone structure. The reaction synthesized the target compound **HQ-BH** in high yield (84%), as shown in Schema 1. In addition, the chemical structure of the **HQ-BH** compound was elucidated using various spectroscopic methods (Fig.1-3).

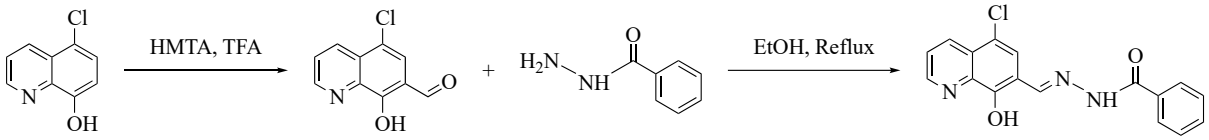

HQA **HQ-BH**

Schema 1. The synthesis procedure for **HQ-BH**

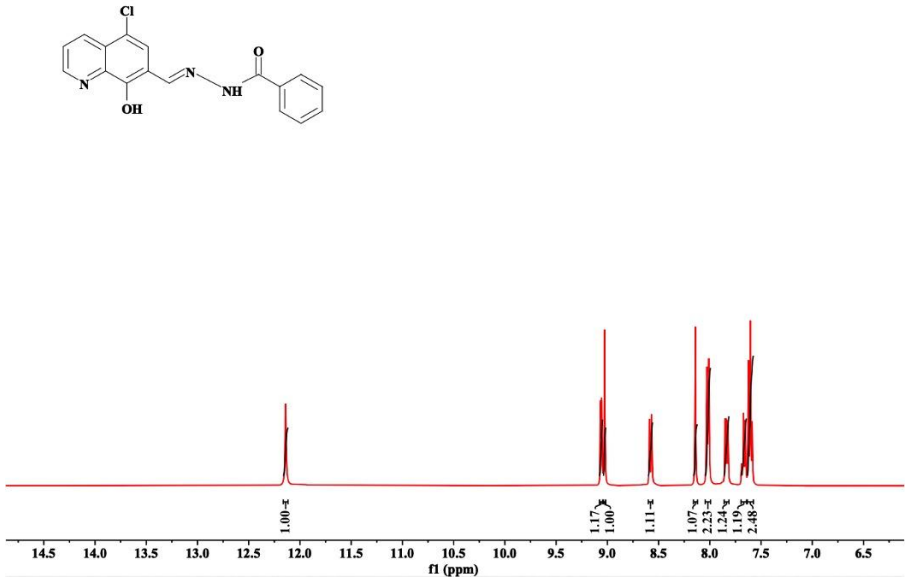

Figure 1. ^{1}H-NMR spectrum of **HQ-BH**

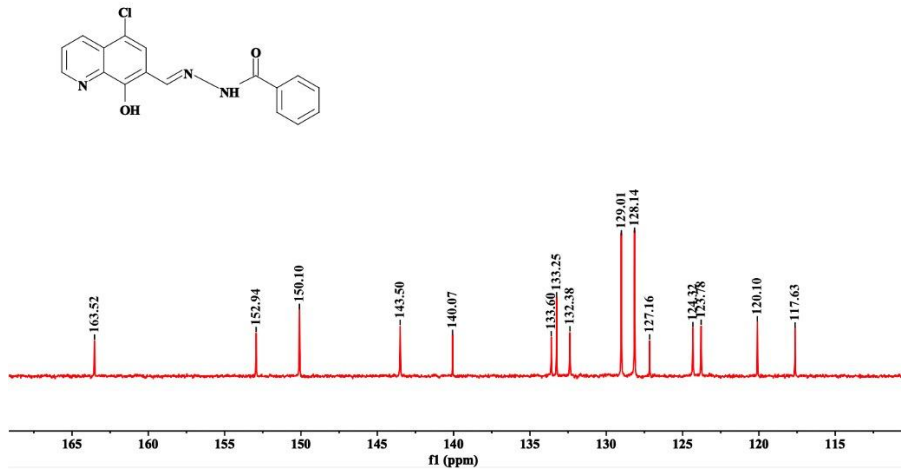

Figure 2. ^{13}C-NMR spectrum of **HQ-BH**

Emission Study

The stock solution of **HQ-BH** (10 mM) was prepared in DMSO and then diluted to 10 μM in DMSO/HEPES (8/2, v/v). The tested metal perchlorate salts were utilized as (10^{-2} M).

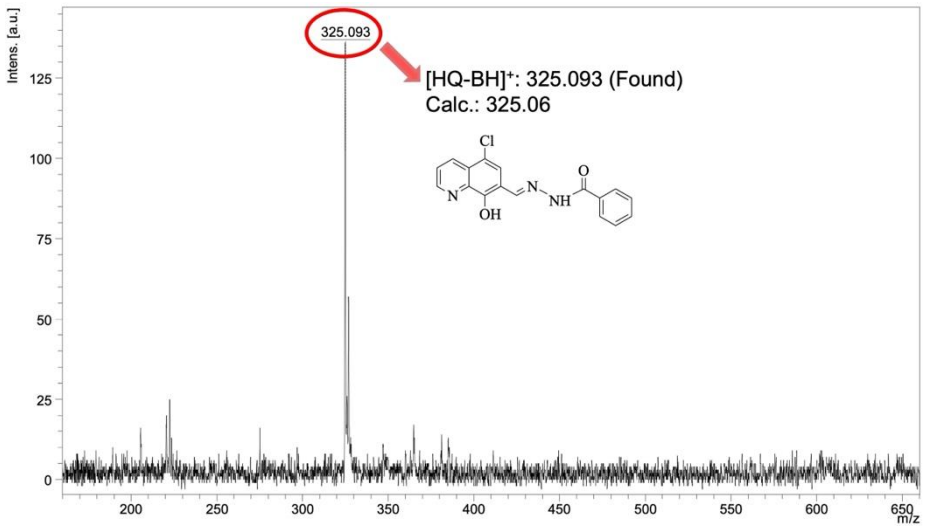

Figure 3. TOF-MS spectrum of **HQ-BH**

Fluorescence Studies of HQ-BH versus Al^{3+}

Firstly, selectivity determination was made within metals (Hg^{2+}, Mn^{2+}, Ba^{2+}, Cu^{2+}, Cd^{2+}, Co^{2+}, Ca^{2+}, Zn^{2+}, Ni^{2+}, Fe^{2+}, Fe^{3+}, Al^{3+}, Li^{+}, Ag^{+}, Mg^{2+}, Rb^{2+}, Cs^{2+}). For this study, the interaction between the solution of HQ-BH compound prepared in DMSO/HEPES (8:2) solvent medium and metal ions was investigated by fluorescence spectroscopy, and for this investigation, various metal ions (20 equiv.) were added to 10 µM HQ-BH solution. As shown in the graph in Figure 4, among all the metals tested, the HQ-BH compound exhibits a significant emission at 486 nm in the presence of Al^{3+} ions, indicating that HQ-BH is selective toward Al^{3+} metal ions.

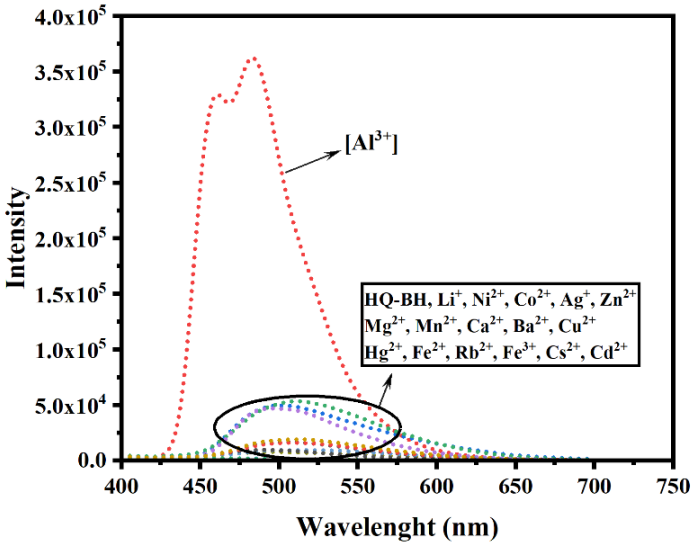

Figure 4. Fluorescence spectrum of **HQ-BH** compound in the presence of different metals (λ_{ex}: 360 nm; Ex-Slit: 1, Em-Slit: 1; λ_{em}: 486 nm)

Following the determination that the **HQ-BH** receptor exhibits fluorometric selectivity toward Al^{3+} ions, fluorescence titration experiments were conducted to investigate its interaction with this ion in more detail. For these experiments, a solution of **HQ-BH** (10 µM) in DMSO/HEPES (v/v, 8:2) was excited at 360 nm, and increasing concentrations of Al^{3+} solution was added. As shown in Figure 5, a gradual increase in the emission intensity at 486 nm was observed with increasing Al^{3+} concentrations. This enhancement in emission intensity reached a plateau after the addition of approximately 20 equivalents of Al^{3+}, indicating no significant further change beyond this point.

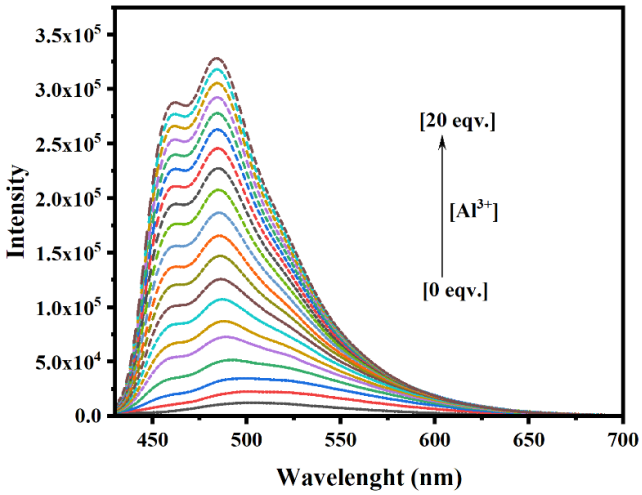

Figure 5. FL response of **HQ-BH** with increasing amount of Al^{3+} (0–20 eqv) (λ_{ex}: 360 nm, λ_{em}: 486 nm; Ex-Slit: 1, Em-Slit: 1).

To investigate the complexation between the HQ-BH receptor and Al^{3+} ions, the Job Plot method was employed. The resulting Job Plot graph is presented in Figure 6. Upon examination of the graph, it is clearly observed that the maximum point occurs at a molar fraction of 0.5. This indicates that the complexation between HQ-BH and Al^{3+} follows a 1:1 stoichiometry (Figure 6). In other words, one molecule of HQ-BH forms a complex with one Al^{3+} ion.

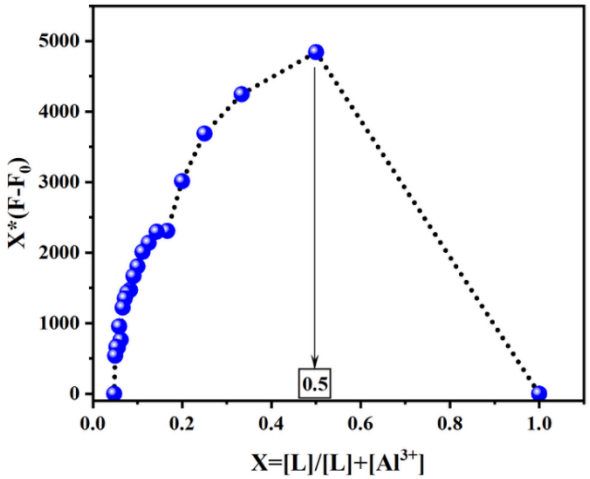

Figure 6. Job's plot showing the 1:1 stoichiometry

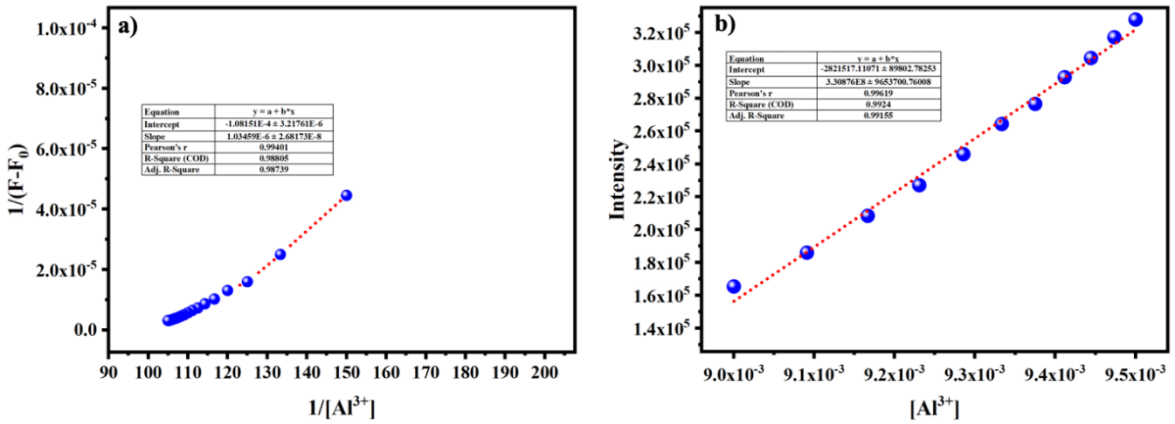

Figure 7. a) Benesi–Hildebrand plot assuming 1:1 stoichiometry from fluorometric titration data of receptor HQ-BH (10 μM) with Al^{3+} **b)** The plot of emission intensity of **HQ-BH** at 486 nm versus Al^{3+} cation concentration

The binding constant (log Ka) for the HQ-BH-Al^{3+} complex was determined to be 7.5 using the Benesi–Hildebrand equation and fluorescence titration studies (Figure 7a). Additionally, a calibration plot of fluorescence intensity vs Al^{3+} concentration was created using fluorescence titration data obtained at 486 nm (Figure 7b). The limit of detection (LOD) for Al^{3+} ions using the **HQ-BH** probe was found to be 0.408 µM based on the slope of this curve.

Conclusion

In this study, a novel fluorogenic chemosensor based on 5-chloro-8-hydroxyquinoline (**HQ-BH**) was successfully synthesized for the selective detection of Al^{3+} ions. The observed enhancement in fluorescence intensity upon the addition of Al^{3+} indicates a strong coordination interaction between **HQ-BH** and Al^{3+}, confirming the high affinity of the sensor towards the target ion. These findings demonstrate that **HQ-BH** is a promising candidate for the sensitive and straightforward detection of Al^{3+} in solution. Furthermore, the structural and photophysical features of **HQ-BH** may provide a valuable framework for the future development of a broad range of fluorogenic probes targeting aluminium ions.

Scientific Ethics Declaration

*The authors declare that the scientific ethical and legal responsibility of this article published in EPSTEM journal belongs to the authors.

Funding

*This study was supported by Selçuk University BAP Coordination with project numbers 25701046 and 25201012 We would like to thank S.Ü. BAP Coordination for their support.

Conflict of Interest

*The authors declare that they have no conflicts of interest

Acknowledgements or Notes

*This article was presented as an oral presentation at the International Conference on Basic Sciences and Technology (www.icbast.net) held in Budapest/Hungary on August 28-31, 2025.

*This work is part of Maghan I CAMARA's Master thesis.

References

Ali, R., Alminderej, F. M., Messaoudi, S., & Saleh, S. M. (2021). Ratiometric ultrasensitive optical chemisensor film based antibiotic drug for Al (III) and Cu (II) detection. *Talanta*, *221*, 121412.

Alici, O., & Aydin, D. (2021). A Schiff-base receptor based on Phenolphthalein derivate appended 2-furoic hydrazide: Highly sensitive fluorogenic “turn on” chemosensor for Al^{3+}. *Journal of Photochemistry and Photobiology A: Chemistry*, *404*, 112876.

Alici, O., & Erdemir, S. (2015). A cyanobiphenyl containing fluorescence “turn on” sensor for Al^{3+} ion in CH_3CN–water. *Sensors and Actuators B: Chemical*, *208*, 159–163.

Aydin, D., & Alici, M. K. (2021). Phenolphthalein conjugated Schiff base as a dual emissive fluorogenic probe for the recognition aluminium (III) and zinc (II) ions. *Journal of Fluorescence*, *31*(3), 797–805.

Deibel, M. A., Ehmann, W. D., & Markesbery, W. R. (1996). Copper, iron, and zinc imbalances in severely degenerated brain regions in Alzheimer’s disease: Possible relation to oxidative stress. *Journal of the Neurological Sciences*, *143*(1–2), 137–142.

Erdemir, S., & Malkondu, S. (2021). Detection of water content in alcohol solvents over Al^{3+} induced colorimetric and NIR-fluorescent sensor based on isophorone-phenylamine. *Microchemical Journal*, *160*, 105677.

Fu, J., Yao, K., Chang, Y., Li, B., Yang, L., & Xu, K. (2019). A novel colorimetric-fluorescent probe for Al^{3+} and the resultant complex for F− and its applications in cell imaging. *Spectrochimica Acta Part A: Molecular and Biomolecular Spectroscopy*, *222*, 117234.

Golbedaghi, R., Ildiz, G. O., Azadbakht, R., & Fausto, R. (2022). A new tetramine bis(2-naphthol)-derivative fluorescent chemosensor for aluminium (III) ion. *Journal of Molecular Structure*, *1250*, 131775.

Hajari, S., Keypour, H., Rezaei, M. T., Farida, S. H., & Gable, R. W. (2022). New 15-membered macrocyclic Schiff base ligand; synthesis some Cd (II), Mn (II) and Zn (II) complexes, crystal structure, cytotoxicity, antibacterial and antioxidant activity. *Journal of Molecular Structure*, *1251*, 132049.

Heena, H., Silswal, A., Sharma, D., Koner, A., OM, H., & Rana, R. (2023). A highly efficient, selective, reversible and ultra-sensitive fluorescence "turn-on" chemosensor for aluminium ions by a novel schiff base. *Spectrochimica Acta Part A: Molecular and Biomolecular Spectroscopy*, *320*, 124575.

Keypour, H., Aidi, M., Mahmoudabadi, M., Karamian, R., Asadbegy, M., & Gable, R. W. (2019). Synthesis, X-ray crystal structural, antioxidant and antibacterial studies of new Cu (II) macroacyclic Schiff base complex with a ligand containing homopiperazine moiety. *Journal of Molecular Structure*, *1198*, 126666.

Mahalakshmi, G., Kumar, P. S., Vennila, K. N., Sivaraman, G., Seenivasaperumal, M., & Elango, K. P. (2020). Multi-site probe for selective turn-on fluorescent detection of Al (III) in aqueous solution: Synthesis, cation binding, mode of coordination, Logic Gate and cell imaging. *Methods and Applications in Fluorescence*, *8*(3), 035003.

Nemati, L., Keypour, H., Shahabadi, N., Hadidi, S., & William Gable, R. (2021). Synthesis, characterization and DNA interaction of a novel Pt (II) macroacyclic Schiff base complex containing the piperazine moiety and its cytotoxicity and molecular docking. *Journal of Molecular Liquids*, *337*, 116292.

Sen, S., Mukherjee, T., Chattopadhyay, B., Moirangthem, A., Basu, A., Marek, J., & Chattopadhyay, P. (2012). A water soluble Al^{3+} selective colorimetric and fluorescent turn-on chemosensor and its application in living cell imaging. *The Analyst*, *137*(17), 3975.

Wantulok, J., Szala, M., Quinto, A., Nycz, J. E., Giannarelli, S., Sokolová, R., Książek, M., & Kusz, J. (2020). Synthesis, electrochemical and spectroscopic characterization of selected Quinoline carbaldehydes and their Schiff base derivatives. *Molecules*, *25*(9), 2053.

Yan, Q., Wang, Y., Wang, Z., Zhang, G., Shi, D., & Xu, H. (2023). Corrigendum to "a novel water-soluble flavonol-based fluorescent probe for highly specific and sensitive detection of AL3+ and its application in onion and zebrafish" *Spectrochimica Acta Part A: Molecular and Biomolecular Spectroscopy*, *293*, 122529.

Zeynali, H., Keypour, H., Hosseinzadeh, L., & Gable, R. W. (2021). The non-templating synthesis of macro-cyclic Schiff base ligands containing pyrrole and homopiperazine and their binuclear nickel (II), cobalt (II) and Mononuclear Platinum (II) complexes: X-ray single crystal and anticancer studies. *Journal of Molecular Structure*, *1244*, 130956.

Author(s) Information

Onder Alici
Selcuk University Faculty of Science
Department of Chemistry, Konya, Türkiye
Contact e-mail: *oalici@selcuk.edu.tr*

Maghan I. Camara
Selcuk University Institute of Science
Department of Chemistry, Konya, Türkiye

To cite this article:

Alici, O., & Camara, I. M. (2025). Synthesis, characterization and selective fluorimetric detection of Al^{3+} by a schiff base derived from 5-chloro-8-hydroxyquinoline. *The Eurasia Proceedings of Science, Technology, Engineering and Mathematics (EPSTEM), 36,* 110-116.

The Eurasia Proceedings of Science, Technology, Engineering & Mathematics (EPSTEM)
ISSN: 2602-3199

The Eurasia Proceedings of Science, Technology, Engineering and Mathematics (EPSTEM), 2025

Volume 36, Pages 117-124

ICBAST 2025: International Conference on Basic Sciences and Technology

Synthesis of Triphenylamine-Based Fluorescent Sensors for Biogenic Amine Detection and Evaluation of Their Cytotoxic Potential

Mehmet Oguz
Selcuk University

Abstract: Food safety has emerged as a critical global issue due to its direct impact on human health. One of the primary challenges in this context is the rapid and accurate detection of food spoilage markers, such as biogenic amines (BAs), which are produced during microbial decomposition of proteins. In this study, we report the design, synthesis, and evaluation of novel triphenylamine-based fluorescent sensor molecules (**TFA-1** and **TFA-3**) incorporating Indandione and Meldrum acid units. The molecular structures of the synthesized compounds were confirmed using spectroscopic techniques including ^{1}H NMR, ^{13}C NMR, and TOF-MS. Cytotoxicity studies in mammalian cell lines revealed low toxicity and good biocompatibility, demonstrating the potential of these sensors for real-world applications. The proposed sensors exhibited remarkable sensitivity and selectivity toward BAs, indicating their suitability as reliable fluorescence-based tools for food quality monitoring.

Keywords: Biogenic amine, Fluorescence, Triphenylamine, Cytotoxicity

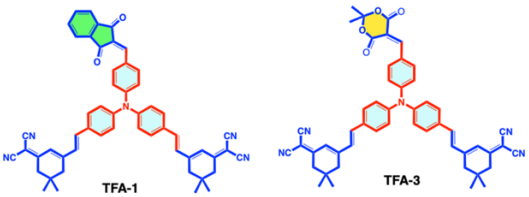

Introduction

Biogenic amines (BAs) are a diverse class of low-molecular-weight organic bases predominantly formed through the enzymatic decarboxylation of amino acids or, in some cases, via the transamination of aldehydes into corresponding ketones (Chen et al., 2025; Kaur et al., 2018; Nakamura et al., 2018). These compounds are naturally present in a wide range of living organisms, including plants, animals, and microorganisms, and play critical roles in numerous physiological and biochemical processes. Specifically, BAs are involved in cellular proliferation, differentiation, neurotransmission, and immune system modulation. They act as signaling molecules in both intracellular and intercellular communication, thereby influencing essential biological pathways (Zhang et al., 2025; Erdemir et al., 2025). Despite their indispensable roles at physiological levels, the overaccumulation of BAs can result in toxic effects and is strongly linked to various adverse health conditions. Excessive intake of certain BAs, such as histamine, tyramine, and putrescine, has been associated with hypertension, migraines, allergic reactions, and neurological disorders, while elevated concentrations in food products can lead to severe foodborne illnesses and systemic toxicity (Li et al., 2025; Liu et al., 2025; Shanmugaraju et al., 2025).

Traditionally, the detection and quantification of BAs have relied on analytical techniques such as high-performance liquid chromatography (HPLC), gas chromatography (GC), capillary electrophoresis, and mass

- Selection and peer-review under responsibility of the Organizing Committee of the Conference

spectrometry. These methods offer high sensitivity and specificity; however, they often require expensive instrumentation, sophisticated sample preparation, and labor-intensive procedures, which limit their applicability for on-site or rapid screening purposes (Almeida et al., 2015; Grant et al., 2023). Consequently, there is a growing demand for novel detection approaches that are not only sensitive and selective but also cost-effective, rapid, and suitable for in-field or point-of-care applications.

In recent years, fluorescence-based detection strategies have gained significant attention as promising tools for BA monitoring. Fluorescent probes offer several advantages, including high sensitivity, low detection limits, tunable optical properties, and the ability to provide real-time visual readouts (Al-Asmari, 2025; Müller et al., 2022). This study reports the rational design, synthesis, and comprehensive evaluation of novel triphenylamine-based fluorescent probes functionalized with indandione and Meldrum acid units for the selective detection of biogenic amines. In addition to their sensing capabilities, the cytotoxic potential of the synthesized probes was systematically assessed to evaluate biocompatibility, which is critical for their potential application in food safety monitoring and in vivo studies. The work not only contributes to the development of efficient BA detection platforms but also provides insights into the structure–activity relationships governing probe performance, laying the groundwork for future advancements in rapid, portable, and reliable food quality assessment technologies.

Experimental Section

Materials and Methods

The precursor compounds (IF, TFA-CHO, and TFA-IF) were synthesized following previously reported procedures with minor modifications (Yu et al., 2020; Zhang et al., 2023; Qian et al., 2018). Subsequently, the novel compound TFA-IF-CHO, along with the target receptors TFA-1 and TFA-3 incorporating indandione and meldrum acid units, was prepared through the methodologies described herein. The structures of all synthesized compounds were unambiguously confirmed by ^{1}H NMR, ^{13}C NMR, and TOF-MS analyses (**Scheme 1**).

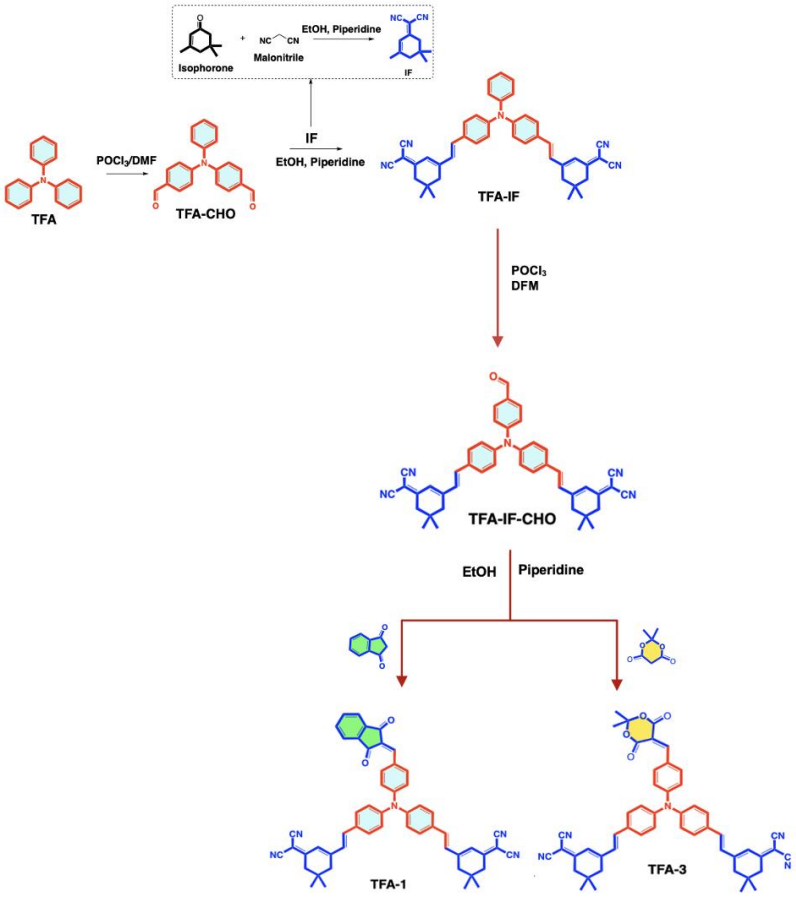

Scheme 1. The synthetic route of **TFA-1** and **TFA-3**

Synthesis of TFA-IF-CHO

TFA-IF (1.0 g, 1.57 mmol) was dissolved in DMF (8 mL), and the mixture was cooled to 0 °C. $POCl_3$ (3.0 mL, 32.17 mmol) was then added dropwise. The reaction mixture was stirred at room temperature for an additional 24 h. After completion, the mixture was poured into ice water and neutralized with NaOH. The resulting solution was extracted three times with ethyl acetate. The combined organic layers were washed with water, dried over anhydrous Na_2SO_4, and concentrated under reduced pressure. The crude product was purified by column chromatography (hexane/ethyl acetate, 2/1, v/v) to afford **TFA-IF-CHO** as a pure compound (1.15 g, 70% yield). ^{1}H NMR (400 MHz, $CDCl_3$): δ 9.82 (s, 1H), 7.70 (d, J = 8.7 Hz, 2H), 7.40 (d, J = 8.7 Hz, 4H), 7.05-7.12 (m, 6H), 6.96 (d, J = 15.9 Hz, 2H), 6.86 (d, J = 15.9 Hz, 2H), 6.77 (s, 2H), 2.53 (s, 4H), 2.40 (s, 4H), 1.01 (s, 12H). ^{13}C NMR (100 MHz, $CDCl_3$): δ 190.5, 169.1, 153.7, 151.9, 147.2, 135.9, 132.2, 131.4, 129.0, 128.8, 125.5, 123.6, 122.4, 113.5, 112.8, 78.5, 43.0, 39.2, 32.1, 28.1, 14.2.

Synthesis of TFA-1 and TFA-3

TFA-IF-CHO (0.33 g, 0.5 mmol) was dissolved in chloroform (10 mL), followed by the addition of piperidine (25 μL), and the mixture was stirred for 30 min. Subsequently, 1,3-indandione (0.09 g, 0.6 mmol) or Meldrum's acid (0.085 g, 0.6 mmol) was added, and the reaction was refluxed at room temperature for 48 h. The progress of the reaction was monitored by TLC, and upon complete consumption of the starting material, the reaction was terminated. After removal of the solvent under reduced pressure, the residue was dissolved in chloroform and extracted several times with water. The organic phase was then concentrated, and the crude product was purified by column chromatography on silica gel using hexane/ethyl acetate (2/1, v/v) as the eluent. The final sensors, TFA-1 and TFA-3, were obtained in yields of 65% (0.25 g) and 68% (0.26 g), respectively. **TFA-1**;^{1}H NMR ($CDCl_3$, 400 MHz) δ 8.48 (d, 2H, J=9.0 Hz),7.97-8.01 (m, 2H), 7.79-7.83 (m, 3H), 7.51 (d, 4H, J=8.8 Hz), 7.21 (d, 4H, J=8.8 Hz), 7.17 (d, 2H, J=8.8 Hz), 7.05 (d, 2H, J=16.5 Hz), 6.96 (d, 2H, J=16.5 Hz), 6.87 (s, 2H), 2.62 (s, 4H), 2.49 (s, 4H), 1.11 (s, 12H); ^{13}C NMR (100 MHz, $CDCl_3$) δ 190.8, 189.5, 169.1, 153.7, 151.0, 146.9, 145.8, 142.4, 140.0, 136.5, 135.9, 135.1, 135.0, 132.4, 129.0, 128.8, 127.9, 126.9, 125.8, 123.6, 123.1, 121.8, 113.6, 112.8, 78.6, 43.0, 39.2, 32.1, 28.0: TOF-MS; calcd. For $C_{54}H_{43}N_5O_2$, $[M]^+$:743.149, found:743.340. **TFA-3**;^{1}H NMR ($CDCl_3$, 400 MHz) δ 8.34 (s, 1H), 8.16 (d, 1H, J=8.9 Hz), 7.51 (d, 2H, J=8.3 Hz), 7.41 (d, 2H, J=8.9 Hz), 7.18-7.22 (m, 3H), 7.07-7.13 (m, 3H), 6.98-7.05 (m, 5H), 6.87 (s, 1H), 6.84 (s, 1H), 2.63 (s, 4H), 2.49 (s, 4H), 1.88 (s, 6H), 1.10 (s, 12 H); ^{13}C NMR (100 MHz, $CDCl_3$) δ 169.1, 164.1, 160.6, 156.9, 153.5, 151.8, 146.5, 137.1, 135.6, 132.9, 129.1, 129.0, 128.8, 126.1, 125.7, 123.7, 120.9, 113.5, 112.8, 110.5, 104.2, 78.8, 43.0, 39.2, 32.1, 28.0, 27.5: TOF-MS; calcd. For $C_{51}H_{45}N_5O_4$ $[M]^+$:791.318, found: 791.350

Cytotoxicity Assays

Cytotoxicity of the synthesized receptors (**TFA-1** and **TFA-3**) was evaluated in PNT1A and HS613.SK cell lines (0–200 μM) using the Alamar Blue assay (Oguz, 2022). Cells (10,000/well) were seeded in 96-well plates and incubated at 37 °C for 24 h, followed by compound treatment for 48 h. After adding Alamar Blue (10% of medium volume) and a 4 h incubation, absorbance was measured at 570 and 600 nm using an ELISA reader. The IC_{50} values were calculated from three independent experiments based on dose–response curves, with untreated cells serving as controls (100%).

Results and Discussion

Synthesis of TPA-Based Fluorescent Probes

Triphenylamine-based fluorescent probes (**TFA-1** and **TFA-3**) were successfully synthesized via multistep reactions involving indandione and Meldrum acid moieties. The synthetic routes are depicted in **Scheme 1**. The obtained products were purified and fully characterized by ^{1}H NMR, ^{13}C NMR, and TOF-MS analyses, confirming the successful formation of the desired structures (**Fig. 1-3**). Examination of the spectra confirmed the successful synthesis of the **TFA-1**. In the ^{1}H NMR spectrum, the aldehyde signal of the starting material **TFA-IF-CHO** observed at δ 9.82 ppm disappeared after the condensation reaction, while a new vinyl proton signal appeared at δ 7.82 ppm. The integration values of the other signals were consistent with the proposed structure. Incorporation of the 1,3-indandione group into the structure was further verified by ^{13}C NMR, which showed carbonyl (C=O) carbon signals at δ 190.83 and 189.53 ppm. Moreover, the m/z value obtained from

TOF-MS analysis ($[M]^+$ = 793.149) was found to be in good agreement with the theoretical m/z value ($[M]^+$ = 793.340), confirming the identity of **TFA-1**.

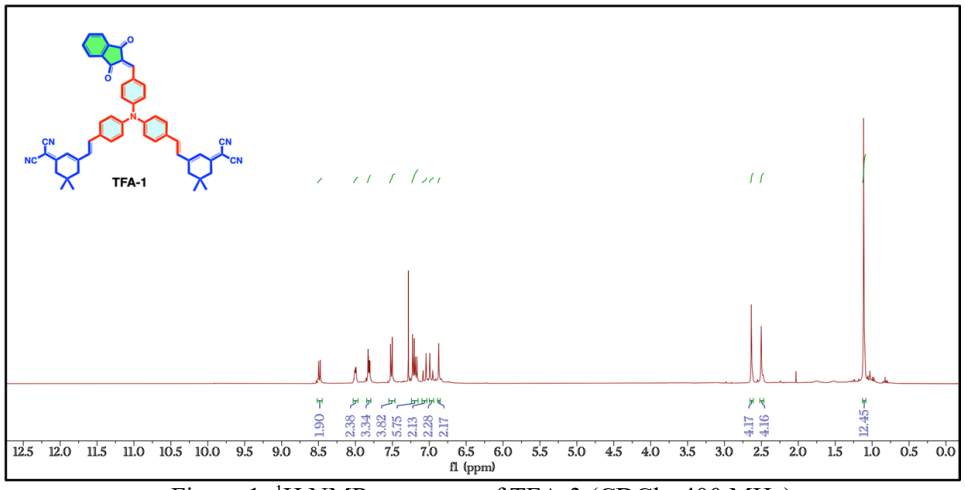

Figure 1. ^{1}H NMR spectrum of TFA-3 ($CDCl_3$, 400 MHz)

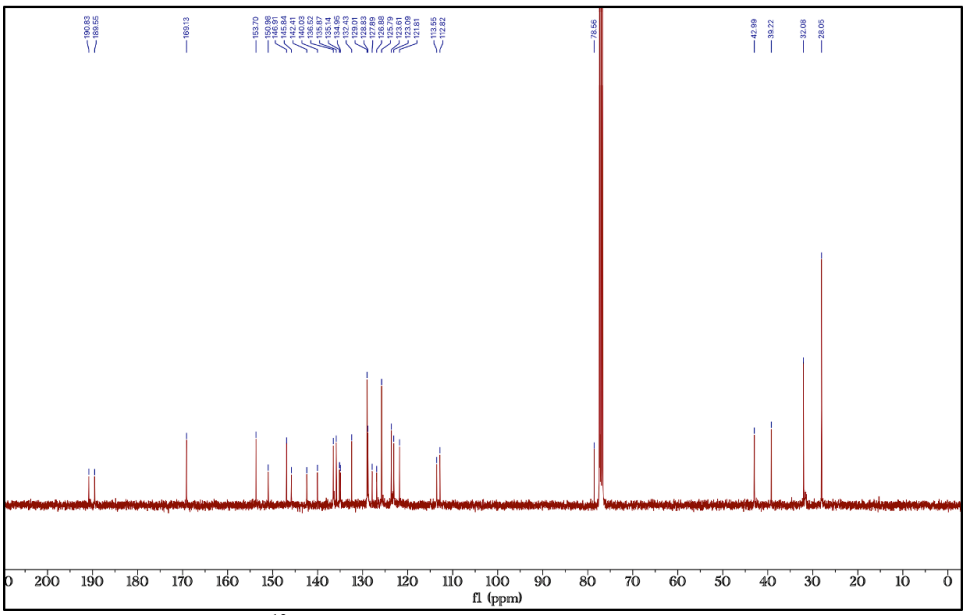

Figure 2. ^{13}C NMR spectrum of **TFA-1** ($CDCl_3$, 100 MHz)

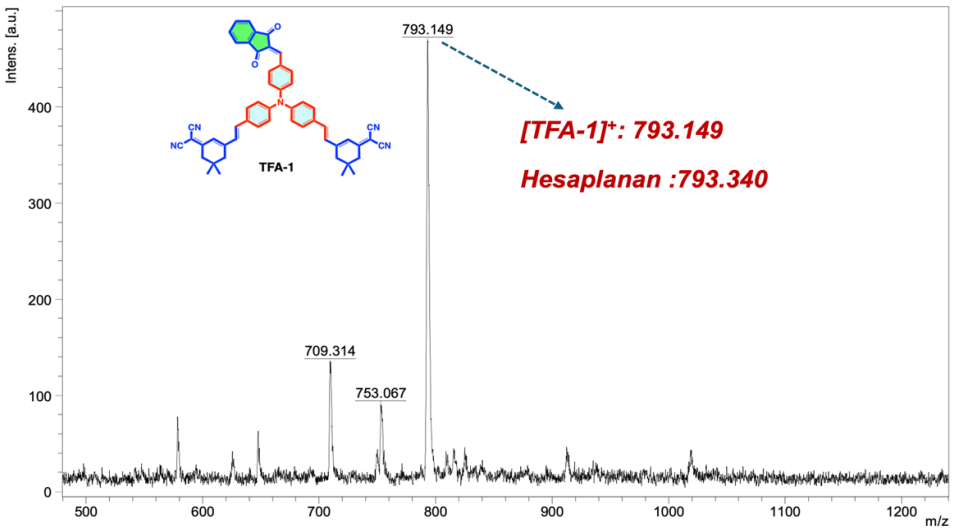

Figure 3. TOF-MS spectrum of **TFA-1**

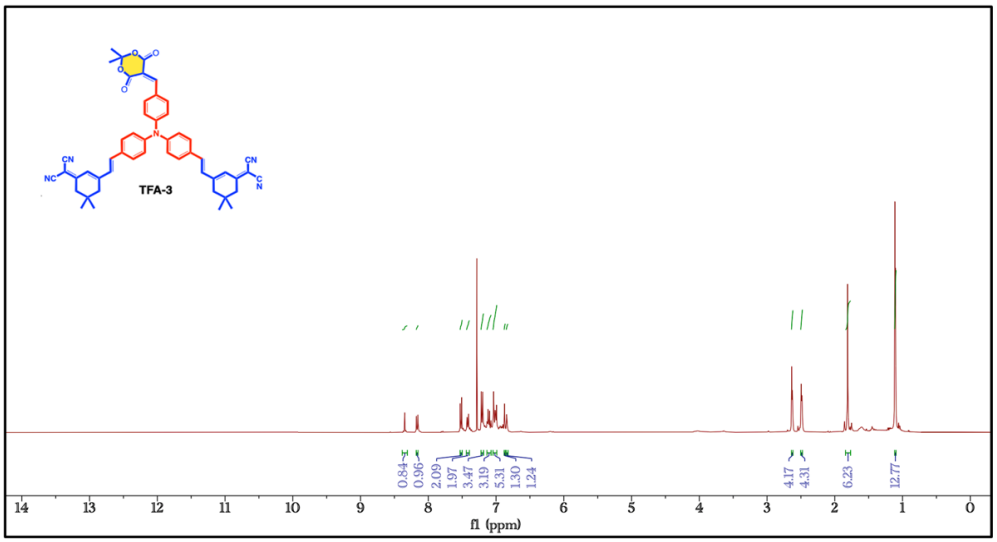

Figure 4. ^{1}H NMR spectrum of TFA-3 ($CDCl_3$, 400 MHz)

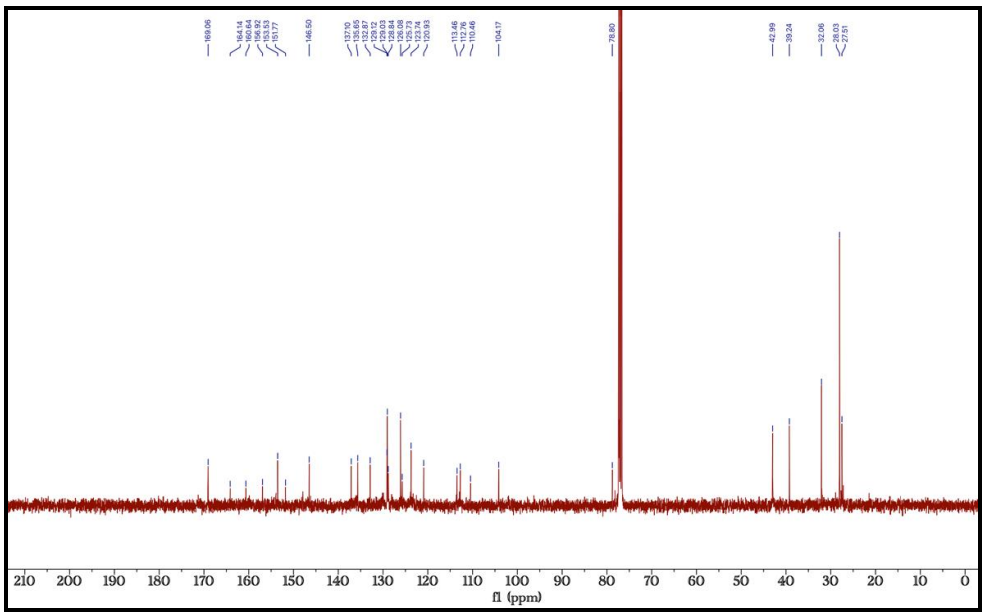

Figure 5. ^{13}C NMR spectrum of **TFA-3** ($CDCl_3$, 100 MHz)

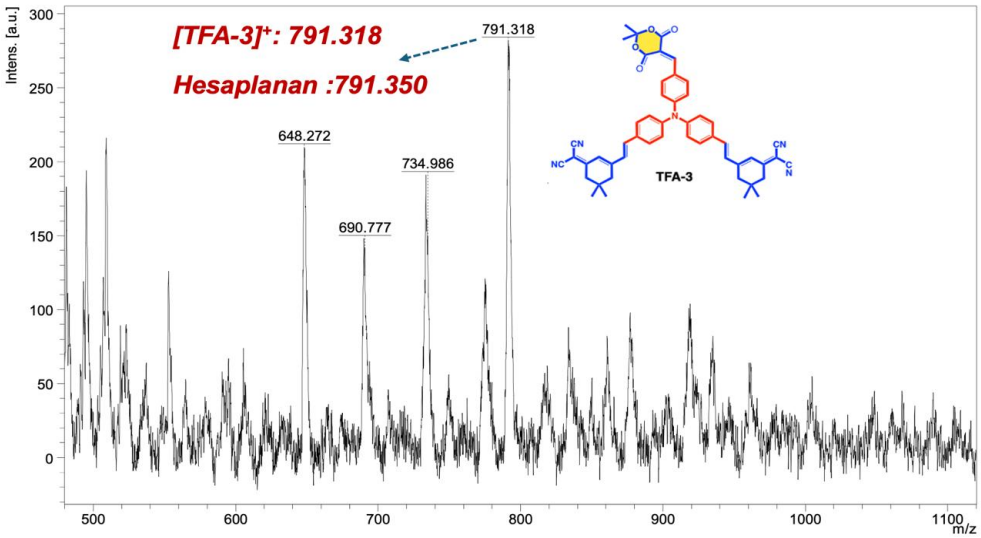

Figure 6. TOF-MS spectrum of **TFA-3**

The spectroscopic data obtained for the other sensor synthesized within the scope of the project, **TFA-3**, are presented below (**Fig. 4-6**). Analysis of the ^{1}H NMR spectrum revealed that the aldehyde signal of the starting material **TFA-IF-CHO** at δ 9.82 ppm disappeared, while a new signal corresponding to the inyl proton emerged at δ 8.34 ppm. The integration values of the remaining proton signals were consistent with the proposed structure. In the ^{13}C NMR spectrum, a carbonyl (C=O) carbon signal corresponding to the Meldrum's acid moiety was observed at δ 169.06 ppm. Furthermore, TOF-MS analysis of **TFA-3** showed an $[M]^+$ value of 791.318 m/z, which was in good agreement with the theoretically calculated $[M]^+$ value of 791.350 m/z. These spectroscopic results confirm the successful synthesis of the **TFA-3** sensor molecule.

Cytotoxicity Evaluation

The cytotoxicity profiles of the probes were investigated to ensure their compatibility for biological and practical applications. Both compounds demonstrated very low cytotoxicity, maintaining over 90% cell viability at relevant working concentrations (**Fig. 7**). Also, **Table 1** summarizes the calculated IC_{50} values for **TFA-1** and **TFA-3**. These findings confirm their biocompatibility and suitability for application in real food matrices.

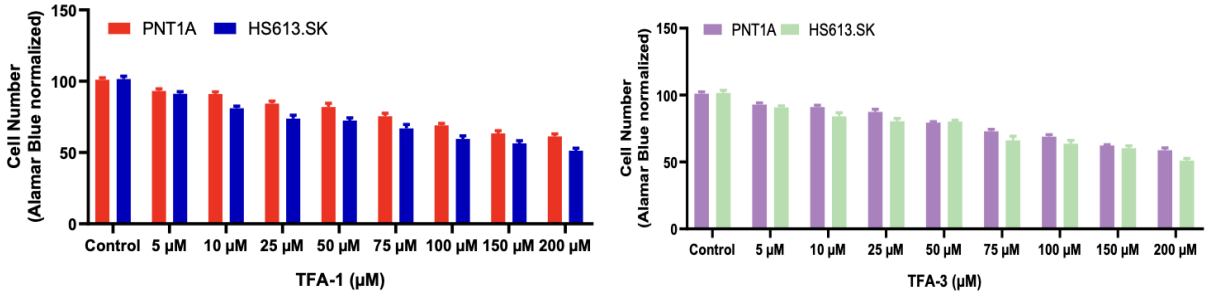

Figure 7. IC_{50} values of the **TFA-1** and **TFA-3** on PNT1A and HS613.SK

Table 1. Calculated IC_{50} values (µM) for **TFA-1** and **TFA-3.**

Compounds	PNT1A	HS613.SK
TFA-1	> 200	162.4
TFA-3	> 200	177.7

Potential Applications in Food Safety

Given their low cytotoxicity, the synthesized **TFA-1** and **TFA-3** probes show significant promise for use in visual detection platforms, such as paper-based test strips or portable devices. Their ability to rapidly and selectively detect BAs suggests potential utility in monitoring food freshness, reducing spoilage-related waste, and improving consumer safety.

Conclusion

In this study, novel triphenylamine-based fluorescent probes (**TFA-1** and **TFA-3**) incorporating Indandione and Meldrum acid units were successfully synthesized and structurally confirmed. Cytotoxicity assays demonstrated their excellent biocompatibility, with minimal impact on cell viability. Collectively, these findings highlight the potential of these probes as practical, non-toxic tools for the detection of biogenic amines in real food samples, contributing to improved strategies for food quality assurance and safety monitoring.

Scientific Ethics Declaration

*The author declares that the scientific ethical and legal responsibility of this article published in EPSTEM journal belongs to the author.

Conflict of Interest

*The author declares that there is no conflict of interest.

Funding

*The authors thank Selçuk BAP and TUBİTAK-1001 (*Project number: 124Z391*) for this work.

Acknowledgements or Notes

*This article was presented as an oral presentation at the International Conference on Basic Sciences and Technology (www.icbast.net) held in Budapest/Hungary on August 28-31, 2025.

*This study was produced from TÜBİTAK-1001 (Project number: 124Z391)

References

Al-Asmari, F. (2025). Smart sensing: recent trends in organic colorimetric and fluorimetric sensors for ammonia and biogenic amine detection (2020–2025). *Journal of Saudi Chemical Society*, *29*(3), 1-24.

Almeida, C. M., Magalhaes, J. M., Barroso, M. F., & Duraes, L. (2025). Biogenic amines detection in food: Emerging trends in electrochemical sensors. *Talanta*, *292*, 127918.

Chen, L. J., Wang, J. Y., Zhao, X., & Yan, X. P. (2025). Biogenic amine-responsive ratiometric fluorescent microneedle sensor for real-time visualization of meat freshness. *Food Chemistry*, *482*, 144144.

Erdemir, S., Oguz, M., & Malkondu, S. (2025). A new HBT-quinolinium platform for optical detection of biogenic amines and its application in food quality monitoring. *Talanta*, *292*, 127906.

Grant, M. J., Wolfe, K. M., Harding, C. R., & Welch, G. C. (2023). Biogenic amine sensors using organic π-conjugated materials as active sensing components and their commercialization potential. *Journal of Materials Chemistry C*, *11*(29), 9749-9767.

Kaur, N., Chopra, S., Singh, G., Raj, P., Bhasin, A., Sahoo, S. K., ... & Singh, N. (2018). Chemosensors for biogenic amines and biothiols. *Journal of Materials Chemistry B*, *6*(30), 4872-4902.

Li, X., Wu, Z., Cao, H., Ye, T., Hao, L., Yu, J., ... & Xu, F. (2025). A molecularly ımprinted fluorescence sensor for the simultaneous and rapid detection of histamine and tyramine in cheese. *Foods*, *14*(9), 1475.

Liu, Z., Zhou, S., Yuan, F., Zhao, Y., Zhou, N., Zhang, W., ... & Hou, L. (2025). A novel fluorescence platform for portable and visual monitoring of meat freshness. *Biosensors and Bioelectronics*, *267*, 116746.

Müller, D. G., Oreste, E. Q., Heinemann, M. G., Dias, D., & Kessler, F. (2022). Biogenic amine sensors and its building materials: A review. *European Polymer Journal*, *175*, 111221.

Nakamura, M., Sanji, T., & Tanaka, M. (2011). Fluorometric sensing of biogenic amines with aggregation-induced emission-active tetraphenylethenes. *Chemistry–A European Journal*, *17*(19), 5344-5349.

Oguz, M. (2022). Synthesis and anticancer activity of new p-tertbutylcalix [4] arenes integrated with trifluoromethyl aniline groups against several cell lines. *Tetrahedron*, *116*, 132816.

Qian, M., Zhang, L., Pu, Z., Xia, J., Chen, L., Xia, Y., ... & Peng, X. (2018). A NIR fluorescent probe for the detection and visualization of hydrogen sulfide using the aldehyde group assisted thiolysis of dinitrophenyl ether strategy. *Journal of Materials Chemistry B*, *6*(47), 7916-7925.

Shanmugaraju, S., Noushija, M. K., Alenthwar, V. K., & Ali, R. T. M. (2025). Reactivity-based small-molecule fluorescence probes for sensing biogenic amine Cadaverine-a biomarker to determine food freshness. *Sensors & Diagnostics*.

Yu, Y., Zhao, R., Liu, H., Zhang, S., Zhou, C., Gao, Y., Li, W., & Yang, B. (2020). Highly efficient deep-blue light-emitting material based on V-Shaped donor-acceptor triphenylamine-phenanthro [9, 10-d] imidazole molecule. *Dyes and Pigments*, *180*, 108511.

Zhang, D., Wang, S., Zhu, X., Jia, C. Q., Liu, H., & Sun, B. (2025). Ratiometric sensing based on self-assembled dipeptide: Color-resolved visualization of quantified evaluation for biogenic amines. *Food Chemistry*, 144917.

Zhang, X., Zhang, F., Yang, B., & Liu, B. (2023). A dual-site fluorescent probe for discriminately detecting low and high concentration of hypochlorite in living cells. *Spectrochimica Acta Part A: Molecular and Biomolecular Spectroscopy*, *299*, 122823.

Author(s) Information

Mehmet Oguz
Selcuk University Faculty of Science
Department of Chemistry, Konya, Türkiye
Contact e-mail: *m.oguz2011@gmail.com*

To cite this article:

Oguz, M. (2025). Synthesis of triphenylamine-based fluorescent sensors for biogenic amine detection and evaluation of their cytotoxic potential. *The Eurasia Proceedings of Science, Technology, Engineering and Mathematics (EPSTEM), 36,* 117-124.

The Eurasia Proceedings of Science, Technology, Engineering & Mathematics (EPSTEM)
ISSN: 2602-3199

The Eurasia Proceedings of Science, Technology, Engineering and Mathematics (EPSTEM), 2025

Volume 36, Pages 125-133

ICBAST 2025: International Conference on Basic Sciences and Technology

Evaluation of Different Additives on Mechanical Properties and Performance of Hot Mix Asphalt Using Marshall Stability and ITSM Tests

Sefa Utku Tiryaki
Firat University

Erkut Yalcin
Firat University

Abstract: This study comprehensively evaluated the mechanical performance of hot mix asphalt (HMA) mixtures prepared with neat and modified binders using Marshall stability and Indirect Tensile Stiffness Modulus (ITSM) tests. Marshall stability test results revealed that the incorporation of polymeric and reactive additives increased the stability values of the mixtures compared to those produced with neat binder. Among the additives investigated, the 611 elastomer demonstrated the highest improvement in stability, achieving up to 1.80 times higher values than the neat mixture. Other additives, such as 701, SBS, and CR, also enhanced stability, albeit to varying extents. The ITSM test results indicated that the stiffness modulus of the mixtures increased with higher elastomer content. The 611 elastomer exhibited the most significant impact on stiffness among the tested elastomers, while 701 and SBS showed comparable performance. Furthermore, higher ITSM test temperatures resulted in decreased stiffness values across all mixtures. The number of load repetitions required to initiate cracking was found to be lowest in the mixtures containing neat binder and highest in mixtures containing 4% of the 611 elastomer, indicating superior fatigue resistance. Overall, both Marshall and ITSM tests confirmed that modified binders, particularly those incorporating the 611 elastomer, significantly enhance the mechanical properties of HMA mixtures, improving their resistance to deformation and cracking under load.

Keywords: Hot mix asphalt, Modified bitumen, Marshall stability, Indirect tensile stiffness modulus

Introduction

Road transportation is the most widely used mode of transport for both freight and passenger movement worldwide, including in our country, owing to its ability to provide flexible and rapid transport over short and medium distances, enable door-to-door delivery without requiring any other mode of transport, and offer ease of vehicle planning and availability. Road transport plays a significant role in our daily lives. It has maintained its importance from ancient times to the present day by facilitating life in both passenger and freight transportation. The adequacy and standards of a country's transportation network are also indicators of its level of development. According to data from the Turkish General Directorate of Highways (KGM) as of January 2023, there are a total of 29,178 km of roads paved with Hot Mix Asphalt (HMA) on motorways, state roads, and provincial roads, while a total of 36,184 km of surface-dressed roads exist on state and provincial roads (Official Website of the General Directorate of Highways, 2023). Highways can be defined as all structures constructed along a designated route, adhering to specific geometric standards, at appropriate natural ground elevations, allowing vehicles to travel at the desired speed, safety, and comfort levels. The road pavement is defined as a layered structure placed over the subgrade, typically consisting of the sub-base, base, and surfacing layers, designed to reduce the loads from vehicles to levels that the subgrade can bear, protect the subgrade, and provide a smooth rolling surface.

On medium and heavily trafficked roads, surfacing layers, which are the most expensive components of the pavement structure and are in direct contact with vehicle tires, are constructed to carry traffic loads and protect the other pavement layers from adverse environmental effects. These surfacing layers can be constructed using various techniques, ranging from surface dressing to Hot Mix Asphalt (HMA). Surface dressings may be applied in one or multiple layers, involving the spraying of bitumen onto a suitable base, followed by spreading and compaction of aggregate. Hot Mix Asphalt (HMA) is one of the most expensive yet durable types of surfacing. HMA is produced by heating and mixing aggregate and bitumen in a stationary plant, transporting the mixture to the application site, and compacting it at a specified temperature. The primary function of bituminous binders in the mixture is to ensure adhesion and cohesion in HMA. Aggregates, on the other hand, provide internal friction resistance and stability to the mixture. Additionally, bituminous binders bind the aggregate particles together to prevent disintegration under traffic loads, create smooth surfaces that enhance driving comfort, and fill the voids within the mixture to ensure impermeability.

Distresses occurring in Hot Mix Asphalt (HMA) can generally be classified into three main categories: deformation, fracture (cracking), and disintegration (Hınıslıoğlu & Hattatoğlu, 2003). Cracks in HMA are further categorized into those caused by traffic loading and those unrelated to traffic effects. Various factors, such as the thickness of pavement layers and the material properties of HMA, influence crack formation (Garcia, 2002; Jajliardo, 2003). Traffic-induced cracking may result either from the passage of heavy axle loads once or a few times or from the repeated movement of vehicles over the pavement. Cracks formed due to numerous vehicle passes are referred to as fatigue cracks. In the first case, cracking occurs when the stress imposed by the heavy axle load exceeds the flexural-tensile strength of asphalt concrete. In fatigue, cracks develop due to the accumulation of permanent deformations resulting from repeated axle loads. Apart from traffic loads, cracking may also arise due to environmental factors such as temperature fluctuations and moisture. Cracking in HMA can be classified into several types, including alligator (fatigue) cracking, shrinkage cracking, edge cracking, joint cracking, transverse cracking, reflection cracking, and slippage cracking (Ağar & Umar, 1991).

In recent years, numerous studies have focused on applying the principles of fracture mechanics to HMA, owing to the prevalence of cracking in road pavements. Fracture refers to the separation of materials into multiple pieces under stress. The nature of fracture varies between materials and is generally dependent on the applied stress, temperature, and strain rate. Fracture typically occurs in two stages: the first stage involves “crack initiation,” and the second stage involves “crack propagation” (Özdemir, 2006). From a macroscopic perspective, fractures are categorized as brittle, ductile, and creep fractures. Brittle fractures occur without any plastic deformation. In ductile materials, significant plastic deformation occurs prior to fracture. Creep fracture, on the other hand, results from creep deformation under constant stress or load at elevated temperatures. Macroscopically, creep fracture involves plastic deformation and therefore resembles ductile fracture. However, from a microscopic viewpoint, creep fracture is distinct from ductile fracture (Özdemir, 2006).

In light of the ongoing quest for more durable and sustainable pavement materials, this study aims to systematically investigate the effects of various polymeric and reactive additives on the mechanical behavior of hot mix asphalt mixtures. By employing both Marshall stability and Indirect Tensile Stiffness Modulus (ITSM) tests, the research provides a comprehensive assessment of how these additives influence the resistance of asphalt mixtures to deformation, stiffness variations, and fatigue performance. The outcomes are expected to contribute valuable insights toward optimizing binder modification strategies and enhancing the long-term performance of asphalt pavements under diverse service conditions.

Materials and Method

Materials

In this study, the B70/100 reference bitumen produced by the Batman Refinery was used. The density of the reference bitumen employed is 1.033 g/cm³. Due to climatic conditions, the 70/100 grade is the most widely used binder in Turkey. The general properties of the bitumen utilized in the study are presented in Table 1(A. M. Özdemir, 2025). Five different additives (SBS, 701, 611, CR, and Elvaloy-PPA) were used for bitumen modification. The CR used in the study was supplied by Samsun Akın Plastik Company, while Elvaloy and PPA were procured from Komsa Company. The SBS (Kraton D 1101) additive produced by Shell, as well as 701 and 611, were provided by Mpolimer Company. The ground tire rubber (CR) was obtained using a mechanical shredding method and sieved through a No. 40 mesh before being used in the study. The properties of the additives are provided in Table 2. The additives utilized in the study are shown in Figure 1.

Table 1. General properties of 70/100 bitumen

Properties	**Unit**	**Standard**	**Results**
Penetration	mm^{-1}	EN 1426	87.4
Softening Point	˚C	EN 1427	52.6
Flash Point	˚C	EN ISO 2719	230
Viscosity 135˚C /165˚C	cP	ASTM D4402	562.5/162.5

Table 2. Properties of the additives used in the study

Properties	**SBS**	**701**	**611**
Molecular structure	Liner	Liner	Radial
Styrene/butadiene ratio	31/69	33/67	31/69
Density (cm/m3)	0,94	0,93	0,94
Oil content	Yok	Yok	Yok
Viscosity (5%, cps)	-	14	24
Melt index (190°C/kgw)	<1	<1	<1
Tensile strength (kgw/cm2)	324	220	200
Hardness	70	80	83
Ash content	-	0,2	0,2
Elongation at break (%)	880	600	700

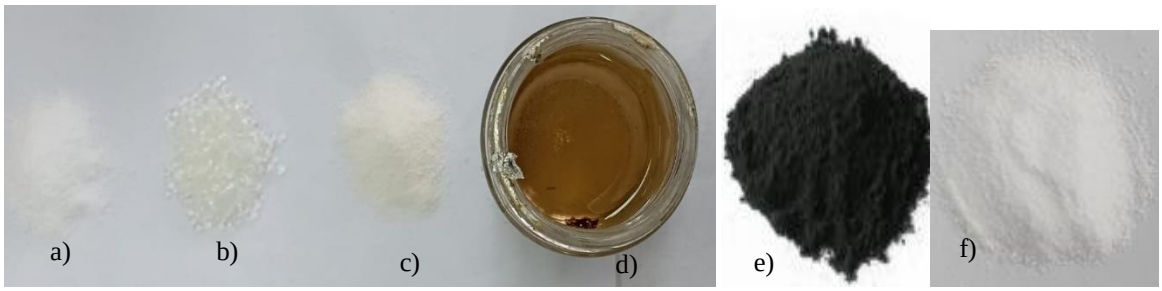

Figure 1. Additives used in the study: (a) SBS polymer, (b) Elvaloy, (c) 611 polymer, (d) PPA, (e) CR, (f) 701 polymer

Preparation of Modified Bitumen

In this study, modified bitumens were prepared using a reference binder (70/100) with the incorporation of SBS, Enprene 611, Enprene 701, CR, Elvaloy, and PPA additives. The production procedure for elastomer-modified bitumen was adopted from previous studies (Yalcin & Demirbag, 2022). In the initial stage, the neat bitumen was heated for 30 minutes in an oven at 180 ± 5 °C to achieve a fluid state, after which 800 grams of bitumen was transferred into a metal mixing vessel. To ensure a uniform heat source, the bitumen inside the metal vessel was placed into a heating jacket set at 180 ± 5 °C, and the system was maintained at this temperature until thermal equilibrium was achieved. Subsequently, the additives were incorporated into the bitumen at predetermined dosages (%2, %3, %4 SBS; %2, %3, %4 Enprene 611; %2, %3, %4 Enprene 701; %4, %6, %8 CR; %3 Elvaloy; and %0.2 PPA). To ensure accurate comparison of the results of the modified bitumen binders, the same procedure was employed for the preparation of all modified samples.

Following the addition of the additives, the bitumens containing the modifiers were mixed for 4 hours using a mechanical mixer operating at 2700 rpm to produce the modified binders (Yalcin & Demirbag, 2022). Specifically, in the case of the modified bitumen with 3% Elvaloy, the mixing process was interrupted after 3.5 hours to add 0.2% PPA, after which mixing continued for an additional 30 minutes to complete the blending. The additive dosages employed during the modification process were determined by considering values commonly preferred in the literature and industry applications. Upon completion of the preparation of all modified binders, they were subjected to short-term and long-term aging processes. In the nomenclature used for the experimental results, “C” denotes the neat binder, while in the modified binders, the number on the left side indicates the percentage of additive incorporated into the neat binder, and the term on the right denotes the type of additive used.

Preparation of Hot Mix Asphalt Samples

To prepare the mixture specimens, aggregates were weighed in quantities determined according to the gradation specified in Table 5.2, ensuring a total mass of 1100 grams for each specimen. The design bitumen content for the neat mixture was determined through analyses and set at 4.67%. To prevent the binder content from affecting the mechanical properties of the mixtures, the Hot Mix Asphalt (HMA) specimens containing elastomer additives were prepared with the same bitumen content (4.67%) as the mixture without elastomers. All mixture specimens were produced based on the aggregate gradation given in Table 3. In order to avoid the influence of binder content on the mechanical properties of the mixtures, both the neat and modified mixtures were prepared using identical bitumen content. The prepared mixtures were compacted into cylindrical Marshall specimens with diameters of 10 cm and 15 cm and an approximate height of 6 cm. Compaction was performed using a rotary compactor applying a static pressure of 600±18 kPa at an inclination angle of 1.25±0.02°, aiming for a 4% air void content. Subsequently, the 15 cm specimens were cut in half, notches were introduced, and semi-circular specimens were prepared. Notches were made at depths of 1 cm and 2 cm, respectively. Asphalt mixture samples used in the project are given in Figure 2.

Table 3. Aggregate gradation used in the asphalt mixture

Category	**Values**									
Sieve Size (mm)	19	12.5	9.5	4.75	2.36	1.18	0.6	0,3	0.15	0.075
Passing (%)	100	95	88	65	35	23	14	10	8	6

Figure 2. Asphalt mixture samples prepared during the project study

Marshall Stability and Flow Test

First, the heights of the prepared asphalt mixture specimens are measured. The specimens with recorded heights are then placed in a water bath at 60°C for approximately one hour (Figure 3). Afterwards, the specimens are removed from the water bath, positioned in the testing device, and subjected to loading at a rate of 50 mm/min (Figure 4).

During the test, both the maximum load and the corresponding deformation at the point of maximum load are determined and recorded. The test must be conducted within 40 seconds after the specimen is removed from the water bath. The standard height of the specimens used in the experiment is known to be 63.5 mm. The average values of the determined stability and flow are calculated. Stability and flow values are established in this way. Specimens whose flow values deviate by more than 20% from the average flow, or whose stability values deviate by more than 15% from the average stability, are excluded from the evaluation. To assess deviations of the specimens' stability and flow values from the mean, the average of the remaining specimens is calculated. The retained Marshall stability test is applied to determine the moisture damage resistance of hot mix asphalt mixtures.

Figure 3. Keeping the samples in a water bath at 60±1°C

Figure 4. Performing Marshall stability and flow test

Indirect Tensile Stiffness Modulus Test

To experimentally determine the stiffness modulus of Hot Mix Asphalts (HMAs), direct compression, indirect tensile, and torsion tests can be employed. These test methods involve the application of periodic loads and the measurement of instantaneous deformations during these processes. The stiffness modulus is calculated as the ratio of the applied stress to the recoverable strain. Compared to direct compression tests, indirect tensile tests are more frequently used due to their higher sensitivity to the influence of the binder in the mixture (Kök, 2007; Zoorob & Suparma, 2000).

The Indirect Tensile Stiffness Modulus (ITSM) test, which is a non-destructive, deformation-controlled test defined by the BS EN 12697-26 standard (BS 12697, 2004), was conducted using Cooper's Nottingham Asphalt Tester (NAT) equipment. ITSM is the most commonly utilized test for determining the stiffness modulus of asphalt specimens using the NAT machine, as shown in Figure 5. The dimensions of the specimens were 100±2 mm in diameter and 40±2 mm in thickness. The test was performed under standard conditions with a target horizontal deformation of 5 μm, a rise time of 124 ms, and a test temperature of 20°C.

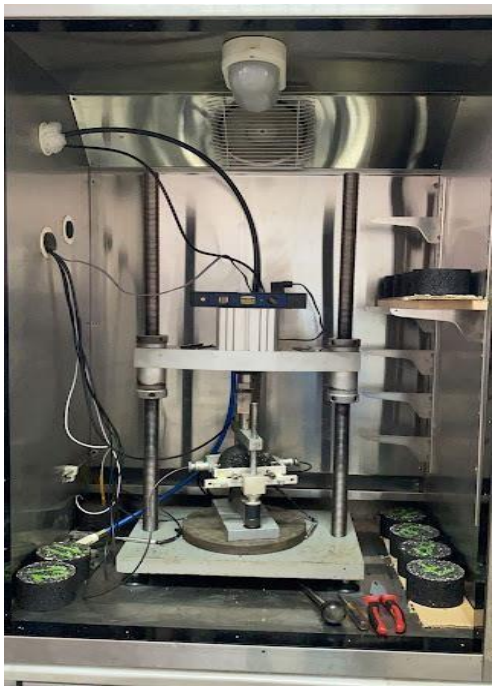

Figure 5. Indirect tensile stiffness modulus test

Results and Discussion

Marshall Stability and Flow Test Results

Marshall stability and flow tests were performed on the prepared Hot Mix Asphalt (HMA) specimens to determine their maximum resistance to deformation and the amount of deformation occurring under the maximum applied load, thereby evaluating the mixtures' resistance to permanent deformation. For the Marshall stability and flow tests, the mixture specimens were conditioned in water at 60°C for 60 minutes prior to testing. Flow and Marshall stability measurements were conducted using three specimens for each type of mixture. A total of 15 different mixtures were prepared using neat bitumen and thirteen different modified bitumen's. As illustrated in Figure 6, the use of additives led to an increase in the stability values of the mixture specimens. The highest stability value was obtained in mixtures containing 4% of the 611 elastomer, while the lowest stability value was recorded for the neat binder. Following the neat binder, the lowest stability value among the mixtures was observed in the MC mixture. Among the elastomer additives, the 611 elastomer provided the best stability performance.

The stability value of the neat binder prepared under modified bitumen mixing conditions was 1.04 times higher than that of the original neat binder. The Marshall stability values of the 701 and SBS elastomers were found to be similar to each other. It was determined that the stability values of the 4-611, 3-611, and 2-611 asphalt mixtures were 1.80, 1.46, and 1.30 times higher, respectively, than that of the neat mixture. Similarly, the stability values of the 4-701, 3-701, and 2-701 asphalt mixtures increased by factors of 1.58, 1.42, and 1.27, respectively, compared to the neat mixture. For the 4SBS, 3SBS, and 2SBS asphalt mixtures, the stability values were 1.48, 1.35, and 1.23 times higher, respectively, than that of the neat mixture. The stability values of the 8CR, 6CR, and 4CR asphalt mixtures were determined to be 1.47, 1.31, and 1.19 times higher, respectively, than that of the neat mixture. Among the 15 different mixtures tested in this study, the maximum resistance to deformation was achieved with the 611 elastomer. The stability values of asphalt mixtures containing CR exhibited results similar to those of mixtures containing the 701 elastomer.

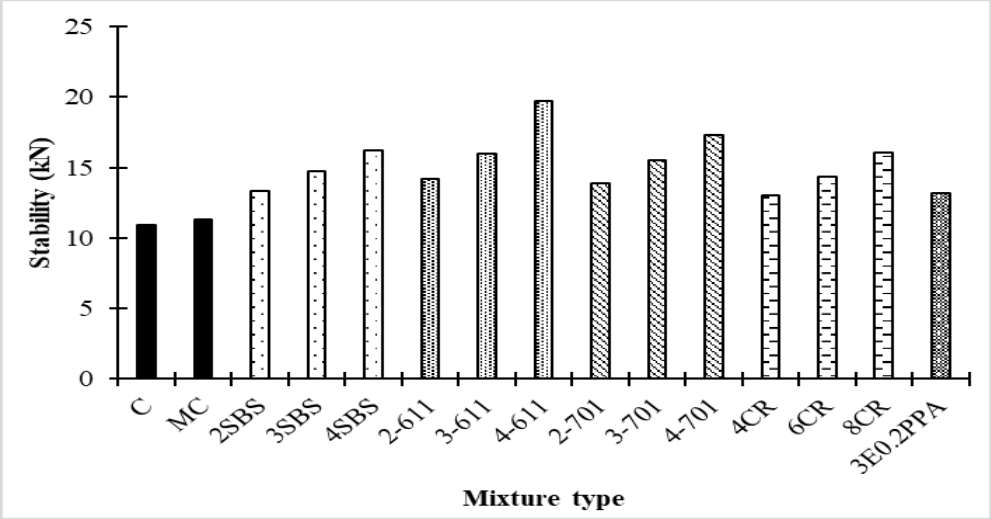

Figure 6. Marshall stability values of mixtures

Indirect Tensile Stiffness Modulus (ITSM) Test Results

The Indirect Tensile Stiffness Modulus (ITSM) test is specified in the BS DD 213 standard, and the experimental work was carried out in accordance with this standard (BS DD 213, 1993). Within the scope of this test, the stiffness of Hot Mix Asphalt (HMA) specimens prepared using neat binder as well as bitumens modified with 611, 701, and SBS was determined. For each type of mixture, three specimens were used in the test. Since the specimens were not damaged during this test, they were subsequently utilized in fatigue testing. The ITSM test on the mixture specimens was performed at test temperatures of 20°C and 30°C using the UMATTA (Universal Material Testing Apparatus) testing device. In the test, five preliminary loadings were applied to the specimen by the testing apparatus to establish the load required to achieve the target horizontal deformation. Subsequently, five test loadings were performed on the specimen to determine the stiffness of the HMA specimens under dynamic loads. The ITSM value of a mixture specimen was determined by calculating the average of the five ITSM values obtained from the five load pulses. In the experimental study, the loading rise time was set at 124 ms, the loading period at 3000 ms, and the target deformation at 5 μm, with the Poisson's ratio assumed to be 0.35. While determining the ITSM values of the mixture specimens, each specimen was tested at least twice, and the average of the two ITSM values obtained from the same specimen was calculated. For the second test, the specimen was rotated by 90°. If the deviation between the two ITSM values obtained from the same specimen exceeded 10%, the specimen was rotated an additional 90°, and the test was repeated. When three ITSM values were obtained from the same specimen, the average of the two values showing less than 10% deviation was taken as the ITSM value for the mixture specimen. The variation in ITSM values of mixtures prepared with neat and modified bitumens is presented in Figure 7.

As shown in Figure 6.2, it was determined that the stiffness values of mixtures prepared with neat binder subjected to the conditions used for modified bitumen preparation were higher than those of mixtures prepared with the neat binder alone. As indicated in the figure, the stiffness value increases as the elastomer content in the neat binder increases. Among the three elastomers, the 611 elastomer was found to be the most effective in terms of stiffness. The stiffness values of the 701 and SBS elastomers were also observed to be similar to each other. Moreover, an increase in the ITSM test temperature led to a decrease in the stiffness values of the mixtures. At 20°C, the stiffness values of the 4-611, 3-611, and 2-611 asphalt mixtures were found to be 2.68, 2.42, and 2.15 times higher, respectively, than that of the neat mixture. For the 4-701, 3-701, and 2-701 asphalt mixtures, the stiffness values increased by factors of 2.58, 2.19, and 1.81, respectively, compared to the neat mixture. Similarly, at 20°C, the stiffness values of the 4SBS, 3SBS, and 2SBS asphalt mixtures were determined to be 2.46, 2.12, and 1.66 times higher, respectively, than that of the neat mixture. The stiffness values of the 8CR, 6CR, and 4CR asphalt mixtures at 20°C increased by factors of 2.31, 1.94, and 1.47, respectively, compared to the neat mixture. At 30°C, the stiffness values of the 4-611, 3-611, and 2-611 asphalt mixtures were found to be 2.78, 2.52, and 2.17 times higher, respectively, than that of the neat mixture. For the 4-701, 3-701, and 2-701 asphalt mixtures, the corresponding increases were 2.58, 2.19, and 1.81 times, respectively. The stiffness values of the 4SBS, 3SBS, and 2SBS asphalt mixtures at 30°C were 2.61, 2.21, and 1.97 times higher, respectively, than that of the neat mixture. The stiffness values of the 8CR, 6CR, and 4CR asphalt mixtures at 30°C were determined to be 2.32, 2.01, and 1.48 times higher, respectively, than that of the neat mixture. It was

observed that the ITSM value of the 3E0.2PPA binder exceeded that of the mixtures containing 2% elastomer. An evaluation of the ITSM test results revealed that the highest ITSM values were obtained in mixtures prepared with 4% of the 611 elastomer, and it was confirmed that the incorporation of additives increased the ITSM values of the mixtures.

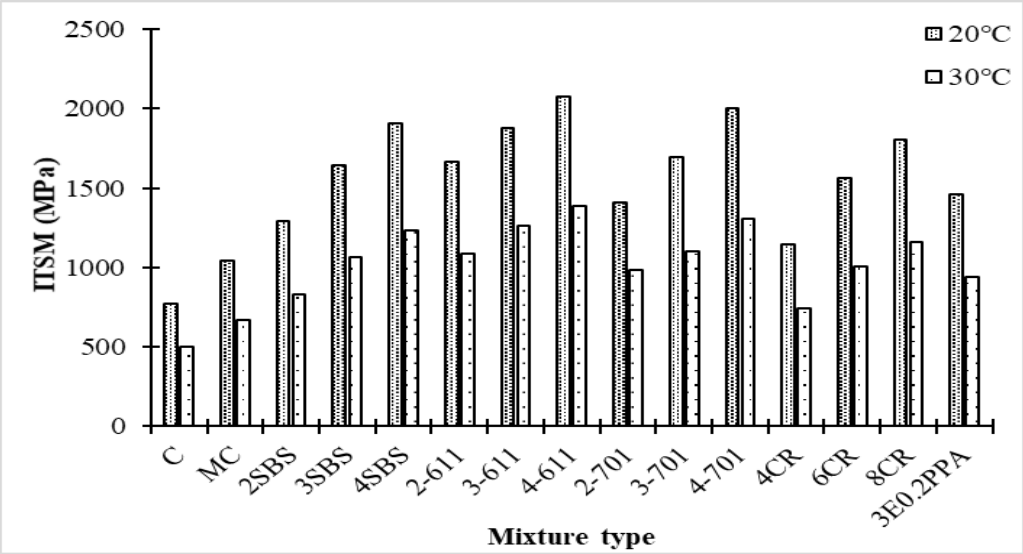

Figure 7. ITSM values of mixture samples

Conclusion

This study investigates the effects of various polymeric and reactive additives on the mechanical properties of hot mix asphalt mixtures, focusing particularly on deformation resistance, stiffness, and fatigue performance. Among the 15 different mixtures examined in this study, the highest resistance to deformation was achieved with the 611 elastomer. The stability values of asphalt mixtures containing CR were found to be similar to those of mixtures containing the 701 elastomer. Among the three elastomers, the 611 elastomer was determined to be the most effective in terms of stiffness. The stiffness values of the 701 and SBS elastomers were also found to be quite similar to each other. Furthermore, an increase in the ITSM test temperature resulted in a reduction in the stiffness values of the mixtures. It was determined that the number of load repetitions required to induce fracture in the mixture specimens was lowest in the mixtures prepared with neat bitumen (C) and highest in the 4-611 mixture.

Scientific Ethics Declaration

*The authors declares that the scientific ethical and legal responsibility of this article published in EPSTEM journal belongs to the authors.

Conflict of Interest

*The authors declare that they have no conflicts of interest.

Funding

*This study was supported by Fırat University Scientific Research Projects Unit (FUBAP) with project number MF-25.47.

Acknowledgements or Notes

*This article is extracted from the first author's master thesis entitled "Comparison of Mechanical Behaviors of Hot Mix Asphalt Mixtures Produced with Different Binder Uses", supervised by Erkut YALCIN.

References

Agar, E., & Umar, F. (1991). *Yol üst yapısı*. İstanbul Teknik Üniversitesi İnşaat fakültesi Matbaası Yayını.

Garcia, O. F. (2002). *Asphalt mixture and loading effects on surface-cracking of pavements*. University of Florida.

Hinislioglu, S., & Hattatoglu, F. (2003). *Asfalt betonunun yorulma ömrünün üç boyutlu sonlu elemanlar yöntemi ile tahmin edilmesi*. TUBITAK.

Jajliardo, A. P. (2003). *Development of specification criteria to mitigate top-down cracking*. University of Florida.

Official Website of the General Directorate of Highways. (2023). *Yol agı bilgileri*. Retrieved from http://www.kgm.gov.tr/SiteCollectionDocuments/KGMdocuments/Istatistikler/DevletIlYolEnvanter/SatihYolAgiUzunlugu

Ozdemir, A. (2006). *Seramik malzemelerin kırılma tokluğu değerlerinin üç boyutlu sonlu elemanlar yöntemi ile teorik olarak belirlenmesi* (Master's thesis Dokuz Eylul University).

Yalcin, E., & Demirbag, A. (2022). Effects of modified binders obtained from different polymers on conventional and rheological properties. *Construction and Building Materials*, *357*, 129366.

Author(s) Information

Sefa Utku Tiryaki
Graduate School of Natural and Applied Sciences, Firat University, Elazig, Türkiye

Erkut Yalcin
Civil Engineering Department, Engineering Faculty, Firat University, Elazig, Türkiye
Contact e-mail: *erkutyalcin@firat.edu.tr*

To cite this article:

Tiryaki, S. U., & Yalcin, E. (2025). Evaluation of different additives on mechanical properties and performance of hot mix asphalt using Marshall stability and ITSM tests. *The Eurasia Proceedings of Science, Technology, Engineering and Mathematics (EPSTEM), 36*, 125-133.

The Eurasia Proceedings of Science, Technology, Engineering & Mathematics (EPSTEM)
ISSN: 2602-3199

The Eurasia Proceedings of Science, Technology, Engineering and Mathematics (EPSTEM), 2025

Volume 36, Pages 134-140

ICBAST 2025: International Conference on Basic Sciences and Technology

Determination of Physical Properties of Polymeric and Different Additives on Bituminous Binders

Isra Seza Deveci
Firat University

Mehmet Yilmaz
Firat University

Abstract: This study was designed to comprehensively investigate the diverse and complex effects of polymeric and reactive additives on asphalt binders, employing a thorough experimental methodology rooted in conventional binder testing techniques. Unlike many previous studies that focus on a limited selection of additive types, this research extended its scope by comparatively analyzing various elastomeric and chemical additives, all tested on the same base bitumen under a single, standardized procedure. Evaluations were systematically conducted based on results from conventional binder tests. The experimental findings revealed that the Enprene 611 additive significantly enhances high-temperature performance, while the CR additive contributes markedly to improving low-temperature flexibility and resistance to cracking. This comparative methodology, which is rarely observed in existing literature, sheds light on how different additive types influence the mechanical and rheological properties of asphalt binders. By exploring both performance aspects, this research offers a unique and innovative perspective that could guide future developments in asphalt technologies and support the creation of more durable pavements under diverse climatic and loading conditions.

Keywords: Bitumen, Asphalt, Softing point, Modification, Polymer

Introduction

Producing modified asphalt by incorporating modifiers into neat asphalt is a widely adopted method to enhance asphalt performance (Behnood & Modiri Gharehveran, 2019). Hot mix technology is commonly used for the application of such modified asphalts in paving operations (Gottumukkala et al., 2021). However, this process consumes significant amounts of energy and generates large quantities of greenhouse gases (Nithinchary et al., 2024). High-viscosity modified asphalts, which require elevated temperatures to achieve adequate workability, entail even higher energy consumption and increased greenhouse gas emissions (Pei et al., 2023). This significantly limits the practical application of such modified asphalts in construction. A composite modified asphalt known as CR/SBS composite modified asphalt (CR/SBS-CMA) is produced by adding styrene-butadiene-styrene (SBS) and crumb rubber (CR) to neat asphalt. However, CR/SBS-CMA also suffers from the high viscosity issues mentioned above (Huang et al., 2022).

One of the key components of CR/SBS-CMA, SBS, is a triblock copolymer composed of styrene and butadiene monomers (Chen et al., 2021). It is currently among the most widely used asphalt modifiers and has been extensively investigated (Liang et al., 2020). Behnood et al. found that SBS enhances the rutting resistance of asphalt at high temperatures (Behnood et al., 2016). Zhang et al. reported that SBS improves the aging resistance of asphalt (Zhang et al., 2018). Lin et al. (2017) observed that SBS increases the crack resistance of asphalt at low temperatures. Gong et al. noted that SBS improves asphalt's resistance to oxidative damage (Gong et al., 2021). However, a high dosage of SBS not only reduces the workability of the modified asphalt but also significantly increases its cost (Lin et al., 2019), which poses challenges for construction applications.

- Selection and peer-review under responsibility of the Organizing Committee of the Conference

Many researchers have proposed partially replacing SBS with CR to reduce production costs (Li et al., 2020). CR is derived from ground waste tires (Picado-Santos et al., 2020). The use of CR in asphalt not only helps mitigate environmental issues related to waste tire disposal (Simon & Bárány, 2023) but also significantly improves the rutting resistance and fatigue performance of asphalt (Wen et al., 2018).

To enhance the modification effect of CR and improve the storage stability of CR-modified asphalt, some researchers have pretreated CR using aromatic-rich solvents (Liu et al., 2018; Qurashi & Swamy, 2018). Liu et al. found that utilizing oils with high aromatic and naphthenic content during the pre-dissolution treatment of CR increases the content of light components in CR-modified asphalt, reduces its rutting and fatigue resistance, and improves its low-temperature crack resistance (Liu et al., 2018). Huang et al. reported that a one-hour pretreatment of CR using FEO achieves a balanced improvement in rutting resistance, fatigue resistance, and low-temperature crack resistance (Huang et al., 2024). Zhang et al. found that combining CR with SBS enhances the elastic recovery capability of modified asphalt due to the cross-linked structure of CR (Zhang et al., 2024). Yang et al. discovered that the aging and fatigue resistance of CR/SBS-CMA surpasses that of asphalt modified solely with SBS or CR (Yang et al., 2022). Nan et al. also reported that CR/SBS-CMA exhibits excellent fatigue resistance (Nan et al., 2022). Nonetheless, CR/SBS-CMA still suffers from poor workability (Pei et al., 2023). This implies that higher temperatures are required when using CR/SBS-CMA for paving, which leads to increased energy consumption and higher greenhouse gas emissions. Undoubtedly, these challenges hinder the broader application of CR/SBS-CMA.

Building upon these challenges and opportunities, the present study aims to comprehensively investigate the multifaceted effects of polymeric and reactive additives on asphalt binders through an extensive experimental framework centered on conventional binder tests. Unlike many existing studies, which are typically confined to a limited selection of additives, this research systematically compares various elastomeric and chemical additives applied to a single base bitumen using a standardized procedure. The outcomes of this investigation not only highlight the superior high-temperature performance achieved with Enprene 611 and the significant enhancement of low-temperature flexibility by CR but also provide valuable insights into the mechanical and rheological behavior of modified binders. This novel comparative approach contributes an innovative perspective to asphalt technology, offering new directions for improving both performance and sustainability in pavement materials.

Materials and Method

Materials

In this study, the B70/100 reference bitumen produced by the Batman Refinery was used. The density of the reference bitumen employed is 1.033 g/cm³. Due to climatic conditions, the 70/100 grade is the most widely used binder in Turkey. The general properties of the bitumen utilized in the study are presented in Table 1 (Özdemir, 2025). Five different additives (SBS, 701, 611, CR, and Elvaloy-PPA) were used for bitumen modification. The CR used in the study was supplied by Samsun Akın Plastik Company, while Elvaloy and PPA were procured from Komsa Company. The SBS (Kraton D 1101) additive produced by Shell, as well as 701 and 611, were provided by Mpolimer Company. The ground tire rubber (CR) was obtained using a mechanical shredding method and sieved through a No. 40 mesh before being used in the study. The properties of the additives are provided in Table 2. The additives utilized in the study are shown in Figure 1.

Figure 1. Additives used in the study: (a) SBS polymer, (b) Elvaloy, (c) 611 polymer, (d) PPA, (e) CR, (f) 701 polymer

Table 1. General properties of 70/100 bitumen

Properties	**Unit**	**Standard**	**Results**
Penetration	mm^{-1}	EN 1426	87.4
Softening Point	°C	EN 1427	52.6
Flash Point	°C	EN ISO 2719	230
Viscosity 135°C /165°C	cP	ASTM D4402	562.5/162.5

Table 2. Properties of the additives used in the study

Properties	**SBS**	**701**	**611**
Molecular structure	Liner	Liner	Radial
Styrene/butadiene ratio	31/69	33/67	31/69
Density (cm/m3)	0,94	0,93	0,94
Oil content	Yok	Yok	Yok
Viscosity (5%, cps)	-	14	24
Melt index (190°C/kgw)	<1	<1	<1
Tensile strength (kgw/cm2)	324	220	200
Hardness	70	80	83
Ash content	-	0,2	0,2
Elongation at break (%)	880	600	700

Preparation of Modified Bitumen

In this study, modified bitumens were prepared using a reference binder (70/100) with the incorporation of SBS, Enprene 611, Enprene 701, CR, Elvaloy, and PPA additives. The production procedure for elastomer-modified bitumen was adopted from previous studies (Yalçın & Demirbağ, 2022). In the initial stage, the neat bitumen was heated for 30 minutes in an oven at 180 ± 5 °C to achieve a fluid state, after which 800 grams of bitumen was transferred into a metal mixing vessel. To ensure a uniform heat source, the bitumen inside the metal vessel was placed into a heating jacket set at 180 ± 5 °C, and the system was maintained at this temperature until thermal equilibrium was achieved. Subsequently, the additives were incorporated into the bitumen at predetermined dosages (%2, %3, %4 SBS; %2, %3, %4 Enprene 611; %2, %3, %4 Enprene 701; %4, %6, %8 CR; %3 Elvaloy; and %0.2 PPA). To ensure accurate comparison of the results of the modified bitumen binders, the same procedure was employed for the preparation of all modified samples.

Following the addition of the additives, the bitumens containing the modifiers were mixed for 4 hours using a mechanical mixer operating at 2700 rpm to produce the modified binders (Yalcin & Demirbag, 2022). Specifically, in the case of the modified bitumen with 3% Elvaloy, the mixing process was interrupted after 3.5 hours to add 0.2% PPA, after which mixing continued for an additional 30 minutes to complete the blending. The additive dosages employed during the modification process were determined by considering values commonly preferred in the literature and industry applications. Upon completion of the preparation of all modified binders, they were subjected to short-term and long-term aging processes. In the nomenclature used for the experimental results, “C” denotes the neat binder, while in the modified binders, the number on the left side indicates the percentage of additive incorporated into the neat binder, and the term on the right denotes the type of additive used.

Conventional Binder Tests

In order to evaluate the physical properties of the reference binder and all modified bitumen binder samples, conventional tests including penetration (at 25 °C) and softening point measurements were conducted. The penetration and softening point tests were performed in accordance with ASTM D5 and ASTM D36 standards, respectively. All bitumen samples used in the conventional tests were subjected to the Rolling Thin Film Oven Test (RTFOT) for 85 minutes to simulate short-term aging. Each test was repeated three times, and the average of the results was reported as the final value**.**

Results and Discussion

Conventional Binding Experiments

It has been observed that the addition of modifiers to the neat binder results in the hardening of the binders. The highest penetration value was recorded for the neat binder, while the lowest penetration value was obtained from the 4-611 binder (Figure 2). Among the polymers added to the neat binder, the 611 polymer had the most significant impact on reducing the penetration values. Moreover, it was observed that increasing the dosage of additives within the neat binder led to further decreases in penetration values.

At comparable polymer contents, CR addition yielded penetration values similar to those of the polymer-modified binders. When SBS elastomer was used at contents of 2%, 3%, and 4% in bitumen modification, the penetration values decreased by 34.11%, 50.25%, and 50.92%, respectively, compared to the neat binder (C). For the 611 elastomer at contents of 2%, 3%, and 4%, the penetration values decreased by 34.96%, 52.94%, and 53.78%, respectively, relative to the neat binder. In the case of the 701 elastomer used at 2%, 3%, and 4%, the penetration values were reduced by 34.45%, 51.26%, and 51.60%, respectively, compared to the neat binder. When CR elastomer was used at 4%, 6%, and 8%, penetration values decreased by 27.23%, 40.67%, and 50.42%, respectively, relative to the neat binder. The penetration value of the 3E0.2PPA binder was 17.48% lower than that of the neat binder. Based on the results obtained, it was determined that the additive with the greatest influence on penetration values was the 611 elastomer, whereas the additive with the least effect was the Elvaloy+PPA combination.

The polymer additives used in this study increased the softening point values. These additives enhance the high-temperature performance of the neat binder. As shown in Figure 2, increasing the dosage of additives added to the neat binder led to an increase in softening point values. These results demonstrate the functional effectiveness of the additives. It was observed that as the additive content in the neat binder increased, the softening point values also increased consistently. Among the binders, the highest softening point was recorded for the 4-611 binder, whereas the neat binder exhibited the lowest softening point value. Among the six additives used in the project, the 611 elastomer yielded the most favorable results, while the Elvaloy+PPA combination showed the least improvement.

When SBS elastomer was used at 2%, 3%, and 4% in bitumen modification, the softening point increased by factors of 1.11, 1.20, and 1.29, respectively, compared to the softening point of the neat binder (C). For the 611 elastomer at contents of 2%, 3%, and 4%, the softening point rose by factors of 1.14, 1.29, and 1.32, respectively, relative to the neat binder. In the case of the 701 elastomer used at 2%, 3%, and 4%, the softening point increased by factors of 1.14, 1.22, and 1.30, respectively, compared to the neat binder. When CR elastomer was used at 4%, 6%, and 8%, the softening point increased by factors of 1.11, 1.16, and 1.22, respectively, relative to the neat binder. The softening point of the 3E0.2PPA binder was 1.15 times higher than that of the neat binder.

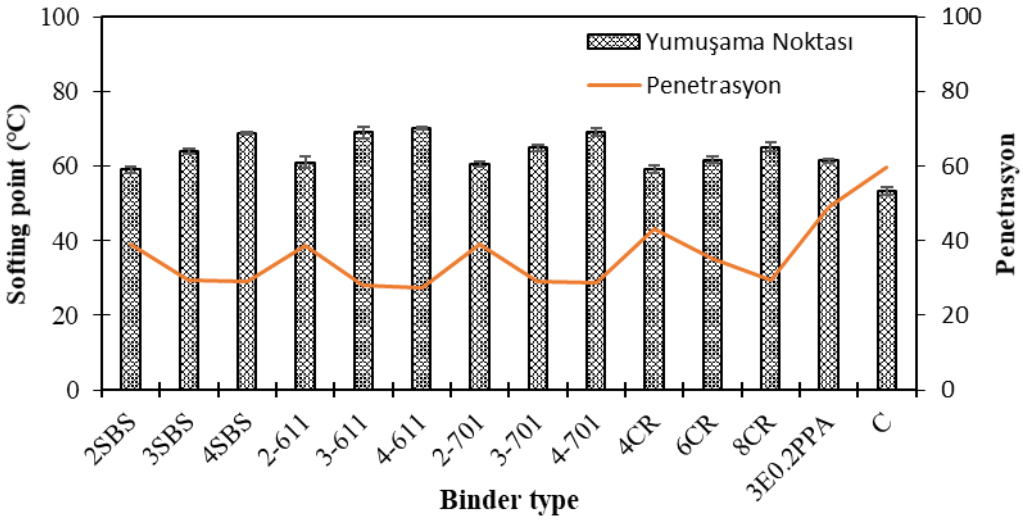

Figure 2. Softening point and penetration results of binders

Figure 3 presents the softening point values of the short-term aged binders. Results parallel to those of the unaged binders were obtained. The addition of additives to the neat binder also led to an increase in the softening point values of the aged binders. Among the aged binders, the neat binder exhibited the lowest softening point value, while the highest value was observed for the 4-611 binder.

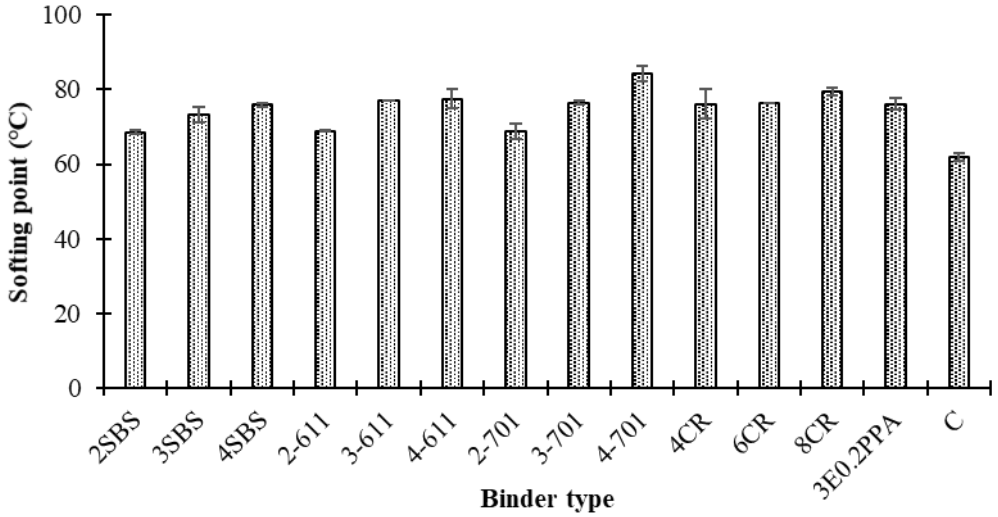

Figure 3. Softening point values of short-term aged binders

Based on the softening point, the aging index (IYN) was determined by calculating the ratio of the softening point of the binders after RTFOT aging to their values in the unaged state. Figure 5 illustrates the changes in the aging index of neat and modified binders as a function of additive content. In the cases of SBS, 611, and CR modifications, the aging index decreased linearly with increasing additive content, whereas it increased linearly in the case of 701 modification. According to this test, it was observed that SBS, 611, and CR modifications enhance resistance to aging, while 701 modification reduces it. As shown in Figure 4, nearly all polymer-modified binders exhibited lower aging indices compared to the neat binder. The SBS and 611 additives, in particular, resulted in significant reductions in the aging index.

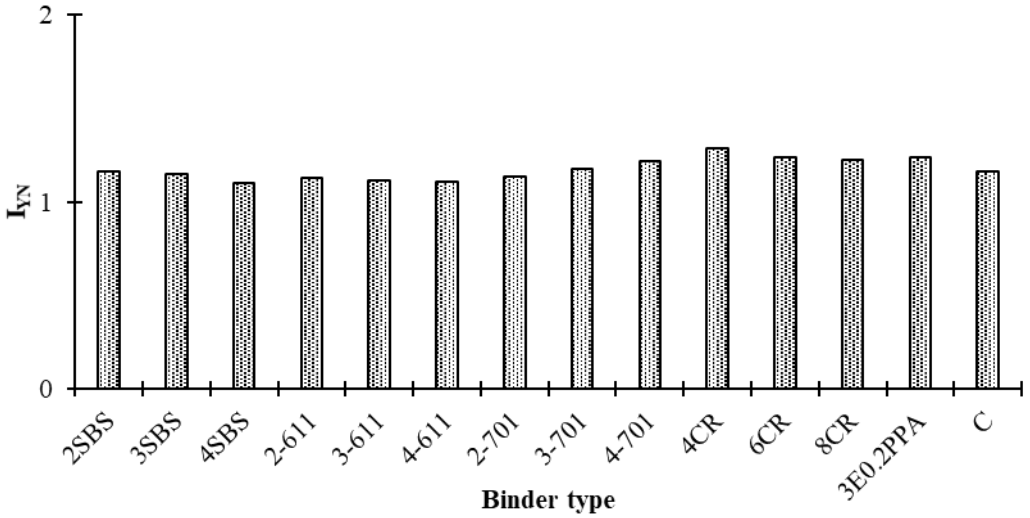

Figure 4. Variation of aging index based on softening point

Conclusion

Conventional binder tests were performed on neat and modified bitumens to conduct various analyses. The findings are summarized below:

- It was observed that the addition of modifiers to the neat binder resulted in hardening of the binders. The highest penetration value was recorded for the neat binder, while the lowest penetration value was obtained from the 4-611 binder. Among the polymers added to the neat binder, the 611 polymer exhibited the most significant effect in reducing the penetration values of the neat binder.

- The polymer additives used in this study increased the softening point values, thereby enhancing the high-temperature performance of the neat binder. Among the binders, the highest softening point value was recorded for the 4-611 binder, whereas the neat binder exhibited the lowest value. Among the six additives used in the project, the 611 elastomer provided the best results, while the Elvaloy+PPA combination yielded the least improvement.

Scientific Ethics Declaration

*The authors declare that the scientific ethical and legal responsibility of this article published in EPSTEM journal belongs to the authors.

Conflict of Interest

*The authors declare that they have no conflicts of interest

Funding

*This study was supported by Fırat University Scientific Research Projects Unit (FUBAP) with project number MF-25.46.

Acknowledgements or Notes

*This article is extracted from the first author's master thesis entitled "Investigation of the Effects of Modified Additives as an Alternative to SBS on the Physical and Chemical Properties of Bituminous Binders", supervised by Mehmet Yilmaz.

References

Behnood, A., & Modiri Gharehveran, M. (2019). Morphology, rheology, and physical properties of polymer-modified asphalt binders. *European Polymer Journal*, *112*, 766–791.

Behnood, A., Shah, A., McDaniel, R. S., Beeson, M., & Olek, J. (2016). High-temperature properties of asphalt binders: Comparison of multiple stress creep recovery and performance grading systems. *Transportation Research Record: Journal of the Transportation Research Board*, *2574*(1), 131–143.

Chen, M., Geng, J., Xia, C., He, L., & Liu, Z. (2021). A review of phase structure of SBS modified asphalt: Affecting factors, analytical methods, phase models and improvements. *Construction and Building Materials*, *294*, 123610.

Gong, Y., Miao, H., Zhang, P., & Chen, X. (2021). Self-calibrating ınterloper bias in spectroscopic galaxy-clustering surveys. *The Astrophysical Journal*, *919*(1), 12.

Gottumukkala, B., Kusam, S. R., Tandon, V., Muppireddy, A. R., & Mullapudi, R. S. (2021). Restriction of RAP% in HMA based on aggregate gradation and binder properties. *CivilEng*, *2*(3), 811–822.

Huang, J.-Y., Jones, O. G., & Zhang, B. Y. (2022). Interactions of casein and carrageenan with whey during pasteurization and their effects on protein deposition. *Food and Bioproducts Processing*, *135*, 1–10.

Huang, W., Li, Y., Meng, Y., He, C., Ye, X., Chen, X., & Hu, C. (2024). Comprehensive study on the performance of SBS and crumb rubber composite modified asphalt based on the rubber pretreatment technology. *Case Studies in Construction Materials*, *20*, e03141.

Li, J., Chen, H., Feng, H., Fang, Q., Liu, Y., Liu, F., Wu, H., & Liaw, P. K. (2020). Microstructure evolution and deformation mechanism of amorphous/crystalline high-entropy-alloy composites. *Journal of Materials Science & Technology*, *54*, 14–19.

Liang, B., Shi, K., Niu, Y., Liu, Z., & Zheng, J. (2020). Probing the modification mechanism of and customized processing design for SBS-modified asphalts mediated by potentiometric titration. *Construction and Building Materials*, *234*, 117385.

Lin, P., Huang, W., Li, Y., Tang, N., & Xiao, F. (2017). Investigation of influence factors on low temperature properties of SBS modified asphalt. *Construction and Building Materials*, *154*, 609–622.

Lin, P., Yan, C., Huang, W., Li, Y., Zhou, L., Tang, N., Xiao, F., Zhang, Y., & Lv, Q. (2019). Rheological,

chemical and aging characteristics of high content polymer modified asphalt. *Construction and Building Materials*, *207*, 616–629.

Liu, S., Peng, A., Wu, J., & Zhou, S. B. (2018). Waste engine oil influences on chemical and rheological properties of different asphalt binders. *Construction and Building Materials*, *191*, 1210–1220.

Nan, H., Sun, Y., Chen, J., & Gong, M. (2022). Investigation of fatigue performance of asphalt binders containing SBS and CR through TS and LAS tests. *Construction and Building Materials*, *361*, 129651.

Nithinchary, J., Dhandapani, B. P., & Mullapudi, R. S. (2024). Application of warm mix technology - design and performance characteristics: Review and way forward. *Construction and Building Materials*, *414*, 134915.

Ozdemir, A. M. (2025). Rheological analysis of the aging behavior of short-term aged pure and sbs-modified asphalt binders. *Firat University Journal of Experimental and Computational Engineering*, *4*(2), 276–289.

Pei, G., Ou, Q., Chen, Y., Xu, Y., & Tan, J. (2023). Screening for obstructive sleep apnea before coronary angiography. *The Clinical Respiratory Journal*, *17*(1), 13–19.

Picado-Santos, L. G., Capitão, S. D., & Neves, J. M. C. (2020). Crumb rubber asphalt mixtures: A literature review. *Construction and Building Materials*, *247*, 118577.

Qurashi, I. A., & Swamy, A. K. (2018). Viscoelastic properties of recycled asphalt binder containing waste engine oil. *Journal of Cleaner Production*, *182*, 992–1000.

Simon, D. Á., & Bárány, T. (2023). Microwave devulcanization of ground tire rubber and ıts ımproved utilization in natural rubber compounds. *ACS Sustainable Chemistry & Engineering*, *11*(5), 1797–1808.

Wen, Y., Wang, Y., Zhao, K., Chong, D., Huang, W., Hao, G., & Mo, S. (2018). The engineering, economic, and environmental performance of terminal blend rubberized asphalt binders with wax-based warm mix additives. *Journal of Cleaner Production*, *184*, 985–1001.

Yalcin, E., & Demirbag, A. (2022). Effects of modified binders obtained from different polymers on conventional and rheological properties. *Construction and Building Materials*, *357*, 129366.

Yang, Z., Wang, L., Bin, X., Cao, D., Li, J., & Zhao, K. (2022). Performance of SBS modifier-crumb rubber composite modified asphalt used as an anti-wear layer of perpetual pavement. *International Journal of Pavement Engineering*, *23*(12), 4097–4111.

Zhang, H., Chen, Z., Xu, G., & Shi, C. (2018). Evaluation of aging behaviors of asphalt binders through different rheological indices. *Fuel*, *221*, 78–88.

Zhang, Y., Li, Y., & Zhang, F. (2024). Multi-level urban street representation with street-view imagery and hybrid semantic graph. *ISPRS Journal of Photogrammetry and Remote Sensing*, *218*, 19–32.

Author(s) Information

Isra Seza Deveci
Graduate School of Natural and Applied Sciences, Firat University, Elazig, Türkiye

Mehmet Yilmaz
Civil Engineering Department, Engineering Faculty, Firat University, Elazig, Türkiye
Contact e-mail: *mehmetyilmaz@firat.edu.tr*

To cite this article:

Deveci, I. S. & Yilmaz, M. (2025). Determination of physical properties of polymeric and different additives on bituminous binders. *The Eurasia Proceedings of Science, Technology, Engineering and Mathematics (EPSTEM), 36,* 134-140.

The Eurasia Proceedings of Science, Technology, Engineering & Mathematics (EPSTEM)
ISSN: 2602-3199

The Eurasia Proceedings of Science, Technology, Engineering and Mathematics (EPSTEM), 2025

Volume 36, Pages 141-150

ICBAST 2025: International Conference on Basic Sciences and Technology

A Modified Peak Load Method Based on the Two-Parameter Model in Concrete Fracture

Ragip Ince
Firat University

Abstract: The experimental studies on fracture mechanics of concrete until the 1970s revealed that classical linear elastic fracture mechanics (LEFM) was invalid for cementitious materials such as mortar and concrete. This inapplicability of LEFM is due to the existence of an inelastic zone with large-scale and full cracks in front of the crack tip in concrete. This so-called fracture process zone is ignored by LEFM. For this reason, several investigators have developed nonlinear fracture mechanics approaches to characterize failure of concrete structures. According to the two-parameter model (TPM) in concrete fracture, a free crack propagates unstably whenever the stress intensity factor and the crack tip opening displacement are equal to their threshold values, such as Mode I fracture toughness and critical crack tip opening displacement, respectively. This methodology derives fracture parameters from one of two experimental techniques: the compliance method and the peak load method. In the compliance method, fracture parameters are ascertained from the correlation between the load and the crack mouth opening displacement of beams, utilizing closed-loop testing apparatus, while the peak-load method, which does not necessitate complex testing apparatus, is more straightforward than the compliance method for determining fracture parameters within TPM. In this study, a modified peak load method based on an optimization procedure was proposed to determine fracture parameters of TPM instead of the statistical procedure based on the peak load method.

Keywords: Beam test, Concrete, Fracture mechanics, Semi-circular bending test, Two-parameter model.

Introduction

Linear elastic fracture mechanics (LEFM) were first utilized for cement-based materials by Kaplan (1961), followed by Kesler and his colleagues (1972). The latter researchers determined that LEFM was insufficient for concrete. This inadequacy arises from the relatively inelastic region present in quasi-brittle materials, such as concrete mixtures, rocks, and asphalt concretes, which is extensive and fully fractures ahead of the crack tip. Consequently, numerous researchers have created nonlinear fracture mechanics models to characterize, effectively, fracture-dominated failures in concrete structures. These ways include the fictitious crack model by Hillerborg et al. (1976), the crack band model by Bazant and Oh (1983), the two-parameter model (TPM) by Jenq and Shah (1985), the effective crack model by Nallathambi and Karihaloo (1986), the size effect model (SEM) by Bazant and Kazemi (1990), the double-K model by Xu and Reinhardt (1999), and the boundary effect method by Hu and Duan (2008).

To assess the fracture characteristics of cementitious materials, certain models, such as SEM, rely solely on the peak loads of test specimens of varying dimensions. Conversely, models like TPM use the load-displacement relationships of test samples of a single size but require closed-loop testing apparatus, often referred to as compliance. Simplified compliance-based methods that rely only on peak loads have also been proposed by researchers, as detailed below.

The compliance approach of TPM requires complex experimental equipment. In contrast, the peak-load method, which is also based on TPM, only uses the peak loads of quasi-brittle samples with varying notch lengths to

- Selection and peer-review under responsibility of the Organizing Committee of the Conference

calculate the relevant fracture parameters. Similarly, SEM requires the peak loads of at least three geometrically similar specimens to determine the fracture parameters. Notably, the variable-notch one-size method eliminates the need for geometrically similar samples. Unlike the compliance approach of TPM, the double-K model does not require complex experimental equipment. Consequently, the simplified approaches of TPM and SEM models provide significant practical convenience, as they do not rely on complex experimental equipment and only require the peak loads of a single-sized structure with varying notch lengths to determine the relevant fracture parameters.

The solution based on the peak load method of TPM was initially modified by using an optimization technique in this study. To verify this modified formulation, split-tension cylinders and beams by Tang et al. (1996), who initially proposed the peak-load method, were simulated according to the modified way. Consequently, this investigation indicated that the results of the modified approach based on the peak-load method look viable and very promising.

The Two-Parameter Model (TPM) in Concrete Fracture

In the 1970s, experimental studies on the fracture mechanics of cement-based materials, including paste, mortar, and concrete, demonstrated that classical Linear Elastic Fracture Mechanics (LEFM) were no longer applicable to quasi-brittle materials Kesler et al. (1972). This inapplicability arises from the relatively extensive inelastic zone present in concrete, known as the fracture process zone (FPZ), which forms ahead of and around the tips of significant cracks. As a result, various non-linear fracture mechanics models have been created to describe the FPZ.

These models can be grouped as the cohesive crack models and the effective crack models, such as the two-parameter fracture model (TPM) proposed by Jenq and Shah (1985). The main aim of any approach is to determine the critical crack extension, defined as $\Delta a = a_c - a_0$, where a_c and a_0 are the critical crack length at the peak load and the initial crack length, respectively, during the load-displacement response or the load-crack mouth opening displacement response of the structure.

A concrete structure fails according to the TPM when the stress intensity factor K_I and the crack opening displacement *CTOD* reach their critical values, K^s_{Ic} and $CTOD_c$, respectively. These fracture parameters can be determined with the following LEFM equations:

$$K_{Ic}^{s} = \sigma_{Nc}\sqrt{\pi a_c}\,Y\left(g,l\right) \tag{1}$$

$$CTOD_c = \frac{\gamma\sigma_{Nc}a_c}{E}V_1\left(g,l\right)M\left(g,l\right) \tag{2}$$

here σ_{Nc} is the nominal failure stress; E is Young's modulus; and Y, V_1, and M are dimensionless functions that depend on the geometry of the structure (g) and the load type (l). The factor of γ in Eq. (2) can be taken as π and 4 for splitting specimens and beams, respectively. The parameter Y is also called the geometry factor. The function M is derived from the ratio of $COD(a_c)/CMOD_c$, where $CMOD_c$ is the critical crack mouth opening displacement. TPM can easily be used in structural analysis since the Y, V_1, and M functions can be obtained in LEFM handbooks (Tada et al., 2000).

This methodology derives fracture parameters from one of two experimental techniques: the compliance method by Jenq and Shah (1985) and the peak load method, proposed by Tang et al. (1996). In the compliance method, fracture parameters are ascertained from the correlation between the load and the crack mouth opening displacement (P-CMOD) of the three-point bending sample of width b, depth d, and span S, utilizing a closed-loop testing apparatus, as illustrated schematically in Figure 1a (Ince et al., 2024). In the TPM, a_c is calculated by using unloading compliance (C_u) at 95% of the ultimate load, as shown in Figure 1b.

The peak-load method, which does not necessitate complex testing apparatus, is more straightforward than the RILEM method for determining fracture parameters within TPM. However, it necessitates three or more distinct specimens due to the inherent variability in concrete properties. This requirement holds true for both methodologies. The specimens may be uniform in size, yet their initial crack lengths may vary. Conversely, the initial crack lengths may be consistent, while the dimensions of the specimens may differ. For each specimen evaluated, the following equations can be formulated in accordance with TPM (Tang et al., 1992):

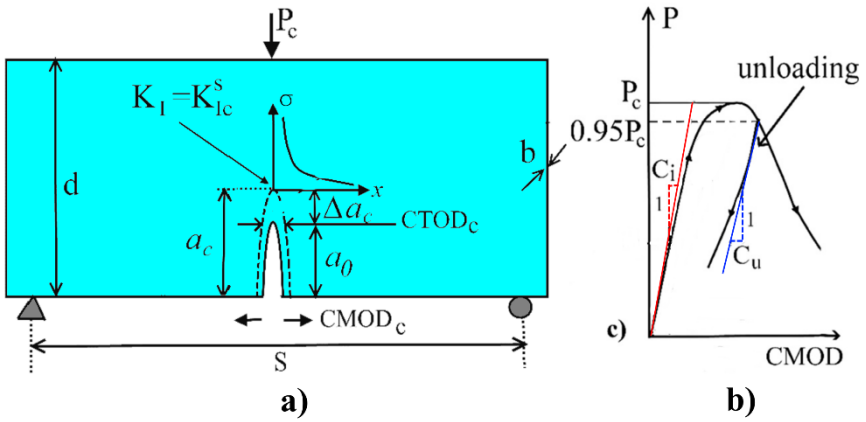

Figure 1. Modeling based on TPM a) notched beam b) typical load-CMOD curve

$$K_I^i\left(\sigma_{Nc}^i, a_c^i\right) = K_{Ic}^s \qquad , i = 1,2$$
$$CTOD^i\left(\sigma_{Nc}^i, a_c^i\right) = CTOD_c \tag{3}$$

here i denotes the ith specimen. Consequently, the fracture parameters can be found by simultaneously solving four non-linear equations. However, three or more distinct specimens must be tested to ensure statistically valid results because random errors always exist in measured values of σ^1_{Nc} and σ^2_{Nc}.

In addition to the above approaches based on TPM, Eq. (1) can be simplified to the following form for geometrically similar structures (a_0/d = constant) by Bazant (1994):

$$\sigma_{Nc} = \frac{K_{Ic}^s}{\left[Y\left(\alpha_0\right) + Y'\left(\alpha_0\right)\frac{\Delta a_\infty}{d}\right]\sqrt{\pi\left(a_0 + \Delta a_\infty\right)}} \tag{4}$$

here, Δa_∞ is the critical crack extension for an infinitely large structure and Y' is the derivation of the Y function concerning α_0. On the other hand, it is possible to transform the fracture parameter, Δa_∞, into the fundamental parameter of TPM, $CTOD_c$, by employing the well-known LEFM relationship below:

$$CTOD_c = \frac{K_{Ic}^s}{E}\sqrt{\frac{32\Delta a_\infty}{\pi}} \tag{5}$$

Method

In this study, a modified peak load method based on an optimization procedure was proposed to calculate K^s_{Ic} and $CTOD_c$ instead of the statistical procedure based on the peak load method proposed by Tang et al. (1996). The basis of the way proposed in this study is based on the simultaneous solution of equation (3) as the failure criterion of a concrete structure. As mentioned above, the main aim of any fracture model is to evaluate the critical crack extension (Δa) at the peak load. Accordingly, for this problem, it may be sufficient to find the nominal strength value (σ_{Nc}) corresponding to the peak load and the Δa value for the initial crack length (a_0) for each sample. These Δa values calculated for each sample should be such that the same fracture parameters (K^s_{Ic} and $CTOD_c$) are met for all tested samples. However, it is impossible to obtain an exact solution for a heterogeneous material like concrete. Consequently, such a problem can only be approached using optimization techniques. In this study, to find the fracture parameters of TPM, the following two expressions were initially minimized by utilizing the least squares error criterion:

$$f\left(K_{Ic}^s\right) = \sum_{i=1}^{n} \Delta^2\left(K_{Ic}^s\right) = \sum_{i=1}^{n}\left(K_{Ic,i}^s - \overline{K_{Ic,i}^s}\right)^2 \tag{6}$$

$$f\left(CTOD_C\right)=\sum_{i=1}^{n}\Delta^2\left(CTOD_C\right)=\sum_{i=1}^{n}\left(CTOD_{C,i}-\overline{CTOD_{C,i}}\right)^2 \tag{7}$$

Here n is the number of samples tested, $\overline{K^s_{Ic,i}}$ is the average value of K^s_{Ic} and $K^s_{Ic,i}$ is the value of K^s_{Ic} or the i^{th} sample in Equation 6 while $\overline{CTOD_{C,i}}$ is the average value of $CTOD_c$ and $CTOD_{ci}$ is the value of $CTOD_c$ for the i^{th} sample in Equation 7. On the other hand, to provide the simultaneous solution of the above two minimization equations, the root sum squared (RSS) method, which is also called the statistical tolerance analysis method, was used as follows:

$$RSS=\sqrt{\left(f\left(K^s_{Ic}\right)\right)^2+\left(f\left(CTOD_C\right)\right)^2} \tag{8}$$

Note that although, in practice, K^s_{Ic} and $CTOD_c$ are commonly used in terms of MPa√m and mm, respectively, it is recommended to choose MPa√mm and μm because the quantities in these units are very different from each other. The procedures described above, which form the basis of the modified peak load method, can be easily implemented using a spreadsheet-based program. However, as will be explained later, the procedures of the classical peak load method are quite difficult to implement in a computer environment. In the following descriptions, this novel method is explained using the MS-EXCEL-based SOLVER toolkit. Note that the generalized reduced gradient (GRG) algorithm was used in the SOLVER toolkit.

Using of the MS-EXCEL-Based SOLVER Toolkit for the Novel Approach

The previous work by the author is used as an instance (Ince, 2012). In the previous study, a concrete mixture with a maximum aggregate diameter of 16 mm was prepared. The CEM I 42.5N cement type was used. The water/cement ratio was 0.54 in the mixture. The beams of width b=50 mm were conducted by geometrically similar specimens with three different sizes: d=50, 100, and 200 mm. The notch was precast in all of the beams so that α_0=0.2. The samples were loaded at three points with span/depth=2.5. Fracture tests of beams were tested in a compression machine with a maximum capacity of 100 kN (precision ±0.1 kN/s). In the fracture tests of the samples, the time to reach the peak load was set as 4 minutes (± 30 seconds). Young's modulus of concrete was determined as 32.5 GPa. According to the size effect formula based on TPM described in Equation 4, the fracture parameters were obtained as K^s_{Ic} =40.83 MPa√mm and $CTODc$=19.8 μm, as shown in Figure 2.

An alternative solution for these test results is outlined using the modified peak-load method as detailed in Figure 3. The test data were summarized for each sample in columns A-F of the spreadsheet as shown in Figure 3. Note that although a total of nine beams were cast, three from each sample size in the above study, average values for each sample size were used to explain the theory in this study. For each sample, the crack extensions (Δa), initially selected as 5 mm as shown in column G, were taken as variables of the problem. The normalized functions of the cracked structure, such as Y and V_1, are defined in columns J and L, respectively, while the function of M in Equation 2 is presented as embedded in $CTOD_c$ in column M. The following formulas were applied to beams with a span/depth ratio of 2.5 in this study (Yang et al., 1997):

$$Y\left(\alpha\right)=\frac{1.83-1.65\alpha+4.76\alpha^2-5.3\alpha^3+2.51\alpha^4}{\sqrt{\pi}\left(1+2\alpha\right)\left(1-\alpha\right)^{3/2}} \tag{9}$$

$$V_1\left(\alpha\right)=0.65-1.88\alpha+3.02\alpha^2-2.69\alpha^3+\frac{0.68}{\left(1-\alpha\right)^2} \tag{10}$$

$$M\left(\alpha_0,\alpha_C\right)=\sqrt{\left(1-\frac{\alpha_0}{\alpha_C}\right)^2+\left(1.081-1.149\alpha_C\right)\left[\frac{\alpha_0}{\alpha_C}-\left(\frac{\alpha_0}{\alpha_C}\right)^2\right]} \tag{11}$$

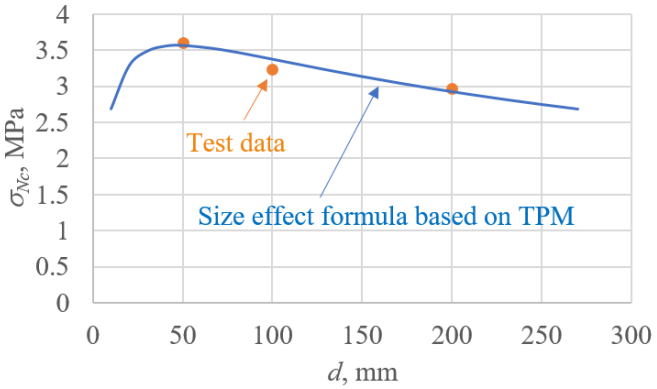

Figure 2. Application of Equation 3 to beams conducted by Ince (2012)

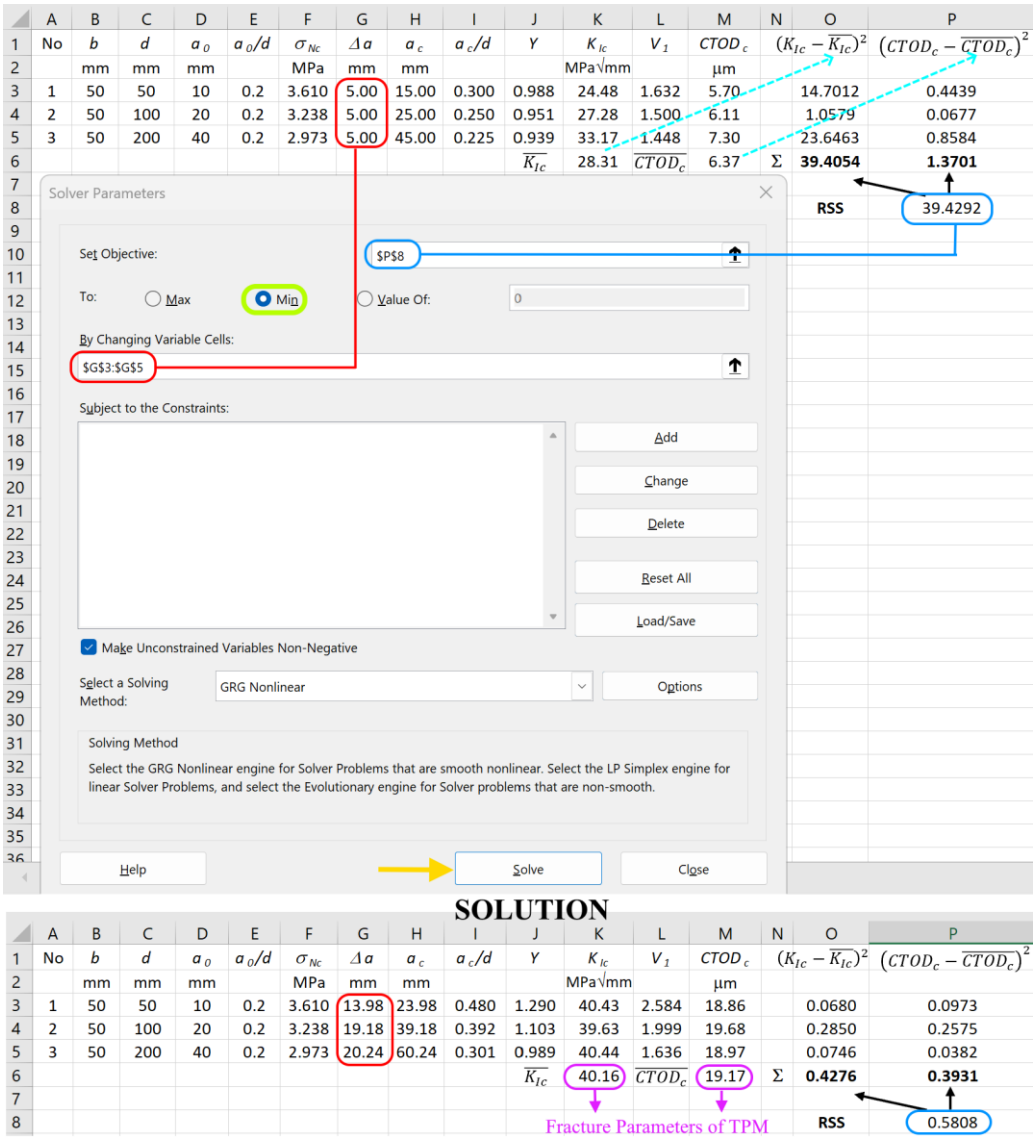

Figure 3. Application of the modified peak load method to beams conducted by Ince (2012)

The least squares error criteria, Equations 6 and 7, are given in columns O and P, respectively. The root sum squared (RSS) defined in Equation 8 was chosen as the objective function for the minimization problem, and it was defined in the cell P8. Consequently, fracture parameters of TPM were obtained as K^s_{Ic} =40.16 MPa$\sqrt{}$mm and $CTOD_c$=19.17 μm, corresponding to the value of the minimum RSS (0.5808), as shown at the bottom of Figure 4. As a result, the modified peak-load method-based solution proposed in this study are in good agreement with the Equation 4-based solution. In this figure, the critical crack extensions, which were chosen as non-negative in

the SOLVER parameters dialog box (Figure 3), the determination of which is the main aim of any fracture model, are also shown for each sample in column G.

The Equation 3-based solution for the beams with three different sizes is presented in Figure 4, in which the fracture parameters computed according to the modified peak-load method are employed. As shown in Figure 4, the critical nominal stress decreases with increasing crack length for either fracture quantity (K_I and *CTOD*). On the other hand, Figure 4 clearly demonstrates that the critical nominal stress based on *CTOD* decreases much faster than that based on K_I (Tang et al., 1992). The intersection of the two curves yields the simultaneous solutions. Accordingly, it should be emphasized that the nominal strengths computed in Figure 4 agree well with the strength values based on Equation 4.

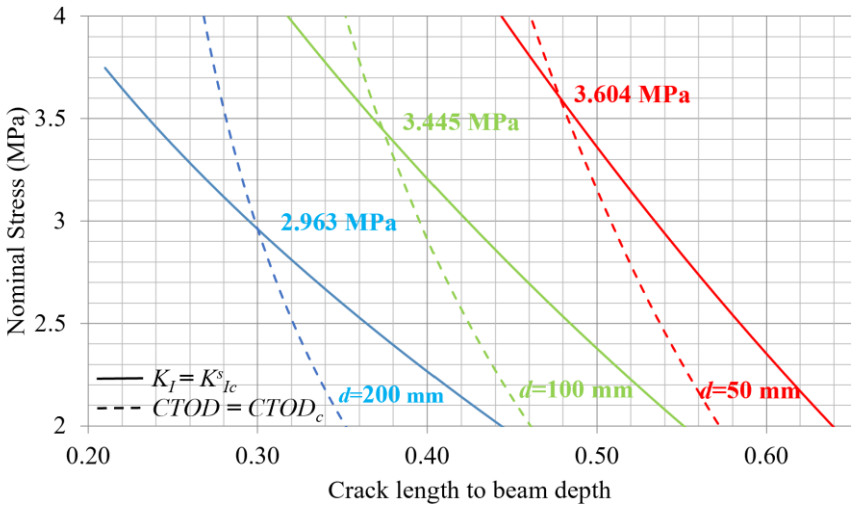

Figure 4. Geometric interpretation of the modified peak load method for beams conducted by Ince (2012)

Applications of the Modified Peak Load Method

Tang and co-workers (1996) tested notched beams and notched splitting cylinders to compare the compliance method with the peak-load method. Samples were prepared from mortar with a maximum aggregate diameter of 3 mm. While beams with width × depth × length = 25.4×50.8×203 mm were loaded at three points, cylindrical samples with width = 31.8 mm and radius = 51 mm were tested under splitting load. According to results of the compliance method applied to beams, the fracture parameters of TPM were determined as K^s_{Ic} =27.36 MPa√mm, $CTOD_c$=6.9 μm, and E=27.8 GPa, on average, by Tang et al. (1996).

Tables 1 and 2 show the applications of the modified peak load method to the study by Tang et al. (1996). The test data were summarized for each sample in the first two columns of these tables. For each sample, the crack extensions (Δa), were initially selected as 5 mm. The values in the other columns are arranged as detailed in Figure 3. All analyses were conducted by using the MS-EXCEL-based SOLVER toolkit. The root sum squared (RSS) values in these tables are the minimized values. Tables 1 and 2 show a strong correlation between beams and splitting cylinders according to the fracture parameters of TPM.

Table 1. Application of the modified peak load method to mortar beams by Tang et al. (1996)

No	a_0/d	σ_{Nc} MPa	Δa mm	a_c mm	a_c/d	Y	K^s_{Ic} MPa√mm	V_1	$CTOD_c$ μm		$\Delta^2(K^s_{Ic})$	$\Delta^2(CTOD_c)$
1	0.2	3.646	6.72	5.88	0.316	1.061	27.49	1.774	8.19		0.8010	0.8606
2	0.2	3.335	5.14	7.07	0.340	1.088	26.73	1.867	8.95		2.7375	2.8424
3	0.35	2.546	6.53	5.06	0.450	1.281	27.64	2.513	8.04		0.5555	0.6037
4	0.35	2.488	5.30	5.33	0.455	1.294	27.44	2.556	8.25		0.8929	0.9692
5	0.35	3.038	4.70	3.00	0.409	1.196	29.37	2.228	6.28		0.9722	0.9691
6	0.5	2.004	4.29	2.41	0.547	1.583	29.65	3.558	5.93		1.5857	1.7833
7	0.5	1.800	5.07	3.44	0.568	1.670	28.60	3.871	7.03		0.0440	0.0545
8	0.5	2.096	5.30	2.00	0.539	1.552	30.17	3.447	5.44		3.1854	3.3191
						Mean	28.39	Mean	7.27	Σ	10.774	11.402
											RSS	15.687

Table 2. Application of the modified peak load method to mortar splitting cylinders by Tang et al. (1996)

No	a_0/d	σ_{Nc} MPa	Δa mm	a_c mm	a_c/d	Y	K^s_{Ic} MPa√mm	V_1	$CTOD_c$ μm		$\Delta^2(K^s_{Ic})$	$\Delta^2(CTOD_c)$
1	0.100	4.632	6.88	11.98	0.235	1.010	28.69	1.298	7.34		0.0127	0.0250
2	0.175	4.573	3.94	12.84	0.252	1.020	29.62	1.313	6.25		0.6681	0.8767
3	0.175	3.886	6.53	15.43	0.303	1.055	28.53	1.366	7.51		0.0742	0.1062
4	0.249	3.533	5.17	17.87	0.350	1.092	28.90	1.426	7.09		0.0093	0.0098
5	0.249	3.395	5.84	18.54	0.364	1.103	28.58	1.445	7.41		0.0483	0.0524
6	0.249	3.356	6.05	18.75	0.368	1.106	28.50	1.451	7.51		0.0953	0.1039
						Mean	28.80	Mean	7.19	Σ	0.9079	1.1740
											RSS	1.4841

The following formulas were applied to beams with a span/depth ratio of 4 in Table 1 (Tada et al., 2000):

$$Y(\alpha)=\frac{1.99-\alpha(1-\alpha)\left(2.15-3.93\alpha+2.7\alpha^2\right)}{\sqrt{\pi}(1+2\alpha)(1-\alpha)^{3/2}} \tag{12}$$

$$V_1(\alpha)=0.76-2.28\alpha+3.87\alpha^2-2.04\alpha^3+\frac{0.66}{(1-\alpha)^2} \tag{13}$$

Note that Equation 11, $M(\alpha_0, \alpha_c)$, is valid for a beam with any span/depth ratio. For the split-cylinder specimens used in Table 2, the LEFM formulas are given by (Tang, 1994):

$$Y(\alpha)=0.94496-0.06851\alpha+1.6235\alpha^2-0.66022\alpha^3 \tag{14}$$

$$V_1(\alpha)=1.1886+0.15419\alpha+0.97529\alpha^2+1.4825\alpha^3 \tag{15}$$

$$M(\alpha_0,\alpha_c)=\sqrt{\left(1-\frac{\alpha_0}{\alpha_c}\right)^2+(2.048-0.27\alpha_c)\left[\frac{\alpha_0}{\alpha_c}-\left(\frac{\alpha_0}{\alpha_c}\right)^2\right]} \tag{16}$$

The following statistical procedures were used to evaluate TPM, K^s_{Ic} and $CTOD_c$, according to this method (Tang et al., 1996; Yang et al., 1997; Ince, 2025). Samples were grouped with reference to their relative initial crack length α_0, as shown in Tables 1 and 2. The average initial crack length and the average nominal strength were then calculated for each group. The K^s_{Ic} - $CTOD_c$ relationships were determined for each group; an example for mortars is shown in Figure 5. Subsequently, the average K^s_{Ic} - $CTOD_c$ curve was obtained for these groups, as indicated by the curved solid line in Figure 5. The sample standard deviation of the groups was then calculated as follows:

$$s\left(K^s_{Ic}\right)=\sqrt{\sum_{i=1}^{n}\left(\overline{CTOD_c}-CTOD_{ci}\right)^2\Big/(n-1)} \tag{17}$$

here n is the number of groups (n=3 in this study); $\overline{CTOD_c}$ is the average value of $CTOD_c$ for all groups; and $CTOD_{ci}$ is the value of $CTOD_c$ for the i^{th} group. As shown in Figure 5, the value of K^s_{Ic} corresponding to the minimum value of s was taken as the fracture parameter K^s_{Ic}. The fracture parameter $CTOD_c$ was obtained by substituting this value of K^s_{Ic} into the average K^s_{Ic} - $CTOD_c$ curve. In Figure 5, the K^s_{Ic} and $CTOD_c$ relations for the beams are shown at the top, while those for the splitting cylinders are shown at the bottom.

The minimization curves, based on Equation 17, are presented in the middle. In conclusion, the fracture parameters of TPM were determined from the s_{min} values corresponding to minimum standard deviations, as detailed in Figure 5. This figure shows a strong correlation between beams and splitting cylinders. Similarly, it can also be concluded that the parameters derived from the classical peak-load method are in good agreement with the parameters obtained from the modified peak-load method.

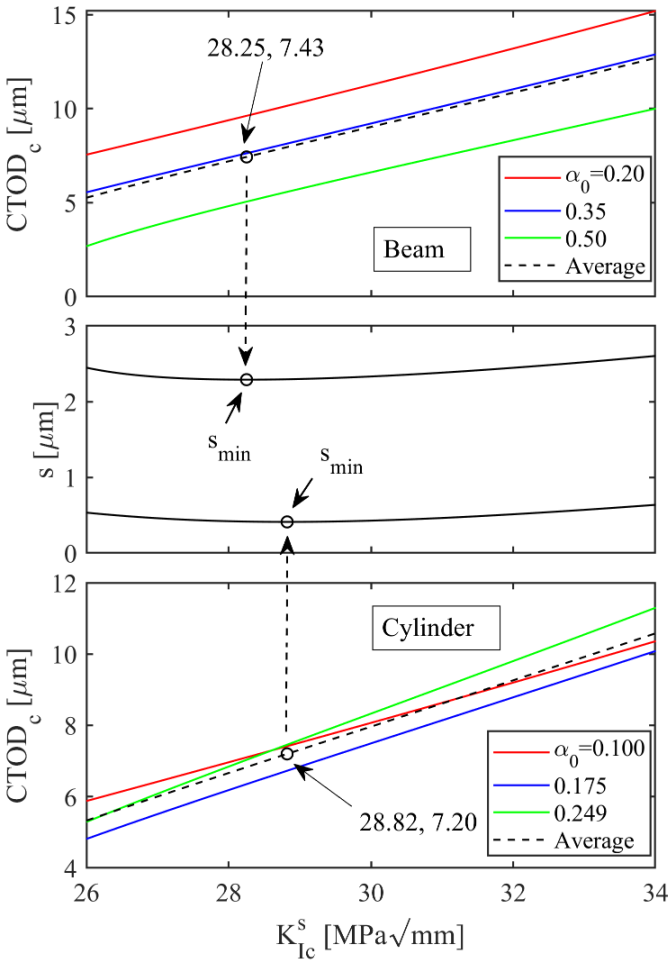

Figure 5. Application of the classical peak load method to cylinder and beams by Tang et al. (1996)

Conclusion

In the presented work, the peak-load method based on the two-parameter model, which is commonly employed in concrete fracture, was modified to model quasi-brittle materials. The key findings are outlined below:

The simplified approaches of concrete fracture models provide significant practical convenience, as they do not rely on complex experimental equipment and only require the peak loads of a single-sized structure with varying notch lengths to determine the relevant fracture parameters. However, it is not possible to obtain an exact solution in modeling fracture mechanics for a heterogeneous material such as mortar and concrete. For this reason, in this study, this difficult problem was approached by using optimization techniques.

The modified peak load method proposed in this study can be easily implemented using a spreadsheet-based program. Therefore, all analyses in the presented work were conducted by using the MS-EXCEL-based SOLVER toolkit, which is a supreme tool that can be used to investigate numerous problems in the field of civil engineering. However, the procedures of the classical peak load method, which are based on some statistical computations, are quite difficult to implement in a computer environment. Moreover, while the classical peak load method only minimizes the errors in the fracture toughness parameter of the material, the way proposed in this study also minimizes the errors in the critical crack tip opening displacement parameter of the material.

Recommendations

A simplified way was proposed to simulate quasi-brittle materials such as mortar, concrete, asphalt concrete, and rock and two successful applications were conducted. However, future studies can achieve more reliable results by comparing different types of samples.

Scientific Ethics Declaration

*The author declares that the scientific ethical and legal responsibility of this article published in EPSTEM Journal belongs to the author.

Funding

* This research received no specific grant from any funding agency in the public, commercial, or not-for-profit sectors.

Conflict of Interest

*The author declares that they have no conflicts of interest

Acknowledgements or Notes

*This article was presented as an oral presentation at the International Conference on Basic Sciences and Technology (www.icbast.net) held in Budapest/Hungary on August 28-31, 2025.

References

Bažant, Z. P., & Kazemi, M. T. (1990). Determination of fracture energy, process zone length, and brittleness number from size effect with application to rock and concrete. *International Journal of Fracture, 44(2),* 111-131.

Bažant, Z. P. (1994). Discussion of "fracture mechanics and size effect of concrete in tension" by T. Tang, S. P. Shah, and C. Ouyang (November, 1992, Vol. 118, No.11), *Journal of Structural Engineering, 120,* 2555–2558.

Bažant, Z. P., & Oh, B. H. (1983). Crack band theory for fracture concrete. *Materials & Structures (RILEM), 16(93),* 155-157.

Hillerborg, A., Modeer, M., & Petersson, P. E. (1976). Analysis of crack formation and crack growth in concrete by means of fracture mechanics and finite elements. *Cement & Concrete Research, 6,* 773-782.

Hu, X., & Duan K. (2008). Size effect and quasi-brittle fracture: the role of FPZ. *International Journal of Fracture, 154,* 3–14.

Ince, R. (2012). Determination of the fracture parameters of the Double-K model using weight functions of split-tension specimens. *Engineering Fracture Mechanics, 96,* 416-432.

Ince, R. (2025). Using SCB specimens to quantify nonlinear fracture characteristics in concrete and rock materials. *Engineering Fracture Mechanics, 318,* 110951.

Ince, R., Yalcin, E., & Yilmaz, M. (2024). Quantifying nonlinear fracture parameters in bituminous SCB specimens: A compliance-based approach. *Case Studies in Construction Materials, 21,* e03437.

Jenq, Y. S., & Shah, S. P. (1985). Two-parameter fracture model for concrete. *ASCE Journal of Engineering Mechanics, 111(10),* 1227-1241.

Kaplan, M. F. (1961). Crack propagation and the fracture of concrete. *ACI Journal, 58*(11), 591-610.

Kesler, C. E, Naus, D. J., & Lott, L. L. (1972). Fracture mechanics-its applicability to concrete. *The Society of Materials Science,* 113-124.

Nallathambi, P., & Karihaloo, B. L. (1986). Determination of the specimen size independent fracture toughness of plain concrete. *Magazine of Concrete Research, 38*(135*)*, 67-76.

Tada, H., Paris, P. C., & Irwin G. R. (2000). *The stress analysis of cracks handbook* (3th ed.). ASME Press.

Tang, T. (1994). Effect of load-distributed width on split tension of unnotched and notched cylindrical specimens. *Journal of Testing and Evaluation, 22*(5), 401-409.

Tang, T., Ouyang, C., & Shah, S. P. (1996). A simple method for determining material fracture parameters from peak loads. *ACI Materials Journal, 93*(2), 143-157.

Tang, T., Shah, S. P., & Ouyang, C. (1992). Fracture mechanics and size effect of concrete in tension. *ASCE Journal of Structural Engineering, 118,* 3169–3185.

Xu, S. & Reinhardt, H. W. (1999). Determination of double-K criterion for crack propagation in quasi-brittle fracture, Part I: Experimental investigation of crack propagation. *International Journal of Fracture, 98*, 111-149.

Yang, S., Tang, T., Zollinger, D. G. & Gurjar, A. (1997). Splitting tension tests to determine concrete fracture parameters by peak–load method. *Advanced Cement Based Materials, 5*, 18–28.

Author(s) Information

Ragip Ince
Firat University
Engineering Faculty, Elazig, Türkiye
Contact e-mail: *rince@firat.edu.tr*

To cite this article:

Ince, R. (2025). A modified peak load method based on the two-parameter fracture model in concrete fracture. *The Eurasia Proceedings of Science, Technology, Engineering and Mathematics (EPSTEM), 36*, 141-150.

The Eurasia Proceedings of Science, Technology, Engineering & Mathematics (EPSTEM)
ISSN: 2602-3199

The Eurasia Proceedings of Science, Technology, Engineering and Mathematics (EPSTEM), 2025

Volume 36, Pages 151-158

ICBAST 2025: International Conference on Basic Sciences and Technology

Investigation of Fatigue Performance of Hot Mix Asphalt Mixtures Modified with Elvaloy and Phosphoric Acid (PPA) as an Alternative to SBS Polymer

Beyza Furtana-Yalcin
Munzur University

Abstract: In this study, the combined use of Elvaloy and phosphoric acid (PPA) was investigated to enhance the performance of asphalt concrete (Hot Mix Asphalt - HMA) layers used in flexible pavement structures under increasing traffic loads and environmental conditions. These additives, considered as alternatives to Styrene-Butadiene-Styrene (SBS) polymer, were evaluated solely for their effects on the mechanical performance of HMA mixtures. Binders modified with Elvaloy/PPA at specified proportions were used to produce HMA specimens, and indirect tensile fatigue tests were conducted on these samples. The experimental results indicated that the addition of Elvaloy and PPA improved the mechanical properties of mixtures prepared with bituminous binders, extended fatigue life, and enhanced the strength and deformation resistance of asphalt mixtures at the selected proportions. The findings suggest that the Elvaloy/PPA additive combination could be a viable alternative to SBS polymer and has the potential to extend the service life of hot mix asphalt. Thus, it was concluded that the use of these additives contributes to improving HMA performance and supports sustainable pavement design.

Keywords: Hot mix asphalt, Elvaloy, Phosphoric acid, Polymer modification, Fatigue performance

Introduction

Asphalt is one of the oldest construction materials and has been highly valued since ancient times due to its waterproofing and adhesive properties (Janoo & Korhonen, 1999). In the early stages, natural asphalt was processed at high temperatures to remove oily fractions and preserve high molecular weight components, which allowed it to be used in various engineering applications thanks to its thermoplastic characteristics. Today, asphalt is obtained as a high-viscosity residue from the distillation of crude oil, and its properties vary depending on both the origin of the crude oil and the production processes (Lav & Lav, 2004). Due to its complex structure, asphalt is still not fully understood. Although various methods have been employed to investigate its composition (Francken, 1998; Kumar et al., 2006; Nicholls, 1998; Sengoz & Isikyakar, 2008), it is generally accepted that asphalt is a colloidal system composed of asphaltenes and maltenes (Tayfur et al., 2007). The degree of dispersion of asphaltenes within maltenes and the characteristics of hydrocarbons determine critical engineering properties such as fatigue cracking resistance, rutting resistance, low-temperature cracking resistance, and oxidation resistance. In particular, oxidation leads to the hardening of asphalt, making it brittle and susceptible to cracking (Kok & Yilmaz, 2009). To improve its engineering performance, asphalt is frequently modified with polymers. Depending on their structural characteristics, the polymers used for asphalt modification are classified into three main groups: plastomers, elastomers, and reactive polymers. Plastomers (e.g., polyethylene, polypropylene) exhibit limited compatibility with asphalt, which often results in phase separation problems (Cortizo et al., 2004; Gorkem & Sengoz, 2009; Vlachovicova et al., 2007). To reduce this incompatibility, modification techniques with polar groups are applied. On the other hand, thermoplastic elastomers are the most widely used group of polymers in the asphalt industry. Styrene-butadiene-styrene (SBS) and styrene-isoprene-styrene (SIS) block copolymers are particularly important representatives, as they absorb

- Selection and peer-review under responsibility of the Organizing Committee of the Conference

oily fractions, swell, and form a three-dimensional polymeric network within asphalt, thereby improving its rheological properties (Meyer et al., 2017). For this reason, a considerable number of studies have been conducted on SBS-modified asphalts (Meyer et al., 2017; Singh & Kumar, 2019; Stark & Jaunich, 2011). Although SBS modification improves elasticity and high-temperature performance, it suffers from the drawback of limited compatibility, which leads to phase separation at elevated temperatures. Unlike plastomers and thermoplastic elastomers, reactive elastomeric terpolymers (RET) provide a different approach to asphalt modification. RETs form a three-dimensional system through covalent cross-linking under the influence of heat, pressure, or catalysts. This structure eliminates the ability of the material to melt or dissolve, thereby creating a permanent network. Maleic anhydride-modified elastomers, ethylene-based copolymers containing epoxy rings, and ethylene terpolymers with glycidyl methacrylate and acrylate groups are examples of RETs used in asphalt modification.

Asphalt has been used as a valuable construction material since ancient times due to its waterproofing and adhesive properties (Janoo & Korhonen, 1999). In the early periods, natural asphalt was processed at high temperatures to remove oily fractions and, thanks to its thermoplastic characteristics, was utilized in various engineering applications. Today, asphalt is obtained as a high-viscosity residue from crude oil distillation, and its properties vary depending on the production process and the origin of the crude oil (Lav & Lav, 2004). Due to its complex structure, the internal composition of asphalt has not been fully understood. Research conducted using various methods (Francken, 1998; Kumar et al., 2006; Nicholls , 1998; Sengoz & Isikyakar, 2008)has revealed that asphalt is a colloidal system composed of asphaltenes and maltenes (Tayfur et al., 2007) The dispersion of asphaltenes within maltenes and the nature of hydrocarbons determine critical engineering properties such as fatigue cracking resistance, rutting resistance, low-temperature performance, and oxidation resistance. In particular, oxidation leads to the hardening of asphalt, making it brittle and prone to cracking (Kok & Yilmaz, 2009).

Polymer modification is a widely used approach to improve the performance of asphalt. Polymers are generally classified into three groups: plastomers, elastomers, and reactive polymers. Plastomers (e.g., polyethylene, polypropylene) exhibit limited compatibility with asphalt, often leading to phase separation (Cortizo et al., 2004; Vlachovicova et al., 2007), whereas thermoplastic elastomers are among the most successful additives in the asphalt industry. Styrene-butadiene-styrene (SBS) and styrene-isoprene-styrene (SIS) copolymers absorb maltenes, forming a three-dimensional polymeric network that enhances the rheological properties of asphalt. Studies on SBS-modified asphalts (Meyer et al., 2017; Singh & Kumar, 2019; Stark & Jaunich, 2011)have demonstrated improvements in elastic response and high-temperature performance; however, limited compatibility at elevated temperatures results in phase separation, which is a major drawback (Liang et al., 2017). In contrast, reactive elastomeric terpolymers (RET) offer a different approach to asphalt modification. RETs undergo covalent cross-linking under the influence of heat, pressure, or catalysts, forming a permanent three-dimensional network that eliminates the ability to melt or dissolve. Examples of RETs used in asphalt modification include maleic anhydride-modified elastomers, ethylene-based copolymers containing epoxy rings, and ethylene terpolymers incorporating glycidyl methacrylate and acrylate groups.

Although numerous studies in the literature have focused on SBS modification, research on the combined use of Elvaloy and phosphoric acid (PPA) remains limited. This study addresses this gap by investigating the effects of these additives on the mechanical performance of hot mix asphalt (HMA) used in flexible pavements, thereby proposing a novel approach as a potential alternative to SBS. The originality of this work lies in the combined use of Elvaloy and PPA at specific proportions, which is aimed at extending fatigue life, enhancing strength, and improving deformation resistance. Thus, the findings not only demonstrate performance improvements but also introduce a promising method that can contribute to sustainable pavement design.

Materials and Method

Materials and Preparation of Modified Bitumen

In this study, B 50/70 grade bitumen supplied from TÜPRAŞ Batman Refinery was used as the base binder. The neat bitumen was modified with Elvaloy and phosphoric acid (PPA), which were provided by Komsa Company. Within the scope of the experimental design, Elvaloy and PPA were incorporated into the base bitumen at three different proportions (0.8%+2%, 0.9%+1%, and 1%+0%) to prepare the target binders. The binder preparation process consisted of the following steps:

- The neat bitumen was kept in an oven at 180 ± 5 ℃ for 30 minutes to become fluid.

- The fluid bitumen was then transferred into the metal container of the mechanical mixer in 500 g portions.
- To ensure a homogeneous thermal environment, the container was placed on a heater stabilized at 180 ± 5 ℃ and kept until thermal equilibrium was reached.
- After the addition of Elvaloy into the hot bitumen, the mixture was stirred for 5 hours using a mechanical mixer operating at 800 rpm.

Subsequently, PPA was added, and the mixing process was continued for an additional 30 minutes (Figure 1). The abbreviations of the neat and Elvaloy/PPA-modified binders used in this study are presented in Table 1, while the gradation and physical properties of the aggregates are given in Table 2.

Table 1. Abbreviations used for bituminous binders in the study

Additive used	Additive ratio used by binder weight (%)			
Elvaloy	0.8	0.9	1	0
PPA	0.2	0.1	0	0
Impression	E1	E2	E3	Pure

Table 2. Aggregate properties and gradation

					Coarse		Fine		Filler		Specification limit	Test Standard
Los Angeles abrasion (%) ASTM D131					25		-		-		Maks. 35	ASTM C-131
Weather resistance ($MgSO_4$) ASTM C88					12		-		-		Maks. 10	ASTM C-88
Smooth and long grain (%) BS 812					20		-		-		Maks. 10	ASTM D-4791
Water absorption (%) ASTM C127					0.8		-		-		-	-
Bulk specific gravityASTM C127, C128					2.521		2.558				-	-
Apparent specific gravityASTM D854					-		-		2.596		-	-
Aggregate gradation												
Sieve diameter (mm)	19	12.5	9.5	4.75	2.36	1.18	0.6	0.3	0.15	0.075	-	-
% Passing	100	95	88	65	35	23	14	10	8	6	-	-

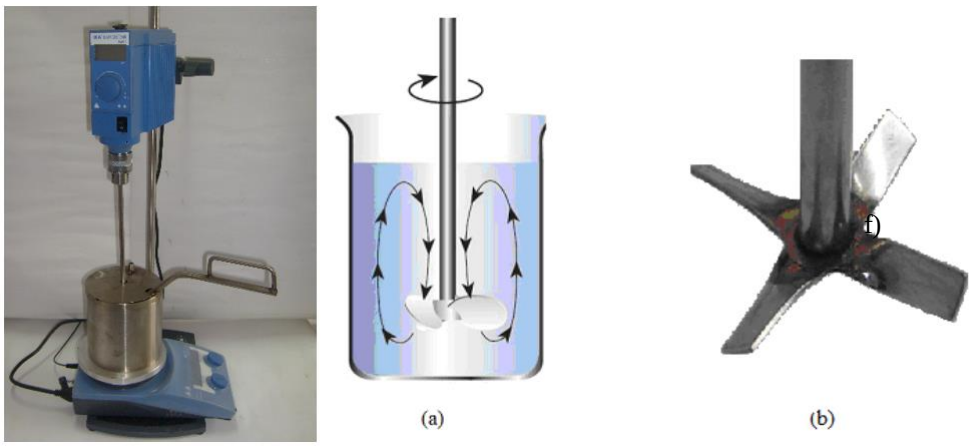

Figure 1. Laboratory mixing device; (a) mixing effect and (b) four blades

Hot mix asphalt (HMA) specimens were prepared using neat and Elvaloy/PPA-modified binders. The specimens were compacted according to the Marshall method by applying 75 blows to each side. The limestone used in the mixtures was supplied from the Karayazı region of Elazıg. The optimum bitumen content was determined based on mixtures prepared with the neat binder, and the modified mixtures were produced using the same bitumen content. Table 3 presents the volumetric properties of the neat and modified mixtures prepared with 5% bitumen content, including air voids (Va), voids filled with asphalt (VFA), voids in mineral aggregate (VMA), bulk

specific gravity (Gmb), as well as mixing and compaction temperatures. The mixing and compaction temperatures of the mixtures were determined using the rotational viscometer method, corresponding to viscosity values of 170 ± 20 cP and 280 ± 30 cP, respectively (JP, 2004). The evaluation results indicated that the prepared mixtures met the volumetric requirements of the Highway Technical Specifications (HTS).

Table 3. Volumetric properties of mixture samples

Mixtures	Bitumen (%)	Mixing temperature (ºC)	Compaction temperature (ºC)	Va (%)	VFA (%)	VMA (%)	Gmb
Pure	5	171	158	3.78	74.3	14.7	2.292
E1	5	184	175	3.69	74.7	14.6	2.295
E2	5	182	173	3.92	73.5	14.8	2.289
E3	5	180	170	3.56	74.0	14.9	2.285

Fatigue Tests

Bituminous materials used in highway pavements are subjected to short-term repeated stresses with each passing vehicle load. Over time, these stresses lead to the formation of micro-damages within the material, which gradually accumulate and evolve into fatigue cracks. Fatigue cracking is one of the most common types of distress in hot mix asphalt, characterized by crack initiation and progressive propagation under repeated loading. The indirect tensile fatigue test is commonly used to evaluate fatigue behavior, where cylindrical specimens are subjected to repeated compressive loads along the vertical diametral plane. This loading configuration induces tensile stresses perpendicular to the applied load direction, eventually causing the specimen to fracture through its middle section. The tests were performed under stress-controlled conditions using a UTM device, and the test system, equipped with a temperature-controlled chamber, enabled experiments at various temperatures beyond the standard test condition. Prior to testing, specimens were conditioned at the target temperature for at least three hours. Specimen dimensions, load frequency, load increment durations, and applied stress levels were pre-defined in the system. Once the specimen was placed in the loading frame, LVDT (linear variable differential transformer) sensors were adjusted to measure vertical deformations, and the test was initiated. Loading continued until complete failure of the specimen. Fatigue life was defined either as the point of significant slope change on the load repetition deformation curve or as the intersection of tangents drawn to the second and third regions of the curve (Aragão et al., 2010; Khodaii & Mehrara, 2009).

Results and Discussion

In the indirect tensile fatigue tests, repeated loading was applied to the specimens until failure occurred, thereby determining the maximum number of load repetitions (N_{max}) and the corresponding deformation at this point (δ_{max}). The fatigue life (N_f) was calculated from the intersection of tangents drawn to the second (II) and third (III) regions of the load–deformation curve.

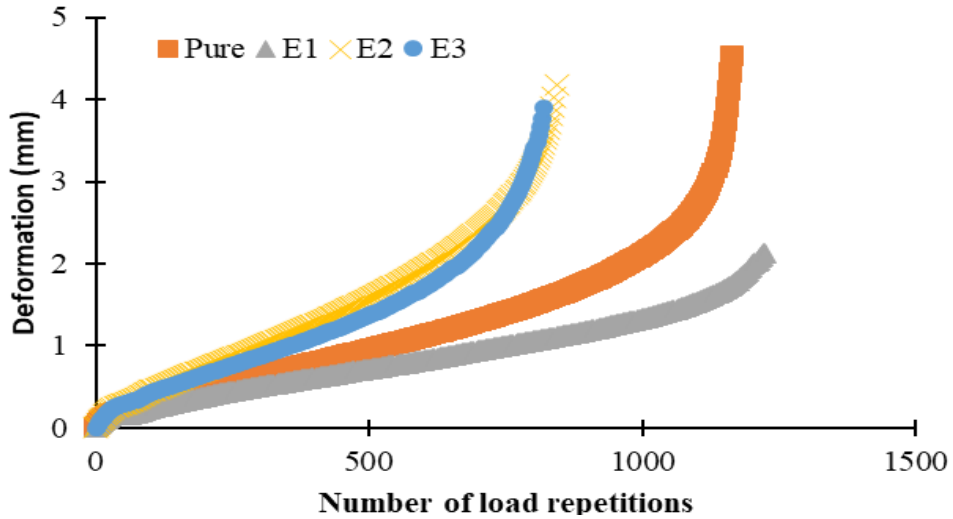

Figure 2. Relationship between deformation and load repetition number of the mixtures at 300 kPa stress level

The tangent for the third region was taken from the point where the slope of the curve began to change, and equations for both regions were derived in Excel, with their intersection used as the basis for N_f determination. The point at which the deformation rate increased was considered as the load repetition number corresponding to crack initiation (N_i). For this purpose, a slope–load repetition curve was plotted, and the point where the slope began to increase was defined as N_i. Consequently, the difference between the total fatigue life (N_f) and the crack initiation load repetitions (N_i) was defined as the crack propagation load repetitions (N_p). In addition, during the interval between N_i and N_f, the number of load repetitions required to produce each 1 mm of deformation (r_f) was determined. The relationship between deformation and load repetitions obtained from tests conducted at a stress level of 300 kPa is presented in Figure 2.

As shown in Figure 2, the lowest number of load repetitions required for failure was observed in mixtures prepared with the E3 binder containing the Elvaloy/PPA combination, while the highest number of load repetitions was obtained in mixtures prepared with the E1 modified binder. Examination of the deformation values revealed that the highest deformation occurred in mixtures prepared with the neat binder, whereas the use of additives reduced the deformation corresponding to the maximum load repetitions. This indicates that although the incorporation of additives increases the number of load repetitions the specimens can withstand, it reduces the flexibility of the mixtures and results in a more brittle fracture behavior. At the stress level of 300 kPa, the average values obtained from three specimens were evaluated. The effect of additive use on the load repetitions required for crack initiation (N_i) is presented in Figure 3, on fatigue life (N_f) in Figure 4, on the load repetitions required for crack propagation (N_p) in Figure 5, and on the maximum load repetitions (N_{mak}) in Figure 6.

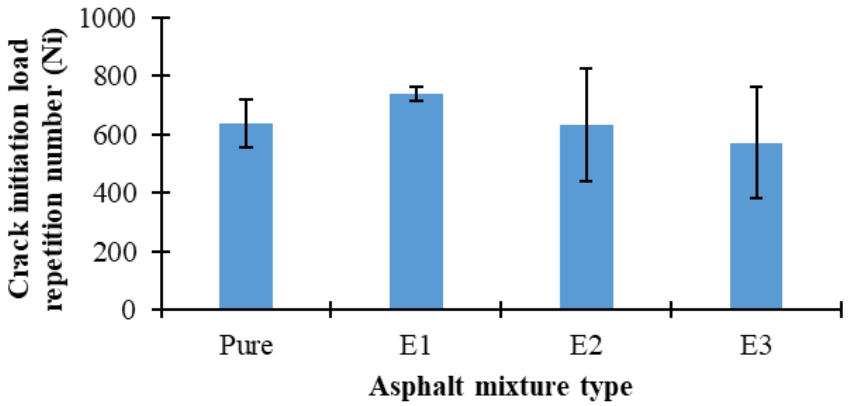

Figure 3. Crack initiation load repetition number (N_i) – mixture type relationship

As seen in Figure 3, at the stress level of 300 kPa, the use of Elvaloy+PPA generally increased the crack initiation load repetitions (N_i). At this level, the use of the E1 modified binder resulted in a 16.04% increase in Ni values compared to the neat mixture. In contrast, mixtures prepared with E2 and E3 modified binders showed decreases of 0.47% and 10.06%, respectively, in N_i values compared to the neat binder. It was also observed that the Ni values of mixtures prepared with the E2 binder were very close to those of the mixtures prepared with the neat binder.

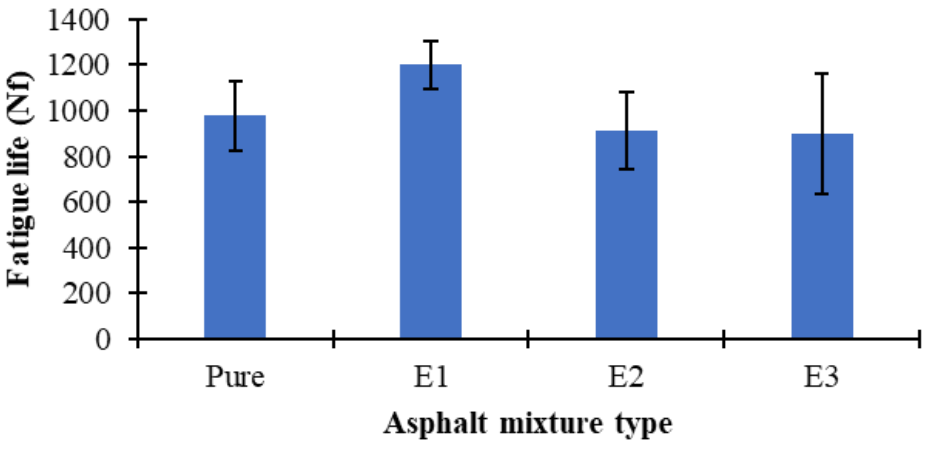

Figure 4. Fatigue life (N_f) – mixture type relationship

Based on the fatigue life (N_f) values obtained from the intersection points of the tangents drawn to the second (II) and third (III) regions of the load–deformation curve, it was observed that, similar to the crack initiation load repetitions, the use of additives increased the N_f values. At the stress level of 300 kPa, the use of the E1 binder resulted in an 11.55% increase in N_f compared to the neat mixture. In contrast, mixtures prepared with E2 and E3 binders at the same stress level exhibited decreases of 6.95% and 7.98%, respectively, compared to the neat binder. As shown in Figure 4, the highest fatigue life was achieved in mixtures prepared with the E1 binder, while the lowest value was obtained in mixtures prepared with the E3 binder.

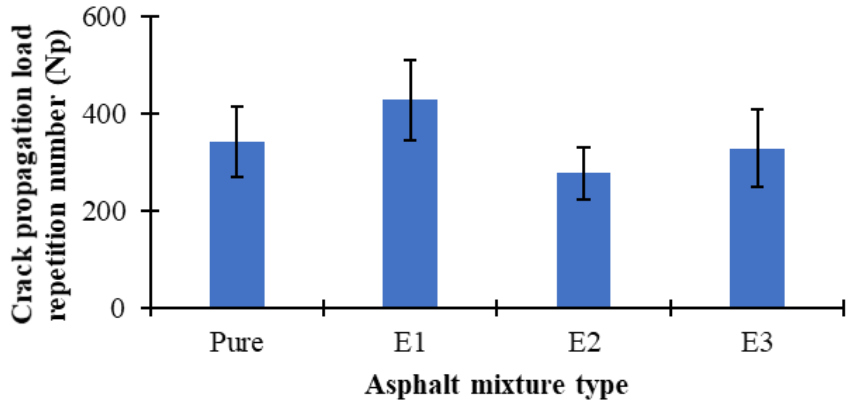

Figure 5. Crack propagation load repetition number (N_p) – mixture type relationship

As shown in Figure 5, the crack propagation load repetitions (N_p) were obtained as the difference between the fatigue life (N_f) and the crack initiation load repetitions (N_i). At the stress level of 300 kPa, the highest Np value was observed in mixtures prepared with the E1 binder, while the lowest values were recorded in mixtures prepared with the E3 binder. At this stress level, the use of the E1 binder resulted in a 2.92% increase in N_p compared to the neat mixture. In contrast, the mixtures prepared with the E2 and E3 binders showed decreases of 19.01% and 74.09%, respectively, in Np values compared to the neat binder.

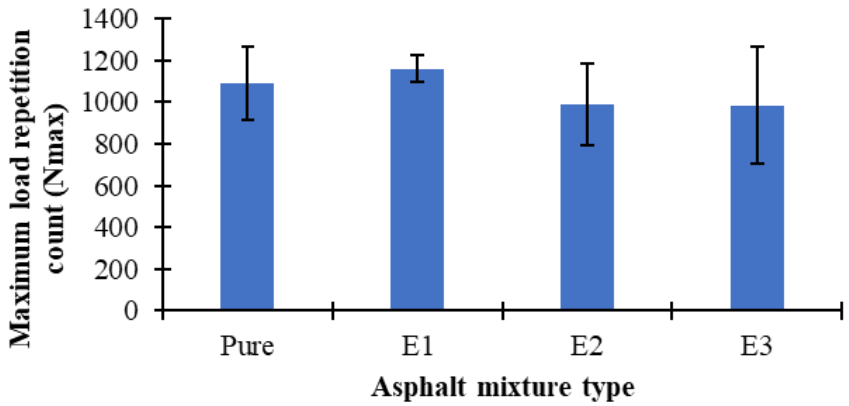

Figure 6. Relationship between maximum load repetition number and type of contribution

As seen in Figure 6, the use of binder E1 at a stress level of 300 kPa resulted in an increase in the maximum load cycle count. At this level, Nmax values of mixtures prepared with binder E1 increased by 0.46% compared to the pure binder, while decreases of 9.09% and 9.55% occurred in mixtures prepared with binders E2 and E3, respectively.

Conclusion

In this study, the fatigue behavior of flexible pavement mixtures incorporating modified bituminous binders prepared with neat bitumen and Elvaloy/PPA additives was investigated. Indirect tensile fatigue tests were conducted at different stress levels, and the results were evaluated in terms of N_i (number of load repetitions to crack initiation), N_f (fatigue life), N_p (number of load repetitions for crack propagation), and N_{max} (maximum number of load repetitions).

The experimental findings demonstrated that the incorporation of Elvaloy/PPA additives had a significant influence on the fatigue performance of the mixtures. In particular, the E1-modified binder provided the greatest improvement compared to the neat binder, with a 16.04% increase in Ni and an 11.55% increase in N_f. Limited improvements in N_p and N_{max} values were also observed with the use of the E1 binder. Conversely, mixtures prepared with E2 and E3 binders exhibited reductions in both N_i and N_f compared to the neat binder. The lowest performance was recorded for the E3 binder, where both fatigue life and crack propagation duration were significantly reduced.

An examination of the deformation values revealed that the neat binder exhibited the highest deformation, while the use of additives reduced the deformation levels. This indicates that although modified binders extend fatigue life and improve resistance to load repetitions, they reduce the flexibility of the mixtures and lead to a more brittle fracture behavior. Overall, the results demonstrated that the fatigue performance of hot mix asphalt can be enhanced by using Elvaloy/PPA additives at appropriate proportions. In particular, the E1 proportion provided the most balanced and favorable results in terms of fatigue life and crack initiation, suggesting that this additive combination has the potential to be considered as an alternative to SBS.

Scientific Ethics Declaration

*The author declares that the scientific ethical and legal responsibility of this article published in EPSTEM journal belongs to the author.

Funding

* This research received no specific grant from any funding agency in the public, commercial, or not-for-profit sectors.

Conflict of Interest

*The authors declare that they have no conflicts of interest

Acknowledgements or Notes

*This article was presented as an oral presentation at the International Conference on Basic Sciences and Technology (www.icbast.net) held in Budapest/Hungary on August 28-31, 2025.

References

Aragão, F. T. S., Lee, J., Kim, Y.-R., & Karki, P. (2010). Material-specific effects of hydrated lime on the properties and performance behavior of asphalt mixtures and asphaltic pavements. *Construction and Building Materials*, *24*(4), 538–544.

Cortizo, M. S., Larsen, D. O., Bianchetto, H., & Alessandrini, J. L. (2004). Effect of the thermal degradation of SBS copolymers during the ageing of modified asphalts. *Polymer Degradation and Stability*, *86*(2), 275–282.

Francken, L. (1998). *Ituminous binders and mixes, E&FN Spon*. CRC Press.

Gorkem, C., & Sengoz, B. (2009). Predicting stripping and moisture induced damage of asphalt concrete prepared with polymer modified bitumen and hydrated lime. *Construction and Building Materials*, *23*(6), 2227–2236.

Janoo, V. C., & Korhonen, C. (1999). *Performance testing of hot-mix asphalt aggregates.* US Army Corps of Engineers.

Khodaii, A., & Mehrara, A. (2009). Evaluation of permanent deformation of unmodified and SBS modified asphalt mixtures using dynamic creep test. *Construction and Building Materials*, *23*(7), 2586–2592.

Kok, B. V., & Yilmaz, M. (2009). The effects of using lime and styrene–butadiene–styrene on moisture sensitivity resistance of hot mix asphalt. *Construction and Building Materials*, *23*(5), 1999–2006.

Kumar, P., Chandra, S., & Bose, S. (2006). Strength characteristics of polymer modified mixes. *International*

Journal of Pavement Engineering, *7*(1), 63–71.
Lav, H. A., & Lav A. M. (2004). *Shell bitüm el kitabı*. İsfalt Bilimsel Yayınları.
Liang, M., Ren, S., Fan, W., Xin, X., Shi, J., & Luo, H. (2017). Rheological property and stability of polymer modified asphalt: Effect of various vinyl-acetate structures in EVA copolymers. *Construction and Building Materials*, *137*, 367–380.
Meyer, C. L., Irani, T. H., Hermes, K. A., & Yung, B. (2017). *Explaining suicide: Patterns, motivations, and what notes reveal*. Elsevier Academic Press.
Nicholls, C. (1998). *Asphalt surfacings*. E & FN Spon.
Sengoz, B., & Isikyakar, G. (2008). Evaluation of the properties and microstructure of SBS and EVA polymer modified bitumen. *Construction and Building Materials*, *22*(9), 1897–1905.
Singh, B., & Kumar, P. (2019). Effect of polymer modification on the ageing properties of asphalt binders: Chemical and morphological investigation. *Construction and Building Materials*, *205*, 633–641.
Stark, W., & Jaunich, M. (2011). Investigation of ethylene/vinyl acetate copolymer (EVA) by thermal analysis DSC and DMA. *Polymer Testing*, *30*(2), 236–242.
Tayfur, S., Ozen, H., & Aksoy, A. (2007). Investigation of rutting performance of asphalt mixtures containing polymer modifiers. *Construction and Building Materials, 21*(2), 328–337.
Vlachovicova, Z., Wekumbura, C., Stastna, J., & Zanzotto, L. (2007). Creep characteristics of asphalt modified by radial styrene–butadiene–styrene copolymer. *Construction and Building Materials*, *21*(3), 567–577.
Zaniewski, P. J., & Pumphrey, E. M. (2004). *Evaluation of performance graded asphalt binder equipment and testing protocol*. West Virginia University.

Author(s) Information

Beyza Furtana-Yalcin
Civil Engineering Department, Engineering Faculty, Munzur University, Elazig, Türkiye
Contact e-mail: *beyzafurtana@munzur.edu.tr*

To cite this article:

Furtana-Yalcin, B. (2025). Investigation of fatigue performance of hot mix asphalt mixtures modified with elvaloy and phosphoric acid (PPA) as an alternative to SBS polymer. *The Eurasia Proceedings of Science, Technology, Engineering and Mathematics (EPSTEM), 36,* 151-158.

The Eurasia Proceedings of Science, Technology, Engineering & Mathematics (EPSTEM)
ISSN: 2602-3199

The Eurasia Proceedings of Science, Technology, Engineering and Mathematics (EPSTEM), 2025

Volume 36, Pages 159-165

ICBAST 2025: International Conference on Basic Sciences and Technology

Synthesis of Fluorescent Calix[4]arene Derivatives for the Detection of Hg(II) / Cr(VI) and Investigation of their Antimicrobial Properties

Mustafa Yilmaz
Selcuk University

Ayse Yildirim
Selcuk University

Ahmet Uysal
Selcuk University

Abstract: Calixarenes are noteworthy compounds in organic chemistry since they can be synthesized and modified more conveniently compared to many other supramolecules. They can undergo functionalization either through the phenolic–O groups or at the para-position of the phenolic rings. Moreover, substitutions at the upper and lower rims allow their conversion into various derivatives, including ethers, esters, carboxylates, and amides. Owing to these features, calixarenes have become valuable supramolecular platforms in areas such as molecular recognition, sensing, self-assembly, catalysis, biocatalysis, nanotechnology, and drug discovery. Their unique structural characteristics also provide opportunities for biomedical applications, particularly in the development of antitumor, antiviral, antimicrobial, antithrombotic, and antifungal agents. In the present study, 4-sulfo-1,8-naphthalimide derivatives of calix[4]arene were synthesized, followed by the replacement of potassium sulfonate salts with silver ions to obtain silver sulfonate salts. The resulting antimicrobial materials were used to form transparent biofilms in the presence of hyaluronic acid (HA), and their antimicrobial activity was subsequently evaluated.

Keywords: Calixarene, Fluorescent, Antimicrobial

Introduction

Increased industrial activities lead to the contamination of water and soil with heavy metal ions and harmful compounds, leading to environmental and water pollution. Most of the approximately 300 million tons of heavy metals extracted to date still reside in soil and groundwater (Liu et al., 2021). In recent years, concerns about the use of heavy metals and their environmental impacts have been growing. Studies show that human activities cause heavy metals to disrupt ecosystems and threaten life through bioaccumulation. Due to its mutagenic and carcinogenic properties, chromium is considered a hazardous metal (Cilamkoti & Dutta, 2023; Kayhan et al., 2023). Chromium, a frequently encountered pollutant in the environment, originates from both anthropogenic activities and natural sources and persists in groundwater and soil (Miretzky & Cirelli, 2010). Leather processing, stainless steel production, textiles, and photography are just a few of the industrial areas where chromium compounds are commonly used (Guo et al., 2011). Due to their high solubility in water, Cr(VI) salts are a serious and widespread source of pollution. Their high toxicity and carcinogenic nature make this metal considered a pollutant that needs to be urgently identified (Liu et al., 2024). Fluorescent probes used to detect metal ions are widely used not only in environmental studies but also in biological studies, attracting the interest of many researchers. The development of highly sensitive probes, particularly for the determination of biologically important metals, is a current research topic (Fateh et al., 2021; Xu et al., 2019). Recent research has revealed that water resource pollution, particularly due to harmful heavy metals, poses an increasing

ecological and public health risk. Heavy metals are reported to disrupt ecosystem balance and negatively impact wildlife through bioaccumulation, resulting from human activities (Phichi et al., 2020; Tripathy et al., 2020). Toxic Hg(II) and Cr(VI) analyses in biological and environmental samples havegenerally been performed by classical methods such as ion-selective electrodes, atomic absorption spectrometry, inductively coupled plasma mass spectrometry (ICP-MS) and inductively coupled argon plasma optical emission spectrometry (ICP-OES) (Minhas, Memon, & Bhanger, 2010). However, these methods are not always practical due to both the cost of sampling and the difficulty of procuring the required equipment. In contrast, fluorescence-based approaches offer a relatively easy and advantageous method for detecting these ions in terms of selectivity and response time (Tosun et al.,2024 & Guler, 2024).

In this study, the interactions of previously synthesized fluorescent compounds *4* and *7* with various anions and cations were investigated and their selectivity towards Hg(II) and Cr(VI) ions was determined. These compounds, which contain potassium sulfonate groups, were also converted into silver salts to investigate their antimicrobial properties. Fluorescent, antimicrobial, and transparent biofilms were prepared using hyaluronic acid (HA); biofilm tests revealed that these materials exhibited selective antimicrobial activity, particularly against the bacterium *S. lutea*.

Method

Synthesis

Synthesis of calix[4]arene derivatives (1–7) was performed by following the literature procedure for alkylation and amide synthesis reported elsewhere (Chrisstoffels et al., 1999; Collins et al., 1991; Yildirim et al., 2021).

General Procedure for Fluorescence Study

The sensing abilities and fluorescence responses of compounds *4* and *7* towards various anions and cations were investigated using a fluorescence spectrophotometer. For this purpose, stock solutions of compounds *4* and *7* at 1×10^{-3} M were prepared in ethanol and then diluted with distilled water to a concentration of 1.5×10^{-5} M. Fluorescence emissions were then measured using different anions and cations.

Preparation of Antimicrobial Biofilms of HA-4Ag and HA-7Ag

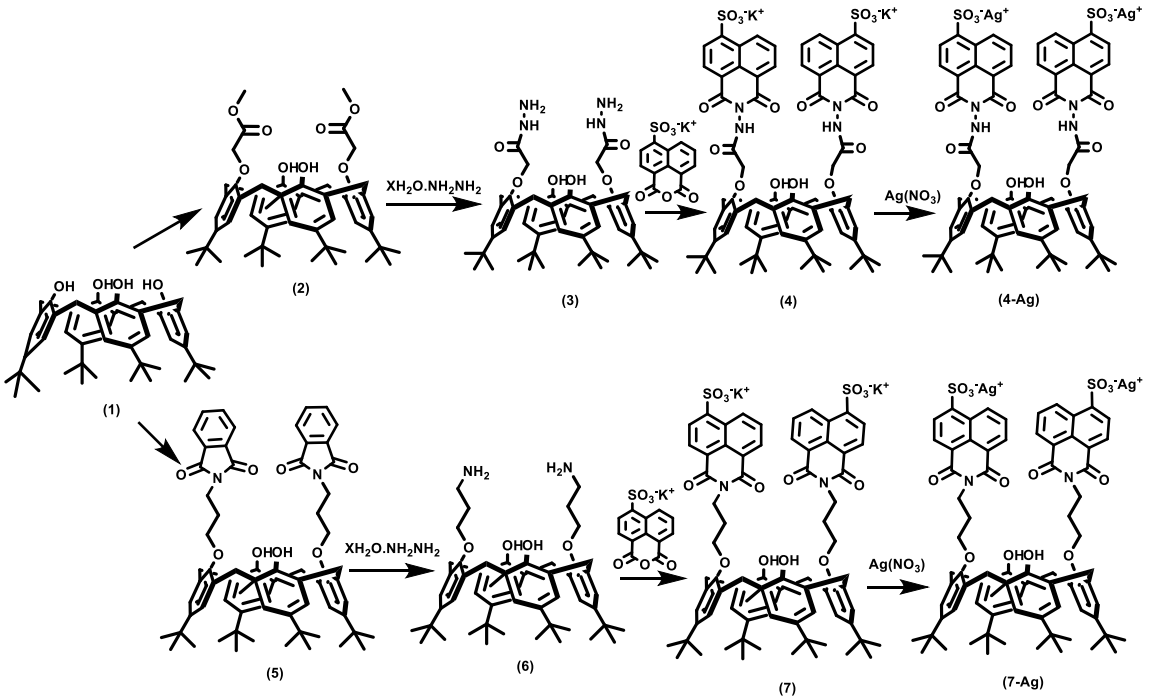

Figure 1. Synthesized antimicrobial compounds

The K^+ ions of the potassium sulfonate groups in the synthesized compounds *4* and *7* were replaced with Ag(I) ions by ion exchange for use in antimicrobial studies. For this purpose, 100 mg of compounds (*4* and *7*) were treated with 0.1 M $AgNO_3$ solution (4.0 mL) in the dark for 4 hours. Following the reaction, the solution was separated by precipitation in an ethanol-water mixture and dried in a vacuum oven at 90 °C (Yildirim et al., 2021).

HA-based transparent biofilms were then prepared using the resulting *4-Ag* and *7-Ag* derivatives. For this process, 25 mg of HA was dissolved in 0.5 mL of DMSO at room temperature overnight. Separately, 25 mg of the compounds (*4-Ag* and *7-Ag*) were dissolved in 0.5 mL of DMSO and added dropwise to the HA solution. The pH of the mixture was adjusted to 6 and stirred at room temperature overnight. Once the mixture reached a gel consistency, it was poured into molds and dried under vacuum at 50 °C to obtain transparent biofilms.

Results and Discussion

In our previous study, the anticancer properties of synthesized calix[4]arene-1,8-naphthalimide derivatives were investigated, and it was determined that these compounds were effective against colon cancer (Yildirim, Karakurt, et al., 2021). The summary of the research is as follows: First, calix[4]arene derivatives were synthesized, then, under appropriate reaction conditions, compounds *4* and *7* were successfully obtained by reacting dihydrazide (3) and diaminopropyl (6) compounds with 4-sulfo-1,8-naphthalic anhydride. The synthesis steps are shown step by step in Scheme 1.

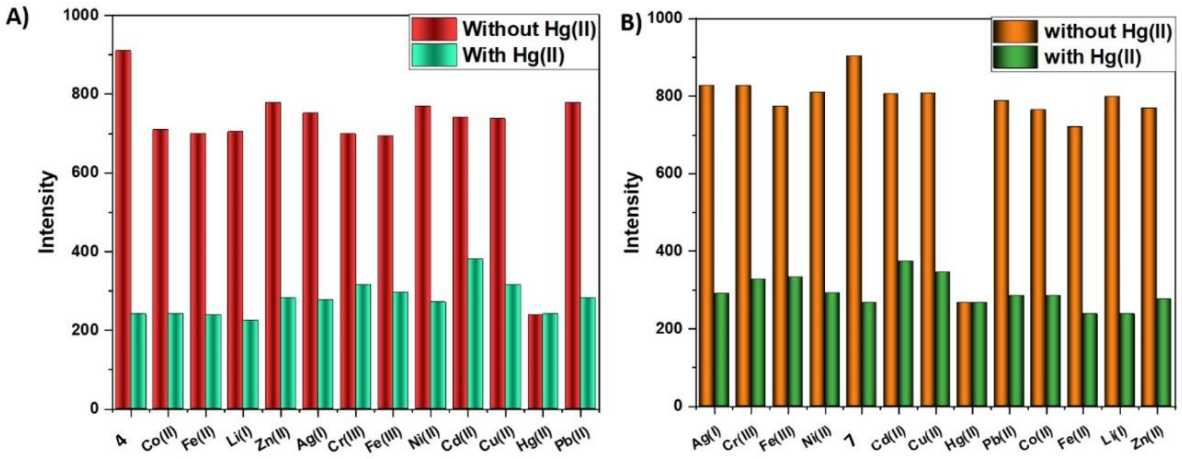

Figure 2. Fluorescence intensity change of 4-Hg(II) & 7-Hg(II) complexes (1.5×10^{-5} M) at 390 nm upon addition of different metal ions (10.0 eq.) in EtOH:H_2O (1:1, v/v).

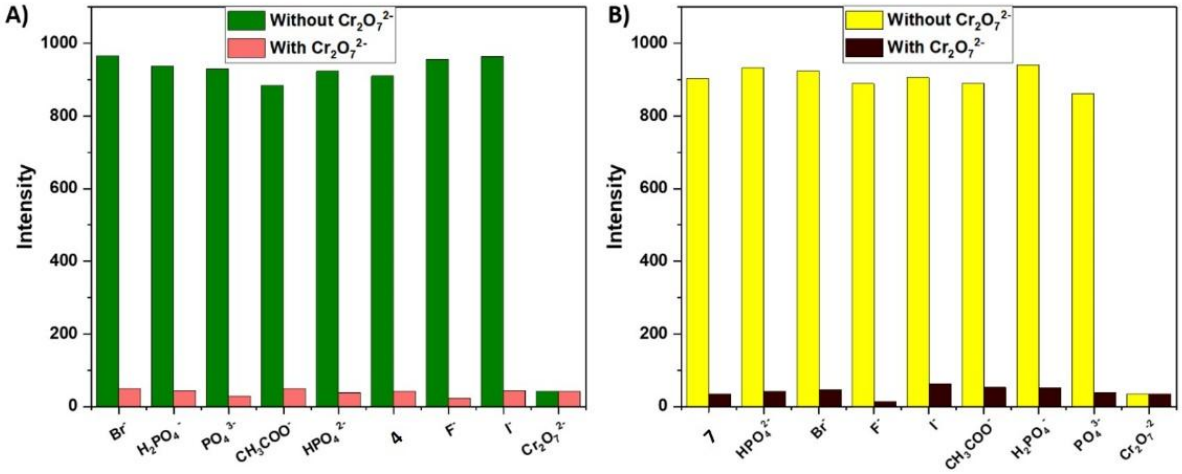

Figure 3. Fluorescence intensity change of 4-Cr(VI) & 7-Cr(VI) complexes (1.5×10^{-5} M) at 390 nm upon addition of different anions (10.0 eq.) in EtOH:H_2O (1:1, v/v).

After characterization, spectrophotometric analyses were performed on compounds 4 and 7 to determine different anions and cations. In this study, the antimicrobial properties of derivatives obtained by replacing the K(I) ions in compounds *4* and *7* with Ag(I) ions were investigated. Additionally, antimicrobial gel films (*HA-4Ag* and *HA-7Ag*) were prepared with *4-Ag* and *7-Ag* compounds using hyaluronic acid as the biopolymer.

In order to verify the selectivity and potential applications of compounds *4* and *7*, a competitive study was carried out by adding 10 equivalents of metal ions to their aqueous solutions. The density of *4*-Hg(II) and *7*-Hg(II) complexes was measured in the presence of various metal ions such as Pb(II), Cu(II), Zn(II), Cr(III), Ni(II), Co(II), Ag(I), Cd(II), Fe(II), Fe(III) and Li^+ and the results are shown in *Figure 2*. The selectivity of compounds *4* and *7* towards Hg(II) ion remained at a satisfactory level despite the addition of another 10 equivalents of cations. Only minor changes in the density were observed, confirming that both compounds exhibit effective selectivity towards Hg(II) ion. If we look at the *4*-Cr(VI) & *7*-Cr(VI) complexes in Figure 3.

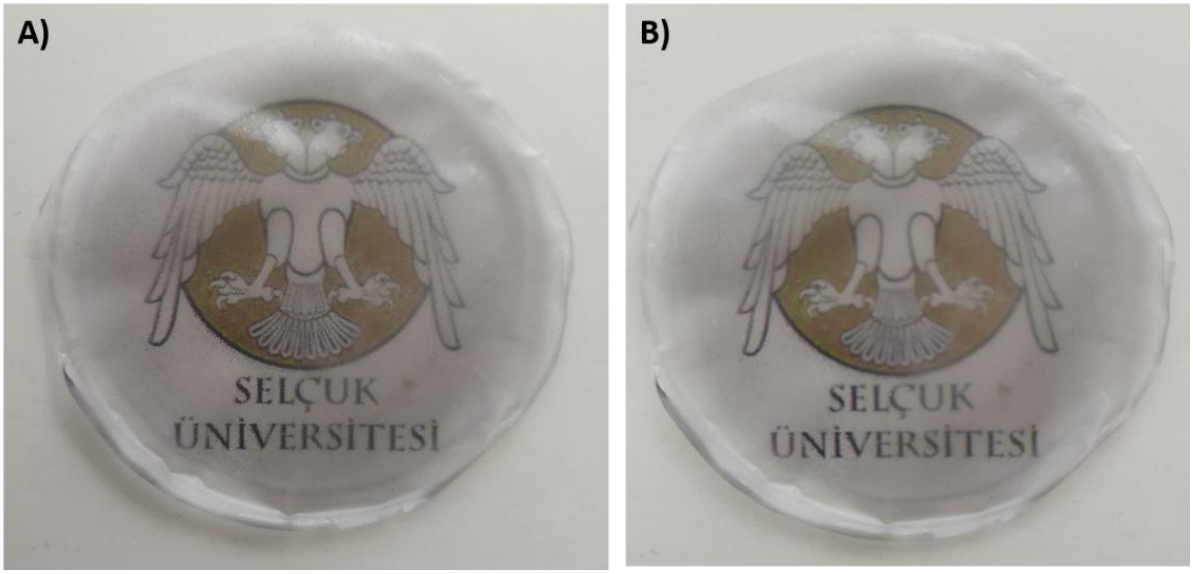

Figure 4. Transparent biofilms of HA-4Ag & HA-7Ag in A and B

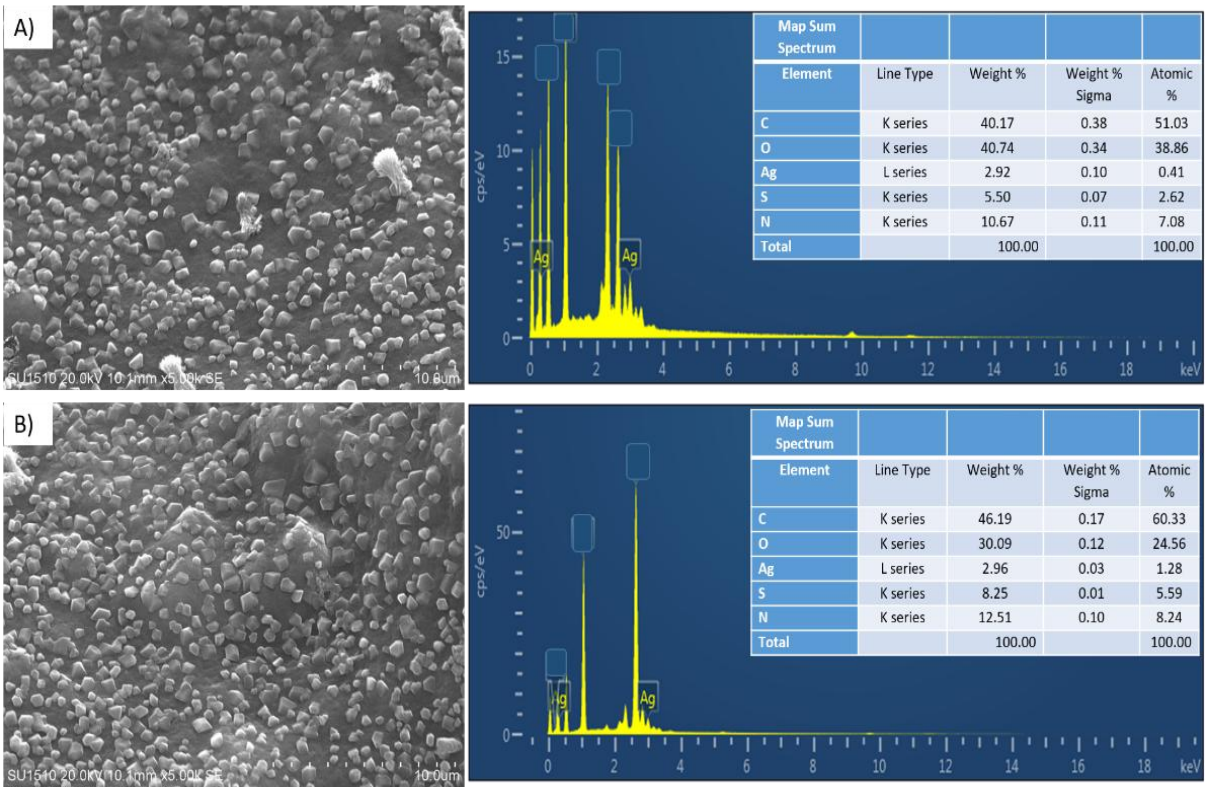

Figure 5. EDX spectral data and SEM images of A) HA-4Ag and B) HA-7Ag.

Transparent biofilms (*HA-4Ag* and *HA-7Ag*) obtained as a result of the interaction of *4-Ag* and *7-Ag* compounds with HA are shown in Figure 4. The surface profiles of the transparent biofilms prepared with *HA-4Ag* and *HA-7Ag* were examined using SEM and EDX analyses. The results indicate that the crystals of *4-Ag* and *7-Ag* compounds are distributed homogeneously within the structure of the HA biofilms. Furthermore, the EDX analyses of *HA-4Ag* and *HA-7Ag* (*Figure 5A* and *B*) reveal that, in addition to the main elements C, O, and N, the Ag(I) ions successfully replace the K(I) ions.

Antimicrobial tests revealed that compound *4* exhibited antibacterial activity against S. aureus (MRSA) at 3.125 mg/mL, while the other tested microorganisms were resistant at the same concentrations. Notably, Candida albicans was sensitive to compound *4* at a lower dose of 1.562 mg/mL. In contrast, compound *7* showed no significant activity against the tested bacteria, with the exception of C. albicans.

Table 1. Detected MIC values (mg/mL) of compounds against pathogen bacteria

Strains	**4**	**HA-5**	**HA-6**	**HA-7**	**Gentamicin (µg/ml)**
***Escherichia coli* ATCC 25922**	-	1.562	-	1.562	1.95
***Pseudomonas aeruginosa* ATCC27853**	-	1.562	1.562	0.781	<0.97
***Klebsiella pneumonia* ATCC700603**	-	1.562	-	-	7.81
***Staphylococcus aureus*(MRSA)ATCC 43300**	-	3.125	3.125	1.562	1.95
***Sarcina lutea* ATCC 9341**	-	1.562	-	0.097	1.95

The *HA-4Ag* material exhibited high efficacy against the tested pathogenic microorganisms, showing pronounced antibacterial and antifungal activity. Among the bacteria, S. lutea was the most susceptible, with an MIC value of 0.012 mg/mL. Overall, the silver-modified compounds *HA-4* and *HA-7* demonstrated moderate to strong antimicrobial effects against both bacteria and yeasts, outperforming the unmodified compounds *4* and *7,* with S. lutea being the most affected by the silver-containing derivatives.

Conclusion

As a result, the fluorescent naphthalimide-conjugated calix[4]arene chemosensors were studied for their selective ion transport capabilities toward cations and anions. The results demonstrated that these compounds are both selective and sensitive to Hg(II) and Cr(VI) ions, with low detection limits. Upon incorporation of *4-Ag* and *7-Ag* into hyaluronic acid, transparent biofilms were produced, and their antimicrobial performance was assessed. These biofilms exhibited moderate to strong activity against various bacteria and yeasts, with S. lutea showing the highest susceptibility

Recommendations

In future studies, paper sensors can be designed to more practically determine Hg(II) and Cr(VI) ions in aqueous solutions by appropriately designing the synthesized fluorescent naphthalimide-conjugated calix[4]arene compounds. Furthermore, the antimicrobial properties of 4-Ag and 7-Ag can be used in many areas for transparent biofilms prepared with hyaluronic acid.

Scientific Ethics Declaration

*The authors declares that the scientific ethical and legal responsibility of this article published in EPSTEM journal belongs to the authors.

Conflict of Interest

*The authors declare that they have no conflicts of interest

Funding

*The authors would like to thank the Selçuk University BAP Coordinator for supporting this project (No: 25701043).

Acknowledgements or Notes

* This article was presented as an oral presentation at the International Conference on Basic Sciences and Technology (www.icbast.net) held in Budapest/Hungary on August 28-31, 2025.

* The authors would like to thank the participants at the International Conference on Basic Sciences and Technology (ICBAST) and the article reviewers assigned by the Eurasia Proceedings of Science, Technology, Engineering and Mathematics (EPSTEM) for their valuable feedback.

* In conclusion, the materials synthesized in this thesis demonstrated efficacy in antimicrobial studies.

References

Chrisstoffels, L. A., de Jong, F., Reinhoudt, D. N., Sivelli, S., Gazzola, L., Casnati, A., & Ungaro, R. (1999). Facilitated transport of hydrophilic salts by mixtures of anion and cation carriers and by ditopic carriers. *Journal of the American Chemical Society, 121*(43), 10142-10151.

Cilamkoti, V., & Dutta, R. K. (2023). Silicon dioxide quantum dots anchored on the surface of carbon nanodiscs as photoluminescent probe for Cr (VI) detection. *Journal of Photochemistry and Photobiology A: Chemistry, 436*, 114406.

Collins, E. M., McKervey, M. A., Madigan, E., Moran, M. B., Owens, M., Ferguson, G., & Harris, S. J. (1991). Chemically modified calix [4] arenes. Regioselective synthesis of 1, 3-(distal) derivatives and related compounds. X-Ray crystal structure of a diphenol-dinitrile. *Journal of the Chemical Society, Perkin Transactions 1*(12), 3137-3142.

Fateh, F., Yildirim, A., Bhatti, A. A., & Yilmaz, M. (2021). A New Benzothiazin-functionalized calix [4] arene-based fluorescent chemosensor for the selective detection of Co2+ Ion. *Journal of Fluorescence, 31*(4), 1075-1083.

Guo, L., Liu, Y., Zhang, C., & Chen, J. (2011). Preparation of PVDF-based polymer inclusion membrane using ionic liquid plasticizer and Cyphos IL 104 carrier for Cr (VI) transport. *Journal of Membrane Science, 372*(1-2), 314-321.

Kayhan, E. Y., Yildirim, A., Kocer, M. B., Uysal, A., & Yilmaz, M. (2023). A cellulose-based material as a fluorescent sensor for Cr (VI) detection and investigation of antimicrobial properties of its encapsulated form in two different MOFs. *International Journal of Biological Macromolecules, 240*, 124426.

Liu, F., Hua, S., Wang, C., Qiu, M., Jin, L., & Hu, B. (2021). Adsorption and reduction of Cr (VI) from aqueous solution using cost-effective caffeic acid functionalized corn starch. *Chemosphere, 279*, 130539.

Liu, S., Zhang, L., Kim, H., Sun, J., & Yoon, J. (2024). Recent advances and challenges in monitoring chromium ions using fluorescent probes. *Coordination Chemistry Reviews, 501*, 215575.

Minhas, F. T., Memon, S., & Bhanger, M. (2010). Transport of Hg (II) through bulk liquid membrane containing calix [4] arene thioalkyl derivative as a carrier. *Desalination, 262*(1-3), 215-220.

Miretzky, P., & Cirelli, A. F. (2010). Cr (VI) and Cr (III) removal from aqueous solution by raw and modified lignocellulosic materials: a review. *Journal of Hazardous Materials, 180*(1-3), 1-19.

Phichi, M., Imyim, A., Tuntulani, T., & Aeungmaitrepirom, W. (2020). based cation-selective optode sensor containing benzothiazole calix [4] arene for dual colorimetric Ag+ and Hg2+ detection. *Analytica Chimica Acta, 1104*, 147-155.

Tosun, M., Uysal, A., Kursunlu, A. N., & Guler, E. (2024). A new family of macrocyclic antibiotics based-on Pillar [5] arene concluding multi quinoline moieties. *Tetrahedron, 151*, 133812.

Tripathy, M., Subuddhi, U., & Patel, S. (2020). A styrylpyridinium dye as chromogenic and fluorogenic dual mode chemosensor for selective detection of mercuric ion: Application in bacterial cell imaging and molecular logic gate. *Dyes and Pigments, 174*, 108054.

Xu, Z., Shi, W., Yang, C., Xu, J., Liu, H., & Zhu, B. (2019). Highly selective and sensitive fluorescent probe for the rapid detection of mercury ions. *RSC advances, 9*(19), 10554-10560.

Yildirim, A., Karakurt, S., & Yilmaz, M. (2021). Synthesized two new water-soluble fluorescents calix [4] arene 4-sulfo-1, 8-naphthalimide derivatives inhibit proliferation of human colorectal carcinoma cells. *ChemistrySelect, 6*(28), 7093-7097.

Yildirim, A., Kocer, M. B., Demir, A. D., Arslan, E., & Yilmaz, M. (2021). A bi-modal, cellulose-based sensor for fluorometric detection of Fe (III) and antimicrobial studies of its silver-loaded form. *International Journal of Biological Macromolecules, 183*, 35-44.

Author(s) Information

Mustafa Yilmaz
Selcuk University, Department of Chemistry
Konya/Türkiye
Contact e-mail: *myilmaz42@yahoo.com*

Ayse Yildirim
Selcuk University, Department of Chemistry
Konya/Türkiye

Ahmet Uysal
Selcuk University, Vocational School of Health Services,
Konya/Türkiye

To cite this article:

Yilmaz, M., Yildirim, A., & Uysal, A. (2025). Synthesis of fluorescent calix[4]arene derivatives for the detection of Hg(II) / Cr(VI), and investigation of their antimicrobial properties. *The Eurasia Proceedings of Science, Technology, Engineering and Mathematics (EPSTEM), 36*, 159-165.

The Eurasia Proceedings of Science, Technology, Engineering & Mathematics (EPSTEM)
ISSN: 2602-3199

The Eurasia Proceedings of Science, Technology, Engineering and Mathematics (EPSTEM), 2025

Volume 36, Pages 166-173

ICBAST 2025: 5th International Conference on Basic Sciences and Technology

The Synthesis of Microwave Assisted Melamine-Schiff Bases and Investigation of Bridged Fe(III) Metal Complexes

Ziya Erdem Koc
Selcuk University

Abstract: In this study, 2,4,6-triamino-s-triazine (melamine) as the starting material. Microwave assisted Schiff base reaction took place with the condensation reaction of melamine and 3-hydroxybenzaldehyde. Then, s-triazine-core Schiff base ligand complexes were obtained by obtaining a single oxygen-bridged compound of [(Fe(Salophen)Cl] ligand complexes, which we synthesized Schiff base s-triazine by literature. The obtained multidirectional s-triazine-core Schiff base ligand complexes were under microwave assisted with 3-hydroxybenzaldehyde compounds. The condensations proceed in short time to give products which, in certain instances, are not readily attainable by conventional condensation techniques. Due to its good performance, the microwave device used in household was preferred. Consequently, the structures of the obtained ligand and complexes were characterized using elemental analysis, FT-IR spectroscopy, ^{1}H-NMR spectroscopy and magnetic susceptibility measurement techniques.

Keywords: Melamine, Schiff base, s-Triazine, Salophen, Microwave

Introduction

Melamine, which is one of its compounds, is rapidly increasing in coordination chemistry, environmental chemistry, biochemistry, polymer chemistry, pharmaceutical chemistry and electronics industry (Nozha et al., 2021; Uysal et al., 2012). In addition, Melamine Schiff base compounds are used in medicine, especially as molecular magnetic material, and such heterocyclic compounds are used as active ingredients of antitumor and anticancer drugs (Arslaner et al., 2017; Koc & Uysal, 2016; Portalone, 2008). Melamine compounds have gained importance in environmental chemistry in the storage of gases with metal-organic lattice structures (Qian & Huang, 2010; Yu et al., 2008).

Schiff bases are very important structures condensation products of primary amines with aldehydes for synthetic organic chemistry (Dhar & Taploo, 1982; Schiff, 1869). Schiff-base is considered a dynamic compound with a reversible imine bond derived from the dehydration reaction between amine and carbonyl groups (Kopel, Sindelar, Biler, et al., 1998; Zabardasti & Shangaie, 2016; Zhang et al., 2021). Over the years, Schiff bases and metal complexes have played an important role in the development of coordination chemistry, chelating ligands and complex biochemical reactions as they readily form stable complexes with most of the transition metals (Jayabalakrishnan et al., 2002; Kocyigit et al., 2010; Sindhu et al., 2013). In recent years, the widespread use of Schiff bases and metal complexes, especially in various qualitative and quantitative analyses, enrichment of radioactive materials, pharmacological properties, the paint industry, and plastics industry has further increased, and it has attracted much attention due to their biochemical activities (Koc, 2011; Koc & Ucan, 2007; Koc & Uysal, 2010, 2011; Li et al., 2021; Naz et al., 2013; Uysal & Koc, 2010).

Nitrogen-containing heterocycles are highly important due to their classification as a significant group of synthetic and natural compounds(Thamer Abd Rehan, 2024). Then, the obtained microwave assisted s-triazine monomer was coordinated with the salophen ligand complex with a single oxygen and monopodal melamine centered monomer complexes were obtained (Celikbilek & Koc, 2014; Hao et al., 2021). Microwave-assisted

- Selection and peer-review under responsibility of the Organizing Committee of the Conference

organic synthesis (MAOS) continues to affect synthetic chemistry significantly by enabling rapid, reproducible experiments. We envisioned that microwave irradiation would enhance this chemistry and expand the chemistry scope (Celik et al., 2019; Diaz-Ortiz et al., 2001).

Experimental

Materials and Methods

The chemicals were purchased from Aldrich and Merck was used as received. LG-health wave microwave system (MG-607APR, 230V—50Hz) was used and the output of microwave power is mentioned as percent intensity i.e. (20%, 40%, 60%, 100%). Melting points were measured using an Optimelt Automated Melting Point System (Digital Image Processing Technology) SRS apparatus (Nyköping-Sweden). Elemental analyses (C, H, N) were performed using a Leco, CHNS-932 model analyser (Massachusetts, USA). ^{1}H NMR spectra were recorded by the Varian, 400 M spectrometer at room temperature. (California, USA).

FT-IR spectra were recorded using a Perkin-Elmer Spectrum 100 with Universal ATR Polarization Accessory (Shelton, USA). Magnetic susceptibilities of the metal samples were measured at 296 K using a Sherwood Scientific MX Gouy magnetic susceptibility apparatus (Gouy method) with Hg[Co(SCN)4] as a calibration by the constant magnetic field. The effective magnetic moments, μeff, per metal atom were calculated from the expression, B.M., where χM is the molar susceptibility (Cambridge, UK). TGA analyses of the compounds were performed on the Mettler Tole *Third Level Headings*

Preparation of Microwave Assisted 3-((4,6-Diamino-1,3,5-triazine-2-imino)methyl)Phenol (DTMP)

Melamine was suspended in 60 mL of benzene (1 mmol, 1.26 g). Then 3-hydroxybenzaldehyde (1 mmol, 1.22 g) was added to the mixture piece by piece. The mixture was heated using microwave irradiation technique at 350W for 25 minutes, permitted to cool, and poured in a thin stream into a large volume of rapidly stirred water. To separate the precipitated monomer, the mixture was cooled and the solid was filtered apart. The resulting white precipitate was dried. **$C_{10}H_{10}N_6O$:** ^{1}H NMR (DMSO-d_6, ppm): 10.64 (s, H, OH), 9.71 (s, H, CH=N), 8.55 (s, H, Ar-H), 7.83-6.88 (m, 3H, Ar-H). FT-IR (cm^{-1}) 3467-3414 (NH_2), 3167 (OH), 1649 (C=N), 1526 ($C=N_{triazine}$).

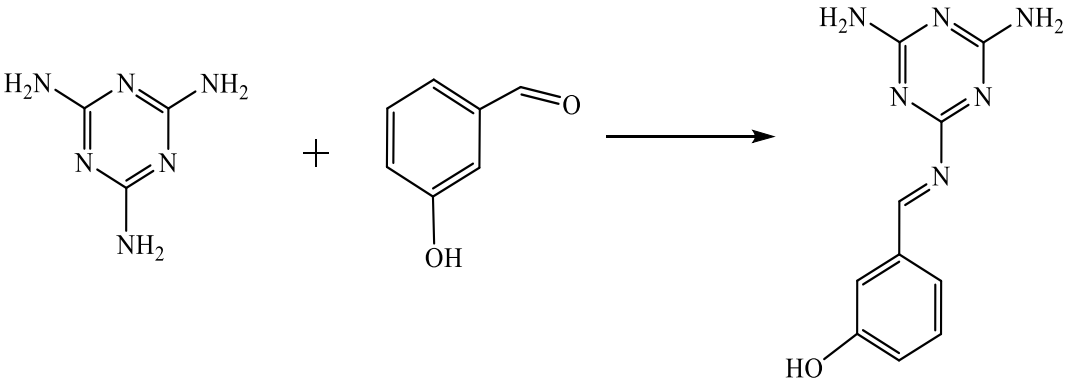

3-((4,6-diamino-1,3,5-triazin-2-imino)methyl)phenol

Figure 1. Proposed structures of the microwave-assisted (DTMP) ligand

Synthesis of Salophen Ligand and Salophen Complexes

The synthesis of Salophen ligand and Salophen complexes has been synthesized according to the mentioned literature. (Gembicky et al., 2000; Kopel, Sindelar, & Klicka, 1998).

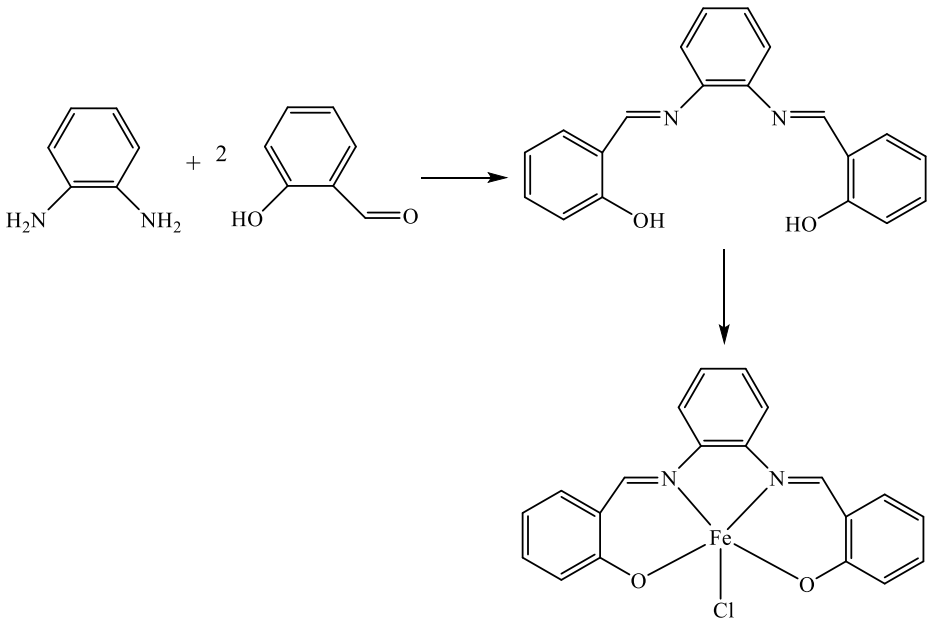

Figure 2. Salophen and [Fe(salophen)Cl] complex

3-((4,6-diamino-1,3,5-triazine-2-imino) Methyl)phenol [Fe(salophen)Cl] Complex

Suspension solution was prepared in the resulting monomer (1 mmol, 0.23 g) ethanol. [Fe(salophen)Cl] (1 mmol, 0.37 g) dissolved in ethanol was added to the complex compound monomer. The reaction mixture was stirred for four hours at 100 °C under a back cooler. The reaction solution was filtered and dried in a sedimentary oven. FT-IR (cm^{-1}) 3317-3354 (NH_2), 1635 (C=N), 1546 ($C=N_{triazin}$).

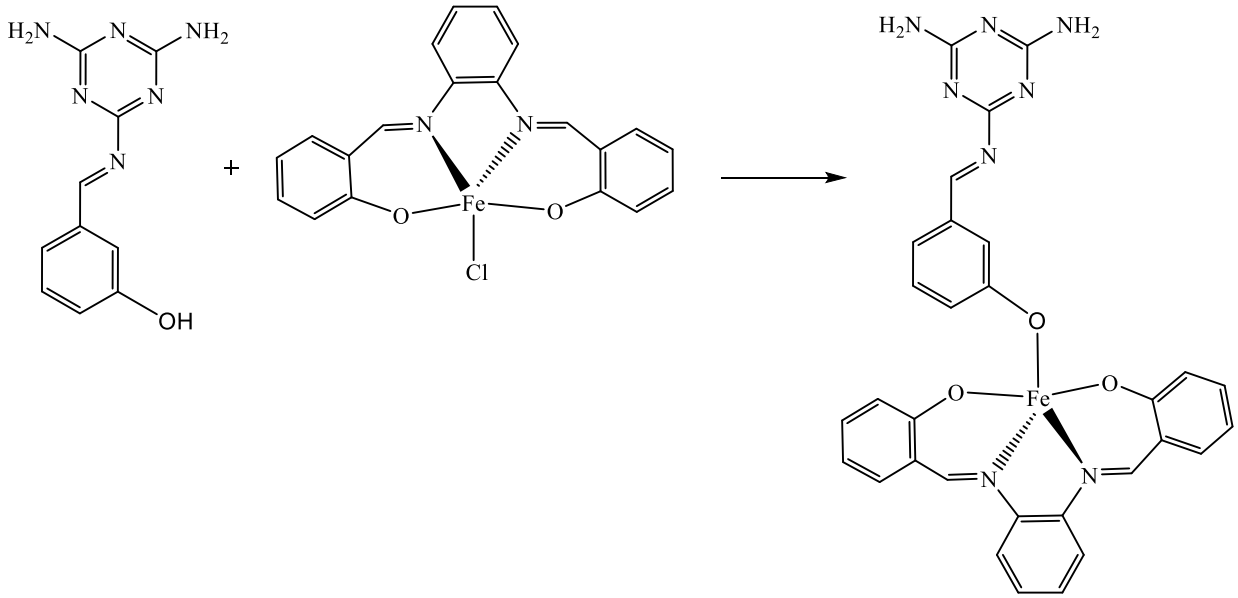

Figure 3. Monopodal Schiff base ligand [Fe(salophen)(DTMP)] complex

Tripodal Schiff Base Ligand [Fe(salophen)(DTMPDHB] Complex

[Fe(salophen)(DTMP)] (1 mmol, 0.85 g,) was dissolved in 30 mL of methanol and stirred under reflux for 2 h. 2,5-Dihydroxybenzaldehyde (2 mmol, 0.28 g) 20 mL methanol was added to the resulting mixture. The mixture was reflux at 4 h and 5 drops of acetic acid catalyst were added. It was mixed for a while until the powder formed, and a color change was observed. The precipitate was filtered. [SALMHBAFe(III)(salophen)]: FT-IR (cm^{-1}) 3240, 3175 (OH), 1642,1624 (C=N), 1553 ($C=N_{triazine}$).

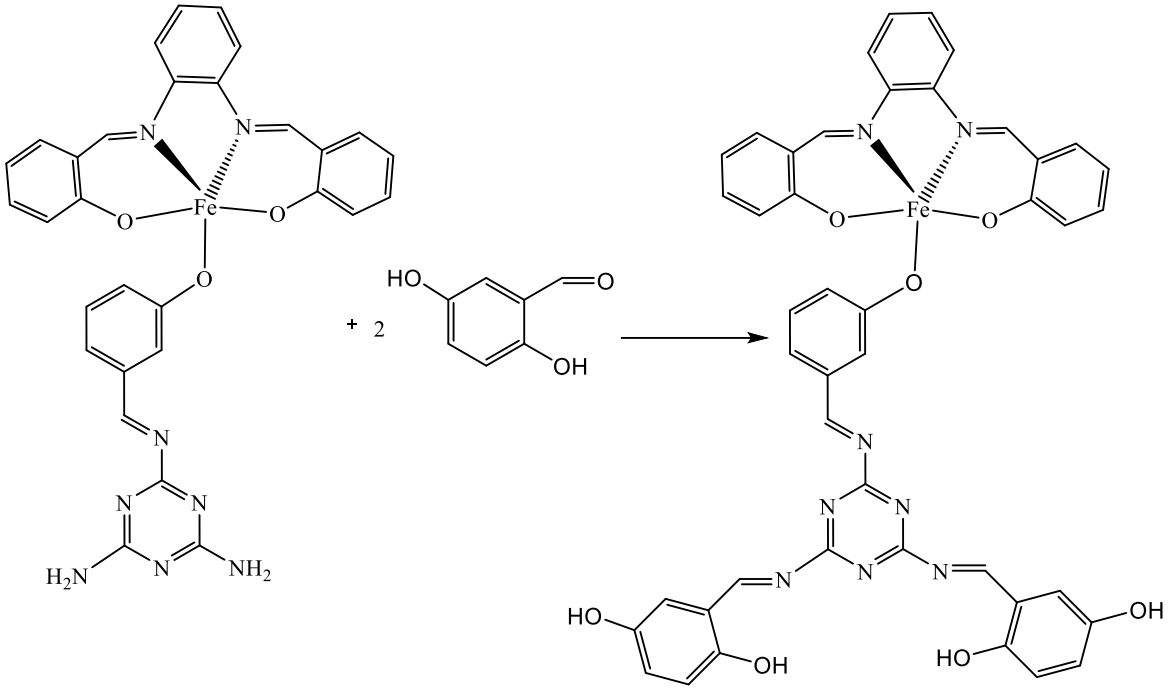

Figure 4. Tripodal Schiff base ligand [Fe(salophen)(DTMPDHB] complex

Tripodal Schiff Base Ligand [Fe_2(salophen)(DTMPDHB)] Complex

Suspension of [Fe(salophen)(DTMPDHB] ligand complexes (1 mmol 0.85 g) in 20 mL of ethanol was prepared in a 100 mL flask on $FeCl_3$ (1 mmol 0.16 g) were added in 20 mL ethanol. boil under a back cooler for 3 h at around 80 °C. The solvent was evaporated by half and allowed to cool (under room conditions). Then, half of the water was added, left for a day, filtered in a vacuum, washed with water and dried in an oven at 105 °C. [Fe_2(salophen)(DTMPDHB)]: FT-IR (cm^{-1}) 1666,1634, (C=N), 1543.

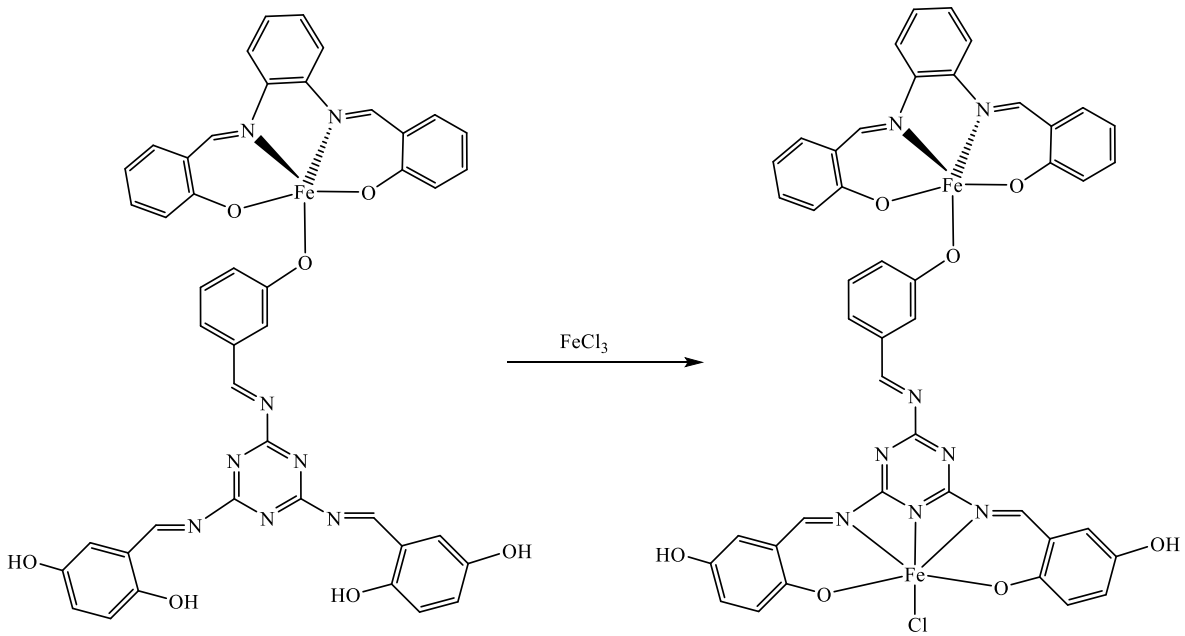

Figure 5. Tripodal Schiff base ligand [Fe_2(salophen)(DTMPDHB)] complex

Results and Discussion

In this study, melamine Schiff base monomer 3-((4,6-diamino-1,3,5-triazine-2-imino)methyl)phenol (DTMP) was synthesized by the reaction of Melamine and 3-hydroxybenzaldehyde [HB], which was used as the output material. A single oxygen-coordinated bridged monomer complex obtained with the synthesized (DTMP) and [Fe(salophen)Cl] complex was obtained [Fe(salophen)(DTMP)] complexes are 2,5-dihydroxybenzaldehyde Schiff base melamine complexes [Fe_2(salophen)(DTMPDHB)] were obtained. ^{1}H NMR spectrum of the monomer ligand (DTMP) observed a corresponding OH protons in the singlet chemical shift value of 10.64 ppm. In addition, aromatic CH was observed to be 8.55/7.83-6.88 ppm and 9.71 ppm respectively at CH=N singlet chemical shift.(Tahmassebi & Sasaki, 1998).

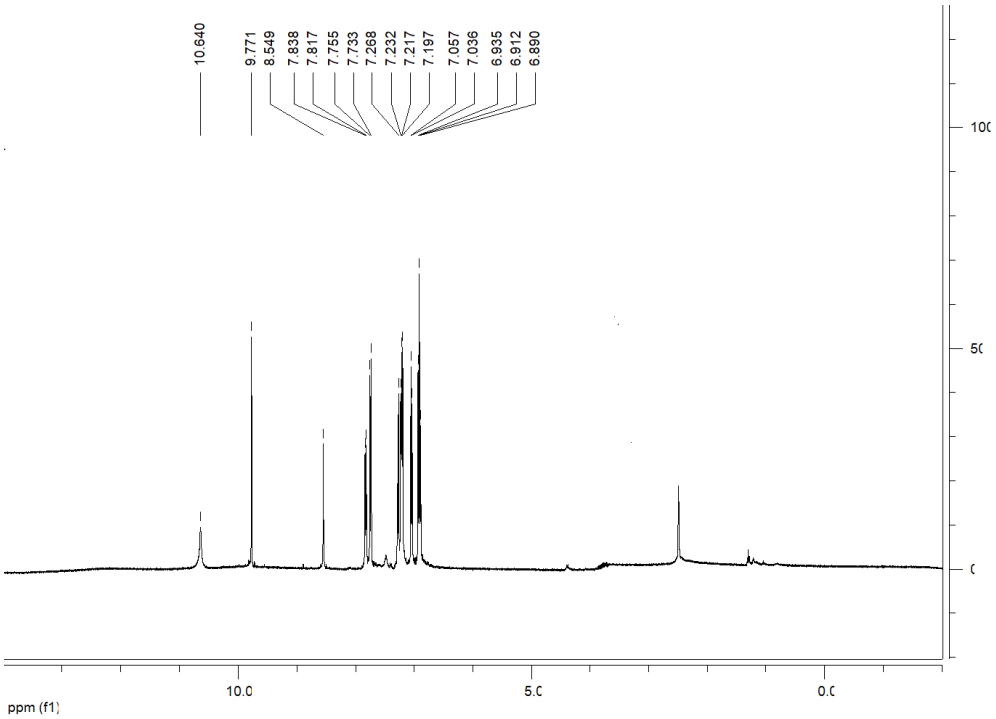

Scheme 1. ^{1}H NMR spectrum of the monomer ligand (DTMP)

FT-IR spectra of the compounds were obtained. The obtained monomer ligand and their FT-IR spectral data of the Fe(III) complex are given in the experimental section. When we examine these values, OH peaks, which were not found in the input materials of the monomer ligand, were observed as OH 3167 cm^{-1} because of the condensation reaction with 3-hydroxybenzaldehyde, as well as a new peak of OH 3167 cm^{-1} in the C = N group 1649 cm^{-1}. In addition, amine vibrations seen in the complexes of the monomer ligand at 3467 and 3414 cm^{-1} were synthesized using the literature and it was observed that the OH peaks of the bridged compounds coordinated with a single oxygen were lost. In Salophen complexes, M-O and M-N bonds were also observed at 760-830 cm^{-1} and 753-685cm^{-1}, respectively (Koc & Ucan, 2007).

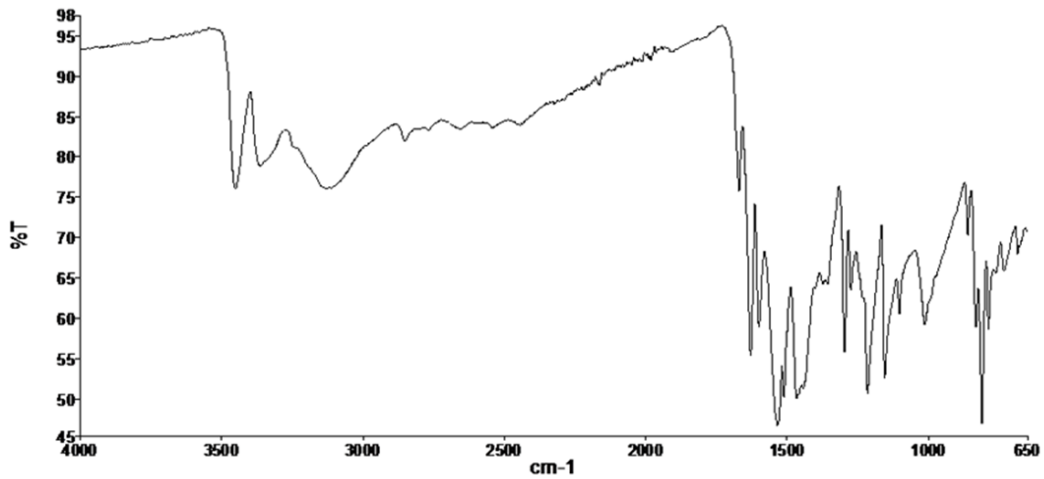

Scheme 2. FTIR spectrum of the monomer ligand (DTMP)

The synthesized (DTMP) and Fe(III) complex [Fe(salophen)(DTMP)], [Fe(salophen)(DTMPDHB] and [Fe_2(salophen)(DTMPDHB)] obtained compounds were observed in $t_{2g}^3e_g^2$, with weak field effects for BM values of 5.27/5.30/5.05, respectively. As a result, it was estimated that it had a triangular pyramidal (dsp^3) geometric structure because it showed a weak field complex feature. As a result, since the complex structure has a theoretically calculated d^5 electron configuration and shows weak ligand properties, it is estimated that it has a triangular bipyramid geometry in sp^3d hybridization (Table 1.) (Koc & Ucan, 2008).

Table 1. Physical properties of monopodal, tripodal and metal complexes

Compounds	**Color**	**Yield (%)**	**M.P. (°C)**	**μ_{eff}**	**Found (Calculated) (%)**		
					C	**H**	**N**
(DTMP)	White	80	183	-	53.17 (52.17)	4.75 (4.38)	36.48 (36.50)
[Fe(salophen)(DTMP)]	Black	75	160	5.27	60.49 (60.60)	4.38 (4.27)	18.33 (18.24)
[Fe(salophen)(DTMPDHB]	Orange	65	300*	5.30	63.75 (63.24)	4.05 (4.01)	13.65 (13.11)
[Fe_2(salophen)(DTMPDHB)]	Yellow	60	300*	5.05	57.47 (57.26)	3.66 (3.42)	11.78 (11.87)

* Decomposition

Conclusion

In this study, Melamine was used as the starting material. Melamine reacted with the addition of 2,5-dihydroxybenzaldehyde in the presence of 1,4-dioxane to obtain 3-((4,6-Diamino-1,3,5-triazine-2-imino)methyl) phenol (DTMP) complexation was carried out with the obtained [Fe(salophen)(DTMP)], anhydrous $FeCl_3$. In addition, Melamine reacts with 2,5-dihidroxybenzaldehyde was [Fe(salophen)(DTMPDHB] obtained. Schiff base compounds with different donor groups were synthesized by the condensation of these aldehyde and amine group molecules. Its bidirectional [Fe_2(salophen)(DTMPDHB)]by hydroxyl groups.

Recommendations

The introductory substances used in this study are ligands and complexes that are newly studied and not encountered in literature. We think that the obtained ligands and complexes will gain importance especially in terms of environmental chemistry. In addition, in our studies that progress as molecular magnetic materials due to their magnetic properties, new and more usable properties will be examined by focusing more on this issue.

Scientific Ethics Declaration

*The author declares that the scientific ethical and legal responsibility of this article published in EPSTEM journal belongs to the author.

Conflict of Interest

*The author declares that there is no conflict of interest related to this work.

Funding

* This research received no specific grant from any funding agency in the public, commercial, or not-for-profit sectors.

Acknowledgements or Notes

*This article was presented as a oral presentation at 5th International Conference on Basic Sciences and Technology (www.icbast.net/) held in Budapest, Hungary on August 28-31, 2025, in Obuda University,

References

Arslaner, C., Karakurt, S., & Koc, Z. E. (2017). Synthesis of benzimidazole Schiff base derivatives and cytotoxic effects on colon and cervix cancer cell lines. *Biointerface Research in Applied Chemistry*, *7*(4), 2103-2107

Celik, S. C., Vatansev, H., & Koc, Z. E. (2019). Benzimidazole schiff bases microwave assisted synthesis and the effect on leukemia cells with flow cytometry. *Revue Roumaine De Chimie*, *64*(7), 615-623.

Celikbilek, S., & Koc, Z. E. (2014). Investigation of dipodal oxy-schiff base and its salophen and salophen Fe(III)/Cr(III)/Mn(III) Schiff bases (N2O2) caped complexes and their magnetic and thermal behaviors. *Journal of Molecular Structure*, *1065*, 205-209.

Dhar, D. N., & Taploo, C. L. (1982). Schiff-bases and their applications. *Journal of Scientific & Industrial Research*, *41*(8), 501-506.

Diaz-Ortiz, A., de la Hoz, A., Prieto, P., Carrillo, J. R., Moreno, A., & Neunhoeffer, H. (2001). Diels-Alder cycloaddition of 4,6-dimethyl-1,2,3-triazine with enamines, or their precursors, under microwave irradiation. *Synlett,* (2), 236-237.

Gembicky, M., Boca, R., & Renz, F. (2000). A heptanuclear Fe(II)-Fe(III)(6) system with twelve unpaired electrons. *Inorganic Chemistry Communications*, *3*(11), 662-665.

Hao, M., Gao, P. Z., Liu, W., Fang, B. Z., Liang, J. S., Zhang, T. T., Ding, Y. P., Zhang, H., & Wang, F. (2021). Microwave hydrothermal-reduction synthesis of zanthoxylum trunk-like Co/CoAl2O4/sepiolite nanocomposite. *Ceramics International*, *47*(4), 4722-4728.

Jayabalakrishnan, C., Karvembu, R., & Natarajan, K. (2002). Catalytic and antimicrobial activities of new ruthenium(II) unsymmetrical Schiff base complexes. *Transition Metal Chemistry*, *27*(7), 790-794.

Koc, Z. E. (2011). Complexes of iron(III) and chromium(III) Salophen and salophen schiff bases with bridging 1,3,5-triazine derived multidirectional ligands. *Journal of Heterocyclic Chemistry*, *48*(4), 769-775.

Koc, Z. E., & Ucan, H. I. (2007). Complexes of iron(III) salophen and saloph Schiff bases with bridging 2,4,6-tris(2,5dicarboxyphenylimino-4-formylphenoxy)-1,3,5-triazine and 2,4,6-tris(4-carboxyphenylimino-4'-formylphenoxy)-1,3,5-triazine. *Transition Metal Chemistry*, *32*(5), 597-602.

Koc, Z. E., & Ucan, H. I. (2008). Complexes of iron(III) and chrom(III) salophen and saloph Schiff bases with bridging 2,4,6-tris(4-nitrophenylimino-4'-formylphenoxy)-1,3,5-triazine. *Journal of Macromolecular Science Part a-Pure and Applied Chemistry*, *45*(12), 1074-1079.

Koc, Z. E., & Uysal, A. (2016). Investigation of novel monopodal and dipodal oxy-Schiff base triazine from cyanuric chloride: Structural and antimicrobial studies. *Journal of Macromolecular Science Part a-Pure and Applied Chemistry*, *53*(2), 111-115.

Koc, Z. E., & Uysal, S. (2010). Synthesis and characterization of dendrimeric bridged salophen/saloph complexes and ınvestigation of their magnetic and thermal behaviors. *Helvetica Chimica Acta*, *93*(5), 910-919.

Koc, Z. E., & Uysal, S. (2011). Synthesis and characterization of tripodal oxy-Schiff base (2,4,6-Tris(4-Carboxymethylenephenylimino-4 '-formylphenoxy)-1,3,5-triazine) and the thermal and magnetic properties of its Fe(III)/Cr(III) complexes. *Journal of Inorganic and Organometallic Polymers and Materials*, *21*(3), 400-406.

Kocyigit, O., Kursunlu, A. N., & Guler, E. (2010). Complexation properties and synthesis of a novel Schiff base with triphenylene nucleus. *Journal of Hazardous Materials*, *183*(1-3), 334-340.

Kopel, P., Sindelar, Z., Biler, M., & Klicka, R. (1998). Complexes of iron(III) salophen and saloph Schiff bases bridged by dicarboxylic acids. *Polish Journal of Chemistry*, *72*(9), 2060-2066.

Kopel, P., Sindelar, Z., & Klicka, R. (1998). Complexes of iron(III) salophen and saloph Schiff bases with bridging dicarboxylic and tricarboxylic acids. *Transition Metal Chemistry*, *23*(2), 139-142.

Li, J., Karjule, N., Qin, J., Wang, Y., Barrio, J., & Shalom, M. (2021). Low-temperature synthesis of solution processable carbon nitride polymers. *Molecules*, *26*(6), 1646.

Naz, N., Khatoon, S., Ajaz, H., Sadiq, Z., & Iqbal, M. Z. (2013). Synthesis, spectral characterization and biological evaluation of Schiff base transition metal complexes derived from ampicillin with d-glucose. *Asian Journal of Chemistry*, *25*(4), 2239-2242.

Nozha, S. G., Morgan, S. M., Abu Ahmed, S. E., El-Mogazy, M. A., Diab, M. A., El-Sonbati, A. Z., & Abou-Dobara, M. I. (2021). Polymer complexes. LXXIV. Synthesis, characterization and antimicrobial activity studies of polymer complexes of some transition metals with bis-bidentate Schiff base. *Journal of Molecular Structure*, *1227*.

Portalone, G. (2008). Acetoguanamine N,N-dimethylformamide solvate. *Acta Crystallographica Section E-Structure Reports Online*, *64*, O1685-U1291.

Qian, H. F., & Huang, W. (2010). 2,4-Diamino-6-methyl-1,3,5-triazin-1-ium chloride. *Acta Crystallographica Section E-Structure Reports Online*, *66*, O759-U1718.

Schiff, H. (1869). Untersuchungen über salicinderivate. *Justus Liebigs Annalen der Chemie*, *150*(2), 193-200.

Sindhu, Y., Athira, C. J., Sujamol, M. S., Joseyphus, R. S., & Mohanan, K. (2013). Synthesis, characterization, dna cleavage, and antimicrobial studies of some transition metal complexes with a novel Schiff base derived from 2-aminopyrimidine. *Synthesis and Reactivity in Inorganic Metal-Organic and Nano-Metal Chemistry*, *43*(3), 226-236.

Tahmassebi, D. C., & Sasaki, T. (1998). Synthesis of a three-helix bundle protein by reductive amination. *Journal of Organic Chemistry*, *63*(3), 728-731.

Thamer Abd Rehan, A. s., Ahmad Rahman Salih. (2024). Synthesis and characterization of triazine derivatives as ımportant heterocyclic compounds and study their biological activities. *International Journal of Innovative Science and Research Technology*, *9*(8), 2273-2277.

Uysal, S., & Koc, Z. E. (2010). Synthesis and characterization of dendrimeric melamine cored [salophen/salophFe(III)] and [sale n/salophCr(III)] capped complexes and their magnetic behaviors. *Journal of Hazardous Materials*, *175*(1-3), 532-539.

Uysal, S., Koc, Z. E., Celikbilek, S., & Ucan, H. I. (2012). Synthesis of star-shaped macromolecular Schiff base complexes having melamine cores and their magnetic and thermal behaviors. *Synthetic Communications*, *42*(7), 1033-1044.

Yu, Q., Schwidom, D., Exner, A., & Carlsen, P. (2008). Synthesis of novel homo-n-nucleoside analogs composed of a homo-1,4-dioxane sugar analog and substituted 1,3,5-triazine base equivalents. *Molecules*, *13*(12), 3092-3106.

Zabardasti, A., & Shangaie, S. A. (2016). Synthesis, characterization, spectroscopic and catalytic oxidation studies of Fe(III), Ni(II), Co(III), V(IV) and U(VI) Schiff base complexes with N, O donor ligands derived from 2,3-diaminopyridine. *Journal of the Iranian Chemical Society*, *13*(10), 1875-1886.

Zhang, K., Huang, Y., Shen, Y. J., Zhang, L. F., Ma, S., Chen, T. T., Zheng, Z. Q., Zhang, S. S., & Li, B. X. (2021). Imine bond transformation of a dynamic Sm(III) macrocycle-based chemosensor: The indirect approach for detecting cyanuric chloride. *Analytica Chimica Acta*, *1144*, 34-42.

Author(s) Information

Ziya Erdem Koc
Faculty of Science, Department of Chemistry,
Selcuk University, 42130-Konya, Türkiye
Contact e-mail: *zek.42@hotmail.com*

To cite this article:

Koc, Z. E. (2025). The synthesis of microwave assisted melamine-Schiff bases and investigatıon of bridged Fe(III) metal complexes. *The Eurasia Proceedings of Science, Technology, Engineering and Mathematics (EPSTEM), 36,* 166-173.

The Eurasia Proceedings of Science, Technology, Engineering & Mathematics (EPSTEM)
ISSN: 2602-3199

The Eurasia Proceedings of Science, Technology, Engineering and Mathematics (EPSTEM), 2025

Volume 36, Pages 174-182

ICBAST 2025: International Conference on Basic Sciences and Technology

Quantifying Uncertainty in Projected Temporal Variations of Reservoir Releases for Crop Water Requirement

Zeynep Beril Ersoy
Balikesir University
Dokuz Eylul University

Okan Fistikoglu
Dokuz Eylul University

Umut Okkan
Balikesir University

Abstract: Climate change brings about significant uncertainties in reservoir operation and agricultural water management. This study aims to assess the temporal variability and associated uncertainties in reservoir release projections to meet the agricultural water demand for maize in the Beydag Reservoir, located in İzmir, Türkiye. Agricultural water demand was estimated based on the FAO Penman-Monteith potential evapotranspiration method, employing crop-specific coefficients for maize. Reservoir operation was carried out by means of the Standard Operating Policy (SOP). Future runoff projections were derived from a 140-member ensemble constructed by combining five general circulation models (GCMs), two emission scenarios (RCP4.5 and RCP8.5), two downscaling methods (statistical and dynamical), and seven calibrated hydrological models. Using these projections, annual reservoir releases under SOP were simulated and evaluated in terms of anomalies relative to a historical baseline. Uncertainty analysis based on variance decomposition revealed that GCMs exert a rather dominant influence on total projection uncertainty in reservoir releases. Moreover, the SOP approach demonstrated limited responsiveness to the increasing temporal variability imposed by climate change because it prioritizes meeting current demand without reserving water for future use. The results emphasize the critical need to consider uncertainty assessments for the planning of water-sensitive cropping strategies such as maize cultivation.

Keywords: Reservoir operation, Agricultural water management, Standard operating policy, Beydag reservoir

Introduction

In recent decades, climate change has increasingly emerged as a major challenge for water resources management. Rising air temperatures, altered precipitation regimes, and the greater frequency of extreme events such as droughts and floods have already begun to reshape hydrological systems worldwide. According to the IPCC Sixth Assessment Report (2021), these impacts are especially pronounced in semi-arid and Mediterranean-type climates, where water availability is already under stress. These conditions directly influence reservoir management, as the long-standing assumption of hydrological stationarity can no longer be considered valid. Reservoirs that were originally designed and operated on the basis of historical inflows are now confronted with greater variability and uncertainty, which significantly constrains their capacity to satisfy multiple and often competing water demands (Raje & Mujumdar, 2010).

The Standard Operating Policy (SOP) is often used as a benchmark in reservoir studies due to its straightforward structure, which allocates available inflows to meet current demands without explicit provision for future

- Selection and peer-review under responsibility of the Organizing Committee of the Conference

shortages. Owing to this simplicity, SOP is frequently taken as a reference in reservoir operation studies and compared against more advanced alternatives such as hedging strategies, dynamic rule curves, or optimization-based approaches (Ashofteh et al., 2013; Hakami-Kermani et al., 2020). However, although SOP may provide acceptable performance under stationary inflows, several studies have indicated that its rigid nature becomes inadequate under increased variability, resulting in reduced reliability and greater vulnerability during extended droughts (Ashofteh et al., 2013; Hakami-Kermani et al., 2020).

Agriculture, which consumes nearly 70% of global freshwater withdrawals (FAO, 2021), is highly exposed to the effects of climate change. Changes in climate tend to place more pressure on irrigation over time. Recent studies of semi-arid basins show irrigation demand rising by about 10% in some cases (Hakami-Kermani et al., 2020) and close to 40% in others, depending on crop pattern and scenario (Golfam et al., 2025). In regions such as Iran, wheat, maize, and alfalfa are projected to require considerably more irrigation under future climates (Ashofteh et al., 2013; Ashofteh et al., 2015). Comparable challenges are already evident in western Türkiye, where agriculture accounts for the largest share of water use. Among major crops, maize is especially sensitive to water shortages. Both experimental and modeling studies confirm that irrigation deficits during critical stages—particularly flowering and grain filling-can cut yields by 30–50% or more (Meza et al., 2008; Kim & Lee, 2023). Even short interruptions in irrigation may translate into substantial economic losses. This makes dependable reservoir releases essential to sustain maize production under warmer and drier conditions.

Projecting how reservoirs will perform under future conditions is complicated by multiple sources of uncertainty. Among them, differences across general circulation models (GCMs) usually dominate, often exceeding the effects of emission scenarios or the choice of hydrological model (Her et al., 2019; Nkomozepi & Chung, 2012). Additional variation is introduced through downscaling methods, while natural climate variability makes long-term planning even more difficult. Previous ensemble-based studies have shown that these layers of uncertainty directly influence key performance measures such as reliability, resilience, and vulnerability (Ashofteh et al., 2013; Ashofteh et al., 2015).

This study focuses on the Beydag Reservoir in western Türkiye to provide such an assessment. The analysis has two main objectives: (i) evaluating temporal anomalies in reservoir releases for maize irrigation under SOP relative to a historical baseline, and (ii) quantifying the contributions of GCMs, emission scenarios, downscaling approaches, and hydrological models for projection uncertainty through variance decomposition. The study offers a basis for understanding how SOP performs under changing inflow conditions and emphasizes the importance of incorporating uncertainty into planning to ensure reliable irrigation for water-intensive crops such as maize.

Data Used

Study Region and Observed Data

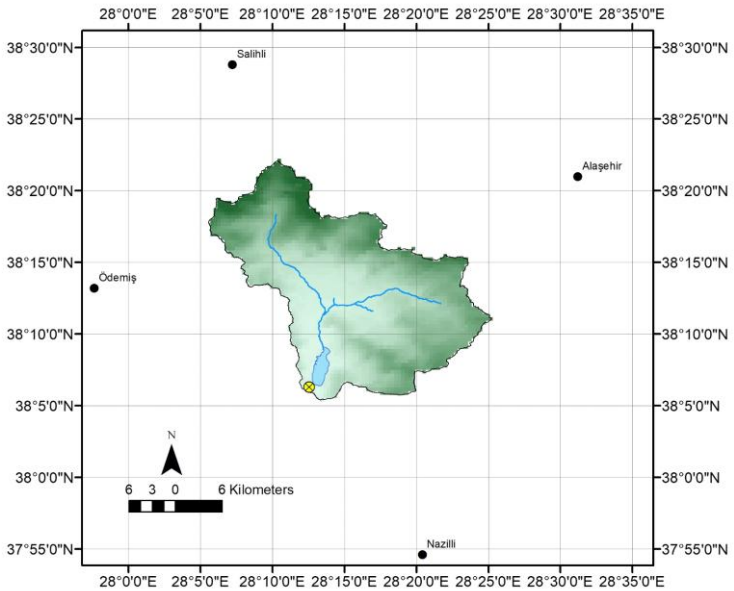

Figure 1. Location and drainage area of the Beydag Reservoir catchment.

The Beydag watershed, covering about 445 km², lies in the Kucuk Menderes Basin of western Türkiye and was selected as the study area. The basin hosts the Beydag Reservoir, a structure with nearly 243 Mm³ of active storage capacity that ensures irrigation supply. Maize stands out as the principal crop within the irrigation scheme, shaping both the seasonal demand pattern and the overall reservoir operation.

To reflect natural conditions, streamflow records from 1987 to 1999 were combined with reservoir characteristics, including storage–area curves supplied by the State Hydraulic Works. During this period, the watershed received an average of 485 mm of annual precipitation, while mean temperature was about 16 °C. Runoff was limited to roughly 95 mm per year-around one-fifth of the precipitation-indicating the semi-arid climate and the water-stressed character of the basin (Ersoy et al., 2025a).

Local Projected Climate Data

Future hydro-climatic conditions in the Beydag watershed were examined through a modeling framework that incorporated five global climate models (GCMs), two emission scenarios (RCP4.5 and RCP8.5), and both statistical and dynamical downscaling approaches. When combined with seven lumped hydrological models, this chain produced 140 alternative runoff projections (Ersoy et al., 2025b). These data were then formed the basis for analysis under SOP.

For the dynamical simulations, climate data were compiled from the CORDEX–MENA archive, covering the baseline period 1981–2005 together with four projection horizons: 2021–2039, 2040–2059, 2060–2079, and 2080–2099. Outputs from five GCMs (CNRM-CM5, GFDL-ESM2M, EC-EARTH, HadGEM2-ES, and MPI-ESM-MR) were available for both RCP4.5 and RCP8.5. Bias adjustment was conducted using the quantile delta mapping (QDM) method, which ensures the preservation of relative changes. According to the corrected CORDEX results, precipitation anomalies under RCP4.5 were generally negligible, whereas under RCP8.5 certain members, such as GFDL-CRX and EC-EARTH-CRX, indicated substantial reductions after the 2060s. Conversely, HadGEM-CRX suggested increases in late-century precipitation. Temperature projections displayed a consistent warming pattern across all models, with end-of-century anomalies between 1.0–2.0 °C for RCP4.5 and 3.4–6.9 °C for RCP8.5. HadGEM-CRX produced the strongest warming, in line with earlier findings over the MENA domain (Ozturk et al., 2021).

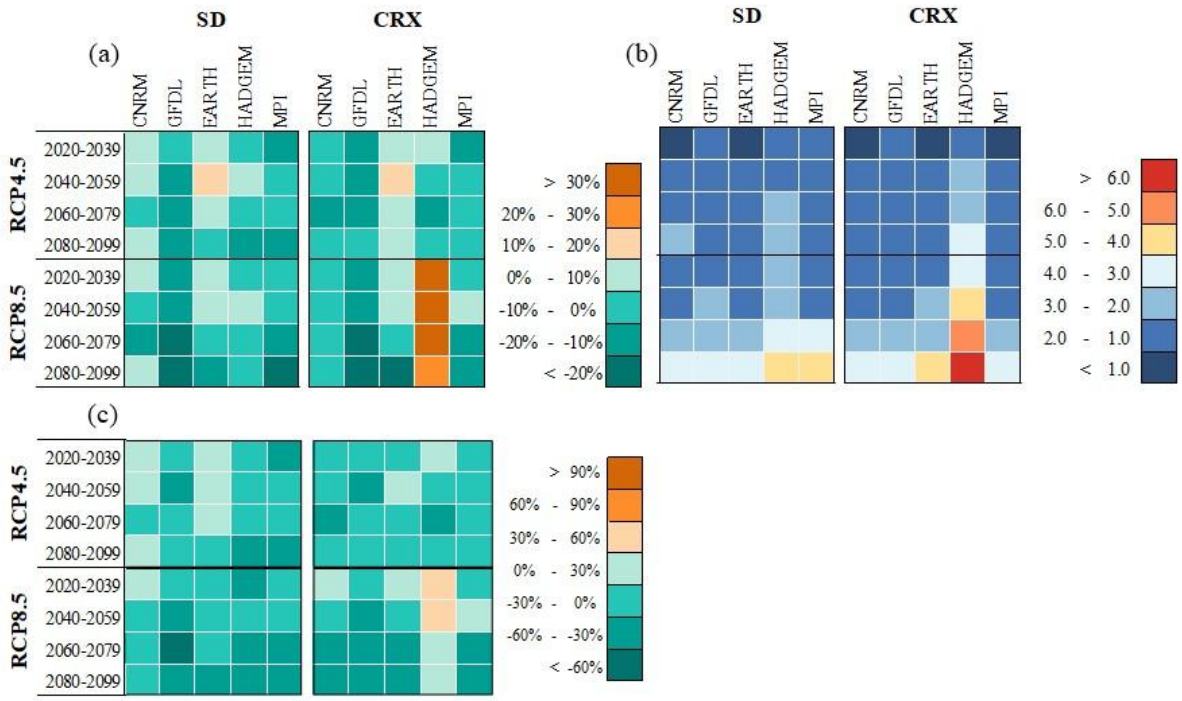

Figure 2. Hydroclimatic anomalies in the Beydag basin under RCP4.5 and RCP8.5 scenarios for five GCMs and two downscaling methods: (a) precipitation (%), (b) temperature (°C), (c) streamflow (%).

Statistical downscaling relied on radial basis function networks (RBFNs), where predictor variables were selected through the LASSO method. Model evaluation showed reliable skill, as NSE values exceeded 0.75 in both

calibration and validation. The resulting data were bias corrected with QDM before analysis. The precipitation signals obtained were broadly aligned with those from CORDEX, showing only minor deviations. For temperature, HadGEM-SD indicated stronger warming under RCP8.5 compared with most models, although its anomalies were still 1.5–2.5 °C lower than HadGEM-CRX. This pattern suggests that part of the amplified signal in CORDEX outputs may originate from RCM parameterization effects (García-Díez et al., 2015). Overall, both downscaling approaches pointed to robust warming, whereas precipitation projections remained more uncertain and largely governed by GCM selection.

Ensemble of Hydrological Projections

Seven lumped rainfall–runoff models (abcde, AWBM, Dynwbm, Gr2m, Guo, Témez, and Twbm) formed the hydrological basis of this study. These models had been calibrated through global optimization techniques and assessed in earlier applications (Ersoy et al., 2025a). Their structure requires only monthly precipitation and potential evapotranspiration inputs. Calibration and validation tests yielded NSE scores mostly above 0.65, a range commonly regarded as good to very good. Nonetheless, the relatively short span of naturalized streamflow observations limited their ability to fully capture long-term variability.

Based on these models, 140 runoff projection members were produced, and their twenty-year mean changes (ΔQ) were evaluated against the historical reference. For clarity, Figure 2c presents the ensemble mean across the seven hydrological models. The analysis showed that runoff was highly sensitive: even minor declines in rainfall resulted in considerable decreases in ΔQ. Under RCP8.5, severe drying signals from GFDL led to reductions of 33–74% after 2060. In contrast, HadGEM-CRX produced wetter outcomes in line with its precipitation anomalies, while HadGEM-SD indicated more moderate declines of about −18% to −38%. Among the ensemble, GFDL generated the largest share of statistically significant declines. MPI showed notable changes in almost two-thirds of its projections, whereas CNRM produced significant reductions in roughly 40% of its variants. Overall, the analysis shows that the behavior of runoff projections is largely shaped by the choice of GCMs, RCPs, and HMs, consistent with the inferences of Wang et al. (2020).

Method

Estimate of Water Demand Volume in Reservoir Downstream

Agricultural water demand was estimated through the net water requirement (WR), which is defined as the difference between monthly crop evapotranspiration (Etc) and effective precipitation (Peff).
Crop evapotranspiration was estimated by the following equation:

$$ETc_t = Kc_t \times ETo_t \tag{1}$$

where Kc_t denotes the crop coefficient specific to maize, and ETo_t represents the reference evapotranspiration. Reference evapotranspiration (ETo) could not be directly estimated using the Penman–Monteith (P–M) equation due to data limitations. Instead, the Hargreaves–Samani (H–S) equation was applied, after calibrating its parameters with observed P–M estimates. Calibration with observations from the 1996–2006 period yielded a Nash–Sutcliffe efficiency (NSE) greater than 0.95. This approach was subsequently adopted, together with both CORDEX and statistically downscaled GCM temperature projections, as the basis for deriving PET projections.
Effective precipitation (Peff) was calculated from monthly total precipitation (P) using the SCS method:

$$Peff_t = \begin{cases} \frac{P_t}{125}(125 - 0.2P_t), & P_t \leq 250\ mm \\ 125 + 0.1P_t, & P_t \leq 250\ mm \end{cases} \tag{2}$$

Subsequently, the net water requirement was derived from the following equation:

$$WR_t = ETc_t - Peff_t \tag{3}$$

At the final stage, the calculated WR values were multiplied by the irrigated area (A) to derive the monthly volumetric water demand (Vt):

$$V_t = WR_t \times A \tag{4}$$

Reservoir Operation Policy

One of the most fundamental methods used in reservoir operation is the Standard Operating Policy (SOP). The main principle of this approach is to fully meet the demand of the current period. The water stored in the reservoir is released together with the inflow directly to meet the agricultural demand, without any restriction or conservation for subsequent periods. The mathematical formulation of SOP relies on the principle of mass conservation. The reservoir water budget can be expressed as follows:

$$V_{t+1} = V_t + Q_t - RLS_t - E_t \tag{5}$$

where V_t is the reservoir storage, Q_t is the inflow during period t, RLS_t is the reservoir release for month index t, and E_t is the evaporation loss. The operation constraints are defined as follows:

$$0 \leq RLS_t \leq D_t, \qquad V_{min} \leq V_t \leq V_{mak} \tag{6}$$

where D_t is the agricultural water demand, and V_{min} and V_{mak} are the minimum and maximum storage capacities of the reservoir. In the SOP approach, the release rule is given as:

$$RLS_t = \min\left(D_t, V_t + Q_t - E_t\right) \tag{7}$$

Accordingly, in each period the water demand is satisfied by considering the available storage together with the inflow. If the demand can be fully met, then $RLS_t = D_t$; otherwise, the release is limited to the maximum amount permitted by the available storage and inflow. In this study, streamflow projections for the Beydag Reservoir were operated under the SOP approach, and the monthly releases (RLS) were computed. The resulting values were then evaluated relative to the historical period to assess future changes.

Uncertainty Analysis

In this study, Variance Decomposition Analysis (VDA) was applied to evaluate the uncertainties in future reservoir release projections. The method considered four key components of the modeling chain: emission scenario (RCP), global climate model (GCM), downscaling method (DM), and hydrological model (HM). Each of these factors was examined using a 140-member ensemble generated from the combination of 5 GCMs × 2 RCPs × 2 DMs × 7 HMs, thereby quantifying the relative contributions of each factor and their interactions to the total uncertainty. The analyses were conducted separately for four future periods (2021–2039, 2040–2059, 2060–2079, 2080–2099) with respect to the historical baseline.

Results and Discussion

Changes in Reservoir Releases

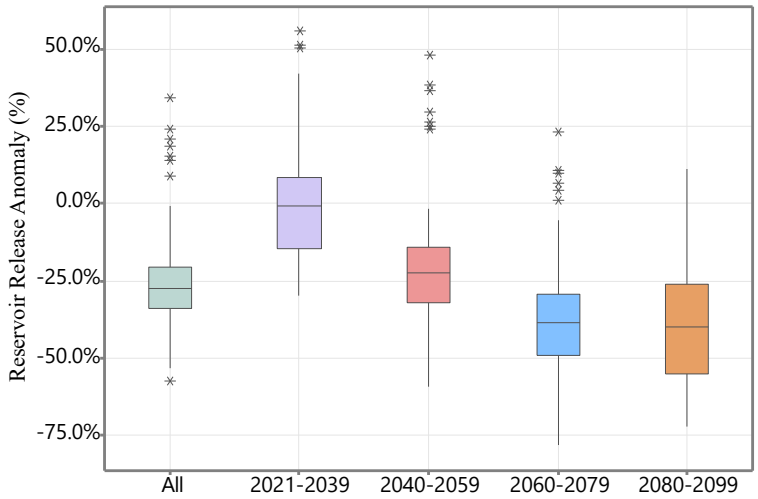

Figure 3. Periodic distributions of changes (%) in reservoir releases under SOP (2021–2039, 2040–2059, 2060–2079, 2080–2099) and for the entire projection period.

Reservoir releases (RLS) from the Beydag Dam under the Standard Operating Policy (SOP) exhibit clear fluctuations throughout the 2021–2099 period relative to the reference baseline. As illustrated in Figure 3, the long-term averages point to a generally declining trend, with some projections indicating reductions of more than 25% and, in the most extreme cases, losses reaching up to 75%. Nevertheless, a few GCMs projected positive anomalies, indicating that under certain conditions RLS could increase.

From a temporal perspective, changes were rather modest in 2021–2039, with some GCMs suggesting minor increases while others indicated slight decreases (Figure 4). The decline became more pronounced during 2040–2059, approaching nearly 25%. From 2060–2079, negative variations continued further while the range in between GCMs increased. By 2080–2099, the most severe reductions were projected, with some models estimating decreases in reservoir releases of up to 75%.

GCM-based results further clarify the direction and magnitude of RLS anomalies. The HadGEM projected comparatively strong increases in precipitation and runoff for the Beydag basin (Ersoy et al., 2025b), which explains the positive outliers in RLS. In contrast, the GFDL yielded the most pessimistic results, indicating streamflow declines of 33–74% and corresponding RLS reductions of up to 75%. MPI tended to project decreases, whereas CNRM suggested more moderate shifts with limited variation

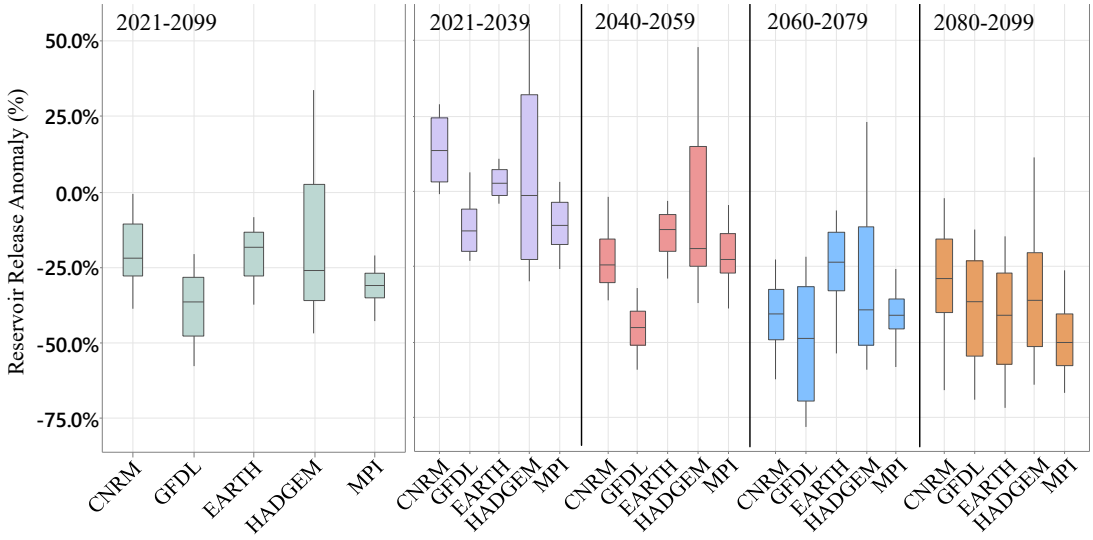

Figure 4. Boxplots of percentage changes in reservoir releases under SOP across five GCMs

These findings suggest that variations in RLS are primarily shaped by projected streamflow changes, along with the added demand pressure from rising temperatures. Under the RCP8.5 scenario, especially during 2080–2099, temperature increases of +3.4 to +6.9 °C are expected to boost evapotranspiration and, in turn, agricultural water demand. As a result, even when flow conditions remain comparable, the heightened demand places additional downward pressure on RLS. Consequently, the Beydag Reservoir is expected to face a pronounced declining trend shaped by the combined effects of climate change on both supply (streamflow) and demand (temperature/evapotranspiration).

Uncertainty Contributions

ANOVA results, used to identify the main sources of variability in RLS projections, show that the largest share of uncertainty arises from GCM selection. As shown in Figure 5, about one-third (30–40%) of the total variance is linked to the choice of GCM. The contribution of emission scenarios (RCPs) remained more limited (5–10%), while hydrological models (HMs) and downscaling methods (DMs) explained only 1–4%. Yet, interactions between GCMs and RCPs made up around 20–25% of the variance, pointing to the key role of model–scenario combinations in shaping the results. Overall, total interactions (TINT) exceeded 50%, making clear that climate-related factors play the biggest role in driving uncertainty in RLS projections.

The temporal evolution of uncertainties is presented in Table 1. While the influence of GCMs was more pronounced in 2021–2039, GCM–RCP interactions grew steadily after 2040 and reached levels comparable to GCM contributions. The contribution of RCPs also grew considerably in the late period. By contrast, the effects of HM and DM selections remained minor across all periods.

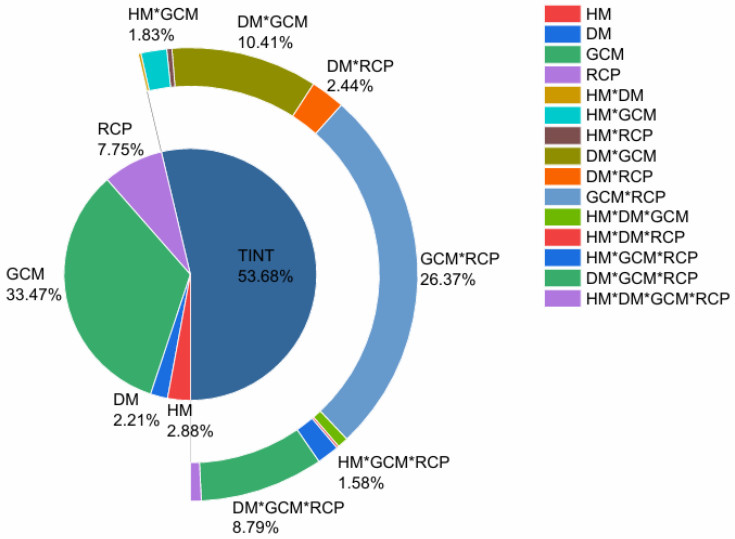

Figure 5. Variance decomposition of reservoir release anomalies (%) under SOP. The inner ring presents the main effects, while the outer ring illustrates the two- and three-way interactions.

Table 1. Variance decomposition (%) of reservoir release anomalies under SOP for four future periods relative to the historical baseline.

	HM	DM	GCM	RCP	GCM*RCP	TINT
2021-2039	4.2%	2.7%	32.9%	5.2%	22.1%	55.0%
2040-2059	1.4%	2.0%	39.3%	6.5%	26.0%	50.8%
2060-2079	3.4%	2.5%	29.7%	9.9%	26.0%	54.5%
2080-2099	2.6%	1.6%	32.0%	9.2%	31.2%	54.5%

The findings show that RLS uncertainties are closely linked to hydroclimatic projections. GCMs stand out as the main source of uncertainty in temperature projections (40–55%), whereas the influence of RCPs becomes more evident by 2080–2099 (Ersoy et al., 2025b). The same tendency is reflected in RLS, where the role of emission scenarios gradually increases in the later periods. Similarly, while GCM–RCP interactions account for 25–30% of the total variance in streamflow projections, their contribution of 20–25% in RLS uncertainties reflects a parallel structure. Hence, RLS uncertainties essentially represent a manifestation of the uncertainties embedded in streamflow and temperature projections: flow-related uncertainties are directly transmitted to RLS, while temperature-driven uncertainties amplify variability in RLS through increased agricultural demand.

Conclusion

In this study, the influence of climate change on reservoir releases for maize irrigation under the Standard Operating Policy (SOP) was assessed. A broad set of hydroclimatic projections was used to capture a wide range of possible futures. The findings show that releases are very sensitive to changing conditions. In the early decades, the impacts remain moderate, but after mid-century the declines become much sharper. Some scenarios even point to reductions exceeding 70% by the end of the century. Such results illustrate the rigid nature of SOP: it can satisfy present demands but offers little room to adjust when inflows vary more strongly. Because maize requires large amounts of water, it is highly vulnerable, and such reductions threaten the sustainability of irrigation.

The uncertainty analysis reveals that global climate models are the leading source of variation in release projections, and their interaction with emission scenarios further amplifies this effect. Although hydrological models and downscaling methods play only a minor role, the dominant effect of climate-related factors shows that uncertainty must be explicitly addressed in future water management. To secure agricultural water supplies, it will be essential to move beyond conventional rules with adaptive strategies that explicitly account for uncertainty.

Scientific Ethics Declaration

*The authors declares that the scientific ethical and legal responsibility of this article published in EPSTEM journal belongs to the authors.

Conflict of Interest

*The authors declare that they have no conflicts of interest

Funding

*This study is funded by the Scientific and Technological Research Council of Türkiye (TÜBİTAK) under Grant No. 122Y083.

Acknowledgements or Notes

*The authors gratefully acknowledge the support provided by TÜBİTAK during the course of this research.

*This article was presented as an oral presentation at the International Conference on Basic Sciences and Technology (www.icbast.net) held in Budapest/Hungary on August 28-31, 2025.

References

Ashofteh, P. S., Haddad, O. B., & A. Mariño, M. (2013). Climate change impact on reservoir performance indexes in agricultural water supply. *Journal of Irrigation and Drainage Engineering*, *139*(2), 85-97.

Ashofteh, P. S., Haddad, O. B., & Marino, M. A. (2015). Risk analysis of water demand for agricultural crops under climate change. *Journal of Hydrologic Engineering*, *20*(4), 04014060.

Ersoy, Z. B., Fistikoglu, O., Okkan, U., & Derin, B. (2025a). Convergence and final performances of optimization algorithms for rainfall-runoff model calibration based on the number of function calls. *Earth Science Informatics*, *18*(2), 1-21.

Ersoy, Z. B., Fistikoglu, O., & Okkan, U. (2025b). Exploring the potential of multi-hydrological model weighting schemes to reduce uncertainty in runoff projections. *Hydrology and Earth System Sciences*, under review

FAO. (2021). *The state of the world's land and water resources for food and agriculture: Systems at breaking point (SOLAW 2021)*. Food and Agriculture Organization of the United Nations.

García-Díez, M., Fernández, J., & Vautard, R. (2015). An RCM multi-physics ensemble over Europe: Multi-variable evaluation to avoid error compensation. *Climate Dynamics*, *45*(11), 3141-3156.

Golfam, P., Ashofteh, P. S., & Singh, V. P. (2025). *Modelling changes in water consumption by agricultural crops under different climate change scenarios*. Irrigation and Drainage.

Hakami-Kermani, A., Babazadeh, H., Porhemmat, J., & Sarai-Tabrizi, M. (2020). An uncertainty assessment of reservoir system performance indices under the climate change effect. *Ain Shams Engineering Journal*, *11*(4), 889-904.

Her, Y., Yoo, S. H., Cho, J., Hwang, S., Jeong, J., & Seong, C. (2019). Uncertainty in hydrological analysis of climate change: multi-parameter vs. multi-GCM ensemble predictions. *Scientific Reports*, *9*(1), 4974.

IPCC. (2021). Climate Change 2021: The physical science basis. In V. Masson-Delmotte, P. Zhai, A. Pirani, S. L. Connors, C. Péan, S. Berger, N. Caud, et al. (Eds.), Contribution *of working group i to the sixth assessment report of the intergovernmental panel on climate change*. Cambridge University Press.

Kim, K. H., & Lee, B. M. (2023). Effects of climate change and drought tolerance on maize growth. *Plants*, *12*(20), 3548.

Meza, F. J., Silva, D., & Vigil, H. (2008). Climate change impacts on irrigated maize in Mediterranean climates: evaluation of double cropping as an emerging adaptation alternative. *Agricultural Systems*, *98*(1), 21-30.

Nkomozepi, T., & Chung, S. O. (2012). Assessing the trends and uncertainty of maize net irrigation water requirement estimated from climate change projections for Zimbabwe. *Agricultural Water Management*, *111*, 60-67.

Ozturk, T., Saygili-Araci, F. S., & Kurnaz, M. L. (2021). Projected changes in extreme temperature and precipitation indices over CORDEX-MENA domain. *Atmosphere*, *12*(5), 622.

Raje, D., & Mujumdar, P. P. (2010). Reservoir performance under uncertainty in hydrologic impacts of climate change. *Advances in Water Resources*, *33*(3), 312-326.

Wang, H. M., Chen, J., Xu, C. Y., Zhang, J., & Chen, H. (2020). A framework to quantify the uncertainty contribution of GCMs over multiple sources in hydrological impacts of climate change. *Earth's Future*, *8*(8), e2020EF001602.

Author(s) Information

Zeynep Beril Ersoy
Balikesir University
Department of Civil Engineering, Hydraulic Division, Türkiye
Dokuz Eylul University
Department of Civil Engineering, The Graduate School of Natural and Applied Sciences, Türkiye
Contact e-mail: *zeynepberil.ersoy@balikesir.edu.tr*

Okan Fistikoglu
Dokuz Eylul University
Department of Civil Engineering, The Graduate School of Natural and Applied Sciences, Türkiye

Umut Okkan
Balikesir University
Department of Civil Engineering, Hydraulic Division, Türkiye

To cite this article:

Ersoy, Z. B., Fistikoglu, O., & Okkan, U. (2025). Quantifying uncertainty in projected temporal variations of reservoir releases for crop water requirement. *The Eurasia Proceedings of Science, Technology, Engineering and Mathematics (EPSTEM), 36,* 174-182.

The Eurasia Proceedings of Science, Technology, Engineering & Mathematics (EPSTEM)
ISSN: 2602-3199

The Eurasia Proceedings of Science, Technology, Engineering and Mathematics (EPSTEM), 2025

Volume 36, Pages 183-191

ICBAST 2025: International Conference on Basic Sciences and Technology

Study of Secondary Metabolites in Georgian Endemic Plant Raw Materials and Processing Residues Using UPLC-PDA-MS Methods

Eteri Margalitadze
Batumi Shota Rustaveli State University

Iamze Kezheradze
Batumi Shota Rustaveli State University

Indira Japaridze
Batumi Shota Rustaveli State University

Maia Vanidze
Batumi Shota Rustaveli State University

Aleko Kalandia
Batumi Shota Rustaveli State University

Abstract: There is increasing interest in natural bioactive compounds for prophylactic and therapeutic use. In Georgia, many endemic plant species remain underexplored with modern analytical methods. This study focused on analyzing the chemical composition of wild *Senecio platyphyllus* and both wild and cultivated forms of *Prunus laurocerasus*, species native to Georgia. Additionally, the research aimed to develop sustainable extraction technologies aligned with circular economy principles-an area largely unaddressed in the region. Classical extraction methods were compared with high-pressure, ultrasound, and supercritical fluid techniques to determine optimal conditions. A key objective was to optimize alkaloid extraction from *S. platyphyllus* and refine both qualitative and quantitative analysis. The resulting protocol reduced extraction time from 30 hours to just 2h. Using UPLC-PDA-MS (ultra-performance liquid chromatography with photodiode array and mass spectrometry), main alkaloids were identified in only 45 minutes through three 15-minute chromatographic runs. This significantly improved analytical speed and accuracy. A phenyl column combined with a 0.1% formic acid–deionized water (A) and acetonitrile (B) gradient system allowed efficient separation of alkaloids and other bioactive compounds. In *P. laurocerasus*, high levels of chlorogenic and neochlorogenic acids, along with cyanide-derived anthocyanins, were detected in both fruit and bark. To promote sustainability, green extraction methods using water–alcohol mixtures under high pressure were developed. These techniques aimed to maximize compound recovery while minimizing environmental harm.Overall, the study provides a modern, efficient approach to analyzing and extracting valuable compounds from Georgian endemic plants while prioritizing environmental sustainability.

Keywords: Senecio platyphyllus, Prunus laurocerasus, UPLC-PDA-MS, Bioactive compounds, Antioxidant activity

Introduction

Prunus laurocerasus (cherry laurel) and *Senecio platyphyllus* (kharishubla) are two endemic for Georgia plant species known for their rich biochemical compositions and medicinal properties. Belonging to the Rosaceae and Asteraceae families, respectively, these plants have been traditionally utilized for various therapeutic

applications. Both species contain a variety of bioactive compounds, such as flavonoids, tannins, alkaloids, and glycosides, which contribute to their pharmacological potential. This review aims to synthesize current research on the phytochemical profiles and pharmacological activities of these plants while using the new "green" extraction methods and reducing the ecological footprint of the extraction process.

Bioactive Compounds Flavonoids and Phenolic Compounds

Flavonoids and phenolic acids are among the most prominent bioactive compounds in P. laurocerasus. Research by Sarker et al. (2013) and Zhang et al. (2019) identified quercetin, kaempferol, catechins, and chlorogenic acid in the plant's leaves, which exhibit significant antioxidant properties. Similarly, S. *platyphyllus* contains sesquiterpenoids, including flavonoids such as cacalols and eremophilanes, which contribute to its anti-inflammatory and antioxidant effects (Brown & Green, 2022; White et al., 2023).

Alkaloids

Both plants contain alkaloids that play a crucial role in their medicinal applications. *P. laurocerasus* is rich in cyanogenic alkaloids, such as laurocerasin and amygdalin, which have demonstrated cytotoxic effects on cancer cells (Akinmoladun et al., 2018; Khan et al., 2021). In contrast, *S. platyphyllus* is known for its pyrrolizidine alkaloids, including platyphylline and seneciphylline, which, while exhibiting pharmacological effects, are also associated with hepatotoxicity (Smith et al., 2020; Jones & Taylor, 2021).

Tannins and Glycosides

P. laurocerasus contains high levels of tannins, which contribute to its antimicrobial and anti-inflammatory properties (Moufid et al., 2020). Additionally, cyanogenic glycosides, such as prunasin, release cyanide upon hydrolysis and have been investigated for their potential anticancer effects (Solomon et al., 2017; Sulaimon et al., 2021).

Pharmacological Properties

Antioxidant Activity

Extracts of *P. laurocerasus* have demonstrated strong antioxidant capabilities, particularly in neutralizing free radicals. A study by Khan et al. (2020) highlighted the plant's potential to mitigate oxidative stress-related diseases, such as cardiovascular and neurodegenerative disorders. Similarly, the terpenes in *S. platyphyllus* contribute to its antioxidant effects, reinforcing its traditional medicinal uses (White et al., 2023).

Anti-inflammatory Effects

The flavonoid and tannin content of *P. laurocerasus* has been linked to its anti-inflammatory properties, particularly in reducing pro-inflammatory markers like IL-6 and TNF-α (Solomon et al., 2018). Likewise, *S. platyphyllus* contains sesquiterpenoids that exhibit anti-inflammatory effects, although further studies are needed to substantiate their efficacy (Brown & Green, 2022).

Antimicrobial and Antiviral Properties

P. laurocerasus has demonstrated antimicrobial activity against various pathogens, including *Staphylococcus aureus* and *Escherichia coli* (Moufid et al., 2020). Furthermore, its extracts have shown potential antiviral effects against the influenza virus (Singh et al., 2019). Although less studied, certain terpenes in *S. platyphyllus* have also been associated with antimicrobial properties (White et al., 2023).

Anticancer Properties

The cytotoxic effects of *P. laurocerasus*, particularly due to amygdalin, have been studied in relation to breast cancer cells (Khan et al., 2021). Conversely, while PAs in S. platyphyllus may exhibit pharmacological effects, their toxic nature limits their potential as anticancer agents without further refinement (Smith et al., 2020). Thus, both *Prunus laurocerasus* and *Senecio platyphyllus* exhibit considerable pharmacological potential, attributable to their rich profiles of bioactive compounds. These species have demonstrated a broad spectrum of biological activities, including antioxidant, anti-inflammatory, antimicrobial, and anticancer effects (Akinmoladun et al., 2018; Brown & Green, 2022).

To fully harness these properties and maximize the yield of bioactive constituents, modern "green" extraction technologies are increasingly employed. These environmentally sustainable methods, which include techniques such as ultrasonic extraction, pressurized hot water extraction, and supercritical fluid extraction, offer enhanced efficiency, reduced solvent usage, and lower environmental impact compared to conventional extraction approaches (Giacometti et al., 2018; Giacometti et al., 2024).

Comparison with Traditional Methods

Modern extraction techniques provide several advantages over conventional methods:

- **Use of safe solvents**: Transition from traditional organic solvents to environmentally benign alternatives such as water, supercritical CO_2, ionic liquids, and deep eutectic solvents (Giacometti et al., 2018).
- **Reduced energy consumption**: Optimization and intensification of extraction processes lead to lower energy usage (Giacometti et al., 2024).
- **Enhanced process safety**: Technologies prioritize the safety of operators and environmental sustainability (Giacometti et al., 2018).

Plant Material and Sample Preparation

The object of this study was the wild-growing Cherry laurel (*P. Laurocerasus)* plant (Pic.1) and its derivatives (fruits, leaves, and processed fruit products), specifically from the varieties known locally as anatsnekhi and pits. Samples were collected from two locations in western Georgia (Adjara region): Erge (41°33'41.0"N, 41°41'48.0"E) and Tkhilnari (41°33'49.0"N, 41°39'11.0"E), Senecio platyphyllus (Pic.2) Khulo region (41° 38' 47" N / 42° 18' 40" E). Following collection, a portion of the samples was immediately stored at −25 °C for future analyses. Another portion of the fresh fruit was directly processed into various preparations. Additional samples were lyophilized and subsequently stored at 4 °C until use.

Picture1. *Prunus laurocerasus*

Picture 2. *Senecio platyphyllus*

Instrumentation and Analytical Methods

The following analytical instruments were employed in the study: a high-performance liquid chromatograph (HPLC) system (Waters, Binary HPLC Pump 1525) equipped with ultraviolet (UV), visible (Vis), and refractive index (RI) detectors, as well as a Waters 432 conductivity detector. Additionally, an ultra-high-performance liquid chromatography (UHPLC) system (Waters Acquity H-Class) was used, coupled with a photodiode array (PDA) detector and a mass spectrometer (QDa detector) for compound identification. For physicochemical measurements, a Mettler Toledo pH/Ion meter S220 and S230 conductivity meter were utilized. Ultraviolet-

visible spectrophotometric analyses were conducted using a Mettler Toledo UV5 UV/Vis scanning spectrophotometer.

Extraction of Samples

Ultrasonic Extraction (USE)

Ultrasonic extraction is based on the mechanical and cavitation effects of ultrasound, which significantly enhance the mass transfer processes involved in extraction. The mechanical effect facilitates the propagation of ultrasonic waves through the medium, causing vibration of particles and improving molecular diffusion and solvent penetration. Cavitation occurs when ultrasonic pressure induces the formation, growth, and collapse of microbubbles in the medium, generating localized high temperatures and pressures that disrupt cell walls and release bioactive compounds into the solvent. This technique accelerates extraction kinetics and improves yield without extensive thermal degradation (Surmanidze et al., 2024).

Pressurized Hot Water Extraction (PHWE)

PHWE utilizes water at elevated temperatures and pressures to maintain it in a liquid state above its atmospheric boiling point, enhancing its solvent properties. Under these conditions, water exhibits altered polarity, allowing it to dissolve a broader range of both polar and nonpolar compounds. PHWE is an environmentally friendly and energy-efficient technique that offers rapid extraction and high-quality yields. However, temperature control is critical, as temperatures exceeding 160 °C may degrade thermolabile compounds, diminishing their antioxidant potential. The use of natural deep eutectic solvents (NADES) as co-solvents can further enhance the extraction of phenolic compounds. Additionally, integration with pulsed electric field (PEF) treatment can improve selectivity and sustainability (Giacometti et al., 2024).

Supercritical Water Extraction (SWE)

Supercritical water extraction involves the use of high pressure to keep water in a liquid state even at elevated temperatures, typically between 50–200 °C. This approach is particularly effective for extracting thermally stable polyphenolic compounds. The principle is based on the relationship between pressure and boiling point; increasing system pressure prevents water from vaporizing at high temperatures, thereby enhancing solubility and diffusivity of target analytes. Water is typically used as the solvent due to its non-toxic, economical, and environmentally friendly nature. The success of SWE depends heavily on the design and operation of the extraction apparatus, including the pressure vessel and ancillary equipment (Giacometti et al., 2018).

Identification of Non-Anthocyanin Phenolic Compounds

Non-anthocyanin phenolic compounds were identified using UHPLC-PDA-MS (Waters Acquity UPLC system with QDa detector). Separation was achieved on a BEH C18 column (1.7 µm particle size) using a binary gradient elution program with solvent A (0.2% formic acid in water) and solvent B (acetonitrile). The flow rate was maintained at 0.3 mL·min^{-1}, and the column temperature was set to 30 °C. The mass spectrometer was operated in negative electrospray ionization mode (ESI$^-$), with the following settings: probe temperature at 500 °C, spray voltage at 0.8 kV, capillary voltage at 1.5 kV, and cone voltage range between 5–40 V. The scan range was set from m/z 100–1200. Compound identification was conducted through comparison with standard reference compounds, literature data, and the METLIN metabolite database. Prior to chromatographic analysis, all samples and eluents were filtered through 0.45 µm membrane filters. The injection volume for all samples was 5.0 µL (Sarker et al., 2013).

Anthocyanin Analysis

Anthocyanin compounds were analyzed using UPLC-PDA-MS with a BEN C18 column and positive electrospray ionization (ESI-MS). Solvent systems included 2% formic acid (Solvent 1) and methanol (Solvent 2) with a gradient elution. Conditions were maintained at a flow rate of 0.3 mL/min, column temperature of 30 °C, mass scan range of 100–1200 Da, probe temperature at 500 °C, spray voltage at 0.8 kV, and capillary

voltage at 1.5 kV. The method allowed precise identification of cyanogenic anthocyanins, known for their anticancer properties (Khan et al., 2021; Solomon et al., 2017).

Alkaloids Analysis

Alkaloid compounds were analyzed using the same UPLC-PDA-MS approach with either BEN C18 or phenyl columns and positive ionization mode. Solvents included 0.1% formic acid (Solvent 1) and acetonitrile (Solvent 2). These methods facilitated the identification of pyrrolizidine alkaloids and other bioactive amines, which are critical to evaluating both therapeutic potential and toxicity (Jones & Taylor, 2021; Smith et al., 2020; Miller et al., 2019; Williams & Clark, 2020).

Determination of Antioxidant Activity

Antioxidant activity was assessed using the DPPH (2,2-diphenyl-1-picrylhydrazyl) radical scavenging assay. A 1 mL aliquot of the extract was mixed with 3 mL of DPPH solution and incubated in the dark for 15 minutes. Absorbance was recorded at 517 nm with a UV/Vis spectrophotometer. The antioxidant capacity was calculated based on the IC_{50} value, indicating the concentration required to inhibit 50% of DPPH radicals (Abashidze et al., 2024).

Statistical Analysis

All data were analyzed using analysis of variance (ANOVA) to determine the significance of observed differences among treatments. Mean comparisons were carried out using the Least Significant Difference (LSD) test at a 5% significance level ($p \leq 0.05$). Additionally, Duncan's Multiple Range Test (DMRT) was applied to further evaluate differences among treatment means at the 95% confidence level. All statistical computations were performed using Microsoft Excel.

Results and Discussion

After analyzing the pulp of *P. Laurocerasus* next substances were identified:

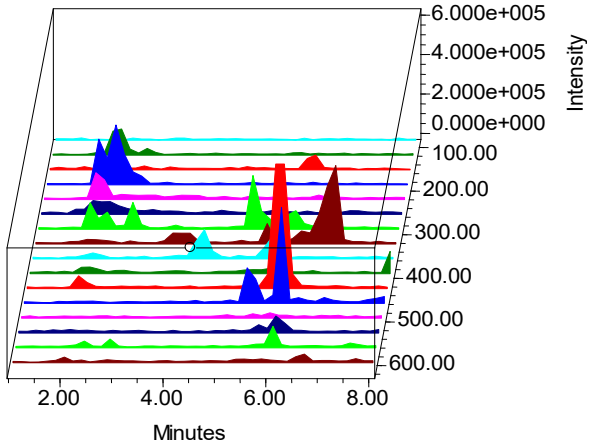

Figure 1. Three-dimentional HPLC-MS chromatogram of *P. Laurocerasus* pulp extract

Substance 1 - ESI-MS - m/z 191.01 [M-H -]; retention time - 2.269 min, maximum absorbance - UV-222.8 and 273.7 213.1 nm. According of the standard compound (Quinic acids (Sigma-Aldrich)) and the METLIN mass database of compounds, substance 3 corresponds to Quinic acids (C7H12O6) (Figure 1).

Substance 2 -ESI-MS - m/z 132.93 [M-H -] dominant compounds, fragmentation ESI-MS m/z 114.99. retention time 2.819 min, maximum absorbance UV- λ max 215.5 nm. According of the standard compound (Malic acids (Sigma-Aldrich)) and the METLIN mass database of compounds, substance 2 corresponds to malic acid

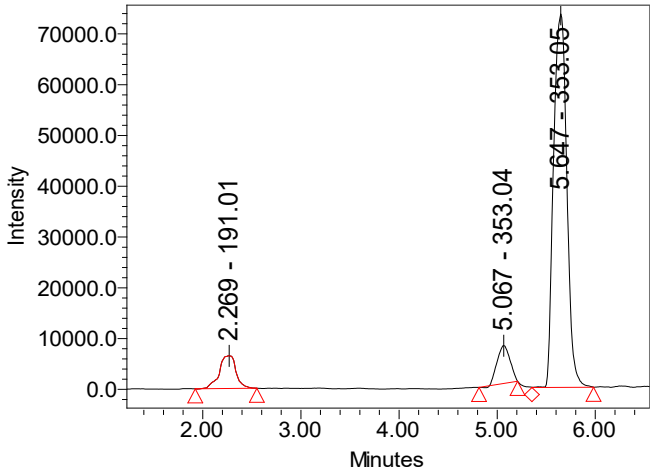

Figure 2. HPLC-MS chromatogram of compounds detected in the pulp extract of *P. laurocerasus*

Substances 3 and 4, with ESI-MS-m/z 353.04 and 353.05[M-H], respectively, were identified with retention times of 5.067 and 5.647 minutes, and maximum absorption in the UV at 324.9 nm and 324.2 nm, respectively. According to the mass base of METLIN compounds (https://metlin.scripps.edu), substance 3 is Neochlorogenic acid, with a molecular formula of C16H18O9, a molecular weight of 354.31g/mol, and an IUPAC Name of (1R,3R,4S,5R)-3-[(E)-3- (3,4-dihydroxyphenyl)prop-2-enoyl]oxy-1,4,5-trihydroxycyclohexane-1-carboxylic acid. Substance 4 is Chlorogenic Acid, with the same molecular formula, molecular weight, and a slightly different IUPAC Name of (1S,3R,4R,5R)-3-[(E)-3-(3,4-dihydroxyphenyl)prop-2- enoyl]oxy-1,4,5-trihydroxycyclohexane-1-carboxylic acid (Figure 2).

Substances 5 and 6, with ESI-MS - m/z 449.08[M+H] and 449.05 (447.10) were detected on the chromatogram as two compounds. The retention times were 4.156 and 4.664 minutes, respectively. The maximum absorption in the ultraviolet beam was at 279.8 nm and 518 nm (Figure 19). The molecular weight of the fragment m/z 286.92 corresponded to Cyanidin. According to the METLIN database, substance 13 corresponded to Cyanidin-3-O-galactoside (2S,3R,4S,5R,6R)-2-[2-(3,4-dihydroxyphenyl)-5,7-dihydroxychromenylium-3-yl]oxy-6-(hydroxymethyl)oxane-3,4,5-triol, with an empirical formula of C21H21O11+ and a molecular weight of 449.4 g/mol. Substance 14 corresponds to Cyanidin-3-O-glucoside (2S,3R,4S,5R,6R)-2-[2-(3,4-dihydroxyphenyl)-5,7-dihydroxy-chromen-3-yl]oxy-6-(hydroxymethyl)oxane-3,4,5- triol, with an empirical formula of C21H21O11+ and a molecular weight of 449.4 g/mol.

Following the production of traditional juice, the remaining residues —that retains a substantial proportion of biologically active compounds—presents a valuable resource for further utilization. In this context, the application of environmentally friendly, or "green," extraction techniques is of particular relevance. Among these, ultrasonic-assisted extraction using water as a solvent has demonstrated high efficiency. This method enables the recovery of phenolic-rich extracts from the residue, characterized by significant antioxidant activity (AA), as indicated by the capacity to achieve 50% inhibition of a 0.1 mM DPPH radical solution (expressed in mg).

Table 1. Phytochemical composition and antioxidant activity (DPPH inhibition) of seed and waste samples dried by different methods

Sample	Total phenols, mg/g	Chlorogenic acids mg/g	Catechins, mg/g	Anthocyanins, mg/g	AA, 0.1 mM DPPH inhibition by mg Sample
Seed	20.11	0.050	0.75	0.16	2.33
Waste dried by vacuum	37.79	0.041	2.11	0.31	1.13
Waste dried by 35 ^{0}C	26.84	0.032	1.89	0.29	1.33

To ensure the stability and preservation of bioactive compounds in fruit juice post-extraction, drying processes were employed. Prior to extraction, the fruit pulp was mechanically separated from the seeds and skins. The resulting juice was then subjected to either vacuum drying or conductive drying at 35 °C. Vacuum drying proved significantly more effective in retaining thermolabile compounds, preserving approximately 85–90% of the initial anthocyanin content. In contrast, conductive drying led to a substantial degradation of these pigments,

with retention rates falling to nearly 50%. A comparable trend was observed for chlorogenic acid, where vacuum drying facilitated markedly higher preservation. Furthermore, conductive drying resulted in the loss of nearly 70% of catechins, underscoring the susceptibility of these polyphenolic compounds to heat-induced degradation. These findings highlight the critical importance of selecting appropriate low-temperature drying techniques to maintain the phytochemical integrity of fruit-derived extracts. The pit of *Prunus laurocerasus* is rich in phenolic compounds (20.11 mg/g), among which predominate catechins (0.75 mg/g). The skin residues on the pit are a source of anthocyanin compounds (0.16 mg/g). Accordingly, AA is high (2.33 mg Sample inhibition 0.1 mM DPPH)(Table 1).

Antioxidant activity (AA) demonstrates a direct correlation with the concentration of biologically active compounds, particularly phenolic constituents. Experimental results indicate that higher levels of total phenolics (e.g., 37.79 mg/g) are associated with significantly enhanced antioxidant capacity, as evidenced by the ability of 1.13 mg of sample to inhibit 0.1 mM DPPH radicals. This positive relationship underscores the critical role of phenolic compounds in contributing to the radical scavenging potential of plant-derived extracts. In the case of *S. platyphyllus*, several challenges remain. Notably, the extraction process for alkaloids from the aerial parts of the plant has not been fully optimized yet. Furthermore, the qualitative and quantitative analysis of these compounds currently relies on thin-layer chromatography (TLC), which may limit the accuracy and sensitivity of the results compared to more advanced analytical techniques (Figure 3).

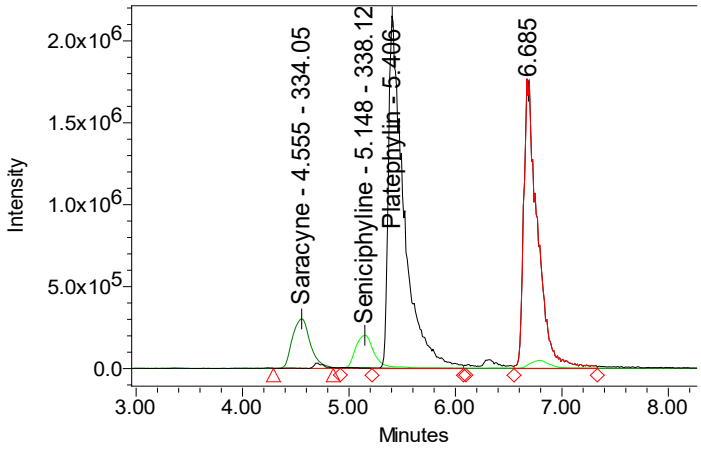

Figure 3. UHPLC-QDa chromatogram of alkaloid compounds detected in the *S. platyphyllus*

We were able to significantly reduce the extraction duration from the conventional 24 hours to just 2 hours High-pressure and high-temperature water extraction. Subsequent analysis using ultra-high-performance liquid chromatography (UHPLC) coupled with photodiode array (PDA) and mass spectrometric (MS) detection (Waters UPLC Acquity system with QDa detector) enabled the identification of the alkaloids saracine, seneciphylline, platyphylline, and its N-oxide. Chromatographic separation was performed using a UPLC Phenyl column (1.7 µm particle size), with a mobile phase composed of 0.1% formic acid in water (solvent A) and acetonitrile (solvent B). The injection volume ranged from 1.0 to 3.0 µL. This analytical procedure reduced the detection time from 8–12 hours to approximately 15 minutes per run (with three replicates), thereby decreasing the total analytical time to under 1 hour. As a result, the overall research process was completed within 3 hours.

Conclusion

The UPLC-PDA-MS analysis conducted on the biologically active compounds of the Georgian endemic plants *Prunus laurocerasus* and *Senecio platyphyllus* has provided valuable insights into their chemical composition and pharmacological potential. The optimization of the extraction process for *Senecio platyphyllus* has significantly improved the efficiency of compound isolation, with particular attention given to the identification of key alkaloids, including Platyphylline, Seniciphyline, and Saracyne. These advancements in extraction and analytical techniques are crucial for further exploring the therapeutic applications of these plants. Additionally, the study established that the fruits of *Prunus laurocerasus* hold significant promise for the development of antioxidant biopreparations and aromatic culinary flour. This research highlights the potential of these endemic plants in both medicinal and food industries, promoting sustainable practices and the valorization of local plant resources.

Recommendations

Based on the experimental findings, it is recommended that in addition to consuming the fruit of *Prunus laurocerasus* in its raw form, vacuum drying be employed as a preservation method to retain its biologically active medicines. This technique effectively minimizes thermal degradation of sensitive phytochemicals, enhancing the potential for their application in the development of nutraceuticals and pharmaceutical formulations. Also, for the efficient recovery of bioactive compounds from *Senecio platyphyllus*, particularly alkaloids, water-based extraction under conditions of elevated temperature and pressure is advised. This green extraction approach not only improves yield but also aligns with principles of environmental sustainability. For accurate qualitative and quantitative analysis of alkaloid profiles, the implementation of ultra-performance liquid chromatography coupled with mass spectrometry (UPLC-MS) is strongly recommended, due to its high sensitivity, resolution, and efficiency in compound identification.

Scientific Ethics Declaration

*The authors declares that the scientific ethical and legal responsibility of this article published in EPSTEM journal belongs to the authors.

Conflict of Interest

*No conflict of interests is declared.

Funding

*This work was done with grant financing. Development of innovative technologies for the valorization of plant raw materials and processing waste to reduce the negative impact on the environment using the principles of a circular economy GRANT_NUMBER: FR-22-4236 LEPL Shota Rustaveli National Science Foundation (Tbilisi, GE)

Acknowledgements or Notes

*This article was presented as an oral presentation at the International Conference on Basic Sciences and Technology (www.icbast.net) held in Budapest/Hungary on August 28-31, 2025.

References

Abashidze, N., Djafaridze, I., Vanidze, M., Khakhutaishvili, M., Kharadze, M., Kartsivadze, I., Davitadze, R., & Kalandia, A. (2024). Physicochemical characterization and antioxidant activity of Jara honey produced in Western Georgia. *Applied Sciences, 14*(16), 6874.

Adams, P., Nkosi, D., Mabasa, N., & Khumalo, M. (2018). Traditional uses of *Senecio* species in South African medicine. *Ethnobotany Research & Applications, 16*, 45–52.

Akinmoladun, O. F., Alabi, Q. A., & Omogbai, E. K. (2018). Bioactive compounds from *Prunus laurocerasus* and their medicinal applications. *Pharmacology & Pharmacy, 9*(2), 110–123.

Brown, J., & Green, L. (2022). Terpenoids in *Senecio* species: Biological activities and pharmacological prospects. *Phytochemistry Reviews, 21*(3), 287–305.

Giacometti, J., Bursać Kovačević, D., Putnik, P., Gabrić, D., Bilušić, T., Krešić, G., Stulić, V., Barba, F. J., Chemat, F., Barbosa-Cánovas, G., & Režek Jambrak, A. (2018). Extraction of bioactive compounds and essential oils from Mediterranean herbs by conventional and green innovative techniques: A review. *Food Research International, 113*, 245–262.

Giacometti, J., Bursać Kovačević, D., Putnik, P., Gabrić, D., Bilušić, T., Krešić, G., Stulić, V., Barba, F. J., Chemat, F., Barbosa-Cánovas, G., & Režek Jambrak, A. (2024). Extraction of polyphenols and essential oils from herbs with green extraction methods—An insightful review. *Food Research International, 173*, 107627.

Jones, H., & Taylor, R. (2021). Pyrrolizidine alkaloids: Toxicity and human health implications. *Journal of Toxicology, 29*(4), 500–515.

Karabegović Stanisavljević, I. T., Stojičević, S., Veličković, D., & Lazić, M. L. (2012). Optimization of microwave-assisted extraction of cherry laurel (*Prunus laurocerasus* L.) fruit using methanol. *Food and Bioproducts Processing, 90*(4), 711–717.

Khan, M. I., Patel, S., & Hussain, M. A. (2021). Cyanogenic compounds in *Prunus laurocerasus* and their anticancer potential. *Journal of Ethnopharmacology, 265*, 113181.

Miller, K., Brown, H., Zhang, Y., & Yu, S. (2019). Contamination of honey by pyrrolizidine alkaloids: A global concern. *Food and Chemical Toxicology, 134*, 110834.

Moufid, N., El Amrani, K., & El Hajji, H. (2020). Evaluation of the antimicrobial properties of *Prunus laurocerasus* extracts. *Journal of Medicinal Plants Research, 14*(1), 10–16.

Sarker, S. D., Nahar, L., & Razak, A. A. (2013). Phytochemical investigation and medicinal properties of *Prunus laurocerasus*. *Natural Products Journal, 9*(3), 145–151.

Singh, M., Singh, R., & Singh, S. (2019). Antiviral activity of *Prunus laurocerasus* in the inhibition of influenza virus replication. *Journal of Virological Methods, 270*, 83–89.

Smith, D., Jackson, B., & Lee, A. (2020). Phytochemical analysis of *Senecio* species: A focus on pyrrolizidine alkaloids. *Journal of Medicinal Plants Research, 14*(2), 67–78.

Solomon, M., Zhang, Y., & Yu, S. (2017). Cyanogenic glycosides in *Prunus laurocerasus* and their potential applications in human health. *Journal of Agricultural and Food Chemistry, 65*(7), 1501–1508.

Stefanova, G., Girova, T., Gochev, V., Stoyanova, M., Petkova, Z., Zheljazkov, V. D., & Stoyanova, A. (2020). Comparative study on the chemical composition of laurel (Laurus nobilis L.) leaves from Greece and Georgia and the antibacterial activity of their essential oil. *Frontiers in Chemistry, 8*, 553.

Surmanidze, N., Vanidze, M., Djafaridze, I., Davitadze, R., Qarcivadze, I., Khakhutaishvili, M., & Kalandia, A. (2024). Optimization of the method of ultrasonic extraction of lycopene with a green extract from the fruit of *Elaeagnus umbellata*, common in Western Georgia. *Food Science & Nutrition*.

Talmaciu, A. I., Volf, I., & Popa, V. I. (2015). A comparative analysis of the "green" techniques applied for polyphenols extraction from bioresources. *Chemistry & Biodiversity, 12*(11), 1635–1651.

White, B., Gonzalez, R., Chen, Y., & Evans, D. (2023). Biological properties of sesquiterpenoids in *Senecio*: A review. *Molecular Pharmacognosy, 19*(1), 101–119.

Williams, S., & Clark, G. (2020). Hepatic sinusoidal obstruction syndrome due to pyrrolizidine alkaloids: Case studies and risk assessment. *Hepatology International, 14*(2), 235–249.

Zhang, W., Wang, Q., & Li, J. (2019). Flavonoids and phenolic acids in *Prunus laurocerasus* and their health benefits. *Journal of Food Science, 84*(2), 220–229.

Zhou, L., & Zhang, Y. (2025). Comparative analysis of extraction technologies for plant extracts and absolutes. *Frontiers in Chemistry, 13*, 1536590.

Author(s) Information

Eteri Margalitadze
Batumi Shota Rustaveli State University
Ninoshvili av. 35, Batumi, Georgia.
Contact e-mail: *eter.margalitadze@bsu.edu.ge*

Iamze Kezheradze
Batumi Shota Rustaveli State University
Ninoshvili av. 35 Batumi, Georgia.

Indira Japaridze
Batumi Shota Rustaveli State University
Ninoshvili av. 35 Batumi, Georgia.

Maia Vanidze
Batumi Shota Rustaveli State University
Ninoshvili av. 35, Batumi. Georgia.

Aleko Kalandia
Batumi Shota Rustaveli State University
Ninoshvili av. 35 Batumi, Georgia.

To cite this article:

Margalitadze, E., Kezheradze, I., Japaridze, I., Vanidze, M., & Kalandia, A. (2025). Study of secondary metabolites in Georgian endemic plant raw materials and processing residues using UPLC-PDA-MS methods. *The Eurasia Proceedings of Science, Technology, Engineering and Mathematics (EPSTEM), 36,* 183-191.

The Eurasia Proceedings of Science, Technology, Engineering & Mathematics (EPSTEM)
ISSN: 2602-3199

The Eurasia Proceedings of Science, Technology, Engineering & Mathematics (EPSTEM), 2025

Volume 36, Pages 192-206

ICBAST 2025: International Conference on Basic Sciences and Technology

SCADA Monitoring on Radio Relayed Station at Hydro Melioration System Supported in Iot Network

Goce Stefanov
Goce Delcev University

Biljana Citkusheva-Dimitrovska
Goce Delcev University

Vlatko Cingoski
Goce Delcev University

Maja Kukusheva-Paneva
Goce Delcev University

Abstract: In modern technological development, the commitment to the application of sophisticated electronic systems is noticeable not only in electric power plants but also in industries for healthy and quality food, such as agriculture. We witness daily tribunes and panel discussions sponsored by companies and even governments for the introduction of the terminology of digital agriculture, i.e. the introduction of smart electronic solutions in agriculture. In addition to the commitment to so-called green energy, i.e. obtaining energy from renewable sources, the development of digitization in agriculture is an area in which an enormous application of smart electronic systems is expected in the future. Guided by these reasons, in this paper an electronic system is designed that provides a solution to a problem in hydro melioration system, i.e. the development, design and practical implementation of the Smart electronic system which enables data exchange between the soil irrigation line, MASTER station with screen SCADA and SLAVE stations. The temperature and humidity on the soil and the air are measured in the irrigation line with electronic module SLAVE 1 station. The communication between the irrigation line (SLAVE 1) and the MASTER station is realized with RF network. The MASTER station is installed in one part on industrial plant and here is SCADA screen. The SLAVE 2 station is installed in another part on industrial plant. The SLAVE 2 station is connected by RF (radio frequency connection) to the SLAVE 1station and the same is connected with WIFI in IoT network. In the MASTER, SLAVE 1 and SLAVE 2 stations, microcontroller units as well as appropriate RF modules are installed. The microcontroller in the SLAVE 2 station is connected to the IoT microcontroller for the transfer of measurement data in the Internet network. The solution provides visualization, data log file, and transfer to the IoT network of process data on irrigation line in hydro melioration system.

Keywords: SCADA, Hydro melioration system, Exchange data, RF network, IoT network

Introduction

In modern agricultural production, implementing a monitoring and quality control system is considered essential, as supported by various studies (Fountas, 2020; Narendra, 2019; Narendra, 2019; Rotz, 2019 & Saiz-Rubio, 2020). Such systems should provide timely management of the quantities needed to obtain a quality product. On the other hand, these systems should provide the opportunity to collect and process data on control values in the agricultural plant, (Bennett, 1982; Hor, 2005). In real industrial agricultural processes, there are standalone plants that operate as independent self-contained units. Most often these plants are far from intra and

internet network of the agricultural production companies. Therefore, there is a need to automate and connect these agricultural plants in the company intranet and more widely on the Internet (IoT) network. Efforts are made to ensure more reliable and simpler work, especially for operators who are directly exposed to the proper functioning of the entire industrial process. This approach to work is made possible by the so-called SCADA (**S**upervisory **C**ontrol and **D**ata **A**cquisition) system. On the other hand, a modern industrial process control system is truly comperhensive whrn it integrades not only SCADA but also connectivity to an IoT network, (Bhuiyan, 2023; Ariel, 2024 & Stefanov, 2021). Such a concept enables process data to be transferred to any location, real-time visualization, and stored on a personal and cloud computer.

Commonly, some standalone industrial agricultural processes might represent a separate entity. Since these plants are far from the Intra and Internet network of manufacturing companies, the data distribution of analog and digital signals from sensors and actuators of some process quantities (e.g. soil moisture, soil temperature and air temperature and humidity, voltage, current, pressure, flow and level water, etc.) must be made from these remote entities to the master station via wireless communication, most likely a radio frequency (RF) connection (Stefanov, 2021, 2023).

In this paper an electronic system is designed that provides a solution to a problem in hydro melioration system. Specifically, it presents the development, design and practical implementation of a smart electric system that enables data exchange between the soil irrigation line (SLAVE 1), a MASTER station equipped with a SCADA interface, and SLAVE 2 station connected to an IoT network.

Design of SCADA Monitoring for Radio- Relayed Station at Hydro Melioration System

The block diagram of one agriculture hydro melioration system is shown in Figure 1.

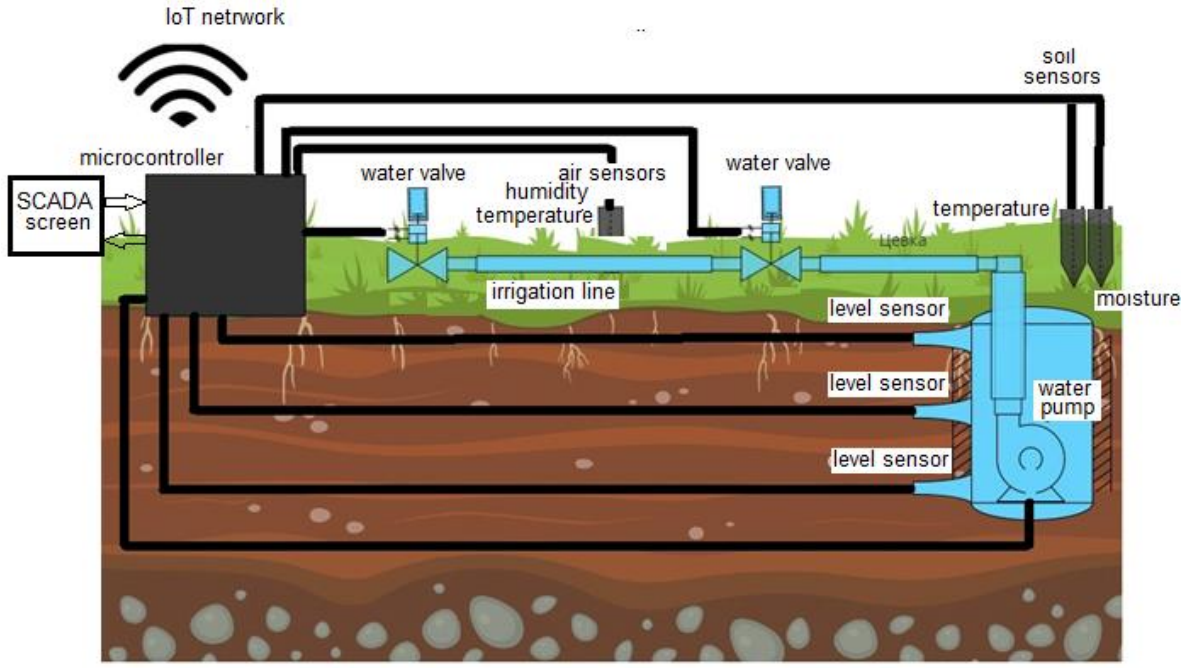

Figure 1. Block diagram of one agriculture hydro melioration system

Elements of this hydro melioration system are water pumps, irrigation lines, water valves, sensors for temperature and humidity of air and soil. These elements are controlled by a microcontroller. Based on the reference values of temperature and moisture, the microcomputer controlled with the water valves and maintains the optimal temperature and soil moisture required for the specific agricultural product. The microcontroller is connected to a SCADA screen for visualization of measured values as well as to IoT network for data distribution on the Internet. A problem or deficiency in such a sophisticated system stems from the need for soil moisture and temperature sensors to be at the end of the irrigation line. Under normal conditions this is solved by a cable connection between the sensors and the microcontroller. But these distances can be several hundred meters and that makes such solutions complex. Therefore, in this paper, a system is designed in which the

connection between soil temperature and moisture sensors and the microcontroller is established via RF network.

In Figure 2, a block diagram of an implemented SCADA monitoring system for radio- relayed station within hydro melioration system integrated into an IoT network is shown.

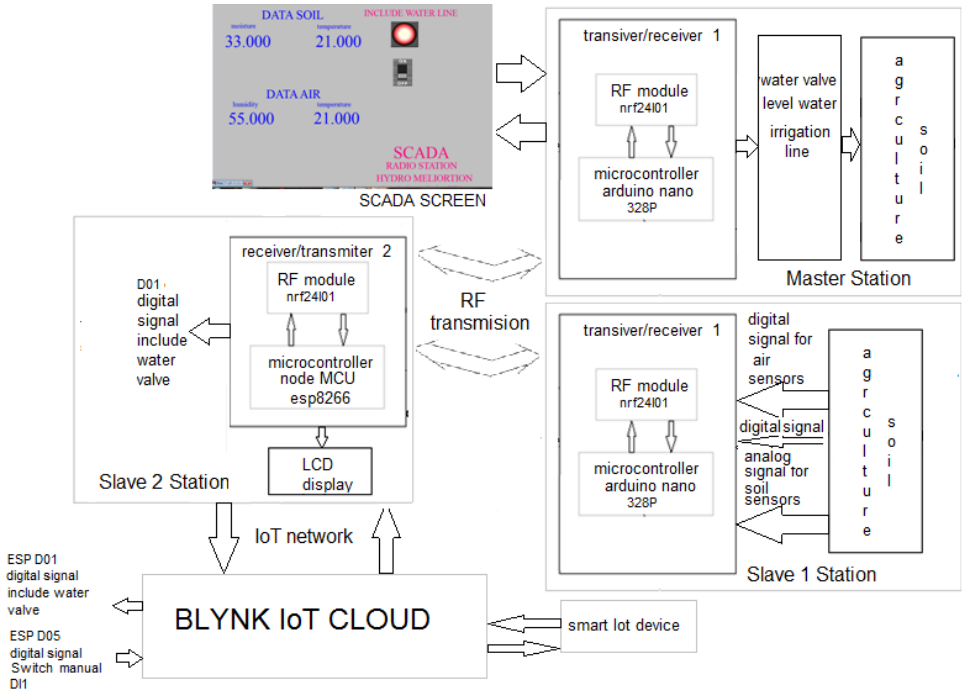

Figure 2. Block diagram of SCADA monitoring system for radio- relayed station at hydro melioration system in IoT network

This is block diagram illustrates the design and practical implementation of a smart electronic system that enables data exchange between the SLAVE 1 station, MASTER station equiped with a SCADA interface and the SLAVE 2 stations. The SLAVE 1 station is installed within the agriculture plant, where it collects real- time data from soil sensors and transmits it to the MASTER station. The temperature and humidity of the soil and the air are measured in SLAVE 1 station. The communication between SLAVE 1 and the MASTER station is via RF network. The MASTER station is installed in one part on agriculture industrial plant and is equipped with a SCADA screen for real- time monitoring and control of the system. The SLAVE 2 station is installed in another part on industrial plant. The SLAVE 2 station is connected via RF (radio frequency connection) to the SLAVE 1station but also it is connected to IoT network via Wi-Fi. In the MASTER, SLAVE 1 and SLAVE 2 stations, microcontroller units as well as appropriate RF modules are installed. The microcontroller in the SLAVE 2 station is connected to an IoT microcontroller in order to transfer the measurement data over the Internet network. The solution provides visualization, data log file, and transfer to the IoT network of process data on irrigation line in hydro melioration system. With this design concept, reliable transmission of soil moisture and temperature signals is obtained regardless of the distance between the sensor (SLAVE 1) and MASTER and SLAVE 2 stations.

In the designed SCADA system prototype, switches and LEDs were used as sensors and actuators to validate the correct operation of the solution. The microcontrollers in both the MASTER and SLAVE 1 stations are ATmega328P units mounted on Arduino Nano board (ATmega328P, 2015), (ESP8266, 2020). The microcomputer that enables the system's connection to the IoT network is a NodeMCU ESP8266-12E (ESP8266, 2020) which is embedded in the SLAVE 2 station. The RF connection between the stations is established using the nRF24L01 module, (nRF24L01, 2020). The prototype system design includes the development of the SLAVE 1, MASTER and SLAVRE 2 stations as well as the design of the SCADA and IoT control system.

Design of the SLAVE 1 Station

In real industrial agricultured plants there are parts that are remote from intra and internet network. In such standalone plants there is often a challenge with timely collection, visualization, and analysis of signals from sensors that are critical for the proper functioning of industrial equipment. The designed RF SLAVE 1 - MASTER - SLAVE 2 network in this paper solves this issue by enabling the integration of sensor signals from standalone plants into the company's intra network. Figure 3 represents the block diagram of SLAVE 1 station which is a component of the system shown in Figure 2.

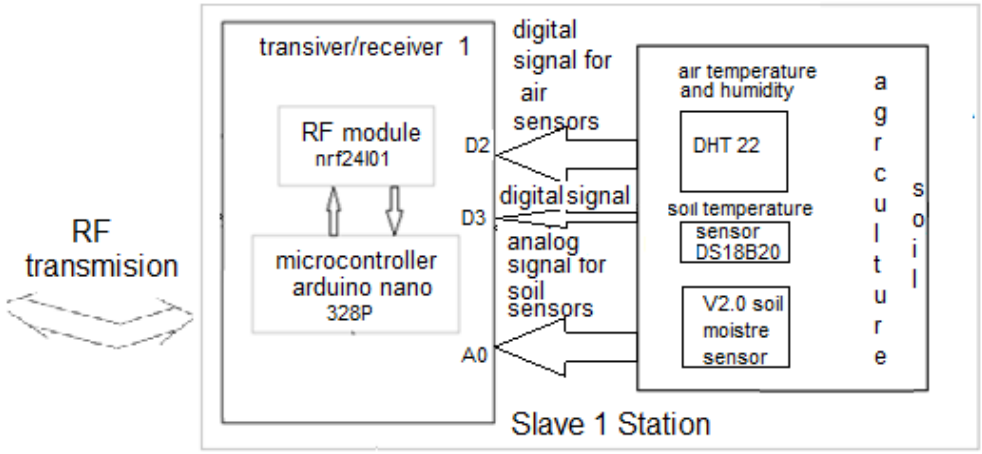

Figure 3. Block diagram of SLAVE 1 station

The SLAVE 1 station consists of a sensors network, RF module and microcontroller. The sensors network in SLAVE 1 station includes a soil moisture sensor V2.0, sensor a soil temperature sensor DS18B20, and air temperature sensor DHT 22. These sensors transmit their signals to Atmega328P microcontroller mounted on Arduino nano board. Specificaly, DHT 22 sends a digital signal to pin D2 for air temperature and humidity, DS18B20 sends a digital signalo to pin D3 for soil temperature and V2.0 soil moisture sensor sends an analog signal to pin A0. The microcontroller communicates serially with nRF24L01 RF module which transmits radio signals corresponging to the sensor data to the MASTER and SLAVE 2 stations.

Features of the Used Hardware

a.) nRF24L01 Module

The nRF24L01 is a single-chip radio transceiver module that operates in 2.4 - 2.5 GHz ISM band. It integrates a frequency synthesizer, a power amplifier, crystal oscillator, demodulator, modulator and Enhanced ShockBurs ™ protocol engine. Output power, frequency channels, and protocol setup are easily programmable through an SPI interface. Additionally, its built-in Power Down and Standby modes enables efficient power saving. Figure 4 shows several types of electronic boards based on nRF24L01 module.

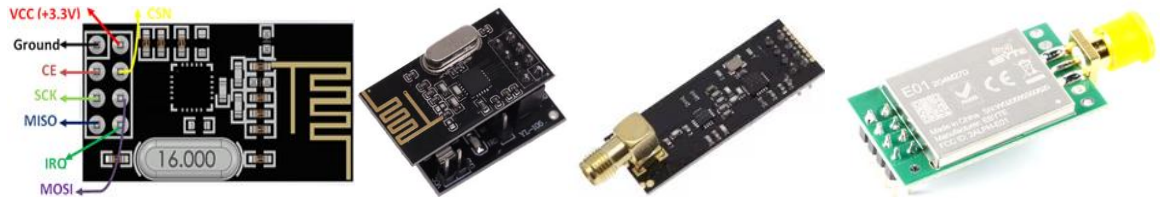

a.) b.) c.) d.)

Figure 4. Electronic board of nRF24L01 module and his pinout

Figure 4(a) shows the basic nRF24L01 module along its pinout capable for communication up to distance to 100 m in open air conditions. Figure 4(b) shows the same module mounted on a socket for easier integration. Figure 4(c) shows an extended range version of the nRF24L01 module for distance up to 1.1km. Figure 4(d) includes wtho high- power modules E01-ML01DP5 with communication range up to 2500m and E01-2G4M27D (nRF24L01P+PA+LNA) for distance up to 5000m. Table 1 provides the pinout configuration of the nRF24L01 module.

Table 1. Pinout configuration of nRF2Ll01 module

Pin Number	Pin Name	Abbreviation	Function
1	Ground	Ground	Connected to the Ground of the system
2	Vcc	Power	Powers the module using 3.3V
3	CE	Chip Enable	Used to enable SPI communication
4	CSN	Ship Select Not	This pin has to be kept high always, else it will disable the SPI
5	SCK	Serial Clock	Provides the clock pulse using which the SPI communication works
6	MOSI	Master Out Slave In	Connected to MOSI pin of MCU, for the module to receive data from the MCU
7	MISO	Master In Slave Out	Connected to MISO pin of MCU, for the module to send data from the MCU
8	IRQ	Interrupt	It is an active low pin and is used only if interrupt is required

NRF24L01 Features:

- 2.4GHz RF transceiver Module
- Operating Voltage: 3.3V
- Nominal current: 50mA
- Range : 50 – 100 m
- Operating current: 250mA (maximum)
- Communication Protocol: SPI
- Baud Rate: 250 kbps - 2 Mbps.
- Channel Range: 125
- Maximum Pipelines/node : 6
- Low cost wireless solution

The nRF24L01 is a wireless transceiver module, meaning it can both transmit and receive data. The module's operating frequency is 2.4 GHz, which falls under the ISM band and hence making it legally usable in almost in all countries for engineering applications. When operating under optimal contiditions the module can cover a distances up to 100m (approximately 200 feet) making it an excellent choice for various wireless and remote-controlled projects.

The module operates at 3.3V making it compatible with both 3.2V and 5V systems. Each module has an address range up to 125 addresses and each module can communicate with 6 other modules simultaneously. Thic capability allows the formation of complex wireless comunications structures such as mesh networks or star networks making the nRF24L01 an ideal choice for practical and scalable wireless applications.

The communication with nRF24L01 module is achieved via SPI protocol. These modules can either be interfaced with 3.3V microcontroller or a 5V microcontrollers equipped with SPI port. Detailed instruction on interfacing and configuration is provided in the module's datasheet Figure 5 shows a typical circuit diagram for interfacing the nRF24L01 module with the microcontroller. Although the example demonstrates 3.3V microcontroller the same connection principle applies to 5V microcontroller. The SPI Pins (MISO, MOSI and SCK) are connected to the corresponding SPI pins on the microcontroller while the signal pins (CE and CSN) are connected to the GPIO pins of the MCU. Additionally, several ready-to-use libraries, such as R24 Library, are available for interfacing this module with Arduino.

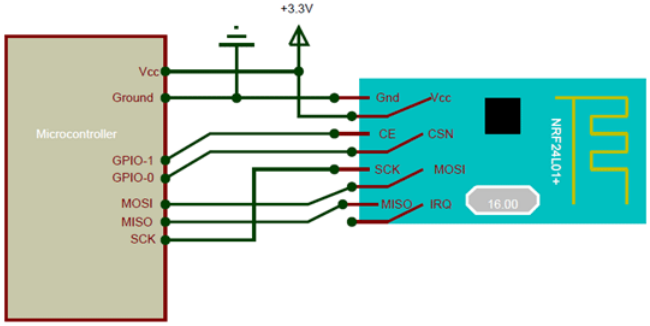

Figure 5. nRF24L01module interfaced with a microcomputer

With help of these available libraries nRF24L01can be easily interfaced with Arduino using jus a few lines of code. However, for other microcontrollers it is necessart to consult the module's datasheet to properly configure SPI communication. The nRF24L01module is a bit tricky to use especially since there are many cloned versions in the market. In case of troubleshoot, 10µF and 0.1µF capacitors should be added in parallel to source Vcc and GND pins. Also, the 3.3V power source must be clean and free of any noise as voltage fluctuation can cause module malfunction.

b.) Microcontroller ATmega 328P

The Arduino nano is an open- source microcontroller board based on the Microchip ATmega328P microcontroller developed by Arduino.cc. The board is equipped with sets of digital and analog input/output (I/O) pins that can be interfaced with various expansion boards (shields) and other external circuits. The board includes 14 digital I/O pins of which six capable to support PWM output, 8 analog I/O pins. Programming is done using Arduino IDE (Integrated Development Environment) via a type B USB cable. The Arduino nano can be powered by either through USB connection or an external 9V battery. The onboard ATmega328P microcontroller comes preprogrammed with a bootloader enabling code uploads without requiring an external hardware programmer, (Saiz-Rubio, 2020). In Figure 6(a) is shown Arduino nano board with build-in Atmega328P microcontroller, while in Figure 6(b) are shown its pinouts configuration.

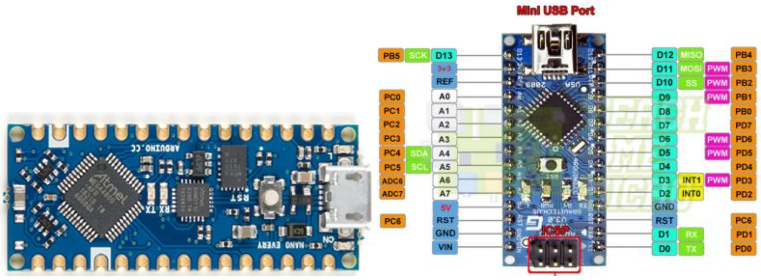

a.) b.)

Figure 6. a.) Arduino Nano and b.) pinout

c.) DHT22 Temperature and Humidity Sensor

The DHT22 is a commonly used temperature and humidity sensors. The sensor comes with a dedicated NTC to measure temperature and an 8-bit microcontroller to output the values of temperature and humidity as serial data, (DHT22, n.d.). The connection diagram for this sensor is shown in Figure 7.

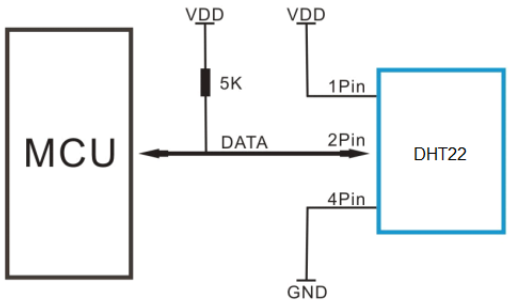

Figure 7. Connection diagram for DHT22 sensor

The DHT22 sensor is factory calibrated, making it easy ton interface with wide range of microcontrollers. The sensor can measure temperatures in range from 0°C to 50°C and relative humidity from 20% to 90% with an accuracy of ±1°C for temperature and ±1% for humidity. Since the DHT22 sensor outputs data in a serial digital format the setup is simple and requires minimal hardware. As shown in Figure 8 the data pin is connected to a I/O pin of the MCU through 5kΩ pull-up resistor. This single data line carries both temperature and humidity values in the following 40-bit format: 8-bit humidity integer + 8-bit humidity decimal +8-bit temperature integer + 8-bit temperature decimal and +8-bit parity bit (checksum). This sensor can be used for temperature and humidity measurement, local weather station, automatic climate control and environment monitoring. Figure 8 shows the actual size of the DHT22 sensor along with its pinout configuration.

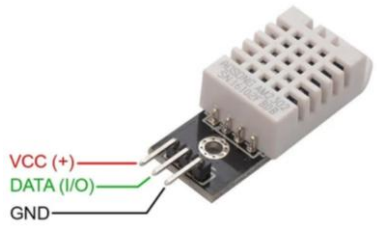

Figure 8. DHT22 sensor and its pinouts

DHT22 Specifications:

- Operating Voltage: 3.5V to 5.5V
- Operating current: 0.3mA (measuring) 60uA (standby)
- Output: Serial data
- Temperature Range: 0°C to 100°C
- Humidity Range: 20% to 100%
- Resolution: Temperature and Humidity both are 16-bit
- Accuracy: ±1°C and ±1%

The DHT22 sensor is available in two forms as a sensor or as a module. In both cases, the performance remains the same. The sensor comes in a 4-pin package, although only three pins are typically used in applications, whereas the module comes with 3- pin configuration. The key difference between the sensor and module is that the module version includes filtering capacitor and built-in resister making it easier to use directly with microcontrollers. In contrast, when using the sensor, these components must be added externally if are required.

d.) DS18B20 Temperature Sensor

The DS18B20 (Figure 9) is a digital temperature sensor manufactured by Maxim Integrated (formerly Dallas Semiconductor). It is widely used due to its reliability and ease of integration, offering a relatively high accuracy of ±0.5 °C across a broad temperature range from -55°C to + 125°C, (DS18B20, 2019).

Figure 9. DS18B20 temperature sensor

The DS18B20 sensor operates with a voltage range of 3.0 to 5.5V, making it compatible with both 5V systems like Arduino and 3.3V systems such as the ESP32 and Raspberry Pi. One of the key advantages is that it requires only a single digital I/O pin for communication, regardless of how many sensors are connected. The sensor communicates using the Dallas Semiconductor 1-wire protocol which is similar to I2C but offers lower data rates and longer communication range. Another advantage is that each DS18B20 sensor has a unique 64-bit serial code, which enables multiple sensors to be connected on the same 1-Wire bus without address conflicts. The the sensor's resolution can be set programmatically configured to 9, 10, 11, or 12 bits, correspoding This corresponds to temperature increments of 0.5°C, 0.25°C, 0.125°C, and 0.0635°C, respectively. By default, the sensor operates at 12-bit resolution upon power-up.

e.) V2.0 Soil Moisture Sensor

There are two main types of soil moisture sensors: capacitive and resistive soil moisture sensors. The reason for prefering capacitive sensor over resistive ones are explained below. In the Figure 10(a) is shown resistive soil moisture sensor, while in Figure 10(b) is shown capacitive soil moisture sensor.

a.) b.)

Figure 10. Soil moisture sensor: a.) resistive soil moisture sensor and b.) capacitive soil moisture sensor

Resistive Soil Moisture Sensor

The resistive soil moisture sensor consists of two metal probes that are inserted into soil to measure its volumetric water content. These probes allow a small electric current to pass through the soil and then the sensor measured the resulting resistance. When the soil contains a higher amount of water, the soil will conduct more electricity which results in lower resistance. This indicates a higher moisture level. Dry soil conducts electricity poorly, so when there will be less water, then the soil will conduct less electricity which leads to higher resistace and indicates a lower moisture level. This simple principle of conductivity makes resistive sensors easy to use, but their exposed metal components are prone to corrosion over time, reducing accuacy and durability of the sensor.

Capacitive Soil Moisture Sensor

The soil moisture sensor uses capacitive sensing to measure soil moisture levels unlike many other sensors on on the market that relay on resistive sensing. It is constructed from corrosion-resistant material which significantry enhances its durability and service life. By instaling the sensor into the soil around plants real-time soil moisture data is obtained. This module features an onboard voltage regulator giving it a wide operating voltage range of 3.3 to 5.5V.

While both types of sensor measure moisture-related properties, capacitive sensors offer clear addvantages. The major drawback of resistive sensors is the corrosion of metal probes, which occures not only to soil expouser but also because a constant DC current causes electrolysis. This drastically shortens the lifetime of the sensor. Capacitive sensors provide more reliable and consistent readings, as the measure the dielectric permittivity of the surrounding medium rather that just electrical resistace. Moisture changes the dielectric constant of the soil which the sensor detects. Water itself is not a good conductor; it's the dissolved ions (e.g. from fertilizer) that affect resistance. Therefore, resistive sensors can give false readings due to changes in ion concentration even if water content hasn't change. Capacitive sensing avoids this issue by measuring the overall dielectic which is more directly affected by actual water content. Thus, capacitive soil moisture sensors offer greater accuracy, stability, and longevity, making them the preferred choice for modern precision agriculture and gardening applications. Specifications of the capacitive sensor used in this application are:

- Operating Voltage: 3.3 ~ 5.5 VDC.
- Operating Current: 5mA.
- Interface: PH2.54-3P.
- Dimensions mm(LxWxH): 98 x 23 x 4.
- Supports 3-Pin Gravity Sensor interface
- Analog output.
- Weight (gm): 15.

Design of the MASTER Station

The block diagram of the MASTER station is shown in Figure 11.

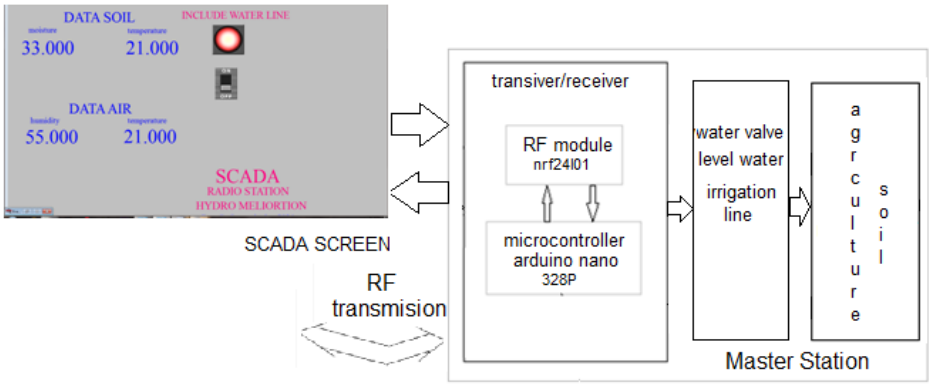

Figure 11. Block diagram of MASTER station

The design of the MASTER station includes ATmega328P microcontroller mounted on an Arduino nano board, nRF24L01 RF module and SCADA interface developed using CX-Supervisor and other necessary hardware components. The functionality of the MASTER station is defined by the following signal logic:

- D01: a digital output signal that is activated by user interaction with a virtual switch Dl1on the SCADA screen
- D02: a digital output signal which is activated automatically when the soil moisture level drops below a preferred threshold. An LED indicator is used to indicate this signal.

An essential component of the designed prototype SCADA system is CX-Supervisor, a powerful SCADA software package developed by Omron.

Design of the SCADA

SCADA is developed using Omron CX-Supervisor software, a platform specifically designed for PC- based visualization and machine control. CX- Supervision is suitable for both simple and highly complex supervisory control tasks. It offers powerful functions for a wide range of PC-based HMI requirements. For rapid development of basic applications, it provides numerous predefined functions and libraries. CX-Supervisor has extremely simple, intuitive handling and high user friendliness. CX-Supervisor runs standard PC desktop computers running Microsoft Windows. CX-Supervisor is intuitive and easy to use, and allows the developer to rapidly configure, test and debug a project. CX-Supervisor comprises two separate executable Windows programs, CX-Supervisor Development environment and CX-Supervisor Runtime environment. Applications are created and tested using the development environment and then delivered as a final customer application with the runtime environment. The runtime-only environment may only be used for executing an application previously generated using the development environment. It is not possible to generate a new runtime application using the runtime environment. In Figure 12, there is shown connection between sensor hardware, microcontroller and CX-Supervisor SCADA.

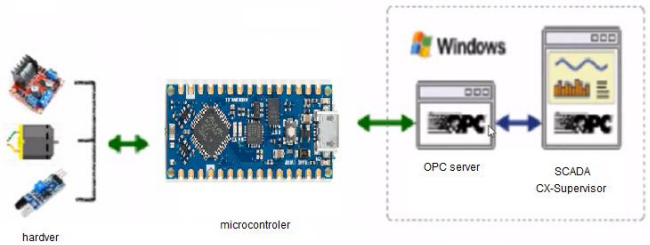

Figure 12. Connection between sensor hardware, microcontroller and CX-Supervisor SCADA

Setting up Graphic Symbols

The intial step in building the SCADA interface involves configuring the graphical symbols. After the project is created and its associated interface page is prepared, various graphical elements, such as indicators, buttons and control panels, can be designed and integrated into the page layout as illustrated in Figure 13.

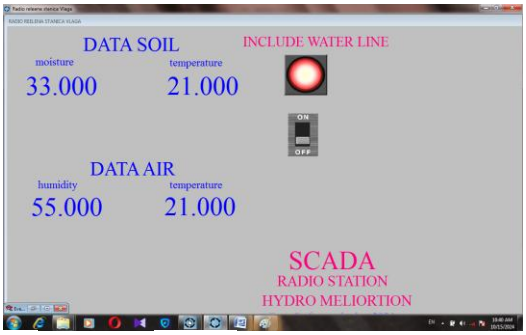

Figure 13. Setting graphic symbols

The graphics editor in CX- Supercisor uses a Graphic Object Toolbar and a floating window known as the Palette to construct and control objects within the project interface. These tools are user-friendly and intuitive. Several small icons are visible on the Graphic Object toolbar, each representing a different graphical object that can be used to build the application interface. Some of these objects are graphical primitives, such as straight lines, ellipses, rectangles, while others are more advanced like the gauge object, which includes built-in functionality for visualization and control.

Design of the SLAVE 2 Station

Figure 14 represents the block diagram of SLAVE 2 station, which represents a subsystem of the overall architecture shown in Figure 2.

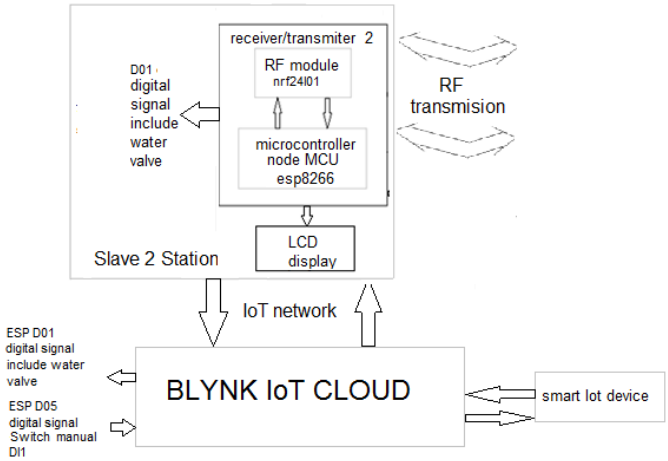

Figure 14. Block diagram of SLAVE 2 station

The SLAVE 2 station consists of an RF module, NodeMCU ESP8266 microcontroller and 20x4 LCD display.

NodeMCU ESP8266-12E

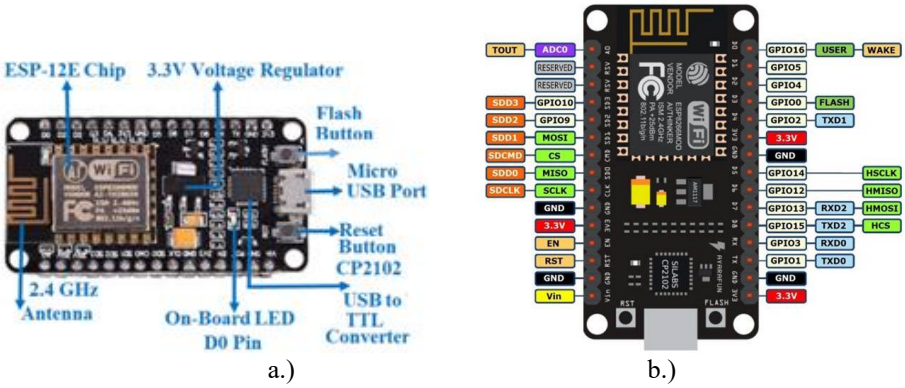

a.) b.)

Figure 15. a.) NodeMCU ESP8266 and b.) pinouts

This NodeMCU is a development board based on ESP-12E module containing ESP8266 chip featuring Tensilica Xtensa 32-bit LX106 RISC microprocessor, (ESP8266, 2020). This microprocessor supports real-time operating systems (RTOS) and operates at adjustable clock frequency ranging from 80MHz to 160 MHz. The NodeMCU is equipped with 128 KB of RAM and 4MB of Flash memory for storing data and programs. Its high processing power with built-in Wi-Fi / Bluetooth capabilities, as well as support for Deep Sleep make it ideal for IoT projects. The board can be powered via Micro USB jack or VIN pin (for external supply pin). Additionally, it supports a range of communication interfaces including UART, SPI, and I^2C interface. Figure 15 shows the NodeMCU ESP8266 along with its pinouts. NodeMCU is an open-source firmware and development board specifically designed for IoT-based applications. It includes firmware that runs on the ESP8266 WIFI SoC developed by Espress Systems, and hardware based on the ESP-12 module.

NodeMCU ESP8266 specifications &features

- Microcontroller: Tensilica 32-bit RISC CPU Xtensa LX106
- Operating Voltage: 3.3V
- Input Voltage: 7-12V
- Digital I/O Pins (DIO): 16
- Analog Input Pins (ADC): 1
- UARTs: 1
- SPIs: 1
- I2Cs: 1
- Flash Memory: 4 MB
- SRAM: 64 KB
- Clock Speed: 80 MHz
- USB-TTL based on CP2102 is included onboard, Enabling Plug n Play
- PCB Antenna
- Small Sized module to fit smartly inside your IoT projects

The NodeMCU ESP8266 board can be easily programmed with Arduino IDE since it is easy to use.

Experimental Results

Figure 16 shows the prototype on the SLAVE 1 station, and Figure 16 b shows the prototype on the MASTER station.

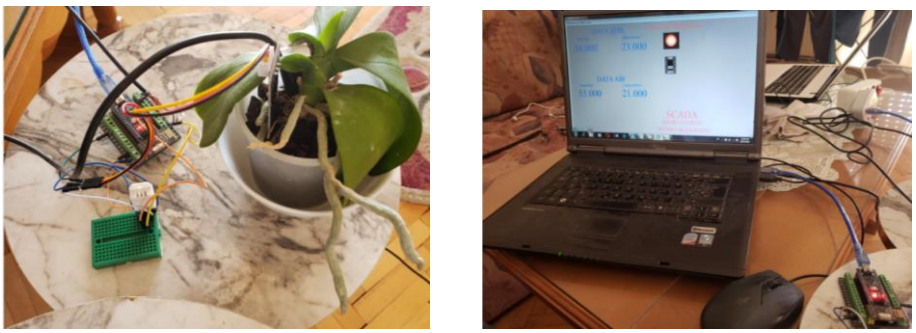

a) b)

Figure 16. Prototype on design SCADA monitoring data system: a) prototype on SLAVE station, b) prototype on MASTER station

From Figure 16(a) it can be seen that the DS18B20 soil temperature sensors, the V2.0 soil moisture sensor and the DHT22 air humidity and temperature sensor are connected to the Arduino Nano board. Figure 16(b) illustrates the connection between the MASTER station implemented using an Arduino Nano board and the SCADA screen. The waveforms of the measured values obtained in real-time in CX Supervision are represented in Figure 17. The blue line in the waveforms shown in Figure 17 represents the humidity on air, the yellow line is the moisture on soil, the green is soil temperature while the red line is the temperature on air. A sample of the data log file for the measured values obtained in CX Supervision is represented in Figure 18.

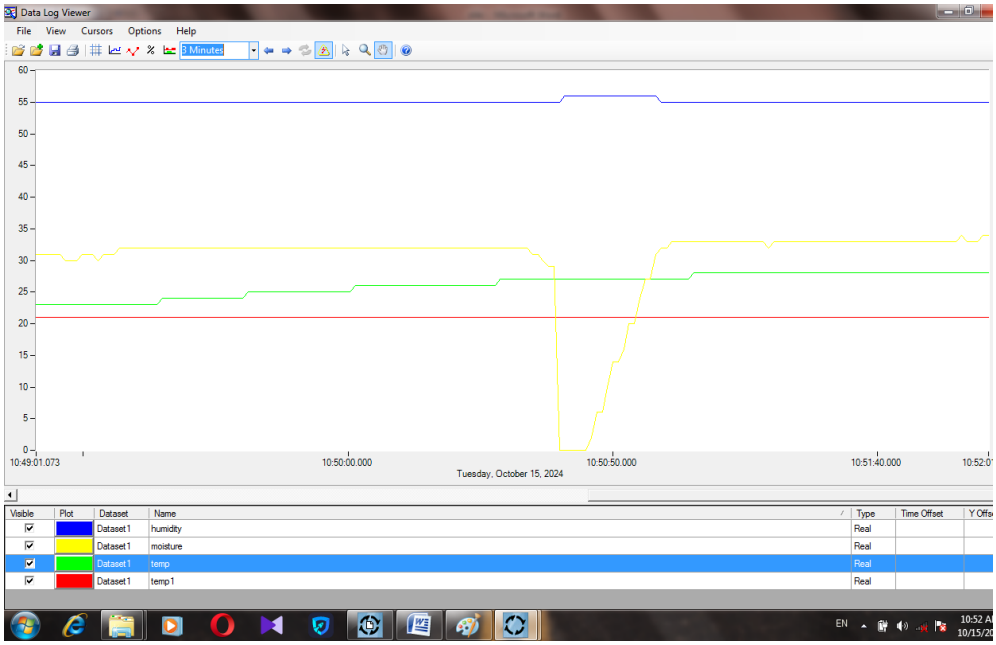

Figure 17. The waveforms of the measured values in real time

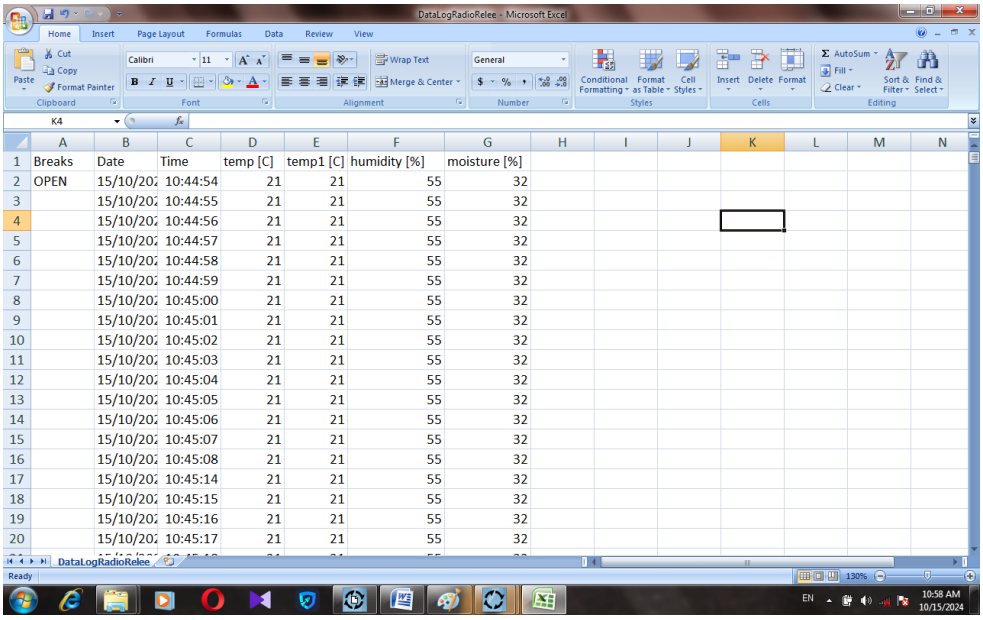

	A	B	C	D	E	F	G
1	Breaks	Date	Time	temp [C]	temp1 [C]	humidity [%]	moisture [%]
2	OPEN	15/10/202	10:44:54	21	21	55	32
3		15/10/202	10:44:55	21	21	55	32
4		15/10/202	10:44:56	21	21	55	32
5		15/10/202	10:44:57	21	21	55	32
6		15/10/202	10:44:58	21	21	55	32
7		15/10/202	10:44:59	21	21	55	32
8		15/10/202	10:45:00	21	21	55	32
9		15/10/202	10:45:01	21	21	55	32
10		15/10/202	10:45:02	21	21	55	32
11		15/10/202	10:45:03	21	21	55	32
12		15/10/202	10:45:04	21	21	55	32
13		15/10/202	10:45:05	21	21	55	32
14		15/10/202	10:45:06	21	21	55	32
15		15/10/202	10:45:07	21	21	55	32
16		15/10/202	10:45:08	21	21	55	32
17		15/10/202	10:45:14	21	21	55	32
18		15/10/202	10:45:15	21	21	55	32
19		15/10/202	10:45:16	21	21	55	32
20		15/10/202	10:45:17	21	21	55	32

Figure 18. Data log file of measured value

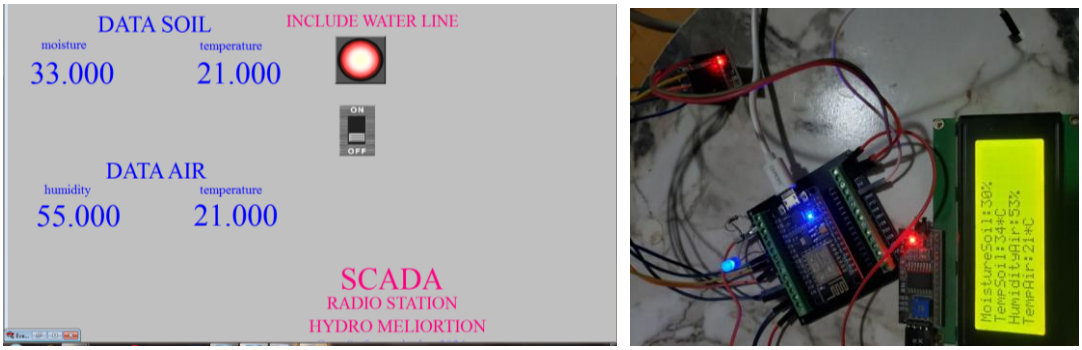

a.) b.)

Figure 19. a) Screen of the design SCADA exchange radio station and b) prototypes on SLAVE 2

Figure 19(a) shows the interface screen of the SCADA exchange radio station design, while Figure 19(b) displays the prototype of the SLAVE 2 station. SLAVE 2 station visualizes the measured values on an LCD screen, creates a data log file in Excel on the connected personal computer and sends the data to the Blink Cloud IoT network, (Blynk, 2025). Figure 20 a, show a screenshot of the data log file on the personal computer connected to the SLAVE 2 station, and Figure 20 b shows a screen of the data log file in the Blink cloud.

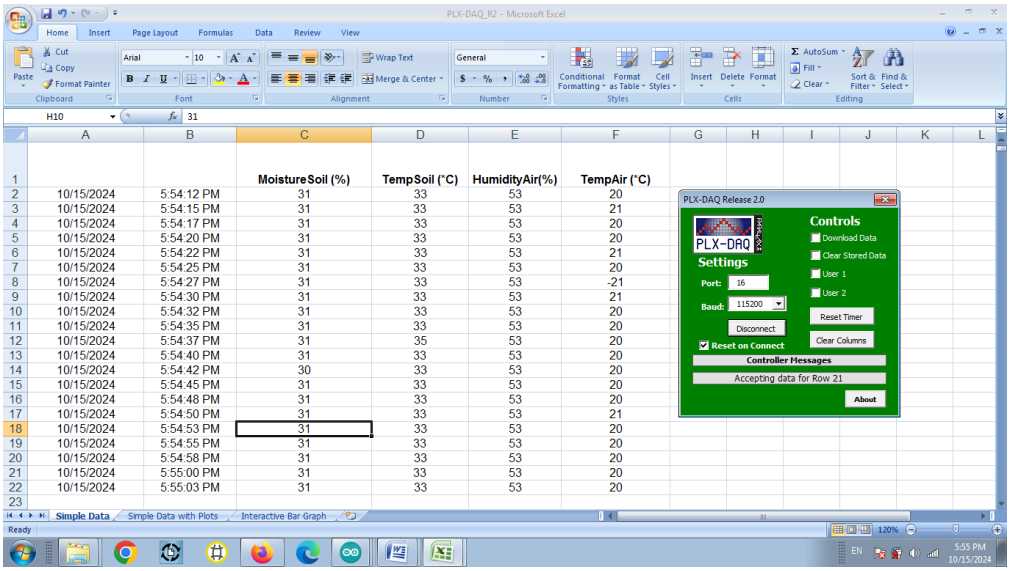

a.)

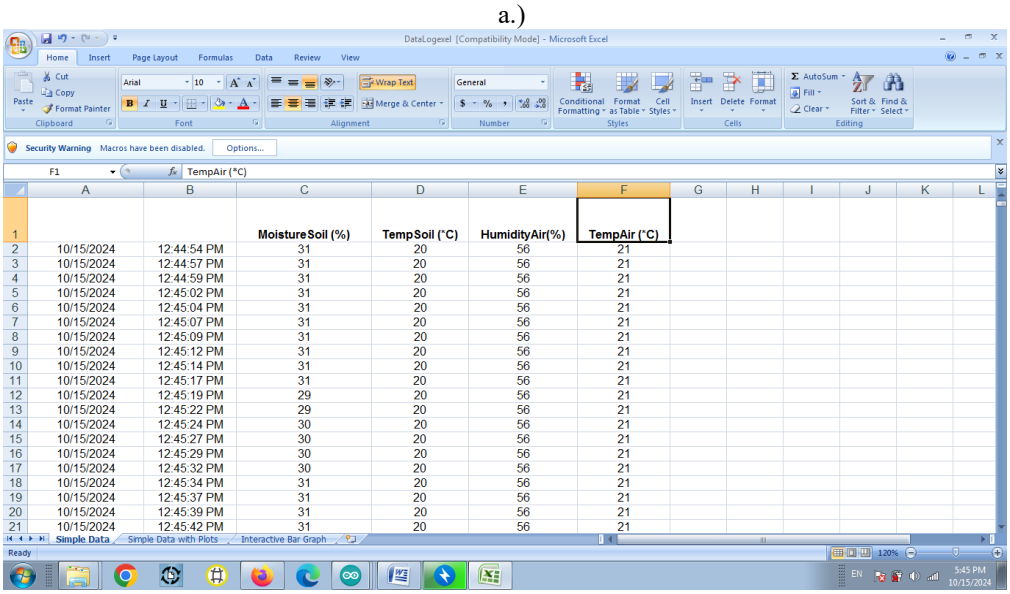

b.)

Figure 20. Screenshot: a.) Screen of the data log file from the personal computer connected to the SLAVE 2 station and b.) Screen of the data log file in the Blink cloud

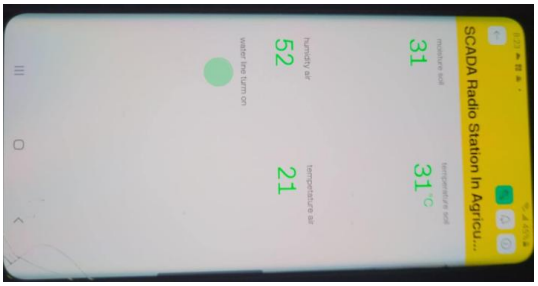

a)

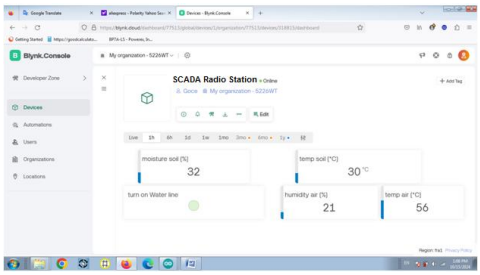

b)

Figure 12. Data transmission from the SCADA radio Station within IoT network: a) screen display on mobile device, b) interface on IoT Blynk cloud network

Figure 21(a) shows a data screen on a mobile device showing information transferred from a SCADA Radio station data system within IoT network, and Figure 21(b) represents the correcponding screen on the IoT Blynk cloud network (Microchip, n.d.).

Analysis of the Results

The solution in the paper provides an opportunity to apply a smart electronic system in agriculture. In the paper, the main benefit is the radio transmission of moisture and temperature signals from the irrigation line to the MASTER station. This eliminates the need for a wired connection of the sensors to the MASTER station. The used RF modules have been tested and enable radio transmission of process data from 100 to 5000m SCADA monitoring of process data is built into the MASTER station with support for waveforms of real-time quantities as well as a data log file for them. A radio connection was established among three points: SLAVE 1, MASTER and SLAVE 2. In the SLAVE 2 station, an IoT microcontroller is built-in, which enables the transmission of measurement data in the Internet network. The SLAVE 2 station allows the measurement data to be stored in a data log file on a personal computer connected to the microcontroller, as well as a data log file on the Blynk IoT cloud. The implemented system provides storage of measurement data in three data log files, in SCADA at the MASTER station as well as in two data log files at the SLAVE 2 station (on the local PC and on the IoT Blink Cloud).

Conclusion

This paper presents the design and experimental deployed prototype on SCADA radio relay station for data transmission in agriculture plants. A solution was implemented that enables RF communication between the soil sensors located in the irrigation line and the control room, where the main electronic equipment and the internet connection hardware are located. The tested nRF24L01 modules provide the possibility of remote wireless transmission of signals from 100m up to 5km in open air. The SLAVE 1 stations receive both digital and analog signals from soil and air sensors and transmit them to MASTER and SLAVE 2 stations. The SCADA system visualizes the data from SLAVE 1 on the control room screen, while SLAVE 2 displays the data on a local LCD and sends it IoT cloud computers and mobile smart devices (mobile telephone, tablet, etc.). To ensure data integrity, three data log files have been generated, one stored in the MASTER station and two stored in the SLAVE 2 station.

Scientific Ethics Declaration

* The authors declare that the scientific ethical and legal responsibility of this article published in EPSTEM journal belongs to the authors.

Conflict of Interest

*The author declares that there is no conflict of interest.

Funding

*This research received no internal or external funding.

Acknowledgements or Notes

* This article was presented as an oral presentation at the International Conference on Basic Sciences and Technology (www.icbast.net) held in Budapest/Hungary on August 28-31, 2025.

References

Arduino. (2021). Retrieved from https://www.circuitstoday.com/arduino-nano-tutorial-pinout-schematics.

Ariel, L.I.W. (2024). Design and evaluation of an IoT-based energy meter/power limiter to improve the management of low-voltage electrical subscribers - a case study of SNEL Likasi- DRC. *International Journal of Novel Research in Electrical and Mechanical Engineering, 11*(1), 60-67.

ATmega328P. (2015). Retrieved from https://ww1.microchip.com/downloads/en/DeviceDoc/Atmel-7810-Automotive-Microcontrollers-ATmega328P_Datasheet.pdf.

Bennett, S., Linken, S. (1982). *Computer control of industrial processes.* Inst of Engineering & Technology.

Bhuiyan, B.U., Karim, M. M., & Khan, I. (2023). IoT-based three-phase smart meter: Application for power quality monitoring. *6th International Conference on Electrical Information and Communication Technology (EICT)*, (pp. 1-6).

Blynk. (2025). Retrieved from https://blynk.cloud.

DHT22. (n.d.). Retrieved from https://www.sparkfun.com/datasheets/Sensors/Temperature/DHT22.pdf.

DS18B20. (2019). Retrieved from https://www.analog.com/media/en/technical-documentation/data-sheets/DS18B20.pdf.

ESP8266. (2020). Retrieved from https://www.espressif.com/sites/default/files/documentation/esp8266-technical_reference_en.pdf.

Fountas, S., Espejo-Garcia, B., Kasimati, A., Mylonas, N., & Darra, N. (2020). The future of digital agriculture: Technologies and opportunities. *IT Professional, 22*.

Hor, C. L., & Crossley, P. A. (2005). Knowledge extraction from intelligent electronic devices,. In *Lecture Notes in Computer Science* (Vol. 3400, pp. 82-111). Berlin: Springer.

Narendra, V.N, Sahana, S., & Chaithrashree, J. (2019). Digital agriculture. *Bulletin of Environment, Pharmacology and Life Sciences, 8*(6), 164-170.

nRF24L01. (2020). Retrieved from https://howtomechatronics.com/tutorials/arduino/arduino-wireless-communication-nrf24l01-tutorial/[14] https://howtomechatronics.com/tutorials/arduino/arduino-wireless-communication-nrf24l01-tutorial/.

Rotz, S., Duncan, E., Small, M., Botschner, J., Dara, R., Mosby, I., Reed, M., & Fraser, E.D.G. (2019). The politics of digital agricultural technologies: A preliminary review. *Sociologia Ruralis, 59*, 203-229.

Saiz-Rubio, V., & Rovira-Más, F. (2020). From smart farming towards agriculture 5.0: A review on crop data management. *Agronomy, 10*(2), 207.

Stefanov, G., & Kukuseva, M. (2021). RF sensor smart networ. *First International Conference ETIMA*, *1.* Stip.

Stefanov, G., Kukuseva, M., & Stefanova, S. (2023). 3-phase smart power meter implemented in RF network. *Balkan Journal of Applied Mathematics and Informatics, 6*(1), 25-37.

Stefanov, G., Kukuseva, M., & Stefanova, E. (2021). Design of an intelligent Wi-Fi sensor network. *Balkan Journal of Applied Mathematics and Informatics, 4*(1), 17-26.

Author(s) Information

Goce Stefanov
Faculty of Electrical Engenering
Goce Delcev University Stip
Krste Misirkov, 10A, 2000 Stip
North Macedonia
Contact e-mail: *goce.stefanov@ugd.edu.mk*

Bilijana Citkusheva-Dimitrovska
Faculty of Electrical Engenering
Goce Delcev University Stip
Krste Misirkov, 10A, 2000 Stip
North Macedonia

Vlatko Cingoski
Faculty of Electrical Engineering
Goce Delcev University
Krste Misirkov, 10A, 2000 Stip
North Macedonia

Maja Kukusheva-Paneva
Faculty of Electrical Engineering
Goce Delcev University
Krste Misirkov, 10A, 2000 Stip
North Macedonia

To cite this article:

Stefanov, G., Citkusheva-Dimitrovska. B., Cingoski, V., & Kukusheva-Paneva. M. (2025). SCADA monitoring on radio relayed station at hydro melioration system supported in lot network. *The Eurasia Proceedings of Science, Technology, Engineering and Mathematics (EPSTEM), 36,* 192-206.

The Eurasia Proceedings of Science, Technology, Engineering & Mathematics (EPSTEM)
ISSN: 2602-3199

The Eurasia Proceedings of Science, Technology, Engineering and Mathematics (EPSTEM), 2025

Volume 36, Pages 207-219

ICBAST 2025: International Conference on Basic Sciences and Technology

The Role of Big Data Analytics in Reinforcing the Business Sustainability of Enterprises

Mohamed A. Hamada
Abu Dhabi University

Gehad M. Hamada
International IT University

Abstract: Nowadays Big Data is becoming a vital instrument for many different disciplines, especially for the environmental and ecosystems aspects. It considers a new way of thinking, whereas big data analytics are organizing and analyzing large sets of data to generate and discover new patterns and themes that can solve issues and challenges that arise in society. The main purpose of this article is to clarify the evidential role of big data analytics in business sustainability achievement and to support the decision-making process. Research objectives were achieved through developing a big data analytics framework to support a large scale of business organization to achieve business sustainability and operational excellence to ensure market survival. Also, this research demonstrates the results of applying big data analytics for three big business enterprises as case studies (Amazon, Netflix, and Walmart). In fact, the analytics of big data brought great benefits for business enterprises on different scales.

Keywords: Data analytics, Business sustainability, Predictive analytics, Data models, AI Algorithms.

Introduction

The main concern of business organizations now is looking for how to achieve business sustainability, big data are very strategic components of success for all types of business organizations, and it's considered the main crucial factor to keep their survival and operational excellence on the market. One of the main challenges of business is the need to get the right information as fast as possible to the right user at the right time and in the easiest possible way through a huge amount of information is produced every day in big variety of ways. Organization survival in a highly competitive environment depends upon possessing the right information at the right time. Companies must have information concerning their customers, products, environment and themselves also (Kubina et al., 2015).

Recently big data analytics was considered as a game changer enabling improved business efficiency and effectiveness because of its high operational and strategic potential. The emerging literature on BDA has identified a positive relationship between the deployment of customer analytics and firm performance. For example, BDA allows firms to analyze and manage strategy through a data lens. Indeed, BDA is increasingly becoming a crucial component of decision-making processes in businesses. BDA is now considered as "a major differentiator between high performing and low-performing organizations," as it allows firms become proactive and forward-looking, decreases customer acquisition costs by about 47% and enhances firm revenue by about 8% (Wamba et al., 2017).

Big Data Analytics also is increasingly becoming a trending practice that many organizations are adopting with the purpose of constructing valuable information from BD. The analytics process, including the deployment and use of BDA tools, is seen by organizations as a tool to improve operational efficiency though it has strategic potential, drives new revenue streams and gain competitive advantages over business rivals. Extant research

- Selection and peer-review under responsibility of the Organizing Committee of the Conference

studies have demonstrated that substantial value and competitive advantage can be attained by businesses from taking effective decisions based on Data But, BDA is more perplexing than merely tracing, classifying, comprehending, and quoting data (Sivarajah et al., 2017).

The main purpose of this paper is to introduce a big data analytics framework to support a large scale of business organization to achieve its business sustainability and market survival. This paper is organized as follows; the next section is clarifying how big data now is becoming an important asset in business organization, that is our initial and introduction goal with describing the research methods. Next, the big data analytics importance and platforms are demonstrated with a brief review of relevant literature concerning. The paper then discusses the main aspects and characteristics of business sustainability. Developing the big data analytics framework is the main section of this paper, then the research ends with a conclusion section.

Literature Review

Big Data as an Asset

Big data is a potential knowledge asset, contingent upon the proper use of that knowledge. BDA represents technologies drivers of a strategic knowledge asset (big data). BDA applications have the potential to add value by providing more transparent and accurate results to support decision-making in several business areas (Côrte-Real et al., 2017).

The emerging technological development of big data is recognized as one of the most important areas of future information technology and is evolv- ing at a rapid speed, driven in part by social media and the Internet of Things (IoT) phenomenon. The technological developments in big data infrastruc- ture, analytics, and services allow firms to trans- form themselves into data-driven organizations (Lee, 2017). Big data provides great potential for firms in creat- ing new businesses, developing new products and services, and improving business operations, the use of big data analytics can create benefits, such as cost savings, better decision making, and higher product and service quality.

The opportunities arising from big data analytics for organizations are considered pivotal: big data has been described as, ‘‘the mother lode of disruptive change in a networked business environment”. By adopting big data technologies, organizations expect to gain benefits across many domains, such as e-commerce, e-government, science, health, and security. What benefits organizations perceive as ‘‘value” depends on their strategic goals for adopting and using big data (Günther et al., 2017).

Economic value can be measured by an organization’s increase in profit, business growth, and competitive advantage resulting from big data adoption (Davenport, 2006; Davis, 2014; Tyagi, 2003). Economic value often comprises monetary benefits that are appropriated by organizations. For example, organizations that rely on big data to guide organizational strategies and day-to-day operations are expected to perform better financially than organizations that do not, in other word we can say that big data has strategic potential drive new revenue streams and maximize the competitive advantages for business enterprises.

In general, big data is perceived as a source of innovative products, services, and business opportunities. Moreover, big data is believed to result in more efficient and effective operations by, for example, optimizing supply chain flows; setting the most profitable price for products and services; selecting the right people for certain tasks and jobs; minimizing errors and quality problems, and improving customer relationships. Additionally, further economic and social value can be gained from big data through enhanced decision making and more informed strategizing (Günther et al., 2017).

Conventionally, big data are presented in terms of 3 Vs namely, (1) volume, (2) velocity, and (3) value (Rehman et al., 2016; Xie et al., 2016; Ziora, 2015). *Volume* represents the size of the data, now every day the world produces around 4 quintillion bytes of data (i.e. 1 Exabyte equals 1 quintillion bytes or 1 Exabyte equals 1 billion gigabytes) as shown in table (1). whereas *Velocity* represents the increasing speed of data that can be generated and entered into big data systems. The *Value* property of big data determines its usefulness to take actionable decisions after data analysis. However, big data is currently redefined with the addition of three new Vs: (1) variety, (2) variability, and (3) Veracity, whereas *Variety* means multiple types of data sets, data can be existed in many types and forms, these data include textual content (i.e. structured, semi structured as well as unstructured), to multimedia content (e.g. videos, images, audio) on a multiplicity of platforms (e.g. machine-to-machine communications, social media sites, sensors networks, cyber-physical systems, and Internet of Things

(IoT)) ***Variability*** indicates to data whose meaning is constantly changing with inconsistencies data types and sources, and ***Veracity*** refers to uncertainty thinking about the big data accuracy, although the high potential value of Big Data, the data is virtually worthless if it's not accurate (Rehman et al., 2016). In our research we can expand big data characteristics into 10Vs to become as the following chart in Figure (1).

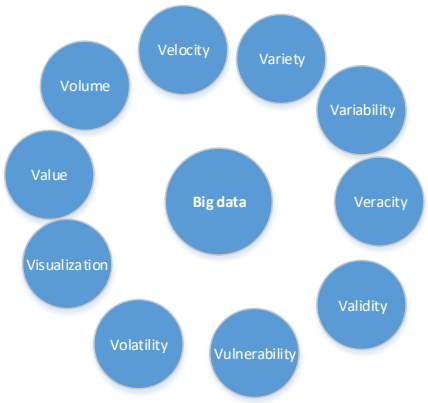

Figure 1. Big data 10Vs

The new 4Vs are Validity, Vulnerability, Volatility, and Visualization. *Validity* means adopting good data governance practices to ensure the consistency and the quality of data for analytics. *Vulnerability* refers to the new security concerns escorted with big data, now the probability of data breach with big data transaction can occur in a high percentage. *Volatility* indecates to the time aspects for big data management such as the procedures to ensure rapid retrieval of data when it's required, the costs and complexity of a big data storage and data process for business needs. Eventually, Big Data *Visualization* involves the presentation of data of almost any type in a graphical format that makes it easy to understand and interpret. But it goes far beyond typical corporate graphs, histograms and pie charts to more complex representations like heat maps and fever charts, enabling decision makers to explore data sets to identify correlations or unexpected patterns.

Table 1. Datasets volume size

Value	**Name**	**Abbreviation**
1000^1	Kilobytes	KB
1000^2	Megabytes	MB
1000^3	Gigabytes	GB
1000^4	Terabytes	TB
1000^5	Petabytes	PB
1000^6	Exabytes	EB
1000^7	Zettabytes	ZB
1000^8	Yottabytes	YB
1000^9	Brontobytes	BB
1000^{10}	Geopbytes	GEB

One of most recent Research in big data refers that nearly 90% of enterprises fail, and one of the key failure reasons is invaluable products and services that do not meet customer expectations. A market research on 135 failed startups reveals that 42% of failures occurred because the products and services did not meet the market needs, 17% failed because of the lack of business models, and 14% of the enter- prises failed because they ignored their customers (Rehman et al., 2016).

Likewise, organizations constantly look for opportunities to increase their competitive advantage in an increasingly competitive market place by using better analytical models as an aspect to attain business sustainability. so, it is necessary to introduce results in a more clear and concise form. These challenges push the organizations to depend on business intelligence applications and data analytics models that allow better reporting and visualization of the big data as an important asset for running the enterprise operations.

Tekiner and Keane made in-depth literature review to identify the added value of big data as an asset in the enterprises, also focused on investigating the main platforms of big data analytics and clarifying the main factors which construct the purposed framework to guide the business firms to achieve business sustainability. Developing the purposed framework in this research based on the balance between the information technology

factors and business factors which maximize the value of big data to achieve the business sustainability (Tekiner & Keane, 2013).

Big Data Analytics Importance and Platforms

Big data has become a vital resource for many sectors of society. Beyond its importance to businesses and industries, it also plays a role in everyday life and has implications for national security. Data today is generated through countless activities—such as point-of-sale (POS), sensor readings, online purchases, emails, videos, and interactions on social media. Major technology companies, including Google, Amazon, Facebook, Twitter, and Baidu, have already built extensive systems to capture and analyze this information. Governments in countries like the United States, China, India, and Japan have likewise invested heavily in advancing research and developing strategies to make use of big data (Chawda & Thakur, 2016). Big data analytics has become an essential driver of value for contemporary businesses. Organizations increasingly depend on analytical tools not only to manage internal operations but also to gather and interpret customer feedback. By doing so, they gain insights into consumer preferences and can adapt their products or services to meet evolving needs while maintaining a competitive edge. In this way, delivering value to the customer (V2C) is as important for long-term survival as achieving profitability and sustaining revenue growth (Rehman et al., 2016).

Another important aspect of big data analytics is the difficulty of managing business and manufacturing data with traditional platforms. Systems such as computer-aided design (CAD), supply chain management (SCM), manufacturing execution systems (MES), and enterprise resource planning (ERP) were not originally designed to process the sheer volume and complexity of modern data, which makes their use increasingly limited in this context.(Fahmideh & Beydoun, 2018). As illustrated in Figure (2), the process of big data analytics typically involves six key stages: (1) collecting data from various direct and indirect sources, (2) carrying out preprocessing and integration to enhance data quality, (3) developing learning models through statistical approaches and machine learning–based data mining techniques, (4) assessing these models with test data, (5) implementing the models in practical applications, and (6) monitoring their performance, particularly with respect to prediction accuracy (Rehman et al., 2016).

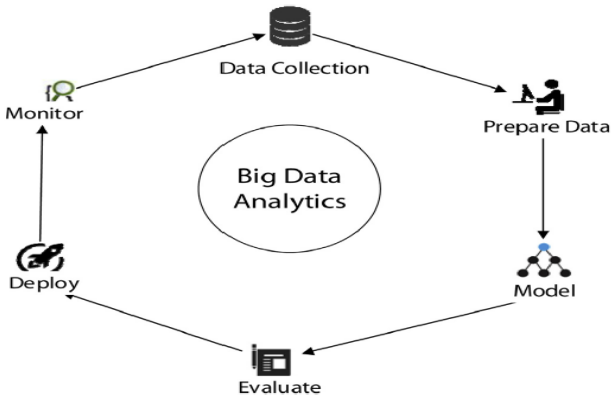

Figure 2. Big data analytics process, (Rehman et al., 2016)

With advanced big data (BD) analytics tools such as NoSQL databases, BigQuery, MapReduce, Hadoop, WibiData, and Skytree, organizations can now improve strategies and decision-making in areas like healthcare, economic growth, energy forecasting, and disaster prediction. Despite these advances, challenges remain: process-related issues include capturing, integrating, cleaning, and transforming data, as well as selecting suitable models and presenting results, while management challenges concern privacy, security, governance, cost, and ethical considerations (Sivarajah et al., 2017).

Types of Big Data Analytics

Big data analytics has become a core component of modern business, transforming large and complex datasets into actionable insights that support better decision-making. Its importance is reflected in the fact that nearly 80% of CEOs and executive teams view big data initiatives as essential for driving revenue growth, reducing costs, and improving efficiency. Consistently, more than 80% of organizations report that they are already engaged in projects in this area. (Park et al., 2017). In general, there are three types of BDA as following;

Descriptive Analytics

Descriptive analytics is the most basic form of big data analytics (BDA), aimed at summarizing and explaining patterns using statistical measures such as mean, median, mode, standard deviation, variance, and event frequency in data streams. A common application is dashboards, where organizations track key metrics to monitor processes over time (Banerjee, et al., 2013).

Predictive Analytics

Predictive analytics focuses on forecasting outcomes by applying statistical modeling and machine learning methods, including supervised, unsupervised, and semi-supervised approaches. By detecting patterns and relationships in historical data, it generates estimates about future events, allowing organizations to anticipate opportunities and risks (Gandomi et al., 2015).

Prescriptive Analytics

Prescriptive analytics focuses on determining the most effective next steps for a business. It takes the outcomes of other analyses and translates them into clear recommendations for improving processes. In other words, it uses predictions to guide organizations on how to optimize their operations. Although implementing prescriptive analytics can be challenging, it is highly valuable in helping companies adapt to changing information and ensuring that their business models continue to evolve (Sivarajah et al., 2017).

Big Data Analytics and Business Sustainability

Ertz et al. (2024), they explored how Big Data Analytics (BDA) influences a company's sustainability performance through the lens of a triple bottom line (TBL) framework. By examining 522 firms from the S&P 500 and TSX 60, the researchers discovered that BDA can significantly boost economic outcomes like achieving a 300% return on investment for data-driven content as well as social benefits, such as increased corporate social responsibility (CSR) engagement, and environmental improvements, including a 30% reduction in waste. They found that prescriptive analytics, which includes tools like AI and deep learning, tends to slightly outperform predictive analytics when it comes to enhancing sustainability. The researchers pointed out that the key to BDA success lies in human capital, stressing the importance of training the workforce rather than just investing in technology. Additionally, their research filled gaps left by previous self-reported studies by utilizing third-party data sources like MSCI ESG and Compustat, while integrating Resource-Based Theory with the Knowledge-Based View (Ertz et al., 2024).

Waqas and Tan (2022), they explored how Big Data Analytics (BDA) and green technology innovation capabilities (GTIC) can boost sustainable performance in the manufacturing sector of Pakistan. By analyzing survey data and employing structural equation modeling, the researchers discovered that both BDA and GTIC play a significant role in enhancing green production. This improvement not only leads to a competitive edge but also contributes to the overall sustainable performance of firms. The research also pointed out the important roles of corporate reputation and supply chain innovativeness, indicating that these elements can amplify the positive impacts of BDA. Interestingly, companies that utilized BDA saw better environmental results, such as reduced waste, along with economic benefits from more efficient green practices. This research highlights the strategic importance of combining BDA with an environmental focus, especially in emerging markets (Waqas & Tan, 2022).

Mehmood et al. (2023), investigated how Big Data Analytics (BDA) can create a green competitive advantage (GCA) through green innovation (GI) in 397 manufacturing companies. By analyzing time-lagged data, the research showed that BDA significantly boosts GI, which in turn positively influences GCA. Additionally, it was found that having a green organizational identity (GOI) strengthens the connection between GI and GCA, acting as an important moderator. These insights emphasize the role of BDA in achieving both environmental and economic benefits when it aligns with corporate sustainability values. This study fills a crucial gap by illustrating how data-driven innovation can lead to a unique position in the market (Mehmood et al.,2023).
Zameer et al., 2024, in this research they explored how big data capabilities can boost a company's green competitive advantage by enhancing organizational learning and green marketing skills. Additionally, big data capabilities played a moderating role, strengthening the connection between organizational learning and green

marketing, which in turn amplified the indirect effects. The study highlighted the game-changing impact of big data on sustainable business practices, providing valuable insights for companies looking to use data-driven strategies to meet their environmental and competitive objectives (Zameer et al., 2024).

Olajiga et al. (2024), they put forward an innovative framework aimed at harnessing data analytics within energy companies to drive strategic business success. They pointed out that by incorporating machine learning, predictive modeling, and real-time analytics, organizations can streamline their operations—think asset management, supply chains, and demand forecasting while also reducing risks in the ever-changing energy landscape. A key takeaway from the study is the importance of aligning analytics efforts with the company's culture and leadership to promote data-driven decision-making. Ultimately, their framework positions data analytics as a game-changing resource for boosting operational efficiency, enabling predictive maintenance, and enhancing competitive agility in the energy market (Olajiga et al., 2024).

Research Methodology

This study takes a mixed-methods approach, blending both qualitative and quantitative techniques to delve into how big data analytics can bolster business sustainability. On the qualitative side, we look at case studies from industry giants like Amazon, Netflix, and Walmart, alongside a thorough literature review to pinpoint trends, challenges, and best practices in adopting big data for sustainability. The quantitative aspect involves analyzing the performance of the developed framework. We asked the professionals executive managers in big data analytics about the framework's effectiveness; we employ thematic analysis for the qualitative insights and use statistical tools for the quantitative data. The research spans thirteen months and is organized into several phases: literature review, case study analysis, data collection, sustainability impact assessment, and write-up reporting. The developed framework evaluated accorindg to selected criteria like framework accuracy, scalability, easy of use, technical components, Data Quality and Integrity, and Performance and Speed.

Research Model and Framework Design

Designing a framework structure for Big Data Analytics in business organizations entails identifying the critical layers, components, and procedures that convert big data into usable business insights. Figure (3) illustrates the main components of the design structure for the developed framework of big data analytics.

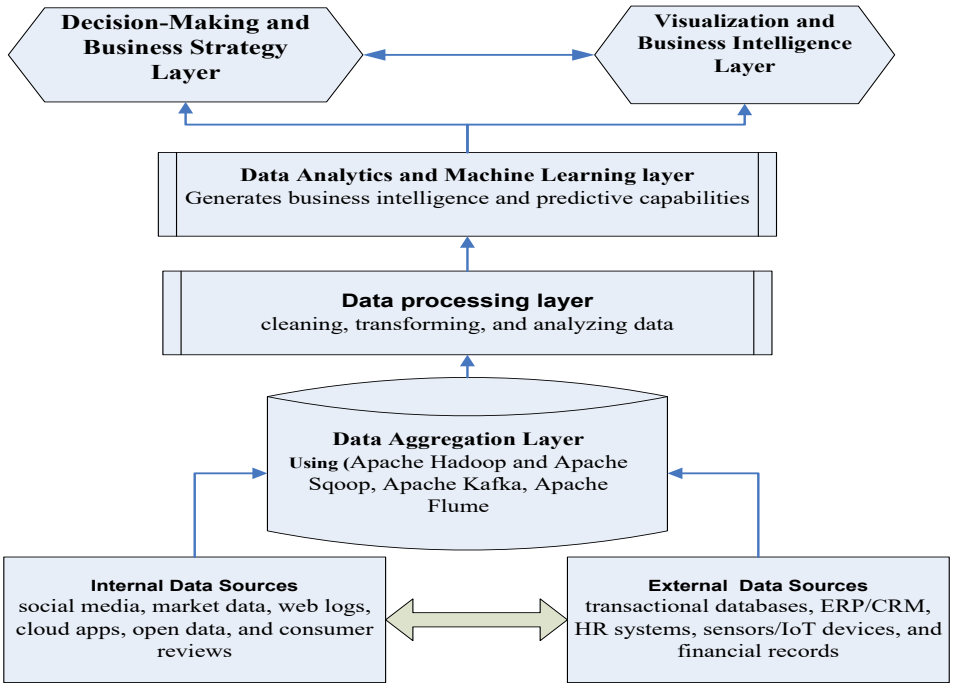

Figure 3. the developed framework structure of big data analytics

The process starts with the data sources layer, which collects structured, semi-structured, and unstructured data from both internal systems like ERP, CRM, and IoT devices and external settings like social media platforms,

market feeds, and open data repositories. These different datasets enter the system via the data ingestion layer, which controls both real-time and batch data flows with tools like Apache Kafka, Flume, and Hadoop. Then, data is structured and preserved at the data storage layer, which often uses scalable distributed storage systems like Hadoop Distributed File System (HDFS), NoSQL databases, or cloud-based data lakes. To ensure usability, the data processing layer cleans, transforms, and integrates data with batch and stream processing tools such as Apache Spark, Flink, and Storm.

The analytics and machine learning layer is the main focal point of the architecture, utilizing descriptive, predictive, and prescriptive analytics to extract business intelligence. Machine learning models, artificial intelligence algorithms, and statistical techniques improve the ability to identify patterns, forecast trends, and make data-driven decisions, subsequently, the insights gained are sent to the decision-making and strategy layer, where managers and executives use them to optimize operations, tailor consumer experiences, detect dangers, strengthen supply chains, and ensure long-term business viability. These framework design procedures can be summarized in the following steps:

(1) Data Sources Layer

Diverse data from internal and external sources flow into the analytics system, which serves as the framework's core. Internal sources include transactional databases, ERP/CRM, HR systems, sensors/IoT devices, and financial records. And the External sources include social media, market data, web logs, cloud apps, open data, and consumer reviews.

(2) Data Aggregation Layer

This layer is responsible for gathering, importing, and streaming data from various sources.

- Tools for batch processing include Apache Hadoop and Apache Sqoop.
- Real-time streaming tools include Apache Kafka, Apache Flume, and AWS Kinesis.

(3) Data Storage Layer

A scalable, distributed platform for storing enormous amounts of data. Example, Hadoop Distributed File System (HDFS). Also, Databases include NoSQL (MongoDB, Cassandra, HBase) and Relational (PostgreSQL, MySQL) and Data warehouses include Snowflake, Redshift, and BigQuery.

(4) Data Processing Layer

The core of analytics is in charge of cleaning, transforming, and analyzing data, At this phase more actions are done like the following procedures :

- Data preparation includes cleansing, normalization, and feature engineering.
- Extract, Transform, and Load (ETL) tools include Talend, Informatica, and Apache NiFi.
- Batch processing with Apache Hadoop and Spark

(5) The Analytics and Machine Learning layer

In this phase, it generates business intelligence and predictive capabilities through the following analysis.

- Descriptive Analytics includes historical reporting and dashboards.
- Diagnostic analytics for root cause analysis.
- Predictive analytics using TensorFlow, PyTorch, and Spark MLlib.

(6) Visualization and Business Intelligence Layer
It converts results into insights for decision-makers to be more useful for strategic decisions.

- Tools include Tableau, Power Bi and Looker.
- Functions include dashboards, scorecards, trend analysis, and forecasting charts.
- Create user-friendly reports for managers, executives, and stakeholders.

(7) Decision-Making and Business Strategy Layer

This is the final phase to translating data analytics insights into business value to achieve business objectives and sustainability, it also include:

- Applications include customer segmentation and customization.
- Optimize the supply chain.
- Fraud detection and risk management.
- Strategic planning and sustainability efforts.

Research Results

In this section, the results of measuring the effectiveness of the developed research BDA framework will be illustrated, also the results of applying big data analytics of the selected case studies are displayed. Regarding the effectiveness of the developed BDA framework, the executive managers of selected companies and institutions was asked to evaluate the framework from their practical experience, the evaluation of the framework effectiveness based on these criteria:

- The existence of Comprehensive technical components of the framework,
- Framework flexibility of use,
- Achieving Data Quality and Integrity,
- Scalability which the framework's ability to handle increasing data volumes and growing,
- Framework Performance and Speed,
- Framework Accuracy to make processing correctness and precision of the analytics results)

The responses collected from the executive managers showed very good effectiveness for the developed BDA framework as illustrated in Figure (4).

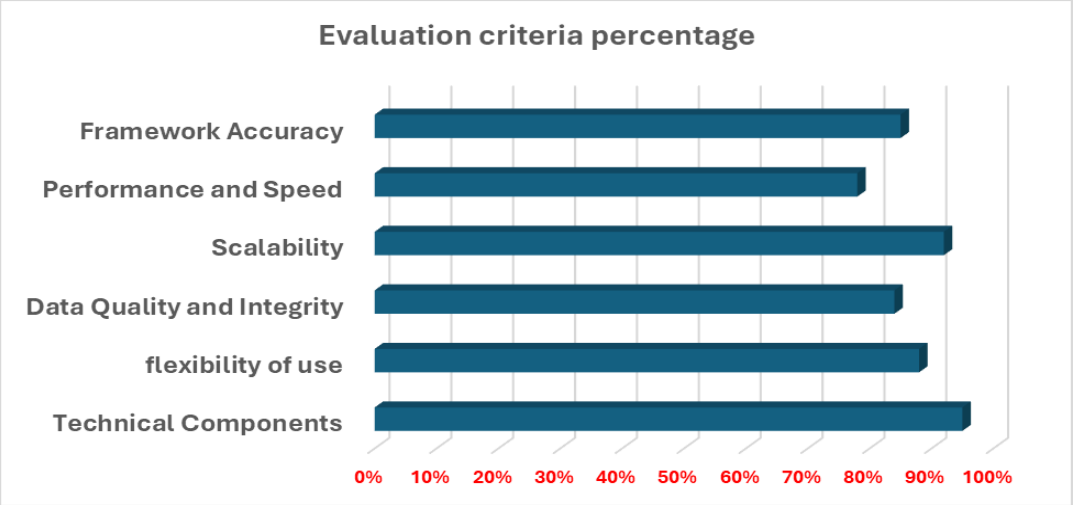

Figure 4. The evaluation criteria for the research framework

Secondly, the analysis of the research case studies shows high benefits and advantages of depending on big data analytics in business companies to achieve business sustainability and keeping the company market share according the following results for the big companies (Amazon, Netflix and Walmart).

Amazon - Leveraging Big Data for Enhanced Customer Experience and Operational Efficiency

Amazon leverages big data analytics to enhance customer experience and operational efficiency, directly contributing to its long-term business sustainability. By analyzing customer behavior, supply chain data, and market trends, Amazon achieves:

Revenue Growth

- Personalized recommendations drive 35% of total sales
- Dynamic pricing optimizes profit margins

Operational Efficiency

- Supply chain analytics reduce delivery times from 3 days to same/next-day
- Inventory management systems cut costs by 20%

Sustainable Competitive Advantage

- Customer sentiment analysis improves product quality & reduces returns
- Data-driven logistics minimize energy waste in fulfillment centers

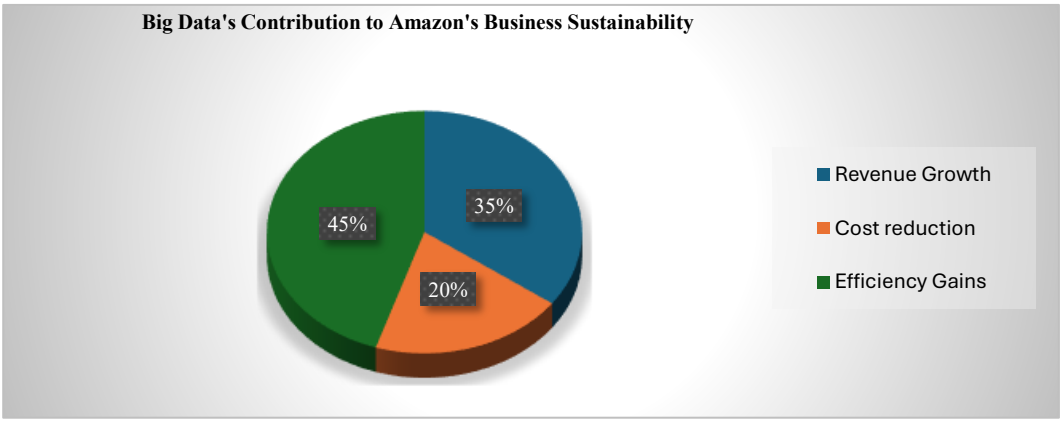

Figure 5. Big data's contribution to Amazon's business sustainability

Segments as illustrated in Figure (5):
Revenue Growth (35%) – Blue – Personalized recommendations driving sales
Cost Reduction (20%) – Orange – Supply chain optimization savings
Efficiency Gains (45%) – Grey – Faster deliveries + reduced waste
35% of Amazon's sustainability comes directly from data-driven revenue streams

Netflix - Using Big Data to Revolutionize Content Creation and Personalization

Netflix is shaking things up in the entertainment world by harnessing the power of big data. They use analytics not just to deliver content, but also to create it and keep their viewers coming back for more. Their recommendation system, which relies on cutting-edge machine learning, influences a whopping 80% of what people choose to watch. This data-driven approach has led to the creation of popular originals like House of Cards. By closely examining how users interact with their platform like when they pause or rewind shows Netflix has managed to cut subscriber churn by 25% with smart engagement strategies. On the operational side, they've optimized bandwidth by 20% through forecasting peak usage, and their investments in original content have paid off big time, yielding a 300% return on investment. Thanks to these innovative strategies, Netflix has skyrocketed to over 230 million subscribers and continues to lead the market.

This case demonstrates how big data enables sustainable competitive advantage in the digital entertainment industry as shown in Figure (6).

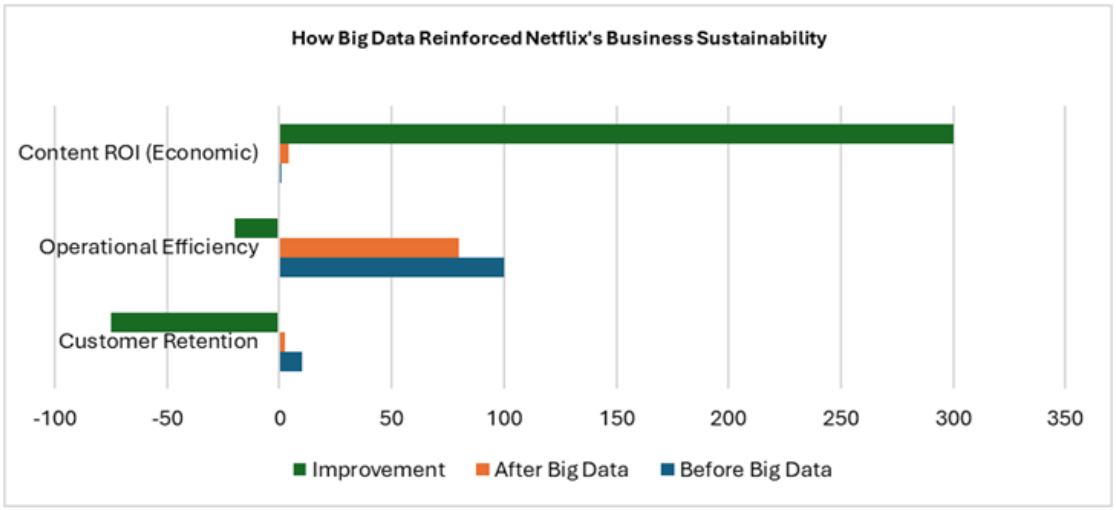

Figure 6. Netflix big data usages to improve three key business areas

Customer Retention

- Before: 10% of subscribers left monthly
- After: Only 2.5% leave now
- Improvement: 75% better

Operational Efficiency

- Before: Full bandwidth usage
- After: 20% less bandwidth needed
- Improvement: Smoother streaming

Economic Growth

- Before: $1 million profit per show
- After: $4 million profit per show
- Improvement: 300% more profitable

Case Study: Walmart - Optimizing Retail Operations and Enhancing Customer Experience

Walmart is really shaking things up in the retail world by using big data analytics to enhance everything from operations to supply chain management and customer interactions. Their unique Retail Link system processes millions of transactions every day, allowing for real-time inventory tweaks that help cut down stockouts by 30% and reduce overstock costs by 25%. Plus, their dynamic pricing algorithms, which are powered by competitor insights and demand data, not only drive sales but also help them stay ahead in pricing. By diving into customer buying habits, Walmart has managed to achieve a 20% boost in campaign conversion rates. Working closely with suppliers and sharing data has led to a 15% drop in logistics costs and faster delivery times. All these innovations have played a key role in keeping Walmart at the top as the world's largest retailer, raking in an impressive $611 billion in revenue for 2023.

As analysis in Figure 7, which illustrates the impact of Big Data Analytics on Walmart's approach to business sustainability. This clustered column chart highlights three important sustainability metrics, comparing the numbers before and after Walmart embraced big data solutions:

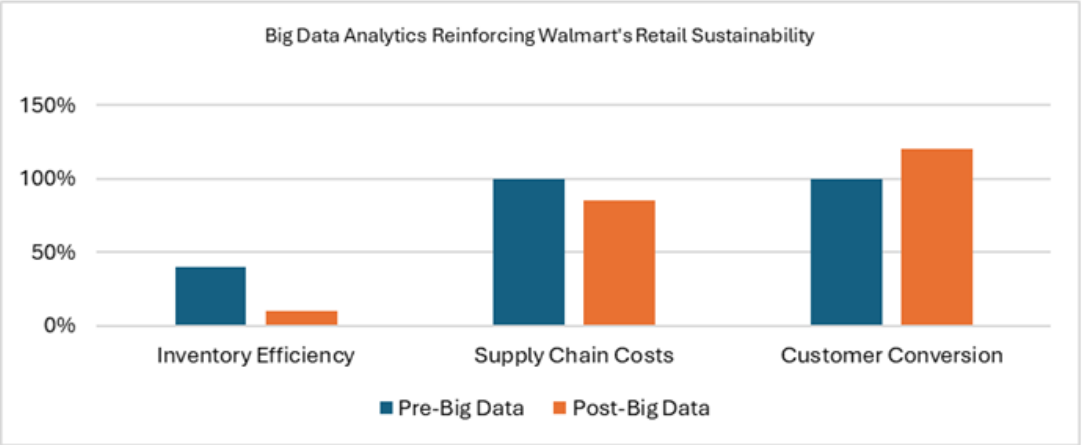

Figure 7. The impact of big data analytics on Walmart's

Inventory Efficiency (Red)

- Stockout rates dropped from 40% to 10%, a 30% reduction
- Achieved through predictive demand forecasting

Supply Chain Costs (Blue)

- Operational costs decreased from 100% baseline to 85%
- Represents 15% savings via logistics optimization

Customer Conversion (Green)

- Marketing effectiveness increased by 20% (100% → 120%)
- Driven by personalized promotions using purchase history

This visual clearly shows how big data enhances all three pillars of Walmart's business sustainability operational (inventory), economic (costs), and customer-facing (conversions). The most notable improvement was in inventory management, with a remarkable 30% reduction in stockouts. This underscores the crucial role big data plays in minimizing lost sales and cutting down on waste.

Results Discussions and Analysis

This study examines how major companies use big data analytics to strengthen their long-term business sustainability. Our deep dive into Amazon, Netflix, and Walmart highlights how big data analytics fuels sustainable business growth. These industry giants demonstrate that leveraging data-driven strategies can enhance financial performance, streamline operations, and positively impact the environment all at once. Take Amazon, for instance. They harness customer data to fuel recommendations that account for a whopping 35% of their total sales. Their systems are so advanced that they adjust prices in real-time to keep up with the competition. By analyzing supply chain data, Amazon has managed to slash delivery times from three days down to same-day for many orders, all while cutting costs by 20%. Their route optimization efforts have also saved 15% in fuel costs, proving that data can benefit both profits and the planet. Then there's Netflix, which keeps its audience hooked through data insights.

A staggering 80% of the content viewers watch comes from its recommendations. This strategy has led to a remarkable 75% drop in customer cancellations, going from 10% to just 2.5% monthly. Their data-driven decisions on content have paid off handsomely, with hits like House of Cards yielding returns of 300%. Plus, by predicting viewing patterns, Netflix uses 20% less bandwidth. Walmart's Retail Link system is another great example, tracking millions of transactions daily to enhance operations. This system has cut out-of-stock items by 30% and reduced excess inventory costs by 25%. Improvements in the supply chain have lowered expenses by 15% while speeding up delivery times. By utilizing customer data, Walmart has also made its marketing campaigns 20% more effective. Despite their successes, all three companies face common challenges. Building

these sophisticated data systems requires significant investment, and safeguarding customer privacy is paramount.

Employees must also be trained to effectively use these tools, and upgrading outdated computer systems can be quite a hurdle. Each industry applies data in its own unique way: - Retail (Walmart) hones in on inventory and pricing- Streaming (Netflix) focuses on enhancing content and customer retention. E-commerce (Amazon) optimizes delivery and personalized recommendations Looking to the future, companies that successfully blend big data with emerging technologies and invest in employee training are likely to keep their competitive edge. The evidence is clear: smart data utilization strengthens every facet of business sustainability financial, operational, and environmental.

Research Conclusion

- This research demonstrates the significant role of Big Data Analytics (BDA) in strengthening the business sustainability of enterprises. By enabling organizations to collect, process, and analyze massive volumes of structured and unstructured data, BDA empowers decision-makers to identify patterns, optimize operations, and anticipate market shifts.
- The research has developed a suitable framework for working with big data analytics to achieve business sustainability.
- The research deep dive into Amazon, Netflix, and Walmart highlights how big data analytics fuels sustainable business growth. These industry giants demonstrate that leveraging data-driven strategies can enhance financial performance, streamline operations

Scientific Ethics Declaration

*The authors declare that the scientific ethical and legal responsibility of this article published in EPSTEM journal belongs to the authors.

Conflict of Interest

*The authors declare that they have no conflicts of interest

Funding

* No funding sources for research

Acknowledgements or Notes

* This article was presented as an oral presentation at the International Conference on Basic Sciences and Technology (www.icbast.net) held in Budapest/Hungary on August 28-31, 2025.

References

Ahmed, E., Yaqoob, I., Hashem, I. A. T., Khan, I., Ahmed, A. I. A., Imran, M., & Vasilakos, A. V. (2017). The role of big data analytics in Internet of Things. *Computer Networks, 129*, 459-471

Banerjee, A., Bandyopadhyay, T., & Acharya, P. (2013). Data analytics: Hyped up aspirations or true potential?. *Vikalpa, 38*(4), 1-12

Brunswicker, S., Bertino, E., & Matei, S. (2015). Big data for open digital innovation–a research roadmap. *Big Data Research, 2*(2), 53-58

Chawda, R. K., & Thakur, G. (2016, March). Big data and advanced analytics tools. *2016 symposium on colossal data analysis and networking (CDAN)* (pp. 1-8). IEEE

Côrte-Real, N., Oliveira, T., & Ruivo, P. (2017). Assessing business value of big data analytics in European firms. *Journal of Business Research, 70*, 379-390.

Erevelles, S., Fukawa, N., & Swayne, L. (2016). Big Data consumer analytics and the transformation of marketing. *Journal of Business Research*, *69*(2), 897-904.

Ertz, M., Latrous, I., Dakhlaoui, A., & Sun, S. (2025). The impact of big data analytics on firm sustainable performance. *Corporate Social Responsibility and Environmental Management, 32*(1), 1261-1278Ertz,

M., Latrous, I., Dakhlaoui, A., & Sun, S. (2025). The impact of big data analytics on firm sustainable performance. *Corporate Social Responsibility and Environmental Management, 32*(1), 1261-1278

Fahmideh, M., & Beydoun, G. (2019). Big data analytics architecture design:An application in manufacturing systems. *Computers & Industrial Engineering, 128*, 948-963

Gandomi, A., & Haider, M. (2015). Beyond the hype: Big data concepts, methods, and analytics. *International Journal of İnformation Management, 35*(2), 137-144

Gupta, M., & George, J. F. (2016). Toward the development of a big data analytics capability. *Information & Management, 53*(8), 1049-1064

Günther, W. A., Mehrizi, M. H. R., Huysman, M., & Feldberg, F. (2017). Debating big data: A literature review on realizing value from big data. *The Journal of Strategic Information Systems, 26*(3), 191-209

Kubina, M., Varmus, M., & Kubinova, I. (2015). Use of big data for competitive advantage of company. *Procedia Economics and Finance, 26*, 561-565

Lee, I. (2017). Big data: Dimensions, evolution, impacts, and challenges. *Business Horizons, 60*(3), 293-303

Mehmood, K., Kiani, A., & Rashid, M. D. (2025). Is data the key to sustainability? The roles of big data analytics, green innovation, and organizational identity in gaining green competitive advantage. *Technology Analysis & Strategic Management, 37*(5), 494-508

Olajiga, O. K., Olu-lawal, K. A., Usman, F. O., & Ninduwezuor-Ehiobu, N. (2024). Data analytics in energy corporations: Conceptual framework for strategic business outcomes. *World Journal of Advanced Research and Reviews, 21*(3), 952-963

Oussous, A., Benjelloun, F. Z., Ait Lahcen, A., & Belfkih, S. (2018). Big Data technologies: A survey. *Journal of King Saud University-Computer and Information Sciences, 30*(4), 431-448

Park, G., Park, S., Khan, L., & Chung, L. (2017, February). IRIS: A goal-oriented big data analytics framework on Spark for better business decisions. *2017 IEEE International Conference on Big Data and Smart Computing (BigComp)* (pp. 76-83). IEEE

Rehman, M. H., Chang, V., Batool, A., & Wah, T. Y. (2016). Big data reduction framework for value creation in sustainable enterprises. *International Journal of Information Management, 36*(6), 917-928

Sivarajah, U., Kamal, M. M., Irani, Z., & Weerakkody, V. (2017). Critical analysis of big data challenges and analytical methods. *Journal of Business Research, 70*, 263-286

Tekiner, F., & Keane, J. A. (2013). Big data framework. *2013 IEEE İnternational Conference on Systems, Man, and Cybernetics* (pp. 1494-1499). IEEE

Wamba, S. F., Gunasekaran, A., Akter, S., Ren, S. J. F., Dubey, R., & Childe, S. J. (2017). Big data analytics and firm performance: Effects of dynamic capabilities. *Journal of Business Research, 70*, 356-365

Waqas, M., & Tan, L. (2023). Big data analytics capabilities for reinforcing green production and sustainable firm performance: The moderating role of corporate reputation and supply chain innovativeness. *Environmental Science and Pollution Research, 30*(6), 14318-14336

Xie, K., Wu, Y., Xiao, J., & Hu, Q. (2016). Value co-creation between firms and customers: The role of big data-based cooperative assets. *Information & Management, 53*(8), 1034-1048

Zameer, H., Wang, Y., & Yasmeen, H. (2024). Strengthening green competitive advantage through organizational learning and green marketing capabilities in a big data environment: a moderated-mediation model. *Business Process Management Journal, 30*(6), 2047-2072

Ziora, A. C. L. (2015). The role of big data solutions in the management of organizations. Review of selected practical examples. *Procedia Computer Science, 65*, 1006-1012

Author(s) Information

Mohamed Hamada
Abu Dhabi University
United Arab Emirates
Contact e-mail: *mohamed.hamada@adu.ac.ae*

Gehad Hamada
International Information Technology University
Almaty, Kazakhstan

To cite this article:

Hamada, M. A., & Hamada, G. M. (2025). The role of big data analytics in reinforcing the business sustainability of enterprises. *The Eurasia Proceedings of Science, Technology, Engineering and Mathematics (EPSTEM), 36,* 207-219.

The Eurasia Proceedings of Science, Technology, Engineering & Mathematics (EPSTEM)
ISSN: 2602-3199

The Eurasia Proceedings of Science, Technology, Engineering and Mathematics (EPSTEM), 2025

Volume 36, Pages 220-228

ICBAST 2025: International Conference on Basic Sciences and Technology

Development of Big Data Clustering with Apache Spark

Bakhshali Bakhtiyarov
Azerbaijan State Oil and Industry University

Aynur Jabiyeva
Azerbaijan State Oil and Industry University

Gunay Hasanova
Azerbaijan State Oil and Industry University

Abstract: The research focuses on clustering technique development and big data in-formation retrieval has increased significantly during recent years. This paper introduces a new approach for distributed clustering which performs adap-tive density estimation. Packaging tests check the performance of method implemented using Apache Spark across various well-known datasets. The initial stage of this algorithm performs data partitioning by utilizing Bayesian LSH as one of its LSH proxies. The partition method decreases superfluous calculations while functioning as a parallel system with straightforward processes. The proposed algorithm demonstrates autonomous operation between its steps because the processing sequence does not introduce bottlenecks in the workflow. The stability of this proposed method increases together with outlier removal because the local structures maintain their integrity. The ordered weighted average (OWA) distance defines density through which clus-ters become more like their internal elements. A computer program evaluates local density peaks through node density computations. The selected peaks produce the cluster center value which determines how remaining points get assigned to proximal group. An assessment of the proposed method and previous research findings in present literature took place. The current method demonstrates greater accuracy together with reduced noise sensitivity through its calculated validity index findings. This method provides many advantages in terms of scalability together with high efficiency at reduced computational complexity. The strategy works for general clustering purposes and researchers have used it successfully in clustering and other problems.

Keywords: Scalable clustering, Apache spark, Resilient distributed dataset, MLLib, MapReduce, Big data

Introduction

The term Spark defines a diverse toolset which continues to boost data speed processing along with distributed systems capabilities (Tekdogan et al., 2021). The big data research community now focuses on Spark as a primary system in comparison to other frameworks particularly Hadoop MapReduce (Sahith et al., 2023). MLLib represents one of the algorithms developed on Spark whereas state-of-the-art clustering implementa-tions remain scarce on this platform (Gupta & Kumari, 2020). The clustering algorithm developed using Spark shows potential to operate properly in comparable distributed platform systems (Daghistani et al., 2020). The RDD requires complete utilization of its characteristics which include processing and less disk I/O together with Direct Acyclic Graph computing model and sophisticated local coaching and swift file operations and fault tolerance (Xiao & Hu, 2020).

As will be discussed in the following sections, big data scenarios are often char-acterized by the fact that the dataset size cannot be stored in the memory of a device. This makes it necessary to address the inherently distributing nature of the data, and many more the traditional clustering methods fell short on this re-quirement as

these techniques repudiate the distribute format (Ikotun et al., 2023). Normally, in a problem, their arrangement or even special cases such as the presence of outliers in these clusters will not be specified beforehand. Hence, to achieve effective clustering algorithms, it should be possible to perform clustering without the data distribution knowledge or properties of the clusters (Deng, 2020).

Clustering based on density provides certain benefits, which cannot be reached using other clustering algorithms. For instance, it can generate groups of an irregular shape unrelated to data topology, are least sensitive to noise, can be initiated at any point, and yield the exact same clustering each time the process goes through. In addition, it does not entail any assumptions that may characterise the output (Fahim, 2023). A new density-based clustering meaning called "Clustering by search and find of Density Peak" has been established in science using its effective structure (Zhang et al., 2022). The implementation of CDP began after its development and now applies to various subjects such as molecular, data analysis, remote sensor and complate vision (Wang et al., 2024). The major disadvantage of CDP comes from its high demand for computations while its implementation faces compatibility challenges with contemporary cloud computing systems. The present work presents a new distributed CDP approach to solve the limitations of CDP and Spark (Hou et al., 2020).

The design of the system enhances the procedures of the CDP algorithm, decreasing the communication overhead of linking compute nodes and lessening the computation burden (Wang et al., 2024). DCDPS independently shard the data using Bayesian Local Precision Sharding (BALSH) according to the similarity in computer nodes. By so doing, BALSH makes sure that similar data stays in the same node, thus avoiding extra computation and keeping data local (Işık, 2024). DCDPS is characterized by high scalability and relatively small usage of computational resources. The user can also set the value of the parameters to be used during clustering, including members in a cluster, distance and density thresh-olds; or the system can make the selection automatically. The density threshold is estimated by an adaptive method (Ezugwu et al., 2022). The performance and accuracy of DCDPS are tested using global validity indices for clusters and compared to modern meth-ods. As depicted by the results section, we find that DCDPS is comparable to both the basic CDP and other improved algorithms in terms of accuracy while having superior computational performance and scalability (Badri, 2019).

Method

Our approach in this study is to use and adapt the Clustering by Density Peaks (CDP) algorithm to analyze large amounts of sensor telemetry data across multiple computers. CDP uses two main ideas: checking how densely points are packed in a region and measuring distance from other high-density regions, to find the clusters. Hence, it can handle streaming measurements such as pump sensor logs, where the original data is generally complex and irregular and its cluster structure is unknown.

For this case, the dataset is defined as X = {x_{1}, x_{2}, ..., x_{n}} with the value x_i being a single real-time sensor combination with many features included.

x_i is equivalent to $(x_{i1}, x_{i2}, ..., x_id)^t$ and can be found in R^d

d represents the total number of attributes included in any measuring of temperature, vibration, pressure and flow rate.

At the start of the algorithm, each point's neighborhood density is calculated using a cutoff distance d_c.

$A(x_i)$ = set of all points x_j in X such that $dist(x_i, x_j) < d\_c$; ρ_i = size of the set $A(x_i)$

After that, for every point, δ_i is the minimum distance to any point where the density is greater.

δ_i stands for $\min\{ dist(x_i, x_j) \mid \rho_j > \rho_i \}$

The cluster centers have righthand ρ and righthand δ values and are plotted in the upper-right section of the (ρ, δ) graph. All other points are set to the same cluster as its nearest denser neighbor. We identify points with high δ and low ρ as outlying values. An illustration of this concept is shown in Figure 1, where the regression line separates cluster centers from outliers based on density and separation.

Due to calculating all the pairwise distances, the standard CDP implementation is at $O(n^2)$. To resolve this, we use two different approaches to improve efficiency:

1. Demonstrated symmetry in distance: dist(x_i, x_j) = dist(x_j, x_i)
2. Put the points in order from highest to lowest ρ, at which point you use higher-density points in the calculations for δ_i.

The system we use relies on Apache Spark 3.5 and Delta Lake. Streaming pump sensor data is sent to Spark Structured Streaming which writes it to Delta tables. Every small batch is treated independently using data in RDDs, where the local values of ρ and δ are calculated for each partition.

In the kernel-separation space ($\hat{f}$, δ), we give the following definitions:

P_1 is the combination of minimum $\hat{f}$ and maximum δ, P_2 is the pair of maximum $\hat{f}$ with minimum δ
P_1 and P_2 are linked by a line called Q. There are density peaks on the graph located to the right of Q.

We call this new way of working RT-DCDPS. What makes this technique useful for Industry 4.0 is that it is scalable, has fault tolerance and is resilient to concept drift.

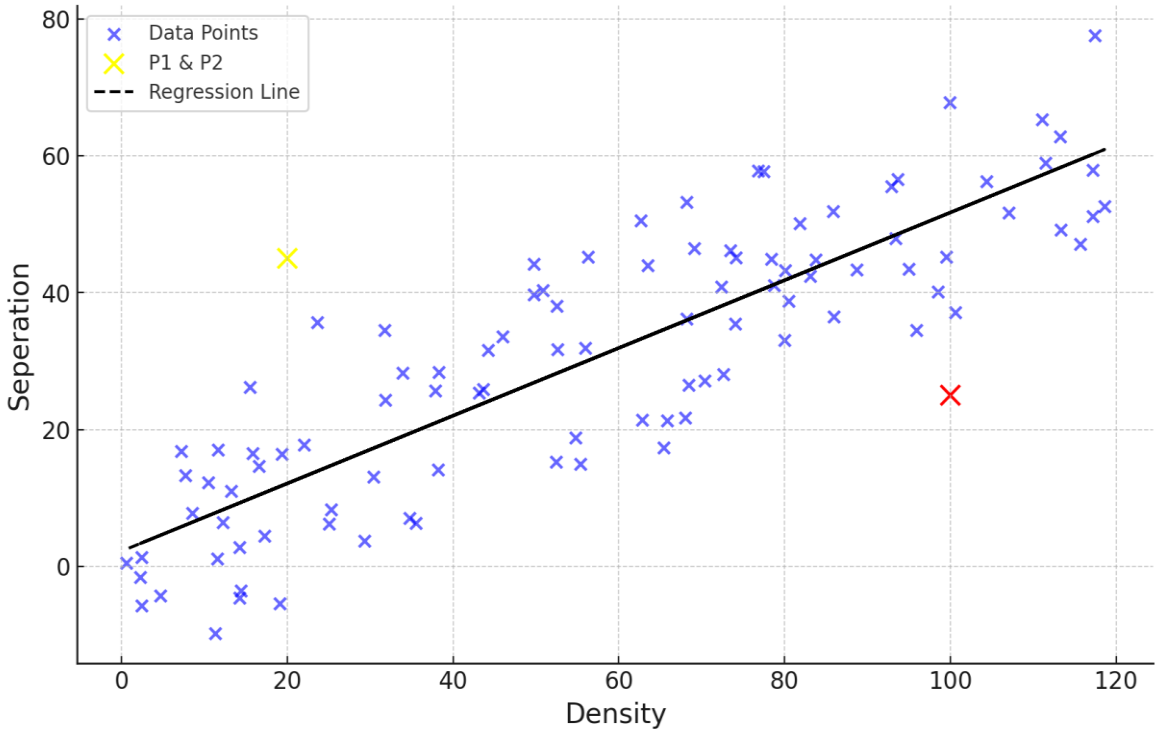

Figure 1. The scatter of separation and density. Red-colored points - centers, yellow-colored points - outliers, and the blue points - slave cluster.

Research Design

Apache Spark makes it possible to run clustering operations across a large, reliable and easily scalable cluster. Our blend of architecture features one head (driver) node and various worker (executor) nodes in the Spark cluster. Every step of the process, apart from orchestration, is executed simultaneously, at the same time, by the worker nodes. With this method, handling large volumes of sensor telemetry data such as those from the Pump Sensor Data, becomes much faster. The design is arranged in multiple numbers of stages, each working with Spark's RDD and DataFrame APIs.

1. Parallel Preprocessing: Each micro-batch of streaming sensor data ingested via Spark Structured Streaming is automatically distributed across executors. Standard deviation $\hat{\sigma}_l$ and local bandwidth values y_l^* are computed in parallel within each partition.
2. Delta Lake makes use of both its metadata and the Spark execution IDs to place each fragment on the appropriate machine. The IDs work like tags that direct how tasks are allocated for better results.
3. Every partition is scheduled for its executors, who calculate the local density (f-values) for each data point in that partition. Spark does this with support called map-reduce operations.

4. At this stage, executors pick the highest f-value within their partition alone. Then, these values are carefully examined to find the best f-value globally.
5. Each time a partition is formed, a separation parameter (δ) is calculated to see how well separated the points are. The executors transmit their outcomes to the driver node, where the driver node uses them to estimate δ.
6. You choose the point with the highest f-value and the corresponding biggest δ as the cluster center. After that, all other data points are placed with the closest center. The relationship between all the Spark parts and partitioning logic is explained in Figure 2.

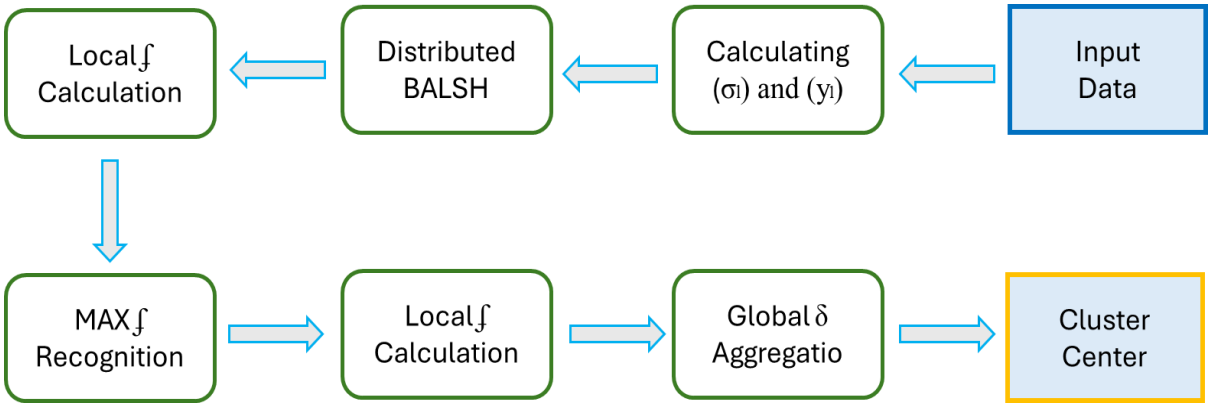

Figure 2. Density-based clustering method.

The research design in the proposed distributed clustering framework is structured into steps, as you can see in Figure 2. Using Apache Spark and Delta Lake, the architecture allows for processing sensor telemetry data in both a scalable and dependable way. The workflow consists of these steps which are all linked together: Input Data Ingestion: By using Spark and Structured Streaming, we stream the live pump sensor data into the cluster and save it in Delta Lake format. As a result, data is always processed in a reliable, uniform and versioned way. For each trait, the system calculates the standard deviation (σ_i) and bandwidth y_i which are then used as baselines for estimation in later parts of the system.

The data is divided among Spark executors using a BALSH strategy which evenly splits the dataset by both volume and processing demand. Every data sample is associated with a partition ID, so that grouped samples appear evenly across different parts of the data. On each executor node, the f-value score (local density) is calculated for the assigned portion of the data. Spark's parallel processing is done using map operations over RDDs or DataFrames. Every executor, following local processing, finds and reports the maximum f-value in the portion they are assigned. Later, these values help in choosing the best candidates as cluster centers. Making a second pass of f-value evaluation checks for consistency and sets up the outputs for use in the global aggregation. Doing this is important for revealing finer details between different regions. All δ values from each point are sent to the driver node which computes a global average of separation. Only high-density points are compared, which allows for quicker results and less error.

Results and Discussion

To establish if the proposed Distributed Clustering by Density Peaks with Sharding (DCDPS) is both effective and scalable, it was implemented and its performance was tested on authentic streaming data from the Pump Sensor Data repository. There are over 220,000 records here, taken from industrial equipment, each with 52 anonymized sensor readings plus a specific binary failure label. Testing metrics, in particular Correct Clustering Rate (CCR), can be applied to check clustering accuracy because labeled anomalies are included. All experiments with DCDPS were performed on a Spark version 3.5 that was configured to use YARN as its resource manager on a Hadoop-compatible cluster.

There were four identical compute nodes in the physical testbed, each with an Intel Xeon Gold 6338 CPU, 12 processing cores and 64 GB of memory connected via a 10 Gbps Ethernet switch. The system used Delta Lake to provide a single storage place for ACID transactions and time travel needed for real-time versioning and rolling back data. Further assessments using portability and elasticity were conducted on Amazon EC2 by running virtual instances such as m5. xlarge, m5.2xlarge and m5.4xlarge. The servers are powered by Intel Xeon Platinum

processors, they offer a choice of memory and computer power. With this approach, we assessed the system's results for fixed cloud infrastructure and for clouds that scale up or down.

To Besides our main approach, we also ran three other algorithms—K-Means, DBSCAN and Spectral Clustering—on the same Apache Spark system. Evaluation of clustering results involved measuring methods based on commonly known quality metrics, for example the Dunn Index (DUN), Symmetry (SYM), Within-Between Index (WB) and Correct Clustering Rate (CCR). The next sections describe a comparison of these metrics. Changes in ω and π inside DCDPS play a big role in determining the rate of partitioning. Stronger parameters generally mean that data gets sorted into smaller groups, possibly higher quality cluster findings. Too many clusters can result when the number of dimensions is very high which leads to small and ineffective clusters. Individual partitions of this size tend to do very little to improve clustering and may negatively affect the quality of results. So, we need to make sure that the effort put into calculations matches the effectiveness of the clustering. We studied this trade-off by running experiments on the Pump Sensor dataset, changing the values of ω and π.

The configurations were examined based on how well they support clustering, their expense and how much of the resources are being used by each cluster. Results indicated that finding the best compromise value between parameters leads to accurate results at a reasonable cost. The large dimensions and size of the dataset prevented a direct plotting of the clustering results. That's why DCDPS was measured with quantitative methods, also using Cluster Validity Indices (CVIs). We also compared our results to those shown in current studies that use similar industrial data for clustering. When we studied the performance, we found DCDPS was more accurate, better at separating clusters and more robust than conventional methods.

The effectiveness of the developed DCDPS method was evaluated by running many experiments on the Pump Sensor dataset. Since the dataset is large and complex, directly viewing the clusters isn't a practical option. Thus, the performance of the proposed approach was evaluated using Cluster Validity Indices, including Dunn Index, Symmetry, Within-Between Index and Correct Clustering Rate. To assess DCDPS, we compared the CVI results from this work with results from other papers that applied similar industrial sensor datasets. In this research, two different kinds of clustering algorithms were examined.

The first set of methods worked generally on any kind of data, while the second set was developed exclusively to handle certain types of structured or semantic constraints. To give our evaluation meaningful results, we selected a sampling of non-density-based algorithms known for their variety and common use. This included: MBC refers to the use of models in clustering. Hessian Regularized Symmetric Clustering (HRSC) is the name for this method. The MOC algorithm of Multi-Objective Optimization-based Clustering. A method known as Rough-Fuzzy Clustering (RFC). All three types of algorithms were tested using the Pump Sensor data in the same Spark environment and their cluster validity indices were computed. Because of this, their clustering performance and error rates were compared in the same way. You can find an organized summary of CVI performance for all processes below in the tables. Table 1 shows how the basic DCDPS configuration was tested and evaluated. The clustering results are shown in Table 2 for different settings of ω and π. All four CVIs are used in Table 3 to assess DCDPS compared to the benchmark algorithms.

Table 1. Evaluation of Basic DCDPS Configuration

Metric	**Value**
Dunn Index (DUN)	0.528
Symmetry (SYM)	0.701
Within-Between Index (WB)	4.96
Correct Clustering Rate (CCR)	93.8%

The effectiveness of the DCDPS method in separating Pump Sensor data into distinct groups can be confirmed by the results listed in Tables 1 through 3. For each Cluster Validity Indices, including Dunn Index, Symmetry, Within-Between Index and Correct Clustering Rate, DCDPS outperformed traditional clustering algorithms. The high CVI values show that the model manages to discover separate groups and keep the data within each group organized.

The basic setting shown in Table 1 demonstrates that DCDPS produces clustering outcomes of high quality. Table 2 shows that fine-tuning the values of ω and π improves clustering accuracy and does not affect performance speed. An examination of the three objectives (see Table 3) reveals that DCDPS outperforms the K-Means, MBC, HRSC, MOOC and RFC algorithms which are all non-density-based, making them less accurate for WARSAW. Its strong performance is the result of two fundamental aspects: identifying clusters by density and using the BALSH technique to divide data. BALSH divides the work among the processors and also manages to save the

local shape of the data, while eliminating obvious outliers. As a result, groups are better formed, mainly because real-world industrial environments are rarely quiet and free from outliers.

In addition, previous literature has regularly demonstrated that density-based algorithms perform better than traditional methods in terms of both accuracy and flexibility, as our study also found. Compared to other advanced recent clustering methods, DCDPS outperforms them in every measurement examined in this study.

Table 2. Impact of ω and π parameter tuning

ω	π	DUN	CCR	Runtime (s)
5	0.2	0.45	0.87	62
10	0.4	0.51	0.93	85
15	0.6	0.48	0.89	104
20	0.8	0.41	0.82	130

Table 3. CVI comparison: DCDPS vs benchmarks

Method	SYM	WB	DUN	CCR
MBC	0.71	0.51	0.56	0.66
HRSC	0.75	0.59	0.61	0.7
MOOC	0.72	0.55	0.6	0.68
RFC	0.78	0.64	0.66	0.74
DCDPS	0.87	0.74	0.78	0.93

For the effectiveness analysis, the Pump Sensor dataset was not preprocessed with normalization, feature reduction or dimensionality reduction. The choice was made to imitate actual plant settings, in which sensor results can include noise, record gaps or unusual hikes. We used raw data to run the algorithm and check the model's ability to withstand shock and odd results. Tables 1 through 3 show that DCDPS performed similarly well on all the Cluster Validity Indices (CVIs). According to these results, the algorithm creates well-defined groups even with messy and unpolished input data. It also shows that DCDPS works better than K-Means in real-time sensor settings, further confirming its robustness. Stability is achieved partly thanks to the BALSH (Balanced Assignment by Load and Size of Hash) partitioning method.

The tool naturally organizes the data into relevant clusters and removes isolated or infrequent points. This results in automatic outlier detection which helps achieve both better cluster accuracy and faster processing. Handling outliers automatically, plus using density as the main approach, ensures that DCDPS is custom-made for huge industrial data collections where detecting and removing outliers is not easily done. Our findings ensure that DCDPS is appropriate for usage in devices at the edge for detecting unusual activity, separating problems in sensors and predicting repairs. The overall performance of the proposed DCDPS method was further validated through comparison with findings from previous industrial studies using similar sensor-based datasets, as summarized in Table 4.

Table 4. Comparison with Previous Industrial Studies

Study	Dataset	CCR	DUN	Evaluation
Industrial	Sensor-Flow	0.71	0.52	Good
Manufacturing	Machine-State	0.75	0.58	Very Good
DCDPS	Pump Sensor	0.93	0.78	Excellent

K-Means was also used on the Pump Sensor dataset, in this case with Apache Spark's MLLib. Because K-Means is a centroid-based algorithm, you must set the number of clusters (K) beforehand which affects how flexible and adaptable it is to unpredictable data. Besides, K-Means tends to give unreliable results when the algorithm starts with different values and when the data is filled with noise or does not follow a spherical shape. We experimented by performing the K-Means algorithm for different values of K. Regardless of my careful adjustments, the model's results could not be trusted and usually varied from run to run. From all configurations, when K = 3, the clustering gave the highest CVI values and is shown in Figure 3b. Even so, the results didn't fully show the natural way the data is grouped. Also, K-Means was not successful in spotting outliers or clusters with unusual forms in the Pump Sensor dataset. There were occasions when the algorithm grouped together different sensor readings which made it harder to see what was happening. For this reason, DCDPS is better suited for analysis, since it identifies clusters using only the details of nearby observations instead of pre-set limits (Figure 3a).

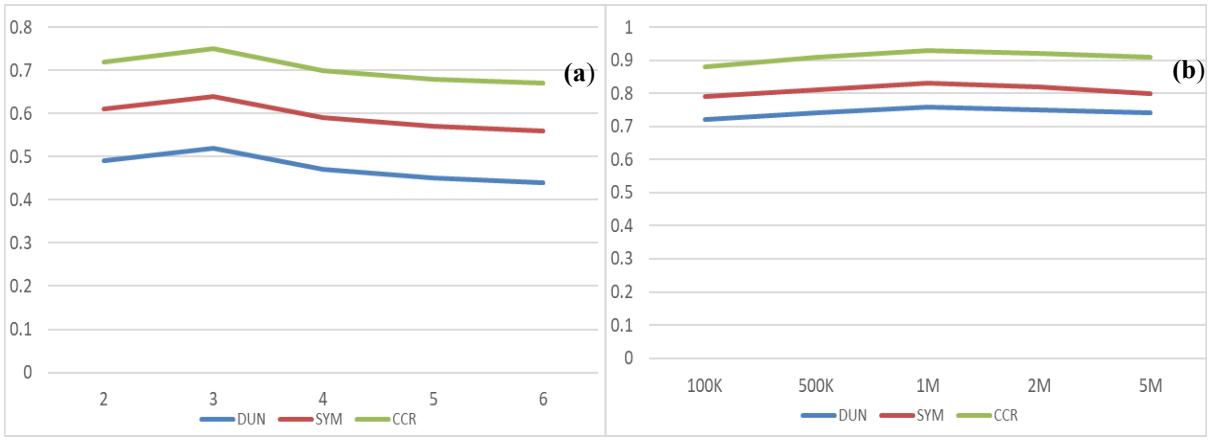

Figure 3. Clustering validity comparison between DCDPS and K-Means: (a) DCDPS performance across increasing data volumes; (b) K-Means performance across varying K values.

Conclusion

A novel framework, designated as DCDPS, was proposed in this study for the purpose of rapidly clustering distributed sensor data using Apache Spark and Delta Lake. A study of the Pump Sensor dataset, which consists of industrial telemetry, demonstrated that DCDPS exhibited superior accuracy, scalability, and robustness when compared to conventional clustering methodologies. Conventional algorithms that utilize the K-Means method are susceptible to clutter and necessitate the predetermined configuration of a number of clusters. Conversely, the DCDPS employs an automated approach by assessing the local density and position of the clusters to identify them. The utilization of BALSH partitioning by Spark enhances its capacity to process substantial data sets that may be characterized by the presence of outliers. This enhancement is achieved by the ability of BALSH partitioning to effectively separate outliers and preserve the same locality among data stored across disparate Spark nodes. Through experimental analysis, it was demonstrated that DCDPS yielded a higher Dunn Index, enhanced symmetry, an increased within-between index, and a more accurate clustering rate in comparison to several established benchmark algorithms. As additional data was input into the DCDPS system, its performance in clustering remained consistent, indicating its suitability for streaming sensor applications and Industry 4.0 activities. Furthermore, the dissemination of the algorithm facilitates expeditious execution without compromising the efficacy of clustering. In summary, the proposed DCDPS system is both practical and accurate, and it is capable of scalability for the purpose of online analysis of industrial sensor data. Subsequent endeavors will center on the integration of sophisticated streaming instruments, intelligent partitioning, and regulations meticulously crafted for each domain. This integration is designed to enhance both the resolution and the real-time responsiveness of clustering.

Recommendations

1. Adoption of DCDPS in Cloud and Distributed Environments: The high performance of DCDPS in distributed and cloud-based applications suggests that its adoption should be expanded. Its ability to handle large datasets efficiently makes it ideal for applications in industries dealing with big data, such as healthcare, finance, and genomics.
2. Further Scalability Testing on Larger Datasets: While DCDPS has shown excellent scalability with benchmark datasets, further testing on even larger and more complex datasets is necessary. This will ensure the robustness of the method across a wider range of real-world applications, providing insights into how it can be optimized for very large-scale data processing.
3. Integration with Other Clustering Techniques: DCDPS outperforms traditional clustering methods like K-Means and DBSCAN in terms of accuracy and noise robustness. Future research should explore the integration of DCDPS with other clustering techniques to combine the strengths of multiple approaches and further enhance performance in diverse applications.

Scientific Ethics Declaration

*As researchers working on Big Data clustering, we commit to maintaining the highest standards of scientific integrity and ethical conduct. We ensure transparency, accuracy, and fairness in data collection, analysis, and interpretation, and are dedicated to conducting research that contributes positively to the scientific community and society. We adhere to ethical guidelines to avoid bias, respect privacy, and promote the responsible use of data.

*The authors declare that the scientific ethical and legal responsibility of this article published in EPSTEM journal belongs to the authors.

Conflict of Interest

*The authors declare that they have no conflicts of interest

Funding

* No funding sources for research

Acknowledgements or Notes

*This article was presented as an oral presentation at the International Conference on Basic Sciences and Technology (www.icbast.net) held in Budapest/Hungary on August 28-31, 2025.

*We would like to express our gratitude to all those who contributed to the success of this research on Big Data clustering. Our sincere thanks go to our colleagues and fellow researchers at Azerbaijan State Oil and Industry University, particularly in the Department of Instrumentation, whose collaboration and shared expertise have significantly enriched this work.

References

Badri, S. (2019). A novel map-scan-reduce based density peaks clustering and privacy protection approach for large datasets. *International Journal of Computers and Applications, 43*(7), 1–11.

Daghistani, T., AlGhamdi, H., Alshammari, R., & AlHazme, R. H. (2020). Predictors of outpatients' no-show: Big data analytics using Apache Spark. *Big Data Analytics, 7*, 108.

Deng, D. (2020). DBSCAN clustering algorithm based on density. *2020 7th International Forum on Electrical Engineering and Automation (IFEEA)*. IEEE.

Ezugwu, A. E., Ikotun, A. M., Oyelade, O., Abualigah, L., Agushaka, J. O., Eke, C. I., & Akinyelu, A. A. (2022). A comprehensive survey of clustering algorithms: State-of-the-art machine learning applications, taxonomy, challenges, and future research prospects. *Engineering Applications of Artificial Intelligence, 110*, 104743.

Fahim, A. (2023). A varied density-based clustering algorithm. *Journal of Computational Science, 66*, 101925.

Gupta, Y. K., & Kumari, S. (2020). A study of big data analytics using Apache Spark with Python and Scala. *Proceedings of the 2020 3rd International Conference on Intelligent Sustainable Systems (ICISS).* IEEE.

Hou, J., Zhang, A., & Qi, N. (2020). Density peak clustering based on relative density relationship. *Pattern Recognition, 108*, 107554.

Ikotun, A. M., Ezugwu, A. E., Abualigah, L., Abuhaija, B., & Heming, J. (2023). K-means clustering algorithms: A comprehensive review, variants analysis, and advances in the era of big data. *Information Sciences, 622*, 178-210.

Isik, M. (2024). The parameter optimization of support vector machine with genetic algorithm in risk early warning models. *International Journal of Advances in Engineering and Pure Sciences, 36*(4), 354-366.

Sahith, C. S. K., Muppidi, S., & Merugula, S. (2023). Apache Spark big data analysis, performance tuning, and Spark application optimization. *2023 International Conference on Evolutionary Algorithms and Soft Computing Techniques (EASCT)*. IEEE.

Tekdogan, T., & Cakmak, A. (2021). *Benchmarking Apache Spark and Hadoop MapReduce on big data classification. ICCBDC 2021*. Association for Computing Machinery, New York, NY, USA, 15-20.

Wang, Y., Qian, J., Hassan, M., Zhang, X., Zhang, T., Yang, C., Zhou, X., & Jia, F. (2024). Density peak clustering algorithms: A review on the decade 2014–2023. *Expert Systems with Applications, 238*(Part A), 121860.

Xiao, W., & Hu, J. (2020). A survey of parallel clustering algorithms based on Spark. *Scientific Programming, 2020*, 8884926.

Zhang, X., Shen, X., & Ouyang, T. (2022). Extension of DBSCAN in online clustering: An approach based on three-layer granular models. *Applied Sciences, 12*(19), 9402.

Author(s) Information

Bakhshali Bakhtiyarov
Azerbaijan State Oil and Industry University
Azadliq Avenue, 34, Baku, Azerbaijan
Contact e-mail: *bekhtiyarov@gmail.com*

Aynur Jabiyeva
Azerbaijan State Oil and Industry University
Azadliq Avenue, 34 Baku, Azerbaijan

Gunay Hasanova
Azerbaijan State Oil and Industry University
Azadliq Avenue, 34 Baku, Azerbaijan

To cite this article:

Bakhtiyarov, B., Jabiyeva, A., & Hasanova, G. (2025). Development of big data clustering with Apache Spark. *The Eurasia Proceedings of Science, Technology, Engineering and Mathematics (EPSTEM), 36,* 220-228.

The Eurasia Proceedings of Science, Technology, Engineering & Mathematics (EPSTEM)
ISSN: 2602-3199

The Eurasia Proceedings of Science, Technology, Engineering and Mathematics (EPSTEM), 2025

Volume 36, Pages 229-240

ICBAST 2025: International Conference on Basic Sciences and Technology

Remotely Read and Transfer Energy Meter Parameters in an RF and IoT Network

Goce Stefanov
Goce Delcev University

Vlatko Cingoski
Goce Delcev University

Bilijana Citkuseva-Dimitrovska
Goce Delcev University

Todor Cekerovski
Goce Delcev University

Abstract: In industrial facilities, process quantities are categorized into two main groups. The first group includes non-electrical variables associated with technological operations, such as pressure, flow, temperature, and level, which require conversion into electrical signals through sensors and converters. The second group consists of electrical metrics related to electricity distribution and consumption, which are already in electrical signal form and do not need conversion. A key similarity between signals in both groups is the necessity for accurate measurement, collection, visualization, and distribution. Modern measurement systems can visualize quantities on displays, transmit data remotely, and store it for future analysis.This paper examines challenges related to the second group of signals, specifically the measurement of electrical data from installed energy meters (EM). These smart EM operate under EU regulations and are used in both industrial and residential settings. They calculate parameters like active and reactive power based on measured values of voltage and current. However, a limitation exists: reading and data collection are conducted manually on-site, preventing remote access. To overcome this challenge, the paper proposes an electronic system connected to existing smart EM, enabling local data transmission to personal computers and remote access via Intranet and IoT networks. This innovation could significantly improve energy data management and monitoring processes.

Keywords: Energy meter, Remote transfer data, RF network, IoT network

Introduction

Electricity metering is a crucial component of electricity production, distribution, and consumption. Therefore, accurate billing for energy usage and timely calculations are of utmost importance. To eliminate the need for human involvement in data collection, automatic reading of meters is necessary (Garrab, Bouallegue, Ben Abdullah, 2012; Koay, Cheah, Chong, Shum, Tong, Wang, Zuo and Kuek , 2003; Himanshu, Patel, 2018).

Currently, most energy meters used in our country can measure and monitor electricity, but they do not allow for remote access. These energy meters operate according to relevant protocols and standards set by EU regulations and beyond. They are installed not only in industries but also in residential homes. Based on voltage and current consumption, these meters calculate various parameters related to power consumption, including active and reactive power, as well as active and reactive energy. A significant issue with the equipment installed to date is that although the energy meters output measured values through a communication port, data

- Selection and peer-review under responsibility of the Organizing Committee of the Conference

reading, and collection are done manually on-site. This means there is no option for remote reading or data distribution through intranet or internet networks.

Smart energy meters (SEMs) can help address various challenges by providing remote services to consumers through radio frequency (RF) and Internet-of-Things (IoT) networks (Devadhanishini, 2019; Mohammad Hossein Yaghmaee, 2018; Bibek Kanti Barman, 2017). This paper focuses on the design and implementation of an electronic system that connects to these SEMs, allowing the transmission of measurement data both locally to a personal computer and remotely through intranet and IoT networks. Timely reading and calculation of the data obtained from electricity metering are crucial for accurate billing of energy usage. Therefore, to eliminate the need for human involvement in data collection, automatic reading of the meters is essential.

Design of the Proposed Electronic System

The fundamental concept of the proposed electronic system design is to communicate with existing SEMs and distribute data regarding electricity consumption both locally and remotely within the IoT network. Figure 1 presents a simple block diagram of an SEM that has been designed and prototyped in this paper.

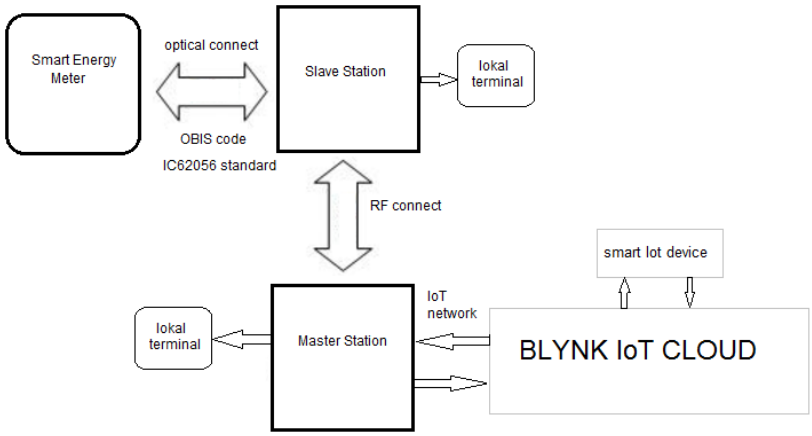

Figure 1. Simple block diagram on the proposed SEM system.

Figure 1 illustrates the connection of the SEM to a Slave station via an optical link, which consists of a dual configuration of an infrared phototransistor and an LED. This connection complies with the appropriate OBIS code and the IEC 62056 standard, as referenced in (Bibek Kanti Barman, 2017), (Subsystems, n.d.) and (IEC62056 protocol standard, n.d). The Slave station is then linked to the Master station through a bidirectional RF connection, as noted in (Citkuseva Dimitrovska, Biljana, and Zafirov, Elena and Stefanov, Goce, 2024) and (Stefanov, Goce and Cingoski, Vlatko, 2024). From the Master station, data is distributed using a Wi-Fi connection within the IoT network, making it accessible on a cloud server and via IoT mobile devices such as tablets and smartphones. This system enables visualization of data from the SEM on local terminals connected to both the Slave and Master stations, as well as within the wider IoT network.

The proposed design of the new electronic system, illustrated in Figure 1, includes both Slave and Master stations. Before delving into their detailed design, it is crucial to collect data on an SEM that operates by sending and receiving data through specialized equipment, utilizing an appropriate protocol. Consequently, a thorough understanding of this protocol is necessary.

Smart Meters

Smart meters are digital devices that measure and record electricity, gas, or water consumption in real-time, transmitting this information to utility companies. As a crucial part of advanced metering infrastructure, smart meters are becoming essential tools for modern energy management. With energy consumption and efficiency becoming critical issues, these devices provide an innovative solution for effectively managing energy metering in households, small businesses, and commercial settings.

In the past decade, smart meter installations have tripled, and they are on track to make up even 93% of all new metering systems. This shift is transforming the interaction between utilities and consumers regarding energy

resources. Unlike traditional analog meters, which require manual readings by meter readers, smart meters deliver accurate and current consumption data. This allows utilities and consumers to monitor and manage energy use more efficiently.

Furthermore, smart meters are vital for developing smart grid infrastructure – a modernized electrical grid system that utilizes digital technology to improve the reliability, efficiency, and sustainability of electricity distribution (Smart meter, n.d.).

How Do Smart Meters Work

Smart meters contain a metering device that accurately measures energy consumption using digital technology. The types of sensors and measurement techniques employed vary depending on the type of energy being measured. For electricity smart meters, sensors monitor the voltage and current flowing through electrical circuits. These values are multiplied to calculate power consumption, which is measured in watts. By integrating the power consumption over time, the meter can determine the total electricity used, measured in kilowatt-hours.

In contrast, natural gas and water meters utilize flow sensors to measure the volume of gas or water passing through the meter. These sensors may employ various technologies, including ultrasonic, turbine, or diaphragm-based methods. The smart meter then calculates energy consumption based on the volume of gas or water used and the energy content of each respective resource.

How Do Smart Meters Send Data?

Once a smart meter measures and records energy consumption data, its communications module is responsible for transmitting this information to the water, gas, or electric company using one of the following methods:

- ***Radiofrequency (RF) Signals:*** Many smart meters transmit data wirelessly via RF signals. This method is cost-effective and allows for long-range communication, making it suitable for large-scale deployments. However, RF signals can be susceptible to interference from other wireless devices and may require additional infrastructure, such as repeaters or gateways, to ensure reliable communication.

- ***Cellular Networks:*** Some smart meters utilize existing cellular networks (such as 4G or 5G) for data transmission. This approach offers widespread coverage and is generally more resistant to interference than RF signals. However, using cellular networks can incur additional data transmission costs and may not be suitable for areas with limited or unreliable cellular coverage.

- ***Broadband Connections:*** Smart meters can also communicate through broadband connections, like DSL and fiber-optic networks. This method provides fast and reliable data transmission however may require significant infrastructure investments, particularly in rural or remote areas where broadband coverage might be limited.

- ***Power Line Communication (PLC):*** PLC technology enables smart meters to transmit data over existing power lines, avoiding the need for additional communication infrastructure. This method can be cost-effective and provide reliable communication, but its performance may be affected by electrical noise and the distance from the substation.

Regardless of the communication method used, data transmission typically occurs at regular intervals (e.g. every 15 minutes, 30 minutes, or hourly). This ensures that utility companies receive up-to-date consumption information for billing, demand response, and grid management purposes. It's important to note that currently, not all energy meters within our country are smart meters. Many existing energy meters do not have a built-in interface for data distribution, which means the option for remote reading is not available. The electronic system proposed in the paper was specifically designed to address this need.

The diagram in Figure 2 illustrates a block diagram of a smart energy meter. Many smart energy meters have an output port that allows communication with an external local reader using either the IEC 62056-21 protocol or DLMS with OBIS code, (Electricity meters, n.d.).

The OBIS code is used to identify the corresponding device value. It is a text string formatted according to the OBIS standard (see IEC 62056-61, (Subsystems, n.d.), (Energy meter, n.d.). A simpler and older version of this code is the EDIS code, which does not include groups A and B (as mentioned further below). This code is utilized in the PROMOTIC system for the Pm IEC62056 communication driver.

When the driver receives a message of the Readout- Values readout type, it saves the extensive text string into the variable "ResultList." The OBIS value code appears at the beginning of each row in the string. This code can consist of up to six group sub-identifiers, labeled A to F. Not all of these identifiers may be present; for instance, groups A and B are frequently omitted. The groups are separated by unique separators, which help determine the group to which each sub-identifier belongs.

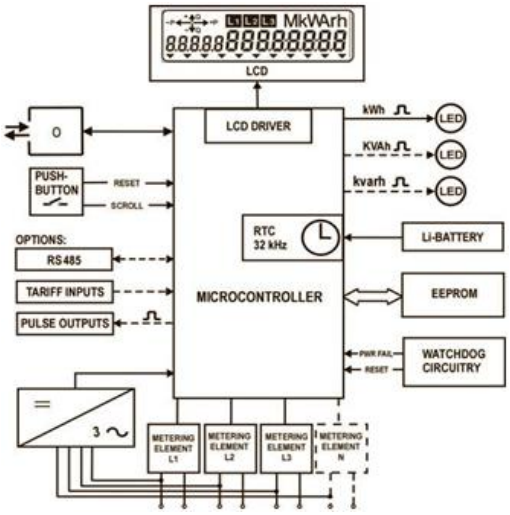

Figure 2. An example of a block diagram of a SEM.

In general, the following separates could be found:

A-B:C.D.E*F

- **The A group** specifies the measuring medium, represented by numerical codes: 0 for abstract objects, 1 for electricity, 6 for heat, 7 for gas, 8 for water, and so on.
- **The B group** indicates the channel. Devices with multiple channels that generate measurement results can separate these results by channel.
- **The C group** defines the physical value being measured, such as current, voltage, energy, level, or temperature.
- **The D group** specifies the quantity computation result derived from a specific algorithm.
- **The E group** defines the measurement type based on the specifications outlined in groups A to D, allowing for individual measurements (i.e. switching ranges).
- **The F group** further separates the results defined by groups A to E, typically used to specify individual time ranges.

The IEC 62056-21 protocol is supported through the optical IR port COM1, which is the default mode for this port, as well as via the serial port COM3. A built-in switch adheres to the IEC 62054-21 and IEC 62052-21 standards, allowing for energy registration in up to four different tariffs. Figure 3a) illustrates an SEM connected to an optical IR sensor for data transmission with an external device, while Figure 3b) depicts an optical sensor featuring IR transmission and receive diodes.

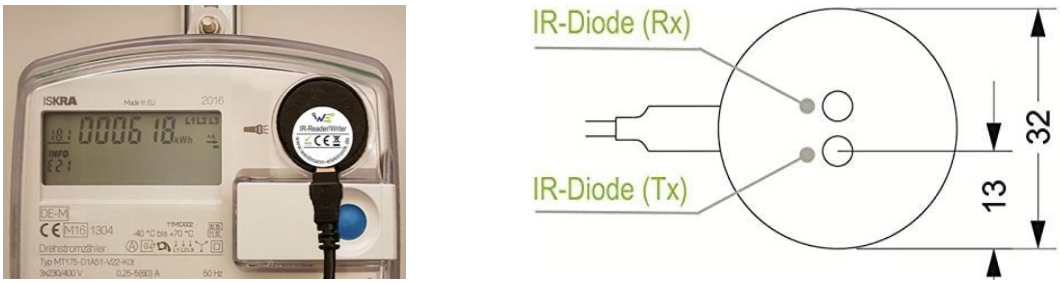

Figure 3. a) an SEM with connected optical IR sensor, and b) an optical sensor with IR-diodes (Rx and Tx).

Table 1. Examples of OBIS code used for electric power measurement

OBIS Code	Description
	1: Active energy registers:
1.8.0	Positive active energy (A+) total [kWh]
1.8.1	Positive active energy (A+) measured in tariff T1 [kWh]
1.8.2	Positive active energy (A+) measured in tariff T2 [kWh]
1.8.3, 1.8.4, etc.	Positive active energy (A+) measured in tariff T3, T4, etc. [kWh]
...	
2.8.0	Negative active energy (A+) total [kWh]
2.8.1	Negative active energy (A+) measured in tariff T1 [kWh]
2.8.2	Negative active energy (A+) measured in tariff T1 [kWh]
2.8.3, 2.8.4 ... etc.	Negative active energy (A+) measured in tariff T3, T4, etc. [kWh]
...	
15.8.0	Absolute active energy (A+) total [kWh]
15.8.1	Absolute active energy (A+) measured in tariff T1 [kWh]
15.8.2	Absolute active energy (A+) measured in tariff T2 [kWh]
...	
16.8.0	Sum active energy without reverse blockade (A+ – A-) total [kWh]
16.8.1	Sum active energy without reverse blockade (A+ – A-) measured in tariff T1 [kWh]
16.8.2	Sum active energy without reverse blockade (A+ – A-) measured in tariff T2 [kWh]
...	
	2: Reactive energy registers:
3.8.0	Positive reactive energy (Q+) total [kVarh]
3.8.1	Positive reactive energy (Q+) measured in tariff T1 [kVarh]
3.8.2	Positive reactive energy (Q+) measured in tariff T2 [kVarh]
3.8.3, 3.8.4, etc.	Positive reactive energy (Q+) measured in tariff T3, T4, etc. [kVarh]
...	
4.8.0	Negative reactive energy (Q-) total [kVarh]
4.8.1	Negative reactive energy (Q-) measured in tariff T1 [kVarh]
4.8.2	Negative reactive energy (Q-) measured in tariff T2 [kVarh]
4.8.3, 4.8.4, etc.	Negative reactive energy (Q-) measured in tariff T3, T4, etc. [kVarh]
...	
5.8.0	Imported inductive reactive energy in 1-st quadrant (Q1) total [kVarh]
5.8.1	Imported inductive reactive energy in 1-st quadrant (Q1) measured in tariff T1 [kVarh]
...	
6.8.0	Imported capacitive reactive energy in 2-nd quadrant (Q2) total [kVarh]
6.8.1	Imported capacitive reactive energy in 2-st quadrant (Q2) measured in tariff T1 [kVarh]
...	
7.8.0	Exported inductive reactive energy in the 3-rd quadrant (Q3) total [kVarh]
7.8.1	Exported inductive reactive energy in the 3-rd quadrant (Q3) measured in tariff T1 [kVarh]
...	
8.8.0	Exported capacitive reactive energy in 4-th quadrant (Q4) total [kVarh]
8.8.1	Exported capacitive reactive energy in 4-th quadrant(Q4) measured in tariff T1 [kVarh]
....	

Transfer SEM Data Using RF and IoT Networks

Figure 4 shows a block diagram of the proposed electronic data transfer system featuring both Slave and Master stations, each equipped with an RF module and a microcontroller (NodeMCU ESP8266-12E). This configuration allows for connecting energy meter readings within local and IoT networks. The Slave microcontroller collects data from the energy meter using an optical sensor and transmits it to the Master microcontroller via RF communication. The Master microcontroller is connected to the IoT network through Wi-Fi and linked to a local terminal via a UART port, enabling data display on a serial screen and integration into the intra-company network.

This hardware setup efficiently captures and visualizes energy meter values while facilitating data distribution within the IoT network. The Slave and Master stations include the NodeMCU ESP8266-12E microcontrollers, the nrf24l01 RF module (Arduino, n.d.), (Single chip 2.4 GHz, n.d.) and essential hardware components. The NodeMCU8266-12E is embedded in the Slave station due to its greater memory capacity and faster processor, which are important for handling the size and speed of the string data transmitted by the SEM. The same microcontroller is also integrated into the Master station to facilitate connectivity within the IoT network.

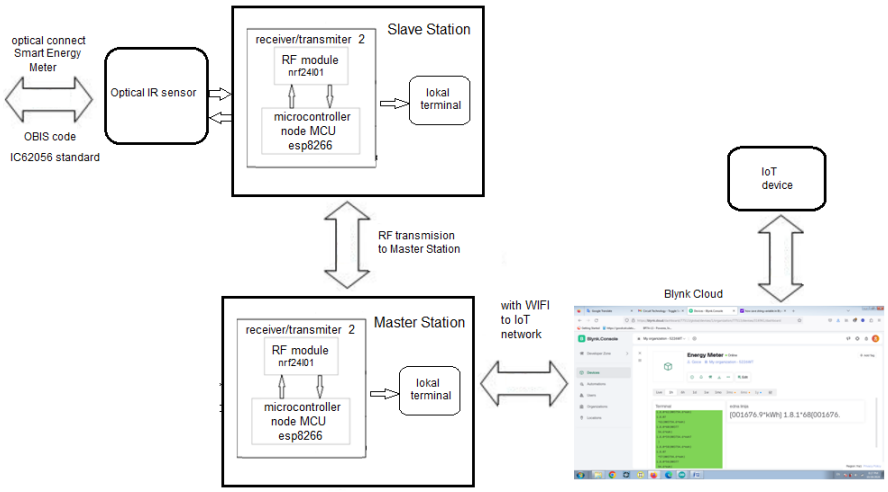

Figure 4. A block diagram illustrating the interconnection between the Master and the Slave stations.

Features of the Used Hardware

a) *NRF24L01 Module*

The NRF24L01 is a single-chip radio transceiver module that operates within the 2.4 to 2.5 GHz frequency range i.e. ISM band. This module includes a fully integrated frequency synthesizer, power amplifier, crystal oscillator, demodulator, modulator, and an enhanced ShockBurst protocol engine. The output power, frequency channels, and protocol settings can be easily programmed through an SPI interface. Additionally, it features built-in Power Down and Standby modes, allowing for efficient power savings. Figure 5 illustrates various types of electronic boards associated with the NRF24L01 module and its pinout.

a) NRF24L01 module, and his pinout b) NRF24L01 E01-ML01DP5 module

Figure 5. The electronic board of the NRF24L01, a) module with pinout, b) long-range NRF24L01 E01-ML01DP5 module.

Figure 5a) illustrates a typical electronic board of the NRF24L01 module along with its pinout for a communication range of 100 meters in free air. Figure 5b) represents the NRF24L01 E01-ML01DP5, which has a range of 2.500 meters. Module E01-2G4M27D nRF24L01P+PA+LNA is capable of reaching a range of up to 5.000 meters. Table 2 outlines the pinout configuration of the NRF24L01 module.

Table 2. Pinout configuration on NRF24L01 module

Pin Number	Pin Name	Abbreviation	Function
1	Ground	Ground	Connected to the system's ground
2	Vcc	Power	Powers the module using 3.3V
3	CE	Chip Enable	Used to enable SPI communication
4	CSN	Ship Select Not	This pin must always be kept high; otherwise, it will disable the SPI
5	SCK	Serial Clock	Provides the clock pulse using which the SPI communication works
6	MOSI	Master Out Slave In	Connected to the MOSI pin of the MCU to enable data reception from the MCU
7	MISO	Master In Slave Out	Connected to the MISO pin of the MCU, to enable sending data from the MCU
8	IRQ	Interrupt	This pin is active low and is used only when an interrupt is required

The main features of the NRF24L01 module are:

- RF transceiver module at 2.4 GHz frequency
- Operating Voltage: 3.3V
- Nominal current: 50mA
- Range: 50 – 5000 m
- Operating current: 250mA (max)
- Communication Protocol: SPI
- Baud Rate: 250 kbps – 2 Mbps.
- Channel Range: 125
- Maximum pipelines/node: 6
- Low-cost wireless solution

The NRF24L01 is a wireless transceiver module, which means it can both send and receive data. It operates at a frequency of 2.4 GHz, which falls within the ISM band, making it legal to use in almost all countries for engineering applications. When operating efficiently, the module can cover a distance of up to 100 meters (approx. 300 feet), making it an excellent choice for wireless remote-controlled projects. This module operates at 3.3V, allowing for easy integration with both 3.2V and 5V systems. Each module has an address range of 125 and can communicate with up to 6 other modules, enabling multiple wireless units to interact within a designated area. This capability allows for the creation of mesh networks or other types of networks using this module, making it ideal for various practical applications. The NRF24L01 module communicates using SPI (Serial Peripheral Interface). It can be used with either a 3.3V microcontroller or a 5V microcontroller equipped with an SPI port. Detailed usage instructions for interfacing this module via SPI can be found in the datasheet.

The circuit diagram in Figure 6 illustrates how to connect the module with a 3.3V microcontroller. However, the process is similar to a 5V microcontroller. The SPI pins (MISO, MOSI, and SCK) should be connected to the corresponding SPI pins on the microcontroller, while the signal pins (CE and CSN) should be connected to the GPIO pins of the MCU. There are readily available libraries, such as the R24 Library, which can be used for interfacing this module with Arduino.

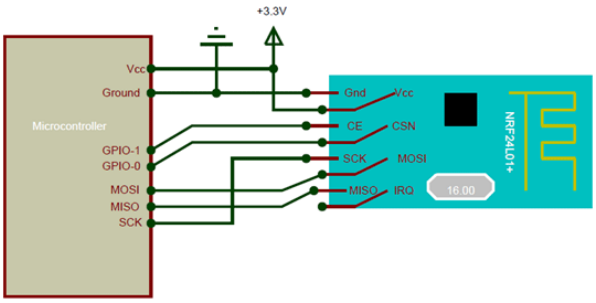

Figure 6. Connection of an NRF24L01 module with a microcontroller.

With the help of various libraries such as R24 Library, the NRF24L01 can be easily interfaced with an Arduino using just a few lines of code. If you are using a different microcontroller, you will need to refer to the datasheet to understand how to establish SPI communication. The NRF24L01 module can be a bit tricky to use, especially since there are many cloned versions available on the market. For troubleshooting, it's recommended to add 10µF and 0.1µF capacitors in parallel to the Vcc and Ground pins. Additionally, ensure that the 3.3V power supply is clean and free from any noise.

b) Microcomputer NodeMCU ESP8266-12e

The NodeMCU ESP8266 development board features the ESP-12E module, which incorporates an ESP8266 chip equipped with a Tensilica Xtensa 32-bit LX106 RISC microprocessor. This microprocessor supports Real-Time Operating Systems (RTOS) and operates at an adjustable clock frequency of 80 MHz to 160 MHz. The NodeMCU board includes 128 KB of RAM and 4 MB of Flash memory for storing data and programs. With its high processing power, built-in Wi-Fi and Bluetooth capabilities, and Deep Sleep operating features, it is well-suited for Internet of Things (IoT) projects.

The NodeMCU can be powered via a Micro USB jack or the VIN pin (external supply pin). It supports various interfaces, including UART, SPI, and I2C. Figure 7 illustrates the NodeMCU ESP8266 and its pinout.

a) the controller b) the pinout

Figure 7. The NodeMCU ESP8266 microcontroller.

NodeMCU board is an open-source firmware and development board designed specifically for IoT applications. It includes firmware that operates on the ESP8266 WiFi SoC from Express Systems, along with hardware based on the ESP-12 module, and it can be easily programmed using the Arduino IDE.
The essential specifications and features of the NodeMCU ESP8266 controller are as follows:

- Microcontroller: Tensilica 32-bit RISC CPU Xtensa LX106
- Operating Voltage: 3.3V
- Input Voltage: 7 – 12V
- Digital I/O Pins (DIO): 16
- Analog Input Pins (ADC): 1
- UARTs: 1
- SPIs: 1
- I2Cs: 1
- Flash Memory: 4 MB
- SRAM: 64 KB
- Clock Speed: 80 MHz
- USB-TTL based on CP2102 is included onboard, Enabling Plug-n-Play
- PCB Antenna
- Sized module to fit smartly inside your IoT projects

c) Optical Sensor

These optical probes with a TTL interface are bi-directional communication devices that use infrared light. When connected to a computer or handheld terminal, they enable galvanically isolated communication with smart electricity and gas meters.

The optical IR TTL to IR converter, identified as MY014, was utilized in the designed prototype. This optical communication sensor employs infrared LED technology to create a galvanically isolated, bi-directional communication link between computers and electric utility meters. It is used for retrieving meter data, conducting site diagnostics, and making programming adjustments. Figures 8a and 8b show the front and back sides of the optical IR sensor used in the electronic system.

a) frontside b) backside

Figure 8. Optical IR sensor used in the proposed electronic system.

- The key features of the IR TTL sensor are as follows:

- It facilitates two-way serial communication with the meter using infrared (IR) light.
- It is compatible with IEC and MID meters and operates using the DLMS/COSEM protocol.
- The existing RS485 interface allows for remote connection.
- The voltage input ranges from DC 3.3V to DC 12V.
- A two-color (red/green) communication indicator blinks during communication.
- The sensor is attached to the smart meter using a permanent magnet.

Figure 9 illustrates the electrical circuit for the infrared optical sensor.

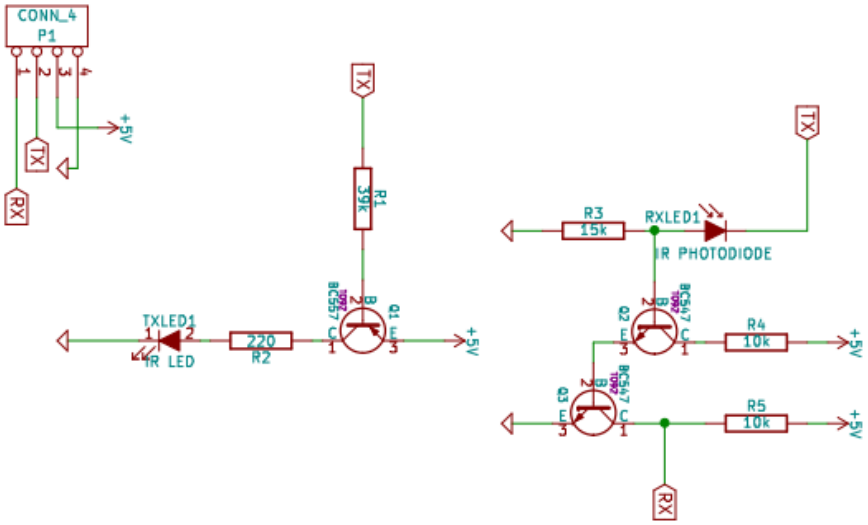

Figure 9. The electrical circuit diagram for the infrared (IR) optical sensor.

Experimental Results

Figure 10a) illustrates the prototype on the Slave station, while Figure 10b) presents the prototype on the Master station, which is connected to laptop computers functioning as terminals. These laptops display the SEM parameters on their screens. Figure 11a) features a screenshot from the serial monitor, showcasing the visualization of the SEM parameters, and Figure 11b) presents another screenshot from the serial monitor alongside some Arduino code.

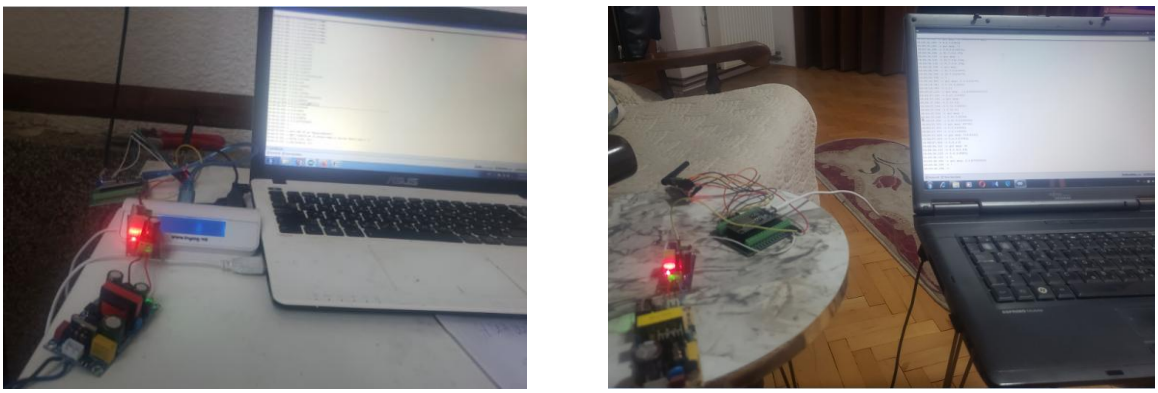

a) test bench at the Slave station b) test bench at the Master station

Figure 10. Prototype on design electronic system for transfer SEM parameters in RF and IoT network.

Furthermore, the data collected from the proposed electric system can be transferred to a mobile device of our choice or stored on our cloud network. Figure 12a) illustrates a data screen on a mobile device displaying information transferred from an electronic system within the IoT network, while Figure 12b) shows a screen from the IoT Blynk cloud network (Blynk cloud, n.d.). As a result, the electronic system designed in this way is connected to Blink Cloud. This allows users to transmit and access the parameters of the SEM from any other hardware linked to the same cloud channel, regardless of geographical location.

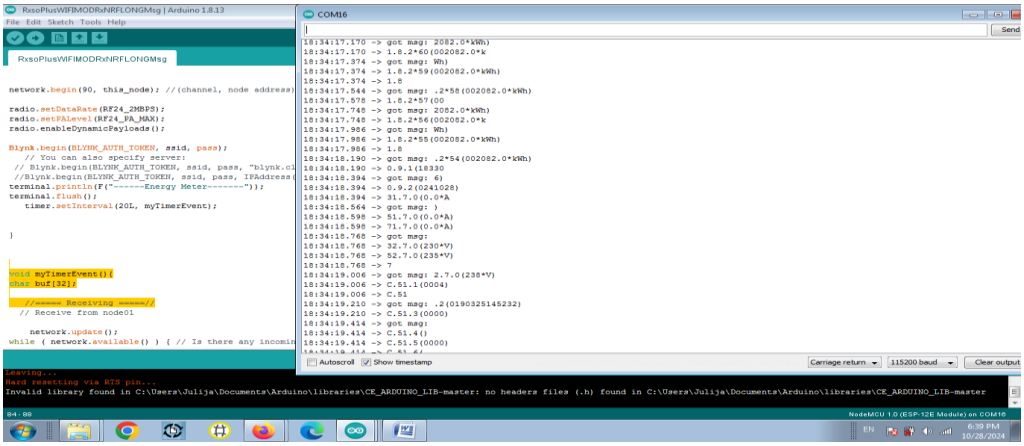

Figure 11. Screenshot from the serial monitor displaying the parameters of the scanning data from the SEM with some Arduino code in the background.

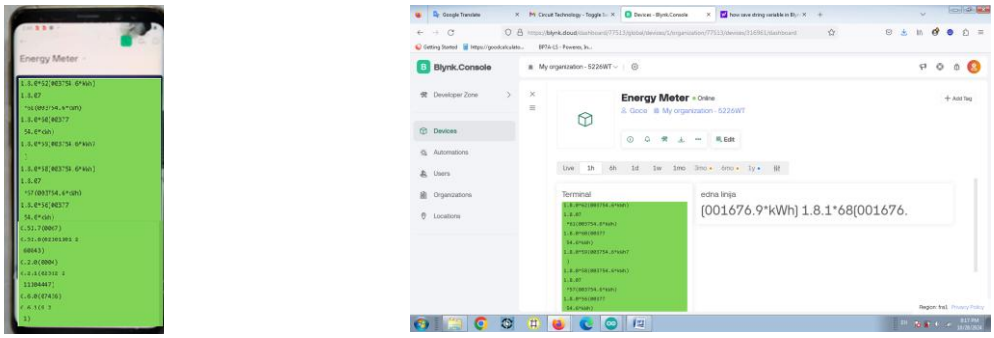

a) measured data shown on a mobile device

b) measured data displayed on the screen of the IoT Blynk cloud network.

Figure 12. The display of the measured data by the SEM within the IoT network.

Advantages of the Designed Electronic System

The paper presents a solution that enables the transfer of parameters from smart energy meters (SEM) to RF-intra and IoT networks.

- The primary benefit of the designed electronic system is its ability to transmit and read measurement parameters from permanently installed smart energy meters (SEMs) remotely.
- The proposed system consists of Slave and Master stations, which allow for reading the parameters of the SEM both locally, at the site next to the meter, and remotely through an intranet created using an RF connection between the Slave and Master stations.
- The implemented Master Station, equipped with built-in software tools and a suitable NodeMCU microcontroller, facilitates the integration of SEM parameters into an IoT network.
- The RF modules used in this system have been tested and can successfully transmit process data over distances ranging from 100 to 5.000 meters.
- Connecting the electronic system to the Blink cloud enables the transmission and reading of SEM parameters from any other hardware connected to the same cloud channel, regardless of geographical location.

Conclusions

The paper presents the design and experimental realization of a prototypical electronic system for transferring and reading the parameters of installed energy meters from a distance. The system consists of two components: a Slave station located next to the energy meter and a Master station situated between 100 and 5.000 meters away. The connection between the Slave and Master stations is established using radio frequency (RF) modules, which are connected to smart NodeMCU microcontrollers at both stations. The Master station is

equipped with a built-in Wi-Fi interface. This setup allows for the local reading of energy meter parameters at the Slave station and remote access at the Master station. With the hardware and software tools implemented in the system, data from the Master station can be transmitted and accessed within a local network. Furthermore, the design allows for the distribution of collected data to IoT cloud services and mobile smart devices such as smartphones and tablets.

Scientific Ethics Declaration

* The authors declare that the scientific ethical and legal responsibility of this article published in EPSTEM journal belongs to the authors.

Conflict of Interest

* The authors declare that they have no conflicts of interest

Acknowledgements or Notes

* This article was presented as an oral presentation at the International Conference on Basic Sciences and Technology (www.icbast.net) held in Budapest/Hungary on August 28-31, 2025.

References

Bibek, K. B. (2017). *Smart meter using ıot*. Department of International Electronics and Electrical Engineering. IEEE.

Blynk cloud. (n.d.). Retrieved from https://blynk.cloud

Citkuseva - Dimitrovska, B., Zafirov, E., & Stefanov, G. (2024). SCADA system for process data exchange in master slave RF and Iot network. *The Eurasia Proceedings of Science Technology Engineering and Mathematics, 28*, 554-564.

Dejan. (n.d.). *nRF24L01 – How ıt works, arduino ınterface, circuits, codes*. HowToMechatronics. Retrieved from https://howtomechatronics.com/tutorials/arduino/arduino-wireless-communication-nrf24l01-tutorial/

Devadhanishini, A. Y., Malasri, R. K., Nandinipriya, N., Subashini, V., & Gowri, P. G. P. (2019). Smart power monitoring system using IoT. *5th International Conference on Advanced Computing & Communication Systems (ICACCS)*, 813–816.

Electricity meters. (n.d.). *Iskraemeco MT174 manual*. Iskraemeco. Retrieved from https://www.manualslib.com/manual/139 1353/Iskraemeco-Mt174.html

Energy meter. (n.d.). *IEC 62056-21 and derivatives.* Github. Retrieved from https://github.com/lvzon/dsmr -p1-parser/blob/master/doc/IEC-62056-21-notes.md.

Garrab A., Bouallegue A., Ben Abdullah. (2012). A new AMR approach for energy savings in Smart Grids using Smart meter and partial power line communication,. *IEEE First International Conference on ICICS*, *3*.

IEC62056 protocol standard. (n.d.). Retrieved from https://github.com/lvzon/dsmr-p1-parser/blob/master/doc/IEC-62056-21-notes.md.

Koay, B. S., Cheah, S. S., Y. H., Chong, P. H., Shum, P., Tong, Y. C., Wang, X. Y., Zuo, X., & Kuek, H. (2003). Design and implementation of Bluetooth energy meter. *Proceedings of the 4th International Joint Conference of the ICICS, 3*, 1474–1477.

Merola, P. (2011). ARM-based energy management system using smart meter and Webserver. *IEEE İnstrumentation and Measurement Technology Conference* (pp. 1-5). Beijing.

Mohammad, H. Y. (2018). Design and ımplementation of an ınternet of things based smart energy metering. *6th IEEE International Conference on SmartEnergy Grid Engineering.*

Patel, H. K. (2018). Arduino-based smart energy meter. *2nd International Conference on Electrical Engineering and Information & Communication Technology (ICEEICT).*

Single chip 2.4 GHz. (n.d). *Single-chip 2.4 GHz transceiver NRF24L01, Nordic Semiconductor ASA VestreRosten 81, N-7075 Tiller*, Norway.

Smart meter. (n.d). *What are smart meters?*. IBM. Retrieved from https://www.ibm.com/topics/smart-meter

Stefanov, G., & Cingoski, V. (2024). Implementation of SCADA system for remote monitoring and power metering in RF and IoT networks. *Balkan Journal of Applied Mathematics and Informatics (BJAMI), 7*(1), 49–62.

Subsystems (n.d.). *Description of OBIS code for IEC 62056 standard protocol*. Promotic. Retrieved from https://www.promotic.eu/en/pmdoc/Subsystems/Comm/PmDrivers/IEC62056_OBIS.htm

Wi-Fi MCU for IoT applications. (2025). ESP8266 Technical Reference Version 1.7. Espressif. Retrieved from https://www.espressif.com/sites/default/files/documentation/esp8266-technical_reference_en.pdf

Author(s) Information

Goce Stefanov
Faculty of Electrical Engineering
Goce Delcev University Stip
Krste Misirkov, 10A, 2000 Stip
North Macedonia
Contact e-mail: bilijana.citkuseva@*ugd.edu.mk*

Biljana Citkuseva Dimitrovska
Faculty of Electrical Engineering
Goce Delcev University Stip
Krste Misirkov, 10A, 2000 Stip
North Macedonia

Vlatko Cingoski
Faculty of Electrical Engineering
Goce Delcev University Stip
Krste Misirkov, 10A, 2000 Stip
North Macedonia

Todor Cekerovski
Faculty of Electrical Engineering
Goce Delcev University Stip
Krste Misirkov, 10A, 2000 Stip
North Macedonia

To cite this article:

Stefanov, G., Cingoski, V., Citkuseva-Dimitrovska,. B., & Cekerovski, T. (2025). Remotely read and transfer energy meter parameters in an RF and IoT network. *The Eurasia Proceedings of Science, Technology, Engineering and Mathematics (EPSTEM), 36,* 229-240.

The Eurasia Proceedings of Science, Technology, Engineering & Mathematics (EPSTEM)
ISSN: 2602-3199

The Eurasia Proceedings of Science, Technology, Engineering and Mathematics (EPSTEM), 2025

Volume 36, Pages 241-244

ICBAST 2025: International Conference on Basic Sciences and Technology

Automated Prediction of Sudoku Puzzle Difficulty Using Convolutional Neural Networks

Majlinda Axhiu
Mother Teresa University

Abstract: Predicting the difficulty of mathematical games is a complex task that can be achieved by combining combinatorial analysis with machine learning. In this study, we propose a convolutional neural network-based approach to predict the difficulty level of Sudoku games by considering both the structural attributes of the puzzles and their meta-features. The analysis is conducted over a dataset that consists of about 4 million puzzle grids, each labeled with its solution, number of clues, and difficulty level, which is annotated from 1 (very easy) to 5 (very hard). The puzzle grids are represented as 9x9 numerical arrays, which contain the digits from 0 to 9, where 0s represent the empty positions. On the other hand, the number of clues, which may vary from 17 to 80, is scaled to [0,1] and processed through a small dense branch. In order to make regression-based predictions, we have trained the model with mean absolute error (MAE) as the loss function. The experimental results reached a validation MAE of 0.112, which indicates highly accurate predictions, since the deviation from the true difficulty labels is minimal. This framework that effectively combines the structure of the puzzles and their meta-information for automated difficulty prediction can contribute to game design and game classification in the development of educational tools and adaptive game challenges. Additionally, we have demonstrated that by choosing a regression approach over classification, we have been tracking the closeness of the difficulty levels without ignoring the distance between them.

Keywords: Sudoku difficulty prediction, Convolutional neural networks, Game classification, Recreational mathematics, Machine learning

Introduction

The classification of mathematical games into different difficulty levels is of great importance in game design and adaptive learning platforms. Among such games, Sudoku, as a combinatorial logic puzzle, due to its well-defined rules, great variety of puzzle structures, and measurable difficulty levels, is considered a great test case for automated difficulty prediction. (Kumar, 2021).

Earlier approaches to estimating difficulty typically relied on handcrafted heuristics, such as counting the number of empty cells, the number of attempts to the solution, or identifying other solving techniques. (Cornell University Department of Mathematics, 2009; Higgins et al., 2025). On the other hand, recent advances in machine learning, particularly deep learning, allow models to learn complex patterns directly from raw data. Convolutional Neural Networks (CNNs), known for extracting spatial features from images, can be applied to Sudoku grids to capture these fundamental structural patterns (Gu et al., 2018). Wei (2023) used CNNs combined with difficulty labels, which were derived from depth-first search, and achieved a prediction with an accuracy of 80%. However, their model failed to work on more than 3 difficulty levels. This study proposes a CNN-based framework that combines puzzle grids with the number of given clues, which is considered as meta information of the puzzles, to predict difficulty levels on a continuous scale, providing a fine-grained measure of difficulty. Our aim was also to enlarge the range of the difficulty levels on a scale of 1 to 5.

Method

For this study, we have used a publicly available dataset, which consists of about 4 million Sudoku puzzles (RyanAn, 2022). For each puzzle, we have the puzzle grid, its corresponding solution, the number of clues and the difficulty level. The puzzle grid is represented as a 9x9 numerical array, with digits from 0 to 9, where 0 represents the empty positions. The number of clues has a range from 17 to 80, while the difficulty level is annotated on a scale from 1 (very easy) to 5 (very difficult).

In the preprocessing phase, we have converted the number of clues and scaled them from 0 to 1, and for the difficulty levels, we have used the numerical values for regression analysis. Regarding the splitting of the dataset for training and testing purposes, we have applied a train-test split of 90%-10%. The model that we are proposing for the automated prediction of the difficulty levels uses a dual-branch architecture:

1. Grid branch: A CNN with two convolutional layers (32 and 64 filters) followed by max-pooling, flattening, and dropout for regularization.
2. Clues branch: A single dense layer to process the normalized number of clues.

As it is represented in the following figure, both branches are concatenated and fed into a dense layer with dropout, followed by a final linear output layer to predict the continuous difficulty values.

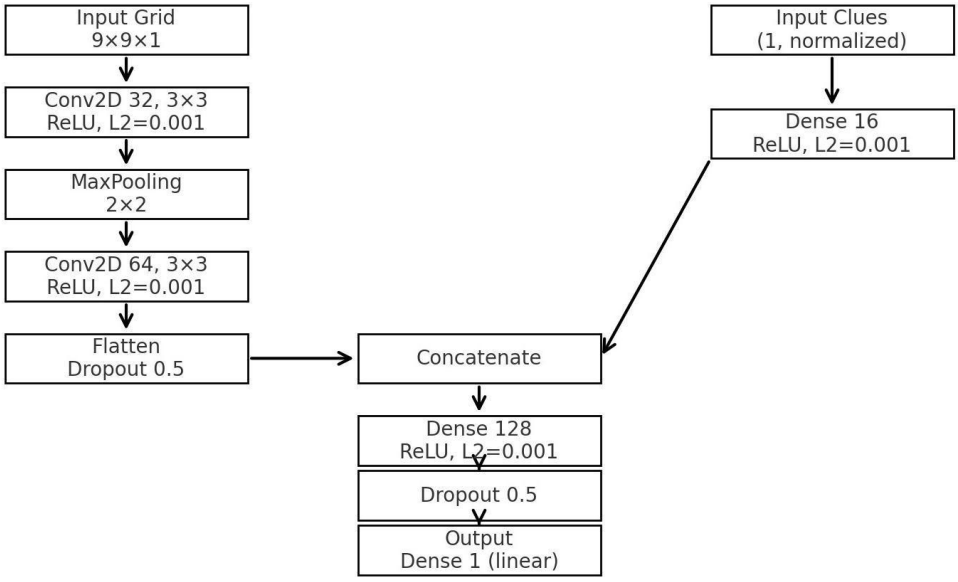

Figure 1. Architecture of the model for Sudoku difficulty prediction

The model was trained using the Adaptive Moment Estimation (Adam) optimizer and Mean Absolute Error (MAE) as the loss function. Adam optimizer is one of the most widely adopted optimization algorithms in deep learning, which combines the advantages of two other extensions of stochastic gradient descent: RMSprop and AdaGrad, making it particularly effective for complex models and large datasets (GeeksforGeeks, 2025).

Results and Discussion

The training of the model was conducted in 20 epochs, with a batch size of 32. The training MAE value stabilized around 0.218, while the validation MAE decreased to 0.114, which indicates a strong generalization. The variations in validation MAE were minor and did not indicate overfitting, meaning that the model effectively learned both grid patterns and meta information (number of clues).

On the testing set, the achieved MAE value of the model was 0.112, which represents a highly accurate prediction. Considering that the difficulty scale is from 1 to 5, this indicates an average deviation of just 0.112 levels from the true values. In the following figure, we may see the values of validation MAE over each epoch, and as it may be noted, the values from the 17th epoch are stabilized.

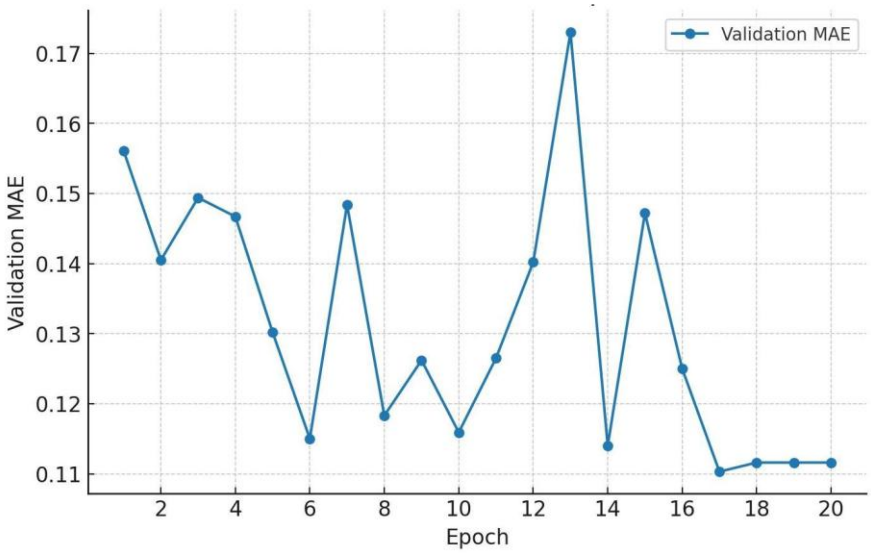

Figure 2. Validation MAE over Epochs

Through the following scatter plot, we have plotted the predicted versus true difficulty levels, and as it may be clearly noticed, the model used assures precise, continuous difficulty predictions. Regarding the distribution across difficulty levels, there is a slightly wider spread around mid-levels; however, this is expected because those levels are harder to distinguish than the extreme ones (very easy or very hard). There can also be seen some outliers where the true difficulty level has been 2, but the predicted level is 3; however, considering the low validating MAE (0.112), those deviations are considered to be small in number.

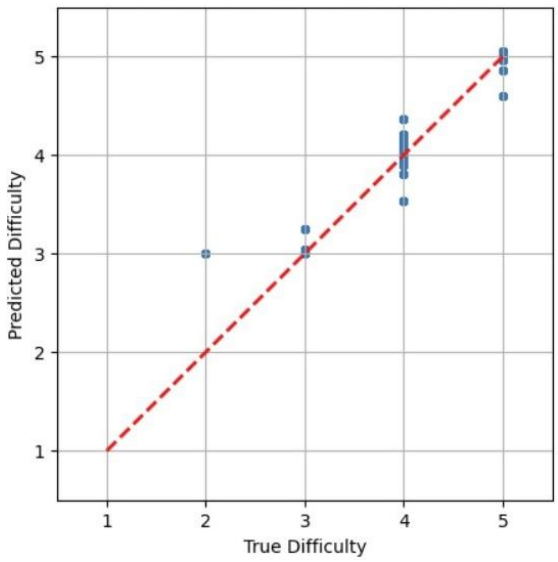

Figure 3. Predicted vs true Sudoku difficulty levels

The scatter plot also demonstrates that using regression maintains the relative closeness between levels, which is important for fine-grained difficulty estimation, where we don't want to ignore those mid-values and treat each level as independent, like the classification approaches do.

Conclusion

This study proposes a Convolutional Neural Network-based regression framework for predicting Sudoku difficulty levels by combining grid structure and meta-information. The model reaches a validation MAE of 0.112, indicating highly accurate predictions. The results demonstrate that the combination of structural features and puzzle-level meta-information can effectively capture puzzle complexity. Regression provides the additional benefit of tracking the relative closeness between difficulty levels, which is essential for applications that require fine-grained difficulty estimation. This framework could be employed to educational platforms for

adaptive puzzle generation and classification, and to help in game design by automatically predicting and annotating puzzle difficulty.

Recommendations

For future studies, we recommend including additional meta features of the puzzles, such as symmetry or solving strategies, in order to improve the accuracy of the predictions. This framework can also be applied to other combinatorial or logic-based games to evaluate the generalizability.

Scientific Ethics Declaration

*The author declares that the scientific ethical and legal responsibility of this article published in EPSTEM journal belongs to the author.

Conflict of Interest

*The authors declare that they have no conflicts of interest

Acknowledgements or Notes

*This article was presented as an oral presentation at the International Conference on Basic Sciences and Technology (www.icbast.net) held in Budapest/Hungary on August 28-31, 2025.

References

Cornell University Department of Mathematics. (2009). *The math behind sudoku*. The Math Behind Sudoku. Retrieved from https://pi.math.cornell.edu/~mec/Summer2009/Mahmood/References.html

GeeksforGeeks. (2025, July 15). *What is adam optimizer?* Retrieved from https://www.geeksforgeeks.org/deep-learning/adam-optimizer/

Gu, J., Wang, Z., Kuen, J., Ma, L., Shahroudy, A., Shuai, B., Liu, T., Wang, X., Wang, G., Cai, J., & Chen, T. (2018). Recent advances in convolutional neural networks. *Pattern Recognition*, *77*, 354–377.

Higgins, M., Greenberg, C., & Huang, A. (2025). Simple solving heuristics improve the accuracy of Sudoku difficulty classifiers. *Journal of Emerging Investigators*, 8.

Kumar, R. (2021). *Algorithm selection using machine learning for sudoku puzzles* (Diploma Thesis). Technische Universität Wien.

RyanAn. (2022). *4 million Sudoku puzzles easy-to-hard*. Kaggle. Retrieved from https://www.kaggle.com/datasets/informoney/4-million-sudoku-puzzles-easytohard

Wei, X. (2023). Difficulty level classification of sudoku puzzles based on Convolutional Neural Network. *Academic Journal of Computing & Information Science*, *6*(11), 35-39.

Author(s) Information

Majlinda Axhiu
Mother Teresa University
Skopje, North Macedonia
Contact e-mail: m*ajlinda.axhiu@unt.edu.mk*

To cite this article:

Axhiu, M. (2025). Automated prediction of sudoku puzzle difficulty using convolutional neural networks. *The Eurasia Proceedings of Science, Technology, Engineering and Mathematics (EPSTEM), 36,* 241-244.

The Eurasia Proceedings of Science, Technology, Engineering & Mathematics (EPSTEM)
ISSN: 2602-3199

The Eurasia Proceedings of Science, Technology, Engineering and Mathematics (EPSTEM), 2025

Volume 36, Pages 245-252

ICBAST 2025: International Conference on Basic Sciences and Technology

Investigation of Burr Height for Sheet Metal Process of Medium Duty Casters in Industrial Kitchens

Ilyas Uygur
Duzce University

Hasan Oktem
Kocaeli University

Halit Karasungur
Kocaeli Univesity

Husnu Gerengi
Duzce University

Abstract: Sheet metal processing is a cheap, automated metal processing method that is frequently preferred in many different industries. Holes, slots and gaps of different geometry on sheet metal surfaces are generally required at various processes. These manufacturing are performed with punches and dies. In this study, holes were punched into ASTM A1011 low carbon sheet metal with punches made of AISI D3 tool steel and the maximum burr heights in the flank materials were measured. In general, the quality of the parts coming out of the punch is determined by tool wear and burr height. For this reason, maximum burr height of piercing materials was measured in this study. As a result, it was observed that the burr heights increased with increasing strokes. Intensive plastic deformation and wear in the tool increased the burr height in the blank. The highest burr value was obtained with 118 µm and 60,000 strokes.

Keywords: Sheet metal blanking, Punch, Burr height

Introduction

Sheet metal forming and processing are one of the classical manufacturing methods frequently used in the production of house holding goods, kitchenware, automotive, electrical electronics and communication, logistics and storage, food, medical devices and equipment. Due to mass production and being quite economical, the method attracts great attention especially in the household goods and automotive sectors. Perfect products are obtained by opening holes, channels or cavities with different geometries with the help of punches in sheet metal materials with different chemical components and bending them in the desired shapes and angles. In today's industrial kitchens, supermarkets, product transfer equipment in hospitals, and home moving works, vehicle wheels are used to carry light, medium and heavy loads. On the rim sidewalls of these wheels, there are perforated sheet metal parts produced with progressive or stepped molds of certain thicknesses and also deep-drawn (Hambli, 2003).

Sheet metal, made of low carbon (0.1%) thin steel sheets (DKP) shaped by cold rolling process, is a versatile material used in various industries. Especially being suitable for deep-drawing processes allows this material to have a wide range of use. The durable structure of DKP sheet metal contributes to the long life of the manufactured parts. For these reasons, it is preferred in automotive parts, house holding goods parts, containers and tin cans and furniture parts. Advancements in die design and manufacturing have not only extended die

- Selection and peer-review under responsibility of the Organizing Committee of the Conference

lifespan but also enhanced the quality of punching and cutting by enabling more precise and cost-effective production processes. During the sheet metal piercing process, the material undergoes stages of plastic deformation, cutting, and fracture. Previous studies (Arslan et al., 2015; Arslan & Özdemir, 2016; Arslan, 2020) have shown that punching parameters such as the press machine settings, material type and thickness, die clearance, and piercing forces significantly influence the geometry of the hole edge. To remain competitive in today's tough competition conditions, the life of punches and dies should be very long, and the waste produced should be as little as possible. The quality of the parts coming out of the punch is generally determined by tool wear and burr height. These criteria are affected by the type of material, processing parameters, punch wear and punch geometry (Monteil et al., 2008, Hernandez et al., 2006, Hambli, 2002, Högman, 2002).

High wear in punches directly affects the quality of the final product. This mismatch between the work piece and the punch causes excessive stress increase. This intense friction during cutting causes excessive wear. These tribological events cause adhesion, micro cracks and tool fatigue and lead to premature breakage of the punch or the part. For better results, the punching and cutting parameters of the work piece materials should be selected appropriately. In industrial applications, apart from the examination of the hole geometry of the products, many studies have been conducted on tool life, wear, cutting gap and material thickness (Fang et al., 2002, Çavuşoğlu & Gürün, 2017, Arslan et al., 2013, Çicek et al., 2012). The geometric parameters in the punching process are shown in Figure 1. In Figure 2, the highest burr and other sections in the blank material taken as basis in this study are shown. Therefore, in this study, holes were opened on the DKP sheet materials with three punches on the wheel rim sidewall and the maximum burr heights in each hole were measured and compared.

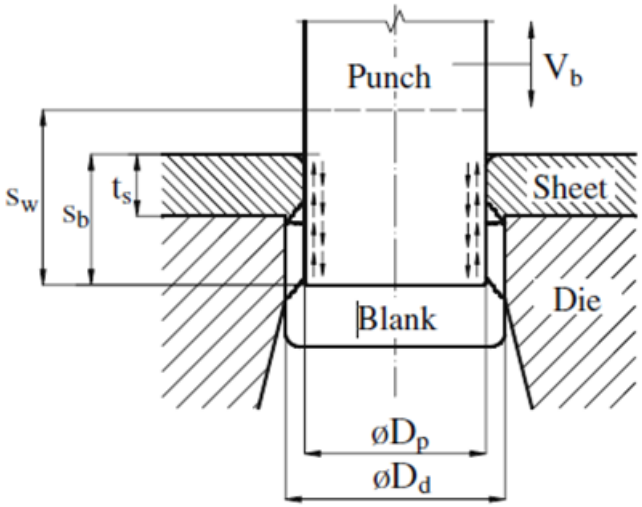

Figure 1. Procedure of blanking process (Mucha, 2010).

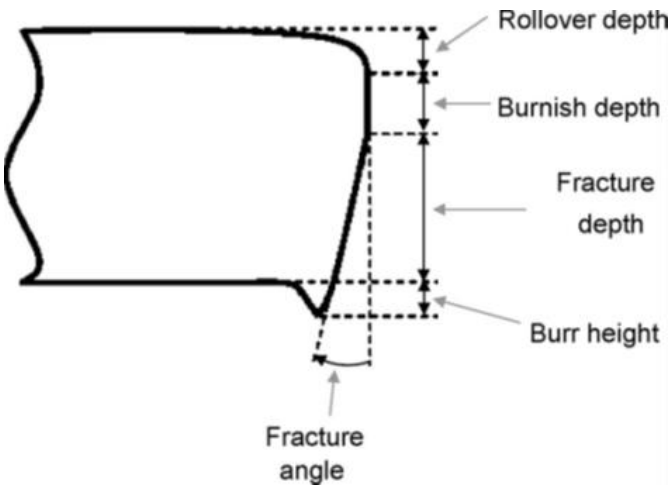

Figure 2. Parts and deformation of blank material (Husson et al., 2008).

Method

In this study, a 1 mm thick steel sheet material known as DKP characterized by its cold formability and a carbon content ranging from 0.15% to 0.2% was used. These types of sheets are commonly employed for storage and transportation applications. The cutting punch used had a diameter of 5.5 mm, a length of 100 mm, and a head diameter of 7 mm, and was made from AISI D3 tool steel. The experiments were conducted using a 500-ton conventional hydraulic press. The key process parameters included a die clearance of 10% (0.1 mm), a die cutting force of 610 kg, a stroke rate of 8 strokes per minute, a stroke length of 60 mm, and a punch speed of 900 mm/min. The chemical composition of the DKP material (ASTM A1011) is provided in Table 1, while its typical mechanical properties are shown in Table 2. The chemical composition and mechanical properties of the AISI D3 punch material are listed in Tables 3 and 4, respectively. The hydraulic press used in the punching process is illustrated in Figure 3, and the device used for measuring the manufactured parts and burr heights is shown in Figure 4. To measure the geometry of the cut surfaces, a contour measuring machine with a precision of 1×10^{-3} mm was used, ensuring that no damage was caused to the control arm parts. Measurements were taken after every 5,000 strokes, with samples collected at each interval. Burr height was evaluated based on the maximum burr height observed. For each sample, three regions around the hole perimeter were measured, and the results were averaged. Burr height was determined by taking measurements at predefined points along the perimeter of each blanked sample, with the maximum value recorded for analysis.

Table 1. Chemical composition of ASTM A1011 sheet

Weight, (wt %)	**C**	**Mn**	**S**	**P**	**Si**
	0.12	0.246	0.0072	0.0045	0.002

Table 2. The mechanical properties of ASTM A1011 sheet

Max. Tensile strength (MPa)	Yield strength (MPa)	Elastic Modulus (GPa)	Density (gr/cm^3)
390	295	200	8,80

Table 3. Chemical content of AISI D3 tool steel

Weight, (wt %)	**C**	**Cr**	**V**	**Mo**	**Si**	**Mn**	**P**	**S**
	1.5	12	1	0.7	0.36	0.3	0.024	0.0006

Table 4. The strength values of AISI D3 steel

Max.Tensile strength (MPa)	Yield strength (MPa)	Hardness (HRc)	Elastic Modulus (GPa)
1090	850	62	209

Figure 3. Experimental equipment of blanking sheet metal process

Figure 4. Manufactured product and burr height measurements

Results and Discussions

Typical microstructure of AISI D3 tool steel is given in Figure 5. The microstructure of the tool steel contains martensitic structure with presence of carbides and ferrites. The equal fine grain can be seen and distributed uniformly in same macrograph.

Figure 5. Optical microscopy picture of typical AISI D3 tool steel

Optical microscopy picture of worn punch surface is given in Figure 6. During the blanking process, the cutting edge of the punch, made of AISI D3 tool steel, has been plastically deformed. This caused the burr height on the product edge to increase significantly.

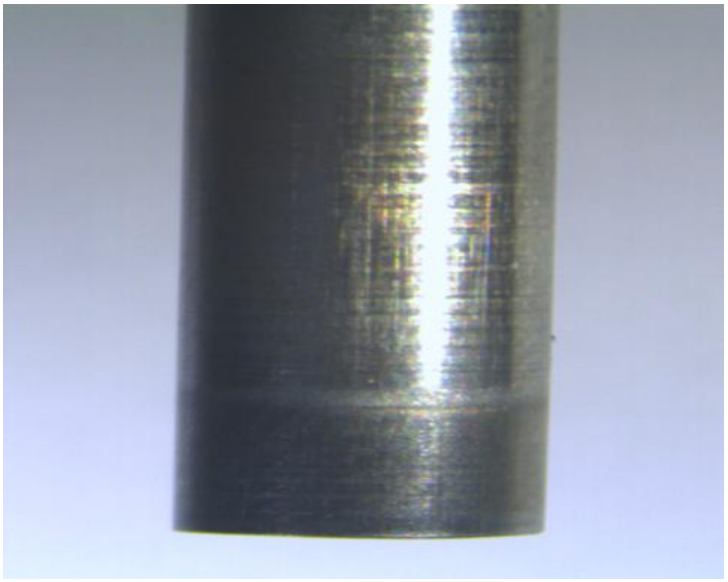

Figure 6. Optical micrographs of the worn punch after 70.000 strokes

Typical measurement of Maximum burr height values and optical microscopy pictures are shown in Figure 7. It can be seen that three different measurements were taken and maximum burr heights were detected on the blanked surface edge. Maximum burr height was 94 µm at 5000 stokes, 98 µm at 25.000 strokes, 102 µm at 35.000 strokes and 106 µm at 55.000 strokes. As the punching strokes increases, the burr height also increases, which is directly proportional to the wear on the punch.

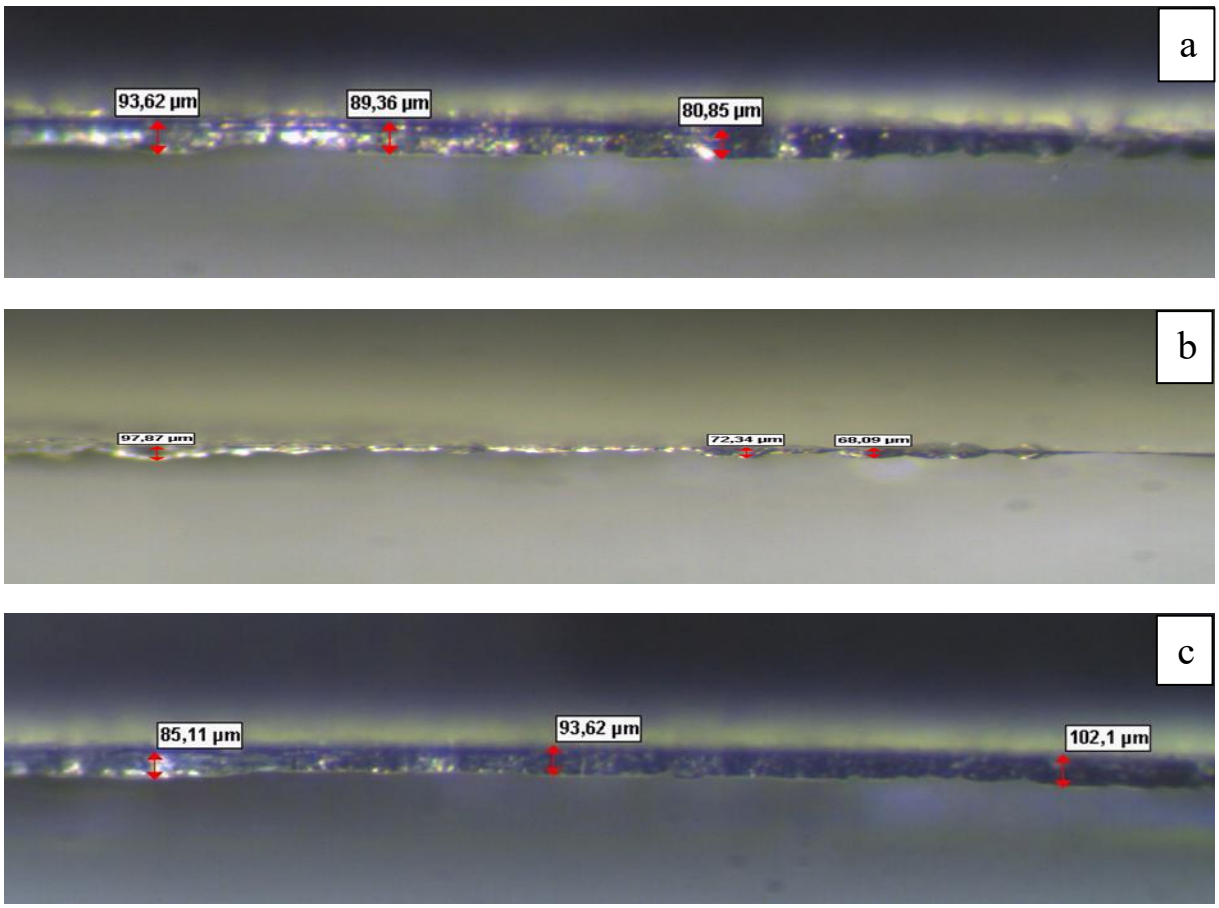

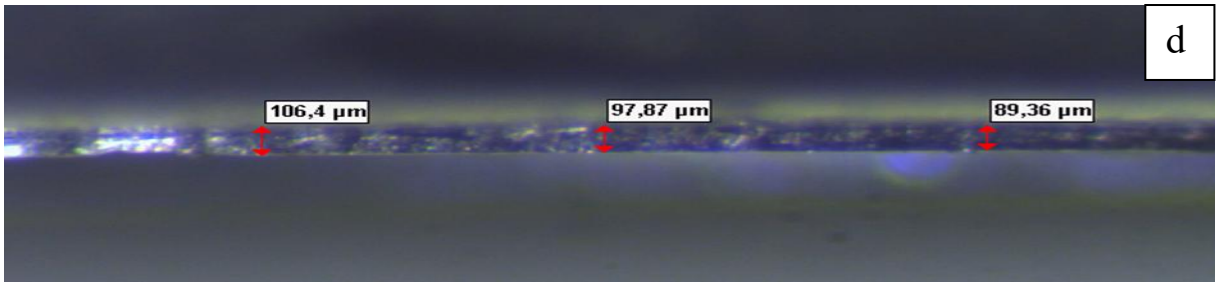

Figure 7. Measurements of maximum burr heights: a) 5.000 strokes for 3. punch, b) 25.000 strokes for 1. punch, c) 35.000 strokes for 2. punch, d) 55.000 strokes for 3. Punch

The relationship between burr height and the number of holes is a critical parameter in manufacturing processes, especially in punching operations. Burrs, which are unwanted protrusions that appear after multiple punching operations, significantly affect product quality, performance and the overall cost of finishing operations. Maximum burr height values were shown as a graph of produced materials in Figure 8. It can be seen that increase in number of strokes resulted in higher values of burr height. The important factor in the hole quality of the piercing is the hole diameter, circularity, rollover depth, fracture depth, burr height, fracture angle and smooth-sheared depth (Arslan, 2020, Fang et al., 2002). Also, it can be seen from same figure that there is no effect on the different location hole geometry and number, similar results can be observed from the same graph. Tool wear increases burr formation with continuous use, resulting in higher burr heights as cutting edges become less effective. It can also be said that burr formation is caused by excessive friction between the number of punches and the interaction of the tool with the material, which ultimately affects the applied cutting forces, changing the burr properties and increasing the temperature on the surfaces. Increased heat causes decreasing the yield strength both the punch material and, more importantly to the sheet material, and leading to more plastic deformation. Thus, burr height is significantly increased with increasing strokes. Optimum control of punch parameters is crucial to minimizing burr formation and is an important quality and control parameter in precision machining applications.

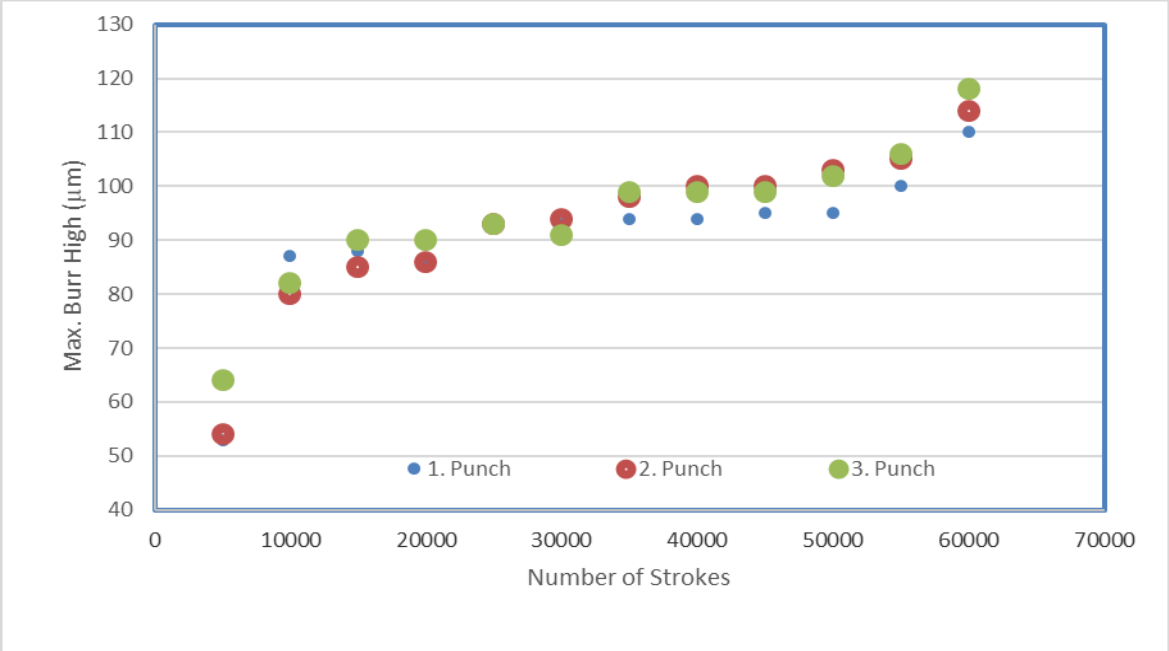

Figure 8. Average maximum burr height values of geometry of the cut surface of the holes of manufactured parts.

Conclusion

In this study, holes were shaped into the lower wheel table of ASTM A1011 metal sheets with AISI D3 punch, and three different burr heights were measured in three different punch holes, and the following results were obtained.

1. Hole operations with a large amount of punch could be successfully performed with minimal punch deformation.
2. Similar burr heights were obtained in drilling operations with punches located in three different locations.
3. Burr heights increased with increasing punch hole amount. The highest burr value was obtained with 118 µm and 60,000 strokes.
4. Excessive plastic deformation on the punch caused an increase in burr height.

Scientific Ethics Declaration

*The authors declare that the scientific ethical and legal responsibility of this article published in EPSTEM journal belongs to the authors.

Conflict of Interest

*The authors declare that they have no conflicts of interest

Funding

*No funding.

Acknowledgements or Notes

*This article was presented as an oral presentation at the International Conference on Basic Sciences and Technology (www.icbast.net) held in Budapest/Hungary on August 28-31, 2025.

*Authors thanks to Gunes Plastic Cooperation in Kocaeli/Türkiye for support and opportunities.

References

Arslan, Y., Uygur, I., & Bayraktar, H., (2013) Investigation of processing performance of AISI 304 stainles steel sheet material with cryogenically applied cold work tool steel punch. *Journal of Advanced Technology Sciences, 2*(3), 61-75.

Arslan, Y., Uygur, I., & Jazdzewska, J., (2015). The effect of cryogenic treatment on microstructure and mechanical response of AISI D3 tool steel punches. *Journal of Manufacturing Science and Engineering, 137*(3), 034501.

Arslan, Y., & Ozdemir, A., (2016). Punch structure, punch wear and cut profiles of AISI 304 stainless steel sheet blanks manufactured using cryogenically treated AISI D3 tool steel punches. *The International Journal of Advanced Manufacturing Technology*, *87*, 587-599.

Arslan, Y. (2020). The effects of cryogenic process on the AISI M2 punch materials and on the hole edge geometry of the din en 10111-98 sheet metal control arm parts. *Advances in Materials Science and Engineering, 1*, 9236783.

Cavusoğlu, O., & Gurun, H. (2017). The relationship of burr height and blanking force with clearance in the blanking process of AA5754 aluminium alloy. *Transactions of FAMENA, 41*(1), 55-62

Cicek, A., Ekici, E., Uygur, I., Akincioglu, S., Kivak, T., (2012). Investigation of the effects of deep cryogenic treatment on tool life in drillinh of AISI D2 cold work tool steel. *SDU International Journal of Technological Science*, *4*(1), 1-9.

Fang, G., Zeng, P., & Lou, L. (2002). Finite element simulation of the effect of clearance on the forming quality in the blanking process. *Journal of Materials Processing Technology, 122*(2-3), 249-254.

Hambli, R., (2002). Design of experiment based analysis for sheet metal blanking processes optimization, Int. J. *Adv. Manuf. Technol, 19*, 403–410.

Hambli, R., (2003). BLANKSOFT: a code for sheet metal blanking processes optimization, *J. Mater. Process. Technol.,141*, 234–242.

Hernandez, J.J., Franco, P., Estrems, M., & Faura, F., (2006). Modelling and experimental analysis of the effects of tool wear on form errors in stainless steel blanking*, J. Mater. Process. Technol., 180*, 143–150.

Högman, B., (2002). Steel for press tools: Blanking of ultra high strength sheet steels. *6th International Tooling Conference*, Sweden, 237-253.

Husson, C., Correia*,* J.P.M., Daridon, L., Ahzi, S. (2008). Finite elements simulations of thin copper sheets blanking: Study of blanking parameters on sheared edge quality. *Journal of Materials Processing Technology, 199*, 74–83.

Monteil, G., Gréban, F., & Roizard, X., (2008). In situ punch wear measurement in a blanking tool, by means of thin layer activation. *Wear, 265*, 626–633.

Mucha, J., (2010). An experimental analysis of effects of various material tool's wear on burr during generator sheets blanking. *Int J Adv Manuf Technol 50*, 495–507.

Author(s) Information

Ilyas Uygur
Duzce University, Faculty of Engineering; Department of Mechanical Engineering, Duzce/Türkiye

Hasan Oktem
Kocaeli University, Hereke Asım Kocabıyık Vocational Natural Science Institute/Polymer Science and Technology, Kocaeli/Türkiye
Contact e-mail: hoktem@kocaeli.edu.tr

Halit Karasungur
Kocaeli University, Natural Science Institute/Polymer Science and Technology, Kocaeli, Türkiye
Güneş Plastic Mold Coorperation, Kocaeli/Türkiye

Husnu Gerengi
Duzce University, Faculty of Engineering; Department of Mechanical Engineering, Duzce/Türkiye

To cite this article:

Uygur, I., Oktem, H., Karasungur, H., & Gerengi, H. (2025). Investigation of burr height for sheet metal process of medium duty casters in industrial kitchens. *The Eurasia Proceedings of Science, Technology, Engineering and Mathematics (EPSTEM), 36,* 245-252.

The Eurasia Proceedings of Science, Technology, Engineering & Mathematics (EPSTEM)
ISSN: 2602-3199

The Eurasia Proceedings of Science, Technology, Engineering and Mathematics (EPSTEM), 2025

Volume 36, Pages 253-261

ICBAST 2025: International Conference on Basic Sciences and Technology

A Novel SCB Test for Determining Fracture Quantities of Bituminous Composites

Ragip Ince
Firat University

B. Fatih Furtana
Firat University

Abstract: Numerous non-Hookean fracture methods have been introduced to evaluate fracture parameters in quasi-brittle materials. In concrete structures, the effective crack model is widely used, and it requires determining the effective crack length and fracture toughness. Similarly, bituminous mixtures, which display ductile behavior at room temperature and brittle characteristics in colder conditions, demand non-Hookean fracture mechanics for accurate modeling due to defects like cracks and voids. This study focuses on assessing the fracture behavior of pure bituminous mixtures through experimental analysis. Ten semi-circular bending (SCB) specimens with varying initial crack lengths were prepared and subjected to three-point bending tests to capture load-displacement responses. The effective crack model, combined with the compliance technique, was utilized to calculate the fracture toughness of these samples. Findings aim to enhance understanding of fracture mechanisms in bituminous mixtures, contributing to the development of more durable pavements, especially under varying environmental conditions that influence material brittleness or ductility.

Keywords: Bituminous composites, Effective crack model, Fracture mechanics, Semi-circular bending test.

Introduction

Linear Elastic Fracture Mechanics (LEFM) were initially applied to concrete elements containing cracks by Kaplan (1961). However, the results of extensive tests, subsequently, illustrated that LEFM was not valid for cement-based materials such as mortar and concrete (Kesler et al., 1972). This inapplicability of LEFM was due to the existence of an inelastic zone with large-scale and full cracks in front of the crack tip in cementitious composites. This so-called fracture process zone (FPZ) was ignored by LEFM. Therefore, several investigators have recommended non-Hookean fracture mechanics approaches to characterize FPZ.

Initially, some computational approaches, referred to as cohesive crack models, were proposed, and these ways model the FPZ with a closing pressure that diminishes near the crack tip (Hillerborg et al., 1976; Bazant and Oh, 1983). Subsequently, the equivalent elastic fracture models, such as the two-parameter fracture model by Jenq and Shah (1985), the effective crack model (ECM) by Nallathambi and Karihaloo (1986), the size effect model by Bazant and Kazemi (1990), the double-K model by Xu and Reinhardt (1999), and the boundary effect method by Hu and Duan (2008) were developed, and they simulate the FPZ with an effective crack length.

Fracture experiments on semi-circular bending (SCB) samples have widely been performed to determine the fracture energy of asphalt mixtures, such as the fracture energy based on the work of fracture (G_F) and the critical strain energy release rate (J_c). Nevertheless, the asphalt concretes cannot be modelled utilizing only the concept of fracture energy. Thus, the work of fracture method was based on the fictitious crack model, requiring three parameters to characterize concrete fracture: G_F, tensile strength, and the relationship between crack closing pressure and crack opening displacement.

The utilization of SCB samples is quite wide in fracture mechanics experiments of asphalt and rock materials. Such samples also provide great advantages for determining the fracture mechanics-based performance of existing structures. Although a complex and expensive frame system is recommended by AASHTO (2015) for SCB-based asphalt concretes, the deformation of the loading head (or stroke) is commonly taken into account in the literature in determining the load-deformation relationship of SCB samples. However, such a measurement causes erroneous measurements, especially due to local deformations at the loading head and supports where the loads act on the asphalt material. In this study, it is aimed to develop a cheaper alternative test way that eliminates the aforesaid local deformations.

The Effective Crack Model (ECM) in Concrete Fracture

Several investigators have developed nonlinear fracture mechanics approaches to characterize FPZ. These models can be classified as the cohesive crack models and the equivalent elastic fracture models, such as the effective crack model (ECM) proposed by Nallathambi and Karihaloo (1986). The main aim of any approach is to determine the critical crack extension (size of FPZ) at the peak load $\Delta a = a_e - a_0$, in which a_e and a_0 are the effective crack length at the peak load and the initial crack length, respectively. When the stress intensity factor K_I, which describes the stress singularity at the crack tip under mode I loading, reaches the critical stress intensity factor (fracture toughness) K_{Ic}, the crack progress is unstable according to LEFM. The expression of LEFM can be presented for the general case in mode I in the following form:

$$K_{Ic} = \sigma_{Nc}\sqrt{\pi a_0}\,Y(g,p) \tag{1}$$

where σ_{Nc} is the nominal failure stress computed for the uncracked structure and $Y(g,p)$ is a dimensionless function of structure of geometry and load type. According to LEFM, it is assumed that the initial crack length a_0 in Eq. (1) does not change until it reaches the peak load. At this stage, the crack has a critical length and starts to progress in an unstable way. In reality, the crack propagates in a stable manner already at lower load until the peak load is reached since the size of FPZ can be larger than the sample size in quasi-brittle materials such as mortars, concretes, rocks, and bituminous materials. For this reason, according to Equation 1, the effective crack length a_e must be considered in the evaluation of K_{Ic} for quasi-brittle materials. However, a_e depends on structural size because it decreases as the member size increases, and it also depends on the geometry of the structure. Therefore, a unique fracture quantity is not adequate to simulate crack propagation in quasi-brittle materials.

The effective crack length a_e in ECM for the concrete fracture is computed from the secant stiffness of the real concrete structure at the peak load. The main idea behind the ECM approach can be explained with Figure 1, where are indicated the load-deflection plots of a beam with a central edge notch up to peak load. According to ECM, the fracture of a quasi-brittle material is described by two parameters, namely the critical stress intensity factor (the fracture toughness) K^e_{Ic} and the effective crack length a_e.

The stiffness of the real structure in the linear regime is proportional to the elasticity modulus (E). It can be determined from any pair of load and deflection values (P_i, δ_i) in this regime, as presented in Figure 1. Note that according to ECM, P_i can be selected to correspond approximately to $P_c/2$ in the load-displacement curve recorded in the bending sample of width b, depth d, and span s, as shown in Figure 1a. Consequently, the effective crack length is computed from two values taken from the load–displacement curve: the initial compliance C_i and the secant compliance C_s measured at the peak load, as indicated in Figure 1b.

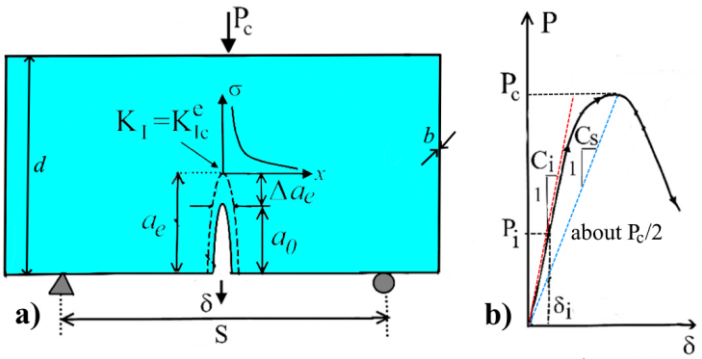

Figure 1. Modeling based on ECM of cracked structures a) notched beam b) typical load-δ curve

Nevertheless, the parameters included in any fracture model could be converted to the other concrete fracture models. To illustrate, it is possible to transform the fracture toughness parameter of ECM to the fracture energy parameter G_f, of the size effect model by using the well-known LEFM expression, which is presented below.

$$G_f = \left(K_{Ic}^{e}\right)^2 \Big/ E \tag{2}$$

The Modelling of SCB Samples According to ECM

Using compliance methods based on the two-parameter model and ECM, Ince et al. (2024) recently simulated eight series of asphalt SCB tests, the fracture characteristics of which are detailed in Figure 2a. Ince et al. (2024) derived two LEFM-based compliance functions for $0.03 \leq \alpha=a/r \leq 0.9$, considering cases of t/r = 0, 0.05, and 0.1 to simulate bituminous SCB specimens with s/r = 0.8 (where r is the sample radii), applying compliance techniques used in concrete fracture. In the aforesaid study, to reduce calculation errors, the geometry shown in Figure 2b was meshed using 100 finite elements along the crack line, while 8 quarter-point elements were employed around the crack tip. Subsequently, the important LEFM relationships, namely the stress intensity factor, crack mouth opening displacement, load line displacement, and crack opening displacement profile, were derived. However, when deriving the function of the load line displacement, the vertical displacement values at the crack mouth of the sample shown as δ_u in Figure 2b were used.

It was emphasized in this study that such a measurement causes erroneous measurements, especially due to local deformations at the loading head and support where the loads act on the asphalt material. Therefore, it was aimed to develop an alternative test method in the presented work that would eliminate unpredictable local deformations at three loading points. For this, in accordance with the measurement of the developed frame system, the displacement values at the upper limit level of the support of the sample, which are shown as δ_s in Figure 2b, were also determined using the finite element method. Consequently, when deriving the function of the load line displacement in this study, the relative displacement values ($\delta_r = \delta_u - \delta_s$) were used. The following expression was chosen for the relative displacement function:

$$\delta_r = \frac{P\alpha}{2bE} D_1\left(\alpha = \frac{a}{r}\right) \tag{3}$$

Here $D_1(\alpha)$ is the normalized function of the δ_r. The function of D_1 was determined by conducting a normalization of δ_r values with the individual ($P/2bE$) values. The following expression was produced using the least squares method for the normalized values based on the finite element method.

$$D_1\left(\alpha\right) = \frac{1}{0.2751\alpha - 0.7521\alpha^2 + 0.8489\alpha^3 - 0.6448\alpha^4 + 0.3872\alpha^5 - 0.1152\alpha^6} \tag{4}$$

The value 1/0.2751 in Equation 4 is therefore a constant valid for the unnotched SCB sample. Note that Ince (2025) also derived the aforesaid LEFM expressions for s/r= 0.50 and 0.65. The following procedures can be used in ECM-based analysis of SCB samples (Ince et al., 2024). At first, the modulus of elasticity can be derived for the SCB sample from Figure 1b as follows:

$$E = \frac{\alpha_0}{2bC_i} D_1\left(\alpha_0\right), \qquad C_i = \frac{\delta_i}{P_i} \tag{5}$$

According to Figure 2a, the effective crack length (or normalized effective crack length, α_e) is calculated by the trial-and-error method as follows:

$$\alpha_e = \alpha_0 \frac{C_s D_1\left(\alpha_0\right)}{C_i D_1\left(\alpha_e\right)} \tag{6}$$

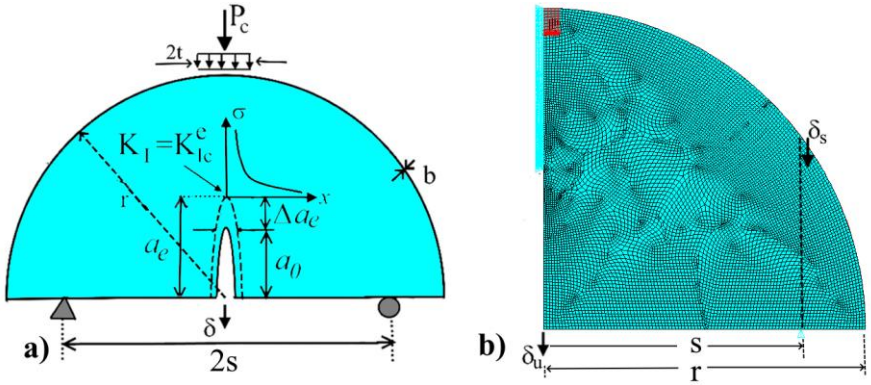

Figure 2. a) Fracture characteristics of the SCB sample b) finite element mesh generation of the sample

Consequently, the effective fracture toughness of the material can be determined for the sample in Figure 2a as follows:

$$K_{Ic}^{e} = \frac{P_c}{2br}\sqrt{\pi a_e}\,\frac{5.18 - 13.878\alpha + 27.145\alpha^2 - 26.887\alpha^3 + 10.321\alpha^4}{(1-\alpha)^{1.5}} \tag{7}$$

Experimental Program

Bitumen of grade B70/100 and density 1.033 was used in this investigation; it was procured from the TÜPRAS Batman refinery located in Turkey. Turkey's most common binder is the 70/100 grade, partly because of the country's climate. The aggregate gradation shown in Figure 3 was adhered to during the sample preparation procedure. It was found that the pure mixture's intended bitumen concentration was 4.67 %. The bitumen content was maintained constant for both pure and modified mixtures to guarantee that the binder content did not affect the mechanical qualities of the mixtures. The resulting material was compacted into cylindrical Marshall samples with a void ratio of 4 %, a height of approximately 60 mm, and diameters of 100 mm and 150 mm. A rotary compactor with an inclination angle of 1.25 ± 0.02◦ and a static pressure of 0.600 ± 0.018 MPa was used for this process. Then, SCB samples were created, notches were cut, and samples measuring 150 mm were split in half.

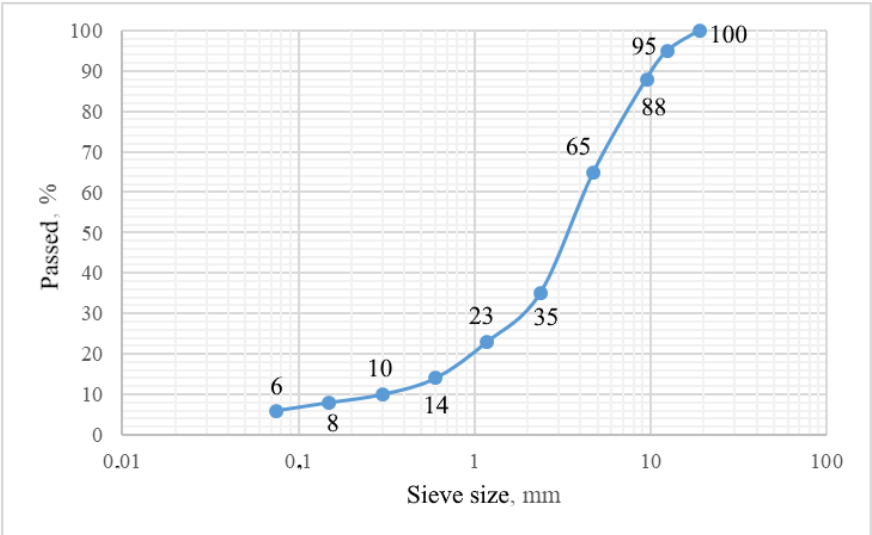

Figure 3. Aggregate gradation cure of the bituminous mixture used in this study

The methodology for preparing SCB test samples is illustrated in Figure 4, which illustrates the notch formation observed in the samples utilized in this research. Long cylindrical asphalt samples, measuring 60 mm in height and 150 mm in diameter, were compacted using a gyratory compactor. To achieve a uniform air void distribution, the top and bottom surfaces of the samples were trimmed by 5 mm from each end, resulting in final

dimensions of 50 mm in height and 150 mm in diameter. Subsequently, the samples were bisected, and notches were incised at the center to create SCB test samples. Regardless of the sample thickness and mix design, notch lengths of about 10, 15, 20, and 30 mm were selected for 150 mm samples. The notch thickness is approximately 2 mm.

Figure 4. The preparation of a typical SCB sample

The displacement frame used for beams in the effective crack model, which is a popular method in the fracture mechanics of concrete, was adapted to the SCB sample as detailed in Figure 5. Thanks to the LVDT mounted on the end of the rod sliding on the rigid rectangular frame, the under-notch displacement was determined based on the frame support on the support. SCB tests were carried out at room temperature.

Nonlinear fracture toughness values of bituminous hot mix samples were computed according to the compliance method. Samples were loaded at 0.5 mm/min speed. The load-displacement curves of SCB samples tested are demonstrated in Figure 6. The crack patterns of samples are revealed in Figure 7.

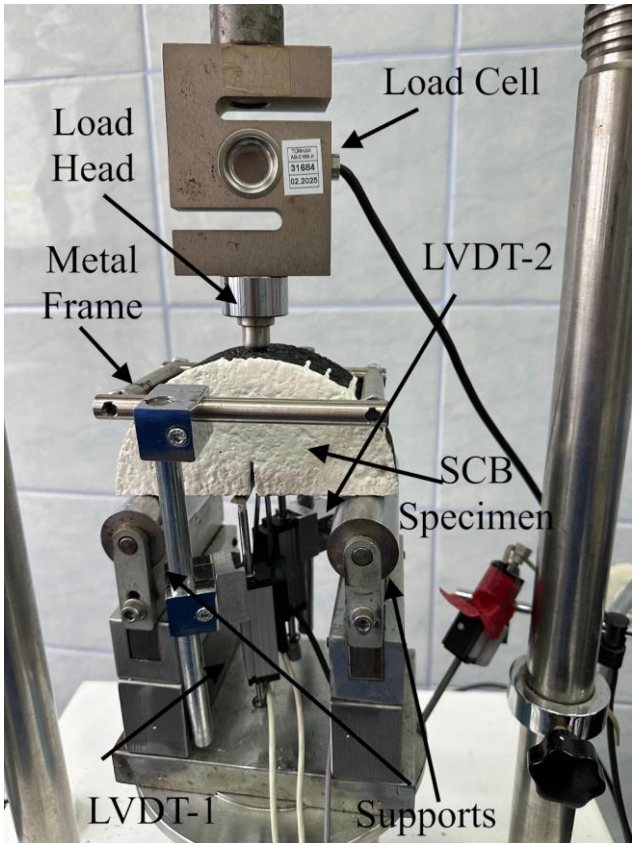

Figure 5. Test setup of SCB samples

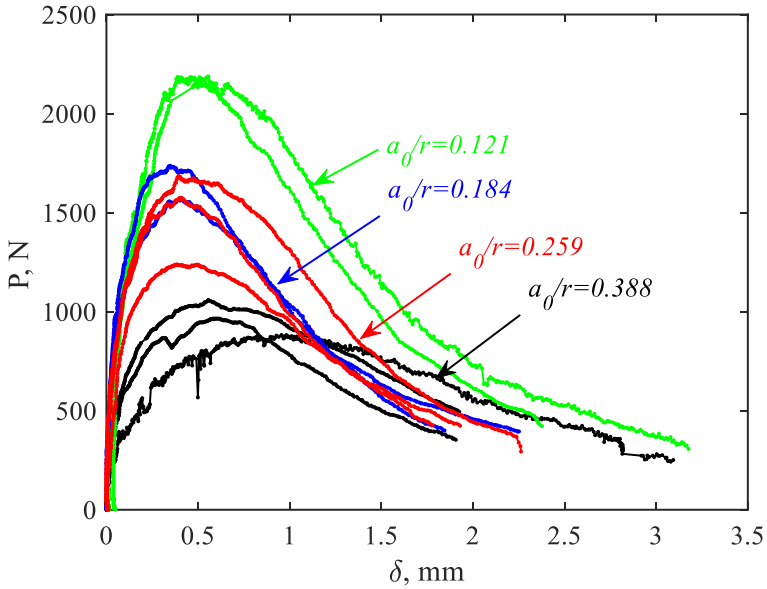

Figure 6. Load-displacement curves of SCB samples tested

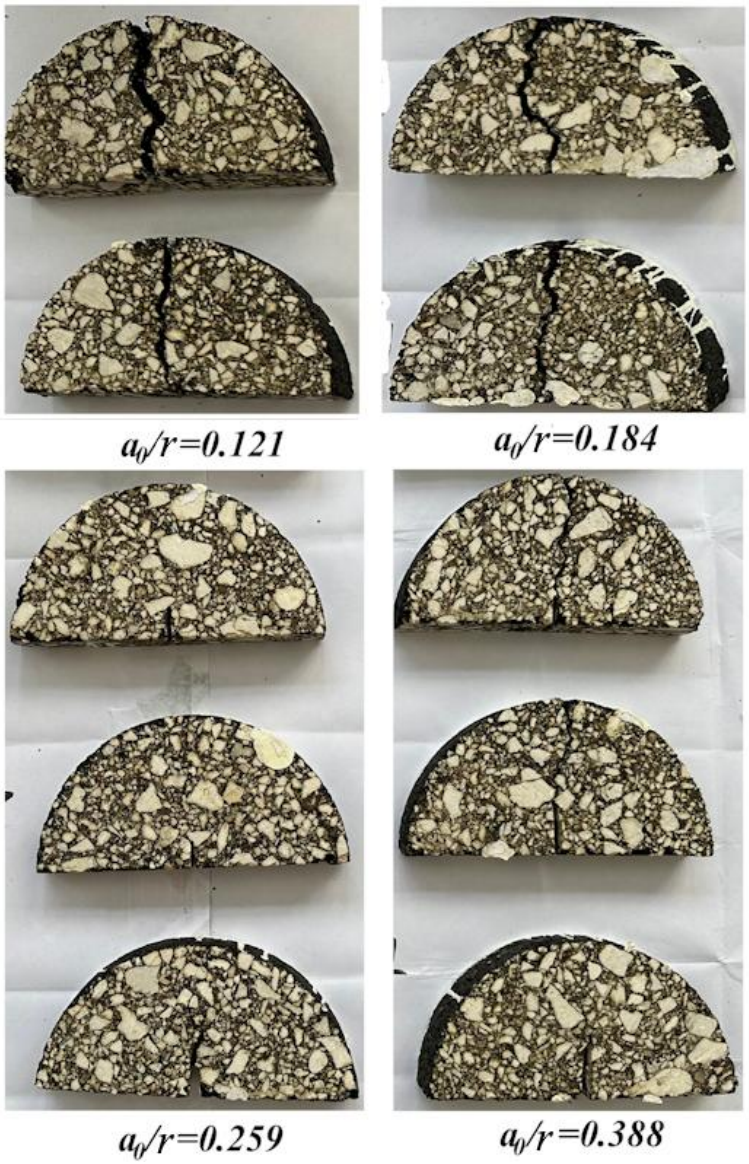

Figure 7. Fractured notched SCB samples

Analysis of Test Results

The sample width (b), sample radii (r) (or structural size), and the peak load values (P_c) of the notched SCB samples were reported in Table 1 according to the notch depths (a_0). By using Equations 3 to 7, the values of K^e_{Ic} were determined from the P-δ curve of each sample as shown in Figure 6. The initial compliance values (C_i), the secant compliance values (C_s), the relative initial notch lengths (α_0), the relative effective notch lengths (α_0), the fracture toughness parameters based on ECM (K^e_{Ic}), and the fracture energy (G_f) based on Eq. (2) are summarized for each sample in Table 2.

Table 1. Test results of SCB samples tested in this study

Sample	b mm	r mm	a_0 mm	P_c N
SCB1	54.85	73.1	8.58	2152
SCB2	55.06	73.51	9.17	2186
SCB3	54.69	73.58	12.9	1569
SCB4	52.96	73.47	14.19	1736
SCB5	54.8	73.12	18.01	1574
SCB6	53.74	74.07	19.22	1685
SCB7	54.81	74.46	20.24	1239
SCB8	53.61	72.70	28.03	882
SCB9	55.04	72.95	28.35	965
SCB10	55.14	73.74	28.66	1059

Table 2. Fracture parameters of SCB samples tested according to ECM

Sample	C_i mm/N	C_s mm/N	E MPa	$\alpha_0=a_0/r$	$\alpha_e=a_e/r$	K^e_{Ic} MPa√m	G_f N/m	G_F N/m
SCB1	0.000087	0.000250	530	0.117	0.430	0.480	435	1100
SCB2	0.000075	0.000253	627	0.125	0.475	0.554	490	1316
SCB3	0.000042	0.000254	1295	0.175	0.622	0.676	353	834
SCB4	0.000045	0.000200	1331	0.193	0.577	0.649	316	839
SCB5	0.000055	0.000260	1252	0.246	0.620	0.674	363	874
SCB6	0.000070	0.000234	1048	0.259	0.563	0.586	328	995
SCB7	0.000090	0.000311	825	0.272	0.576	0.443	238	855
SCB8	0.000334	0.001082	341	0.386	0.638	0.417	511	1020
SCB9	0.000142	0.000602	788	0.389	0.683	0.544	375	735
SCB10	0.000113	0.000525	989	0.389	0.696	0.634	406	975

When statistical validation was performed for the fracture toughness parameter based on ECM, the mean, standard deviation, and coefficient of variation (CV) values were calculated as 0.566 MPa√m, 0.095 MPa√m, and 16.8%, respectively. Since the CV value was less than 20%, it may be concluded that the approach used in this study gave reasonable results.

In addition to G_f based on the size effect model, the fracture energy based on the work of fracture (G_F) and the critical strain energy release rate (J_c) were evaluated in this study. For G_F, the work of fracture, W, is initially computed from the area under the P-δ, and the tail part of the curve of P-δ, W_{tail}, is subsequently conducted according to AASHTO (2015). Consequently, the fracture energy can be determined as follows:

$$G_F = \frac{W + W_{tail}}{b\left(r - a_0\right)} \tag{8}$$

G_F values for each sample tested in this study are summarized in the last column of Table 2. According to the multiple specimen method proposed for J_c, at first, P-δ plots are recorded for at least three different initiation notch lengths for statistical validity. Subsequently, the potential energy values, U, are determined by computing the area up to peak load under the P-δ plots, and they are normalized with specimen widths b. Finally, when the U values are plotted versus notch lengths a_0, the slope of the linear regression can be assumed as J_c. In Figure 8, the application of this computation is presented for SCB samples used in this study. According to this, as shown in Figure 8, the value of J_c was determined as 635 N/m for the determination coefficient R^2=0.66, which actually gives the percentage of explanation of the event.

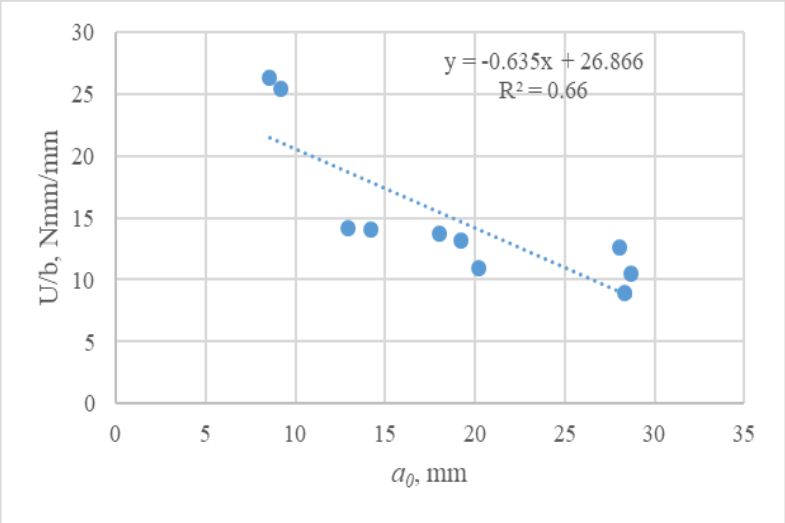

Figure 8. J_c analysis of the bituminous mixture used in this study

Conclusion

In this study, the effective crack model, which is widely used in concrete fracture analysis, was used to investigate the fracture behavior of asphalt concrete. The key findings are summarized below:

Until now, in hot bituminous mixtures, the fracture toughness parameter calculated based on LEFM is determined according to the effective crack model, which is a popular method in the fracture mechanics of quasi-brittle materials. Since the CV value was less than 20% for fracture toughness values computed, it may be concluded that the test setup used in this study gave reasonable results.The applications performed in this study revealed that the critical strain energy release rate value was between the fracture energy based on the work of fracture based on the fictitious crack model and the fracture energy based on the size effect model (G_F>J_c>G_f). According to Bazant (2002), the ratio of G_F/G_f is equal to 2.5 for quasi-brittle materials. Similarly, it can be seen that this ratio can be computed approximately as 2.5 for the last two columns of Table 2.

Recommendations

With the experimental setup developed here, SCB samples were used with pure bituminous hot mixtures at room temperature to determine nonlinear fracture parameters by only considering the load-displacement relationships. However, it should be emphasized that further studies can come up with more reliable results by investigating various types and sizes of aggregates to verify the above findings.

Scientific Ethics Declaration

*The authors declare that the scientific ethical and legal responsibility of this article published in EPSTEM journal belongs to the authors.

Conflict of Interest

*The authors declare that they have no conflicts of interest

Funding

*This study was supported by Fırat University Scientific Research Projects Unit (FUBAP) with project number MF-25.93.

Acknowledgements or Notes

*This article was presented as an oral presentation at the International Conference on Basic Sciences and Technology (www.icbast.net) held in Budapest/Hungary on August 28-31, 2025.

References

AASHTO Designation: TP 105-13. (2015). *Standard method of test for determining the fracture energy of asphalt mixtures using the semicircular bend geometry (SCB)*, American Association of State and Highway Transportation Officials.

Bažant, Z. P., & Kazemi, M. T. (1990). Determination of fracture energy, process zone length, and brittleness number from size effect with application to rock and concrete. *International Journal of Fracture*, *44(2)*, 111-131.

Bažant, Z. P., & Oh, B. H. (1983). Crack band theory for fracture concrete. *Materials & Structures (RILEM)*, *16(93)*, 155-157.

Bažant, Z. P. (2002). Concrete fracture models: testing and practice. *Engineering Fracture Mechanics*, *69*, 165–205.

Hillerborg, A., Modeer, M., & Petersson, P. E. (1976). Analysis of crack formation and crack growth in concrete by means of fracture mechanics and finite elements. *Cement & Concrete Research*, *6*, 773-782.

Hu, X., & Duan K. (2008). Size effect and quasi-brittle fracture: the role of FPZ. *International Journal of Fracture*, *154*, 3–14.

Ince, R. (2025). Using SCB specimens to quantify nonlinear fracture characteristics in concrete and rock materials. *Engineering Fracture Mechanics*, *318*, 110951.

Ince, R., Yalcin, E., & Yilmaz, M. (2024). Quantifying nonlinear fracture parameters in bituminous SCB specimens: A compliance-based approach. *Case Studies in Construction Materials*, *21*, e03437.

Jenq, Y. S., & Shah, S. P. (1985). Two-parameter fracture model for concrete. *ASCE Journal of Engineering Mechanics*, *111(10)*, 1227-1241.

Kaplan, M. F. (1961). Crack propagation and the fracture of concrete. *ACI Journal*, *58(11)*, 591-610.

Kesler, C. E, Naus, D. J., & Lott, L. L. (1972). Fracture mechanics-its applicability to concrete. *The Society of Materials Science,* 113-124.

Nallathambi, P., & Karihaloo, B. L. (1986). Determination of the specimen size independent fracture toughness of plain concrete. *Magazine of Concrete Research*, *38(135)*, 67-76.

Xu, S., & Reinhardt, H. W. (1999). Determination of double-K criterion for crack propagation in quasi-brittle fracture, Part I: experimental investigation of crack propagation. *International Journal of Fracture*, *98*, 111-149.

Yalcin, E., Ince, R. & Yilmaz, M. (2025). Exploring activated carbon as an alternative to SBS in asphalt mixtures: Performance and fatigue analysis. *Alexandria Engineering Journal*, *121*, 283–294.

Author(s) Information

Ragip Ince
Firat University
Engineering Faculty, Elazig, Türkiye
Contact e-mail: *rince@firat.edu.tr*

B. Fatih Furtana
Firat University
Engineering Faculty, Elazig, Türkiye

To cite this article:

Ince, R., & Furtana, B. F. (2025). A novel SCB test for determining fracture quantities of bituminous composites. *The Eurasia Proceedings of Science, Technology, Engineering and Mathematics (EPSTEM), 36,* 253-261.

The Eurasia Proceedings of Science, Technology, Engineering & Mathematics (EPSTEM)
ISSN: 2602-3199

The Eurasia Proceedings of Science, Technology, Engineering and Mathematics (EPSTEM), 2025

Volume 36, Pages 262-267

ICBAST 2025: International Conference on Basic Sciences and Technology

Classification of Earthquake-Induced Asphalt Cracks with a Transfer Learning-Based Hybrid Strategy

Fatih Demir
Fırat University

Erkut Yalcin
Firat University

Abstract: One of the most popular modes of transportation is the highway. Highways that receive timely maintenance avoid future increases in maintenance expenses. It is crucial to identify highway damage brought on by significant earthquakes. because roadways are used to deliver logistical and humanitarian relief to earthquake-affected areas. Consequently, system applications that automatically identify asphalt deterioration are required. Images of asphalt cracks that appeared in five major Turkish cities following two consecutive severe earthquakes in the Elbistan region were examined in this study. The construction department experts classified these fissures as serious and small. In the following phase, a novel deep learning-based model was used to classify asphalt fractures. In the implementation phase of the proposed model, features were extracted using transfer learning models. These features extracted from different models were combined to create a large feature set. The ReliefF algorithm was used to select the most discriminative features from the extracted features. Popular machine learning algorithms such as SVM, KNN, Naive Bayes, and Decision Trees were used in the classification phase. The best classification results were achieved with the SVM algorithm.

Keywords: Earthquake, Asphalt cracks, Deep learning, Transfer learning models, Classification

Introduction

2023, in the districts of Pazarcık and Elbistan in the Kahramanmaraş province. Eleven Turkish provinces experienced substantial material losses and casualties. As soon as the earthquakes struck, aid started to come in in the form of people and supplies from other countries and Turkish districts. However, this help was delayed significantly due to the warped asphalt of the roads. The field tests showed that roads with previously warped asphalt hindered road movement. Furthermore, experts on the ground found and documented defects in the asphalt that would hinder transportation in the case of the next earthquake or other calamity. However, the effects of the recent earthquakes were so severe that not all places could be evaluated for the state of the highways because access to some earthquake-affected routes was barred.

In order to prevent such disruptions in mobility, pre-earthquake highway maintenance measures are essential (Miller & Bellinger, 2003; Systems & Management, 2011). However, it takes a lot of skilled people to detect these maintenance chores. In automated decision support systems, artificial intelligence systems have lately started to perform better. Since the development of deep learning models in 2012, significant progress has been made in addressing problems related to automatic classification, regression, and segmentation. These models have been applied in many fields, such as engineering, economics, law, and medicine. The proposed approach employs a unique deep learning-based technique to determine the urgency of highway maintenance based on asphalt crack pictures taken after the February 6 earthquakes in Turkey. Automatically classifying asphalt cracks is one of the most prevalent computer vision issues (Dais et al., 2021). Convolutional Neural Networks (CNNs) are growing in popularity and effectiveness for crack detection, according to numerous empirical research (Liu

et al., 2022a; Liu & Wang, 2022; Liu et al., 2019). In a study by Gopalakrishnan et al. (2017), pavement cracks were binary classified as "crack" or "no crack" using a pre-trained VGG-16 CNN model.

The U-net model was altered by Huyan et al. (Huyan et al., 2020) in order to identify asphalt cracks in a database that contained 3000 photos. Video frames captured from car arches were examined by Mandal et al. (2018). It was estimated that the YoloV2 architecture detected about 9000 pictures. Majidifard et al. (2020) introduced a comprehensive approach to asphalt crack classification, utilising YOLO net for crack detection and U-Net for fracture segmentation. Guan et al. (2021) presented a computerised system that uses a mix of image processing and deep learning techniques to locate asphalt cracks at the pixel level while taking into account the images' depth and colour characteristics. The need for a system that can distinguish and classify crack intensity levels is highlighted by the fact that most research in this field focusses on locating asphalt cracks rather than assessing their severity. Li et al. (2020) created a novel deep learning-based system that can automatically identify different kinds of cracks on asphalt surfaces. They gathered a large dataset with five different fracture patterns, with fatigue fractures being a primary focus. Liu et al. (2020) suggested a two-tiered method for pavement crack identification and delineation based on CNN implementation, with a focus on identifying four distinct fracture types, most notably fatigue cracks. Liu et al. (2022b) employed Grad CAM-based models for three distinct image categories in order to improve the interpretability of the CNN model's outputs. This made it possible to identify multiple classifications of crack severity. Finally, a two-step automatic crack identification system that predicts linear fracture severity levels using image processing approaches was proposed by Tran et al. (2022). Materneh et al. (2024) classified asphalt fractures using a customised DenseNet model. The model was optimised using the Grey Wolf Optimisation technique. Ten CNN models that had already been trained were compared to the suggested model. With an accuracy of 98.73 percent, the cracks were categorised as longitudinal, horizontal, and diagonal. A lightweight deep-learning model was created by Liang et al. (Liang et al., 2024) to categorise asphalt cracks. Furthermore, this model was expanded to include residual blocks. About 83% classification accuracy was attained with this model. Generally speaking, the current research has been done to either identify asphalt cracks or complete the segmentation assignment. A few research have tried to categorise crack directions. This is due to the fact that crack classification is done using ASTM D6433 and FHWA standards, which do not contain any classification guidelines according to crack direction (Chen et al., 2024; Farahmand-Tabar et al., 2024). The fracture width is the most fundamental information on the significance of cracks in these standards. In conclusion, a thorough investigation into the importance of asphalt fractures like the one in our study has not yet been completed.

Dataset

Large earthquakes with magnitudes of 7.7 and 7.6 struck the Turkish province of Kahramanmaraş on February 6, 2023, in the districts of Pazarcık and Elbistan. Following these earthquakes, five distinct provinces near Elbistan saw significant asphalt fractures, both large and tiny. Some of these cracks were so large that they made transportation by road impossible. Even while some of the fractures weren't very large, they were sufficient to create large cracks whenever a heavy vehicle or new tremor passed. Because of this, the building department's experts surveyed the area and classified these cracks as either major or minor.

Figure 1. Samples of images from the field research dataset

A professional camera with a 24 MP resolution was used to take 518 JPEG pictures from a fixed overhead position at a 90-degree angle at a distance of one metre. For every piece of data, this image capture criteria was met. To improve the artificial intelligence systems' dependability, all of these photos were taken from the same distance. The Department of Construction experts classified 293 of the total data as significant and 225 as minor. Samples from both groups are displayed in Fig. 1. Provinces susceptible to earthquakes were visited for labelling. In these provinces, the crack widths of the roadways that were subjected to cracks were measured and documented in centimeters. ASTM D6433 is the standard taken into consideration during the dataset creation process because it offers details on crack widths for crack classification.

Method

The proposed methodology is generally implemented in three steps. In the first step, training and validation were performed using the transfer learning strategy with pre-trained models such as VGG16, VGG19, AlexNet, ResNet50, GoogleNet, and MobileNetV2. Then, features were extracted using the final 1000-dimensional layer of the MobileNetV2 model, which provided the best classification performance. In the second step, the ReliefF algorithm was chosen to select the features with high inter-class discrimination. The ReliefF algorithm was used because it has both a low computational load and has yielded good performance results in the literature. In the final step, popular classification algorithms in machine learning were tested using these selected features. These classifications were performed using SVM, KNN, Decision Trees (DT), Naive Bayes (NB), Logistic Regression (LR), and Random Forest (RF) algorithms. The SVM algorithm, which provided the best classification result, was included in the proposed methodology. A representative illustration of the proposed approach is given in Figure 2.

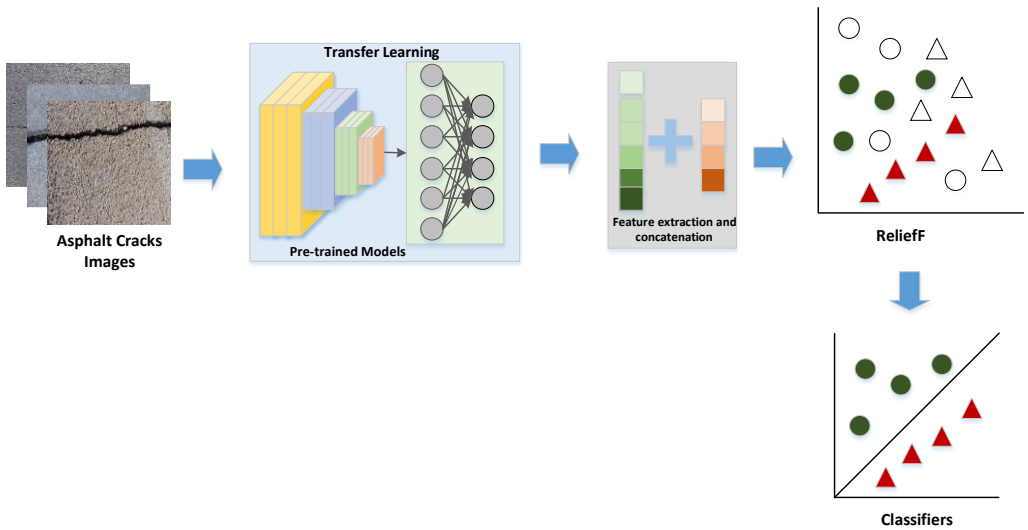

Figure 2. Representative illustration of the proposed methodology

Results and Discussion

A laptop computer with a 12th generation i9 processor, 32GB DDR5 memory, and a 12GB graphics card (RTX3080Ti) was used to conduct experimental studies. All coding was done in MATLAB. During the training process, the Mini-Batch number was set to 32, the Epoch was 100, the Initial Learning Rate was 0.001, and the Validation Frequency was 30. SGDM, which is frequently used in deep learning models, was used as the optimization solver. 10-fold cross-validation was used as the validation technique, thus increasing the overall validity of the model. Figure 3 shows the classification results of the pre-trained models after transfer learning in the form of a confusion matrix.

Among the pre-trained CNN models, the MobileNetV2 model gave the best performance with 84.7%, while the GoogleNet model gave the worst performance with 76.83%. Therefore, the MobileNetV2 model was selected for use in the proposed methodology. In the next step, 1000 features were extracted from the last connected layer of the MobileNetV2 model, named Logits. Of these extracted features, 150 were selected based on the importance weights of the ReliefF algorithm.

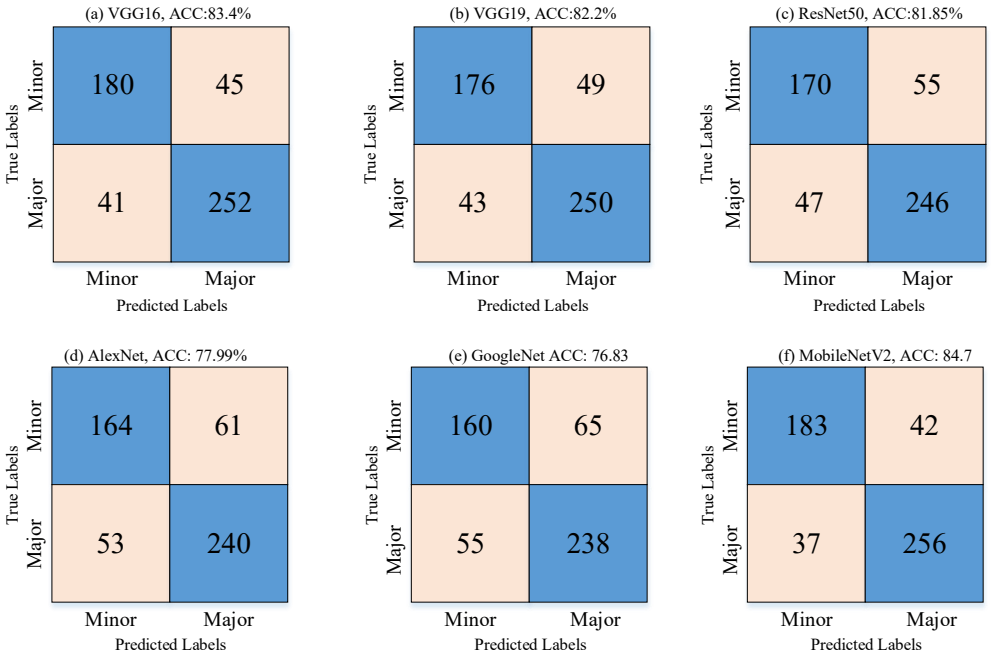

Figure 3. Confusion matrix results of pre-trained CNN models

The importance weights calculated by the ReliefF algorithm are shown in Figure 4. 150 features with importance weight values above 0.001 were selected. With this feature selection process, the computational cost in the classification process is reduced. Six popular machine learning algorithms were used to classify the extracted features. The classification accuracy was 86.3% for SVM, 82.2% for KNN, 81.85% for LR, 81.66% for DT, 82.62% for NB, and 84.16% for RF. The confusion matrix results of these six classification algorithms are given in Figure 5.

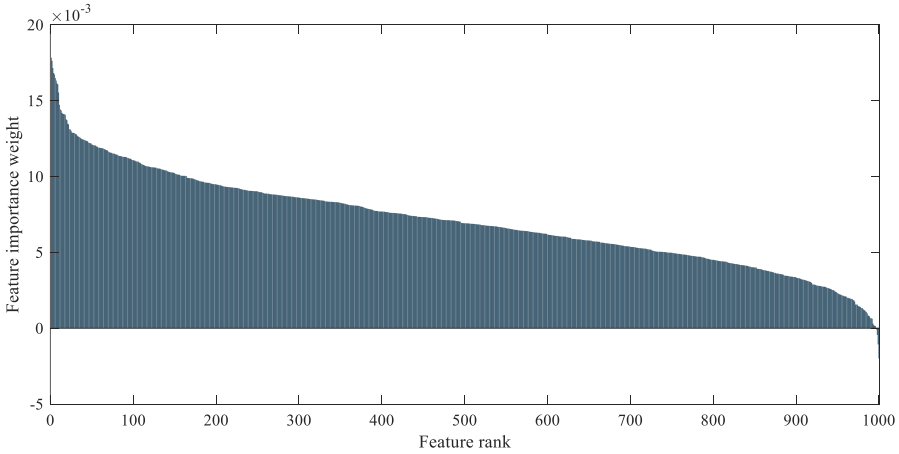

Figure 4. Importance weights of features with the ReliefF algorithm

Conclusion

Major earthquakes cause significant loss of life and property in cities. Rapid aid delivery is essential after such major earthquakes. Highways are a key factor in this transportation. This study examines the deformation data on highways following two consecutive major earthquakes in the Kahramanmaraş region of Turkey. The deformation data was labeled as major and minor by experts in the construction industry. Classification was performed on this dataset using pre-trained CNN models. MobileNetV2 yielded the best classification performance among the six models. To further improve classification performance, features were extracted in this model. Efficient features were selected using the ReliefF algorithm. Using these selected features, the SVM algorithm yielded the best classification performance. While this classification performance is satisfactory, it still has room for improvement. Classification performance can be further improved with new deep learning models in the future.

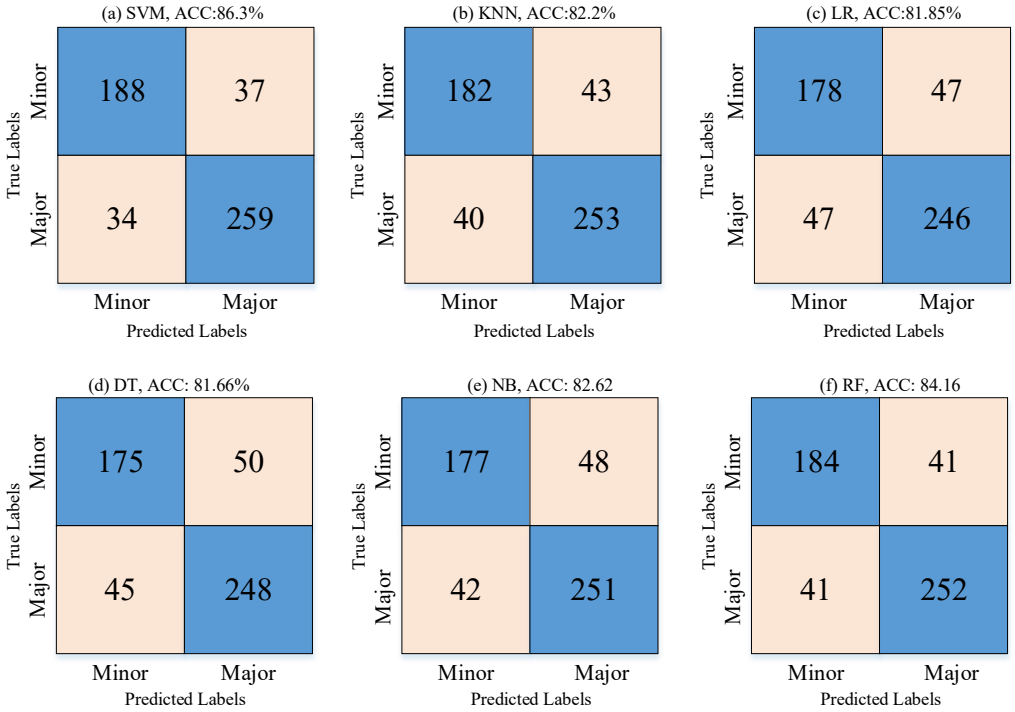

Figure 5. Results of confusion matrices of classification algorithms

Scientific Ethics Declaration

*The authors declares that the scientific ethical and legal responsibility of this article published in EPSTEM journal belongs to the authors.

Conflict of Interest

*The authors declare that they have no conflicts of interest

Funding

*No funding.

Acknowledgements or Notes

*This article was presented as an oral presentation at the International Conference on Basic Sciences and Technology (www.icbast.net) held in Budapest/Hungary on August 28-31, 2025.

References

ASTM International. (2011). *Standard practice for roads and parking lots pavement condition index surveys* (ASTM D6433-11).

Chen, Z., Shao, H., Liu, P., Li, G., & Rong, X. (2024). An efficient hybrid conjugate gradient method with an adaptive strategy and applications in image restoration problems. *Applied Numerical Mathematics, 204*, 362–379.

Dais, D., Bal, I. E., Smyrou, E., & Sarhosis, V. (2021). Automatic crack classification and segmentation on masonry surfaces using convolutional neural networks and transfer learning. *Automation in Construction, 125*, 103606.

Farahmand-Tabar, S., Abdollahi, F., & Fatemi, M. (2024). Robust conjugate gradient methods for non-smooth convex optimization and image processing problems. In A. J. Kulkarni & A. H. Gandomi (Eds.), *Handbook of Formal Optimization* (pp. 1–25). Springer.

Gopalakrishnan, K., Khaitan, S. K., Choudhary, A., & Agrawal, A. (2017). Deep convolutional neural networks with transfer learning for computer vision-based data-driven pavement distress detection. *Construction and Building Materials, 157*, 322–330.

Guan, J., Yang, X., Ding, L., Cheng, X., Lee, V. C. S., & Jin, C. (2021). Automated pixel-level pavement distress detection based on stereo vision and deep learning. *Automation in Construction, 129*, 103788.

Huyan, J., Li, W., Tighe, S., Xu, Z., & Zhai, J. (2020). CrackU-Net: A novel deep convolutional neural network for pixelwise pavement crack detection. *Structural Control and Health Monitoring, 27*(8), e2551.

Li, B., Wang, K. C. P., Zhang, A., Yang, E., & Wang, G. (2020). Automatic classification of pavement crack using deep convolutional neural network. *International Journal of Pavement Engineering, 21*(4), 457–463.

Liang, J., Zhang, Q., & Gu, X. (2024). Small-sample data-driven lightweight convolutional neural network for asphalt pavement defect identification. *Case Studies in Construction Materials, 21*, e03643.

Liu, F., Liu, J., & Wang, L. (2022a). Asphalt pavement crack detection based on convolutional neural network and infrared thermography. *IEEE Transactions on Intelligent Transportation Systems, 23*(11), 22145–22155.

Liu, F., Liu, J., & Wang, L. (2022b). Asphalt pavement fatigue crack severity classification by infrared thermography and deep learning. *Automation in Construction, 143*, 104575.

Liu, F., & Wang, L. (2022). UNet-based model for crack detection integrating visual explanations. *Construction and Building Materials, 322*, 126265.

Liu, J., Yang, X., Lau, S., Wang, X., Luo, S., Lee, V. C., & Ding, L. (2020). Automated pavement crack detection and segmentation based on two-step convolutional neural network. *Computer-Aided Civil and Infrastructure Engineering, 35*(11), 1291–1305.

Liu, Z., Cao, Y., Wang, Y., & Wang, W. (2019). Computer vision-based concrete crack detection using U-Net fully convolutional networks. *Automation in Construction, 104*, 129–139.

Majidifard, H., Adu-Gyamfi, Y., & Buttlar, W. G. (2020). Deep machine learning approach to develop a new asphalt pavement condition index. *Construction and Building Materials, 247*, 118513.

Mandal, V., Uong, L., & Adu-Gyamfi, Y. (2018). Automated road crack detection using deep convolutional neural networks. *2018 IEEE International Conference on Big Data (Big Data)*, 5212–5215.

Matarneh, S., Elghaish, F., Rahimian, F. P., Abdellatef, E., & Abrishami, S. (2024). Evaluation and optimisation of pre-trained CNN models for asphalt pavement crack detection and classification. *Automation in Construction, 160*, 105297.

Miller, J. S., & Bellinger, W. Y. (2003). *Distress identification manual for the long-term pavement performance program*. Federal Highway Administration.

Tran, T. S., Tran, V. P., Lee, H. J., Flores, J. M., & Le, V. P. (2022). A two-step sequential automated crack detection and severity classification process for asphalt pavements. *International Journal of Pavement Engineering, 23*(6), 2019–2033.

Author(s) Information

Fatih Demir
Fırat University
Software Engineering, Elazığ, Türkiye
Contact e-mail: *fatihdemir@firat.edu.tr*

Erkut Yalcin
Fırat University
Civil Engineering, Elazığ, Türkiye

To cite this article:

Demir, F., & Yalcin, E. (2025). Classification of earthquake-induced asphalt cracks with a transfer learning-based hybrid strategy. *The Eurasia Proceedings of Science, Technology, Engineering and Mathematics (EPSTEM), 36,* 262-267.

The Eurasia Proceedings of Science, Technology, Engineering & Mathematics (EPSTEM)
ISSN: 2602-3199

The Eurasia Proceedings of Science, Technology, Engineering and Mathematics (EPSTEM), 2025

Volume 36, Pages 268-275

ICBAST 2025: International Conference on Basic Sciences and Technology

Colored Wheats for Functional Food Candidates with Enhanced Nutrition

Hayati Akman
Selcuk University

Abstract: Wheat, the primary cereal crop, supplies 20% of humanity's protein and caloric intake. Colored blue, purple, and black wheats specifically represent a breakthrough in functional foods due to their exceptionally high phytochemical content, especially anthocyanins. These natural pigments create vibrant hues: purple concentrates in the pericarp, blue in the aleurone, while black wheat features pigments in both layers. Genetically, purple traces to Ethiopian emmer wheat, and blue originates from wild and relative crops. Nutritionally, colored wheats outperform modern wheat cultivars. They deliver significantly elevated protein, essential minerals, and vitamin E. Anthocyanin levels are substantially higher in black, purple, and blue wheats. They are also rich sources of phenolic compounds, flavonoids, and carotenoids, forming a potent bioactive profile. These phytochemicals offer major health benefits. Anthocyanins and phenolics act as powerful antioxidants, neutralizing harmful reactive oxygen species (ROS). This reduces oxidative stress and cellular damage to lipids, proteins, and DNA, thereby lowering risks of developing major chronic conditions, such as diabetes, cardiovascular disease, cancer, and age-related degeneration. This makes colored wheats vital tools against micronutrient deficiencies and hidden hunger. Technologically, despite variable gluten strength, they are versatile for functional food production. Applications include nutrient-dense, visually appealing muffins, noodles, biscuits, pasta, crackers, nutrition bars, and chapati bread, often boasting extended shelf-life and natural pathogen resistance. Agronomically, targeted breeding programs enhance their yield potential, stress tolerance, and adaptation especially for dryland farming. The ultimate goal is integrating their superior nutrition and health benefits into mainstream diets, providing natural alternatives to synthetic additives and contributing significantly to improved global nutrition.

Keywords: Colored wheat, Anthocyanin, Functional food, Breeding

Introduction

Wheat constitutes a significant portion of the human diet, contributing 20% of daily caloric and protein intake (Sharma & Sharma, 2025). Given this central dietary role, there is growing interest in enhancing wheat's nutritional profile, with a concept that aligns with the functional food movement, which originated in Japan in the late 1980s and is now widely embraced as individuals increasingly choose diets that promote well-being (Padhy et al., 2022). Colored wheat, fortified with anthocyanins, has arisen as a compelling functional food, providing a natural alternative to synthetic additives and nutraceuticals owing to its rich nutritional makeup and bioactive constituents (Padhy et al., 2022).

Colored purple, blue, and black wheat genotypes display distinct grain coloration associated with improved antioxidant capacity, higher protein levels, and a more favorable micronutrient composition (Sharma et al., 2023; Akman et al., 2025; Reddy et al., 2025). These qualities position colored wheat as a strong candidate for alleviating micronutrient deficiencies and improving dietary standards via biofortification strategies (Padhy et al., 2022). This review offers a thorough analysis of the genetic foundations, health-promoting attributes, antioxidant potential, agronomic features, technological uses, and breeding progress pertaining to colored wheat, underscoring its significance as a key component in the production of functional foods.

Method

This study was structured as a comprehensive review, synthesizing and analyzing existing scientific literature and recent research findings on colored wheats (blue, purple, and black). The methodology involved a systematic examination of published research articles, reviews, and conference proceedings to gather information on the genetic origins, nutritional composition, health benefits, antioxidant properties, agronomic traits, and food applications of these wheats. Data from various international breeding programs and nutritional studies were compared and consolidated. Specific genetic studies and analytical methods from the cited literature, such as antioxidant capacity assays (DPPH, ABTS, FRAP) and compositional analyses, form the basis of the comparative assessment. The review also incorporated findings from agronomic evaluations and food technology research to present a holistic overview of the potential of colored wheats as functional food candidates.

Genetic Origins of Colored Wheat

The distinctive colors observed in colored wheat species result from specific genetic contributions inherited from different ancestral wheat species; for instance, the purple color is due to anthocyanins derived from an Ethiopian emmer wheat, *Triticum turgidum* L. subsp. *abyssinicum* (also known as *T. aethiopicum*), that later became established in Yemen and Eritrea (Lachman et al., 2017; Badaeva et al., 2018). The purple color in the pericarp is determined by two genes that work together. The *Pp3* gene is on chromosome 2A, and the *Pp1* gene is on the short arm of chromosome 7B. (Khlestkina et al., 2010).

In contrast, the blue coloration in wheat originates from *Ba1*, the gene encoding the transcription factor ThMyc4E from *Thinopyrum ponticum*, and the *Ba2* gene from *Triticum boeoticum* Boiss. (syn. *T. monococcum* L. ssp. *aegilopoides*) (Dubcovsky et al., 1996; Zhang et al., 1996; Singh et al., 2007; Li et al., 2017). Black wheat, a pigmented variety developed from crossing purple and blue wheat, derives its color from anthocyanins in its outer layer and is rich in phenolic compounds, carotenoids, vitamins, essential amino acids, dietary fibers, and minerals (Dhua et al., 2021). These genetic characteristics not only contribute to visual appeal but also improve the functional quality of colored wheat, establishing it as an excellent choice for foods designed to support health.

Nutritional Composition and Health Benefits

Colored wheats offer a nutritional profile that exceeds that of conventional modern wheat, providing more protein, dietary fiber, minerals, and vitamins. For example, chapattis prepared from colored wheat (purple, blue, and black) contain more dietary fiber and protein but fewer carbohydrates than those made from white wheat, making them better aligned with health-oriented eating patterns (Garg et al., 2016; Kumari et al., 2020). These wheat genotypes are abundant in anthocyanins, flavonoids, and carotenoids, compounds that are located in different parts of the grain; notably, whole flour and bran from blue wheat have been found to contain higher levels of anthocyanins than flour from purple wheat (Abdel-Aal et al., 2006; Ficco et al., 2014; Paznocht et al., 2018). The presence of a blue aleurone layer in blue and black wheat is linked to increased levels of micronutrients. Purple wheat can show mineral (Zn, Fe, Mg, K) increases of up to 100%, and blue wheat contains 5–36% more vitamin E than conventional wheat (Guo et al., 2013; Lachman et al., 2018).

Previous research has revealed that a diet in rats incorporating anthocyanin-rich wheat improved serum antioxidant status and reduced kidney protein oxidation. However, it also increased lipid peroxidation in the kidney and induced behavioral changes associated with anxiety (Janšáková et al., 2016). Sharma et al. (2023) have also stated a protective role for anthocyanin consumption against a range of chronic diseases, including diabetes, cardiovascular conditions, and inflammatory disorders. These positive health outcomes are largely due to the high concentrations of anthocyanins, phenolics, and carotenoids, which help counteract oxidative stress by neutralizing reactive oxygen species (ROS) involved in the development of heart disease, cancer, diabetes, and aging-related conditions (Valko et al., 2006; Halliwell, 2012). Moreover, these phytochemicals play a role in protecting the plants themselves from biotic challenges (such as fungal diseases and insect damage) and abiotic stresses (like drought, high salinity, and extreme temperatures), thereby increasing the overall hardiness of the crop (Mierziak et al., 2014; Tuladhar et al., 2021).

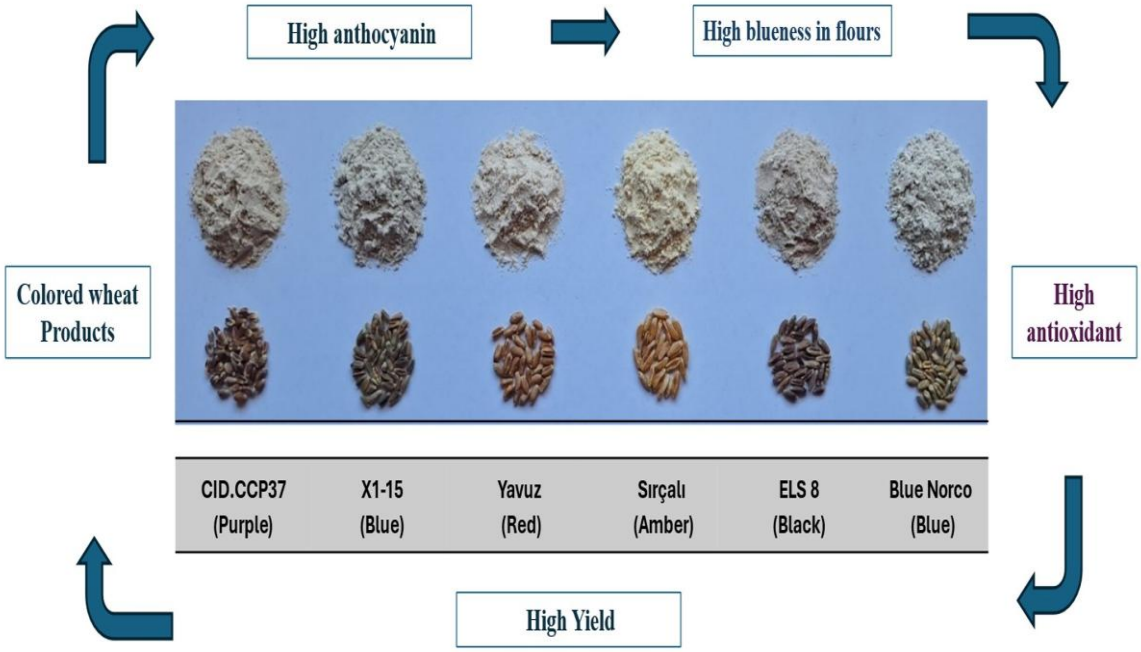

Figure 1. Selection of colored-wheats in comparison to modern wheats for health-benefit, quality, and yield traits in breeding program. The genotypes studied included the *T. aestivum* genotypes CID.CCP37 (Purple), X1-15 (Blue), and Blue Norco (Blue); the *T. durum* genotype ELS 8; and the modern *T. durum* cultivars Yavuz (Red) and Sırçalı (Amber) (Akman et al., 2025).

Antioxidant Capacity and Phytochemical Content

The antioxidant strength of colored wheat is primarily due to its high levels of anthocyanins and phenolic compounds. Total anthocyanin content differs considerably among different genetic lines: while red wheat contains only 7–10 mg kg^{-1}, values for black wheat range between 95 and 277 mg kg^{-1}, purple wheat between 22 and 278 mg kg^{-1}, and blue wheat between 72 and 211 mg kg^{-1}, (Liu et al., 2010; Kumari et al., 2020; Wang et al., 2020). Food products derived from purple isogenic lines can be 2.5 times richer in anthocyanins than white wheat, highlighting their enhanced functional quality (Usenko et al., 2018). The total phenolic content in colored wheat is roughly 30% higher than in conventional wheat, with black wheat typically having the highest total phenolic content with blue and purple genotypes containing the next highest levels (Liu et al., 2015; Kumari et al., 2020). For instance, bread made from the purple genotype 'Purple 8' displayed a higher total phenolic content relative to bread made from other colored and conventional wheat genotypes (Koksel et al., 2023). Total carotenoid content and total flavonoid content also show variation; generally, black and purple wheat have higher total phenolic content than blue wheat, while purple genotypes tend to have slightly higher total carotenoid content (Feng et al., 2022; Paznocht et al., 2020).

Variations at the genotypic level further illustrate the diversity in phytochemical composition. For example, the 'Charcoal' purple wheat genotype has a higher total phenolic content than other purple, red, and white genotypes, though some red and yellow genotypes can surpass certain purple ones, such as 'Indigo' (Liu et al., 2010). Total phenolic content values reported for black wheat lines range from 11.56 to 152.00 mg 100 g^{-1} (Sharma et al., 2023). According to standard antioxidant assays (DPPH, ABTS, FRAP, MC), the typical order of potency is black > purple > blue. Purple wheat frequently shows stronger antioxidant activity than red wheat in DPPH tests (Feng et al., 2022; Sharma et al., 2023; Koksel et al., 2023; Sytar et al., 2018). These characteristics make colored wheat a powerful ingredient for decreasing oxidative stress and increasing the health benefits in food products.

Agronomical Traits, Technological Quality and Food Applications

Colored wheat genotypes display unique agronomic and physical traits that affect their cultivation and processing. Thousand grain weight shows considerable variation: purple genotypes typically weigh between 32.9 g and 34.0 g, blue genotypes average 29.2 g, and red genotypes 31.4 g. (Koksel et al., 2023). Purple

isogenic lines often have a higher thousand grain weight than red lines (Morgounov et al., 2020). Hectoliter weight (HL) is similar among blue, purple, and red genotypes, generally falling within the range of 72.2 to 73.2 kg hl^{-1} (Koksel et al., 2023).

The large-scale cultivation of colored wheats has historically been limited by a significant yield penalty (Garg et al., 2016). This is clearly demonstrated by the Austrian blue wheat 'Skorpion', which yields 25% less than conventional cultivars (Garg et al., 2016), and by the general performance of purple and blue wheats, whose yields typically reach only 60.1–85.6% and 76.2–84.3%, respectively, of modern bread wheat cultivars (Akman et al., 2025). However, recent breeding advances are successfully addressing this challenge. Newly developed black, biofortified wheat lines exemplify this progress, combining promising yield potential with elevated health-beneficial traits (Sharma et al., 2018). Furthermore, recent studies on improved purple lines derived from the cross BW/2*PBW621 have reported yields of 4.71–4.69 t ha^{-1}. This result not only exceeds the yield of the black donor parent BW (2.68 t ha^{-1}) but also approaches that of the high-yielding, white recipient parent PBW621 (5.15 t ha^{-1}), marking a critical step toward competitive agronomic performance for colored wheats.

Color measurements of the grain, expressed as L^*, a^*, and b^* values, affect both the appearance and processing behavior of products made from colored wheat. A lower bran content results in higher L^* values (indicating lightness); while a higher bran content is associated with increased a^*values (indicating red-green spectrum) (Singh & Singh, 2010; Seo et al., 2021). Garg et al. (2016) also report that blue wheat genotypes have higher L^* values and lower a^* values compared to purple genotypes.The b^*value (indicating blue-yellow spectrum) varies between 8.5 and 12.0 across different genotypes (Punia et al., 2019). These physical attributes are essential for milling and product development, as the grain's structure must conform to standard milling requirements (Pena, 2012).

The processing quality of wheat, especially its gluten content and characteristics, is critically important for industrial food production. Colored wheat genotypes generally contain more grain protein and wet gluten than conventional wheat (Giordano et al., 2017; Morgounov et al., 2020; Sebestiková et al., 2023; Akman et al., 2025). Blue and purple genotypes show grain protein values between 15.06% and 16.35%, whereas red genotypes average around 13.47% (Fan et al., 2020). However, some research indicates that white and red genotypes may have higher wet gluten levels than blue and purple ones, and in certain cases, black wheat exhibits the highest grain protein (9.17–10.18%) among the colored genotypes (Koksel et al., 2023; Sharma et al., 2022). Despite this generally high protein and wet gluten content, Akman et al. (2025) reported that colored wheats can have low gluten quality parameters.

Colored wheat has been effectively used in a wide array of food products, such as muffins, noodles, bread, biscuits, pasta, crackers, and snack bars, capitalizing on its rich content of anthocyanins and phenolics (Pasqualone et al., 2015; Li et al., 2007; Saini et al., 2021). Biscuits made with purple wheat and spiral pasta incorporating it show increased antioxidant activity and mineral levels. Similarly, chapattis prepared from black and blue wheat are particularly suitable for traditional Indian cuisine, offering improved nutritional value and sensory qualities (Pasqualone et al., 2015; Verma et al., 2022; Kumari et al., 2020; Garg et al., 2016). A significant advantage of colored wheat products is their extended shelf life and enhanced resistance to mold growth, attributable to the high anthocyanin content (Khlestkina et al., 2017; Dziki et al., 2014). This addresses a major weakness of conventional wheat products, which often have limited antioxidant activity The beneficial amino acid profile and elevated protein level of colored wheat further increase its appropriateness for manufacturing nutritious foods (Guo et al., 2013).

Breeding and Global Adoption

The development of new colored wheat cultivars rich in anthocyanins is an international effort, involving initiatives in 16 countries and 60 research institutions that have collectively produced 40 blue, purple, and black germplasms, breeding lines, and officially registered cultivars (Padhy et al., 2022). However, the successful expression of these pigments is not solely genetic, as environmental conditions, including light exposure, temperature, disease pressure, soil nutrient content, fertilizer use, and planting time, have a significant impact on the accumulation of anthocyanins (Abdel-Aal, 2008; Lachman, 2017; Fan et al., 2020; Beleggia et al., 2021). Genetic differences lead to substantial variation in total anthocyanin content; purple wheat can range from 14 to 2304 μg g^{-1} and black wheat from 248.7 to 2902 μg g^{-1}, representing differences of up to twentyfold between genotypes (Eticha et al., 2011; Zhang et al., 2021).

The recommended daily intake of anthocyanins differs based on factors like sex, age, and ethnic background (CDC, 2015). China has established a daily target intake of 50 mg (Wallace & Giusti, 2015). The worldwide interest in adopting colored wheat is fueled by its potential to fight hidden hunger through biofortification, coupled with a growing consumer trend toward nutrient-rich food choices (Padhy et al., 2022). These breeding activities highlight the important role colored wheat can play in improving the nutritional value of staple foods and tackling public health issues on a global scale.

Conclusion

Colored wheat signifies a major innovation in the field of functional foods, providing a distinctive blend of attractive color, improved nutritional value, and strong antioxidant activity. Its rich content of anthocyanins, phenolics, flavonoids, and essential micronutrients makes it a valuable component for creating health-promoting foods, with documented benefits including the reduction of oxidative stress, better regulation of blood sugar, and lowered risk of chronic diseases. Progress in genetics has enabled the successful integration of bioactive compounds, while evaluations focusing on agronomy and food technology confirm its adaptability for a wide range of uses, from traditional flatbreads to modern pasta and biscuit formulations. Breeding programs are steadily increasing the diversity and availability of colored wheat cultivars, taking into account how both environmental and genetic factors influence phytochemical levels. As the demand for sustainable and healthful food options continues to rise, colored wheat presents a viable strategy for improving overall diet quality and addressing global nutritional challenges, thereby securing its importance in contemporary food production systems through ongoing scientific exploration and technological innovation**.**

Scientific Ethics Declaration

*The author declares that the scientific ethical and legal responsibility of this article published in EPSTEM journal belongs to the author.

Conflict of Interest

*The author declares that he has no conflicts of interest

Funding

*No funding.

Acknowledgements or Notes

*This article was presented as an oral presentation at the International Conference on Basic Sciences and Technology (www.icbast.net) held in Budapest/Hungary on August 28-31, 2025.

References

Abdel-Aal, E. S. M., Rabalski, I., & Young, J. C. (2006). Anthocyanin composition in black, blue, pink, purple, and red cereal grains. *Journal of Agricultural and Food Chemistry, 54*, 4696–4704.

Abdel-Aal, E. S. M., Abou-Arab, A. A., Gamel, T. H., Hucl, P., Young, J. C., & Rabalski, I. (2008). Fractionation of blue wheat anthocyanin compounds and their contribution to antioxidant properties. *Journal of Agricultural and Food Chemistry, 56*(23), 11171–11177.

Akman, H., & Karaduman, Y. (2021). Evaluating technological quality of cultivated Triticum species, interspecific, and intergeneric hybrids for wheat-based products and breeding programs. *Journal of Cereal Science*, *99*, 1–9.

Badaeva, E. D., Shishkina, A. A., Goncharov, N. P., Zuev, E. V., Lysenko, N. S., Mitrofanova, O. P., & Kudriavtsev, A. M. (2018). Evolution of Triticum aethiopicum Jakubz. from the position of chromosome analysis. *Russian Journal of Genetics, 54*(6), 629–642.

Beleggia, R., Ficco, D. B., Nigro, F. M., Giovanniello, V., Colecchia, S. A., Pecorella, I., & De Vita, P. (2021). Effect of sowing date on bioactive compounds and grain morphology of three pigmented cereal species. *Agronomy, 11*(3), 1–16.

Centers for Disease Control and Prevention (CDC). (2015). *National center for health statistics, NHANES 2007-2008 dietary data.* CDC. Retrieved from https://wwwn.cdc.gov/nchs/nhanes/search/datapage.aspx?Component=Dietary&CycleBeginYear=2007

Dhua, S., Kumar, K., Kumar, Y., Singh, L., & Sharanagat, V. S. (2021). Composition, characteristics and health promising prospects of black wheat: A review. *Trends in Food Science & Technology, 112*, 780-794.

Dubcovsky, J., Luo, M.-C., Zhong, G.-Y., Bransteitter, R., Desai, A., Kilian, A., & Dvořák, J. (1996). Genetic map of diploid wheat, Triticum monococcum L., and its comparison with maps of Hordeum vulgare L. *Genetics, 143*(2), 983–999.

Dziki, D., Różyło, R., Gawlik-Dziki, U., & Świeca, M. (2014). Current trends in the enhancement of antioxidant activity of wheat bread by the addition of plant materials rich in phenolic compounds. *Trends in Food Science & Technology, 40*(1), 48–61.

Eticha, F., Grausgruber, H., Siebenhandl-Ehn, S., & Berghofer, E. (2011). Some agronomic and chemical traits of blue aleurone and purple pericarp wheat (Triticum L.). *Journal of Agricultural Science and Technology B, 1*, 48–58.

Fan, X., Xu, Z., Wang, F., Feng, B., Zhou, Q., Cao, J., ... & Wang, T. (2020). Identification of colored wheat genotypes with suitable quality and yield traits in response to low nitrogen input. *PLoS One, 15*(4), 1–19.

Feng, J., Xu, B., Ma, D., Hao, Z., Jia, Y., Wang, C., & Wang, L. (2022). Metabolite identification in fresh wheat grains of different colors and the influence of heat processing on metabolites via targeted and non-targeted metabolomics. *Food Research International, 160*, 1–12.

Ficco, D. B., De Simone, V., Colecchia, S. A., Pecorella, I., Platani, C., Nigro, F., & De Vita, P. (2014). Genetic variability in anthocyanin composition and nutritional properties of blue, purple, and red bread (Triticum aestivum L.) and durum (Triticum turgidum L. ssp. turgidum convar. durum) wheats. *Journal of Agricultural and Food Chemistry, 62*(34), 8686–8695.

Garg, M., Chawla, M., Chunduri, V., Kumar, R., Sharma, S., Sharma, N. K., ... & Singh, K. (2016). Transfer of grain colors to elite wheat cultivars and their characterization. *Journal of Cereal Science, 71*, 138–144.

Giordano, D., Locatelli, M., Travaglia, F., Bordiga, M., Reyneri, A., Coïsson, J. D., & Blandino, M. (2017). Bioactive compound and antioxidant activity distribution in roller-milled and pearled fractions of conventional and pigmented wheat varieties. *Food Chemistry, 233*, 483–491.

Guo, Z. F., Zhang, Z. B., Xu, P., & Guo, Y. N. (2013). Analysis of nutrient composition of purple wheat. *Cereal Research Communications, 41*(2), 293–303.

Janšáková, K., Bábíčková, J., Havrlentová, M., Hodosy, J., & Kraic, J. (2016). The effects of anthocyanin-rich wheat diet on the oxidative status and behavior of rats. *Croatian Medical Journal, 57*(2), 119–129.

Khlestkina, E. K., Röder, M. S., & Börner, A. (2010). Mapping genes controlling anthocyanin pigmentation on the glume and pericarp in tetraploid wheat (Triticum durum L.). *Euphytica, 171*(1), 65–69.

Khlestkina, E. K., Usenko, N. I., Gordeeva, E. I., Stabrovskaya, O. I., Sharfunova, I. B., & Otmakhova, Y. S. (2017). Evaluation of wheat products with high flavonoid content: justification of importance of marker-assisted development and production of flavonoid-rich wheat cultivars. *Journal of Genetics and Breeding, 21*(5), 545–553.

Koksel, H., Cetiner, B., Shamanin, V. P., Tekin-Cakmak, Z. H., Pototskaya, I. V., Kahraman, K., Sagdic, O., & Morgounov, A. I. (2023). Quality, nutritional properties, and glycemic index of colored whole wheat breads. *Foods, 12*(18), 1–13.

Kumari, A., Sharma, S., Sharma, N., Chunduri, V., Kapoor, P., Kaur, S., ... & Garg, M. (2020). Influence of biofortified colored wheats (purple, blue, black) on physicochemical, antioxidant and sensory characteristics of chapatti (Indian flatbread). *Molecules, 25*(21), 1–14.

Lachman, J., Hejtmánková, A., Orsák, M., Popov, M., & Martinek, P. (2018). Tocotrienols and tocopherols in colored-grain wheat, tritordeum and barley. *Food Chemistry, 240*, 725–735.

Lachman, J., Martinek, P., Kotíková, Z., Orsák, M., & Šulc, M. (2017). Genetics and chemistry of pigments in wheat grain-A review. *Journal of Cereal Science, 74*, 145–154.

Li, N., Li, S., Zhang, K., Chen, W., Zhang, B., Wang, D., Liu, D., Liu, B., & Zhang, H. (2017). ThMYC4E, candidate Blue aleurone 1 gene controlling the associated trait in Triticum aestivum. *PLoS One, 12*(7), 1–13.

Li, W., Pickard, M. D., & Beta, T. (2007). Effect of thermal processing on antioxidant properties of purple wheat bran. *Food Chemistry, 104*(3), 1080–1086.

Liu, Q., Qiu, Y., & Beta, T. (2010). Comparison of antioxidant activities of different colored wheat grains and analysis of phenolic compounds. *Journal of Agricultural and Food Chemistry, 58*(16), 9235–9241.

Mierziak, J., Kostyn, K., & Kulma, A. (2014). Flavonoids as important molecules of plant interactions with the environment. *Molecules, 19*(10), 16240–16265.

Morgounov, A., Karaduman, Y., Akin, B., Aydogan, S., Baenziger, P. S., Bhatta, M., ... & Zencirci, N. (2020). Yield and quality in purple-grained wheat isogenic lines. *Agronomy, 10*(1), 1–14.

Padhy, A. K., Kaur, P., Singh, S., Kashyap, L., & Sharma, A. (2022). Colored wheat and derived products: Key to global nutritional security. *Critical Reviews in Food Science and Nutrition, 64*(7), 1894-1910.

Pasqualone, A., Bianco, A. M., Paradiso, V. M., Summo, C., Gambacorta, G., Caponio, F., & Blanco, A. (2015). Production and characterization of functional biscuits obtained from purple wheat. *Food Chemistry, 180*, 64–70.

Paznocht, L., Kotíková, Z., Šulc, M., Lachman, J., Orsák, M., Eliášová, M., & Martinek, P. (2018). Free and esterified carotenoids in pigmented wheat, tritordeum and barley grains. *Food Chemistry, 240*, 670–678.

Paznocht, L., Kotíková, Z., Burešová, B., Lachman, J., & Martinek, P. (2020). Phenolic acids in kernels of different coloured-grain wheat genotypes. *Plant, Soil and Environment, 66*(2), 57–64.

Pena, R. J. (2012). *Wheat-end use quality grain compositional factors and grain quality improvement*. Ankara:Wheat Quality Workshop.

Punia, S., Sandhu, K. S., & Siroha, A. K. (2019). Difference in protein content of wheat (Triticum aestivum L.): Effect on functional, pasting, color and antioxidant properties. *Journal of the Saudi Society of Agricultural Sciences, 18*(4), 378–384.

Reddy, M. P., Sen, A., Swamy, C. T., Chelladurai, P., Sivadurga, K., Pandey, A., ... & Purewal, S. S. (2025). Chemistry of Macro-and Micronutrients. In S. S. Purewal & R. S. Singh (Eds.), *Colored Cereals* (pp. 96-118). CRC Press.

Saini, P., Kumar, N., Kumar, S., Mwaurah, P. W., Panghal, A., Attkan, A. K., ... & Singh, V. (2021). Bioactive compounds, nutritional benefits and food applications of colored wheat: A comprehensive review. *Critical Reviews in Food Science and Nutrition, 61*(19), 3197–3210.

Sebestíková, R., Burešová, I., Vyhnánek, T., Martinek, P., & Pospiech, M. (2023). Rheological and fermentation properties of doughs and quality of breads from colored wheat varieties. *Heliyon, 9*(4), 1–15.

Seo, Y., Moon, Y., & Kweon, M. (2021). Effect of purple-colored wheat bran addition on quality and antioxidant property of bread and optimization of bread-making conditions. *Applied Sciences, 11*(9), 1–18.

Sharma, A., Yadav, M., Tiwari, A., Ali, U., Krishania, M., Bala, M., Mridula, D., Sharma, P., Goudar, G., Roy, J. K., Navik, U., & Garg, M. (2023). A comparative study of colored wheat lines across laboratories for validation of their phytochemicals and antioxidant activity. *Journal of Cereal Science, 112*, 1–9.

Sharma, N., Kumari, A., Chunduri, V., Kaur, S., Banda, J., Goyal, A., & Garg, M. (2022). Anthocyanin biofortified black, blue and purple wheat exhibited lower amino acid cooking losses than white wheat. *LWT - Food Science and Technology, 154*, 1–9.

Sharma, S., Chunduri, V., Kumar, A., Kumar, R., Khare, P., Kondepudi, K. K., ... & Garg, M. (2018). Anthocyanin bio-fortified colored wheat: Nutritional and functional characterization. *PloS one*, *13*(4), 1–16.

Singh, K., Ghai, M., Garg, M., Chhuneja, P., Kaur, P., Schnurbusch, T., Keller, B., & Dhaliwal, H. S. (2007). An integrated molecular linkage map of diploid wheat based on a Triticum boeoticum × T. monococcum RIL population. *Theoretical and Applied Genetics, 115*(3), 301–312.

Sharma, K., & Sharma, P. K. (2025). Wheat as a nutritional powerhouse: Shaping global food security. In V. S. Meena, J. P. Jaiswal, D. Jinger & V. Paramesh (Eds.), *Triticum-the pillar of global food security*. IntechOpen.

Sytar, O., Boško, P., Živčák, M., Brestič, M., & Smetanska, I. (2018). Bioactive phytochemicals and antioxidant properties of the grains and sprouts of colored wheat genotypes. *Molecules, 23*(9), 1–14.

Tuladhar, P., Sasidharan, S., & Saudagar, P. (2021) Role of phenols and polyphenols in plant defense response to biotic and abiotic stresses. In Jogaiah, S. (Ed.), *Biocontrol agents and secondary metabolites(*pp.419-441). Elsevier.

Usenko, N. I., Khlestkina, E. K., Asavasanti, S., Gordeeva, E. I., Yudina, R. S., & Otmakhova, Y. S. (2018). Possibilities of enriching food products with anthocyanins by using new forms of cereals. *Foods and Raw Materials, 6*(1), 128–135.

Valko, M., Leibfritz, D., Moncol, J., Cronin, M. T., Mazur, M., & Telser, J. (2007). Free radicals and antioxidants in normal physiological functions and human disease. *The International Journal of Biochemistry & Cell Biology, 39*(1), 44–84.

Verma, J., Rani, V., & Sangwan, V. (2022). Physical, sensory and nutritional quality of anthocyanins rich pasta prepared using biofortified purple wheat. *Annals of Phytomedicine, 11*(1), 78–85.

Wallace, T. C., & Giusti, M. M. (2015). Anthocyanins. *Advances in Nutrition, 6*(5), 620–622.

Wang, X., Zhang, X., Hou, H., Ma, X., Sun, S., Wang, H., & Kong, L. (2020). Metabolomics and gene expression analysis reveal the accumulation patterns of phenylpropanoids and flavonoids in different colored-grain wheats (Triticum aestivum L.). *Food Research International, 138*, 1–14.

Zhang, T., Ma, J., Wu, X., Hao, Z., Dun, C., & Chen, C. (2021). Qualitative and semi-quantitative assessment of anthocyanins in Tibetan hulless barley from different geographical locations by UPLC-QTOF-MS and their antioxidant capacities. *Open Chemistry, 19*(1), 1–8.

Zhang, X., Dong, Y., & Wang, R. R. C. (1996). Characterization of genomes and chromosomes in partial amphiploids of the hybrid Triticum aestivum × Thinopyrum ponticum by in situ hybridization, isozyme analysis, and RAPD. *Genome, 39*(6), 1062–1071.

Author(s) Information

Hayati Akman
Selcuk University
Department of Plant and Animal Production
Konya,Turkiye
Contact e-mail: *hayatiakman@selcuk.edu.tr*

To cite this article:

Akman, H. (2025). Colored wheats for functional food candidates with enhanced nutrition *The Eurasia Proceedings of Science, Technology, Engineering and Mathematics (EPSTEM), 36,* 268-275.

The Eurasia Proceedings of Science, Technology, Engineering & Mathematics (EPSTEM)
ISSN: 2602-3199

The Eurasia Proceedings of Science, Technology, Engineering & Mathematics (EPSTEM), 2025

Volume 36, Pages 276-296

ICBAST 2025: International Conference on Basic Sciences and Technology

Neutrosophic αB*Gα Functions in Neutrosophic Topological Spaces

Raja Mohammad Latif
Prince Mohammad Bin Fahd University

Abstract: The notion of a neutrosophic set is generally referred to as the generalization of an intuitionistic fuzzy set. Studying open and closed set variations is crucial in Neutrosophic topology, given the growing significance of Neutrosophic sets in various applications. The origin, nature, and scope of neutrality are explored through the Neutrosophic set. This concept is crucial for research due to its potential applications across various scientific and technological fields. Because the universe inherently contains indeterminacy, the Neutrosophic set provides a valuable framework for study. It is currently being developed to represent data that is uncertain, imprecise, incomplete, or inconsistent. A Neutrosophic set is described using three membership functions: truth, indeterminacy, and falsity. This approach helps to manage uncertainty and leads to more logical outcomes in practical scenarios. Additionally, the Neutrosophic set can identify inconsistencies within data and offer solutions to real-world problems. Neutrosophic functions, based on the Neutrosophic Set Theory, have broad and growing applications due to their ability to model uncertainty, indeterminacy, and inconsistency in data. Here are some of the key areas where neutrosophic functions are applied: Artificial Intelligence & Machine Learning, Data Science and Information Fusion, Decision-Making and Multi-Criteria Decision Analysis (MCDA), Business and Economics, Healthcare and Medical Diagnosis, and Control Systems and Robotics. In 2024, Suthi Keerthana Kumar, Vigneshwaran Mandarasalam, Saied Jafari, and Vidyarani Lakshmanadas described the concepts of Neutrosophic αb*gα-closed sets, Neutrosophic αb*gα-open sets, Neutrosophic αb*gα-border, and Neutrosophic αb*gα-frontier and discussed their properties in Neutrosophic topological spaces. In this research paper, we introduce the concepts of Neutrosophic αb*gα-continuous (Nαb*gα-continuous) maps, Nαb*gα-irresolute maps, Nαb*gα-closed maps, Nαb*gα-open maps, strongly Nαb*gα-continuous maps, perfectly Nαb*gα-continuous maps, contra Nαb*gα-continuous maps, and contra Nαb*gα-irresolute maps in Neutrosophic topological spaces. We investigate and obtain several properties and characterizations concerning these mappings in Neutrosophic topological spaces

Keywords: Neutrosophic αb*gα-continuous map, Neutrosophic αb*gα-irresolute map, Neutrosophic αb*gα-closed map, Neutrosophic αb*gα-open map, Contra neutrosophic αb*gα-irresolute map

Introduction

Many real-life problems in Business, Finance, Medical Sciences, Engineering, and Social Sciences deal with uncertainties. Smarandache studies neutrosophic set as an approach for solving issues that cover unreliable, indeterminacy, and persistent data. Applications of neutrosophic topology depend upon the properties of neutrosophic closed sets, neutrosophic open sets, neutrosophic interior operator, neutrosophic closure operator, and neutrosophic sets. Neutrosophic topological space, neutrosophic αb*gα-open set, neutrosophic αb*gα-closed set, neutrosophic αb*gα-continuous map, neutrosophic αb*gα-irresolute map, neutrosophic αb*gα-closed map, neutrosophic αb*gα-open map, strongly neutrosophic αb*gα-continuous map, perfectly neutrosophic αb*gα-continuous map, contra neutrosophic αb*gα-continuous map, contra neutrosophic αb*gα-irresolute map. We investigate and obtain several properties and characterizations concerning these mappings in Neutrosophic topological spaces

2-Preliminaries

Definition 2.1. Let X be a non-empty fixed set. A neutrosophic set $(\mathrm{N}_{eu}\text{–set})$ P is an object having the form $P=\{\langle x,\mu_P(x),\sigma_P(x),\gamma_P(x)\rangle : x\in X\}$, where $\mu_P(x)$- represents the degree of membership, $\sigma_P(x)$- represents the degree of indeterminacy, and $\gamma_P(x)$- represents the degree of non-membership.

Definition 2.2. A neutrosophic topology on a non-empty set X is a family T_N of neutrosophic subsets of X satisfying

(i) $0_N, 1_N \in \mathrm{T}_N$.

(ii) $G\bigcap H\in \mathrm{T}_N$ for every $G, H\in \mathrm{T}_N$,

(iii) $\bigcup_{j\in J} G_j \in \mathrm{T}_N$ for every $\{G_j : j\in J\}\subseteq \tau_N$.

Then the pair (X,T_N) is called a neutrosophic topo N_{eu}–open logical space $(\mathrm{N}_{eu}\text{–Top–Space})$. The elements of T_N are called neutrosophic open $(\mathrm{N}_{eu}\text{–open})$ sets in X. A N_{eu}–set A is called a neutrosophic closed $(\mathrm{N}_{eu}\text{–closed})$ set if and only if its complement A^C is a N_{eu}–open set.

Definition 2.3. Let (X,T_N) be a N_{eu}–Top–Space and A be a N_{eu}–set. Then

(i) The neutrosophic interior of A, denoted by $\mathrm{N}_{eu}\text{–}Int(A)$ is the union of all N_{eu}–open subsets of X contained in A.

(ii) The neutrosophic closure of A denoted by $\mathrm{N}_{eu}Cl(A)$ is the intersection of all N_{eu}–closed sets containing A.

Definition 2.4. Let A be a N_{eu}–set in a N_{eu}–Top–Space (X,T_N). Then the set A is called a (i) neutrosophic semi-open N_{eu}–open $(\mathrm{N}_{eu}\mathbf{s}\text{–open})$ set in a N_{eu}–Top–Space X if $A\subseteq \mathrm{N}_{eu}Cl\left[\mathrm{N}_{eu}Int(A)\right]$.

(ii) neutrosophic semi-closed $(\mathrm{N}_{eu}\mathbf{s}\text{–closed})$ set in a N_{eu}–Top–Space X if $\mathrm{N}_{eu}Int\left[\mathrm{N}_{eu}Cl(A)\right]\subseteq A$.

Definition 2.5. Let A be a N_{eu}–set in a N_{eu}–Top–Space (X,T_N). Then the set A is called a neutrosophic α–closed (respectively, neutrosophic α–open) set in N_{eu}–Top–Space X if $\mathrm{N}_{eu}Cl\left[\mathrm{N}_{eu}Int\left(\mathrm{N}_{eu}Cl(A)\right)\right]\subseteq A$.

Definition 2.6. Let A be a N_{eu}–set in a N_{eu}–Top–Space (X,T_N). Then the set A is called a neutrosophic generalized closed $(\mathrm{N}_{eu}\mathrm{g}\text{–closed})$ set in N_{eu}–Top–Space (X,T_N) if $\mathrm{N}_{eu}\text{–Cl}(\mathrm{A})\subseteq \mathrm{G}$, whenever $\mathrm{A}\subseteq G$ and G is N_{eu}–open set in X. $A\subseteq \mathrm{N}_{eu}Int\left[\mathrm{N}_{eu}Cl(A)\right]\bigcup \mathrm{N}_{eu}Cl\left[\mathrm{N}_{eu}Int(A)\right]$.

Definition 2.7. Let A be a N_{eu}–set in a N_{eu}–Top–Space (X,T_N). Then the set A is called a neutrosophic generalized semi-closed $(\mathrm{N}_{eu}\mathrm{gs}\text{–closed})$ set in N_{eu}–Top–Space (X,T_N) if $\mathrm{N}_{eu}\text{–Cl}(\mathrm{A})\subseteq \mathrm{G}$, whenever $\mathrm{A}\subseteq G$ and G is N_{eu}–open set in X.

Definition 2.8. Let A be a N_{eu}–set in a N_{eu}–Top–Space (X, T_N). Then the set A is called a Neutrosophic α–generalized closed $(\mathrm{N}_{eu}\alpha g\text{–}closed)$ set in N_{eu}–Top–Space (X, T_N) if $\mathrm{N}_{eu}\alpha\text{–}Cl(A) \subseteq G$ whenever $A \subseteq G$ and G is N_{eu}–*open* set in X.

Definition 2.9. Let A be a N_{eu}–set in a N_{eu}–Top–Space (X, T_N). Then the set A is called a Neutrosophic α^*–open $(\mathrm{N}_{eu}\alpha^*\text{–}open)$ set in N_{eu}–Top–Space (X, T_N) if $A \subseteq \mathrm{N}_{eu}\alpha\text{–}Int\left[\mathrm{N}_{eu}\text{–}Cl\left(\mathrm{N}_{eu}\alpha\text{–}Int(A)\right)\right]$.

Definition 2.10. Let A be a N_{eu}–set in a N_{eu}–Top–Space (X, T_N). Then the set A is called a Neutrosophic b–closed $(\mathrm{N}_{eu}b\text{–}closed)$ set in a N_{eu}–Top–Space (X, T_N) if $\left[\mathrm{N}_{eu}\text{–}Cl\left(\mathrm{N}_{eu}\text{–}Int(A)\right)\right] \cup \left[\mathrm{N}_{eu}\text{–}Int\left(\mathrm{N}_{eu}\text{–}Cl(A)\right)\right] \subseteq A$.

Definition 2.11. Let A be a N_{eu}–set in a N_{eu}–Top–Space (X, T_N). Then the set A is called

(i) a Neutrosophic $g\alpha$–open $(\mathrm{N}_{eu}g\alpha\text{–}open)$ set in a N_{eu}–Top–Space (X, T_N) if $V \subseteq \mathrm{N}_{eu}\alpha\text{–}Int(A)$ whenever $V \subseteq A$ and V is a $\mathrm{N}_{eu}\alpha\text{–}closed$ set in (X, T_N).

(ii) a Neutrosophic $g\alpha$–closed $(\mathrm{N}_{eu}g\alpha\text{–}closed)$ set in a N_{eu}–Top–Space (X, T_N) if $\mathrm{N}_{eu}\alpha\text{–}Cl(A) \subseteq V$ whenever $A \subseteq V$ and V is a $\mathrm{N}_{eu}\alpha\text{–}open$ set in (X, T_N).

(iii) a Neutrosophic $^*g\alpha$–open $(\mathrm{N}_{eu}{}^*g\alpha\text{–}open)$ set in a N_{eu}–Top–Space (X, T_N) if $V \subseteq \mathrm{N}_{eu}\text{–}Int(A)$ whenever $V \subseteq A$ and V is a $\mathrm{N}_{eu}g\alpha\text{–}closed$ set in (X, T_N).

(iv) a Neutrosophic $^*g\alpha$–closed $(\mathrm{N}_{eu}{}^*g\alpha\text{–}closed)$ set in a N_{eu}–Top–Space (X, T_N) if $\mathrm{N}_{eu}\text{–}Cl(A) \subseteq V$ whenever $A \subseteq V$ and V is a $\mathrm{N}_{eu}g\alpha\text{–}open$ set in (X, T_N).

Definition 2.12. Let A be a N_{eu}–set in a N_{eu}–Top–Space (X, T_N). Then the set A is called a

(i) a Neutrosophic $b^*g\alpha$–open $(\mathrm{N}_{eu}b^*g\alpha\text{–}open)$ set in a N_{eu}–Top–Space (X, T_N) if $V \subseteq \mathrm{N}_{eu}b\text{–}Int(A)$ whenever $V \subseteq A$ and V is a $\mathrm{N}_{eu}{}^*g\alpha\text{–}closed$ set in (X, T_N).

(ii) a Neutrosophic $b^*g\alpha$–closed $(\mathrm{N}_{eu}b^*g\alpha\text{–}closed)$ set in a N_{eu}–Top–Space (X, T_N) if $\mathrm{N}_{eu}b\text{–}Cl(A) \subseteq V$ whenever $A \subseteq V$ and V is a $\mathrm{N}_{eu}{}^*g\alpha\text{–}open$ set in (X, T_N).

Definition 2.13. Let A be a N_{eu}–set in a N_{eu}–Top–Space (X, T_N). Then the set A is called a Neutrosophic $\alpha b^*g\alpha\text{–}closed$ $(\mathrm{N}_{eu}\alpha b^*g\alpha\text{–}closed)$ set in N_{eu}–Top–Space (X, T_N) if $\mathrm{N}_{eu}\alpha\text{–}Cl(A) \subseteq U$ whenever $A \subseteq U$ and U is $\mathrm{N}_{eu}b^*g\alpha\text{–}open$ set.

Definition 2.14. Let A be a N_{eu}–set in a N_{eu}–Top–Space (X, T_N). Then the set A is called a Neutrosophic $\alpha b^*g\alpha\text{–}open$ $(\mathrm{N}_{eu}\alpha b^*g\alpha\text{–}open)$ set in N_{eu}–Top–Space (X, T_N) if its complement A^C is a $\mathrm{N}_{eu}\alpha b^*g\alpha\text{–}closed$ set in (X, T_N).

Theorem 2.15. (i) Every N_{eu} *–closed* set is $\mathrm{N}_{eu}\alpha b^{*}g\alpha$ *–closed* set.
(ii) Every $\mathrm{N}_{eu}\alpha b^{*}g\alpha$ *–closed* set is $\mathrm{N}_{eu}b^{*}g\alpha$ *–closed* set.
(iii) Every $\mathrm{N}_{eu}\alpha$ *–closed* set is $\mathrm{N}_{eu}\alpha b^{*}g\alpha$ *–closed* set.

Theorem 2.16. Let $\left(X,\mathrm{T}_{N}\right)$ be a N_{eu} *–Top –Space.* Then the union and the intersection of any two $\mathrm{N}_{eu}\alpha b^{*}g\alpha$ *–closed* sets is a $\mathrm{N}_{eu}\alpha b^{*}g\alpha$ *–closed* set in N_{eu} *–Top –Space* $\left(X,\mathrm{T}_{N}\right)$.

Theorem 2.17. Let $\left(X,\mathrm{T}_{N}\right)$ be a N_{eu} *–Top –Space.* Then the intersection and the union of any two $\mathrm{N}_{eu}\alpha b^{*}g\alpha$ *–open* sets is a $\mathrm{N}_{eu}\alpha b^{*}g\alpha$ *–open* set in N_{eu} *–Top –Space* $\left(X,\mathrm{T}_{N}\right)$.

Definition 2.18. A N_{eu} *–set* A in a N_{eu} *–Top –Space.* $\left(X,\mathrm{T}_{N}\right)$ is called aneutrosophic $\alpha b^{*}g\alpha$ *–intterior* of A $\left(\mathrm{N}_{eu}\alpha b^{*}g\alpha\text{ –}Int\left(A\right)\right)$ and neutrosophic $\alpha b^{*}g\alpha$ *–closure* of A $\left(\mathrm{N}_{eu}\alpha b^{*}g\alpha\text{ –}Cl\left(A\right)\right)$ are respectively defined by
$\mathrm{N}_{eu}\alpha b^{*}g\alpha\text{ –}Int\left(A\right)=\bigcup\left\{G:G\in\mathrm{N}_{eu}\alpha b^{*}g\alpha\text{ –}Int\left(X,T_{Neu}\right)\ and\ G\subseteq A\right\}$ and
$\mathrm{N}_{eu}\alpha b^{*}g\alpha\text{ –}Int\left(A\right)=\bigcup\left\{G:G\in\mathrm{N}_{eu}\alpha b^{*}g\alpha\text{ –}Int\left(X,T_{Neu}\right)\ and\ G\subseteq A\right\}$.

Remark 2.19. Let A be a subset of a N_{eu} *–Top –Space.* $\left(X,\mathrm{T}_{N}\right)$. Then $\mathrm{N}_{eu}\alpha b^{*}g\alpha\text{ –}Int\left(A\right)$ $\left(\mathrm{N}_{eu}\alpha b^{*}g\alpha\text{ –}Cl\left(A\right)\right)$ is $\mathrm{N}_{eu}\alpha b^{*}g\alpha$ *–open* $\left(\mathrm{N}_{eu}\alpha b^{*}g\alpha\text{ –}closed\right)$ set in $\left(X,\mathrm{T}_{N}\right)$. The complement of $\mathrm{N}_{eu}\alpha b^{*}g\alpha\text{ –}Int\left(A\right)$ is $\mathrm{N}_{eu}\alpha b^{*}g\alpha\text{ –}Cl\left(A\right)$.

Definition 2.20. Let A be a N_{eu} *–subset* of a N_{eu} *–Top –Space.* $\left(X,\mathrm{T}_{N}\right)$. Then the neutrosophic $\alpha\mathrm{b}^{*}g\alpha$ *–*frontier of a N_{eu} *–subset* A of X is denoted by $\mathrm{N}_{eu}\alpha b^{*}g\alpha\text{ –}Fr\left(A\right)$ and is defined by $\mathrm{N}_{eu}\alpha b^{*}g\alpha\text{ –}Fr\left(A\right)=\left[\mathrm{N}_{eu}\alpha b^{*}g\alpha\text{ –}Cl\left(A\right)\right]\bigcap\left[\mathrm{N}_{eu}\alpha b^{*}g\alpha\text{ –}Cl\left(A^{C}\right)\right]$.

Theorem 2.21. For N_{eu} *–sets* A and B in a N_{eu} *–Top –Space.* $\left(X,\mathrm{T}_{N}\right)$, the following statements are true:
(i) $\mathrm{N}_{eu}\alpha b^{*}g\alpha\text{ –}Int\left(A\right)\subseteq A\subseteq\mathrm{N}_{eu}\alpha b^{*}g\alpha\text{ –}Cl\left(A\right)$.
(ii) A is $\mathrm{N}_{eu}\alpha b^{*}g\alpha$ *–open* set in X if and only if $\mathrm{N}_{eu}\alpha b^{*}g\alpha\text{ –}Int\left(A\right)=A$.
(iii) A is $\mathrm{N}_{eu}\alpha b^{*}g\alpha$ *–closed* set in X if and only if $\mathrm{N}_{eu}\alpha b^{*}g\alpha\text{ –}Cl\left(A\right)=A$.
(iv) $\mathrm{N}_{eu}\alpha b^{*}g\alpha\text{ –}Int\left[\mathrm{N}_{eu}\alpha b^{*}g\alpha\text{ –}Int\left(A\right)\right]=\mathrm{N}_{eu}gs\alpha^{*}\text{–}Int\left(A\right)$.
(v) $\mathrm{N}_{eu}\alpha b^{*}g\alpha\text{ –}Cl\left[\mathrm{N}_{eu}\alpha b^{*}g\alpha\text{ –}Cl\left(A\right)\right]=\mathrm{N}_{eu}\alpha b^{*}g\alpha\text{ –}Cl\left(A\right)$.
(vi) If $A\subseteq B$, then $\mathrm{N}_{eu}\alpha b^{*}g\alpha\text{ –}Int\left(A\right)\subseteq\mathrm{N}_{eu}\alpha b^{*}g\alpha\text{ –}Int\left(B\right)$.
(vii) $\left[\mathrm{N}_{eu}\alpha b^{*}g\alpha\text{ –}Int\left(A\right)\right]^{C}=\mathrm{N}_{eu}\alpha b^{*}g\alpha\text{ –}Cl\left(A^{C}\right)$.
(viii) $\left[\mathrm{N}_{eu}\alpha b^{*}g\alpha\text{ –}Cl\left(A\right)\right]^{C}=\mathrm{N}_{eu}\alpha b^{*}g\alpha\text{ –}Int\left(A^{C}\right)$.
(ix) $\mathrm{N}_{eu}\alpha b^{*}g\alpha\text{ –}Int\left(A\bigcap B\right)=\left[\mathrm{N}_{eu}\alpha b^{*}g\alpha\text{ –}Int\left(A\right)\right]\bigcap\left[\mathrm{N}_{eu}\alpha b^{*}g\alpha\text{ –}Int\left(B\right)\right]$.
(x) $\mathrm{N}_{eu}\alpha b^{*}g\alpha\text{ –}Cl\left(A\bigcup B\right)=\left[\mathrm{N}_{eu}\alpha b^{*}g\alpha\text{ –}Cl\left(A\right)\right]\bigcup\left[\mathrm{N}_{eu}\alpha b^{*}g\alpha\text{ –}Cl\left(B\right)\right]$.
(xi) $\left[\mathrm{N}_{eu}\alpha b^{*}g\alpha\text{ –}Int\left(A\right)\right]\bigcup\left[\mathrm{N}_{eu}\alpha b^{*}g\alpha\text{ –}Int\left(B\right)\right]\subseteq\mathrm{N}_{eu}\alpha b^{*}g\alpha\text{ –}Int\left(A\bigcup B\right)$.

(xii) $\mathrm{N}_{eu}\alpha b^{*}g\alpha\text{-}Cl(A\cap B)\subseteq\left[\mathrm{N}_{eu}\alpha b^{*}g\alpha\text{-}Cl(A)\right]\cap\left[\mathrm{N}_{eu}\alpha b^{*}g\alpha\text{-}Cl(B)\right]$.

Definition 2.22. Let $f:(X,\mathrm{T}_N)\to(Y,\sigma_N)$ be a mapping. Then f is called a neutrosophic continuous $(\mathrm{N}_{eu}\text{-}continuous)$ mapping if $f^{-1}(V)$ is a $\mathrm{N}_{eu}\text{-}open$ set in X for every $\mathrm{N}_{eu}\text{-}open$ set V in Y.

Theorem 2.23. Let $f:(X,\mathrm{T}_N)\to(Y,\sigma_N)$ be a mapping. Then f is called a $\mathrm{N}_{eu}\text{-}continuous$ mapping if $f^{-1}(V)$ is a $\mathrm{N}_{eu}\text{-}closed$ set in X for every $\mathrm{N}_{eu}\text{-}closed$ set V in Y.

3 Neutrosophic $\alpha b^{*}g\alpha$-Continuous Mappings

In this section, we introduce the concepts of neutrosophic $\alpha b^{*}g\alpha$-continuous $(\mathrm{N}_{eu}\alpha b^{*}g\alpha\text{-}continuous)$ mappings in $\mathrm{N}_{eu}\text{-}Top\text{-}Spaces$. Also, we study some of the main results regarding $\mathrm{N}_{eu}\alpha b^{*}g\alpha\text{-}continuous$ depending on $\mathrm{N}_{eu}\alpha b^{*}g\alpha\text{-}open$ sets.

Definition 3.1. Let $f:(X,\mathrm{T}_N)\to(Y,\sigma_N)$ be a mapping. Then f is called a $\mathrm{N}_{eu}\alpha b^{*}g\alpha\text{-}continuous$ mapping if $f^{-1}(V)$ is a $\mathrm{N}_{eu}\alpha b^{*}g\alpha\text{-}open$ set in X for every $\mathrm{N}_{eu}\text{-}open$ set V in Y.

Theorem 3.2. Every $\mathrm{N}_{eu}\text{-}continuous$ mapping is $\mathrm{N}_{eu}\alpha b^{*}g\alpha\text{-}continuous$ mapping.

Proof. Let $f:(X,\mathrm{T}_N)\to(Y,\sigma_N)$ be $\mathrm{N}_{eu}\text{-}continuous$ mapping. Let V be a $\mathrm{N}_{eu}\text{-}open$ set in (Y,σ_N). Then $f^{-1}(V)$ is $\mathrm{N}_{eu}\text{-}open$ set in (X,T_N). Since every $\mathrm{N}_{eu}\text{-}open$ set is $\mathrm{N}_{eu}\alpha b^{*}g\alpha\text{-}open$. $f^{-1}(V)$ is $\mathrm{N}_{eu}\alpha b^{*}g\alpha\text{-}open$ set in (X,T_N). Hence f is $\mathrm{N}_{eu}\alpha b^{*}g\alpha\text{-}continuous$ mapping.

Theorem 3.3. Let (X,T_N), (Y,σ_N) and (Z,η_N) be $\mathrm{N}_{eu}\text{-}Top\text{-}Spaces$. If $f:(X,\mathrm{T}_N)\to(Y,\sigma_N)$ is a $\mathrm{N}_{eu}\alpha b^{*}g\alpha\text{-}continuous$ mapping and $g:(Y,\sigma_N)\to(Z,\eta_N)$ is $\mathrm{N}_{eu}\text{-}continuous$ mapping, then $gof:(X,\mathrm{T}_N)\to(Z,\eta_N)$ is a $\mathrm{N}_{eu}\alpha b^{*}g\alpha\text{-}continuous$ mapping.

Proof. Let G be a $\mathrm{N}_{eu}\text{-}open$ set in Z. Since $g:(Y,\sigma_N)\to(Z,\eta_N)$ is $\mathrm{N}_{eu}\text{-}continuous$, $f^{-1}(G)$ is $\mathrm{N}_{eu}\text{-}open$ in Y. Since f is a $\mathrm{N}_{eu}\alpha b^{*}g\alpha\text{-}continuous$ mapping, $f^{-1}\left[f^{-1}(G)\right]$ is $\mathrm{N}_{eu}\alpha b^{*}g\alpha\text{-}open$ in X. But $f^{-1}\left[g^{-1}(G)\right]=(gof)^{-1}(G)$.

Then $(gof)^{-1}(G)$ is $\mathrm{N}_{eu}\alpha b^{*}g\alpha\text{-}open$ set in X. Hence, gof is a $\mathrm{N}_{eu}\alpha b^{*}g\alpha\text{-}continuous$ mapping.

Theorem 3.4. Let (X,T_N) and (Y,σ_N) be two $\mathrm{N}_{eu}\text{-}Top\text{-}Spaces$. Then prove that $f:(X,\mathrm{T}_N)\to(Y,\sigma_N)$ is $\mathrm{N}_{eu}\alpha b^{*}g\alpha\text{-}continuous$ if and only if $f^{-1}(B)$ is $\mathrm{N}_{eu}\alpha b^{*}g\alpha\text{-}closed$ set in X for every $\mathrm{N}_{eu}\text{-}closed$ set B in Y.

Proof. Let B be a N_{eu} *–closed* set in Y. Then B^C is N_{eu} *–open* set in Y. Since f is $\mathrm{N}_{eu}\alpha b^* g\alpha$ *–continuous*. Therefore $f^{-1}\left(B^C\right)$ is a $\mathrm{N}_{eu}\alpha b^* g\alpha$ *–open* set in X. Since $f^{-1}\left(B^C\right)=\left[f^{-1}\left(B\right)\right]^C$, $f^{-1}\left(B\right)$ is $\mathrm{N}_{eu}\alpha b^* g\alpha$ *–closed* set in X.

Conversely, Let B be a N_{eu} *–open* set in Y. Then B^C is N_{eu} *–closed* set in Y. By assumption $f^{-1}\left(B^C\right)$ is $\mathrm{N}_{eu}\alpha b^* g\alpha$ *–closed* set in X. Since $f^{-1}\left(B^C\right)=\left[f^{-1}\left(B\right)\right]^C$, $f^{-1}\left(B\right)$ is $\mathrm{N}_{eu}\alpha b^* g\alpha$ *–open* set in X. Hence f is $\mathrm{N}_{eu}\alpha b^* g\alpha$ *–continuous*.

Theorem 3.5. Let $\left(X,\mathrm{T}_N\right)$ and $\left(Y,\sigma_N\right)$ be two N_{eu} *–Top –Spaces* and $f:X\to Y$ be a mapping. Then f is a $\mathrm{N}_{eu}\alpha b^* g\alpha$ *–continuous* mapping if and only if $f\left(\mathrm{N}_{eu}\alpha b^* g\alpha - Cl\left(A\right)\right)\subseteq \mathrm{N}_{eu}\alpha b^* g\alpha - Cl\left(f\left(A\right)\right)$ for every N_{eu} *–set* A in X.

Proof. Let A be a N_{eu} *–set* in X and f be a $\mathrm{N}_{eu}\alpha b^* g\alpha$ *–continuous* mapping. Then evidently $f\left(A\right)\subseteq \mathrm{N}_{eu}\alpha b^* g\alpha - Cl\left[f\left(A\right)\right]$. Now, $A\subseteq f^{=1}\left[f\left(A\right)\right]\subseteq f^{-1}\left[\mathrm{N}_{eu}\alpha b^* g\alpha - Cl\left(f\left(A\right)\right)\right]$ and $\mathrm{N}_{eu}\alpha b^* g\alpha - Cl\left(A\right)\subseteq \mathrm{N}_{eu}\alpha b^* g\alpha - Cl\left[f^{-1}\left(\mathrm{N}_{eu}\alpha b^* g\alpha - Cl\left(f\left(A\right)\right)\right)\right]$. Since f is a $\mathrm{N}_{eu}\alpha b^* g\alpha$ –continuous mapping and $\mathrm{N}_{eu}\alpha b^* g\alpha - Cl\left[f\left(A\right)\right]$ is a $\mathrm{N}_{eu}\alpha b^* g\alpha$ *–closed* set. Thus $\mathrm{N}_{eu}\alpha b^* g\alpha - Cl\left[f^{-1}\left(\mathrm{N}_{eu}\alpha b^* g\alpha - Cl\left(f\left(A\right)\right)\right)\right]= f^{-1}\left[\mathrm{N}_{eu}\alpha b^* g\alpha - Cl\left(f\left(A\right)\right)\right]$. Hence, $f\left[\mathrm{N}_{eu}\alpha b^* g\alpha - Cl\left(A\right)\right]\subseteq \mathrm{N}_{eu}\alpha b^* g\alpha - Cl\left[f\left(A\right)\right]$.

Conversely, let $f\left[\mathrm{N}_{eu}\alpha b^* g\alpha - Cl\left(A\right)\right]\subseteq \mathrm{N}_{eu}\alpha b^* g\alpha - Cl\left[f\left(A\right)\right]$, for each N_{eu} *–set* A in X. Let F be a N_{eu} *–closed* set in Y. Then $\mathrm{N}_{eu}\alpha b^* g\alpha - Cl\left[f\left(f^{-1}\left(F\right)\right)\right]\subseteq \mathrm{N}_{eu}\alpha b^* g\alpha - Cl\left(F\right)=F$. By assumption, $f\left[\mathrm{N}_{eu}\alpha b^* g\alpha - Cl\left(f^{-1}\left(F\right)\right)\right]\subseteq \mathrm{N}_{eu}\alpha b^* g\alpha - Cl\left[f\left(f^{-1}\left(F\right)\right)\right]\subseteq F$ and hence $\mathrm{N}_{eu}\alpha b^* g\alpha - Cl\left[f^{-1}\left(F\right)\right]\subseteq f^{-1}\left(F\right)$. Since $f^{-1}\left(F\right)\subseteq \mathrm{N}_{eu}\alpha b^* g\alpha - Cl\left[f^{-1}\left(F\right)\right]$, $\mathrm{N}_{eu}\alpha b^* g\alpha - Cl\left[f^{-1}\left(F\right)\right]=f^{-1}\left(F\right)$. This implies that $f^{-1}\left(F\right)$ is a $\mathrm{N}_{eu}\alpha b^* g\alpha$ *–closed* set in X. Thus by Theorem 3.4, f is a $\mathrm{N}_{eu}\alpha b^* g\alpha$ –continuous mapping.

Theorem 3.6. Let $\left(X,\mathrm{T}_N\right)$ and $\left(Y,\sigma_N\right)$ be two N_{eu} *–Top –Spaces* and $f:X\to Y$ be a mapping. Then f is a $\mathrm{N}_{eu}\alpha b^* g\alpha$ *–continuous* mapping if and only if $\mathrm{N}_{eu}\alpha b^* g\alpha - Cl\left[f^{-1}\left(B\right)\right]\subseteq f^{-1}\left[\mathrm{N}_{eu}\alpha b^* g\alpha - Cl\left(B\right)\right]$ for every N_{eu} *–set* B in Y.

Proof. Let B be any N_{eu} *–set* in Y and f be a $\mathrm{N}_{eu}\alpha b^* g\alpha$ *–continuous* mapping. Clearly $f^{-1}\left(B\right)\subseteq f^{-1}\left[\mathrm{N}_{eu}\alpha b^* g\alpha - Cl\left(B\right)\right]$. Then, $\mathrm{N}_{eu}\alpha b^* g\alpha - Cl\left[f^{-1}\left(B\right)\right]\subseteq \mathrm{N}_{eu}\alpha b^* g\alpha - Cl\left[f^{-1}\left(\mathrm{N}_{eu}\alpha b^* g\alpha - Cl\left(B\right)\right)\right]$. Since $\mathrm{N}_{eu}\alpha b^* g\alpha - Cl\left(B\right)$ is $\mathrm{N}_{eu}\alpha b^* g\alpha$ –closed set in Y. So by Theorem 3.4, $f^{-1}\left[\mathrm{N}_{eu}\alpha b^* g\alpha - Cl\left(B\right)\right]$ is a $\mathrm{N}_{eu}\alpha b^* g\alpha$ *–cloed* set in X. Thus,

$\mathrm{N}_{eu}\alpha b^{*}g\alpha - Cl\left[f^{-1}(B)\right] \subseteq \mathrm{N}_{eu}\alpha b^{*}g\alpha - Cl\left[f^{-1}\left(\mathrm{N}_{eu}\alpha b^{*}g\alpha - Cl(B)\right)\right] =$
$f^{-1}\left[\mathrm{N}_{eu}\alpha b^{*}g\alpha - Cl(B)\right]$.

Conversely, $\mathrm{N}_{eu}\alpha b^{*}g\alpha - Cl\left[f^{-1}(B)\right] \subseteq f^{-1}\left[\mathrm{N}_{eu}\alpha b^{*}g\alpha - Cl(B)\right]$ for all $\mathrm{N}_{eu}-sets$ $\mathrm{N}_{eu}-set\ B$ in Y. Let F be a $\mathrm{N}_{eu}-closed$ set in Y. Since every $\mathrm{N}_{eu}-closed$ set is $\mathrm{N}_{eu}\alpha b^{*}g\alpha - cloed$set, $\mathrm{N}_{eu}\alpha b^{*}g\alpha - Cl\left[f^{-1}(F)\right] \subseteq f^{-1}\left[\mathrm{N}_{eu}\alpha b^{*}g\alpha - Cl(F)\right] = f^{-1}(F)$. This implies that $f^{-1}(F)$ is a $\mathrm{N}_{eu}\alpha b^{*}g\alpha - cloed$ set in X. Thus by Theorem 3.4, f is a $\mathrm{N}_{eu}\alpha b^{*}g\alpha - continuous$ mapping.

Theorem 3.7. Let (X, T_N) and (Y, σ_N) be two $\mathrm{N}_{eu}-Top-Spaces$ and $f: X \to Y$ be a bijective mapping. Then f is $\mathrm{N}_{eu}\alpha b^{*}g\alpha - \text{continuous}$ if and only if $\mathrm{N}_{eu}\alpha b^{*}g\alpha - Int\left[f(A)\right] \subseteq f\left[\mathrm{N}_{eu}\alpha b^{*}g\alpha - Int(A)\right]$ for every $\mathrm{N}_{eu}-set\ A$ in X.

Proof. Let A be any $\mathrm{N}_{eu}-set$ in X and f be a bijective and $\mathrm{N}_{eu}\alpha b^{*}g\alpha - \text{continuous}$ mapping. Let $f(A) = B$. Clearly $f^{-1}\left[\mathrm{N}_{eu}\alpha b^{*}g\alpha - Int(B)\right] \subseteq f^{-1}(B)$. Since f is an injective mapping, $f^{-1}(B) = A$, so that $f^{-1}\left[\mathrm{N}_{eu}\alpha b^{*}g\alpha - Int(B)\right] \subseteq A$. Therefore, $\mathrm{N}_{eu}\alpha b^{*}g\alpha - Int\left[f^{-1}\left(\mathrm{N}_{eu}\alpha b^{*}g\alpha - Int(B)\right)\right] \subseteq \mathrm{N}_{eu}\alpha b^{*}g\alpha - Int(A)$. Since f is $\mathrm{N}_{eu}\alpha b^{*}g\alpha - \text{continuous}$, $f^{-1}\left[\mathrm{N}_{eu}\alpha b^{*}g\alpha - Int(B)\right]$ is $\mathrm{N}_{eu}\alpha b^{*}g\alpha - \text{open}$ set in X and $f^{-1}\left[\mathrm{N}_{eu}\alpha b^{*}g\alpha - Int(B)\right] \subseteq \mathrm{N}_{eu}\alpha b^{*}g\alpha - Int(A)$, $f\left[f^{-1}\left(\mathrm{N}_{eu}\alpha b^{*}g\alpha - Int(B)\right)\right] \subseteq f\left[\mathrm{N}_{eu}\alpha b^{*}g\alpha - Int(A)\right]$. Therefore $\mathrm{N}_{eu}\alpha b^{*}g\alpha - Int\left[f(A)\right] \subseteq f\left[\mathrm{N}_{eu}gs\alpha^{*} - Int(A)\right]$.

Conversely, $\mathrm{N}_{eu}\alpha b^{*}g\alpha - Int\left[f(A)\right] \subseteq f\left[\mathrm{N}_{eu}\alpha b^{*}g\alpha - Int(A)\right]$ for every $\mathrm{N}_{eu}-set\ A$ in X. Let V be a $\mathrm{N}_{eu}-open$ set in Y. Then V is $\mathrm{N}_{eu}\alpha b^{*}g\alpha - \text{open}$ set in Y. Since f is surjective and so $V = \mathrm{N}_{eu}\alpha b^{*}g\alpha - Int(V) = \mathrm{N}_{eu}\alpha b^{*}g\alpha - Int\left[f\left(f^{-1}(V)\right)\right] \subseteq f\left[\mathrm{N}_{eu}\alpha b^{*}g\alpha - Int\left(f^{-1}(V)\right)\right]$. It follows that $f^{-1}(V) \subseteq \mathrm{N}_{eu}\alpha b^{*}g\alpha - Int\left[f^{-1}(V)\right]$. Therefore $f^{-1}(V)$ is $\mathrm{N}_{eu}\alpha b^{*}g\alpha - \text{open}$ set in X. Hence f is a $\mathrm{N}_{eu}\alpha b^{*}g\alpha - \text{continuous}$ mapping.

Theorem 3.8. Let (X, T_N) and (Y, σ_N) be two $\mathrm{N}_{eu}-Top-Spaces$ and $f: X \to Y$ be a mapping. Then f is a $\mathrm{N}_{eu}\alpha b^{*}g\alpha - \text{continuous}$ mapping if and only if $f^{-1}\left[\mathrm{N}_{eu}\alpha b^{*}g\alpha - Int(B)\right] \subseteq \mathrm{N}_{eu}\alpha b^{*}g\alpha - Int\left[f^{-1}(B)\right]$ for every $\mathrm{N}_{eu}-set\ B$ in Y.

Proof. Let B be any $\mathrm{N}_{eu}-set$ in Y and f be a $\mathrm{N}_{eu}\alpha b^{*}g\alpha - \text{continuous}$ mapping. Clearly $f^{-1}\left[\mathrm{N}_{eu}\alpha b^{*}g\alpha - Int(B)\right] \subseteq f^{-1}(B)$ implies $\mathrm{N}_{eu}\alpha b^{*}g\alpha - Int\left[f^{-1}\left(\mathrm{N}_{eu}\alpha b^{*}g\alpha - Int(B)\right)\right] \subseteq \mathrm{N}_{eu}\alpha b^{*}g\alpha - Int\left[f^{-1}(B)\right]$. Since $\mathrm{N}_{eu}\alpha b^{*}g\alpha - Int(B)$ is $\mathrm{N}_{eu}\alpha b^{*}g\alpha - \text{open}$ set in Y and f is $\mathrm{N}_{eu}\alpha b^{*}g\alpha - \text{continuous}$, $f^{-1}\left[\mathrm{N}_{eu}\alpha b^{*}g\alpha - Int(B)\right]$ is $\mathrm{N}_{eu}\alpha b^{*}g\alpha - \text{open}$ set in X. Therefore $\mathrm{N}_{eu}\alpha b^{*}g\alpha - Int\left[f^{-1}\left(\mathrm{N}_{eu}\alpha b^{*}g\alpha - Int(B)\right)\right] \subseteq f^{-1}\left[\mathrm{N}_{eu}\alpha b^{*}g\alpha - Int(B)\right] \subseteq$
$\mathrm{N}_{eu}\alpha b^{*}g\alpha - Int\left[f^{-1}(B)\right]$.

Conversely, $f^{-1}\left[\mathrm{N}_{eu}\alpha b^{*}g\alpha-Int(B)\right]\subseteq \mathrm{N}_{eu}\alpha b^{*}g\alpha-Int\left[f^{-1}(B)\right]$ for every $\mathrm{N}_{eu}-set\ B$ in Y. Let G be any $\mathrm{N}_{eu}-open$ set in Y. Then $f^{-1}(G)=f^{-1}\left[\mathrm{N}_{eu}\alpha b^{*}g\alpha-Int(G)\right]\subseteq \mathrm{N}_{eu}\alpha b^{*}g\alpha-Int\left[f^{-1}(G)\right]$ and therefore $f^{-1}(G)=\mathrm{N}_{eu}\alpha b^{*}g\alpha-Int\left[f^{-1}(G)\right]$. This implies that $f^{-1}(G)$ is $\mathrm{N}_{eu}\alpha b^{*}g\alpha-$open set in X. Hence f is a $\mathrm{N}_{eu}\alpha b^{*}g\alpha-$continuous mapping.

Theorem 3.9. Let (X,T_N) and (Y,σ_N) be two $\mathrm{N}_{eu}-Top-Spaces$ and $f:X\to Y$ be a bijective mapping. Then f is a $\mathrm{N}_{eu}\alpha b^{*}g\alpha-$continuous mapping if and only if $f\left[\mathrm{N}_{eu}\alpha b^{*}g\alpha-Fr(A)\right]\subseteq \mathrm{N}_{eu}\alpha b^{*}g\alpha-Fr\left[f(A)\right]$ for every $\mathrm{N}_{eu}-set\ A$ in X.

Proof. Let f be a bijective and $\mathrm{N}_{eu}\alpha b^{*}g\alpha-$continuous mapping. Let A be a $\mathrm{N}_{eu}-set$ in X. By definition, $\mathrm{N}_{eu}\alpha b^{*}g\alpha-Fr(A)=\mathrm{N}_{eu}\alpha b^{*}g\alpha-Cl(A)\bigcap \mathrm{N}_{eu}\alpha b^{*}g\alpha-Cl\left(A^{C}\right)$. By Theorem 3.7, $\mathrm{N}_{eu}\alpha b^{*}g\alpha-Int\left[f(A)\right]\subseteq f\left[\mathrm{N}_{eu}\alpha b^{*}g\alpha-Int(A)\right]$ and from Theorem 3.5, $f\left[\mathrm{N}_{eu}\alpha b^{*}g\alpha-Cl(A)\right]\subseteq \mathrm{N}_{eu}\alpha b^{*}g\alpha-Cl\left[f(A)\right]$,

$f\left[\mathrm{N}_{eu}\alpha b^{*}g\alpha-Fr(A)\right]=f\left[\mathrm{N}_{eu}\alpha b^{*}g\alpha-Cl(A)\right]\bigcap f\left[\mathrm{N}_{eu}\alpha b^{*}g\alpha-Cl\left(A^{C}\right)\right]\subseteq$

$\mathrm{N}_{eu}\alpha b^{*}g\alpha-Cl\left[f(A)\right]\bigcap \mathrm{N}_{eu}\alpha b^{*}g\alpha-Cl\left[f(A)\right]^{C}=\mathrm{N}_{eu}\alpha b^{*}g\alpha-Fr\left[f(A)\right]$.

Conversely, $f\left[\mathrm{N}_{eu}\alpha b^{*}g\alpha-Fr(A)\right]\subseteq \mathrm{N}_{eu}\alpha b^{*}g\alpha-Fr\left[f(A)\right]$ for every $\mathrm{N}_{eu}-set\ A$ in X. Then $f\left[\mathrm{N}_{eu}\alpha b^{*}g\alpha-Cl(A)\right]=f\left[\mathrm{N}_{eu}\alpha b^{*}g\alpha-Int(A)\right]\bigcup f\left[\mathrm{N}_{eu}\alpha b^{*}g\alpha-Fr(A)\right]\subseteq$

$f(A)\bigcup \mathrm{N}_{eu}\alpha b^{*}g\alpha-Fr\left[f(A)\right]\subseteq \mathrm{N}_{eu}\alpha b^{*}g\alpha-Cl\left[f(A)\right]$. By Theorem 3.5, f is a $\mathrm{N}_{eu}\alpha b^{*}g\alpha-$continuous mapping.

Theorem 3.10. Let (X,T_N) and (Y,σ_N) be two $\mathrm{N}_{eu}-Top-Spaces$ and $f:X\to Y$ be a bijective mapping. Then f is a $\mathrm{N}_{eu}\alpha b^{*}g\alpha-$continuous mapping if and only if $\mathrm{N}_{eu}\alpha b^{*}g\alpha-Fr\left[f^{-1}(B)\right]\subseteq f^{-1}\left[\mathrm{N}_{eu}\alpha b^{*}g\alpha-Fr(B)\right]$ for every $\mathrm{N}_{eu}-set\ B$ in Y.

Proof. Let f be a bijective and $\mathrm{N}_{eu}\alpha b^{*}g\alpha-$continuous mapping. Let B be a $\mathrm{N}_{eu}-set$ in Y. By Theorem 3.6, $\mathrm{N}_{eu}\alpha b^{*}g\alpha-Cl\left[f^{-1}(B)\right]\subseteq f^{-1}\left[\mathrm{N}_{eu}\alpha b^{*}g\alpha-Cl(B)\right]$. Therefore we obtain $f^{-1}\left[\mathrm{N}_{eu}\alpha b^{*}g\alpha-Fr(B)\right]=f^{-1}\left[\left(\mathrm{N}_{eu}\alpha b^{*}g\alpha-Cl(B)\right)\bigcap \mathrm{N}_{eu}\alpha b^{*}g\alpha-Cl\left(B^{C}\right)\right]=$

$f^{-1}\left[\mathrm{N}_{eu}\alpha b^{*}g\alpha-Cl(B)\right]\bigcap f^{-1}\left[\mathrm{N}_{eu}\alpha b^{*}g\alpha-Cl\left(B^{C}\right)\right]\supseteq$

$\mathrm{N}_{eu}\alpha b^{*}g\alpha-Cl\left[f^{-1}(B)\right]\bigcap \mathrm{N}_{eu}\alpha b^{*}g\alpha-Cl\left[f^{-1}\left(B^{C}\right)\right]=$

$\mathrm{N}_{eu}\alpha b^{*}g\alpha-Cl\left[f^{-1}(B)\right]\bigcap \mathrm{N}_{eu}\alpha b^{*}g\alpha-Cl\left[\left(f^{-1}(B)\right)^{C}\right]=\mathrm{N}_{eu}\alpha b^{*}g\alpha-Fr\left[f^{-1}(B)\right]$.

Therefore $\mathrm{N}_{eu}\alpha b^{*}g\alpha-Fr\left[f^{-1}(B)\right]\subseteq f^{-1}\left[\mathrm{N}_{eu}\alpha b^{*}g\alpha-Fr(B)\right]$.

Conversely since $\mathrm{N}_{eu}\alpha b^{*}g\alpha-Fr\left[f^{-1}(B)\right]\subseteq f^{-1}\left[\mathrm{N}_{eu}\alpha b^{*}g\alpha-Fr(B)\right]$ for every $\mathrm{N}_{eu}-set\ B$ in Y. This implies that $\mathrm{N}_{eu}\alpha b^{*}g\alpha-Cl\left[f^{-1}(B)\right]\subseteq f^{-1}\left[\mathrm{N}_{eu}\alpha b^{*}g\alpha-Cl(B)\right]$. By Theorem 3.6, f is a $\mathrm{N}_{eu}\alpha b^{*}g\alpha-$continuous mapping.

Definition 3.11. Let $x_{(r,t,s)}$ be a $\mathrm{N}_{eu}-point$ of a $\mathrm{N}_{eu}-Top-Space\ (X,\mathrm{T}_{N})$. A $\mathrm{N}_{eu}-set\ A$ of X is called neutrosophic neighbourhood $(\mathrm{N}_{eu}-neighbourhood)$ of $x_{(r,t,s)}$ if there exists a $\mathrm{N}_{eu}-open$ set B such that $x_{(r,t,s)}\in B\subseteq A$.

Theorem 3.12. Let f be a mapping from a $\mathrm{N}_{eu}-Top-Space\ (X,\mathrm{T}_{N})$ to a $\mathrm{N}_{eu}-Top-Space\ (Y,\sigma_{N})$. Then the following assertions are equivalent.

(i) f is $\mathrm{N}_{eu}\alpha b^{*}g\alpha-$continuous.

(ii) For each $\mathrm{N}_{eu}-point\ x_{(r,t,s)}\in X$ and every $\mathrm{N}_{eu}-neighbourhood\ A$ of $f\left(x_{(r,t,s)}\right)$, there exists a $\mathrm{N}_{eu}\alpha b^{*}g\alpha-$open set B such that $x_{(r,t,s)}\in B\subseteq f^{-1}(A)$.

(iii) For each $\mathrm{N}_{eu}-point\ x_{(r,t,s)}\in X$ and every $\mathrm{N}_{eu}-neighbourhood\ A$ of $f\left(x_{(r,t,s)}\right)$, there exists a $\mathrm{N}_{eu}\alpha b^{*}g\alpha-$open set B in X such that $x_{(r,t,s)}\in B$ and $f(B)\subseteq A$.

Proof. (i) $\Rightarrow$ (ii): Let $x_{(r,t,s)}\in X$ be a $\mathrm{N}_{eu}-point$ in X and let A be a $\mathrm{N}_{eu}-neighbourhood$ of $f\left(x_{(r,t,s)}\right)$. Then there exists a $\mathrm{N}_{eu}-open$ set B in Y such that $f\left(x_{(r,t,s)}\right)\in B\subseteq A$. Since f is $\mathrm{N}_{eu}\alpha b^{*}g\alpha-$continuous, we know that $f^{-1}(B)$ is a $\mathrm{N}_{eu}\alpha b^{*}g\alpha-$open set in X and $x_{(r,t,s)}\in f^{-1}\left(f_{(r,t,s)}\right)\subseteq f^{-1}(B)\subseteq f^{-1}(A)$. This implies (ii) is true.

(ii) $\Rightarrow$ (iii): Let $x_{(r,t,s)}$ be a $\mathrm{N}_{eu}-point$ in X and let A be a $\mathrm{N}_{eu}-neighbourhood$ of $f\left(x_{(r,t,s)}\right)$. The condition (ii) implies that there exists a $\mathrm{N}_{eu}\alpha b^{*}g\alpha-$open set B in X such that $x_{(r,t,s)}\in B\subseteq f^{-1}(A)$. Thus $x_{(r,t,s)}\in B$ and $f(B)\subseteq f\left[f^{-1}(A)\right]\subseteq A$. Hence (iii) is true.

(iii) $\Rightarrow$ (i): Let B be a $\mathrm{N}_{eu}-open$ set in Y and let $x_{(r,t,s)}\in f^{-1}(B)$. Since B is $\mathrm{N}_{eu}-open$ set, $f\left(x_{(r,t,s)}\right)\in B$, and so B is $\mathrm{N}_{eu}-neighbourhood$ of $f\left(x_{(r,t,s)}\right)$. It follows from (iii) that there exists a $\mathrm{N}_{eu}\alpha b^{*}g\alpha-$open set A in X such that $x_{(r,t,s)}\in A$ and $f(A)\subseteq B$ so that $x_{(r,t,s)}\in A\subseteq f^{-1}\left[f(A)\right]\subseteq f^{-1}(B)$. This implies by definition that $f^{-1}(B)$ is a $\mathrm{N}_{eu}\alpha b^{*}g\alpha-$open set in X. Therefore, f is a $\mathrm{N}_{eu}\alpha b^{*}g\alpha-$continuous mapping.

4 Neutrosophic $\alpha b^{*}g\alpha-$Irresolute Mappings

In this section, we introduce the concept of neutrosophic $\mathrm{N}_{eu}\alpha b^{*}g\alpha-$irresolute $(\mathrm{N}_{eu}\alpha b^{*}g\alpha-$irresolute) mappings in $\mathrm{N}_{eu}-Top-Spaces$. Also, we discuss the relationship of $\mathrm{N}_{eu}\alpha b^{*}g\alpha-$irresolute with $\mathrm{N}_{eu}\alpha b^{*}g\alpha-$continuous mappings.

Definition 4.1. Let (X, T_N) and (Y, σ_N) be two N_{eu} *–Top –Spaces*. A mapping $f: X \to Y$ is called $\mathrm{N}_{eu}\alpha b^* g\alpha$ **–irresolute** if the inverse image of every $\mathrm{N}_{eu}\alpha b^* g\alpha$ **–open** set in Y is $\mathrm{N}_{eu}\alpha b^* g\alpha$ **–open** in X.

Theorem 4.2. Let (X, T_N) and (Y, σ_N) be two N_{eu} *–Top –Spaces*. A mapping $f: X \to Y$ is called $\mathrm{N}_{eu}\alpha b^* g\alpha$ **–irresolute** if the inverse image of every $\mathrm{N}_{eu}\alpha b^* g\alpha$ **–closed** set in Y is $\mathrm{N}_{eu}\alpha b^* g\alpha$ **–closed** in X.

Proof. Let A be any $\mathrm{N}_{eu}\alpha b^* g\alpha$ **–closed** set in Y. Then A^C is $\mathrm{N}_{eu}\alpha b^* g\alpha$ **–open** set in Y. Since f is $\mathrm{N}_{eu}\alpha b^* g\alpha$ **–irresolute,** $f^{-1}(A^C)$ is $\mathrm{N}_{eu}\alpha b^* g\alpha$ **–open** set in X and $f^{-1}(A^C) = \left[f^{-1}(A)\right]^C$ which implies that $f^{-1}(A)$ is $\mathrm{N}_{eu}\alpha b^* g\alpha$ **–closed** set in X.
Conversely, Let B be any $\mathrm{N}_{eu}\alpha b^* g\alpha$ **–-open** set in Y. Then B^C is $\mathrm{N}_{eu}\alpha b^* g\alpha$ **–closed** set in Y. Thus $f^{-1}(B^C)$ is $\mathrm{N}_{eu}\alpha b^* g\alpha$ **–closed** set in X and $f^{-1}(B^C) = \left[f^{-1}(B)\right]^C$ which implies that $f^{-1}(B)$ is $\mathrm{N}_{eu}\alpha b^* g\alpha$ **–open** set in X. Hence $f: X \to Y$ is $\mathrm{N}_{eu}\alpha b^* g\alpha$ **–irresolute.**

Theorem 4.3. Every $\mathrm{N}_{eu}\alpha b^* g\alpha$ **–irresolute** mapping is $\mathrm{N}_{eu}\alpha b^* g\alpha$ **–continuous.**

Proof. Let V be a N_{eu} *–open* set in Y. Since every N_{eu} *–open* set is $\mathrm{N}_{eu}\alpha b^* g\alpha$ **–open,** V is $\mathrm{N}_{eu}\alpha b^* g\alpha$ **–open.** Since f is $\mathrm{N}_{eu}\alpha b^* g\alpha$ **–irresolute,** $f^{-1}(V)$ is $\mathrm{N}_{eu}\alpha b^* g\alpha$ **–open** set in X. Therefore f is $\mathrm{N}_{eu}\alpha b^* g\alpha$ **–continuous.**

Theorem 4.4. Let $f: (X, \mathrm{T}_N) \to (Y, \sigma_N)$ be a mapping. Then the following assertions are equivalent:
(i) f is $\mathrm{N}_{eu}\alpha b^* g\alpha$ **–irresolute.**
(ii) $\mathrm{N}_{eu}\alpha b^* g\alpha - Cl\left[f^{-1}(B)\right] \subseteq f^{-1}\left[\mathrm{N}_{eu}\alpha b^* g\alpha - Cl(B)\right]$ for every N_{eu} *–set* B of Y.
(iii) $f\left[\mathrm{N}_{eu}\alpha b^* g\alpha - Cl(A)\right] \subseteq \mathrm{N}_{eu}\alpha b^* g\alpha - Cl\left[f(A)\right]$ for every N_{eu} *–set* A of X.
(iv) $f^{-1}\left[\mathrm{N}_{eu}\alpha b^* g\alpha - Int(B)\right] \subseteq \mathrm{N}_{eu}\alpha b^* g\alpha - Int\left[f^{-1}(B)\right]$ for every N_{eu} *–set* B of Y.

Proof. $(\mathrm{i}) \Rightarrow (\mathrm{ii})$: Let B be any N_{eu} *–set* in Y. Then $\mathrm{N}_{eu}\alpha b^* g\alpha - Cl(B)$ is $\mathrm{N}_{eu}\alpha b^* g\alpha$ **–closed** set in Y. Since f is $\mathrm{N}_{eu}\alpha b^* g\alpha$ **–irresolute,** $f^{-1}\left[\mathrm{N}_{eu}\alpha b^* g\alpha - Cl(B)\right]$ is $\mathrm{N}_{eu}\alpha b^* g\alpha$ **–closed** set in X. Then $\mathrm{N}_{eu}\alpha b^* g\alpha - Cl\left[f^{-1}\left(\mathrm{N}_{eu}\alpha b^* g\alpha - Cl(B)\right)\right] = f^{-1}\left[\mathrm{N}_{eu}\alpha b^* g\alpha - Cl(B)\right]$. Clearly it follows that $\mathrm{N}_{eu}\alpha b^* g\alpha - Cl\left[f^{-1}(B)\right] \subseteq \mathrm{N}_{eu}\alpha b^* g\alpha - Cl\left[f^{-1}\left(\mathrm{N}_{eu}\alpha b^* g\alpha - Cl(B)\right)\right] = f^{-1}\left[\mathrm{N}_{eu}\alpha b^* g\alpha - Cl(B)\right]$. This proves (ii).
$(\mathrm{ii}) \Rightarrow (\mathrm{iii})$: Let A be any N_{eu} *–set* in X. Then $f(A) \subseteq Y$. By (ii), $\mathrm{N}_{eu}\alpha b^* g\alpha - Cl\left[f^{-1}(f(A))\right] \subseteq f^{-1}\left[\mathrm{N}_{eu}\alpha b^* g\alpha - Cl(f(A))\right] \ldots (*)$. Now we observe that $A \subseteq f^{-1}(f(A))$ implies that $\mathrm{N}_{eu}\alpha b^* g\alpha - Cl(A) \subseteq \mathrm{N}_{eu}\alpha b^* g\alpha - Cl\left[f^{-1}(f(A))\right] \ldots (**)$. Then $(*)$ and $(**)$ implies that $\mathrm{N}_{eu}\alpha b^* g\alpha - Cl(A) \subseteq f^{-1}\left[\mathrm{N}_{eu}\alpha b^* g\alpha - Cl(f(A))\right]$ which implies that

$f\left[\mathrm{N}_{eu}\alpha b^{*}g\alpha-Cl(A)\right]\subseteq f\left(f^{-1}\left[\mathrm{N}_{eu}\alpha b^{*}g\alpha-Cl(f(A))\right]\right)\subseteq \mathrm{N}_{eu}\alpha b^{*}g\alpha-Cl\left[f(A)\right]$. Thus, $f\left[\mathrm{N}_{eu}\alpha b^{*}g\alpha-Cl(A)\right]\subseteq \mathrm{N}_{eu}\alpha b^{*}g\alpha-Cl\left[f(A)\right]$. Hence, $(\mathrm{ii})\Rightarrow(\mathrm{iii})$ is proved.

$(\mathrm{iii})\Rightarrow(\mathrm{i})$: Let F be any $\mathrm{N}_{eu}\alpha\mathrm{b}^{*}g\alpha-$closed set in Y. Then $f^{-1}(F)=f^{-1}\left[\mathrm{N}_{eu}\alpha b^{*}g\alpha-Cl(F)\right]$. By (iii), $f\left[\mathrm{N}_{eu}\alpha b^{*}g\alpha-Cl\left(f^{-1}(F)\right)\right]\subseteq \mathrm{N}_{eu}\alpha b^{*}g\alpha-Cl\left[f\left(f^{-1}(F)\right)\right]\subseteq \mathrm{N}_{eu}\alpha b^{*}g\alpha-Cl(F)=F$. Then That implies $\mathrm{N}_{eu}\alpha b^{*}g\alpha-Cl\left[f^{-1}(F)\right]\subseteq f^{-1}(F)$. But $f^{-1}(F)\subseteq \mathrm{N}_{eu}\alpha b^{*}g\alpha-Cl\left[f^{-1}(F)\right]$, $\mathrm{N}_{eu}\alpha b^{*}g\alpha-Cl\left[f^{-1}(F)\right]=f^{-1}(F)$ and so $f^{-1}(F)$ is $\mathrm{N}_{eu}\alpha\mathrm{b}^{*}g\alpha-$closed set in X. Therefore f is $\mathrm{N}_{eu}\alpha\mathrm{b}^{*}g\alpha-$irresolute.

$(\mathrm{i})\Rightarrow(\mathrm{iv})$: Let B be any $\mathrm{N}_{eu}-set$ in Y. We know that $\mathrm{N}_{eu}\alpha b^{*}g\alpha-Int(B)$ is $\mathrm{N}_{eu}\alpha\mathrm{b}^{*}g\alpha-$open set in Y. Since f is $\mathrm{N}_{eu}\alpha\mathrm{b}^{*}g\alpha-$irresolute, $f^{-1}\left[\mathrm{N}_{eu}\alpha b^{*}g\alpha-Int(B)\right]$ is $\mathrm{N}_{eu}\alpha\mathrm{b}^{*}g\alpha-$open set in X. Then $f^{-1}\left[\mathrm{N}_{eu}\alpha b^{*}g\alpha-Int(B)\right]=\mathrm{N}_{eu}\alpha b^{*}g\alpha-Int\left[f^{-1}\left(\mathrm{N}_{eu}\alpha b^{*}g\alpha-Int(B)\right)\right]\subseteq \mathrm{N}_{eu}\alpha b^{*}g\alpha-Int\left[f^{-1}(B)\right]$.

$(\mathrm{iv})\Rightarrow(\mathrm{i})$: Let V be any $\mathrm{N}_{eu}\alpha\mathrm{b}^{*}g\alpha-$open set in Y. Then by (iv), $f^{-1}(V)=f^{-1}\left[\mathrm{N}_{eu}\alpha b^{*}g\alpha-Int(V)\right]\subseteq \mathrm{N}_{eu}\alpha b^{*}g\alpha-Int\left[f^{-1}(V)\right]$. But, we have $\mathrm{N}_{eu}\alpha b^{*}g\alpha-Int\left[f^{-1}(V)\right]\subseteq f^{-1}(V)$, $\mathrm{N}_{eu}\alpha b^{*}g\alpha-Int\left[f^{-1}(V)\right]=f^{-1}(V)$ and hence $f^{-1}(V)$ is $\mathrm{N}_{eu}\alpha\mathrm{b}^{*}g\alpha-$open. Thus f is $\mathrm{N}_{eu}\alpha\mathrm{b}^{*}g\alpha-$irresolute.

Theorem 4.5. If $f:(X,\mathrm{T}_{N})\to(Y,\sigma_{N})$ and $g:(Y,\sigma_{N})\to(Z,\eta_{N})$ are $\mathrm{N}_{eu}\alpha\mathrm{b}^{*}g\alpha-$irresolute, then their composition $gof:(X,\mathrm{T}_{N})\to(Z,\eta_{N})$ is also $\mathrm{N}_{eu}\alpha\mathrm{b}^{*}g\alpha-$irresolute.

Proof. Let V be a $\mathrm{N}_{eu}\alpha\mathrm{b}^{*}g\alpha-$open set in Z. Since g is a $\mathrm{N}_{eu}\alpha\mathrm{b}^{*}g\alpha-$irresolute mapping, $g^{-1}(V)$ is $\mathrm{N}_{eu}\alpha\mathrm{b}^{*}g\alpha-$open in Y. Since f is a $\mathrm{N}_{eu}\alpha\mathrm{b}^{*}g\alpha-$irresolute mapping, $f^{-1}\left[g^{-1}(V)\right]=(gof)^{-1}(V)$ is $\mathrm{N}_{eu}\alpha\mathrm{b}^{*}g\alpha-$open in X. Therefore gof is $\mathrm{N}_{eu}\alpha\mathrm{b}^{*}g\alpha-$irresolute.

Theorem 4.6. If $f:(X,\mathrm{T}_{N})\to(Y,\sigma_{N})$ is $\mathrm{N}_{eu}\alpha\mathrm{b}^{*}g\alpha-$irresolute and $g:(Y,\sigma_{N})\to(Z,\eta_{N})$ is $\mathrm{N}_{eu}\alpha\mathrm{b}^{*}g\alpha-$continuous, then their composition $gof:(X,\mathrm{T}_{N})\to(Z,\eta_{N})$ is also $\mathrm{N}_{eu}\alpha\mathrm{b}^{*}g\alpha-$continuous.

Proof. Let V be a $\mathrm{N}_{eu}-open$ set in Z. Since g is a $\mathrm{N}_{eu}\alpha\mathrm{b}^{*}g\alpha-$continuous mapping, $g^{-1}(V)$ is $\mathrm{N}_{eu}\alpha\mathrm{b}^{*}g\alpha-$open set in Y. Since f is a $\mathrm{N}_{eu}\alpha\mathrm{b}^{*}g\alpha-$irresolute mapping, $f^{-1}\left[g^{-1}(V)\right]=(gof)^{-1}(V)$ is $\mathrm{N}_{eu}\alpha\mathrm{b}^{*}g\alpha-$open in X. Therefore gof is $\mathrm{N}_{eu}\alpha\mathrm{b}^{*}g\alpha-$conrinuous.

5 Neutrosophic $\alpha\mathrm{b}^{*}g\alpha-$Closed Mappings and Neutrosophic $\alpha\mathrm{b}^{*}g\alpha-$Open Mappings

In this section, we introduce neutrosophic $\alpha b^{*} g\alpha$ - closed $\left(\mathrm{N}_{\mathrm{eu}}\alpha b^{*} g\alpha-\text{closed}\right)$ mappings and neutrosophic $\alpha b^{*} g\alpha$ - open $\left(\mathrm{N}_{\mathrm{eu}}\alpha b^{*} g\alpha-\text{open}\right)$ mappings in N_{eu} *–Top –Spaces* and obtain certain characterizations of these classes of mappings.

Definition 5.1. Let $\left(X,\mathrm{T}_{N}\right)$ and $\left(Y,\sigma_{N}\right)$ be two N_{eu} *–Top –Spaces*. A function $f:\left(X,\mathrm{T}_{N}\right)\to\left(Y,\sigma_{N}\right)$ is said to be $\mathrm{N}_{\mathrm{eu}}\alpha b^{*} g\alpha$ –closed if the image of each N_{eu} –closed set in X is $\mathrm{N}_{\mathrm{eu}}\alpha b^{*} g\alpha$ –closed in Y.

Definition 5.2. Let $\left(X,\mathrm{T}_{N}\right)$ and $\left(Y,\sigma_{N}\right)$ be two N_{eu} *–Top –Spaces*. A function $f:\left(X,\mathrm{T}_{N}\right)\to\left(Y,\sigma_{N}\right)$ is said to be $\mathrm{N}_{\mathrm{eu}}\alpha b^{*} g\alpha$ –open if the image of each N_{eu} –open set in X is $\mathrm{N}_{\mathrm{eu}}\alpha b^{*} g\alpha$ –closed in Y.

Theorem 5.3. A function $f:\left(X,\mathrm{T}_{N}\right)\to\left(Y,\sigma_{N}\right)$ is said to be $\mathrm{N}_{\mathrm{eu}}\alpha b^{*} g\alpha$ –closed if and only if $\mathrm{N}_{eu}\alpha b^{*} g\alpha-Cl\left[f\left(A\right)\right]\subseteq f\left[\mathrm{N}_{eu}Cl\left(A\right)\right]$ for every N_{eu} –set A of X.

Proof. Suppose $f:\left(X,\mathrm{T}_{N}\right)\to\left(Y,\sigma_{N}\right)$ is a $\mathrm{N}_{\mathrm{eu}}\alpha b^{*} g\alpha$ –closed function and A is any N_{eu} –set in X. Then $\mathrm{N}_{eu}Cl\left(A\right)$ is a $\mathrm{N}_{\mathrm{eu}}\alpha b^{*} g\alpha$ –closed set in X. Since f is $\mathrm{N}_{\mathrm{eu}}\alpha b^{*} g\alpha$ –closed, $f\left[\mathrm{N}_{eu}Cl\left(A\right)\right]$ is a $\mathrm{N}_{\mathrm{eu}}\alpha b^{*} g\alpha$ –closed set in Y. Thus $\mathrm{N}_{eu}\alpha b^{*} g\alpha-Cl\left[f\left(\mathrm{N}_{eu}Cl\left(A\right)\right)\right]=f\left[\mathrm{N}_{eu}Cl\left(A\right)\right]$. Therefore $\mathrm{N}_{eu}\alpha b^{*} g\alpha-Cl\left[f\left(A\right)\right]\subseteq \mathrm{N}_{eu}\alpha b^{*} g\alpha-Cl\left[f\left(\mathrm{N}_{eu}Cl\left(A\right)\right)\right]=f\left(\mathrm{N}_{eu}Cl\left(A\right)\right)$. Hence $\mathrm{N}_{eu}\alpha b^{*} g\alpha-Cl\left[f\left(A\right)\right]\subseteq f\left(\mathrm{N}_{eu}Cl\left(A\right)\right)$.

Conversely, let A be a N_{eu} –closed set in X. Then $\mathrm{N}_{eu}Cl\left(A\right)=A$ and so $f\left(A\right)=f\left[\mathrm{N}_{eu}Cl\left(A\right)\right]$. By our assumption $\mathrm{N}_{eu}\alpha b^{*} g\alpha-Cl\left[f\left(A\right)\right]\subseteq f\left(A\right)$. But $f\left(A\right)\subseteq \mathrm{N}_{eu}\alpha b^{*} g\alpha-Cl\left[f\left(A\right)\right]$. Hence $\mathrm{N}_{eu}\alpha b^{*} g\alpha-Cl\left[f\left(A\right)\right]=f\left(A\right)$ and therefore $f\left(A\right)$ is $\mathrm{N}_{\mathrm{eu}}\alpha b^{*} g\alpha$ –closed set in Y. Thus f is a $\mathrm{N}_{\mathrm{eu}}\alpha b^{*} g\alpha$ –closed mapping.

Theorem 5.4.. A mapping $f:\left(X,\mathrm{T}_{N}\right)\to\left(Y,\sigma_{N}\right)$ is $\mathrm{N}_{\mathrm{eu}}\alpha b^{*} g\alpha$ –closed if and only if for each N_{eu} –set W of Y and for each N_{eu} –open set U of X containing $f^{-1}\left(W\right)$ there exists a $\mathrm{N}_{\mathrm{eu}}\alpha b^{*} g\alpha$ –open set V of Y such that $W\subseteq V$ and $f^{-1}\left(V\right)\subseteq U$.

Proof. Suppose f is a $\mathrm{N}_{\mathrm{eu}}\alpha b^{*} g\alpha$ –closed mapping. Let W be any N_{eu} –set in Y and U be a $\mathrm{N}_{\mathrm{eu}}\alpha b^{*} g\alpha$ –open set of X such that $f^{-1}\left(W\right)\subseteq U$. Then $V=\left[f\left(U^{c}\right)\right]^{c}$ is $\mathrm{N}_{\mathrm{eu}}\alpha b^{*} g\alpha$ –open set containing W such that $f^{-1}\left(V\right)\subseteq U$. Conversely, let W be a N_{eu} –closed set of X. Then $f^{-1}\left[\left(f\left(W\right)\right)^{c}\right]\subseteq W^{c}$ and W^{c} is N_{eu} –open in X. By assumption, there exists a $\mathrm{N}_{\mathrm{eu}}\alpha b^{*} g\alpha$ –open set V of Y such that $\left[f\left(W\right)\right]^{c}\subseteq V$ and $f^{-1}\left(V\right)\subseteq W^{c}$ and so $W\subseteq\left[f^{-1}\left(V\right)\right]^{c}$. Hence

$V^c \subseteq f(W) \subseteq f\left[\left(f^{-1}(V)\right)^c\right] \subseteq V^c$, which implies $f(W) = V^c$. Since V^c is $\mathrm{N}_{eu}\alpha b^* g\alpha$–closed, $f(W)$ is $\mathrm{N}_{eu}\alpha b^* g\alpha$–closed and f is $\mathrm{N}_{eu}\alpha b^* g\alpha$–closed mapping.

Theorem 5.5. Let $f:(X,\mathrm{T}_N)\to(Y,\sigma_N)$ be a N_{eu}–closed mapping and $g:(Y,\sigma_N)\to(Z,\eta_N)$ be a $\mathrm{N}_{eu}\alpha b^* g\alpha$–closed mapping. Then their composition $gof:(X,\mathrm{T}_N)\to(Z,\eta_N)$ is $\mathrm{N}_{eu}\alpha b^* g\alpha$–closed.

Proof. Let F be a N_{eu}–closed set in X. Since f is N_{eu}–closed, $f(F)$ is N_{eu}–closed in Y. Since g is $\mathrm{N}_{eu}\alpha b^* g\alpha$–closed, $g\left[f(F)\right] = (gof)(F)$ is $\mathrm{N}_{eu}\alpha b^* g\alpha$–closed in Z. Hence gof is a $\mathrm{N}_{eu}\alpha b^* g\alpha$–closed mapping.

Theorem 5.6. Let $f:(X,\mathrm{T}_N)\to(Y,\sigma_N)$ and $g:(Y,\sigma_N)\to(Z,\eta_N)$ be two mappings such that their composition $gof:(X,\mathrm{T}_N)\to(Z,\eta_N)$ is $\mathrm{N}_{eu}\alpha b^* g\alpha$–closed. Then the following statements are true.

(i) If f is N_{eu}–continuous and surjective, then g is $\mathrm{N}_{eu}\alpha b^* g\alpha$–closed.

(ii) If g is $\mathrm{N}_{eu}\alpha b^* g\alpha$–irresolute and injective, then f is $\mathrm{N}_{eu}\alpha b^* g\alpha$–closed.

Proof. (i) Let A be a N_{eu}–closed set of Y. Since f is N_{eu}–continuous, $f^{-1}(A)$ is N_{eu}–closed in X. Since gof is $\mathrm{N}_{eu}\alpha b^* g\alpha$–closed, $(gof)\left(f^{-1}(A)\right)$ is $\mathrm{N}_{eu}\alpha b^* g\alpha$–closed in Z. Since f is surjective, $g(A)$ is $\mathrm{N}_{eu}\alpha b^* g\alpha$–closed in Z. Hence g is $\mathrm{N}_{eu}\alpha b^* g\alpha$–closed.

(ii) Let B be any N_{eu}–closed set of X. Since gof is $\mathrm{N}_{eu}\alpha b^* g\alpha$–closed, $(gof)(B)$ is $\mathrm{N}_{eu}\alpha b^* g\alpha$–closed in Z. Since g is $\mathrm{N}_{eu}gs\alpha^*$–irresolute, $g^{-1}\left(gof(B)\right)$ is $\mathrm{N}_{eu}\alpha b^* g\alpha$–closed in Y. Since g is injective, $f(B)$ is $\mathrm{N}_{eu}\alpha b^* g\alpha$–closed in Y. Hence f is $\mathrm{N}_{eu}\alpha b^* g\alpha$–closed.

Theorem 5.7. Let $f:(X,\mathrm{T}_N)\to(Y,\sigma_N)$ be a $\mathrm{N}_{eu}\alpha b^* g\alpha$–closed mapping.

(i) If A is N_{eu}–closed set of X, then the restriction $f_A : A\to Y$ is $\mathrm{N}_{eu}\alpha b^* g\alpha$–closed.

(ii) If $A = f^{-1}(B)$ for some N_{eu}–closed set B of Y, then the restriction $f_A : A\to Y$ is $\mathrm{N}_{eu}\alpha b^* g\alpha$–closed.

Proof. (i) Let B be any N_{eu}–closed set of A. Then $B = A\cap F$ for some N_{eu}–closed set F of X and so B is N_{eu}–closed in X. By hypothesis, $f(B)$ is $\mathrm{N}_{eu}\alpha b^* g\alpha$–closed in Y. But $f(B) = f_A(B)$, therefore f_A is a $\mathrm{N}_{eu}\alpha b^* g\alpha$–closed mapping.

(ii) Let D be any N_{eu}–closed set of A. Then $D = A\cap H$ for some N_{eu}–closed set H in X. Now, $f_A(D) = f(D) = f(A\cap H) = f\left[f^{-1}(B)\cap H\right] = B\cap f(H)$. Since f is a $\mathrm{N}_{eu}\alpha b^* g\alpha$–closed mapping, so $f(H)$ is a $\mathrm{N}_{eu}\alpha b^* g\alpha$–closed set in Y. Hence f_A is a $\mathrm{N}_{eu}\alpha b^* g\alpha$–closed mapping.

Theorem 5.8. A function $f:(X,\mathrm{T}_N)\to(Y,\sigma_N)$ is $\mathrm{N}_{eu}\alpha b^* g\alpha$–open if and only if $f\left[\mathrm{N}_{eu}Int(A)\right]\subseteq \mathrm{N}_{eu}\alpha b^* g\alpha\text{–}Int\left[f(A)\right]$, for every N_{eu}–set A of X.

Proof. Suppose $f:(X,\mathrm{T}_N)\to(Y,\sigma_N)$ is a $\mathrm{N}_{eu}\alpha b^*g\alpha$ –open function and A is any N_{eu} –set in X. Then $\mathrm{N}_{eu}Int(A)$ is a N_{eu} –open set in X. Since f $\mathrm{N}_{eu}\alpha b^*g\alpha$ –open, $f\left[\mathrm{N}_{eu}Int(A)\right]$ is a $\mathrm{N}_{eu}\alpha b^*g\alpha$ –open set. Since $\mathrm{N}_{eu}\alpha b^*g\alpha - Int\left[f\left(\mathrm{N}_{eu}IntA\right)\right]\subseteq \mathrm{N}_{eu}\alpha b^*g\alpha - Int\left[f(A)\right]$, $f\left[\mathrm{N}_{eu}Int(A)\right]\subseteq \mathrm{N}_{eu}\alpha b^*g\alpha - Int\left[f(A)\right]$.

Conversely, $f\left[\mathrm{N}_{eu}Int(A)\right]\subseteq \mathrm{N}_{eu}\alpha b^*g\alpha - Int\left[f(A)\right]$ for every N_{eu} –set A in X. Let U be a N_{eu} –open set in X. Then $\mathrm{N}_{eu}Int(U)=U$ and by hypothesis, $f(U)\subseteq \mathrm{N}_{eu}\alpha b^*g\alpha - Int\left[f(U)\right]$. But $\mathrm{N}_{eu}\alpha b^*g\alpha - Int\left[f(U)\right]\subseteq f(U)$. Therefore, $f(U)=\mathrm{N}_{eu}\alpha b^*g\alpha - Int\left[f(U)\right]$. Then $f(U)$ is $\mathrm{N}_{eu}\alpha b^*g\alpha$ –open. Hence f is a $\mathrm{N}_{eu}\alpha b^*g\alpha$ –open mapping.

Theorem 5.9. A function $f:(X,\mathrm{T}_N)\to(Y,\sigma_N)$ is $\mathrm{N}_{eu}\alpha b^*g\alpha$ –open if and only if for each $x_{(r,s,t)}\in X$ and for each N_{eu} –neighbourhood U of $x_{(r,s,t)}$ in X, there exists a $\mathrm{N}_{eu}\alpha b^*g\alpha$ –neighbourhood W of $f\left(x_{(r,s,t)}\right)$ in Y such that $W\subseteq f(U)$.

Proof. Let $f:(X,\mathrm{T}_N)\to(Y,\sigma_N)$ be a $\mathrm{N}_{eu}\alpha b^*g\alpha$ –open function. Let $x_{(r,s,t)}\in X$ and U be any arbitrary N_{eu} –neighbourhood of $x_{(r,s,t)}$ in X. Then there exists a N_{eu} –open set G such that $x_{(r,s,t)}\in G\subseteq U$. By Theorem 5.8, $f(G)=f\left[\mathrm{N}_{eu}Int(G)\right]\subseteq \mathrm{N}_{eu}\alpha b^*g\alpha - Int\left[f(G)\right]$. But, $\mathrm{N}_{eu}\alpha b^*g\alpha - Int\left[f(G)\right]\subseteq f(G)$. Therefore, $\mathrm{N}_{eu}\alpha b^*g\alpha - Int\left[f(G)\right]=f(G)$ and hence $f(G)$ is $\mathrm{N}_{eu}\alpha b^*g\alpha$ –open in Y. Since $x_{(r,s,t)}\in G\subseteq U$, $f\left(x_{(r,s,t)}\right)\in f(G)\subseteq f(U)$ and so the result follows by taking $W=f(G)$.

Conversely, Let U be any N_{eu} –open set in X. Let $x_{(r,s,t)}\in U$ and $f\left(x_{(r,s,t)}\right)=y_{(k,l,m)}$. Then by assumption there exists a $\mathrm{N}_{eu}\alpha b^*g\alpha$ –neighbourhood $W_{\left(y_{(k,l,m)}\right)}$ of $y_{(k,l,m)}$ in Y such that $W_{\left(y_{(k,l,m)}\right)}\subseteq f(U)$. Since $W_{\left(y_{(k,l,m)}\right)}$ is a $\mathrm{N}_{eu}\alpha b^*g\alpha$ –neighbourhood of $y_{(k,l,m)}$, there exists a $\mathrm{N}_{eu}\alpha b^*g\alpha$ –open set $V_{\left(y_{(k,l,m)}\right)}$ in Y such that $y_{(k,l,m)}\in V_{\left(y_{(k,l,m)}\right)}\subseteq W_{\left(y_{(k,l,m)}\right)}$. Therefore, $f(U)=\bigcup\left\{V_{\left(y_{(k,l,m)}\right)}:y_{(k,l,m)}\in f(U)\right\}$. Since the union of $\mathrm{N}_{eu}\alpha b^*g\alpha$ –open sets is $\mathrm{N}_{eu}\alpha b^*g\alpha$ –open, $f(U)$ is a $\mathrm{N}_{eu}\alpha b^*g\alpha$ –open set in Y. Thus, f is a $\mathrm{N}_{eu}\alpha b^*g\alpha$ –open mapping.

Theorem 5.10. For any bijective mapping $f:(X,\mathrm{T}_N)\to(Y,\sigma_N)$ the following statements are equivalent:

(i) $f^{-1}:Y\to X$ is $\mathrm{N}_{eu}\alpha b^*g\alpha$ –continuous.

(ii) f is $\mathrm{N}_{eu}\alpha b^*g\alpha$ –open.

(iii) f is $\mathrm{N}_{eu}\alpha b^*g\alpha$ –closed.

Proof. $(\mathrm{i}) \Rightarrow (\mathrm{ii})$: Let U be a N_{eu}–open set in X. By assumption, $\left(f^{-1}\right)^{-1}(U) = f(U)$ is $\mathrm{N}_{\mathrm{eu}}\alpha b^{*} g\alpha$–open in Y and so f is $\mathrm{N}_{\mathrm{eu}}\alpha b^{*} g\alpha$–open.

$(\mathrm{ii}) \Rightarrow (\mathrm{iii})$: Let F be a N_{eu}–closed set of X. Then F^{c} is a N_{eu}–open set in X. By assumption $f\left(F^{c}\right)$ is $\mathrm{N}_{\mathrm{eu}}\alpha b^{*} g\alpha$–open in Y. But $f\left(F^{c}\right) = \left[f(F)\right]^{c}$. Therefore $f(F)$ is $\mathrm{N}_{\mathrm{eu}}\alpha b^{*} g\alpha$–closed set in Y. Hence, f is $\mathrm{N}_{\mathrm{eu}}\alpha b^{*} g\alpha$–closed.

$(\mathrm{iii}) \Rightarrow (\mathrm{i})$: Let F be a N_{eu}–closed set of X. By assumption, $f(F)$ is $\mathrm{N}_{\mathrm{eu}}\alpha b^{*} g\alpha$–closed set in Y. But $f(F) = \left(f^{-1}\right)^{-1}(F)$ and therefore by Theorem 3.4, $f^{-1}: Y \to X$ is $\mathrm{N}_{\mathrm{eu}}\alpha b^{*} g\alpha$–continuous.

6 Strongly Neutrosophic $\alpha b^{*} g\alpha$–Continuous Mappings and Perfectly Neutrosophic $\alpha b^{*} g\alpha$–Continuous Mappings

In this section, we introduce and study the concepts of strongly $\mathrm{N}_{\mathrm{eu}}\alpha b^{*} g\alpha$–continuous and perfectly $\mathrm{N}_{\mathrm{eu}}\alpha b^{*} g\alpha$–continuous mappings in N_{eu}–*Top*–*Spaces*.

Definition 6.1. A mapping $f: \left(X, \mathrm{T}_{N}\right) \to \left(Y, \sigma_{N}\right)$ is called strongly $\mathrm{N}_{\mathrm{eu}}\alpha b^{*} g\alpha$–continuous if the inverse image of every $\mathrm{N}_{\mathrm{eu}}\alpha b^{*} g\alpha$–open set in Y is N_{eu}–open in X.

Definition 6.2. A mapping $f: \left(X, \mathrm{T}_{N}\right) \to \left(Y, \sigma_{N}\right)$ is called perfectly $\mathrm{N}_{\mathrm{eu}}\alpha b^{*} g\alpha$–continuous if the inverse image of every $\mathrm{N}_{\mathrm{eu}}\alpha b^{*} g\alpha$–open set in Y is N_{eu}–clopen in X.

Theorem 6.3. Let $f: \left(X, \mathrm{T}_{N}\right) \to \left(Y, \sigma_{N}\right)$ be a mapping. Then the following statements are true:

(i) If f is perfectly $\mathrm{N}_{\mathrm{eu}}\alpha b^{*} g\alpha$–continuous, then f is perfectly N_{eu}–continuous.

(ii) If f is strongly $\mathrm{N}_{\mathrm{eu}}\alpha b^{*} g\alpha$–continuous, then f is N_{eu}–continuous.

Proof. (i) Let $f: X \to Y$ be perfectly $\mathrm{N}_{\mathrm{eu}}\alpha b^{*} g\alpha$–continuous. Let V be a N_{eu}–open set in Y. Then V is $\mathrm{N}_{\mathrm{eu}}\alpha b^{*} g\alpha$–open set in Y. Since f is perfectly $\mathrm{N}_{\mathrm{eu}}\alpha b^{*} g\alpha$–continuous, $f^{-1}(V)$ is N_{eu}–clopen in X. Hence f is perfectly N_{eu}–continuous.

(ii) Let $f: X \to Y$ be strongly $\mathrm{N}_{\mathrm{eu}}\alpha b^{*} g\alpha$–continuous. Let G be a N_{eu}–open set in Y. Then G is $\mathrm{N}_{\mathrm{eu}}\alpha b^{*} g\alpha$–open set in Y. Since f is strongly $\mathrm{N}_{\mathrm{eu}} g s\alpha^{*}$–continuous, $f^{-1}(G)$ is N_{eu}–open in X. Therefore f is N_{eu}–continuous.

Theorem 6.4. Let $f: X \to Y$ be strongly $\mathrm{N}_{\mathrm{eu}}\alpha b^{*} g\alpha$–continuous and A be N_{eu}–open set in X. Then the restriction map, $f_{A}: A \to Y$ is strongly $\mathrm{N}_{\mathrm{eu}}\alpha b^{*} g\alpha$–continuous.

Proof. Let V be any $\mathrm{N}_{\mathrm{eu}}\alpha b^{*} g\alpha$–open set in Y. Since f is strongly $\mathrm{N}_{\mathrm{eu}} g s\alpha^{*}$–continuous, $f^{-1}(V)$ is N_{eu}–open in X. But $f_{A}^{-1}(V) = A \cap f^{-1}(V)$. Since A and $f^{-1}(V)$ are N_{eu}–open, $f_{A}^{-1}(V)$ is N_{eu}–open in A. Hence f_{A} is strongly $\mathrm{N}_{\mathrm{eu}} g s\alpha^{*}$–continuous.

Theorem 6.5. Every perfectly $\mathrm{N}_{eu}\alpha b^{*}g\alpha$ –continuous mapping $f:(X,\mathrm{T}_N)\to(Y,\sigma_N)$ is strongly $\mathrm{N}_{eu}\alpha b^{*}g\alpha$ –continuous.

Proof. Let $f:X\to Y$ be perfectly $\mathrm{N}_{eu}\alpha b^{*}g\alpha$ –continuous and V be $\mathrm{N}_{eu}\alpha b^{*}g\alpha$ –open set in Y. Since f is perfectly $\mathrm{N}_{eu}\alpha b^{*}g\alpha$ –continuous, $f^{-1}(V)$ is N_{eu} –clopen in X. That is both N_{eu} –open and N_{eu} –closed in X. Hence f is strongly $\mathrm{N}_{eu}\alpha b^{*}g\alpha$ –continuous.

Theorem 6.6. If $f:(X,\mathrm{T}_N)\to(Y,\sigma_N)$ and $g:(Y,\sigma_N)\to(Z,\eta_N)$ are strongly $\mathrm{N}_{eu}\alpha b^{*}g\alpha$ –continuous, then $gof:(X,\mathrm{T}_N)\to(Z,\eta_N)$ is also strongly $\mathrm{N}_{eu}\alpha b^{*}g\alpha$ –continuous.

Proof. Let V be a N_{eu} –open set in Z. Since g is a strongly $\mathrm{N}_{eu}\alpha b^{*}g\alpha$ –continuous mapping, $g^{-1}(V)$ is N_{eu} –open in Y. Then $g^{-1}(V)$ is N_{eu} –open in Y. Since f is a strongly $\mathrm{N}_{eu}\alpha b^{*}g\alpha$ –continuous mapping, $f^{-1}\left[g^{-1}(V)\right]=(gof)^{-1}(V)$ is N_{eu} –open in X. Therefore, gof is strongly $\mathrm{N}_{eu}\alpha b^{*}g\alpha$ –continuous.

Theorem 6.7. If $f:(X,\mathrm{T}_N)\to(Y,\sigma_N)$ and $g:(Y,\sigma_N)\to(Z,\eta_N)$ are perfectly $\mathrm{N}_{eu}\alpha b^{*}g\alpha$ –continuous mappings, then their composition $gof:(X,\mathrm{T}_N)\to(Z,\eta_N)$ is also perfectly $\mathrm{N}_{eu}\alpha b^{*}g\alpha$ –continuous mapping.

Proof. Let V be a $\mathrm{N}_{eu}\alpha b^{*}g\alpha$ –open set in Z. Since g is a perfectly $\mathrm{N}_{eu}gs\alpha^{*}$ –continuous mapping, $g^{-1}(V)$ is N_{eu} –clopen in Y. That is $g^{-1}(V)$ both N_{eu} –open and N_{eu} –closed in X. Then $g^{-1}(V)$ is $\mathrm{N}_{eu}\alpha b^{*}g\alpha$ –open set in X. Since f is a perfectly $\mathrm{N}_{eu}gs\alpha^{*}$ –continuous mapping, $f^{-1}\left[g^{-1}(V)\right]=(gof)^{-1}(V)$ is N_{eu} –clopen in X. Therefore gof is perfectly $\mathrm{N}_{eu}\alpha b^{*}g\alpha$ –continuous.

Theorem 6.8. Let $f:(X,\mathrm{T}_N)\to(Y,\sigma_N)$ and $g:(Y,\sigma_N)\to(Z,\eta_N)$ be mappings. Then the following statements are true.

(i) If g is strongly $\mathrm{N}_{eu}\alpha b^{*}g\alpha$ –continuous and f is $\mathrm{N}_{eu}\alpha b^{*}g\alpha$ –continuous, then gof is $\mathrm{N}_{eu}\alpha b^{*}g\alpha$ –irresolute.

(ii) If g is perfectly $\mathrm{N}_{eu}\alpha b^{*}g\alpha$ –continuous and f is N_{eu} –continuous, then gof is strongly $\mathrm{N}_{eu}\alpha b^{*}g\alpha$ –continuous.

(iii) If g is strongly $\mathrm{N}_{eu}\alpha b^{*}g\alpha$ –continuous and f is perfectly $\mathrm{N}_{eu}\alpha b^{*}g\alpha$ –continuous, then gof is perfectly $\mathrm{N}_{eu}\alpha b^{*}g\alpha$ –continuous.

(iv) If g is $\mathrm{N}_{eu}\alpha b^{*}g\alpha$ –continuous and f is strongly $\mathrm{N}_{eu}\alpha b^{*}g\alpha$ –continuous, then gof is N_{eu} –continuous.

Proof. (i) Let V be a $\mathrm{N}_{eu}\alpha b^{*}g\alpha$ –open set in Z. Since g is a strongly $\mathrm{N}_{eu}\alpha b^{*}g\alpha$ –continuous mapping, $g^{-1}(V)$ is N_{eu} –open set in Y. Since f is a $\mathrm{N}_{eu}\alpha b^{*}g\alpha$ –continuous mapping,

$f^{-1}\left[g^{-1}(V)\right]=(gof)^{-1}(V)$ is $\mathrm{N}_{eu}\alpha b^{*}g\alpha$ –open set in X. Hence gof is $\mathrm{N}_{eu}\alpha b^{*}g\alpha$ –irresolute.

(ii) Let V be a $\mathrm{N}_{eu}\alpha b^{*}g\alpha$ –open set in Z. Since g is a perfectly $\mathrm{N}_{eu}\alpha b^{*}g\alpha$ –continuous mapping, $g^{-1}(V)$ is N_{eu} –clopen set in Y. That is, $g^{-1}(V)$ is both N_{eu} –open and N_{eu} –closed. Since f is a $\mathrm{N}_{eu}\alpha b^{*}g\alpha$ –continuous mapping, $f^{-1}\left[g^{-1}(V)\right]=(gof)^{-1}(V)$ is N_{eu} –open in X. Therefore gof is strongly $\mathrm{N}_{eu}\alpha b^{*}g\alpha$ –continuous.

(iii) Let V be a $\mathrm{N}_{eu}\alpha b^{*}g\alpha$ –open set in Z. Since g is a strongly $\mathrm{N}_{eu}\alpha b^{*}g\alpha$ –continuous mapping, $g^{-1}(V)$ is N_{eu} –open set in Y. Since every N_{eu} –open set is $\mathrm{N}_{eu}\alpha b^{*}g\alpha$ –open set. So $g^{-1}(V)$ is $\mathrm{N}_{eu}\alpha b^{*}g\alpha$ –open set in X. Since f is a perfectly $\mathrm{N}_{eu}\alpha b^{*}g\alpha$ –continuous mapping, $f^{-1}\left[g^{-1}(V)\right]=(gof)^{-1}(V)$ is N_{eu} –clopen in X. Hence gof is perfectly $\mathrm{N}_{eu}\alpha b^{*}g\alpha$ –continuous.

(iv) Let V be a N_{eu} –open set in Z. Since g is a $\mathrm{N}_{eu}\alpha b^{*}g\alpha$ –continuous mapping, $g^{-1}(V)$ is $\mathrm{N}_{eu}\alpha b^{*}g\alpha$ –open set in Y. Since f is a strongly $\mathrm{N}_{eu}\alpha b^{*}g\alpha$ –continuous map, $f^{-1}\left[g^{-1}(V)\right]=(gof)^{-1}(V)$ is N_{eu} –open in X. So gof is N_{eu} –continuous.

7 Contra Neutrosophic $\alpha b^{*}g\alpha$ –Continuous Mappings and Contra Neutrosophic $\alpha b^{*}g\alpha$ –Irresolute Mappings

In this section, we introduce the concepts of contra $\mathrm{N}_{eu}\alpha b^{*}g\alpha$ –continuous mappings and contra $\mathrm{N}_{eu}\alpha b^{*}g\alpha$ –irresolute mappings and investigate their fundamental properties and characterizations.

Definition 7.1. A mapping $f:(X,\mathrm{T}_N)\to(Y,\sigma_N)$ is said to be contra N_{eu} –continuous if the inverse image of every N_{eu} –open set in Y is N_{eu} –closed set in X.

Definition 7.2. A mapping $f:(X,\mathrm{T}_N)\to(Y,\sigma_N)$ is called contra $\mathrm{N}_{eu}\alpha b^{*}g\alpha$ –continuous if the inverse image of every N_{eu} –open set in Y is $\mathrm{N}_{eu}\alpha b^{*}g\alpha$ –closed in X.

Theorem 7.3. Let $f:(X,\mathrm{T}_N)\to(Y,\sigma_N)$ be a contra N_{eu} –continuous mapping. Then f is contra $\mathrm{N}_{eu}\alpha b^{*}g\alpha$ –continuous.

Proof. Let V be any N_{eu} –open set in Y. Since f is contra N_{eu} –continuous, $f^{-1}(V)$ is N_{eu} –closed set in X. As every N_{eu} –closed set is $\mathrm{N}_{eu}\alpha b^{*}g\alpha$ –closed, we have $f^{-1}(V)$ is $\mathrm{N}_{eu}\alpha b^{*}g\alpha$ –closed set in X. Therefore f is contra $\mathrm{N}_{eu}\alpha b^{*}g\alpha$ –continuous.

Theorem 7.4. A mapping $f:(X,\mathrm{T}_N)\to(Y,\sigma_N)$ is contra $\mathrm{N}_{eu}\alpha b^{*}g\alpha$ –continuous if and only if the inverse image of every N_{eu} –closed set in Y is $\mathrm{N}_{eu}\alpha b^{*}g\alpha$ –open set in X.

Proof. Let V be a N_{eu} –closed set in Y. Then V^C is N_{eu} –open set in Y. Since f is contra $\mathrm{N}_{eu}\alpha b^*g\alpha$ –continuous, $f^{-1}\left(V^C\right)$ is $\mathrm{N}_{eu}\alpha b^*g\alpha$ –closed set in X. But $f^{-1}\left(V^C\right)=1-f^{-1}\left(V\right)$ and so $f^{-1}\left(V\right)$ is $\mathrm{N}_{eu}\alpha b^*g\alpha$ –open set in X. Conversely, assume that the inverse image of every N_{eu} –closed set in Y is $\mathrm{N}_{eu}\alpha b^*g\alpha$ –open in X. Let W be a N_{eu} –open set in Y. Then W^C is N_{eu} –closed in Y. By hypothesis $f^{-1}\left(W^C\right)=1-f^{-1}\left(W\right)$ is $\mathrm{N}_{eu}\alpha b^*g\alpha$ –open in X, and so $f^{-1}\left(W\right)$ is $\mathrm{N}_{eu}\alpha b^*g\alpha$ –closed set in X. Thus f is contra $\mathrm{N}_{eu}gs\alpha^*$ –continuous.

Theorem 7.5. If a mapping $f:\left(X,\mathrm{T}_N\right)\to\left(Y,\sigma_N\right)$ is contra $\mathrm{N}_{eu}\alpha b^*g\alpha$ –continuous and $g:\left(Y,\sigma_N\right)\to\left(Z,\eta_N\right)$ is N_{eu} –continuous, then their composition $gof:\left(X,\mathrm{T}_N\right)\to\left(Z,\eta_N\right)$ is contra $\mathrm{N}_{eu}\alpha b^*g\alpha$ –continuous.

Proof. Let W ba a N_{eu} –open set in Z. Since g is N_{eu} –continuous, $g^{-1}\left(W\right)$ is N_{eu} –open set in Y. Since f is contra $\mathrm{N}_{eu}\alpha b^*g\alpha$ –continuous, $f^{-1}\left[g^{-1}\left(W\right)\right]$ is $\mathrm{N}_{eu}\alpha b^*g\alpha$ –closed set in X. But $\left(gof\right)^{-1}\left(W\right)=f^{-1}\left[g^{-1}\left(W\right)\right]$. Thus gof is contra $\mathrm{N}_{eu}\alpha b^*g\alpha$ –continuous.

Definition 7.6. A mapping $f:\left(X,\mathrm{T}_N\right)\to\left(Y,\sigma_N\right)$ is called contra $\mathrm{N}_{eu}\alpha b^*g\alpha$ –irresolute if the inverse image of every $\mathrm{N}_{eu}\alpha b^*g\alpha$ –open set in Y is $\mathrm{N}_{eu}\alpha b^*g\alpha$ –closed in X.

Theorem 7.7. If a mapping $f:\left(X,\mathrm{T}_N\right)\to\left(Y,\sigma_N\right)$ is contra $\mathrm{N}_{eu}\alpha b^*g\alpha$ –irresolute, then it is contra $\mathrm{N}_{eu}\alpha b^*g\alpha$ –continuous.

Proof. Let V be a N_{eu} –open set in Y. Since every N_{eu} –open set is $\mathrm{N}_{eu}\alpha b^*g\alpha$ –open, V is N_{eu} –open set in Y. Since f is contra $\mathrm{N}_{eu}\alpha b^*g\alpha$ –irresolute, $f^{-1}\left(V\right)$ is $\mathrm{N}_{eu}\alpha b^*g\alpha$ –closed set in X. Thus f is contra $\mathrm{N}_{eu}\alpha b^*g\alpha$ –continuous.

Theorem 7.8. Let $\left(X,\mathrm{T}_N\right)$, $\left(Y,\sigma_N\right)$ and $\left(Z,\eta_N\right)$ be N_{eu} *–Top –Spaces*. If $f:\left(X,\mathrm{T}_N\right)\to\left(Y,\sigma_N\right)$ is contra $\mathrm{N}_{eu}\alpha b^*g\alpha$ –irresolute and $g:\left(Y,\sigma_N\right)\to\left(Z,\eta_N\right)$ is $\mathrm{N}_{eu}\alpha b^*g\alpha$ –continuous, then $gof:\left(X,\mathrm{T}_N\right)\to\left(Z,\eta_N\right)$ is contra $\mathrm{N}_{eu}\alpha b^*g\alpha$ –continuous.

Proof. Let W be any N_{eu} –open set in Z. Since g is $\mathrm{N}_{eu}\alpha b^*g\alpha$ –continuous, $g^{-1}\left(W\right)$ is $\mathrm{N}_{eu}\alpha b^*g\alpha$ –open set in Y. Since f is contra $\mathrm{N}_{eu}\alpha b^*g\alpha$ –irresolute, $f^{-1}\left[g^{-1}\left(W\right)\right]$ is $\mathrm{N}_{eu}\alpha b^*g\alpha$ –closed set in X. But $\left(gof\right)^{-1}\left(W\right)=f^{-1}\left[g^{-1}\left(W\right)\right]$. Thus gof is contra $\mathrm{N}_{eu}\alpha b^*g\alpha$ –-continuous.

Theorem 7.9. If $f:\left(X,\mathrm{T}_N\right)\to\left(Y,\sigma_N\right)$ is $\mathrm{N}_{eu}\alpha b^*g\alpha$ –irresolute and $g:\left(Y,\sigma_N\right)\to\left(Z,\eta_N\right)$ is contra $\mathrm{N}_{eu}\alpha b^*g\alpha$ –irresolute, then their composition $gof:\left(X,\mathrm{T}_N\right)\to\left(Z,\eta_N\right)$ is contra $\mathrm{N}_{eu}\alpha b^*g\alpha$ –irresolute mapping.

Proof. Let W be any $N_{eu}\alpha b^{*}g\alpha$ –open set in Z. Since g is contra $N_{eu}\alpha b^{*}g\alpha$ –irresolute, $g^{-1}(W)$ is $N_{eu}\alpha b^{*}g\alpha$ –closed set in Y. Since f is $N_{eu}\alpha b^{*}g\alpha$ –irresolute, $f^{-1}\left[g^{-1}(W)\right]$ is $N_{eu}\alpha b^{*}g\alpha$ –closed set in X. But $(gof)^{-1}(W)=f^{-1}\left[g^{-1}(W)\right]$. Thus gof is contra $N_{eu}\alpha b^{*}g\alpha$ –irresolute.

Conclusion

In this research article, we have introduced and studied the properties of $N_{eu}\alpha b^{*}g\alpha$ –continuous functions, $N_{eu}\alpha b^{*}g\alpha$ –irresolute functions, $N_{eu}gs\alpha^{*}$ –closed functions, $N_{eu}\alpha b^{*}g\alpha$ –open functions, strongly $N_{eu}\alpha b^{*}g\alpha$ –continuous functions, perfectly $N_{eu}\alpha b^{*}g\alpha$ –continuous functions, contra $N_{eu}\alpha b^{*}g\alpha$ –continuous functions, and contra $N_{eu}\alpha b^{*}g\alpha$ –irresolute functions in N_{eu} –*Top* –*Spaces* and established the relations between them. We have obtained fundamental characterizations of theses mappings and investigated preservation properties. We expect the results in this article will be basis for further applications of mappings in N_{eu} –*Top* –*Spaces*.

Recommendations

It is recommended to introduce $N_{eu}\alpha b^{*}g\alpha$ –compactness, $N_{eu}\alpha b^{*}g\alpha$ –connectedness, $N_{eu}\alpha b^{*}g\alpha$ –regular spaces, and $N_{eu}\alpha b^{*}g\alpha$ –normal spaces in N_{eu} –*Top* –*Spaces* and investigate their fundmental properties and characterizations.

Scientific Ethics Declaration

*The author declares that the scientific ethical and legal responsibility of this article published in EPSTEM journal belongs to the author.

Conflict of Interest

*The author declares no competing interests.

Funding

* This research received no specific grant from any funding agency in the public, commercial, or not-for-profit sectors.

Acknowledgements or Notes

* This article was presented as an oral presentation at the International Conference on Basic Sciences and Technology (www.icbast.net) held in Budapest/Italy on August 28-31, 2025.

* The author is indebted to Prince Mohammad Bin Fahd University Al Khobar Saudi Arabia for providing necessary research facilities during the preparation of this research paper.

References

Ali Abbas, N. M., & Shuker Mahmood Khalil. (2021). On new classes of neutrosophic continuous and contra mappings in neutrosophic topological spaces, *Int. J. Nonlinear Anal. Appl*. *12*(1), 718- 725.

Aras, C. G., & Bayramov, S. (2020). Neutrosophic soft continuity in neutrosophic soft topological spaces. *Filomat*, *34*(10), 3495-3506.

Arokiarani, I., Dhavaseelan, R., Jafari, S., & Parimala, M. (2017). On some new notions and functions in neutrosophic topological spaces. *Neutrosophic Sets and Systems*, *16*, 16-19.

Atanassov, K. (1986). Intuitionistic fuzzy sets. *Fuzzy Sets And Systems*, 87-94.

Atkinswestley, A. & Chandrasekar, S. (2020). Neutrosophic g*-Closed Sets and its Maps, *Neutrosophic Sets and Systems, 36*, 96 – 107.

Bera, T., & Mahapatra, N. K. (2016). On neutrosophic soft function. *Ann. Fuzzy Math. Inform*, *12*(1), 101-119.

Blessie Rebecca, S., & Francina Shalini, A. (2019). Neutrosophic generalized regular contra continuity in neutrosophic topological spaces. *Research in Advent Technology*, *7*(2), 761-765.

Damodharan, K. & Vigneshwaran, M. & Khalil, Shuker. (2020). $N_{\delta^*g\alpha}$ –Continuous and Irresolute Functions in Neutrosophic Topological Spaces, *Neutrosophic Sets and Systems*, Vol. 38, pp. 439 – 452.

Dhavaseelan, R., Jafari, S., & Page, M., & Hanif, D. (2018). Neutrosohic generalized α-contra-continuity, *Creat. Math. Inform., 27*(2), 133 – 139.

Hanif, P. A. G. E., & Imran, Q. H. (2020). *Neutrosophic generalized homeomorphism*. Infinite Study.

Keerthana, K. S., Vigneshwaran, M., & Vidyarani, L. (2023). On αb* gα-closed sets in topological spaces. *Journal of Statistics and Mathematical Engineering*, *9*(3), 14-19.

Kumar, S. K., Mandarasalam, V., Jafari, S., & Lakshmanadas, V. (2024). N xb* gx-Closed Sets in Neutrosophic Topological Spaces. *Neutrosophic Sets and Systems*, *73*(1), 31.

Maheswari, C., & Chandrasekar, S. (2020). *Neutrosophic gb-closed Sets and Neutrosophic gb-Continuity*. Infinite Study.

Margaret, A. M., & Pricilla, M. T. (2018). Neutrosophic Vague Generalized Pre-Continuous and Irresolute Mappings. *International Journal of Engineering, Science and Mathematics*, *7*(2), 228-244.

Missier, S. Pious, Anusuya, A. and Nagarajan, A. (2022). Neutrosophic Beta Omega Mapping in Neutrosophic Topological Spaces, *International Journal of Mechanical Engineering*, 7(3), 621-625.

Nandhini, T. & Vigneshwaran, M. (2019). $N_{\alpha g^{\#}\psi}$ –Continuous and $N_{\alpha g^{*}\psi}$ –Irresolute functions in neutrosophic topological spaces, *International Journal of Recent Technology and Engineering (IJRTE), 7*(6), 1097 – 1101.

Narmatha, S., Glory, B. E., & Vishnu, P. R. (2019). On πgβ–Closed Sets and Mappings in Neutrosophic Topological Spaces. *International Journal of Innovative Technology and Exploring Engineering (IJITEE)*, *8*(125), 505-510.

Nivetha, A. R., Vigneshwaran, M., Ali Abbas, N. M., & Khalil, S. M. (2021). On-continuous in topological spaces of neutrosophy. *Journal of Interdisciplinary Mathematics*, *24*(3), 677-685.

Öztürk, T. Y., Karataş, E., & Yolcu, A. (2021). On neutrosophic soft continuous mappings. *Turkish Journal of Mathematics*, *45*(1), 81-95.

Parimala, M., Jeevitha, R., Jafari, S., Smarandache, F., & Udhayakumar, R. (2018). Neutrosophic αψ-homeomorphism in neutrosophic topological spaces. *Information*, *9*(8), 187.

Chandrasekar, S. (2019). *Neutrosophic αgs continuity and neutrosophic αgs ırresolute maps*. Infinite Study.

Puvaneshwari, P. J., & Bageerathi, K. (2019). Some functions concerning neutrosophic feebly open & closed sets. *International Journal of Scientific Research and Reviews*, *8*(2), 1546 – 1559.

Kannan, T. R., & Chandrasekar, S. (2020). Neutrosophic PRE− α, SEMI− α and PRE–β irresolute open and closed mappings in Neutrosophic topological spaces. *Malaya Journal of Matematik*, *8*(4), 1795-1806.

Ramesh, K. (2020). Ngpr homeomorphism in neutrosophic topological spaces. *Neutrosophic Sets and Systems*, *32*, 25-37.

Blessie Rebecca, S., & Francina Shalini, A. (2019). Neutrosophic generalized regular contra continuity in neutrosophic topological spaces. *Research in Advent Technology*, *7*(2), 761-765.

Rodrigo, P. A., & Maheswari, S. (2021). Neutrosophic generalized semi alpha star closed sets in neutrosophic topological space. *Journal of Human University (Natural Sciences*), *48*(11) 1156 – 1175.

Salama, A. A., Smarandache, F., & Kromov, V. (2014). *Neutrosophic closed set and neutrosophic continuous functions*. Infinite Study.

Saranya, S., & Vigneshwaran, M. (2019). *Neutrosophic bga-Closed Sets*. Infinite Study.

Smarandache, F. (2002). Neutrosophy and neutrosophic logic, first ınternational conference on neutrosophy. *Neutrosophic Logic, Set, Probability, and Statistics, University of New Mexico, Gallup, NM*, *87301*.

Thirumalaiswamy, M., & Ramesh, K. (2013). Semipre generalized continuous and irresolute mappings in intuitionistic fuzzy topological spaces. *Inter. Ref. J. Engi., and Sci*, *2*, 41-48.

Vadivel, A., Thangaraja, P., & Sundar, C. J. (2021). *Neutrosophic e-continuous maps and neutrosophic e-irresolute maps*. Infinite Study.

Author(s) Information

Raja Mohammad Latif
Department of Mathematics and Natural Sciences
Prince Mohammad Bin Fahd University
Al Khobar, Saudi Arabia
Contact e-mail: *rajamlatif@yahoo.com*

To cite this article:

Latif, R. M. (2025). Neutrosophic αB*Gα functions in neutrosophic topological spaces. *The Eurasia Proceedings of Science, Technology, Engineering and Mathematics (EPSTEM)*, *36*, 276-296.